Instituto Português da Qualidade

espaço Q

edição especial • maio 2026







PUBLICAÇÕES DE METROLOGIA

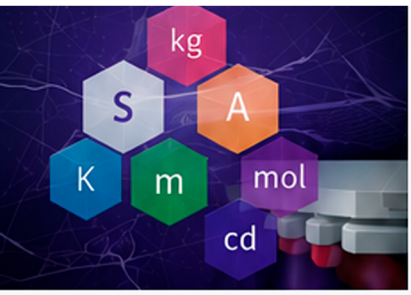


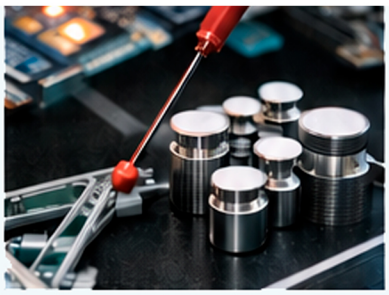


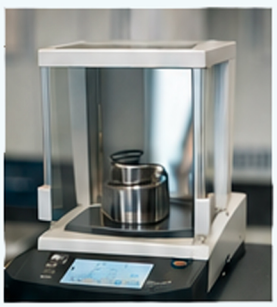




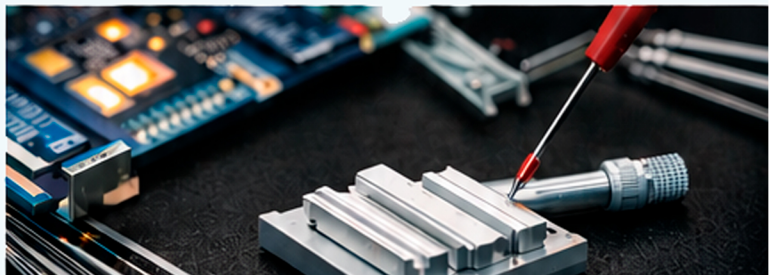

ÍNDICE

Publicação *online*, que desde 2005, tem vindo a divulgar e partilhar com uma comunidade, cada vez mais alargada de subscritores e leitores, as iniciativas e os acontecimentos mais relevantes que têm ocorrido nos domínios da Metrologia, da Normalização e da Qualificação, cumprindo os objetivos que estão na sua génese.

Trata-se de um espaço informativo institucional que complementa a missão do Instituto Português da Qualidade de promover e divulgar os temas da qualidade, enquanto organismo nacional responsável pela coordenação da infraestrutura que constitui o enquadramento legal da Qualidade em Portugal: o Sistema Português da Qualidade (SPQ).

Instituto Português da Qualidade

CONSELHO DIRETIVO | **MARIA JOÃO GRAÇA**
CONSELHO EDITORIAL | **MARIA JOÃO GRAÇA (COORDENAÇÃO), ANA PINTO, ETELVINA NABAIS, INÊS JUDAS, ISABEL GODINHO, SUSANA SANTOS, CATARINA LOPES**
EDIÇÃO GRÁFICA | **UNIDADE DE PLANEAMENTO, COMUNICAÇÃO E QUALIDADE**

ISSN 1646-1916

EDITORIAL

Caros/as leitores/as

É com grande satisfação que apresentamos a primeira edição especial da **Espaço Q** de 2026, dedicada a destacar algumas das publicações técnico-científicas mais relevantes desenvolvidas pelo Instituto Português da Qualidade ao longo de 2025.

Enquanto Instituição Nacional de Metrologia, o Instituto Português da Qualidade (IPQ) desempenha um papel central no avanço da ciência da medição e das suas aplicações. Esta edição reflete a diversidade, abrangência e profundidade das atividades desenvolvidas, evidenciando contributos em múltiplos domínios científicos e tecnológicos, desde áreas clássicas da metrologia até campos emergentes de elevada complexidade.

Nesta edição da Espaço Q, os trabalhos apresentados encontram-se organizados em publicações em revistas científicas internacionais com revisão por pares, bem como em comunicações e posters apresentados em conferências internacionais. Nos casos em que as publicações não estejam disponíveis em acesso aberto, é disponibilizado o respetivo resumo (*abstract*).

Esta edição contempla um conjunto alargado de áreas de atuação, nomeadamente a metrologia aplicada aos cuidados de saúde, incluindo instrumentação e terapias de perfusão; as medições no domínio elétrico e o desenvolvimento de componentes de elevada precisão; a metrologia química e ambiental, com enfoque na preparação e estabilidade de materiais de referência, bem como em medições relevantes para a monitorização ambiental e a descarbonização; e ainda a metrologia aplicada a sistemas microfluídicos, abrangendo a caracterização de propriedades físicas, o controlo de escoamentos e o desenvolvimento de técnicas avançadas de calibração a micro e nanoescala.

Destacam-se igualmente contributos na área da metrologia de fluxo e de pressão, na avaliação de desempenho de instrumentos em contextos regulados, como os sistemas de medição de combustíveis e a proteção radiológica, bem como estudos no domínio da química analítica, incluindo medições de pH em diferentes matrizes e a deteção de microplásticos recorrendo a técnicas espectroscópicas avançadas.

Esta edição evidencia também avanços na metrologia quântica e no desenvolvimento de padrões do Sistema Internacional de Unidades, sublinhando o papel crescente das tecnologias quânticas na definição e realização das unidades de medida. Paralelamente, são abordados aspetos fundamentais como a rastreabilidade das medições e a importância das comparações interlaboratoriais, pilares essenciais para assegurar a fiabilidade, comparabilidade e reconhecimento internacional dos resultados.

Os trabalhos apresentados resultam, em grande medida, de colaborações com outros Institutos Nacionais de Metrologia e com instituições científicas e académicas de referência, tanto a nível nacional como internacional, reforçando o papel do IPQ em redes globais de conhecimento e inovação.

Esperamos que esta edição especial da **Espaço Q** seja simultaneamente informativa e inspiradora, refletindo o compromisso contínuo do IPQ com a excelência científica, a inovação e o desenvolvimento sustentável da Metrologia.

Boa leitura!

O Conselho Diretivo
Maria João Graça

REVISTAS E CONGRESSOS INTERNACIONAIS

nature nanotechnology

Analysis

https://doi.org/10.1038/s41565-025-02037-5

A quantum resistance memristor for an intrinsically traceable International System of Units standard

Received: 7 January 2025

Accepted: 15 September 2025

Published online: 27 October 2025

Check for updates

Gianluca Milano[1] ✉, Xin Zheng[2], Fabio Michieletti[3], Giuseppe Leonetti[1,3], Gabriel Caballero[4,5], Ilker Oztoprak[6], Luca Boarino[1], Özgür Bozat[7], Luca Callegaro[8], Natascia De Leo[1], Isabel Godinho[9], Daniel Granados[4], Itir Koymen[7,10], Mariela Menghini[4], Enrique Miranda[11], Luís Ribeiro[9], Carlo Ricciardi[3], Jordi Suñe[11], Vitor Cabral[9] ✉ & Ilia Valov[2,12] ✉

The recent revision of the International System of Units (SI)—which fixed the numerical values of nature's fundamental constants—has opened new perspectives for practical realizations of SI units. Here we demonstrate an intrinsic resistance standard based on memristive nanoionic cells that operate in air at room temperature and are directly accessible to end users. By driving these devices into the quantum conductance regime and using an electrochemical-polishing-based programming strategy, we achieved quantum conductance levels that can be exploited as intrinsic standard values. An interlaboratory comparison confirmed metrological consistency, with deviations of −3.8% and 0.6% from the agreed SI values for the fundamental quantum of conductance, G_0, and $2G_0$, respectively. These results lay the groundwork for the implementation of national metrology institute services on chip and for the development of self-calibrating measurement systems with zero-chain traceability.

Guaranteeing reliability and accuracy of measurements in all spheres of human knowledge is of ultimate priority to ensure the proper function of science and technology, and for the comfort and quality of our daily activities. To comply with this objective, national metrology institutes (NMIs) realize, develop and maintain primary standards of measurement units. The revision of the International System of Units (SI) in 2019[1,2] represented a historic change of paradigm for metrology, opening a new perspective on the mise en pratique of the SI base units. Indeed, SI units are now mainly defined in terms of fundamental constants of nature defined by fixed numerical values. These fixed values are exact with zero uncertainty, and therefore no longer need to be measured. Accordingly, any experiment able to correlate measurable physical quantities to a fundamental constant, or a set of fundamental constants, fixed by the SI becomes a direct realization of the corresponding SI unit. This new paradigm is expected to revolutionize metrology as the science of measurement, making it possible to bring

[1]Advanced Materials Metrology and Life Sciences Division, INRiM (Istituto Nazionale di Ricerca Metrologica), Turin, Italy. [2]Forschungszentrum Jülich, Peter Grünberg Institute (PGI-7), Jülich, Germany. [3]Department of Applied Science and Technology, Politecnico di Torino, Turin, Italy. [4]IMDEA Nanociencia, Cantoblanco, Madrid, Spain. [5]Facultad de Ciencias Físicas, Universidad Complutense de Madrid, Madrid, Spain. [6]Department of Physics, Gebze Technical University, Gebze, Kocaeli, Turkey. [7]TUBITAK National Metrology Institute (UME), Gebze, Turkey. [8]Quantum Metrology and Nanotechnologies Division, INRiM (Istituto Nazionale di Ricerca Metrologica), Turin, Italy. [9]Instituto Português da Qualidade, Caparica, Portugal. [10]Department of Electrical and Electronics Engineering, TOBB University of Economics and Technology, Ankara, Turkey. [11]Departament d'Enginyeria Electrònica, Universitat Autònoma de Barcelona, Cerdanyola del Valles, Spain. [12]Institute of Electrochemistry and Energy Systems, Bulgarian Academy of Sciences (BAS), Sofia, Bulgaria. ✉e-mail: g.milano@inrim.it; vcabral@ipq.pt; i.valov@fz-juelich.de

https://doi.org/10.1038/s41565-025-02037-5

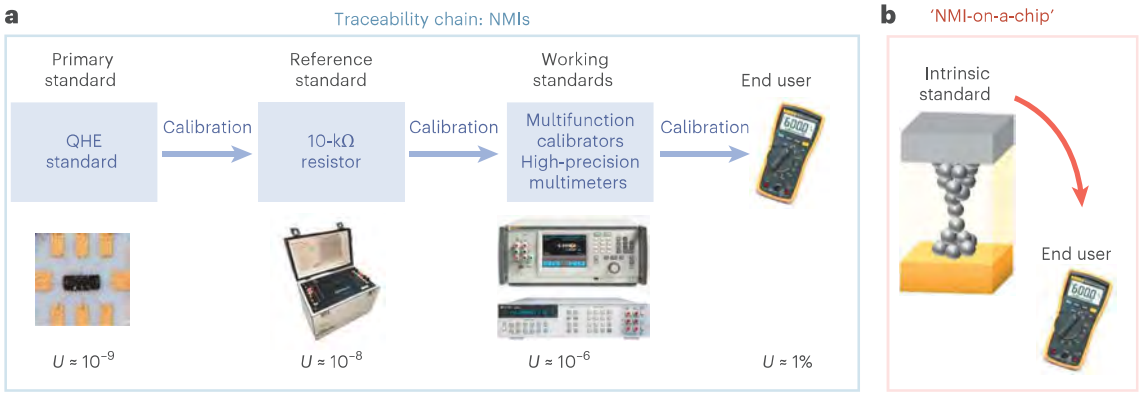

Fig. 1 | NMI on-a-chip. a, Conventional traceability chain for electrical resistance measurements. The chain starts with a comparison of the primary standard based on QHE with a first-level standard resistor (10 kΩ in the example given). In the second step of the traceability chain, this resistor standard is used to calibrate a second-order level of working standards as high-accuracy multifunction calibrators or digital multimeters. At the end of the chain, working standards are exploited to calibrate end-user equipment. Each step of the chain results in an increase of the measurement relative uncertainty *U*. The relative uncertainty *U* for the 10-kΩ example goes from some parts in 10^9 (the uncertainty related to the limitations in the practical implementation of the quantum Hall resistance values) to some parts in 10^6 (the typical specifications of precise multifunction calibrators or digital multimeters in the 10-kΩ range). At the end of the chain, we can find, for example, a hand-user multimeter with an accuracy specification of the order of 1%. **b**, Implementation of the memristive intrinsic standard of resistance directly in the end-user equipment, bringing NMI services on chip and allowing the realization of self-calibrating systems with zero-chain traceability.

measurement technology and metrology out of NMIs directly to the end-user. In particular, the miniaturization and integration of NMI services on chip (for example, the NIST on a Chip programme[3]) working according to the principles of quantum physics can enable the realization of reliable SI-traceable self-referenced systems. In the field of electrical metrology, quantum phenomena such as the quantum Hall effect, the Josephson effect and single-electron transport effect have been widely explored for the practical realization of resistance, voltage and current electrical units, respectively[4]. Despite the recognized performances of metrological devices based on these quantum phenomena, the involved large size experimental set-ups and complexity of related measurements limit their realization almost exclusively to universities and metrology institutions. In the framework of the SI, the fundamental quantum of conductance, G_0, is a quantity having a fixed numerical value with zero uncertainty (Supplementary Section 1). Hence, an experiment or device exhibiting a physical observable related to G_0 can be exploited as a standard of resistance. Although it has been suggested that quantum effects in memristive devices could be exploited to overcome the main issues related to on chip integration of electrical standards[5], an experimental verification is still missing. While several approaches have been followed to obtain quantum conductance levels in memristive devices[6–28], their practical application has been hindered by a lack of substantial progress in programming and controlling such quantum levels.

In this Article, we report on a programmable resistance standard based on nanoionic memristive devices working in air, at room temperature, and implementable on chip. Besides introducing the electrochemical polishing effect to achieve reliable quantum conductance levels as multiples of G_0, we provide a programming strategy that enables practical exploitation of quantum conductance effects even in presence of variability. Based on the results from an interlaboratory comparison involving three NMIs and three academic/research centres, we established consensus values of conductance states related to G_0 and $2G_0$ that deviates from SI values by −3.8% and 0.6%, respectively. These results establish the basis for the realization of self-calibrating systems embedding intrinsic standards directly traceable to the SI.

NMI services on chip

Metrological traceability is a fundamental requirement for any measurement process and is at the base of the intercomparability and validity of measurement outcomes, an essential need in science and in our daily activities. Traceability is defined as a property of a measurement result whereby the result can be related to a reference standard through a documented unbroken chain of calibrations, each calibration contributing to the overall measurement uncertainty[29]. In this framework, a chain of calibrations (or traceability chain) ensures the link between a common established reference (which underpins the comparability of measurement results) at the top of the chain and the measurement result given by an instrument on a lower step along the chain. Uncertainty increases after every step of the chain as the result of the contribution of the uncertainty associated with a new measurement that relates the instrument under calibration with the reference standard corresponding to that step.

Figure 1a shows an example of the conventional traceability chain for electrical resistance measurements. The reference standard for resistance based on the quantum Hall effect (QHE) (the standard having the highest metrological properties[30,31]) has been established for decades and is based on the von Klitzing constant R_K (ref. 32). Notably, the potential use of the quantum anomalous Hall effect in metrology, which enables the realization of a resistance standard operating at zero external magnetic field, but still at cryogenic temperatures (~35 mK) and vacuum conditions, has recently been demonstrated[33]. The traceability chain relies on a comparison of the primary standard based on the QHE with a first-level standard resistor that is then used to calibrate a second-order level of working standards such as multifunction calibrators or digital multimeters. Each step of the chain results in an increase of the measurement uncertainty *U* and, at the end of the chain, we can find, for example, a hand-user multimeter with a specification of the order of 1%. Each calibration in the traceability chain must be periodically repeated due to possible drifts of each measurement standard caused by operating time, environmental conditions and/or use. This means cost, long periods of unavailability of the measurement equipment and a lot of effort in the management process. Moreover, the QHE primary method has expensive and complex systems with highly demanding operating conditions because it need to operate in vacuum conditions, at very low temperatures (~1 K) and under high applied magnetic fields (6–12 T) (Supplementary Section 2).

Memristive nanoionic devices, showing quantum conductance levels that are multiples of the fundamental quantum of conductance in air, at room temperature and implementable on chip, are therefore ideal candidates to be exploited as intrinsic standards of resistance. In this context, memristive devices make it possible to have an 'NMI

https://doi.org/10.1038/s41565-025-02037-5

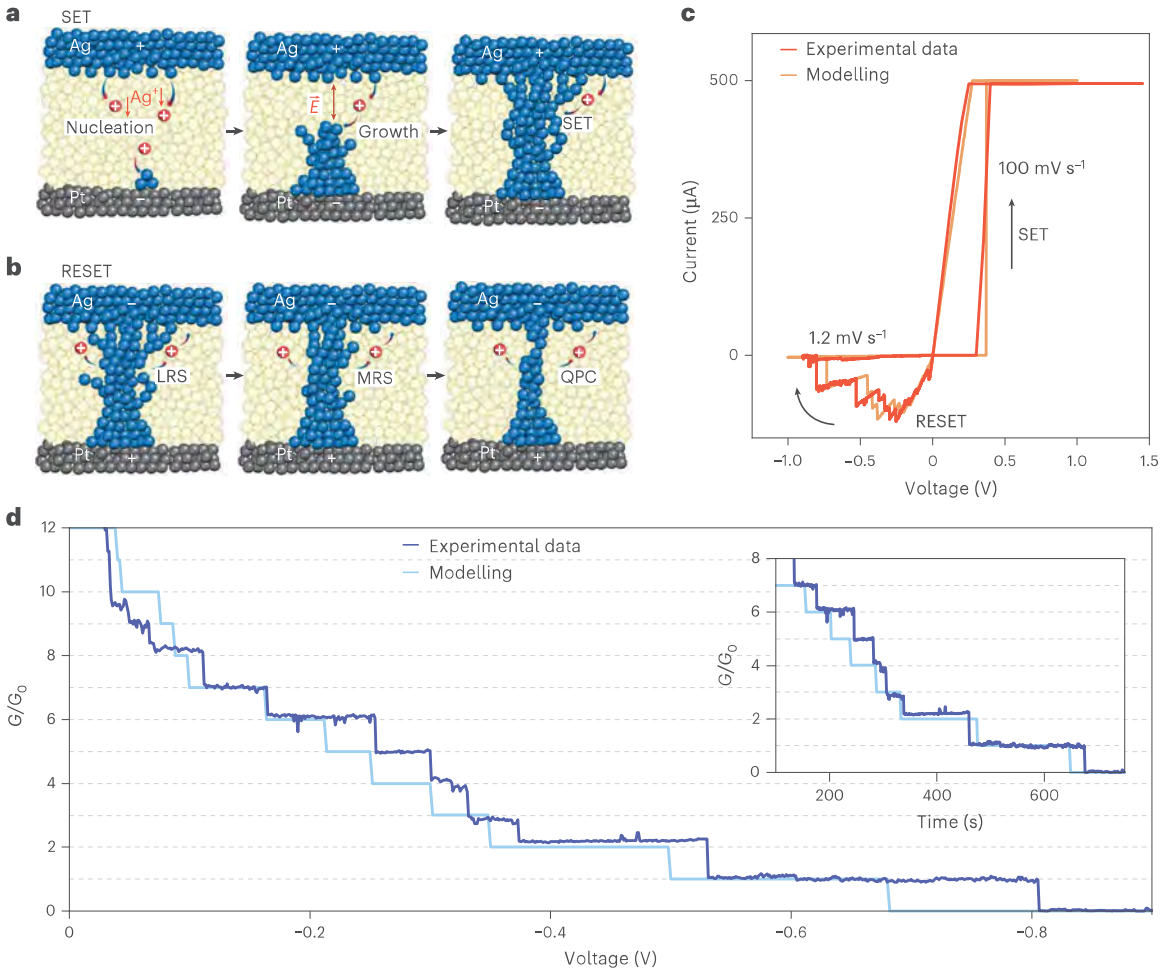

Fig. 2 | Quantum conductance levels stabilized by electrochemical polishing. **a**, Schematic representation of the SET process in a memristive cell, that is, an electrochemically driven process additionally accelerated by the electric field formed at the tip apex. The harsh conditions during filament growth in these nanoscale devices, characterized by extremely high current densities exceeding 10^6 A cm^{-2} in conditions of high electric field acceleration (>10^8 V cm^{-1}), typically led to high unpredictability and variability of quantum conductance levels. **b**, The electrochemical polishing effect makes it possible to obtain more reliable quantum conductance levels by removing/dissolving first the unstable atoms at the contact configuration during the RESET process, but keeping the more stable ones. In this framework, the system evolves through discrete levels of conductance from a low-resistance state (LRS) to an intermediate metastable-resistance state (MRS) to a QPC. **c**, Example of a cycle showing abrupt SET obtained through a voltage sweep rate of 100 mV s^{-1} and RESET with discrete levels obtained by electrochemical polishing through a slow voltage sweep (1.2 mV s^{-1}). **d**. The RESET process obtained through electrochemical polishing shows stable quantum conductance plateaus that are multiples of G_0. Inset: the stability over time of the quantum conductance plateaus while sweeping the applied voltage.

on chip' available where the above-described traceability chain is no longer required (zero-chain traceability, Supplementary Section 3), enabling the realization of systems embedding the intrinsic standard that do not require any calibration (self-calibrating systems) (Fig. 1b).

Electrochemical polishing in memristive devices

Redox-based memristive devices are two-terminal nanoionics devices in which an ion-conductive (switching) film is sandwiched between two metal electrodes. The operation principle and functionalities of these cells rely on resistive switching effects related to the formation and rupture of a nanosized conductive filament within thin films (typically oxides or other chalcogenides) under the action of an electric field[34]. As a consequence of the progressive growth of the nanosized metallic whisker, quantum point contacts (QPCs) have been reported for short circuit conditions. The latter are typically achieved during the SET process (that is, the process that turns the device from an high-resistance state to a low-resistance state; Supplementary Section 4)[6,7,9], which is electrochemically driven, but it is characterized by extremely high current densities and high electric fields (Fig. 2a). The electric field even increases during operation, due to the exponentially reducing distance between the tip apex and the electrode surface during the filament growth, until metallic contact is reached. Due to these extreme conditions, it is practically very difficult to control the filament growth process, resulting in large stochasticity in the shape, number of small dendrites/needles and the effective area of the formed contact. Accordingly, formation of QPCs is highly unpredictable and rather large filament(s) are formed under these harsh conditions. As a result, QPCs formed during the SET process largely vary in resistance value, and/or are highly unstable, even if formed at low voltages and currents. Alternatively, we propose forming QPCs during the RESET process (that is, the process that turns the device from a low-resistance state to a high-resistance state) in Ag/SiO_2/Pt devices (Methods; details of materials and device configuration are given in Supplementary Section 5), exploiting the effect of electrochemical polishing (Supplementary Section 6). To obtain reliable QPC during RESET operation, after the SET process where a large filament is formed, we applied a sequence of voltages high enough to oxidize/dissolve the energetically unstable atoms in the filament and the peripheral nanoneedles in the contact

https://doi.org/10.1038/s41565-025-02037-5

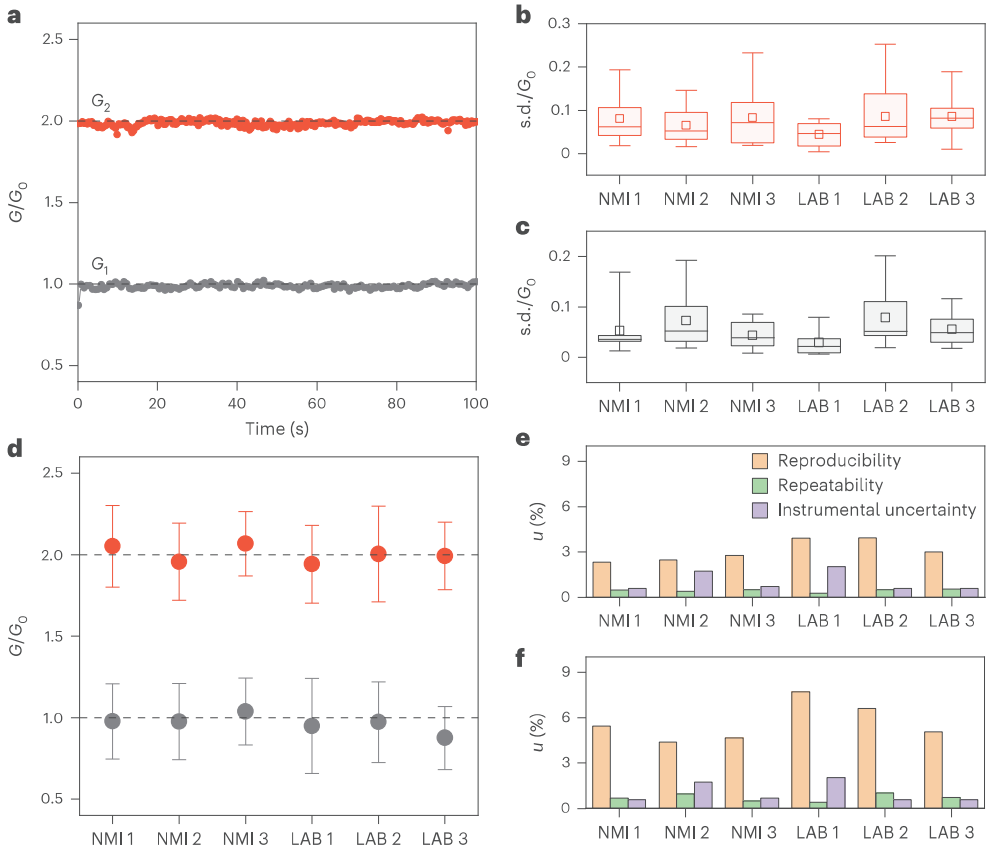

Fig. 3 | Quantum conductance levels and uncertainty budget. a, Stability of G_1 and G_2 quantum conductance levels achieved through a program-and-verify strategy in air and at room temperature. **b**,**c**, Repeatability of conductance values for G_2 (**b**) and G_1 (**c**), evaluated in terms of the s.d. over consecutive measurements of the programmed quantum levels, for the different NMIs and academic/research laboratories (LABs) participating in the interlaboratory comparison (see 'Interlaboratory comparison' in Methods for explanation of abbreviations). The sample size (N, the number of s.d. values for each participant) and the number of different devices used are presented in Supplementary Section 16. In box-plots, the midline represents the median of the N s.d. values, boxes show the 25th and 75th percentiles, and whiskers are the 5th and 90th percentiles. **d**, Reproducibility of conductance values for all participants in terms of the mean value of N mean values; the error bar represents the corresponding s.d. for G_1 and G_2. The sample size (N, the number of mean values) and the number of different devices used are presented in Supplementary Section 16. **e**,**f**, Relative standard uncertainty components of G_2 (**e**) and G_1 (**f**), related to reproducibility, repeatability and instrumental uncertainty for each participant.

configuration, but at the same time sufficiently low not to remove the more stable core atoms (Fig. 2b). Using this approach, despite Joule heating effects, we avoid high Faradaic currents and electric field acceleration of ionic reactions and transport, which ultimately results in more reproducible and reliable QPCs. During the partial RESET process, we neither break the contact, nor dissolve the filament entirely, but the filament is progressively narrowed, achieving $G < 10G_0$, opposite to the abrupt SET process (Fig. 2c). In the partial RESET regime, the stepwise conductance changes correspond to integer multiples of G_0 (Fig. 2d). Importantly, the quantum conductance states prepared by electrochemical polishing remain stable for several tens of seconds even under increasing negative voltage (Fig. 2d, inset), demonstrating a much higher stability and reliability compared with the QPC reached during the SET process. Thus, electrochemical polishing allows for predictable adjustment of stable quantum point levels, as required for the development of a quantum-based standard of resistance. A detailed discussion on the effect of electrochemical polishing in memristive devices can be found in Supplementary Section 7. It is worth remarking that the electrochemical polishing effect is best suited for memristive devices relying on the electrochemical metallization mechanism (ECM), as in our case (see Supplementary Section 8 for details).

Based on the electropolishing approach which aimed to slow RESET transitions, a stochastic model that considers conductance jumps ~G_0 accelerated by temperature (local power dissipation) and not by the electric field is proposed (Methods and Supplementary Section 9). This is related to the fact that redox dynamics and/or out-diffusion of metallic species that control the filament dissolution are sufficiently suppressed during the RESET process. As can be observed in Fig. 2c,d, the behavioural model results nicely track the experimental data (additional data in Supplementary Section 10).

Interlaboratory comparison

An interlaboratory comparison study involving three NMIs and three academic/research laboratories was carried out with the purpose of measuring the achieved quantum reference values (see Methods for details). This activity included the establishment of a measurement protocol and data processing according to international standards and well-recognized best practices[35–37]. The measurement protocol was based on a 'program-and-verify' approach that aimed to generate and sustain the desired quantum conductance reference levels, making it possible to exploit memristive devices as a quantum standard of resistance while dealing with conductance fluctuations. This approach consists of selecting the desired discrete quantum conductance level during the gradual step-like RESET obtained through electrochemical polishing, and subsequent evaluation of the conductance level to be used as reference value by means of a constant applied voltage that, at the same time, sustains the conductance state (Extended Data Fig. 1). This applied read voltage is expected to stabilize the quantum conductance state

https://doi.org/10.1038/s41565-025-02037-5

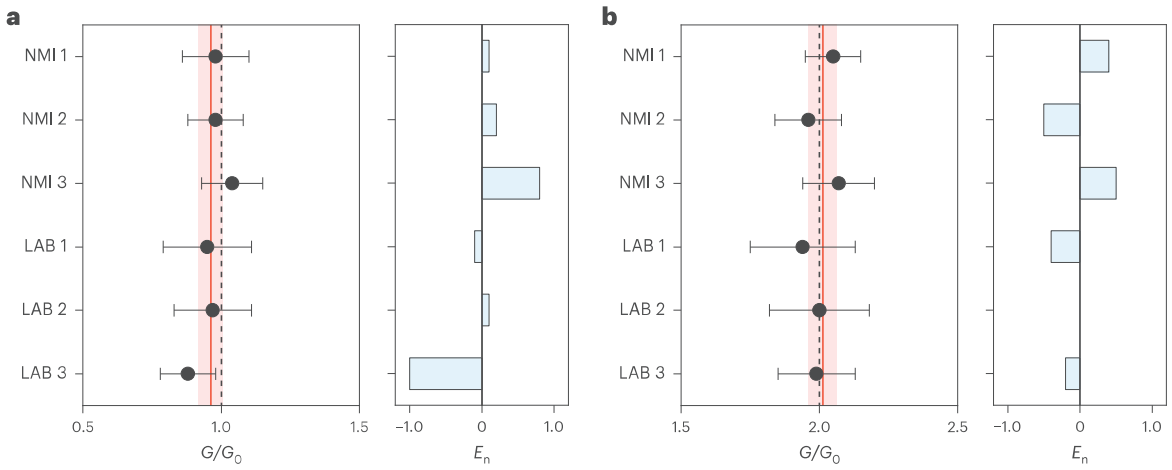

Fig. 4 | Resistance standard. a,**b**, Mean values of resistance standards based on memristive devices and corresponding expanded uncertainty (error bars) evaluated in different NMIs and laboratories (LABs) for G_1 (**a**, left) and G_2 (**b**, left). The red line is the consensus value G_{cons} of the participant's results, the red shading is the corresponding expanded uncertainty $U(G_{cons})$, and the black dashed line shows the G_0 and $2G_0$ SI values. Right: the normalized error E_n of each participant exploited to qualify results with respect to the consensus value.

by exerting quantum pressure forces due to recoil of flowing charge carriers that stabilize atomic-scale filaments and, thus, the quantum conductance level[38]. The program-and-verify approach reported here does not aim to fine-tune the device resistance as in conventional programming schemes for in-memory computing[39], but rather to nudge the device towards the quantum conductance operational regime while checking if the desired quantum conductance level is achieved. Note also that a similar program-and-verify approach is conventionally exploited for the practical realization of a d.c. voltage standard based on the Josephson effect to appropriately select the desired voltage level to be used as the reference standard (Supplementary Section 11)[40]. Figure 3a reports examples of devices programmed in air and at room temperature through the program-and-verify approach at G_1 and G_2 conductance values related to the G_0 and $2G_0$ quantum states, respectively. This program-and-verify approach makes it possible to achieve and sustain quantum conductance levels for up to 16,000 s (Extended Data Fig. 2). A comparison of the stability of quantum conductance values with previous works, including a comparison of device structures, switching mechanisms and programming approaches, is reported in Supplementary Section 12.

For the interlaboratory comparison, each laboratory performed a series of programming levels, and for each programmed level a time series of conductance measurements was carried out. For each time series, a mean value of the measurement conductance was evaluated. The repeatability was defined as the s.d. of the time series values (Methods and Supplementary Section 13). The reproducibility of the conductance value was defined as the s.d. of the mean values corresponding to each programming level. The uncertainty related to the measurement equipment was extracted from the instrument specifications and measurement conditions (Methods and Supplementary Section 14). The repeatability, reproducibility and uncertainty of the experimental set-up all contribute to the overall uncertainty. The complete set of measurements is reported in Extended Data Figs. 3 and 4. The validation of the programming methodology is detailed in Supplementary Section 15.

Figure 3b,c shows consistent repeatability in all laboratories in terms of the distribution of s.d. values for G_2 and G_1, respectively. No significant trends were observed in the s.d. as a function of the measurement time interval, showing that the contribution of repeatability to the measurement result can be evaluated based on consecutive measurements performed at relatively short time intervals, <100 s (Extended Data Fig. 5). This means that, for practical applications, it is possible to exploit the programmability of the memristive cell by on-demand programming it on the desired quantum conductance level when required without the need of long-term stability of the filament.

Figure 3d reports for each participant the mean value of the measured mean values and the corresponding s.d. of mean values of the considered quantum levels, and shows comparable reproducibility of programmed quantum levels in all the laboratories. As can be observed, the results for G_1 and G_2 are statistically consistent with expected G_0 and $2G_0$ quantum values and no s.d. values can be observed among the laboratories, revealing that laboratory-to-laboratory variability can be considered negligible compared with the variabilities related to the reproducibility of quantum steps. In addition, it can be observed that cycle-to-cycle variability dominates over device-to-device variability (Supplementary Section 16). The cycle-to-cycle variability can be attributed to the peculiar dynamic trajectories of nanofilament reconfiguration leading to slightly different atomic configurations near the quantum point contact, resulting in slight variations of quantum conductance levels around integer multiples of G_0, as analysed in a previous work[41]. Similarly, slight deviations from integer multiples of G_0 were previously observed also in mechanically controllable break junctions[42–44].

Figure 3e,f shows results for the estimation of the relative standard uncertainty components related to reproducibility, repeatability and measurement equipment of each partner for values of G_2 and G_1, respectively. The figure shows that the component of uncertainty related to reproducibility is dominant. In terms of percentage, higher reproducibility and repeatability can be observed when considering values of G_2 with respect to G_1 (Fig. 3e,f). However, statistical results show no significant discrepancies in terms of reproducibility and repeatability between the G_2 and G_1 conductance states when considering absolute uncertainty component values (Extended Data Fig. 6). Although the contribution from the uncertainty related to the measurement equipment is comparable among all laboratories, it is not negligible.

Memristive devices as a standard of resistance

A consensus value G_{cons} and its corresponding expanded uncertainty $U(G_{cons})$ were established based on the participant's results for the investigated quantum conductance plateaus[36,37]. The aim of establishing a consensus value is to investigate a possible systematic deviation with respect to the exact quantization value. We choose as an estimate for G_{cons} the weighted mean of the values measured by participants[35], while the combined uncertainty of the consensus value $U(G_{cons})$ was

estimated based on the participant's combined uncertainties, which take into account all sources of uncertainties previously discussed and the coverage factor k calculated for a confidence level of 95% (see Methods for details). The normalized error E_n expresses the consistency of the results obtained by each participant with the consensus value[35,37] (see Methods for details). Mean values of quantum levels with the corresponding expanded uncertainties for all laboratories and normalized error with respect to the consensus value for G_1 and G_2 are reported in Fig. 4a,b, respectively. The evaluation of $|E_n|$ values ($\leq$1.0 for all participants) shows that the measured conductance values belong to consistent datasets (Fig. 4a,b, right). G_{cons} was calculated to be $(0.962 \pm 0.043)G_0$ and $(2.012 \pm 0.051)G_0$ for G_1 and G_2, respectively. It turns out that the error of the consensus values for G_1 and G_2 is −3.8% and 0.6% with respect to the expected G_0 and $2G_0$ SI values, respectively. In summary, consensus values agree with SI values because their deviation from SI values is well covered by the expanded measurement uncertainty.

Conclusions

In this work, we demonstrated an intrinsic and programmable resistance standard, based on quantum physics, that, at the cost of higher uncertainty with respect to conventional standards based on QHE, operates in air, at room temperature and can be miniaturized down to the nanometre scale. This standard has the significant advantage of low operating voltages (of the order of 10 mV) and low operating currents (of the order of 1 μA) during reading operations that are ideally suited for practical applications. It is worth mentioning that, even if electrochemical processes underlying filament formation/rupture are affected by temperature[45], electronic transport phenomena leading to quantum conductance levels arising at the QPC is theoretically not affected by temperature and, in principle, traceability of the physical observable is not affected when the device is operating at different temperatures (Supplementary Section 17). All these characteristics enable the realization of an intrinsic quantum standard of electrical resistance/conductance that can be made available at the lower levels of the presently adopted traceability chain and can be directly implementable on chip, opening new opportunities for metrological traceability of electrical quantities. This makes possible its incorporation into any type of electronic measurement instrumentation, including multimeters, resistance bridges, temperature bridges, voltage dividers, voltage amplifiers, current amplifiers, temperature controllers, reference resistors in analogue-to-digital converters, etc. By means of autocalibration and autoadjustment processes, the on-chip standard allows the realization of electrical equipment with zero-chain traceability. In this context, it must be acknowledged also that a standard of resistance coupled with a voltage standard can enable the practical realization of a current standard according to the Bureau International des Poids et Mesures.

At the present stage, the deviations of quantum conductance states of memristive devices with respect to SI values are higher than the accuracy required by primary metrology achieved in NMIs. Nevertheless, the availability of on-chip realization of the resistance standard can find applications (at lower levels of the traceability chain) where the periodical calibration of meters or sensors becomes inconvenient or impossible, and measurement traceability must be maintained over years or decades, in the spirit of the 'NMI-on-a-chip' paradigm. Examples lie in space applications, marine offshore environments, underground probes, sensing in remote locations, sensing in harsh environments and sensor networks.

For all these applications, several strategies can be exploited to improve the actual accuracy. From the device point-of view, further engineering of involved materials and stacked configurations combined with a refinement of the measurement protocol can be exploited to reduce the cycle-to-cycle variability, which is the dominant contribution to uncertainty. For example, the host matrix can be engineered to promote electrochemical dynamics leading to only selected atomic configurations closely related to the G_0 SI value. Further strategies to reduce stochastic effects related to cycle-to-cycle variability, to improve the stability of the filament and to reduce conductance drifts over extended timescales include (1) optimizing the sweep rate during electrochemical polishing, (2) combining electrochemical polishing with a partial RESET process to reduce stochastic effects related to the formation of a completely new filament during each SET/RESET operation, and (3) electropolishing of the filament in a small voltage window after programming (here the strategy is to vary not only the total voltage range, but also components in the positive and negative voltage sign and the sweep rate) (Supplementary Section 7). Moreover, for practical applications, the accuracy can be improved by using n independent devices in parallel to produce an average value of quantum levels that could improve variability by an order of $\sqrt{n}$. Similarly, a viable strategy includes also the mitigation of variability by mediating among multiple realizations of the same desired quantum conductance value, by leveraging the device programmability.

While the on-chip implementation of a resistance standard based on memristive cells necessarily requires additional circuitry to drive and control its operations, the complexity and costs of this control circuit (which can be easily miniaturized through conventional complementary metal-oxide-semiconductor technology) is significantly lower than the complexity and costs associated with the maintenance of the traceability chain and routine calibrations based on the conventional QHE-based resistance standard. In this context, we envision that the practical implementation of the self-calibration concept can be based on the artefact calibration paradigm[46], where an on-chip memristive cell coupled with a mixed-signal application-specific integrated circuit that takes care of cell programming/reading could replace the external reference standard. For all these purposes, the circuit design can exploit the here-described behavioural model of memristive devices working in the quantum regime which can be implemented in conventional circuit simulators.

Online content

Any methods, additional references, Nature Portfolio reporting summaries, source data, extended data, supplementary information, acknowledgements, peer review information; details of author contributions and competing interests; and statements of data and code availability are available at https://doi.org/10.1038/s41565-025-02037-5.

References

1. *The International System of Units (SI), 9th edition*, (Bureau International des Poids et Mesures, 2019); https://www.bipm.org/en/publications/si-brochure
2. Fischer, J. & Ullrich, J. The new system of units. *Nat. Phys.* **12**, 4–7 (2016).
3. *NIST on a Chip* (National Institute of Standards and Technology, accessed 3 October 2025); https://www.nist.gov/noac
4. Mise en pratique for the definition of the ampere and other electric units in the SI. *The International System of Units (SI), 9th edition* (Bureau International des Poids et Mesures, 2019).
5. Milano, G. et al. Memristive devices for quantum metrology. *Adv. Quantum Technol.* **3**, 2000009 (2020).
6. Milano, G. et al. Quantum conductance in memristive devices: fundamentals, developments, and applications. *Adv. Mater.* **34**, 2201248 (2022).
7. Xue, W. et al. Recent advances of quantum conductance in memristors. *Adv. Electron. Mater.* **5**, 1800854 (2019).
8. Li, Y. et al. Conductance quantization in resistive random access memory. *Nanoscale Res. Lett.* **10**, 420 (2015).
9. Terabe, K., Hasegawa, T., Nakayama, T. & Aono, M. Quantized conductance atomic switch. *Nature* **433**, 47–50 (2005).

10. Tsuruoka, T., Hasegawa, T., Terabe, K. & Aono, M. Conductance quantization and synaptic behavior in a Ta_2O_5-based atomic switch. *Nanotechnology* **23**, 43 (2012).
11. Wagenaar, J. J. T., Morales-Masis, M. & Van Ruitenbeek, J. M. Observing quantized conductance steps in silver sulfide: two parallel resistive switching mechanisms. *J. Appl. Phys.* **111**, 014302 (2012).
12. Zhu, X. et al. Observation of conductance quantization in oxide-based resistive switching memory. *Adv. Mater.* **24**, 3941–3946 (2012).
13. Tappertzhofen, S., Valov, I. & Waser, R. Quantum conductance and switching kinetics of AgI-based microcrossbar cells. *Nanotechnology* **23**, 145703 (2012).
14. Long, S. et al. Quantum-size effects in hafnium-oxide resistive switching. *Appl. Phys. Lett.* **102**, 18 (2013).
15. Chen, C. et al. Conductance quantization in oxygen-anion-migration-based resistive switching memory devices. *Appl. Phys. Lett.* **103**, 043510 (2013).
16. Gao, S. et al. Conductance quantization in a Ag filament-based polymer resistive memory. *Nanotechnology* **24**, 335201 (2013).
17. Mehonic, A. et al. Quantum conductance in silicon oxide resistive memory devices. *Sci. Rep.* **3**, 2708 (2013).
18. Younis, A., Chu, D. & Li, S. Voltage sweep modulated conductance quantization in oxide nanocomposites. *J. Mater. Chem. C* **2**, 10291–10297 (2014).
19. Yi, W. et al. Quantized conductance coincides with state instability and excess noise in tantalum oxide memristors. *Nat. Commun.* **7**, 11142 (2016).
20. Nandakumar, S. R., Minvielle, M., Nagar, S., Dubourdieu, C. & Rajendran, B. A 250 mV $Cu/SiO_2/W$ memristor with half-integer quantum conductance states. *Nano Lett.* **16**, 1602–1608 (2016).
21. Krishnan, K., Muruganathan, M., Tsuruoka, T., Mizuta, H. & Aono, M. Highly reproducible and regulated conductance quantization in a polymer-based atomic switch. *Adv. Funct. Mater.* **27**, 1605104 (2017).
22. Banerjee, W. & Hwang, H. Quantized conduction device with 6-bit storage based on electrically controllable break junctions. *Adv. Electron. Mater.* **5**, 1900744 (2019).
23. Deswal, S., Malode, R. R., Kumar, A. & Kumar, A. Controlled inter-state switching between quantized conductance states in resistive devices for multilevel memory. *RSC Adv.* **9**, 9494–9499 (2019).
24. Chen, Q. et al. Controlled construction of atomic point contact with 16 quantized conductance states in oxide resistive switching memory. *ACS Appl. Electron. Mater.* **1**, 789–798 (2019).
25. Xue, W. et al. Controllable and stable quantized conductance states in a Pt/HfO_x /ITO memristor. *Adv. Electron. Mater.* **6**, 1901055 (2020).
26. Zhao, X. et al. Natural acidic polysaccharide-based memristors for transient electronics: highly controllable quantized conductance for integrated memory and nonvolatile logic applications. *Adv. Mater.* **33**, 2104023 (2021).
27. Song, M. et al. Self-compliant threshold switching devices with high on/off ratio by control of quantized conductance in Ag filaments. *Nano Lett.* **23**, 2952–2957 (2023).
28. Maudet, F., Hammud, A., Wollgarten, M., Deshpande, V. & Dubourdieu, C. Insights on the variability of Cu filament formation in the SiO_2 electrolyte of quantized-conductance conductive bridge random access memory devices. *Nanotechnology* **34**, 245203 (2023).
29. *International Vocabulary of Metrology —Basic and General Concepts and Associated Terms (VIM)* (Bureau International des Poids et Mesures, 2012).
30. Rigosi, A. F. & Elmquist, R. E. The quantum Hall effect in the era of the new SI. *Semicond. Sci. Technol.* **34**, 093004 (2019).
31. Hartland, A. The quantum Hall effect and resistance standards. *Metrologia* **29**, 175–190 (1992).
32. Klitzing, K. V., Dorda, G. & Pepper, M. New method for high-accuracy determination of the fine-structure constant based on quantized Hall resistance. *Phys. Rev. Lett.* **45**, 494–497 (1980).
33. Patel, D. K. et al. A zero external magnetic field quantum standard of resistance at the 10^{-9} level. *Nat. Electron.* https://doi.org/10.1038/s41928-024-01295-w (2024).
34. Wang, Z. et al. Resistive switching materials for information processing. *Nat. Rev. Mater.* **5**, 173–195 (2020).
35. Cox, M. G. The evaluation of key comparison data. *Metrologia* **39**, 589–595 (2002).
36. *ISO/IEC 17043: 2023-05, Ed. 2 Conformity Assessment—General Requirements for the Competence of Proficiency Testing Providers* (International Organization for Standardization, 2023).
37. *ISO 13528: 2022-08, Ed. 3—Statistical Methods for Use in Proficiency Testing by Interlaboratory Comparison* (International Organization for Standardization, 2022)
38. Kharlanov, O. G., Shvetsov, B. S., Rylkov, V. V. & Minnekhanov, A. A. Stability of quantized conductance levels in memristors with copper filaments: toward understanding the mechanisms of resistive switching. *Phys. Rev. Appl.* **17**, 054035 (2022).
39. Milo, V. et al. Accurate program/verify schemes of resistive switching memory (RRAM) for in-memory neural network circuits. *IEEE Trans. Electron Devices* **68**, 3832–3837 (2021).
40. Benz, S. P. & Hamilton, C. A. Application of the Josephson effect to voltage metrology. *Proc. IEEE* **92**, 1617–1629 (2004).
41. Milano, G. et al. Electrochemical rewiring through quantum conductance effects in single metallic memristive nanowires. *Nanoscale Horiz.* **9**, 416–426 (2024).
42. Krans, J. M. et al. One-atom point contacts. *Phys. Rev. B* **48**, 14721–14724 (1993).
43. Yanson, A. I., Bollinger, G. R., van den Brom, H. E., Agraït, N. & van Ruitenbeek, J. M. Formation and manipulation of a metallic wire of single gold atoms. *Nature* **395**, 783–785 (1998).
44. Rodrigues, V., Fuhrer, T. & Ugarte, D. Signature of atomic structure in the quantum conductance of gold nanowires. *Phys. Rev. Lett.* **85**, 4124–4127 (2000).
45. Menzel, S., Tappertzhofen, S., Waser, R. & Valov, I. Switching kinetics of electrochemical metallization memory cells. *Phys. Chem. Chem. Phys.* **15**, 6945 (2013).
46. Rietveld, G. Artifact calibration—the role of software in metrology. In *National Conference of Standard Laboratories (NCSL) Workshop and Symposium, Monterey, CA* 315–322 (NCSLI, 1996).

Methods

Device fabrication

Memristive devices were fabricated by sandwiching a SiO_2 insulator in between a platinum bottom electrode and a silver top electrode. The choice of silver as the top electrode is based on its electrochemical activity which allows dissolution of silver atoms and migration of Ag^+ ions at lower voltages compared to other noble metals, while platinum was chosen as the counter-electrode because it is electrochemical inert (details on the selection of materials and device configuration can be found in Supplementary Section 5). The pad structure devices were fabricated on a thermally oxidized silicon substrate starting with the d.c. magnetron sputtering deposition (power, 200 W) of a TiO_2 (10 nm) adhesion layer and a platinum (100 nm) bottom electrode. The homogeneous SiO_2 film (20 nm) with a purity of 8N was deposited by radiofrequency (RF) magnetron sputtering with a sputtering power of 150 W in a processing gas mixture of 9 sccm argon and 1 sccm oxygen at 150 °C. Note that the choice of the 8 N SiO_2 matrix is related to the very low level of impurities, a potential disturbing factor for achieving controlled conductance states. Also, the resulting SiO_2 is rather stoichiometric and chemical and physical interactions with silver are not thermodynamically favourable. Following switching layer deposition, feature sizes of 50 × 50 μm^2 were patterned by negative photolithography. Then, the Ag (20 nm) active top electrode was deposited by e-beam evaporation with a deposition rate of 0.01 nm s^{-1}, followed by a d.c.-sputtered platinum (50 nm) capping layer. The role of the capping layer is to prevent degradation of the silver active electrode over time as required for long-term use of the device. A standard lift-off process was utilized for the final cleaning of devices, obtaining an Ag/SiO_2/Pt cell with a top electrode size of 50 × 50 μm^2.

Device modelling

Departing from the experimental observation of well-defined conductance jumps and states, we model the RESET transition (the SET transition is also considered for generality) as a random generation of events related to the destruction of single quantum mode channels with conductance $\sim G_0$. This is a stochastic version of a continuous behavioural compact model[47] which has been successfully applied to memristors with different material systems, different switching modes (bipolar, unipolar, complementary and threshold switching) and for the SPICE simulation of neuromorphic circuits. The stochastic version of the model presented here was recently applied to valence change memory devices which show variability, but not quantum conductance jumps[48].

The stochastic resistive switching model follows Chua's approach[49] to memristors and is based on two equations, one for the current and one for the internal memory variable. In our case, the memory state variable is the number of conducting channels, n_{ch}, each of these channels contributing $\sim G_0$ to the filament conductance. In a naive interpretation, each of these channels can be considered either as 'atomic chains' or as 'quantized quantum transport modes' in the filament constriction. This is a simple implementation of the Landauer theory for ballistic transport through an atomic-size constriction[50]. We consider that the SET/RESET transitions occur by successive discrete conductance jumps (events) corresponding to the creation/destruction of single conduction channels. For simplicity, we assume that each switching event increases or decreases the conductance by the same amount. However, this might not be completely realistic because several channels can be created/destroyed at the same time. During the RESET transition, we will consider that each jump is $|\Delta G| = G_0$. Given the experimental results, we impose that the first SET event is abrupt so that the device reaches the compliance limit in a single conductance jump. The creation/destruction of single channels will occur at random times during the application of the external electrical signal (voltage/current). For the sake of generality, we limit the number of channels to n_{max}. This parameter is related to the maximum area of the filament created during electroforming. Under these conditions, the proposed memory equation is:

$$\frac{dn_{ch}}{dt} = \frac{n_{max} - n_{ch}}{\tau_S} - \frac{n_{ch}}{\tau_R} \quad (1)$$

where the two terms of the right-hand side (RHS) represent the SET and RESET transitions, and τ_S and τ_R are the SET and RESET characteristic times, respectively. Because the SET transition resembles the dielectric breakdown process and is strongly accelerated by the electric field, an exponential voltage dependence for τ_S is assumed:

$$\tau_S(V) = \tau_{S0} \exp\left[-\gamma_S(V - IR_S)\right] \quad (2)$$

where γ_S is the acceleration factor, τ_{S0} is the time scale prefactor, I is current, V is voltage and R_S is the series resistance. On the other hand, consistently with the electropolishing interpretation, the RESET transition is assumed to be controlled by the oxidation/reduction dynamics and/or by the out-diffusion of species to the filament surroundings. Because both processes are strongly accelerated by temperature, we neglect voltage acceleration (as discussed within the electropolishing interpretation) and we only consider the local temperature rise related to the power dissipated in the filament, $P = I(V - IR_S)$. Assuming an Arrhenius temperature dependence as a first-order approximation, the characteristic RESET time, τ_R, can be described as:

$$\tau_R(V) = \tau_{R0} \exp\left[\frac{E_a}{K_B(T + R_{TH}P)}\right] \quad (3)$$

where τ_{R0} is the RESET scale prefactor, E_a is the activation energy, K_B is the Boltzman constant, T is the external temperature and R_{TH} is the thermal resistance. The thermal resistance has been described in the literature in terms of two parallel paths for heat evacuation[51]. The longitudinal thermal resistance, R_L, corresponding to heat transport along the channel (related to the electrical conductivity) and the transverse resistance, R_T, associated with heat transport towards the surrounding material. The latter is independent of the filament size to the first order, while R_L is inversely proportional to the filament area, represented here by n_{ch}, which is proportional to the area. Thus, we can write $R_L = K_L/n_{ch}$, where K_L is a constant. The total thermal resistance is given by the parallel combination of R_L and R_T, so that $R_{TH} = (K_L R_T)/(n_{ch}R_T + K_L)$. It is worth remarking that we included only description of thermal dissipation with a phenomenological approach based on macroscopic parameters such as thermal resistances. While in principle quantum thermal effects cannot be ruled out, experimental works pointed out that these effects only become not negligible in the low-temperature regime[52], that is, far away from the room temperature conditions of our work.

Because τ_S has a strong exponential dependence on voltage, it emerges that $\tau_S \ll \tau_R$ for positive voltages and $\tau_S \gg \tau_R$ for negative voltages. Because of this, we can separately consider the SET and RESET transitions with two separate differential equations. One for the SET:

$$\frac{dn_{ch}}{dt} = \frac{n_{max} - n_{ch}}{\tau_S} \quad (4)$$

And one for the RESET:

$$\frac{dn_{ch}}{dt} = -\frac{n_{ch}}{\tau_R} \quad (5)$$

As far as the current is concerned, we have considered:

$$I(V) = \frac{n_{ch}G_0}{1 + n_{ch}G_0R_S}V + I_B \sinh\left[\eta(V - IR_S)\right] \quad (6)$$

where η is a shape parameter related to the potential barrier at the constriction when there are no conducting channels. The first term corresponds to the conduction through the n_{ch} channels, and the second to the background tunnelling regime, that is, when the filament has a gap. Although the considered voltage dependence of the background current can be discussed, this is not relevant to our work because we focus on situations where there is at least one conducting channel with a conductance which is generally much larger than that of the background. Finally, notice that n_{ch} couples the current and memory equations.

For the generation of random events, we follow an 'on-the-fly' method. If the number of events (conductance jumps) is $n(t)$, the event generation rate is $\lambda(t) = \mathrm{d}n(t)/\mathrm{d}t$. During the SET transition, $n_{ch} = n(t)$ so that $\lambda(t) = \mathrm{d}n_{ch}/\mathrm{d}t$, while during RESET $n_{ch} = n_{max} - n(t)$, so that $\lambda(t) = -\mathrm{d}n_{ch}/\mathrm{d}t$. Thus, the event generation rates can be obtained from equations (4) and (5) so that $\lambda_S = (n_{max} - n_{ch})/\tau_S$ and $\lambda_R = n_{ch}/\tau_R$ during SET and RESET, respectively. Since $n_{max} > n_{ch}$ at any time, both generation rates are always positive as they must be. For the RESET transition, we will depart from an initial number of channels, n_{init}, which are the ones generated during the previous SET transition.

The events are generated with a random number u uniformly distributed between 0 and 1 along the simulation time. The simulation time is discretized in steps Δt which are small enough so that λ(t) can be assumed to be constant during Δt. It can be shown that under these conditions, the random time to a subsequent event at time t is $\Delta t_u = -\ln(u)/\lambda(t)$. During the simulation, if $\Delta t_u < \Delta t$ an event is generated at time t, otherwise, the event is rejected. Details on modelling are discussed in Supplementary Section 9.

Interlaboratory comparison

An interlaboratory comparison involving six participants was carried out for the electrical characterization of quantum conductance levels in memristive devices, with the aim of testing the intrinsic standard of electrical conductance (or resistance) and for evaluating laboratory-to-laboratory variability. For this purpose, samples assumed to be identical were distributed among participants and a common measurement protocol was defined. The participants were the following institutions: Istituto Nazionale di Ricerca Metrologica (Italian Institute of Metrology, NMI 1), Instituto Português da Qualidade (Portuguese Institute of Metrology, NMI 2), Turkiye Bilimsel ve Teknolojik Arastirma Kurumu (Turkish Institute of Metrology, NMI 3), Forschungszentrum Juelich GmbH (LAB 1), Fundación IMDEA Nanociencia (LAB 2) and Politecnico di Torino (LAB 3).

Measurement protocol

The equivalence of the measurements across the different laboratories was ensured by establishing and agreeing a measurement protocol that defines standardized measurement conditions to program, accept and stabilize the quantum conductance level, and defines the methodology to measure its conductance value under steady conditions (an example of the device programming methodology is reported in Extended Data Fig. 1). The generation of the quantum conductance states is achieved by running sequential SET/RESET cycles where an applied voltage to the two terminals of the device is swept between +1.5 V and −0.9 V. The positive part of the sweep (SET cycle) has a sweep rate of 96 mV s^{-1} (voltage steps of 50 mV). The negative sweep (RESET cycle) has a slower sweep rate of 2 mV s^{-1} (voltage steps of 1 mV). The current compliance was established as 500 µA and 10 mA for the positive and negative cycles, respectively. The voltage at the terminals of the device and the current that flows through it are continuously measured over SET/RESET cycles, and the corresponding conductance state is obtained for each applied voltage step. The formation of the quantum conductance steps during the RESET is continuously verified and a criterion to detect and accept G_1 and G_2 conductance states related to G_0 and $2G_0$ quantum values, respectively, was established. If the last five consecutive measurements of the conductance state lay within either $G_0 \pm 0.5G_0$ or $2G_0 \pm 0.5G_0$ (censoring interval), the sweep RESET cycle is interrupted, and a continuous read voltage of 10 mV is applied. The measurement of the step conductance value starts under this fixed applied control voltage and continues as long as it remains in the intervals $[0.5G_0; 1.5G_0]$ or $[1.5G_0; 2.5G_0]$. The measurements were made at room temperature and under normal environmental conditions. The equipment used was a source meter (different equipment was used by the participants, as detailed in Supplementary Section 14) in autorange mode. The above-described methodology makes it possible to deal with the stochasticity of the conductive filament formation process establishing an initial limit to the variability around the nominal values of the desired quantum conductance steps (the validation of this programming methodology is discussed in Supplementary Section 15). Note that all measurements not strictly following the established comparison protocol were not considered for the interlaboratory comparison.

Evaluation of results and uncertainty budget

The evaluation of the average value and the variability of the programmed quantum steps was made from the observation of the measurements taken under repeatability and reproducibility conditions (described in appendix 2 of ref. 4). Here, repeatability conditions are understood as measurements of a specific device taken consecutively, while reproducibility is considered as the variability of the measurements taken from cycle-to-cycle operation of a specific device and programmed state as well as from device-to-device operations.

For each participant, j, the arithmetic mean and the experimental standard deviation were calculated for each series i of n_i values:

$$\bar{G}_{j,i} = \frac{1}{n_i}\sum_{a=1}^{n_i} G_{i,a} \tag{7}$$

$$s_{j,i} = \sqrt{\frac{1}{n_i - 1}\sum_{a=1}^{n_i}\left(G_{i,a} - \bar{G}_{j,i}\right)^2} \tag{8}$$

The s.d. given by equation (8) is an estimate of the repeatability[53,54] associated with series i of a programmed quantum conductance state measured by participant j. Only series with a minimum of 30 consecutive values and limited to a maximum of 100 values were considered as a fixed condition in this data evaluation (Supplementary Section 13). As each participant measured N_j series and there are series with different numbers of values, a polled standard deviation[55] $s^2_{p,j}$ is calculated based on the following equation for its variance:

$$s^2_{p,j} = \frac{\sum_{i=1}^{N_j}(n_i - 1) \times s^2_{j,i}}{\sum_{i=1}^{N_j}(n_i - 1)} \tag{9}$$

$s_{p,j}$ is therefore a weighted average of the N_j s.d. where the number of degrees of freedom $(n_i - 1)$ is the weight of each series.

For each participant, an average of the mean values obtained from the N_j series and the experimental s.d. is calculated as:

$$\bar{\bar{G}}_j = \frac{1}{N_j}\sum_{i=1}^{N_j}\bar{G}_{j,i} \tag{10}$$

$$S_j = \sqrt{\frac{1}{N_i - 1}\sum_{i=1}^{N_j}\left(\bar{G}_{j,i} - \bar{\bar{G}}_j\right)^2} \tag{11}$$

The evaluation of the reproducibility of the programmed quantum conductance steps was based on the s.d.[53,54] given by equation (11). Because the values obtained by each participant for each step are from

different cycles and different devices, the reproducibility obtained is the result of cycle-to-cycle and device-to-device variability.

The measurement of quantum conductance states associated with each participant is expressed by the following measurement equation:

$$G_j = \bar{\bar{G}}_j + S_j + s_{p,j} + e_j \tag{12}$$

where $\bar{\bar{G}}_j$ is the mean value calculated by participant j, S_j is the related experimental s.d. according to equations (10) and (11), $s_{p,j}$ is the repeatability of the measurements according to equation (9), and e_j is the error related to the accuracy of the measurement equipment used. It is assumed that these input variables are statistically random variables where S_j, $s_{p,j}$ and e_j have an expectation value equal to zero and a s.d. estimated based on the experimental values presented before (S_j and $s_{p,j}$) and in the manufacturing specifications of the equipment used (for e_j). Note that random effects, including cycle-to-cycle variability but also variations related to small variations in the room temperature, humidity levels or even small fluctuations from the measurement set-up, are included in the estimation of the uncertainty component of the quantities S_j and $s_{p,j}$, even if each specific contribution has not been disentangled.

The measuring uncertainty of G_j can be estimated by applying the law of propagation of uncertainties[55] to equation (12):

$$u^2(G_j) = u^2(S_j) + u^2(s_{p,j}) + u^2(e_j) \tag{13}$$

where $u^2(x)$ is the variance (square of standard uncertainty) associated with the variable x and $u^2(G_j)$ is the square of the combined uncertainty of G_j.

The standard uncertainties of S_j and $s_{p,j}$ are estimated by the corresponding s.d. of the mean:

$$u(S_j) = \frac{1}{\sqrt{N_j}} S_j \tag{14}$$

$$u(s_{p,j}) = \frac{1}{\sqrt{\sum_{i=1}^{N_j}(n_i)/N_j}} s_{p,j} \tag{15}$$

The relative standard uncertainty of e_j is calculated from the combined relative uncertainty of the measurement of the voltage, $u_r^2(U)$, and current, $u_r^2(I)$:

$$u_r(e) = \sqrt{u_r^2(U) + u_r^2(I)} \tag{16}$$

The relative uncertainties of the measured voltage U and current I are estimated assuming a rectangular probability distribution for the voltage and the current measuring error with the plus/minus limits given by the manufacturing specifications of the equipment, usually identified as 'accuracy' (Supplementary Section 14):

$$u_r(U) = \frac{1}{\sqrt{3}} \frac{U_{accuracy}}{U} \tag{17}$$

$$u_r(I) = \frac{1}{\sqrt{3}} \frac{I_{accuracy}}{I} \tag{18}$$

Following the international recommendation to express the final measuring uncertainty with a coverage probability of approximately 95%[56,57], the expanded uncertainty $U(G_j)$ is calculated following the equation:

$$U(G_j) = k \times u(G_j) \tag{19}$$

where k is the coverage factor calculated according to annex G of ref. 55.

Evaluation of consensus value

The evaluation of the results achieved by the participants was done by comparing individual results with a consensus value[36,37]. The consensus value is established based on all results from the participants[37], using a weighted average of their values[35]:

$$G_{cons} = \left(\sum_{j=1}^{6} w_j \times G_j\right) \Big/ \left(\sum_{j=1}^{6} w_j\right) \tag{20}$$

where the weighting factors are given by:

$$w_j = 1/u^2(G_j) \tag{21}$$

The combined uncertainty of the consensus value is estimated based on the participant uncertainties as follows:

$$u(G_{cons}) = \sqrt{1 \Big/ \sum_{j=1}^{6} w_j} \tag{22}$$

And the related expanded uncertainty is given assuming a coverage factor $k = 2$ (ref. 35):

$$U(G_{cons}) = 2 \times u(G_{cons}) \tag{23}$$

To identify an overall consistency of the results produced by this approach, a chi-square test was applied to the input values[35]:

$$\chi^2_{obs} = \sum_{j=1}^{n} \left[(G_j - G_{cons})^2 / u^2(G_j)\right] \tag{24}$$

The result of the test is considered to fail if $\Pr\{\chi^2(\nu) > \chi^2_{obs}\} < 0.05$ where Pr is the 'probability of', $\chi^2(\nu)$ is the expected theoretical value of a chi-squared distribution for ν, and ν is the degrees of freedom, which is the number of input values n minus 1 (in this case, 5). If the consistency check does not fail, then G_{cons} can be accepted as the consensus value and $U(G_{cons})$ can be accepted as its expanded uncertainty. Values obtained for the interlaboratory comparison were $\chi^2_{obs} = 6.3$ and $\chi^2(5) = 11.1$. As $\chi^2_{obs} \leq \chi^2(5; 0.05)$, the consistency of the participant's values and the calculated consensus value was demonstrated, thus the obtained G_{cons} is the consensus value and $U(G_{cons})$ is its expanded uncertainty.

To qualify the result of each participant related to the consensus value, the normalized error[35,37], $E_{n,j}$, was calculated by:

$$E_{n,j} = (G_j - G_{cons}) / \sqrt{U^2(G_j) - U^2(G_{cons})} \tag{25}$$

The value of $E_{n,j}$ has the following meaning: if $|E_{n,j}| \leq 1.0$, the result is consistent (passed); if $|E_{n,j}| > 1.0$, the result is inconsistent (failed). For all participants, results were observed to be consistent with the established consensus value. Based on statistical analysis, higher values of $|E_{n,j}|$ (even if always ≤1.0) cannot be ascribed to eventual systematic errors affecting the measurement that are not being adequately corrected or considered in the evaluation of measurement uncertainty.

Data availability

The data that support the findings of this study are available via Zenodo at https://doi.org/10.5281/zenodo.16788655 (ref. 58). All other data are available from the corresponding authors.

References

47. Miranda, E. & Sune, J. Memristive state equation for bipolar resistive switching devices based on a dynamic balance model and its equivalent circuit representation. *IEEE Trans. Nanotechnol.* **19**, 837–840 (2020).

48. Suñé, J., Bargalló-González, M., Saludes, M., Campabadal, F. & Miranda, E. Event-driven stochastic compact model for resistive switching devices. *IEEE Trans. Electron Devices* **71**, 4649–4654 (2024).
49. Chua, L. Resistance switching memories are memristors. *Appl. Phys. A* **102**, 765–783 (2011).
50. Landauer, R. Spatial variation of currents and fields due to localized scatterers in metallic conduction. *IBM J. Res. Dev.* **1**, 223–231 (1957).
51. Russo, U., Ielmini, D., Cagli, C. & Lacaita, A. L. Filament conduction and reset mechanism in NiO-based resistive-switching memory (RRAM) devices. *IEEE Trans. Electron Devices* **56**, 186–192 (2009).
52. Pekola, J. P. & Karimi, B. Colloquium: Quantum heat transport in condensed matter systems. *Rev. Mod. Phys.* **93**, 041001 (2021).
53. *ISO 5725-1: 2023-07—Accuracy (Trueness and Precision) of Measurement Methods and Results—Part 1: General Principles and Definitions* (International Organization for Standardization, 2023).
54. *ISO 3534-2: 2006—Statistics—Vocabulary and Symbols—Part 2: Applied Statistics* (International Organization for Standardization, 2006).
55. *JCGM 100: 2008—Evaluation of Measurement Data—Guide to the Expression of Uncertainty in Measurement* (Bureau International des Poids et Mesures, 2008).
56. *ILAC-G17:01/2021—ILAC Guidelines for Measurement Uncertainty in Testing* (International Laboratory Accreditation Cooperation, 2021).
57. *ILAC-P14:09/2020—ILAC Policy for Measurement Uncertainty in Calibration* (International Laboratory Accreditation Cooperation, 2020).
58. Milano, G. et al. A quantum resistance memristor for an intrinsically traceable International System of Units standard - Dataset. *Zenodo* https://doi.org/10.5281/zenodo.16788655 (2025).

Acknowledgements

This work was supported by the European project MEMQuD, code 20FUN06. This project (EMPIR 20FUN06 MEMQuD) has received funding from the European Metrology Programme for Innovation and Research (EMPIR) cofinanced by the participating states and from the European Union's Horizon 2020 research and innovation programme.

Author contributions

G.M., V.C. and I.V. generated the idea. G.M., V.C. and I.V. supported by X.Z. and F.M. designed the experiments. X.Z. designed and performed device fabrication. G.M., V.C. and F.M. supported by X.Z. developed the measurement protocol for the interlaboratory comparison. X.Z., F.M., G.L., G.C., I.O. and V.C. performed electrical measurements. V.C., J.S. and G.M. performed data analysis. J.S. and E.M. developed the model. G.M., L.B., O.B., L.C., N.D.L., I.G., D.G., I.K., M.M., E.M., L.R., C.R., J.S., V.C. and I.V. supervised the research.

Funding

Open access funding provided by Forschungszentrum Jülich GmbH.

Competing interests

The authors declare no competing interests.

Additional information

Extended data is available for this paper at https://doi.org/10.1038/s41565-025-02037-5.

Supplementary information The online version contains supplementary material available at https://doi.org/10.1038/s41565-025-02037-5.

Correspondence and requests for materials should be addressed to Gianluca Milano, Vitor Cabral or Ilia Valov.

Peer review information *Nature Nanotechnology* thanks Run-Wei Li and the other, anonymous, reviewer(s) for their contribution to the peer review of this work.

https://doi.org/10.1038/s41565-025-02037-5

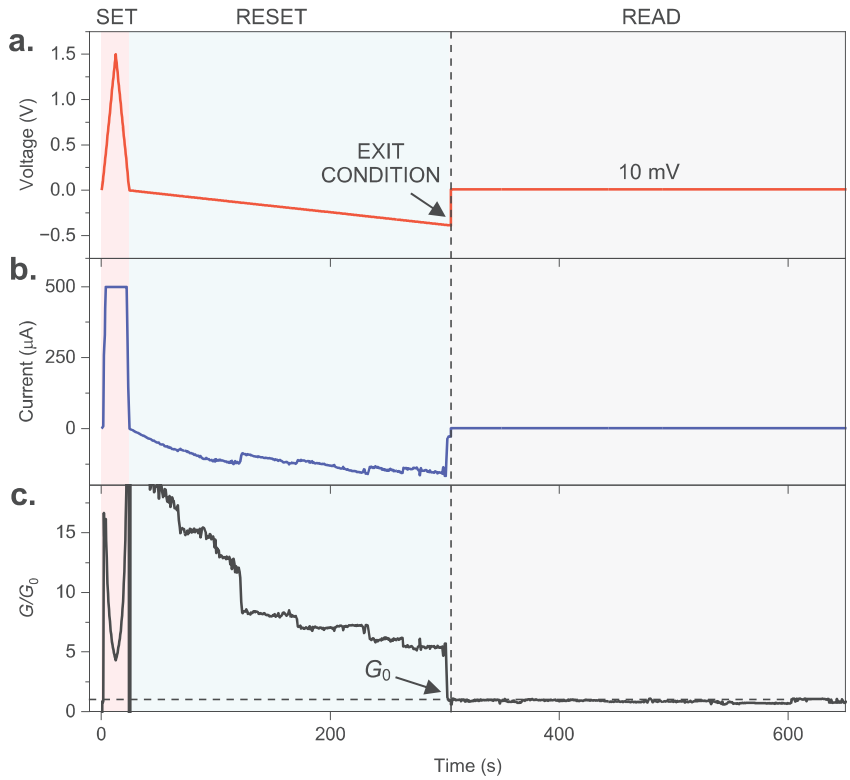

Extended Data Fig. 1 | Program-and-verify approach to program the device to the desired quantum conductance levels. This approach consists in the following steps: *i)* SET of the device through a positive voltage sweep cycles in between 0 and 1.5 V (sweep rate of 96 mV s^{-1}, compliance current of 500 μA externally controlled to avoid hard breakdown of the device) (red shadowed region); *ii)* RESET the device through a negative slow voltage sweep (2 mV s^{-1}) from 0 down to -0.9 V to achieve a step-like decrease of device conductance due to quantum conductance effects (blue shadowed region); *iii)* READ of the desired quantum level with a continuous constant voltage, if the exit condition has been satisfied during the RESET step, the RESET cycle is interrupted and the control changes to a continuously positive read voltage of 10 mV (grey shadowed region). The exit condition is considered satisfied if the device exhibits during the time series at least 5 consecutive conductance measurements in the desired quantum level $\pm 0.5G_0$. Note that the device is continuously cycled until the desired quantum level has been obtained. **a**, Programming voltage; **b**, measured current; **c**, the device conductance.

https://doi.org/10.1038/s41565-025-02037-5

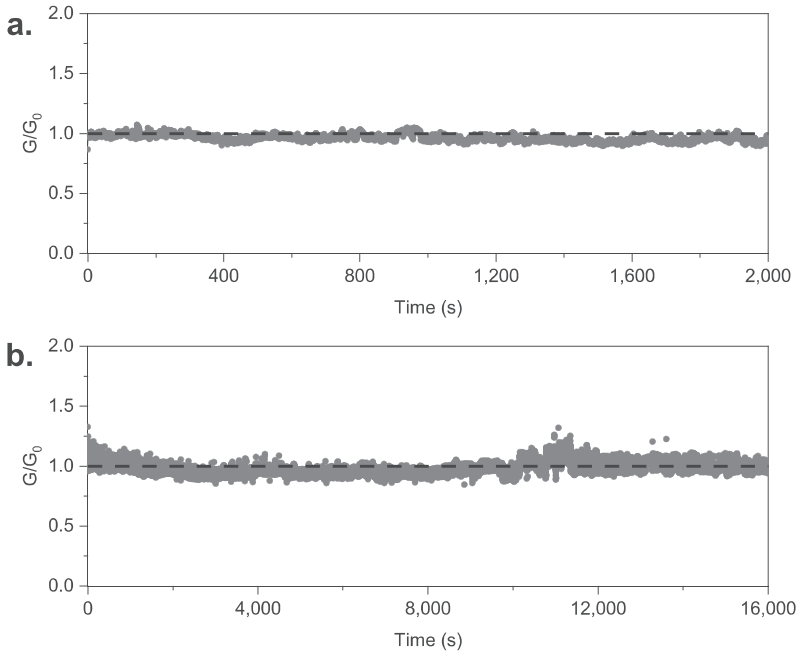

Extended Data Fig. 2 | Stability of programmed quantum conductance levels. **a**. Example of a quantum conductance level measured at NMI 1 observed to be stable up to 2000 s under constant voltage reading of 10 mV (initial data are reported in Fig. 3a). **b**. Example of a quantum conductance level measured at NMI 3 observed to be stable up to 16000 s under constant reading voltage of 10 mV. Dashed lines represent the G_0 reference value. Quantum conductance levels in panels a and b have been obtained through the program-and-verify approach, with negative voltage sweep for gradual RESET of 2 mV s^{-1} and 80 mV s^{-1}, respectively.

https://doi.org/10.1038/s41565-025-02037-5

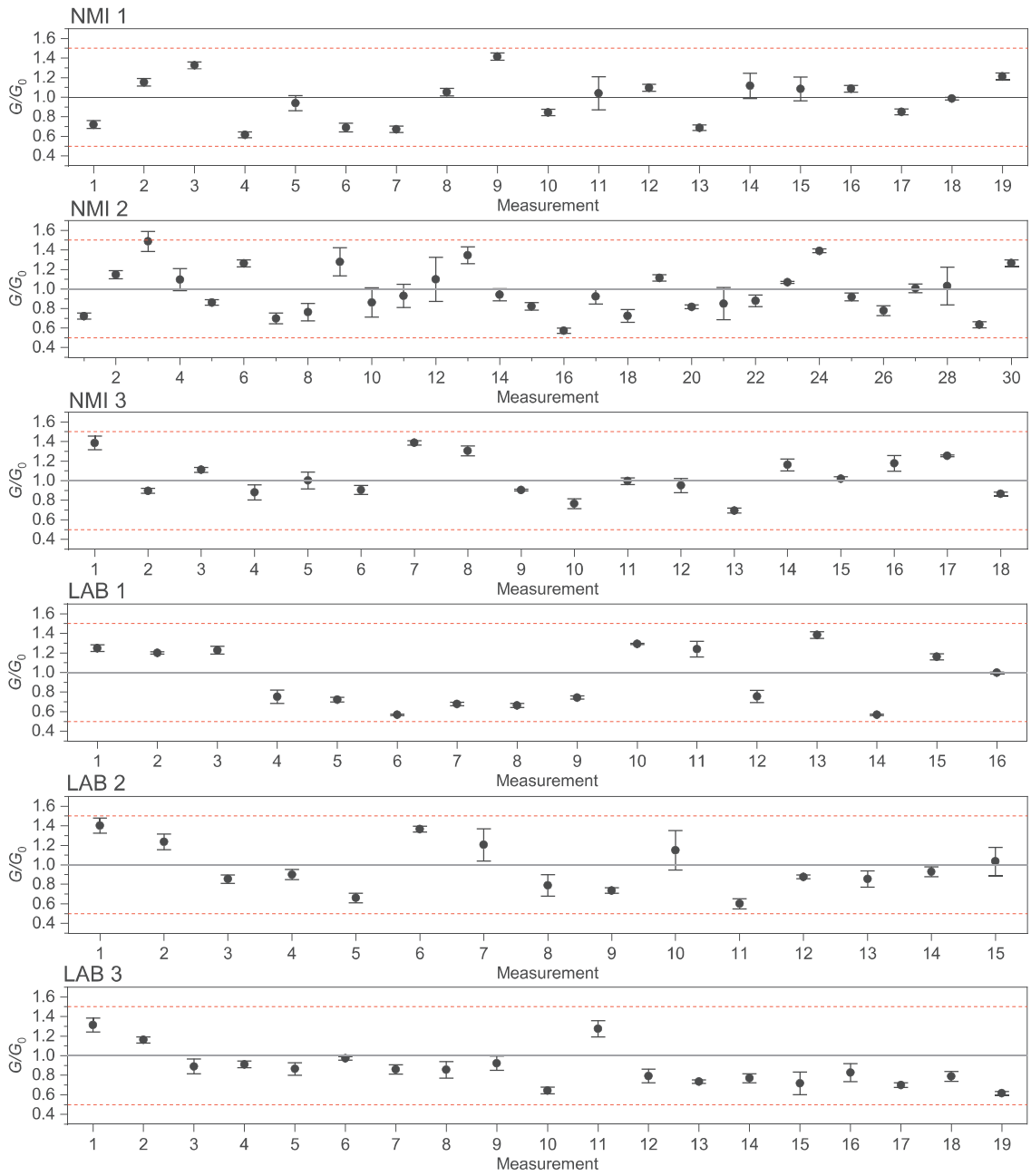

Extended Data Fig. 3 | G_1 conductance plateaus related to the G_0 quantum level from the interlaboratory comparison. Each data point is the mean value and error bar is the standard deviation representing the repeatability evaluated over n (30 to 100) repeated measurements of the same conductance value. Red dashed lines represent boundaries of the exit condition of the program-and-verify approach, while grey line represents the G_0 reference line.

https://doi.org/10.1038/s41565-025-02037-5

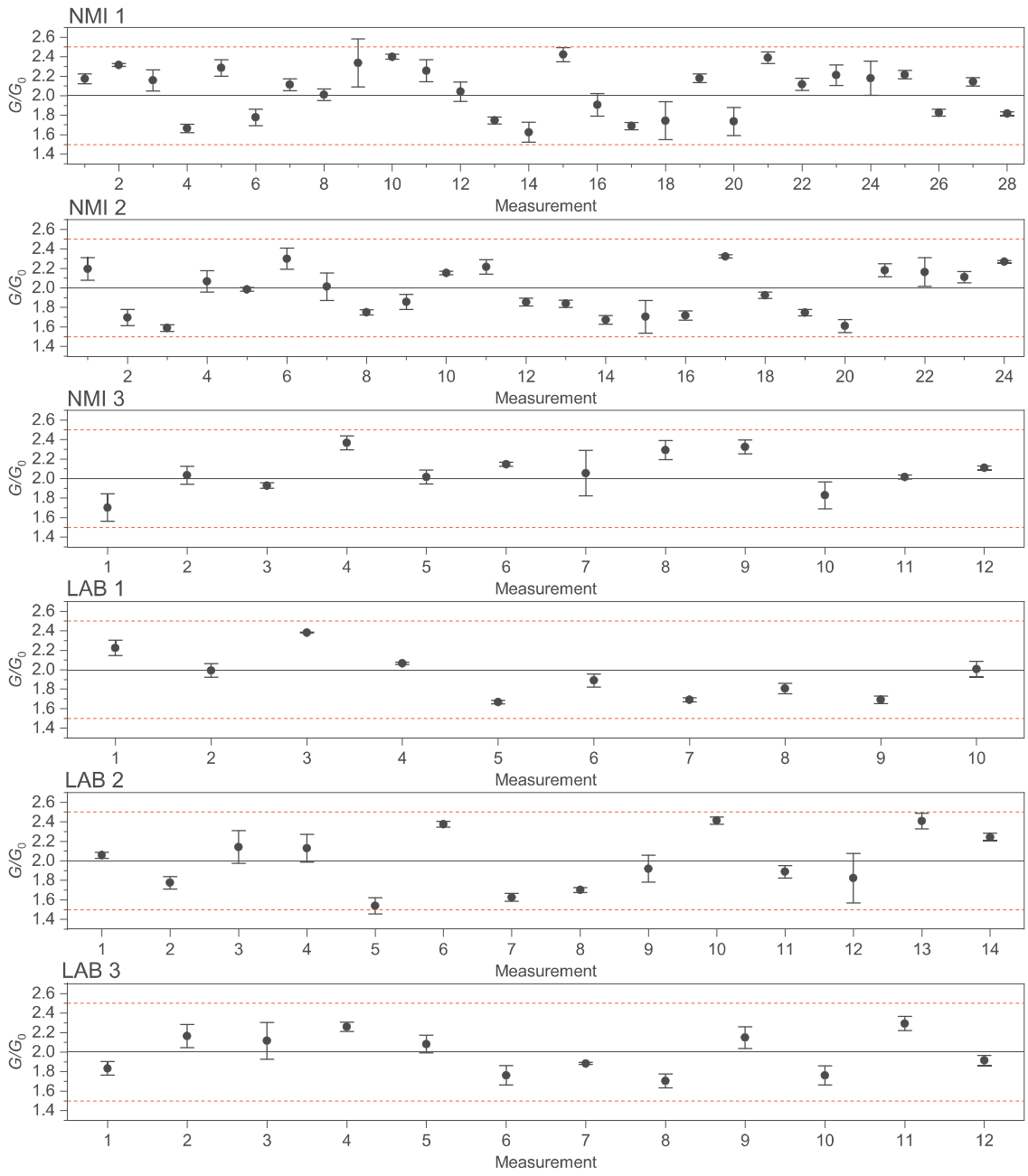

Extended Data Fig. 4 | G_2 conductance plateaus related to the $2G_0$ quantum level from the interlaboratory comparison. Each data point is the mean value and error bar is the standard deviation representing the repeatability evaluated over n (30 to 100) repeated measurements of the same conductance value. Red dashed lines represent boundaries of the exit condition of the program-and-verify approach, while grey line represents the $2G_0$ reference line.

https://doi.org/10.1038/s41565-025-02037-5

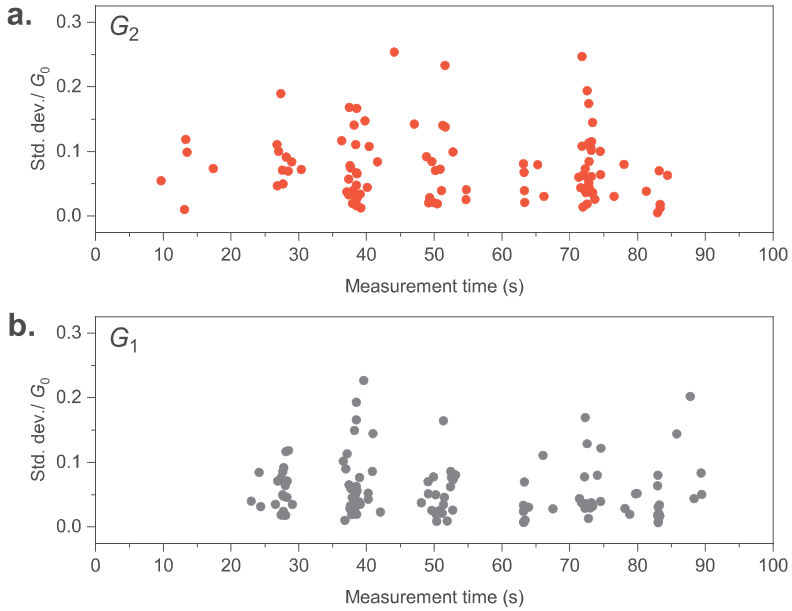

Extended Data Fig. 5 | Measurement repeatability and time interval of consecutive measurements. Repeatability in terms of the standard deviation of n consecutive measurements evaluated for conductance levels related to $2G_0$ (panel **a.**) and to G_0 (panel **b.**), for a measurement time up to 100 s. Each point has been evaluated by programming the device to a desired programmed quantum level and then evaluating the standard deviation of n (30 to 100) consecutive measurements of the conductance step. Graphs have been obtained through aggregated data analysis of results obtained by different labs in the interlaboratory comparison. In case of equal number of consecutive measurements, different measurement time intervals arise from different sample rates of measurement arising from different experimental equipment and their configuration parameters (for example NPLC – Number of Power Line Cycles, Filter, etc) exploited for the interlaboratory comparison. As can be observed, no significant trend can be observed in the standard deviation as a function of the measurement time interval, suggesting that the repeatability can be evaluated based on consecutive measurements performed on a small-time interval.

https://doi.org/10.1038/s41565-025-02037-5

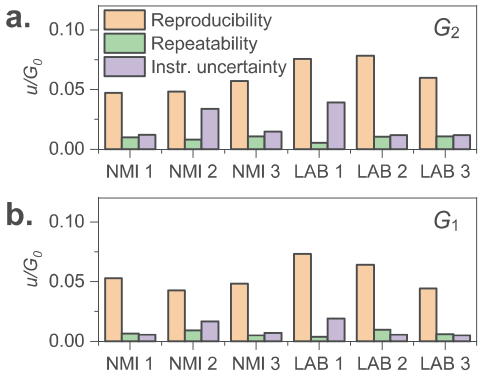

Extended Data Fig. 6 | Uncertainty budget – absolute values. Absolute standard uncertainty components of G_2 (panel a.) and G_1 (panel b.) related to reproducibility, repeatability, and measurement equipment for each participant.

frontiers | Frontiers in Nanotechnology

TYPE Original Research
PUBLISHED 11 June 2025
DOI 10.3389/fnano.2025.1600426

OPEN ACCESS

EDITED BY
Eliana B. Souto,
University College Dublin, Ireland

REVIEWED BY
Zimu Zhou,
Western Digital, United States
Mohsen Mahmoudysepehr,
University of Waterloo, Canada

*CORRESPONDENCE
E. Batista,
ebatista@ipq.pt

RECEIVED 26 March 2025
ACCEPTED 02 June 2025
PUBLISHED 11 June 2025

CITATION
Batista E, Martins RF, Silverio V and Godinho I (2025) Advancing calibration techniques for accurate micro and nanoflow measurements. *Front. Nanotechnol.* 7:1600426. doi: 10.3389/fnano.2025.1600426

Advancing calibration techniques for accurate micro and nanoflow measurements

E. Batista[1]*, Rui F. Martins[2], Vania Silverio[3,4] and Isabel Godinho[1]

[1]Metrology Department, Instituto Português da Qualidade, Caparica, Portugal, [2]NOVA School of Science and Technology, Caparica, Portugal, [3]INESC MN Microsistemas e Nanotecnologias, Lisboa, Portugal, [4]Department of Physics, Instituto Superior Tecnico, Universidade de Lisboa, Lisboa, Portugal

The lack of established protocols and standards for calibrating flow measuring instruments operating in the microflow range raises concerns about the reliability and precision of such measurements results. This work focuses on developing and improving innovative calibration methodologies to enhance the accuracy of microflow and nanoflow measurements. The gravimetric method already implemented at IPQ from 120 µL/h to 2000 mL/h was used and improved for low flow rates down to 10 µL/h. Additionally, three other optical methods were developed to calibrate micro/nano flows in a non-intrusive way: the interferometric, pending drop and front track. The methodology best suited for each specific flow instrument (e.g., syringe pumps and flow meters) and each for measurement range, with the lowest uncertainty, was successfully identified during this work. Also, it was possible to increase the measuring range of the Portuguese Institute for Quality–Volume and Flow Laboratory (IPQ-LVC) down to 5 nL/min (0.3 µL/h) with a 3% target uncertainty (k = 2). This was not only achieved but improved further with the interferometric method, where measurements were performed down to 1.6 nL/min (0.1 µL/h) with 2% uncertainty (k = 2). Furthermore, this method was external validated by a comparison performed under the EURAMET project 1508. The methodologies here described were the basis of the development of EURAMET guide cg 27 - Guidelines for the Calibration of Drug Delivery Devices and Infusion Device Analysers. This document provides standardized procedures for testing microflow and nanoflow instruments aiming to improve the accuracy and comparability of measurement results.

KEYWORDS

calibration, uncertainty, flow, validation, methods

1 Introduction

Metrology, the science of measurement, plays a crucial role in ensuring the accuracy and reliability of flow measurements across various applications. Flow measurements are essential in numerous fields, including healthcare, pharmaceuticals, environmental monitoring, microfluidic technology and industrial processes. Accurate flow measurement is vital for maintaining product quality, ensuring safety, and optimizing performance but most of the instruments used to measure flow rate, especially in health applications and particularly those operating at the micro and nanoscale, have not been sufficiently studied regarding their flow accuracy and traceability. This lack of comprehensive research and validation raises concerns about the reliability and precision of these measurements, which are critical for ensuring patient safety and

effective treatment outcomes. Furthermore, the absence of established protocols and standards for calibrating these instruments at such low flow ranges exacerbates the issue. Without standardized calibration procedures, it is challenging to verify the accuracy of flow measurements, leading to potential discrepancies and inconsistencies in the results. Addressing these gaps through rigorous studies and the development of robust calibration methods is essential for advancing the reliability and efficacy of flow rate measurements. In this work, new methodologies for calibration of syringe pumps, flow meters and microfluidic chips were developed and validated. The primary objective of this work is to enhance the gravimetric procedure described by Bissig et al. (Batista et al., 2020a) and to develop three innovative methods to ensure the traceability of micro and nanoflow measuring instruments. These instruments are increasingly being introduced to the market and are used in various applications, such as healthcare. In this work, various calibration methods were employed to measure flow, including gravimetry and newly developed techniques such as interferometry, pending drop, and the front track method. The front track method, in particular, was also described by Ogheard et al. (Bissig et al., 2015).

The gravimetric method, currently used at the IPQ-LVC laboratory, was improved and the lower limit 120 µL/h was extended to 10 µL/h. In the interferometry technique, an interferometer is used to measure the distance travelled by a pusher block of a syringe pump, over time, to determine the flow rate. The pending drop method uses high-resolution cameras to determine the growth of a drop over time. In the front track method, the cameras follow the meniscus of the liquid displacement in a close tube over time.

The methods developed in this work were validated internally or externally by the participation of IPQ-LVC in the EURAMET pilot project 1508 (Batista et al., 2020b).

The information described in this paper was the basis for the development of EURAMET guide cg 27 - Guidelines for the Calibration of Drug Delivery Devices and Infusion Device Analysers (EURAMET guide cg 27, 2024).

The development of the new methods has also allowed flow measurements (Batista et al., 2024) to be extended to another field–microfluidics and led to the publication of a new EURAMET Technical Guide 4 - Evaluation of flow related quantities in microfluidic devices (EURAMET, 2024).

2 Methods

The gravimetric method, interferometric method, front track and pending drop method were used to calibrate various microflow measuring instruments, namely, syringes pumps, flow meters and microfluidic chips in different flow ranges. The results were compared in terms of % of error and uncertainty mainly due to manufactures specification information. In general, 20 to 30 points were collected in each performed test.

2.1 Gravimetric method

The primary method used for flow determination is the gravimetric method (EURAMET, 2022), which involves weighing the mass of water delivered over a fixed period (Figure 1). The flow rate is calculated as the quotient of the mass of the reference liquid, typically water with specific characteristics, and the time interval, with corrections for buoyancy, evaporation, and fluid properties. This method is widely adopted by several National Metrology Institutes globally and is applied across a broad range of applications.

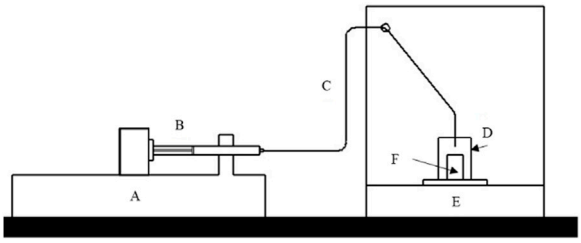

FIGURE 1
Gravimetric schematic of the flow circuit. The fluid goes from a glass syringe **(B)** of a flow generator **(A)** to the balance **(E)** through tubing **(C)** that is immersed in the weighing vessel **(F)** that is inside an evaporation trap **(D)**.

At IPQ, a microflow setup was developed, consisting of two different assemblies using METTLER balances: an AX 26 with a resolution of 0.001 mg and a maximum capacity of 20 g, and an XP 2015 with a resolution of 0.01 mg and a maximum capacity of 220 g. In both assemblies, mass and time data are acquired and statistically processed using an application developed in LABVIEW software. Several tube diameters from 0.09 cm to 0.32 cm and different types and sized of plastic and glass syringes were used in the setup.

The setup was applied to calibrate syringe pumps, flow meters and microflow chips. The uncertainty components of this method are described in Table 1. The uncertainty calculation was determined based on the Guide to the expression of uncertainty in measurement, GUM (BIPM et al., 2008) and can be found in detail in (Sousa et al., 2021).

2.2 Interferometric method

The interferometric method developed (Batis et al., 2020) incorporates a laser unit (Hewlett-Packard, model 5528 A) operating at 633 nm, with signal processing managed by a LABVIEW script specifically developed for this purpose. The optical arrangement consists of two retroreflector cubes, complemented by a control unit, a pusher block, a flow generator, and a syringe. Figure 2 illustrates an example of the experimental setup.

In practice, the flow generation was accomplished by a stepper motor that drove a screw connected to a pusher block that itself pushed the syringe piston. One of the reflector cubes was added on top of this pusher block.

Knowing the internal diameter of the syringe (made of glass or plastic) with very high precision (see 2.5), the travelled distance, and the time needed for that travelled distance (elapse time), it is possible to calculate the flow rate of the fluid inside the syringe.

TABLE 1 Uncertainty components of the gravimetric method.

Uncertainty components	Standard uncertainty	Evaluation process	Distribution
Temperature of the water	$u(T)$	Calibration certificate	Normal
Density of water	$u\ (\rho_W)$	Literature	Rectangular
Density of air	$u\ (\rho_A)$	Literature	Rectangular
Density of mass pieces	$u\ (\rho_B)$	Calibration certificate	Normal
Initial time	$u\ (t_i)$	Estimation (1 μs)	Rectangular
Final time	$u\ (t_f)$	Estimation (1 μs)	Rectangular
Initial mass	$u\ (I_{E,i})$	Calibration certificate	Normal
Final mass	$u\ (I_L)$	Calibration certificate	Normal
Expansion coefficient	$u(\gamma)$	Literature	Rectangular
Evaporation	$u\ (\delta Q_{evap})$	Standard deviation of the measurements	Normal
Buoyancy	$u\ (\delta Q_{mbuoy})$	Calibration certificate (depends on the radius determination)	Normal
Repeatability	$u\ (\delta Q_{rep})$	Standard deviation of the measurements	Normal

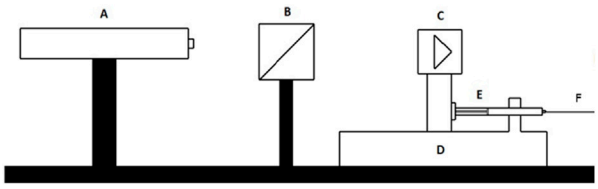

FIGURE 2
Interferometric schematic. **(A)** Is the interferometer, **(B)** and **(C)** are retroreflector cubes, **(D)** is a flow generator, **(E)** is a glass syringe that is filled with the calibration fluid connected to a tubing **(F)**.

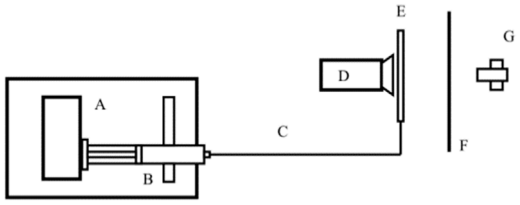

FIGURE 3
Schematic of the general experimental setup for the front track method, where **(A)** is the flow generator, **(B)** is the syringe, **(C)** is the connection line, **(D)** is the camera, **(E)** is the capillary tube, **(F)** is the translucent paper and **(G)** is the LED light.

TABLE 2 Uncertainty components of the interferometric method.

Uncertainty components	Standard uncertainty	Evaluation process	Distribution
Distance	$u(d)$	Calibration certificate	Normal
Inner diameter	$u(r)$	Calibration certificate	Normal
Time	$u(t)$	Calibration certificate	Normal
Temperature	$u(T_W)$	Calibration certificate	Normal
Expansion coefficient	$u(\gamma)$	Literature	Rectangular
Stability	$u\ (\delta Q_{sta})$	Standard deviation of stability measurements	Normal
Repeatability	$u\ (\delta Q_{rep})$	Standard deviation of the mean of the flow measurements	Normal

This method was used to calibrate flow meters and syringe pumps.

The uncertainty components of this method are described in Table 2. In addition, the uncertainty calculation can be found in detail in (Alvares, 2020).

2.3 Front track method

The front tracking method involves monitoring the position of the meniscus (liquid/air interface) inside a capillary tube over time. By knowing the displacement of the meniscus and the internal cross-sectional area of the capillary, the flow rate can be calculated. A high-resolution Alvium 1800 U-1240 camera with a 12 MP resolution and a Qioptic Optem 7:1 telecentric zoom lens was used for this purpose. The camera is connected to a computer and utilizes Python programming to identify the meniscus and determine its position, a translucent paper and a LED light are used as background illumination, allowing to decrease the reflection caused by ambient light, and obtain a good contrast between the background and the liquid meniscus. The setup is illustrated in Figure 3.

TABLE 3 Uncertainty components of the front track method.

Uncertainty components	Standard uncertainty	Evaluation process	Distribution
Meniscus displacement	$u(\Delta)$	Experimental and calibration certificate	Normal
Capillary radius	$u(r)$	Experimental and calibration certificate	Normal
Time	$u(t)$	Calibration certificate	Normal
Temperature	$u(T_W)$	Calibration certificate	Normal
Expansion coefficient	$u(\gamma)$	Literature	Rectangular
Stability	$u\ (\delta Q_{sta})$	Standard deviation of stability measurements	Normal
Repeatability	$u\ (\delta Q_{rep})$	Standard deviation of the mean of the flow measurements	Normal

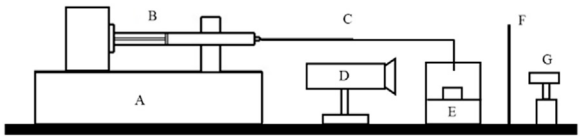

FIGURE 4
Schematic of the second experimental setup of the pending drop method, where **(A)** is a flow generator, **(B)** is the glass syringe, **(C)** is the connection line, **(D)** is the camera, **(E)** is the evaporation trap, **(F)** is the paper and **(G)** the LED light.

The front track method can be applied in several type of flow measurement instruments like syringe pumps, microflow chips and flow meters down to 1.6 nL/min (0.1 µL/h) with 7% uncertainty.

The front track method can be applied in several types of flow measurement instruments, such as syringe pumps, microflow chips and flow meters. More information on this method and the uncertainty calculation can be found in (Bissig et al., 2015) and (Alvares, 2020). The uncertainty components of this method are described in Table 3.

2.4 Pending drop method

The pending drop method (Batista et al., 2021) involves measuring the volume (V) of a drop, its growth over time (t), and applying an evaporation correction (evap). This method is based on visualizing the increase in the volume of a drop over time, using a high-resolution Alvium 1800 U-1240 camera with a 12 MP resolution and a Qioptic Optem 7:1 telecentric zoom lens (Figure 4). The camera is connected to a computer, which processes the data. The image analysis program developed in Python consists of four steps: scale definition, image segmentation, contour determination and volume calculation. It can be used to calibrate syringe pumps from 100 µL/h to 1,000 µL/h.

TABLE 4 Uncertainty components of the pending drop method.

Uncertainty components	Standard uncertainty	Uncertainty evaluation process	Uncertainty distribution
Radius	$u(r)$	Experimental and calibration certificate	Normal
Time	$u(t)$	Calibration certificate	Normal
Evaporation	$u\ (\delta Qevap)$	Experimental tests	Normal
Repeatability	$u\ (\delta Q_{rep})$	Standard deviation of the mean of the flow measurements	Normal

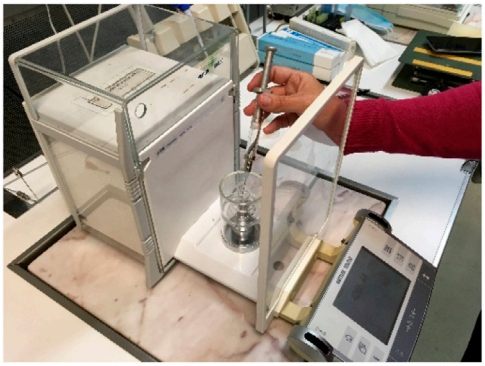

FIGURE 5
Gravimetric experimental setup for the syringe volume determination.

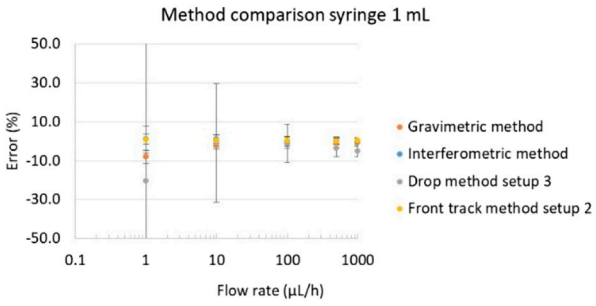

FIGURE 6
Comparison of Nexus pump calibration results with a 1 mL syringe.

TABLE 5 Calibration results of nexus pump calibration.

Nominal flow (mL/h)	Interferometric		Front track		Gravimetric		Pending drop	
	Error (%)	*U* (%)	Error (%)	*U* (%)	Error (%)	*U* (%)	Error (%)	*U* (%)
1	−7.6	3.2	0.9	6.9	−8.0	23.0	−20.4	87.1
10	−1.7	2.1	0.3	3.0	−2.0	3.7	−1.0	30.4
100	−1.8	2.8	0.4	2.1	−0.7	2.4	−1.0	9.8
500	−0.7	2.5	0.0	1.4	−0.6	1.2	−3.7	4.4
1,000	−1.1	1.9	0.3	1.5	−0.6	1.0	−4.9	3.2

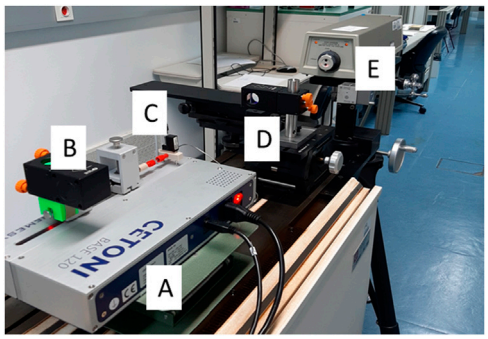

FIGURE 7
Cetoni pump calibration setup using the interferometric method, where **(A)** is the Cetoni syringe pump; **(B)** is the Retroreflector cube; **(C)** is the 100 µL glass syringe; **(D)** is the other Retroreflector cube; **(E)** is the Laser unit.

More information on this method and the uncertainty calculation can be found in (Batista et al., 2021). The uncertainty components of this method are described in Table 4.

This method has still some limitation of use for high flow rates and at lower flow range has high uncertainty values. It can be used for the calibration of syringe pumps from 100 µL/h to 1,000 µL/h with an average standard uncertainty of 5%. More information on this method can be found in (Alvares, 2020; Batista et al., 2020).

2.5 Inner diameter measurements of glass syringes and capillaries

In all the methods described above a flow generator using glass syringes is used. The inner diameter determination of the syringe is critical for assuring the precision of the flow determination and it must be done using appropriate and traceable methods. In this work the gravimetric method is used to determine the inner diameter of all the used syringes (Figure 5) and also the capillaries used in the front track method. This procedure consists in measuring the liquid volume of a specific length of the glass tube. Knowing these two quantities it is possible to determine the average inner diameter of a capillary or syringe. More information on this method can be found in (Batista et al., 2023).

3 Results and discussion

The measurement error presented in this paper was determined according to the International Vocabulary of Metrology (VIM) (BIPM et al., 2012), as is defined as the measured quantity value minus a reference quantity value, Equation 1.

$$\text{Metrological error: } A_{Metro} = \frac{\left(Q_{set} - Q_{ref}\right)}{Q_{ref}} 100\,(\%) \qquad (1)$$

TABLE 6 Calibration results of a thermal sensirion flow meter.

Nominal Flow rate (nL/min)	Nominal flow rate (mL/h)	Interferometric method		Front track method	
		Error (%)	Uncertainty (%)	Error (%)	Uncertainty (%)
1,500	90	1.0	2.0	0.3	3.4
1,000	60	2.7	2.0	4.0	3.4
500	30	4.0	2.1	2.2	3.4
100	6	5.8	2.4	2.3	3.9
70	4.2	5.8	2.4	4.3	4.4
50	3	5.2	3.0	5.1	5.1
20	1.2	4.6	5.1	0.4	9.9

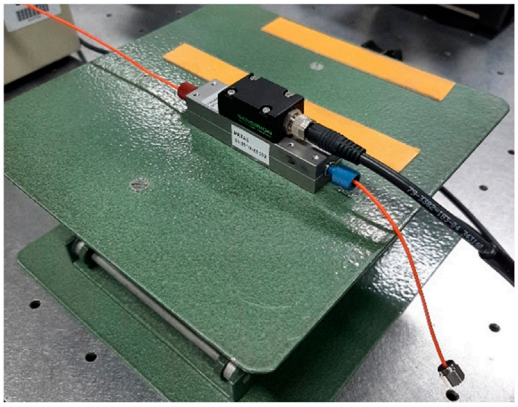

FIGURE 8
Sensirion flow meter.

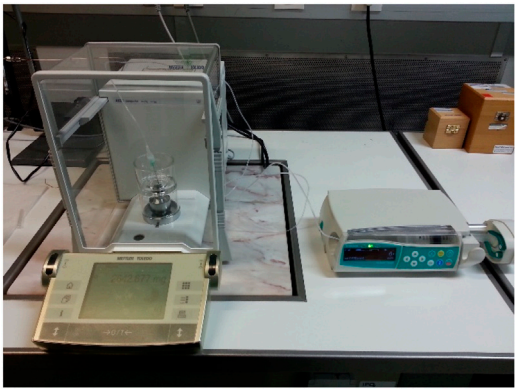

FIGURE 10
Calibration of BBraun pump with a 10 mL syringe using the gravimetric method.

where:

A_{Metro} is the relative flow measurement error or systematic error as defined by VIM (BIPM et al., 2012), Q_{ref} is the reference flow rate determined by the reference measurement method (e.g., gravimetric method), Q_{set} is the flow rate set or the indicated flow rate at the instrument under calibration (e.g., 1 mL/h).

A precision Nexus 3,000 pump with 1 mL glass syringe was calibrated using the methods described above at the following flow rates: 1,000 µL/h, 500 µL/h, 100 µL/h, 10 µL/h, 1 µL/h.

The results are presented in Figure 6 and Table 5.

From the figure above it can be seen that the results from all the methods are consistent on all points.

The method with the larger uncertainty in Figure 6 is the pending drop method, which is recommended to be used only above 100 mL/h with an expanded uncertainty from 5% to 10%.

In the gravimetric method, it was possible to measure down to 10 µL/h with an acceptable expanded uncertainty of 2.6%; this allowed a decrease of range in the volume and flow laboratory of IPQ that was previously of 120 mL/h with 2.5% uncertainty.

The front track method can go to 1 µL/h with an expanded uncertainty of 7%.

The method with the smaller uncertainty is the interferometric method, especially at low flow rates. However, the instruments need to have an external piston for this method to be employed.

Tests were also performed with a Cetoni pump (Figure 7) at 0.1 mL/h using a 100 µL glass syringe with the interferometric method. The results were really outstanding, with an error of 1.7% and an expanded uncertainty of 1.9%.

This interferometric method can calibrate flow meters and syringe pumps from 5,000 mL/h down to 1.6 nL/min (0.1 µL/h) with an expanded uncertainty range of (1.9–0.9) %. The calibration of a thermal Sensirion flow meter (Figure 8) was performed with the interferometer method and the front track method, tested at 1,500 nL/ min, 1,000 nL/min, 500 nL/min, 100 nL/min, 70 nL/min, 50 nL/ min and 20 nL/min.

The results are presented Table 6 and Figure 8.

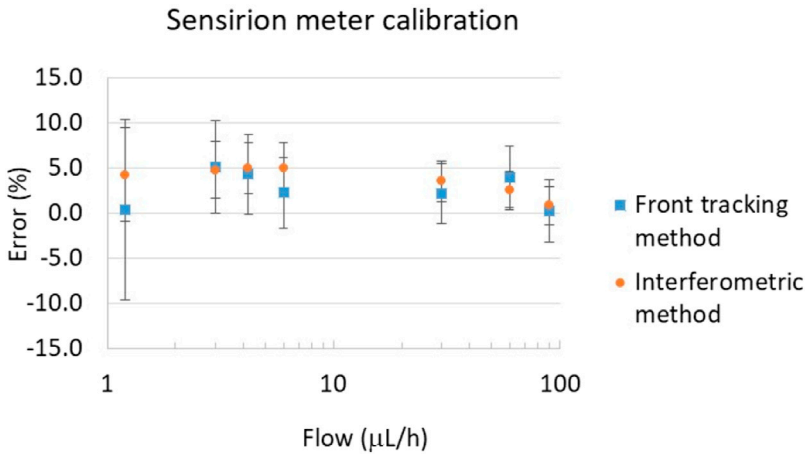

FIGURE 9
Calibration of a thermal sensirion flow meter.

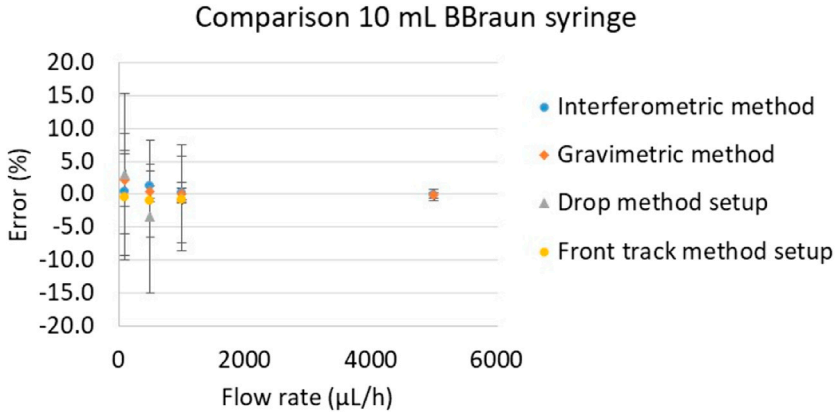

FIGURE 11
Calibration of BBraun pump with a 10 mL syringe.

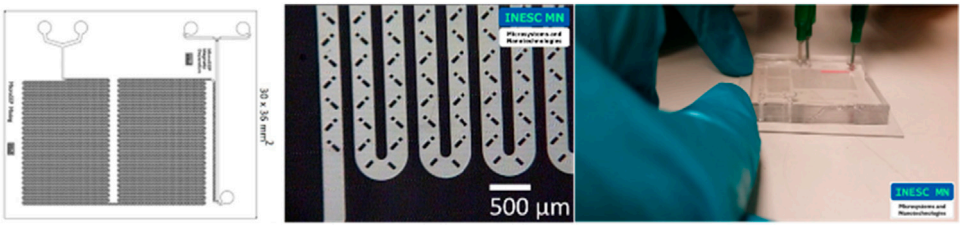

FIGURE 12
Microfluidic Lab-On-a-Chip device for passive mixing and magnetic separation of bioanalytes.

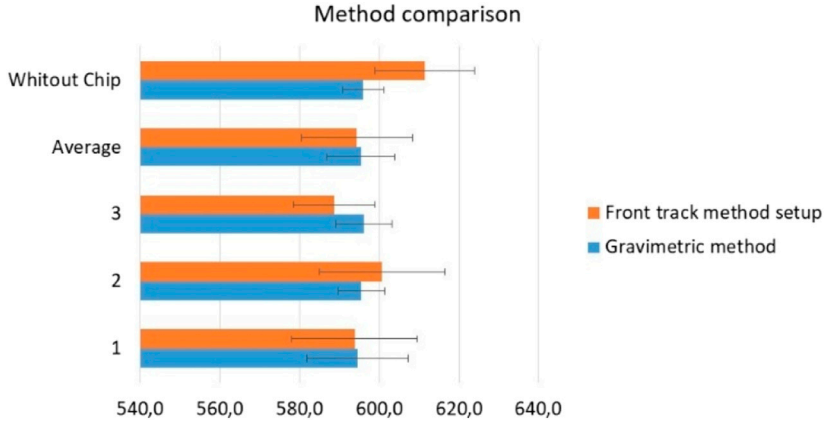

FIGURE 13
Comparison methods for microchips calibration.

It can be verified from Figure 9 that the results are consistent in both methods used in the tests, and the uncertainty in general, smaller for the interferometer method.

In order to test the methods with an instrument used in real life application a perfusor space BBraun syringe pump, used in hospitals to administrate drug to patients (Figure 10), was calibrated with water at flow rates 5,000 µL/h, 1,000 µL/h, 500 µL/h, 100 µL/h, using the methods described in section 2.

The results presented in Figure 11 are consistent for all methods and in all flow rate points. The uncertainty values are very similar for

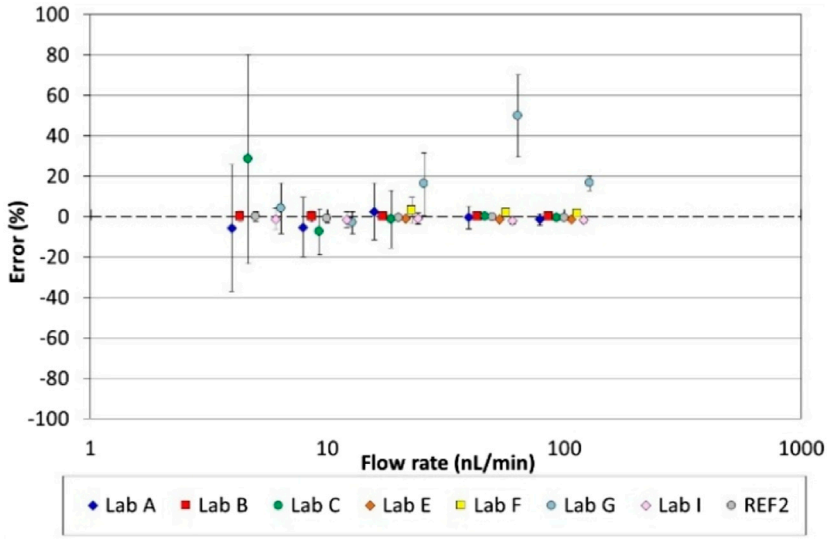

FIGURE 14
Intercomparison results for a cetoni pump calibration.

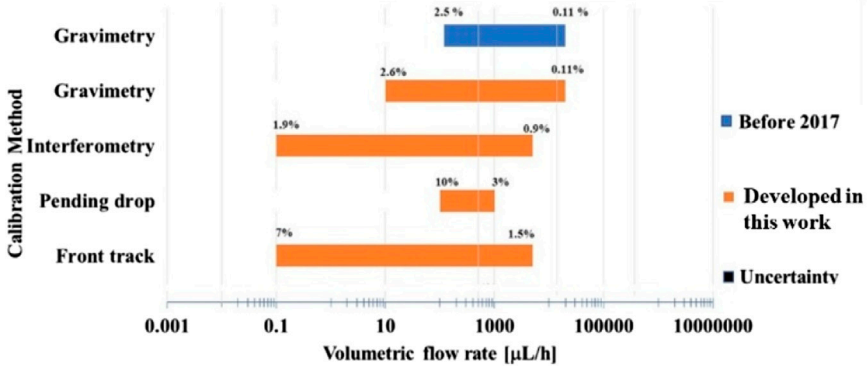

FIGURE 15
Comparison of methods used in micro and nano flow measurements.

all methods regarding each calibration point. More results on this pump can be found in (Batista, 2022).

Finally, a microfluidic Lab-On-a-Chip device (Figure 12) for passive mixing and magnetic separation of bioanalytes with square channel cross-section and obstacles that promotes a mixture of components for sample preparation was also characterized using the front track method and the gravimetric method.

The chips were tested at 600 µL/h because this is the flow rate at which this chip is used. Water was used as a calibration liquid. The total acquisition time was 15 min, with one data point obtained at every 30 s. Tests were performed with and without the chip and three replicates were performed for each method. All the results, including the average of the replicates, are presented in Figure 13.

The results in Figure 13 were consistent for the two methods used. The uncertainties values were very similar for the two methods, being higher for the front track method, probably due to the short acquisition time arising from the limitations of the capillary used.

4 Methods validation

To validate the methods developed, especially the interferometric method that gives a smaller uncertainty and can go down to 0.1 µL/h, IPQ participated in EURAMET project 1508. The results for the calibration of a Cetoni precision pump are presented in Figure 14 (EURAMET, 2022). The results of IPQ are consistent with the reference value, which was estimated based on the weighting mean of all participants at all points.

5 Methods comparison, applications, advantages and limitations

In Figure 15 is possible to see summarizes the range of application and uncertainty of the methodologies developed in the scope of this work for flow measurements.

The developed interferometric method demonstrated exceptional performance, enabling flow measurements as low as 0.1 µL/h with uncertainty values below 2%. It is compatible with any flow generator equipped with an external motor, where the pusher block and the interferometer reflector cube are added (e.g., Nexus syringe pump). However, despite its precision, the method can be costly to implement in a laboratory setting due to the high price of the required instrumentation. Additionally, successful deployment necessitates specialized technical knowledge in interferometry.

The front track method offers a viable option for measuring flow rates as low as 0.1 µL/h across various flow generators, flow meters, insulin pumps and microfluidic chips. However, the method currently exhibits high uncertainty levels. To improve accuracy, testing with smaller capillaries is recommended, as this could reduce the measurement range and extend testing time—potentially achieving acceptable uncertainty levels between 2% and 3%. Despite its limitations, the method is characterized by its ease of implementation, straightforward handling procedures, and low cost.

In this work, the gravimetric method was successfully extended to measure flow rates down to 10 µL/h, compared to the previous limit of 100 µL/h. However, there remains potential for further improvement in both measurement range and uncertainty. This method is compatible with any flow generator, flow meter, or microfluidic device that work down to 10 µL/h, though it generally exhibits higher uncertainty than the interferometric method. Similar to the front track method, it is easy to implement and operate, and it involves relatively low costs.

The pending drop method also presents significant potential for improvement, particularly in controlling evaporation, which currently contributes to higher uncertainty values compared to the interferometric, gravimetric, and front track methods. Additionally, its operational range is more limited. Nevertheless, the method is highly versatile, suitable for use with many microfluidic or flow measurement device that work up to 100 µL/h. It is also easy to use and cost-effective to implement in a laboratory setting.

6 Conclusion

The implementation of the methodologies explored in this work was designed to enable the calibration of various types of instruments with different characteristics, such as precision syringes, perfusion syringes, microchips, and flowmeters, which are commonly used in the health and pharmaceutical industries as well as in microfluidic technologies. This calibration is crucial for ensuring the accuracy and reliability of these instruments.

It is essential that this information is disseminated not only to the scientific community but also to the medical and biomedical communities. Sharing these findings with healthcare professionals and researchers can foster collaboration and innovation, leading to further advancements in medical technology and practices. Additionally, manufacturers of medical instruments and other flow devices should be informed of these methodologies to ensure that their products meet the highest standards of accuracy and reliability.

In this work, the gravimetric method was improved for microflow measurements but there is still room for improvement. Three new methods were developed, and microfluidic chips were manipulated and tested for the first time at IPQ-LVC.

The interferometric method had the best performance regarding all methods tested but has some limitation in the type of instrument used (it must have an external motor) and cost of installation. The front track method is a good option that can be used for any type of flow measuring instrument or microfluidic device but more work is needed in order to decrease the uncertainty. The pending drop method has the worst performance of the four methods but is easy to use and low-cost i2mplementation.

All methods were internally validated by comparison with each other in the calibration of several flow measuring instruments.

This work served as the basis for the development of the EURAMET Guide CG-27, “Guidelines for the Calibration of Drug Delivery Devices and Infusion Device Analysers” (EURAMET guide cg 27, 2024). This document provides standardized procedures for testing microflow and nanoflow instruments aiming to improve the accuracy and comparability of measurement results Additionally, it contributed to the publication of the new EURAMET Technical Guide 4, “Evaluation of Flow-Related Quantities in Microfluidic Devices (EURAMET, 2024), but despite advancements in flow measurement techniques, challenges remain, particularly in microfluidics applications such has organ-on-chip. Ensuring traceability and accuracy at these scales requires ongoing research and development.

The development of standardized calibration methods and advanced measurement techniques for validating manufacturing, performance, and safety are essential in shaping the future of healthcare and microfluidic technology. The new EPM MFMET II project aims to fill these gaps by developing protocols and guidelines to support standardization efforts (Mfmet.eu, 2025).

Metrology is a key enabler of innovation and patient safety in healthcare. By ensuring the accuracy and reliability of drug delivery systems and diagnostic devices, like organ-on-chips, metrology helps reduce errors, enhance treatment efficacy, and save lives.

Going forward, standardized calibration methods, advanced measurement techniques, and collaborative research will be essential in shaping the future of healthcare technology.

Data availability statement

The data analyzed in this study is subject to the following licenses/restrictions: No restrictions. Requests to access these datasets should be directed to ebatista@ipq.pt.

Author contributions

EB: Conceptualization, Investigation, Methodology, Validation, Visualization, Writing – original draft. RM: Supervision,

Writing – review and editing. VS: Investigation, Resources, Validation, Writing – review and editing. IG: Writing – review and editing.

Funding

The author(s) declare that financial support was received for the research and/or publication of this article. The EMPIR and EPM projects "18HLT08 MeDD2" and "24NRM03 MFMET II" have received funding from the EMPIR and EPM programme co-financed by the Participating States and from the European Union's Horizon 2020 research and innovation programme.

Acknowledgments

The EMPIR projects "18HLT08 MeDD2" and "24NRM03 MFMET II" have received funding from the EMPIR and EPM programme co-financed by the Participating States and from the European Union's Horizon 2020 research and innovation programme.

Conflict of interest

The authors declare that the research was conducted in the absence of any commercial or financial relationships that could be construed as a potential conflict of interest.

The author(s) declared that they were an editorial board member of Frontiers, at the time of submission. This had no impact on the peer review process and the final decision.

Generative AI statement

The author(s) declare that Generative AI was used in the creation of this manuscript. The AI tool was used for text improving.

Publisher's note

References

Alvares, M. (2020). Implementação de um sistema de medição de microcaudais com recurso a métodos óticos (Master Thesis in Mechanical Engineering, FCT/UNL).

Batista, E. (2022). Calibration methodologies of microflow measuring instruments (PhD Thesis in Mechanical Engineering, FCT/UNL).

Batista, E., Álvares, M., Martins, R., Ogheard, F., Geršl, J., and Godinho, I. (2023). Measurement of internal diameters of capillaries and glass syringes using gravimetric and optical methods for microflow applications. *Biomed. Eng./Biomed. Tech.* 68 (1), 29–38. doi:10.1515/bmt-2022-0033

Batista, E., Alves e Sousa, J., Cardoso, S., and Silvério, V. (2020b). Experimental testing for metrological traceability and accuracy of liquid microflows and microfluidics. *Flow Meas. Instrum.* 71, 101691. doi:10.1016/j.flowmeasinst.2020.101691

Batista, E., Mendes, R., Furtado, A., Ferreira, M. C., Godinho, I., Sousa, J. A., et al. (2020). Calibration of syringe pumps using interferometry and optical methods. *Int. J. Biomed. Biol. Eng.* 14, 10.

Batista, E., Furtado, A., Pereira, J., Ferreira, M., Bissig, H., Graham, E., et al. (2020a). New EMPIR project - metrology for drug delivery. *Flow Meas. Instrum.* 72, 101716. doi:10.1016/j.flowmeasinst.2020.101716

Batista, E., Godinho, I., Martins, R. F., Mendes, R., and Robarts, J. (2020). Development of an experimental setup for microflow measurement using interferometry. *Flow Meas. Instrum.* 75, 101789. doi:10.1016/j.flowmeasinst.2020.101789

Batista, E., Silverio, V., Romieu, K., Alves e Sousa, J., and Daugbjerg, T. (2024). Development of measurement procedures for volume and flow related quantities in microfluidic devices. *Sensors*, 101551. doi:10.1016/j.measen.2024.101551

Batista, E., Sousa, J. A., Alvares, M., Afonso, J., and Martins, R. (2021). Development of an experimental setup for micro flow measurement using the front tracking method. *Meas. Sensors* 18, 100152. doi:10.1016/j.measen.2021.100152

BIPM, IEC, IFCC, ILAC, ISO (2008). IUPAC, IUPAP, and OIML. Evaluation of measurement data | Guide to the expression of uncertainty in measurement. Joint Committee for Guides in Metrology. *JCGM* 100.

BIPM, IEC, IFCC, ILAC, ISO, IUPAC, IUPAP (2012). International vocabulary of metrology | Basic and general concepts and associated terms (VIM). Joint Committee for Guides in Metrology. *JCGM*. 200

Bissig, H., Batista, E., Lucas, P., Filipe, E., Almeida, N., Ribeiro, L., et al. (2015). Primary standards for measuring flow rates from 100 nl/min to 1 ml/min – gravimetric principle. *Biomed. Eng.* 60 (4), 301–316. doi:10.1515/bmt-2014-0145

EURAMET (2024). EURAMET Technical Guide 4 - Evaluation of flow related quantities in microfluidic devices.

EURAMET guide cg 27 (2024). EURAMET guide cg 27 - guidelines for the calibration of drug delivery devices and infusion device Analysers.

EURAMET (2022). Pilot study intercomparison of ultra-low liquid flow rates in range below 100 nL/min. Available online at: https://www.euramet.org (Accessed March 13, 2022).

Mfmet.eu (2025). Mfmet.eu

Sousa, J. A., Batista, E., Demeyer, S., Fischer, N., Pellegrino, O., Ribeiro, A., et al. (2021). Uncertainty calculation methodologies in microflow measurements: comparison of GUM, GUM-S1 and Bayesian approach. *Measurement* 181, 109589. doi:10.1016/j.measurement.2021.109589

Characterization of passive components for use in a precision integrating analogue-to-digital converter

O Power[1], G McMahon[1], S Prendergast[1], V Cabral[2], L Ribeiro[2], N Beev[3,4] and R Lapuh[5]

[1] National Standards Authority of Ireland, Glasnevin, Dublin, D11 E527, Ireland
[2] Instituto Português da Qualidade, Rua António Gião,2, 2829-513 Caparica, Portugal
[3] High Precision Measurements Section, Electrical Power Converters Group, Accelerator Systems Department, CERN, Esplanade des Particules 1, CH-1211 Geneva, Switzerland
[4] Institute of Electrical Engineering, Faculty of Electrical Engineering and Information Technology, Slovak University of Technology in Bratislava, Ilkovicova 3, 841 04 Bratislava, Slovakia
[5] Left Right s.p., Ulica bratov Učakar 40, 1000 Ljubljana, Slovenia

Corresponding Author: vcabral@ipq.pt

Abstract – This paper presents a comprehensive characterization of precision passive components used in the design of integrating analogue-to-digital converters (IADCs). The tests are focussed on ceramic capacitors and metal foil resistor networks, evaluating their dependence on temperature and humidity, as well as dielectric absorption effects. The work is motivated by the necessity for metrological traceability of the measured characteristics of the key components within a narrow ambient range to meet the requirements of precision applications such as an IADC design.

Keywords: passive components, temperature coefficient, humidity sensitivity, dielectric absorption, IADC

1. Introduction

Integrating analogue-to-digital converters (IADCs), also known as charge-balancing ADCs, are widely recognized for their high accuracy in DC and low-frequency measurements [1, 2]. While most ADCs are realized monolithically, the highest-performance IADCs are built from discrete components whose imperfections (nonlinearity, drift, dielectric absorption) limit the achievable accuracy [3, 4].

To improve ADC modelling and performance prediction, accurate characterisation of passive components is essential. Manufacturers often provide specifications over wide temperature ranges (commercial, industrial, military), while metrology and precision devices operate in controlled environments with narrower variations of temperature and humidity. In this regime, actual component performance can exceed datasheet expectations, especially for temperature-compensated devices like NP0 capacitors and metal foil resistors [5], where non-linear temperature behaviour is common.

Additionally, humidity poses a more significant and difficult-to-control influence compared to temperature. Humidity variations often dominate measurement error on hourly to daily timescales, thereby influencing recalibration schedules. Traceability and detailed performance knowledge are essential due to manufacturing and batch variation.

This work evaluates several surface-mount capacitors and resistor networks [6] under controlled environmental conditions, including detailed dielectric absorption studies.

2. Influence of temperature and humidity on components

2.1. Capacitor Temperature Dependence

Tests were performed on 470 pF ceramic C0G (NP0) capacitors in 1206 packages from two manufacturers, including different batches.

The capacitor under test was fitted in a specially fabricated, spring-loaded fixture which allows a three-terminal measurement of its capacitance (figure 1). The fixture was placed in a climatic chamber whose temperature and humidity can be varied. The capacitance was measured using an accurate, high resolution, digital bridge. Temperature and humidity measurements were made over the ranges 23 to 43 °C and 40 %rh to 80 %rh respectively. Figure 2 shows a photograph of the test setup with the main components labelled.

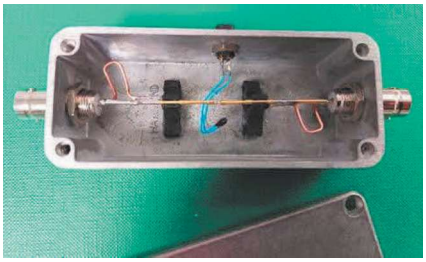

Figure 1. Capacitance Test fixture.

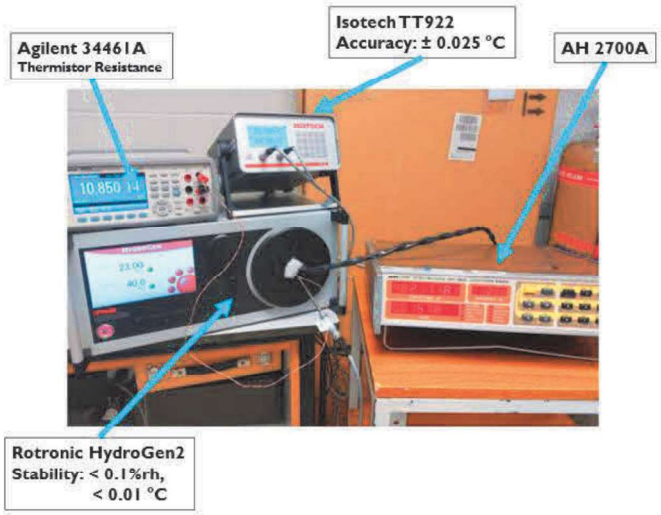

Figure 2. Test setup for the measurement of the temperature and humidity sensitivities of capacitors.

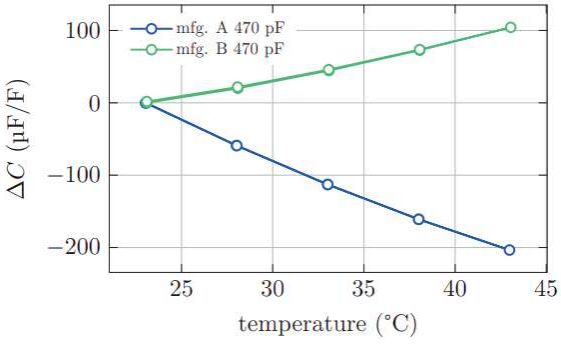

Figure 3. Capacitor temperature dependence.

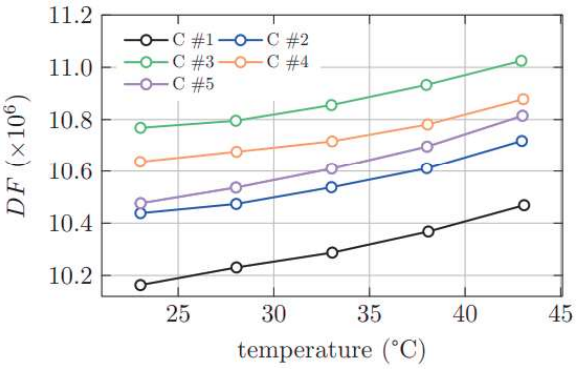

Figure 4. Capacitor dissipation factor temperature dependence for five samples from mfr. B.

The temperature was varied from 23 °C to 43 °C and back in 5 °C steps, with 1 hour stabilization at each level. Capacitance was recorded using a high-resolution digital bridge. Figure 3 plots the observed capacitance variation. A quadratic temperature model was fit to the data. Table 1 summarizes the observed temperature coefficients and inter-sample variability.

Table 1. Temperature Coefficients @ 23 °C - sample means and relative standard deviations (σ).

Manufacturer	No. of samples	Mean TC @ 23 °C (K^{-1})	σ (K^{-1})
A (batch 1)	10	-12.2×10^{-6}	0.25×10^{-6}
A (batch 2)	4	-12.6×10^{-6}	0.14×10^{-6}
B	5	$+3.1 \times 10^{-6}$	0.57×10^{-6}

The dissipation factor (loss component) was also monitored across temperature, showing measurable variation for all samples (see figure 4).

2.2. Capacitor Humidity Dependence

Humidity was varied from 40 %rh to 80 %rh and back at 23 °C. Capacitance showed increasing sensitivity with higher humidity and noticeable hysteresis (see figure 5). A short-term step test (40 %rh to 80 %rh, 8 hours duration) was used to reveal variation between manufacturers and batches. Figure 6 plots capacitance dependence on humidity for five capacitors from a batch of five manufacturer B 470 pF capacitors. The response of devices from manufacturer A to humidity changes was found to be considerably smaller and more consistent.

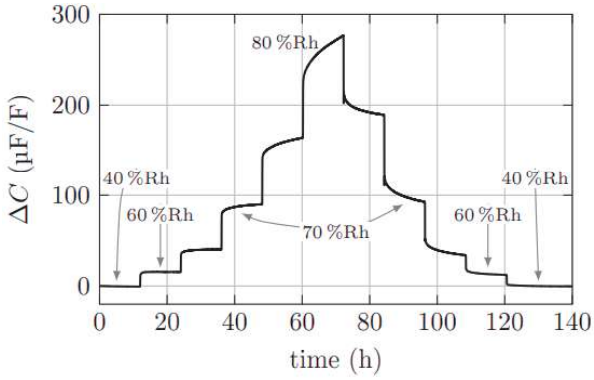

Figure 5. Capacitor humidity dependence.

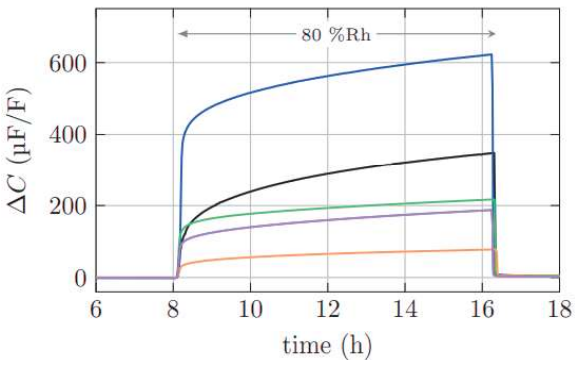

Figure 6. Variability of capacitor humidity dependence.

2.3. Resistor Network Temperature Characterization

Metal foil resistor networks were tested for their ratio stability under temperature and humidity variations. These components are frequently used in high-accuracy analogue front-ends due to their excellent ratio tracking, thermal matching, and relatively compact form factors.

Figure 7. Test setup for the measurement of the thermal and humidity coefficients of the resistor networks ratio.

Figure 7 shows the setup used for the resistor networks testing where a climatic chamber provided the temperature and humidity cycling conditions and a low-thermal quad scanner (16 input channels) allowed the simultaneous test of several resistor networks whose ratio was measured by a high resolution-multimeter.

The core measurements were performed using the ohms ratio function of a high-resolution multimeter (Figure 8 shows a schematic of the setup). This function allows sequential two-channel measurements and outputs the resistance ratio directly, offering a balance between precision and test efficiency. Unlike resistance bridges, which can offer superior absolute accuracy, the multimeter facilitates rapid, repeatable measurements over long-duration environmental sweeps. When both input channels operate in the same range, measurement uncertainty is dominated by short-term noise and ADC linearity. To suppress thermoelectric voltages, particularly critical during temperature ramps, the “true ohm” function was employed. This mode averages bidirectional current measurements to cancel polarity-dependent offsets.

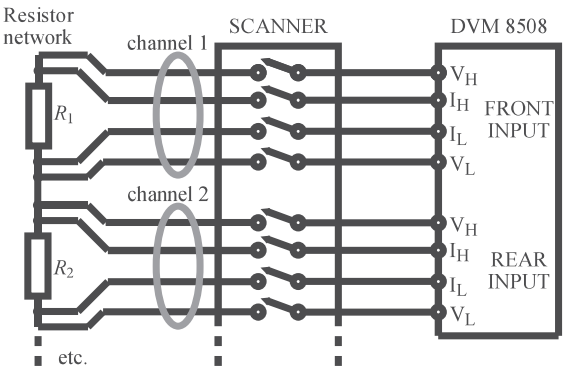

Figure 8. Resistor networks test setup.

A validation test using two matched 10 kΩ standards over six days in a temperature-controlled bath produced 337 data points. The resulting relative standard deviation of the individual measurements was 9×10^{-8}, decreasing with $\sqrt{n}$ (n is number of points) for the mean. This establishes the intrinsic resolution and repeatability limits of the setup. A validation of the observed readings showed that white noise with Gaussian distribution can be assumed for periods of approximately 14 hours of continuous measurements.

Three resistor networks with the same nominal ratio 1:1 were characterized:

- R_1 10 kΩ / 10 kΩ Hermetic 3-pin (through-hole)
- R_2 4 x 10 kΩ Plastic 8-pin (surface-mount)
- R_3 10 kΩ / 10 kΩ Plastic 3-pin (surface mount)

Resistors were cycled from 15 °C to 45 °C and back in 10 °C steps at 50 %rh, with a stabilisation period between 12 and 14 hours at each plateau. Initial preconditioning at 15 °C and 50 %rh for approximately 2.5 days ensured thermal and moisture equilibrium. At each temperature step, ~40 consecutive measurements were taken after the system stabilized. This approach excluded transient effects and ensured representative statistics for each condition.

Figure 9 shows the variation of the ratio with temperature for R_1 and R_2. A slight hysteresis between ascending and descending cycles was observed, attributed to thermal lag or material relaxation. Mean values of the ratio errors (δr) and their standard deviations (σ) are summarized in Table 2.

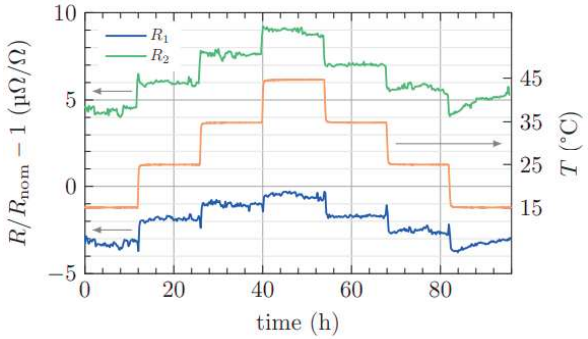

Figure 9. Observed variation of resistance ratio with temperature for two different resistor networks, where the nominal ratio was 1:1.

Table 2. Mean value and standard deviation of the mean for the relative error of the measurement ratio.

T (°C)	$\delta r(R_1)$ (μΩ/Ω)	σ (μΩ/Ω)	$\delta r(R_2)$ (μΩ/Ω)	σ (μΩ/Ω)	$\delta r(R_3)$ (μΩ/Ω)	σ (μΩ/Ω)
15	–3.31	0.02	4.36	0.03	–27.22	0.04
25	–1.85	0.02	5.99	0.02	–27.25	0.03
35	–1.06	0.02	7.59	0.02	–28.01	0.03
45	–0.48	0.02	8.95	0.02	–28.47	0.03
35	–1.71	0.01	7.02	0.01	–28.60	0.01
25	–2.53	0.02	5.75	0.02	–27.80	0.03
15	–3.30	0.02	4.96	0.03	–26.81	0.03

The calculated relative thermal coefficients (TC) of the ratios, obtained by linear regression, were as follows:

- R_1: Slight positive TC (~ $+0.09\times10^{-6}$ K^{-1})
- R_2: More pronounced positive TC (~ $+0.14\times10^{-6}$ K^{-1})
- R_3: Negative TC of -0.05×10^{-6} K^{-1}

These trends indicate that while all resistors show predictable, smooth drift, the "dual-in-line" isolated resistor network, R_2, exhibits more thermal sensitivity compared to the 3-pin voltage divider type, R_1 and R_3. Moreover, the hermetic and plastic packaged devices show the same order of magnitude for the absolute value of TC tracking.

2.4. Resistor Network Humidity Characterization

To isolate the influence of humidity, the relative humidity was swept from 10 %rh (initial conditioning) to 80 %rh and back in 20 %rh steps at a constant 25 °C. Each step involved 14 h stabilization. Like in the thermal tests, ~40 readings were averaged per level.

Results shown in figure 10 reveal that R_1 is largely immune to humidity effects, with a very small coefficient of 0.003×10^{-6} / %rh, one order of magnitude below the noise of the measurements. This fact highlights the protective advantage of hermetic packaging. In contrast, R_2 displayed (and R_3 not shown) monotonic ratio drifts (0.03×10^{-6} / %rh and -0.05×10^{-6} / %rh, respectively), consistent with moisture absorption and dielectric changes in plastic-encapsulated packages.

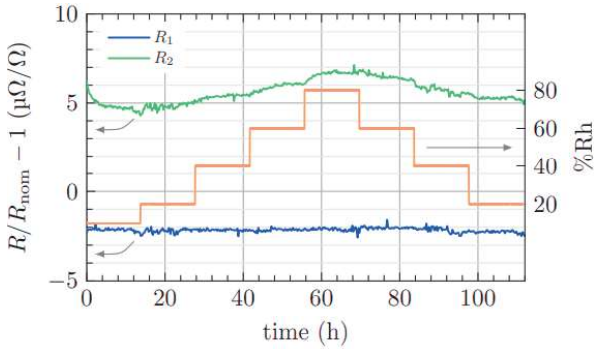

Figure 10. Resistor ratio error as a function of humidity.

R_3 showed a humidity coefficient matching its thermal coefficient, suggesting a similar magnitude of environmental influence. Full results are tabulated in Table 3.

It is worth noting that the manufacturer specifications of the tested devices do not provide information related to this sensitivity to humidity, but only a climatic test for the effect of prolonged exposure to high humidity levels.

Table 3. Mean value and standard deviation of the mean for the relative error of the measurement ratio.

RH (%rh)	$\delta r(R_1)$ (μΩ/Ω)	σ (μΩ/Ω)	$\delta r(R_2)$ (μΩ/Ω)	σ (μΩ/Ω)	$\delta r(R_3)$ (μΩ/Ω)	σ (μΩ/Ω)
20	–2.22	0.02	4.78	0.02	–26.68	0.05
40	–2.17	0.01	5.41	0.01	–28.25	0.02
60	–2.14	0.01	5.95	0.02	–29.12	0.01
80	–2.12	0.01	6.71	0.01	–29.43	0.02
60	–2.03	0.01	6.44	0.01	–27.96	0.03
40	–2.20	0.03	5.65	0.03	–27.19	0.03
30	–2.24	0.01	5.29	0.01	–26.48	0.01

3. Dielectric Absorption and modelling

Dielectric absorption was measured using the standard charge-discharge protocol per IEC 60384-1 [7]. Figure 11 shows a schematic of the test setup.

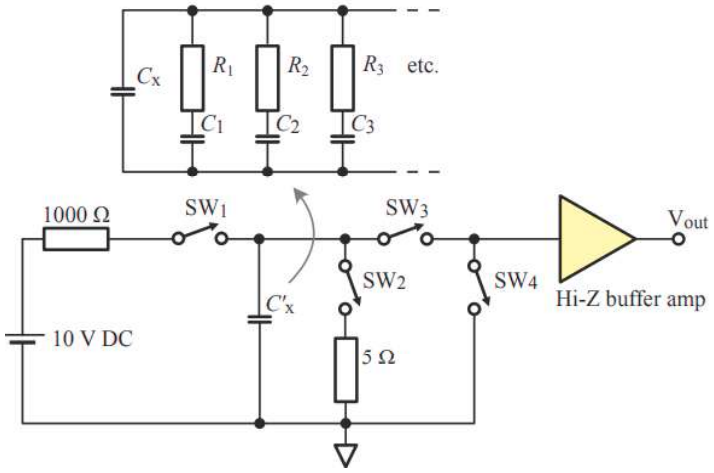

Figure 11. Dielectric absorption test setup.

Capacitors were charged to 10 V for 900 s via relay SW1, discharged for 1 s via relay SW2, then allowed to recover with relay SW3 closed. Recovery voltage was monitored for 990 s using an electrometer-buffered DMM.

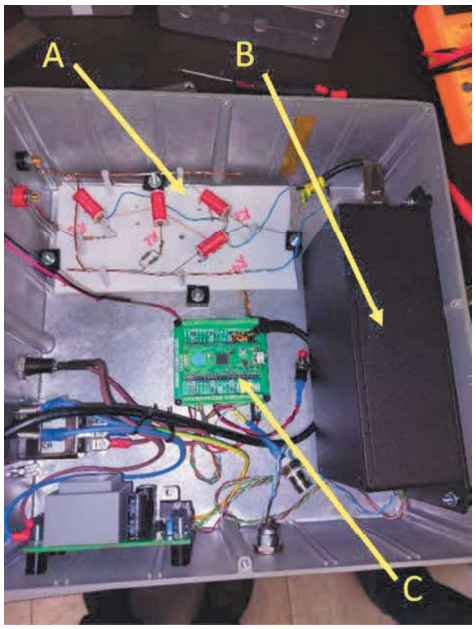

Figure 12. Relay board (A), buffer amplifier (B) and control board for dielectric absorption measurements.

An important requirement of the setup was the minimization of the effects of leakage across the test capacitor and of the bias current generated by the buffer amplifier. Low leakage, glass encapsulated relays mounted on a PTFE base were used. A high impedance, low bias current buffer amplifier using a ADA4530-1 electrometer op amp was constructed. Connection to the test fixture is via a triaxial connection. The op-amp's guard voltage is used to minimize leakage in the input cable and to drive the relay guards. The amplifier is housed in a shielded case to reduce noise. The bias current of the buffer amplifier was measured and found to be less than 5 fA. An external DC source is used to charge the capacitor. The output of the buffer amplifier (i.e. the recovery voltage) was measured using a Fluke 8588A multimeter.

The relay board (A), buffer amplifier (B) and the relay control board (C) were mounted in an earthed metal enclosure as shown in figure 12 where the top cover of the enclosure has been removed.

Recovery curves for five samples from each manufacturer were averaged across seven runs (see figure 13). The magnitude of the dielectric absorption effect, defined as the recovery voltage at 990 s divided by the charging voltage, ranged from 1.0 % to 1.6 %. Typical type A standard uncertainty was 0.05 %.

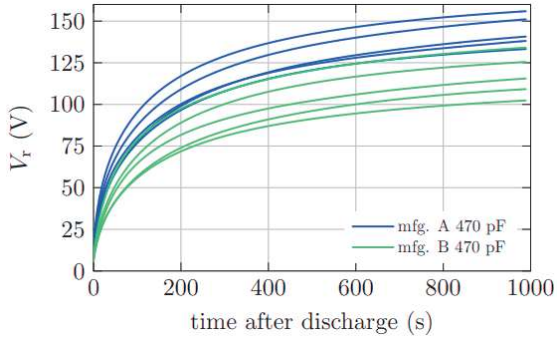

Figure 13. Observed voltage recovery profiles.

A model using five parallel RC branches (see figure 11) was used to fit the data [8, 9]

$$V_{rec}(t) = \sum_{i=1}^{5} V_i \left(1 - e^{\frac{t}{R_i C_i}}\right) \quad (1)$$

Fitted component values are listed in Table 4.

Table 4. RC model components obtained by fitting to the recovery voltage.

Component Nr.	R_i (TΩ)	C_i (pF)
1	82.5	1.780
2	255.0	2.410
3	25.6	1.620
4	18.1	0.571
5	16.1	0.031

4. Conclusion

The results show the variation in temperature and humidity sensitivities of capacitors and resistor networks, both between and within manufacturers and batches. These differences are especially relevant for precision IADC applications where ambient control and stability are assumed.

For some devices humidity was found to induce larger and more variable effects than temperature, which would require frequent recalibration of any IADC in which they are used. Dielectric absorption in ceramic capacitors was measured with high resolution and modelled using a five-element RC network, offering a useful tool for IADC design simulations.

Accurate and traceable component data are essential to predict and mitigate error mechanisms in high-performance digitizers. As component quality improves, the limitations of legacy test measurement procedures must also be addressed.

5. References

[1] Goeke W C 1989 An 8½ digit Integrating ADC with 16-bit 100,000 per second performance *HP Journal* 8-14

[2] Beev N 2018 Analog-to-digital conversion beyond 20 bits IEEE Intern. Instrum. and Meas. Tech. Conf. (I2MTC) Houston TX USA 1-6

[3] Buchanan J E 1975 Dual-Ramp A/D Converter Error Due to Nonideal Integrator Capacitor *IEEE Trans. on Instrum. and Meas.* **24** no. 1 33-39

[4] Michaeli L, Šaliga J, Buša J, Dolinskỳ P and Andráš I 2016 Influence of the capacitor's dielectric absorption on the dual slope ADC *IMEKO TC4 Intern. Symp.* Budapest

[5] Yarborough B 2020 *White Paper - Temperature coefficient of resistance for current sensing – how temperature and construction affect resistance stability* Vishay Doc. 30405

[6] IEC 60115-1 2020 Fixed resistor for use in electronic equipment – Part 1: Generic specification

[7] IEC 60384-1 Fixed capacitors for use in electronic equipment – Part 1: Generic specifications

[8] Dow P C 1958 Analysis of certain errors in electronic differential analyzers *IRE Trans. Electr. Comp*. 17-22

[9] Iorga C 2000 Compartmental Analysis of Dielectric Absorption in Capacitors *IEEE Trans. on Diel. and Elec. Insul.* **7** no. 2 187-192

Acknowledgement

The project 22RPT02 True8DIGIT has received funding for the European Partnership on Metrology. Co-financed from the European Unions' Horizon Europe Research and Innovation programme and by the Participating States. The UK participant in Horizon Europe Project 22RPT02 True8DIGIT is supported by UKRI grant number 10,084,012 (Signal Conversion Ltd).

metrology

MDPI

Article

Comparison of Measurement Protocols for Internal Channels of Transparent Microfluidic Devices

Joris Kaal [1], Nicolas Feltin [2], Marc Lelong [2], Huabing Yin [3], Andrew Glidle [3], Kevin Romieu [4] and Elsa Batista [5,*]

1 CEA-Leti, Commissariat à l'Énergie Atomique et aux Énergies Alternatives, Université Grenoble Alpes, F-38000 Grenoble, France; joris.kaal@cea.fr
2 Laboratoire National de Métrologie et d'Essais-Nanometrology, CEDEX, 78197 Trappes, France; nicolas.feltin@lne.fr (N.F.); marc.lelong@lne.fr (M.L.)
3 Division of Biomedical Engineering, School of Engineering, University of Glasgow, Glasgow G12 8LT, UK; huabing.yin@glasgow.ac.uk (H.Y.); andrew.glidle@glasgow.ac.uk (A.G.)
4 CETIAT, Centre Technique des Industries Aérauliques et Thermiques, F-69603 Villeurbanne, France; kevin.romieu@cetiat.fr
5 Metrology Department, Portuguese Institute for Quality (IPQ), 2829-513 Caparica, Portugal
* Correspondence: ebatista@ipq.pt; Tel.: +351-212948167

Abstract: The microfluidic industry faces a significant challenge due to the lack of sensitive and standardized methods. One critical need is the measurement of internal channel dimensions in fully assembled chips. This study presents and compares several protocols for measuring these dimensions, including optical profilometry, optical microscopy, and tiled digital imagery. Standardized chips made from two materials commonly used in microfluidics (borosilicate glass and Cyclic Olefin Copolymer) were evaluated using each protocol. A consistency analysis using normalized error statistics identified optical profilometry as the most reliable method, offering the lowest uncertainty and the highest consistency with nominal geometry values. However, all protocols encountered difficulties with vertical depth measurements of internal structures. Future research should focus on addressing these limitations, including investigating the influence of multiple refractive surfaces on optical profilometry and exploring confocal microscopy. In conclusion, this work provides a comprehensive comparison of measurement protocols for internal microfluidic structures and offers a practical solution for applications in the microfluidic industry, while also identifying important directions for future research.

Keywords: microfluidic chips; optical measurements; channels dimensions; methods validation

Academic Editors: Michele Norgia, Rahul Kumar and Han Haitjema

Received: 2 September 2024
Revised: 4 December 2024
Accepted: 6 January 2025
Published: 10 January 2025

Citation: Kaal, J.; Feltin, N.; Lelong, M.; Yin, H.; Glidle, A.; Romieu, K.; Batista, E. Comparison of Measurement Protocols for Internal Channels of Transparent Microfluidic Devices. *Metrology* **2025**, *5*, 4. https://doi.org/10.3390/metrology5010004

1. Introduction

Microfluidics has long held the potential to disrupt a wide range of fields [1–3]. Aiming at the miniaturization of analytical and chemical methods [4], microfluidics continues to promise revolutionary advancements across many industries [5].

In recent years, the microfluidics industry has experienced remarkable growth, driven by applications such as chemical analysis, point-of-care diagnostics [6,7], and pharmaceutical research [8,9], including microphysiological systems [10,11]. The growth is projected to continue at a compound annual growth rate of 2.2% until 2028 [12].

Regardless of the application, the internal geometry of microfluidic channels is often crucial to the functionality of the device. For example, point-of-care diagnostic devices required precise dilution ratios, while microphysiological systems need physiologically

relevant shear stresses [13,14], both of which impose strict geometrical constraints on chip manufacturers.

Given the importance of the internal geometry to a device's functionality, it is crucial for the industry to be able to accurately characterize the internal dimensions of a chip. Microfluidic chips are often made of multiple structured layers that are sealed together to form the final product. While measuring the dimensions of the structure before assembly is feasible (for example, using optical microscopy or stylus profilometry), once sealed, the channels are encapsulated inside the chip. This makes their characterization more difficult due to material properties and physical constraints. This issue is significant because the assembly process can change the structure of the chip compared to its pre-assembled state, leaving both the manufacturer and the user uncertain about the actual geometry and dimensions of the flow circuit in use.

The industry itself has identified the lack of sensitive and standardized testing methods as one of the major hurdles preventing microfluidics from fulfilling its promises [15,16]. To help address this challenge, this work presents multiple protocols for measuring the internal dimensions of fully assembled transparent chips. The reproducibility and precision of each protocol are analyzed and compared. Both glass and polymer chips are used as substrates to evaluate the influence of material on measurement reproducibility.

The protocols described in this study enable automated, non-destructive, reproducible characterization of the internal geometry of transparent microfluidic chips after assembly, making them suitable for industrial applications. By removing the uncertainty caused by potential deformation during assembly, these protocols ensure that users can trust the devices they are using, and manufacturers can be confident in the quality of the chips they are providing.

Here, we describe the chip designs and different measuring techniques. The different sets of results are analyzed through consistency tests between the protocols and nominal values. Finally, we examined the influence of two different materials on dimension measurements.

2. Chips Geometries

Batches of chips were designed and manufactured using two different materials: D263©bio glass [17] (a common type of borosilicate glass) and COC (Cyclic Olefin Copolymer, tradename TOPAS© [18]). The chips made from each material have different internal dimensions and designs. The choice of geometries was based on different applications for these chips within the EURAMET 20NRM02 MFMET project [19] (MFMET–Establishing Metrology Standards in Microfluidic devices [20]). These tests mainly include leakage tests [21], flow resistivity tests [22], and the dimensional measurements described here.

All designs adhere to the ISO 22916:2022 standard on interoperability requirements for dimensions, connections, and initial classification of microfluidic devices [23]. This standard has a notable influence on the chips' footprint, as well as the positions and dimensions of their connections. This allows different participants to use the same connector and be confident that the chips were compatible with each other's measurement setup. In addition, these chips are intended to serve as transfer standards for other laboratories. By adhering to ISO 22916:2022, compatibility with laboratories outside the scope of this project will also be facilitated.

2.1. Glass Transfer Standard Chips

Eight designs (footprint 15 mm × 45 mm) were developed for glass chips (see Figure 1). Each design has one or several main channels, with some connected to one or multiple "leakage channels"—these are significantly smaller in cross-section compared to the main

channels, simulating a leak. All designs, except Design 08, include a reference channel (Channel 01 in Figure 1) that does not have any additional side channels. Figure 2 shows an example of Design 04 chips. Technical design drawings of these glass transfer standard chips are available in the Electronic Supplementary Information.

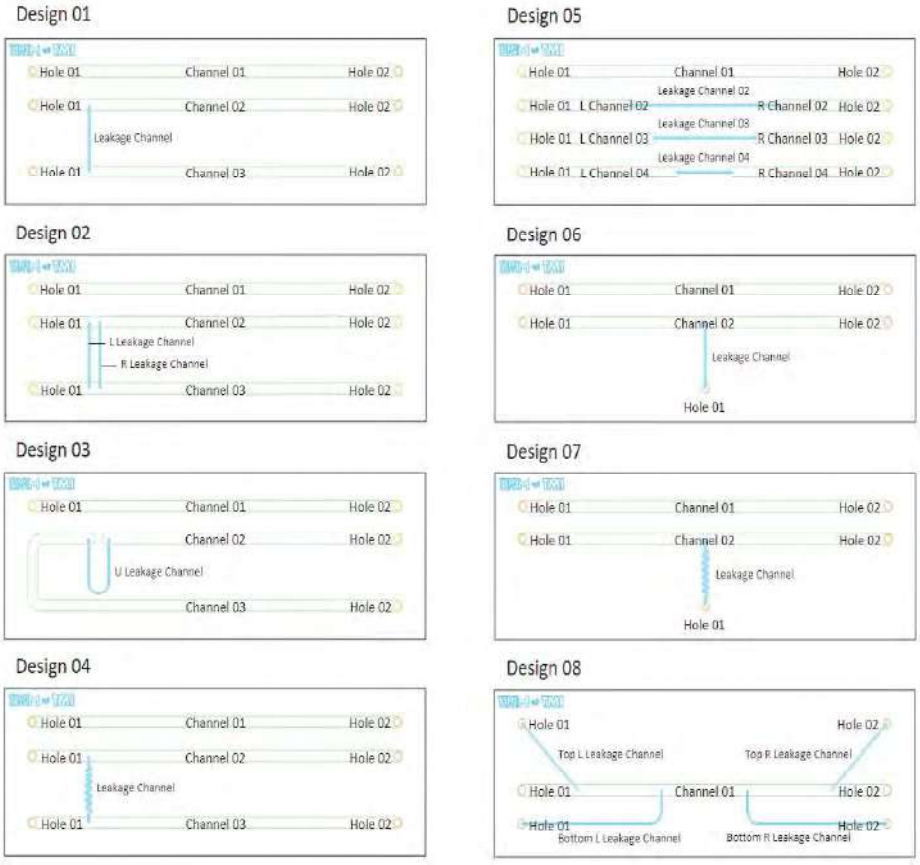

Figure 1. Different glass chip designs and their geometry nomenclature for measurements.

Figure 2. Example of a glass transfer standard chip, Design 04.

The glass chips were fabricated by IMT Masken und Teilungen AG, Greifensee, Switzerland, using D263©bio glass [17], via isotropic wet-etching techniques, employing hydrofluoric acid-based etching solutions commonly used in the semiconductor industry. The final chips consist of two halves that were individually fabricated and then bonded together. The critical dimensions of the device were verified during and after processing for quality assurance. For Designs 01 to 05, four chips were produced, while Design 06 and 07 had three chips each, and Design 08 had two. One chip from each design was reserved as a backup.

2.2. Polymer Transfer Standard Chips

The polymer transfer standard chip has the same footprint as a standard microscope slide and contains eight different designs on a single chip (see Figure 3). Each design consisted of two main channels with a "leakage channel". The leakage channels came in two distinct lengths: four designs had longer leakage channels, and the other four had shorter ones. The cross-section of the leakage channels is rectangular and varies between designs. Figure 4 shows an example of one of the polymer chips. Detailed designs, technical drawings, and CAD files of the polymer chip design can be found in the Electronic Supplementary Information.

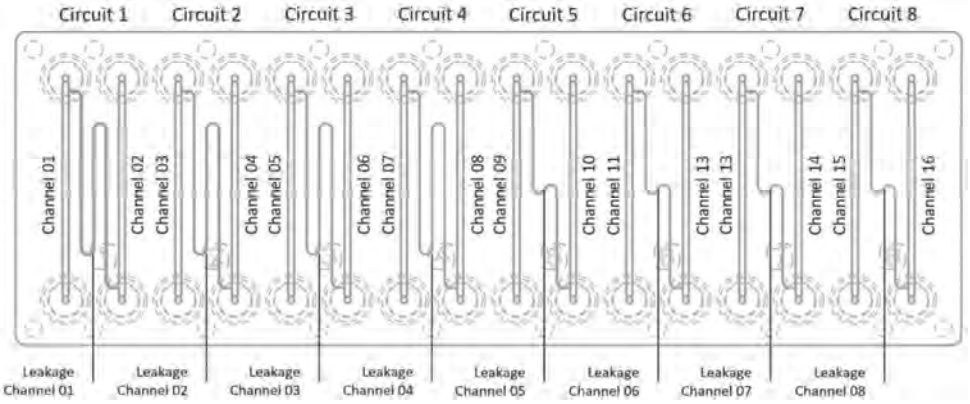

Figure 3. Polymer chip design and its geometry nomenclature for measurements.

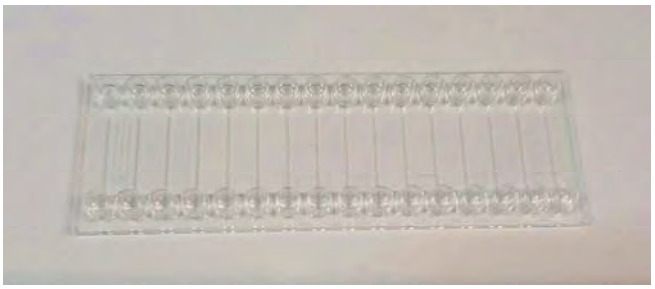

Figure 4. Example of a polymer transfer standard chip.

The polymer chips were produced by microfluidic ChipShop GmbH, Jena, Germany, using injection molding.

Once the fabrication process is complete, the top part containing the microfluidic structure is sealed onto a thin bottom slide to close the chip. The entire chip is made of COC (Cyclic Olefin Copolymer, tradename TOPAS© [18]).

3. Three Different Measurement Protocols

The different pieces of equipment used for the measurement protocols set out below are shown in Figure 5, with specifications given in Table 1.

Table 1. Specifications of the different instruments used for dimension measurements.

Instrument	Lens	Lighting	Calibration	Uncertainty Linked to Calibration
OGP SmartScope ZIP®250	×1 ×2	Substage LED profile Coaxial LED surface SmartRing™ LED ring light	Annual calibration report by OGP	In plane (XY): ±2 µm + 4 L/1000 Vertically (Z): ±2.5 µm + 5 L/1000 In-image: <1 µm

Table 1. *Cont.*

Instrument	Lens	Lighting	Calibration	Uncertainty Linked to Calibration
Olympus BX53M	×1.5 ×5 ×15	Substage tungsten bulb lighting	Test pattern (see Figure 5)	0.1%
Leica Wild M3Z	×2.56	Overhead LED ring light	Test pattern (see Figure 5)	2%
Nikon D5300	×1, f/2.8, 105 mm macro lens	Fluorescent tube lighting below sample	Test pattern (see Figure 5)	In-image: 0.45% On tiled images: 0.76%
Zeiss AxioObserver	×2.5	Transmission lighting from quartz halogen bulb	Test pattern (see Figure 5)	0.15%

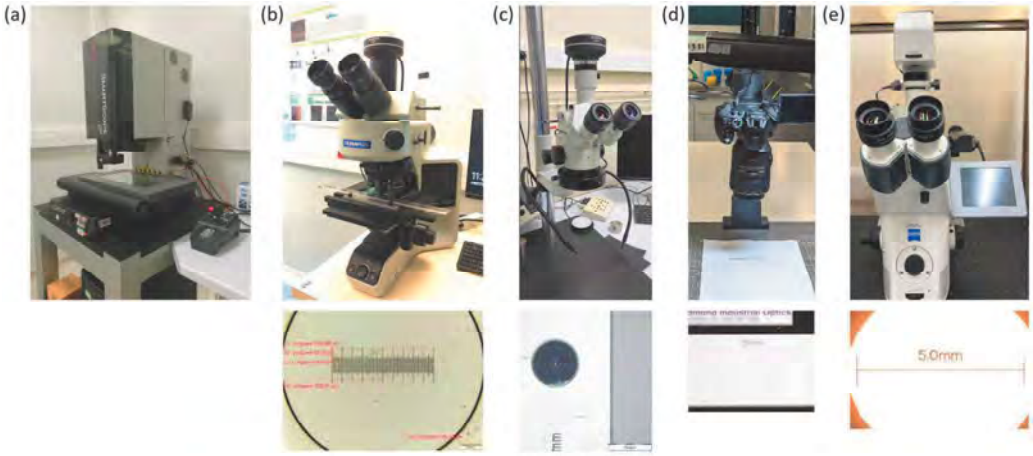

Figure 5. The different setups used for dimension measurements. (**a**) Optical profilometer OGP SmartScope ZIP®250. (**b**) Optical microscope Olympus BX53M with its calibration gauge. (**c**) Stereo binocular microscope Leica Wild M3Z with its calibration gauge. (**d**) Digital camera Nikon D5300 with its calibration gauge. (**e**) Optical microscope Zeiss AxioObserver with its calibration gauge.

Examples of the optical images obtained from each of the techniques are given in Figure 6, together with details showing which points in the images were used as reference criteria from which the measurement values were obtained.

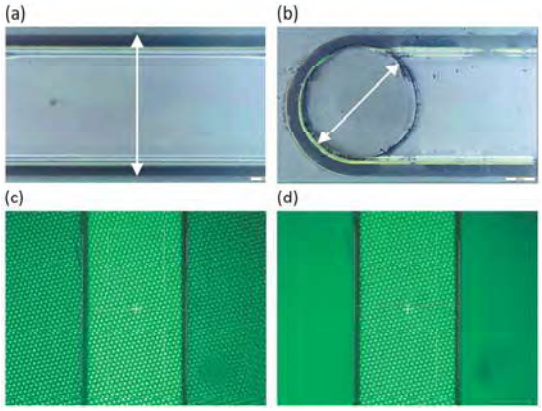

Figure 6. *Cont.*

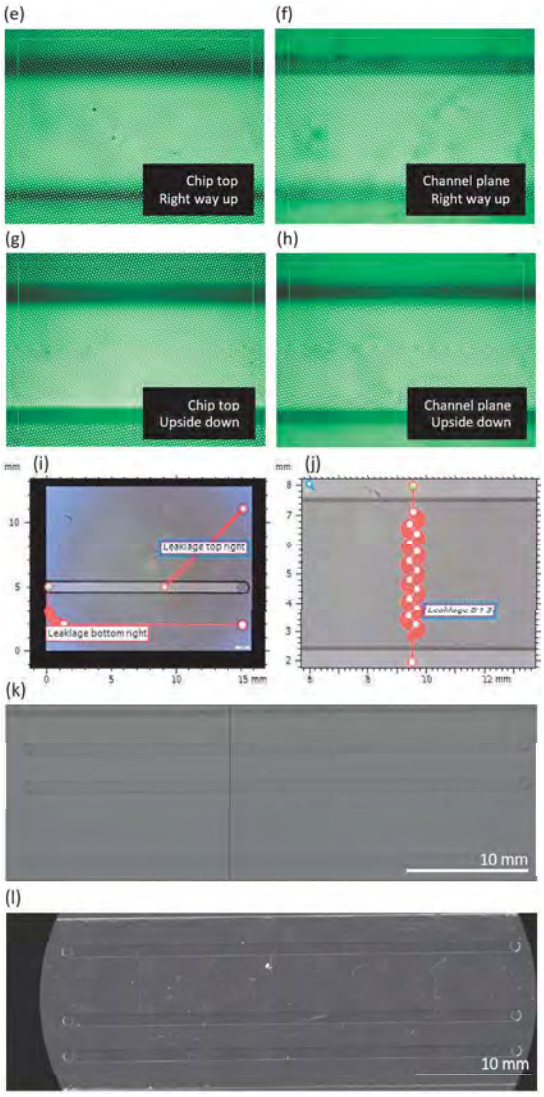

Figure 6. Definition of measurement points (images (**b**–**h**) from the Optical Profiler; (**i**) from the Leica Wild M3Z; (**j**) from the Olympus BX53M; (**k**) from the Nikon D5300; and (**l**) from the Zeiss AxioObserver). (**a**) The width of the channels is taken as the maximum width. (**b**) The diameter of the holes is measured by recognizing the internal hole features. (**c**) Point at the bottom Z-plane of the polymer channel. (**d**) Point at the top Z-plane of the polymer channel. (**e**) Point at the top plane of the glass chip when the chip is the right way up (see Section 3.1). (**f**) Point at the measurable channel plane of the glass chip when the chip is the right way up. (**g**) Point at the top plane of the glass chip when the chip is upside down (see Section 3.1). (**h**) Point at the measurable channel plane of the glass chip when the chip is upside down. (**i**) MountainsMap©'s "Distance between two points" and "Customized path" tools applied to Design 08. (**j**) MountainsMap©'s "Distance between two points" and "Customized path" tools applied to S-channel in design 04. (**k**) A stitched image of Design 01 created using the Nikon D5300 camera. (**l**) A stitched image of Design 04 created using the Zeiss AxioObserver with Ludl BioPoint2 stage showing the ability to discern the leakage channel (left hand side of image) when using higher NA optics.

3.1. Protocol 1: Optical Profilometry

The first protocol entails optical profilometry, a method that uses light instead of a physical probe to characterize geometries. This allows non-destructive measurements without direct contact with the object, making it particularly suitable for transparent substrates.

A SmartScope ZIP®250 (with its accompanying software, ZONE3©, both from Optical Gaging Products (OGP), part of Quality Vision International (QVI), Rochester, NY, USA)

was used to perform measurements of the internal geometries. Table 1 gives details of the instrument, and the setup is shown in Figure 5a.

The instrument is annually recalibrated by OGP staff, ensuring the accuracy shown in Table 1 (Calibration report available in the Electronic Supplementary Information). It is important to note the difference in uncertainty between measurements where the stage moves a distance, L, between two measured points and static in-image measurements.

The OGP SmartScope ZIP®250 can automatically focus on a plane within a user-defined margin. The software identifies geometrical features from the focused image and measures the dimension of interest. For example, to determine the width of a channel, the profilometer finds the focus plane at the top of the channel, identifies the outermost edges, and measures the width between these edges (see Figure 6).

Depth measurements proved to be more challenging, particularly in glass compared to polymer chips. For polymer chips, the depths of all channels were measured by determining focus planes at the top and bottom of the channel using the software's "Focus" tool, which establishes a 3D point on each plane. The software then calculates the channel depth by measuring the distance in Z-axis between these two points (Figure 6).

However, depth measurements inside transparent materials using optical profilometry are subject to distortion due to the material's refractive index, which depends on both material and the wavelength of light used to determine the focus plane. The SmartScope ZIP®250 uses grid light with a wavelength range from 575 nm to 625 nm. For polymer chips, a refractive index (RI) of n_D = 1.53 for 589 nm at 25 °C (provided by microfluidic ChipShop GmbH, Germany) was used to correct for the difference between and optical path length and physical distance measurement [24]; thus, all depth measurements in polymer chips were multiplied by n_D.

For glass, the optical profilometer struggled to differentiate between the focus planes at the top and bottom of the channels. Therefore, a more complex approach was used to estimate the channel depth. The profilometer could determine the top and bottom planes of the chip and one plane of the channel (Figure 6). The assumption was made that this plane belonged to the upper channel. In this method, when the chip is right-side up, the top of the chip, the top of the channel, and the bottom of the chip are measured. When the chip is flipped upside down, the bottom of the chip, the bottom of the channel, and the top of the chip are measured. The following formula was then used to estimate the depth of the channel:

$$D = ((z_{chnl,2} - z_{top,2}) - (z_{chnl,1} - z_{top,1})) \cdot n_D \quad (1)$$

where D is the estimated channel depth; z_(chnl,2) and z_(top,2) are the z-coordinates of the measurable channel plane and the top plane measured when the chip is upside down; z_(top,1) and z_(chnl,1) are the z-coordinates of the measurable channel plane and the top plane measured when the chip is right-side up; and n_D is the refractive index of D263©bio glass. Based on the OGP light wavelength range, a refractive index = 1.5230 for 589.2938 nm [25], provided by Schott AG, Germany, was used to correct for RI effects [17].

The length of the main channels was defined as the maximum distance between the inlet and outlet hole centers. Hole diameters were determined using the "Feature finder" tool, which measures the internal circumference of the holes (Figure 6). Leakage channel lengths were measured using start and end reference points taken from the mid-point of a line drawn across the intersection of the leakage channel with the wall of a main channel.

Measuring the lengths of more complex, non-linear channels (such as L-, U-, and S-shaped channels) posed difficulties. Despite multiple attempts using different settings and ZONE3© tools, no reproducible parameters were found.

All the above steps are programmable on the OGP SmartScope ZIP®250. This allows a specific measurement protocol—including positions, fields of view, focus zones, lighting,

and image processing settings—to be stored and repeated for identical objects. Once established, the measurement program was run three times on each chip.

Using the data from each run, an average and a standard deviation (s_r) were determined. Together with the uncertainty from the instrument's calibration (u_c), noted in Table 1, the standard uncertainty (u) of the measurement was calculated using the following formula:

$$u = \sqrt{u_c^2 + s_r^2} \quad (2)$$

The calculation assumes that these are the two largest sources of uncertainty. For the purpose of this article, variability in the refractive index was not considered, which could be investigated in future research.

3.2. Protocol 2: Optical Microscopy

The second protocol uses standard optical microscopy. Depending on the size of the microfluidic geometries, two different microscopes were employed: an optical microscope (Olympus BX53M) or a stereo binocular microscope (Leica Wild M3Z) was used. Details of both instruments are provided in Table 1.

Each instrument has its own calibration gauge structure (Figure 5), ensuring that measurement results are traceable to the International System of Units (SI). The uncertainties associated with the calibration of each instrument can be found in Table 1.

The width and length of the leakage channels, the width of the main channels, and the diameters of the holes were all measured using the Olympus BX53M (with the ×5 or ×10 lens). Images were taken and analyzed using Olympus Stream Essentials 2.3.3 (Build 17023). This software has the capability to continuously capture images and automatically detect different focal planes, creating a merged image where measurements were made.

Similar to the optical profilometer in Protocol 1, the largest dimension was used to define the channel width (Figure 6). The length of the main channels was measured as the maximum distance between the inlet and outlet holes, using the Leica Wild M3Z binocular microscope. The focal plane was manually adjusted for these measurements.

For hole diameter measurements, a circle tool was used. However, identifying the correct focal plane was difficult, as multiple focal planes were closely spaced. It was hypothesized to be due to the hole-drilling process during chip manufacturing. Several measurements were performed, and an uncertainty value was assigned to take into account the various focal planes and irregularities in the structure.

The length of non-linear channels (both main and leakage channels) was measured using specific tools from the MountainsMap© version 10 software package (from Digital Surf, France). Depending on the channel shape's complexity, either the "Distance between two points" tool or the "Customized path" tool was used (Figure 6). In both cases, the length was determined along the median line of the channel width.

As with Protocol 1, each chip was measured three times, and the results were used to calculate a standard uncertainty using the same approach.

3.3. Protocol 3: Tiled Digital Imagery

The third protocol uses two different instruments, both with a wide field of view: a Nikon D5300 digital camera fitted with a 105 mm, 1×, f/2.8 macro lens; and a Zeiss AxioObserver optical microscope equipped with a Ludl BioPoint2 motorized stage, Zeiss EC Plan Neofluar 2.5×/0.085 objective, and Zeiss HRc camera. Details of both devices are included in Table 1.

Digital cameras, such as the Nikon D5300, offer portability, affordability, and high resolution. Since they can detect events within entire microfluidic devices, they have been widely used with paper–microfluidic devices for on-site diagnosis [26,27] and high-speed

imaging and detection of events within microfluidic devices [28]. The Zeiss AxioObserver, similar to the microscope used in Protocol 2, provides more precise measurements.

Both instruments were calibrated using standard reference bars (Figure 6), which allowed for the determination of the resolution of the instruments and the uncertainty linked to calibration (Table 1). The calibration report is available in the Electronic Supplementary Information.

In this protocol, measurements were made using image processing. For hole diameters and channel widths, both instruments could produce results from a single image. The uncertainty in these measurements was based solely on the consistency associated with the instruments' calibration.

For measuring the lengths of the main channels, tiled images were used. The number of frames needed to cover the entire microfluidic channel depended on the field of view of the instrument. The accuracy of the measurement was affected by how well the frames were stitched together, the quality of images, and the uncertainty linked to the instrument's calibration.

The Nikon D5300 camera, with its large field of view, required only two frames to cover an entire main channel in the glass chips (see Figure 6 for an example). The images were taken with overlapping areas such that they could be stitched together in ImageJ by overlaying blemishes in successive frames. The uncertainty from stitching was 3 pixels/frame (1 pixel = 8.44 μm according to calibration). Due to the lower image quality, there was a significant uncertainty in defining the ends of the channels. This was approximately 6 pixels at each end, resulting in a total uncertainty of 15 pixels, which equals 0.31% of the total length of 39,800 μm. Furthermore, the leakage channels were not sufficiently visible in the images, making accurate measurements unreliable. Including the instrument uncertainty (0.45%; see Table 1), the potential total uncertainty for length measurements using this system was 0.76%.

The Zeiss AxioObserver, equipped with a motorized Ludl BioPoint2 stage, also used stitched images (see Figure 6 for an example). However, the precision and reproducibility of the Ludl BioPoint2 stage (<1 μm) were sufficient, so the results were highly consistent. The main advantage of this instrument was the higher numerical aperture (NA) of the 2.5× objective (NA = 0.085), which gave clearer images. This improved clarity made it easier to define channel and hole borders, resulting in a notable improvement in measurement precision. Therefore, the uncertainty in defining the channel ends was negligible, with an error of at most 1 pixel. Hence, the total uncertainty for the length measurements using the Zeiss AxioObserver was the same as its in-image uncertainty from calibration (i.e., 0.15%; see Table 1).

Both instruments were used to measure multiple glass chips, and the average of multiple measurements from each method was taken as final value. Given this combination of two different methods, the standard uncertainty definition from Equation (2) needs to be updated as follows:

$$u = \sqrt{u_{c1}^2 + u_{c2}^2 + s_r^2} \tag{3}$$

where u_{c1} is the standard uncertainty associated with the Nikon D5300 (which differs between in-image and tiled-image measurements, as shown in Table 1), u_{c2} is the uncertainty associated with the calibration of the Zeiss AxioObserver, and s_r remains the standard deviation between the two values.

3.4. Evaluation of the Measurement Results

To evaluate the consistency of the three protocols, their results are compared against a reference value. For each measurement (for example the diameter of Hole 01 in Channel 01 of Design 01), a reference value can be defined. This reference value (called RV) is

determined as the mean of the measurement values from the three protocols combined, using the weighted means formula. The inverse square of the standard uncertainty (u_n) associated with the average of a protocol's measurement values (x_n) serves as its weighting factor [29]:

$$RV = \frac{x_1/u^2(x_1) + \ldots + x_n/u^2(x_n)}{1/u^2(x_1) + \ldots + 1/u^2(x_n)} \quad (4)$$

The following formula gives the standard uncertainty, u(RV), associated with the reference value [29]:

$$u(RV) = \sqrt{\frac{1}{\frac{1}{u^2(x_1)} + \ldots + \frac{1}{u^2(x_n)}}} \quad (5)$$

Once the reference value and its standard uncertainty are determined, the measurement values from each protocol can be tested for consistency with this reference value. To identify this consistency, the normalized error (E_n) is calculated [30]:

$$E_n = \frac{x_n - RV}{\sqrt{U^2(x_n) - U^2(RV)}} \quad (6)$$

where E_n is a protocol's consistency indicator for a specific measurement; x_n is the average of a protocol's measurement values; RV is the reference value of the same measurement; and U (x_n) and U (RV) are their associated expanded uncertainties, calculated as U = k × u with k = 2.

The value of E_n leads to the following conclusions:

- If $|E_n| \leq 1$, the protocol's measurement values are consistent for a certain measurement (test passed).
- If $|E_n| > 1$, the protocol's measurement values are inconsistent for a certain measurement (test failed).

This approach allows for a comparison of the protocols between each other. However, it does not necessarily indicate the accuracy of all protocols. Besides a reference value, a nominal value can also be defined for all measurements. These nominal values and their standard uncertainties are based on the design drawings with quality assurance measurements and statistical tolerances provided by IMT Masken und Teilungen AG. The nominal values represent the theoretical dimensions that the geometry should have.

For the diameters of the holes, no statistical data were available, so the nominal value from the design (i.e., 800 µm) was used. Based on IMT's experience, a standard uncertainty of 15 µm was assumed, resulting in an expanded uncertainty of 30 µm.

The depth was measured by IMT during quality assurance, with values falling within a range of (98.3 ± 0.4) µm, giving an expanded uncertainty of 0.8 µm.

The width of the main channels was estimated using the known depth, leading to a calculated nominal width of (996.6 ± 2.66) µm for this specific batch of chips.

Finally, the length of the main channels, defined as the maximum distance between the inlet and outlet holes (designed at 39,800 µm), depends on the precision of hole placement. Based on IMT's experience, a precision of 7.5 µm per hole was assumed, leading to a total standard uncertainty of 15 µm for the length of the main channels and, thus, an expanded uncertainty of 30 µm.

Using these estimations, the consistency of the measurement values of each protocol with the nominal values can be tested.

To investigate the influence of material on measurements, a straightforward approach was adopted. Protocol 1 was applied to both glass and polymer chips, and the standard uncertainty of the measurements was compared. This standard uncertainty, defined in Equation (2), consists of a standard deviation term (s_r), related to the actual measurements,

and an uncertainty term (u_c), related to the calibration of the machine used. Since the calibration uncertainty for the OGP SmartScope ZIP®250 is identical for both polymer and glass measurements, it is more informative to compare the standard deviations of the actual measurements. Thus, the standard deviations from Protocol 1 for both polymer and glass measurements will be compared.

4. Results

4.1. Glass Chips

Each protocol naturally gave a set of results for the glass chips. The three complete sets of results can be found in the Electronic Supplementary Information. For analysis purposes, the results from a single chip, Design 01—series 01, and only its first channel, Channel 01, will be treated here. In this channel, the protocols performed the following measurements:

- The diameter of Hole 01;
- The diameter of Hole 02;
- The width of the channel;
- The depth of the channel;
- The length of the channel.

The subsequent figures (Figures 7–11) show the resulting values from all three protocols, their associated reference value, and the nominal value of each measurement.

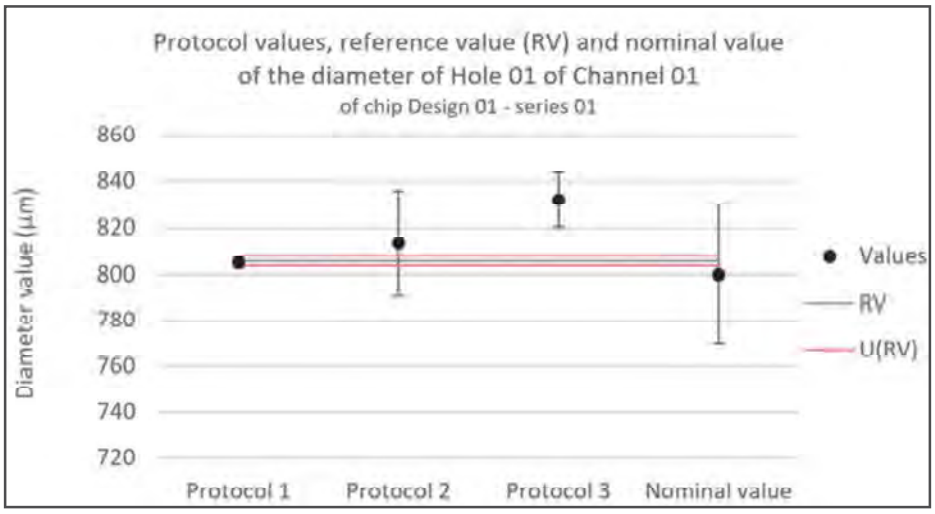

Figure 7. Consistency test for the diameter of Hole 01 in Channel 01 of chip Design 01—series 01. Error bars represent the expanded uncertainty. Likewise, U(RV) is the expanded uncertainty associated with the reference value.

To determine the consistency between the different protocols and their resulting reference value, the normalized error values (E_D) are shown in Table 2.

Table 2. Normalized error values between protocols and their resulting reference value (RV) for each measurement. Values that indicate inconsistency are marked in red.

	Diameter Hole 01	Diameter Hole 02	Width	Depth	Length
Protocol 1	−1.78	−4.44	−1.57	N/A	1.48
Protocol 2	0.33	4.14	1.65	N/A	0.32
Protocol 3	2.30	1.12	−0.40	N/A	−1.95

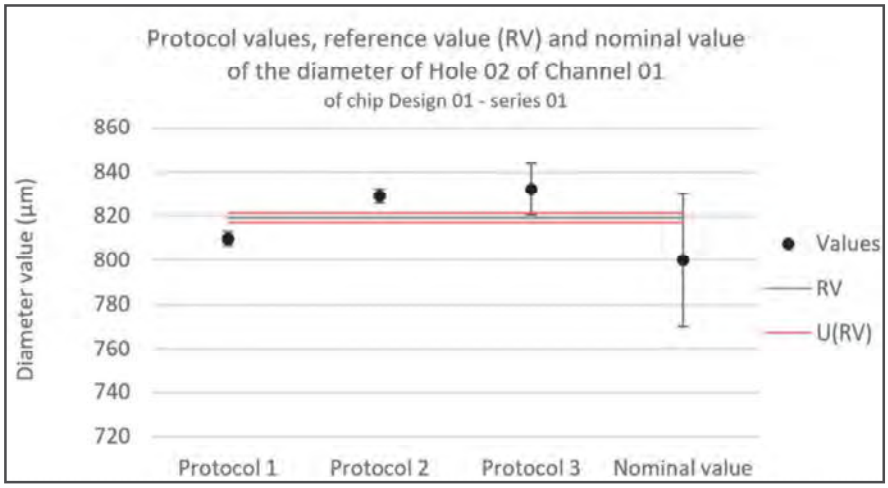

Figure 8. Consistency test for the diameter of Hole 01 in Channel 01 of chip Design 01—series 01. Error bars represent the expanded uncertainty. Likewise, U(RV) is the expanded uncertainty associated with the reference value.

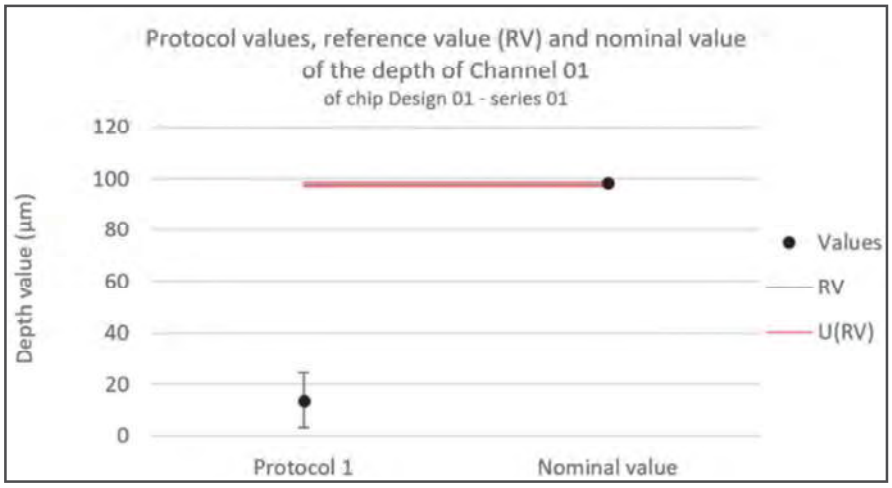

Figure 9. Consistency test for the depth of Channel 01 of chip Design 01—series 01. Error bars represent the expanded uncertainty. Likewise, U(RV) is the expanded uncertainty associated with the reference value.

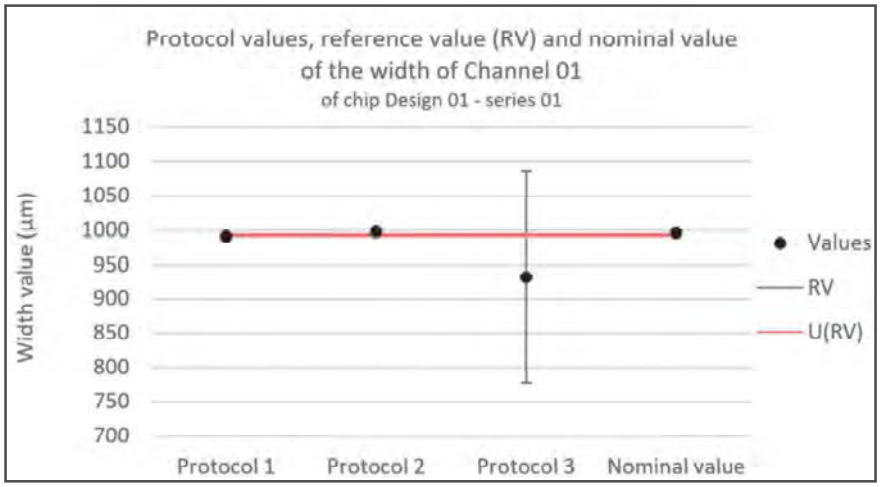

Figure 10. Consistency test for the width of Channel 01 of chip Design 01—series 01. Error bars represent the expanded uncertainty. Likewise, U(RV) is the expanded uncertainty associated with the reference value.

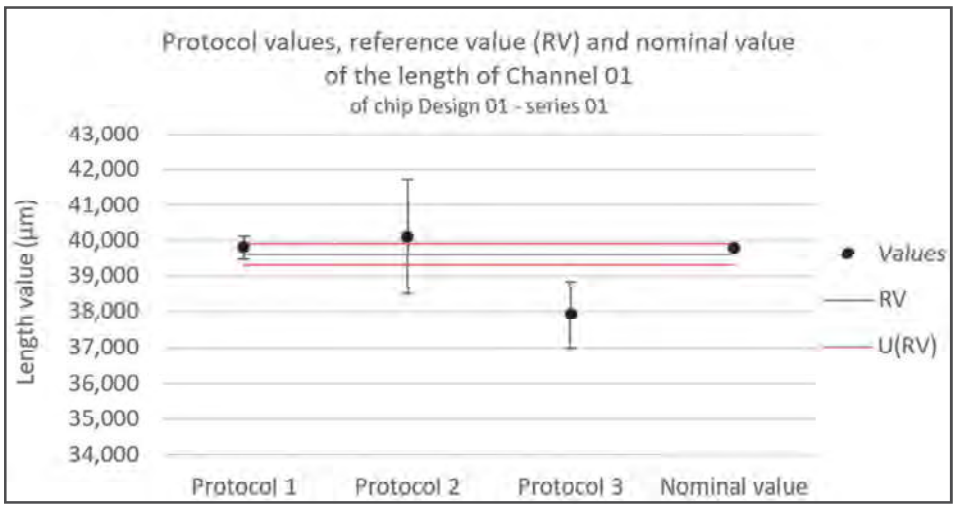

Figure 11. Consistency test for the length of Channel 01 of chip Design 01—series 01. Error bars represent the expanded uncertainty. Likewise, U(RV) is the expanded uncertainty associated with the reference value.

Given that the depth was only measured with Protocol 1, there is no reference value or normalized error for a consistency test.

Finally, the consistency between the protocols and the nominal value was determined for each measurement. The normalized errors for this consistency test are shown in Table 3.

Table 3. Normalized error values between protocols and the nominal value for each measurement. Values that indicate inconsistency are marked in red.

	Diameter Hole 01	Diameter Hole 02	Width	Depth	Length
Protocol 1	0.16	0.33	−0.93	−7.81	0.02
Protocol 2	0.35	0.96	0.23	N/A	0.20
Protocol 3	0.99	0.99	−0.42	N/A	−2.04

4.2. Polymer Chips

The full set of results from the polymer chips acquired with Protocol 1 can be found in the Electronic Supplementary Information. As an excerpt, Table 4 shows the width and depth measurements, as well as their standard deviations, for the first design of one of the COC chips. To facilitate a more meaningful comparison of these standard deviations against those from measurements made on glass chips, they are expressed in percentages.

Table 4. Measurements of the width and depth of the channels in Circuit 1 of one of the TOPAS© COC chips, as well as their associated standard deviations.

	Width		Depth	
	Average Measured	Standard Deviation	Average Measured	Standard Deviation
Channel 01	503.1 µm	0.1 µm (0.0%)	358.0 µm	1.7 µm (0.5%)
Leakage Channel 01	108.5 µm	0.1 µm (0.1%)	123.6 µm	1.8 µm (1.4%)
Channel 02	508.1 µm	0.1 µm (0.0%)	372.9 µm	2.7 µm (0.7%)

For comparison purposes, Table 5 provides measurements and uncertainties from Protocol 1 for the measurement directions corresponding to those of Table 4.

Table 5. Measurements of the width and depth of the channels of glass chip Design 01—series 01, as well as their associated standard deviations.

	Width		Depth	
	Average Measured	**Standard Deviation**	**Average Measured**	**Standard Deviation**
Channel 01	991.3 µm	0.2 µm (0.0%)	13.8 µm	4.6 µm (33.0%)
Channel 02	992.1 µm	0.2 µm (0.0%)	17.9 µm	1.3 µm (7.6%)
Channel 03	992.4 µm	0.2 µm (0.0%)	20.2 µm	3.3 µm (16.3%)
Leakage channel	143.0 µm	0.5 µm (0.3%)	N/A	N/A

5. Discussion

5.1. Comparison of Protocols

The normalized error values in Table 2 suggest that the protocols are often inconsistent with the reference values. On the contrary, Table 3 shows the protocols mostly consistent with the nominal values. The consistency of Protocol 1 with the nominal values slightly outperforms that of Protocol 2, which in turn slightly outperforms Protocol 3. This implies while the different protocols produce different values, they remain consistent with the nominal values and their expanded uncertainties. This also indicates the need for a more detailed exportation of the uncertainty calculations, as they are likely underestimated across all protocols.

In particular, for longer dimensions, such as the channel length, the accuracy of the optical profilometer is higher than that of the other protocols.

Several factors may explain the decreased accuracy of the length measurements in Protocol 3. The most evident reason is the extra uncertainty term introduced in the standard uncertainty definition due to the combination of two different methods (see the comparison between Equation (2) to Equation (3)). Additionally, the uncertainty of each method includes an extra factor related to image stitching, on top of the uncertainty associated with calibration. Lastly, the average and standard deviations for Protocol 3 are based on two measurement points, one from each method. Improving any of these three factors might potentially improve the consistency of this protocol with the nominal values for length.

In terms of uncertainty, Protocol 1 presents smaller values than the others in all measurement dimensions.

5.2. Close-Up on Depth Measurements

For the depth measurements shown in Figure 10, only Protocol 1 was capable of providing results, but these were inconsistent with the nominal values (see Table 3 and, additionally, Table 5). Several factors could explain this inconsistency and suggest potential improvements.

First, the measurements were corrected with the refractive index of the material. The refractive index is given for a specific wavelength (589 nm), which may not exactly match the wavelength of the SmartScope ZIP®250 used in Protocol 1. OGP indicated that the wavelength of the grid light for measurements in Z could range from 575 to 625 nm (Table 6).

However, even if the wavelength is different slightly, considering the material's refractive index variations, it is unlikely to cause significant changes in the measured values [17,25].

Table 6. Refractive indices of D263©bio glass for different wavelengths spanning the SmartScope.

$n_{C'}$ (643.8469 nm) ZIP®250 focus light range.	1.5209
n_D (589.2938 nm)	1.5230
n_e (546.074 nm)	1.5255 ± 0.0015

If the value of the refractive index is not the issue, then it may be the method of applying it. The straightforward multiplication of the measured values with the refractive index to correct for deformation is regularly used for structures with a single refractive interface. However, for an internal channel with two refractive interfaces, this assumption might not hold, and further investigation is warranted, which would also take into account the NA of the imaging optic and its influence on the estimated optical path length.

Another possibility is that the optical profilometer did not accurately measure either of the two surfaces. Given the high surface quality of wet-etched channels and the proximity of its top and bottom planes, the channel itself might act as a lens. In this case, the low surface roughness, which is usually considered an advantage, might impede proper measurement. This too would be worth further investigation.

It seems unrealistic to hypothesize that the bonding process has altered the channel depth from the quality assurance value of 98.3 ± 0.4 µm to the measured values in Table 5. A destructive test could verify this; however, other tests performed on these chips within the 20NRM02 MFMET project would likely have detected such a drastic geometry change.

To suggest further improvements in depth measurement for internal microfluidic channels, an additional method was tested. The following paragraph describes preliminary results obtained during this work, which could provide an interesting avenue for future work on depth measurement protocols for internal microfluidic channels.

Leakage Channel 02 of a polymer chip was measured using a Zeiss LSM 510 confocal fluorescence microscope. The instrument operates based on a confocal principle, which eliminates out-of-focus light from focal planes (called optical sections) and collects serial optical sections. In comparison to conventional epifluorescence microscopy, confocal microscopy can produce three-dimensional images by stacking up a series of Z-images. Confocal microscopy is well suited to measure the depth of an enclosed microfluidic channel. It must be noted that a fluorophore solution was injected into the chip for these measurements.

The obtainable resolution in Z depends on the NA value and the magnification of the microscope's objectives. Two objectives were used: an ×20 NA = 0.5 objective and an ×100 NA = 1.3 objective, allowing for a resolution in Z of 2.07 µm and 0.44 µm, respectively. The higher NA value objective thus enables thinner optical slicing. With this objective, however, for optical sections further away from the base of the channel, the fluorescence intensity significantly decreases because of fluorescence self-absorption effects. This effect is clearly visible in Figure 12.

Figures 13 and 14 show the resulting Z-stacks of the confocal fluorescence measurements made with the ×20 N = 0.5 objective and the ×100 NA = 1.3 objective, respectively.

To estimate the channel height using these confocal measurements, first it is necessary to determine the sections at which the fluorescence intensity in the channel is significant compared to outside the channel. This can be performed by comparing the intensity at the center of the channel to the intensity measured outside of the channel (as shown in Figure 12).

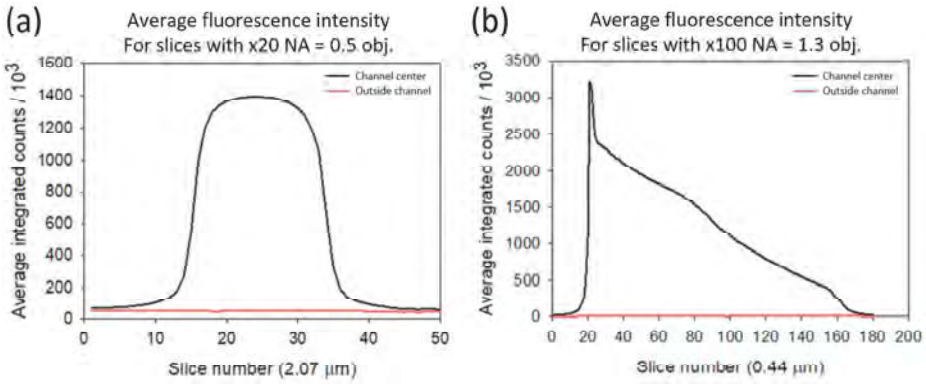

Figure 12. Average fluorescence intensity for successive optical sections (slices) measured in the center of the channel (black) and to the side of the channel (red). Base of the channel at slice 0. (**a**) Measurements from the ×20 NA = 0.5 objective, 2.07 µm sections. (**b**) Measurements from the ×100 NA = 1.3 objective, 0.44 µm sections.

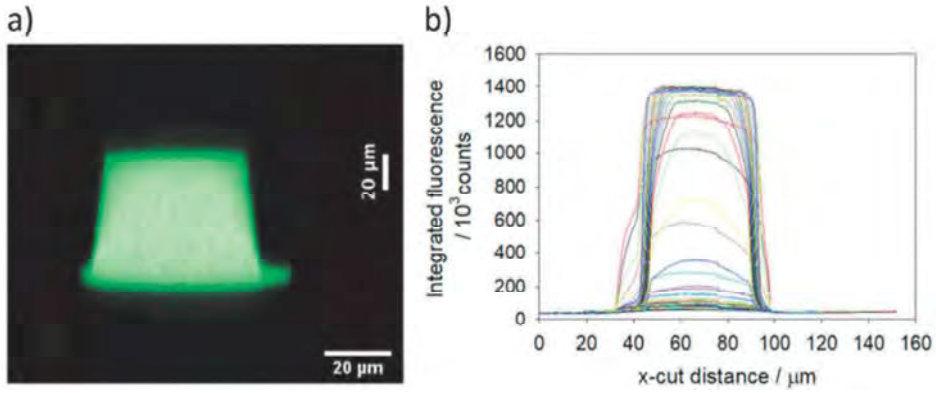

Figure 13. Integrated fluorescence intensity from Z-stack of all 50 optical sections taken with the ×20 NA = 0.5 objective. (**a**) Cross-section of channel height. (**b**) Fluorescence Intensity profile of all optical sections over an x-cut perpendicular to both the long channel axis and the channel height axis.

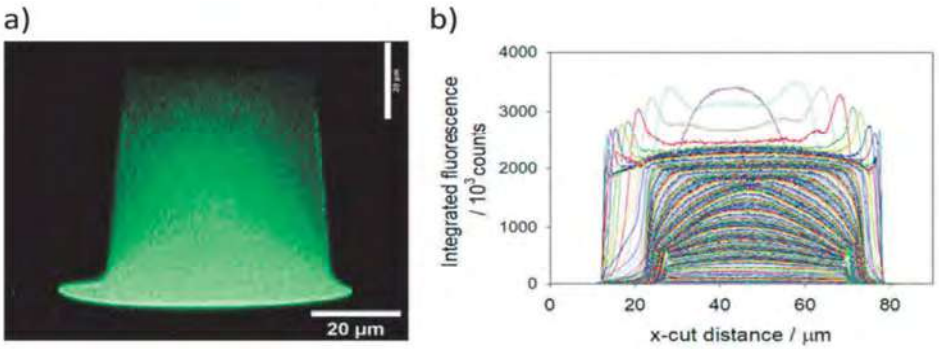

Figure 14. Integrated fluorescence intensity from Z-stack of all 180 optical sections taken with the ×100 NA = 1.3 objective. (**a**) Cross-section of channel height. (**b**) Fluorescence Intensity profile of all optical sections over an x-cut perpendicular to both the long channel axis and the channel height axis.

Secondly, a decision needs to be made about the minimum value of fluorescence intensity within an optical section corresponds to that confocal slice being substantially within the channel. This decision is necessary because the confocality is not perfect: for all practical pinhole sizes, light from a range of Z-distances will pass through. For a homogeneous fluorescence solution, such as the one in use here, a lower limit for fluorescence intensity to determine whether an optical section is substantially within the channel could, for example, be taken as 1% of that found at the channel's mid-height.

Using this 1% criteria, it is possible to estimate that 37 of the 50 optical sections from the ×20 NA = 0.5 objective are substantially within the channel. With its resolution in Z of 2.07 μm (calibrated to be accurate to 0.1 μm using an internal encoder), the channel height of the polymer device is estimated at (74.5 ± 4) μm (there will be at least on slice uncertainty at both the top and bottom of the channel).

Despite the fact that the profiles collected using the ×100 NA = 1.3 objective appear noisy (especially at sections further from the channel base), it is possible to make an accurate estimate of which slices have a fluorescence intensity above the 1% threshold. For the ×100 NA = 1.3 objective, there are 166 out of 180 optical sections above the 1% fluorescence intensity criteria, corresponding to a channel height estimate of (73.0 ± 0.8) μm.

Thus, the two measurements are consistent with each other, with the ×100 NA = 1.3 objective having greater precision.

There is a channel height discrepancy between the design specifications and the height measured by confocal microscopy. These parts are made by sealing an upper piece, which bears the imprinted channel profile, to a lower piece that is a plain (flat) plastic substrate. A significant fraction of this discrepancy in heights is most likely due to the bonding process used to seal the two pieces together. As can be seen from the fluorescence x-cut profiles of Figures 13 and 14, the measured width of the lowest 5–10 μm of the channel is significantly larger than the main part of the channel (at approximately 30 μm above the base). If this lower, wider part of the channel profile is disregarded, and the fluorescence criteria used to define the channel height is relaxed from 1% to 5% of the main channel intensity, then the measurement of upper piece channel height becomes 56 μm, significantly closer to the design specification of 50 μm.

These preliminary results hint in the direction of another interesting method worth investigating in future work for depth measurements of internal channels in transparent microfluidic devices.

5.3. The Influence of Different Materials

Following the comparison between protocols, the influence of different materials on measurements will be considered. Measurements taken on polymer and glass chips in the XY-plane will be considered separately from those taken in the *Z*-axis.

The standard deviations in the XY-plane (width measurements from Tables 4 and 5) are generally within the range of a few tenths of micrometers for both polymer and glass measurements. When expressed as percentages, it becomes even more evident that the standard deviation is negligible for both materials.

It would be interesting for future research to investigate whether this observation holds true for other materials commonly used in microfluidics (e.g., PP, PC, COP, and PMMA) and other measurement methods (e.g., optical or confocal microscopy). Experience suggests that the SmartScope ZIP®250's apparent indifference to material type may not necessarily extended to other techniques.

In contrast, the standard deviations of the depth measurements in TOPAS© COC are much lower than those for D263©bio glass.

During the measurements, it was noticed that the SmartScope ZIP®250 seemed to distinguish more clearly between the top and bottom planes of the internal channels in the polymer chips. For this reason, the Z-coordinates of the top and the bottom planes were subtracted directly to calculate the channel depth. As mentioned earlier, it is hypothesized that the polymer chips' higher surface roughness, which is usually a disadvantage, might have helped the optical profilometer better define a focus plane compared to the near-perfect smoothness of the wet-etched glass channels. Testing this hypothesis would be an interesting avenue for future research.

It is worth noting that, regardless of whether the standard deviation is low or high, the accuracy of depth measurements in both materials is questionable. In both TOPAS© COC and D263©bio glass, the depth measurements were inconsistent with their nominal values. In addition, although the profilometer was seemingly capable of distinguishing between the top and bottom of the internal channels in the polymer chips, it is difficult to differentiate it from the actual bottom of the chip. This might explain the overestimation of the depth of Leakage Channel 01, as shown in Table 4.

6. Conclusions

Accurately measuring internal structures after chip assembly is a well-recognized challenge in the microfluidic industry. This study, conducted as part of the EMPIR MFMET project, compared three different protocols, namely optical profilometry, optical microscopy, and tiled digital imagery, for measuring different internal microfluidic structures in chips made from D263©bio glass and TOPAS© COC.

A consistency analysis using normalized error statistics revealed Protocol 1, optical profilometry, as the preferred method due to its low uncertainty compared to the other protocols and its higher consistency with nominal geometry values.

However, challenges were encountered in measuring the depth of the internal geometries. The only protocol able to provide a measurement of the internal channel depth, optical profilometry, gave results that are highly inconsistent with their nominal values. Several avenues for future research are proposed, including a study of how to apply the refractive index for deformation compensation when dealing with multiple refraction interfaces. Another promising method is confocal fluorescence microscopy, which showed promising preliminary results.

The performance of TOPAS© COC chips was not significantly better or worse than that of D263©bio glass chips. This suggests that both materials are equally compatible with optical profilometry. However, depth measurements presented an exception, as channels with poorer surface roughness were easier to measure using the optical profilometer. Despite that, the depth measurements for the TOPAS© COC chips were also unsatisfactory. Further research comparing other common materials in microfluidics and different measurement techniques is recommended.

The results of this work directly address the current lack of accurate, robust, and validated measurement methods for internal microfluidic structures, offering a comprehensive comparison of different protocols and ultimately suggesting a preferred option for immediate application in the microfluidic industry. Additionally, this study offers valuable directions for future research, taking an important step toward overcoming a significant challenge that has hindered the microfluidic industry from reaching its full potential. The information obtained in this work also indicates the need for standardization in the field of dimensional measurements in microfluidic technology, especially after the chip's assembly. New European standardization projects will help in the development of standards for microfluidic dimension application within ISO/TC48/WG4 microfluidic devices, as foreseen in their new roadmap.

Supplementary Materials: The following supporting information can be downloaded at: https://www.mdpi.com/article/10.3390/metrology5010004/s1, Table S1: Glass Measurements Analysis; Table S2: Glass measurements for Analysis; Table S3: Glass Measurements protocol 1 CEA; Table S4: Glass Measurements protocol 2 LNE; Table S5: Glass Measurements protocol 3 UofG; Table S6: Polymer Measurements protocol 1 CEA; File S1: ChipDesign GlassTransferStandard IMT; File S2: ChipDesign PolymerTransferStandard MCS (pdf); File S3: ChipDesign PolymerTransferStandard MCS (stp); File S4: Calibration Report protocol1 CEA; File S5: Calibration Report protocol3 UofG.

Author Contributions: E.B. and K.R. were responsible for the conceptualization and supervision of the study. J.K. performed investigations of Protocol 1, defining its methodology and providing the required resources. N.F. did the same for Protocol 2, with assistance with the investigations from M.L., as did H.Y. for Protocol 3 and the confocal microscopy assisted in the investigations by A.G. Formal analysis of all results was performed by E.B. and J.K. The original draft was written by J.K., starting with input from E.B., H.Y. and N.F. for their respective parts. All authors have read and agreed to the published version of the manuscript.

Funding: This project 20NRM02 MFMET has received funding from the EMPIR programme co-financed by the Participating States and from the European Union's Horizon 2020 Research and Innovation Programme.

Data Availability Statement: The original data presented in the study are openly available on the Zenodo repository Establishing Metrology Standards in Microfluidic Devices at https://doi.org/10.5281/zenodo.11621010 (accessed on 4 December 2024).

Acknowledgments: This study is part of the work performed in the MFMET project. The authors recognize the contribution of all project participants and thank them for it. Secondly, the authors would like to express their gratitude to IMT Masken und Teilungen AG, Switzerland, and microfluidic ChipShop GmbH, Germany, for their contribution to the project, including but not limited to the development of the transfer standard chips used in this work. Finally, the authors want to thank all academic and industrial partners for continuously providing insights into microfluidic challenges and needs through discussions, workshops, or surveys conducted by The Microfluidics Association.

Conflicts of Interest: The authors declare no conflicts of interest.

References

1. Whitesides, G.M. The origins and the future of microfluidics. *Nature* **2006**, *442*, 368–373. [CrossRef] [PubMed]
2. Sackmann, E.K.; Fulton, A.L.; Beebe, D.J. The present and future role of microfluidics in biomedical research. *Nature* **2014**, *507*, 181–189. [CrossRef] [PubMed]
3. Elvira, K.S.; i Solvas, X.C.; Wootton, R.C.; Demello, A.J. The past, present and potential for microfluidic reactor technology in chemical synthesis. *Nat. Chem.* **2013**, *5*, 905–915. [CrossRef] [PubMed]
4. Berlanda, S.F.; Breitfeld, M.; Dietsche, C.L.; Dittrich, P.S. Recent Advances in Microfluidic Technology for Bioanalysis and Diagnostics. *Anal. Chem.* **2021**, *93*, 311–331. [CrossRef] [PubMed]
5. Convery, N.; Gadegaard, N. 30 years of microfluidics. *Micro Nano Eng.* **2019**, *2*, 76–91. [CrossRef]
6. Rosen, Y.; Gurman, P. MEMS and microfluidics for diagnostics devices. *Curr. Pharm. Biotechnol.* **2010**, *11*, 366–375. [CrossRef] [PubMed]
7. Behera, P.P.; Kumar, N.; Kumari, M.; Kumar, S.; Mondal, P.K.; Arun, R.K. Integrated microfluidic devices for point-of-care detection of bio-analytes and disease. *Sens. Diagn.* **2023**, *2*, 1437–1459. [CrossRef]
8. Huh, D.; Leslie, D.C.; Matthews, B.D.; Fraser, J.P.; Jurek, S.; Hamilton, G.A.; Thorneloe, K.S.; McAlexander, M.A.; Ingber, D.E. A Human Disease Model of Drug Toxicity–Induced Pulmonary Edema in a Lung-on-a-Chip Microdevice. *Sci. Transl. Med.* **2012**, *4*, 159ra147. [CrossRef] [PubMed]
9. Levner, D.; Ewart, L. Integrating Liver-Chip data into pharmaceutical decision-making processes. *Expert Opin. Drug Discov.* **2023**, *18*, 1313–1320. [CrossRef] [PubMed]
10. Quintard, C.; Tubbs, E.; Jonsson, G. A microfluidic platform integrating functional vascularized organoids-on-chip. *Nat. Commun.* **2024**, *15*, 1452. [CrossRef] [PubMed]
11. Middelkamp, H.; Weener, H.; Gensheimer, T.; van der Meer, A.D. Embedded macrophages induce intravascular coagulation in 3D blood vessel-on-chip. *Biomed. Devices* **2023**, *26*, 2. [CrossRef] [PubMed]
12. Yole Intelligence. *Status of the Microfluidics Industry 2023 Maturity of Microfluidics Devices Applications*; Yole Intelligence: Lyon, France, 2023.
13. Wang, K.; Man, K.; Liu, J.; Chen, Q.; Zhou, Y.; Yang, Y. Microphysiological Systems: Design, Fabrication, and Applications. *ACS Biomater. Sci. Eng.* **2020**, *6*, 3231–3257. [CrossRef] [PubMed]
14. Kim, H.; Lee, J.B.; Kim, K.; Sung, G.Y. Hydrophobic Sponge Structure-Based Triboelectric Nanogenerator. *J. Ind. Eng. Chem.* **2022**, *115*, 279–286. [CrossRef]

15. Gurkan, U.A.; Wood, D.K.; Carranza, D.; Herbertson, L.H.; Diamond, S.L.; Du, E.; Guha, S.; Di Paola, J.; Hines, P.C.; Papautsky, I.; et al. Next generation microfluidics: Fulfilling the promise of lab-on-a-chip technologies. *Lab Chip* **2024**, *24*, 1867–1874. [CrossRef] [PubMed]
16. van Heeren, H. Trends and Challenges in the Microfluidic Industry. 2021. Available online: https://enablingmnt.com/wp-content/uploads/2021/01/Trends-and-Challenges-in-the-Microfluidic-Industry-Henne-van-Heeren-January-2021.pdf (accessed on 4 December 2024).
17. Schott AG. D263©. Available online: https://www.schott.com/en-nl/products/d-263-P1000318/technical-details?tab=830fa6759ac84d07a3d53bfbe4535a90 (accessed on 17 April 2024).
18. TOPAS Advanced Polymers/Polyplastics, TOPAS© COC Datasheets. Available online: https://topas.com/wp-content/uploads/2023/05/TDS_6015S-04_english-units.pdf (accessed on 4 December 2024).
19. Batista, E.; Reyes, D.R. Publishable Summary Establishing Metrology Standards in Microfluidic Devices (20NRM02). 2023. Available online: https://mfmet.eu/wp-content/uploads/2023/11/20NRM02-MFMET-Publishable-Summary-M27.pdf (accessed on 4 December 2024).
20. MFMET—Establishing Metrology Standards in Microfluidic Devices. Available online: https://mfmet.eu/ (accessed on 18 April 2024).
21. Silverio, V.; Guha, S.; Keiser, A.; Natu, R.; Reyes, D.R.; van Heeren, H.; Verplanck, N.; Herbertson, L.H. Overcoming technological barriers in microfluidics: Leakage testing. *Front. Bioeng. Biotechnol.* **2022**, *10*, 958582. [CrossRef] [PubMed]
22. Copeland, M.; Ogheard, F.; Batista, E.; van Heeren, H. Whitepaper Flow Resistivity Testing. Zenodo. 2023. Available online: https://zenodo.org/records/7919134 (accessed on 4 December 2024).
23. *ISO 22916:2022*; Microfluidic Devices Interoperability Requirements for Dimensions, Connections and Initial Device Classification. International Organization for Standardization: Geneva, Switzerland, 2022.
24. microfluidic ChipShop GmbH. Material Data Sheet mcs-COC 13. 2024. Available online: https://www.microfluidic-chipshop.com/microfluidics/materials-in-microfluidics/polymers-in-microfluidics/topas/ (accessed on 4 December 2024).
25. Schott AG. TIE-29 Refractive Index and Dispersion. 2016. Available online: https://www.schott.com/shop/medias/tie-29-refractive-index-and-dispersion-eng.pdf?context=bWFzdGVyfHJvb3R8MTg4OTQ2NHxhcHBsaWNhdGlvbi9wZGZ8aDQ3L2hjYS84ODE3NDA5NTg5Mjc4LnBkZnxkMTc5MjMyYjI5YmRlZTAzZmFmYzIxZmVlNTMyMmE5NzBiNWI5OGJhODM3YWRjYmM5NmY1ZTczMjY1ZWM3NDdk (accessed on 4 December 2024).
26. Martinez, A.W.; Phillips, S.T.; Carrilho, E.; Thomas, S.W.; Sindi, H.; Whitesides, G.M. Simple telemedicine for developing regions: Camera phones and paper-based microfluidic devices for real-time, off-site diagnosis. *Anal. Chem.* **2008**, *80*, 3669–3707. [CrossRef] [PubMed]
27. Wang, B.; Li, Y.; Zhou, M. Smartphone-based platforms implementing microfluidic detection with image-based artificial intelligence. *Nat. Commun.* **2023**, *14*, 1341. [CrossRef] [PubMed]
28. Howell, J.; Hammarton, T.C.; Altmann, Y.; Jimenez, M. High-speed particle detection and tracking in microfluidic devices using event-based sensing. *Lab Chip* **2020**, *20*, 3024–3035. [CrossRef] [PubMed]
29. Cox, M.G. The evaluation of key comparison data. *Metrologia* **2002**, *39*, 589–595. [CrossRef]
30. *ISO 13528:2022*; Statistical Methods for Use in Proficiency Testing by Interlaboratory Comparison. International Organization for Standardization: Geneva, Switzerland, 2022.

Measurement: Sensors 38 (2025) 101560

Contents lists available at ScienceDirect

Measurement: Sensors

journal homepage: www.sciencedirect.com/journal/measurement-sensors

Comparison of primary standards for liquid flow in the range from 0.1 μL/min to 10 μL/min

ARTICLE INFO

Keywords:
Key comparison
Liquid flow
Micro flow
Degree of equivalence

ABSTRACT

The CCM.FF-K1.2022 comparison was organized to determine the degree of equivalence of national standards for liquid flow in the range from 0.1 μL/min to 10.0 μL/min. A Coriolis mass flow meter and a thermal flow meter were used as transfer standards. Six laboratories from three regional metrology organizations (RMOs) participated between April 2023 and December 2023; EURAMET: METAS (Switzerland), CETIAT (France), IPQ (Portugal); SIM: NIST (United States of America); APMP: CMS (Taiwan, R.O.C.), NMIJ (Japan). METAS was the pilot laboratory and performed preliminary tests of the transfer standards to quantify their repeatability and reproducibility and to assess the stability of the artifacts. The key comparison reference values (KCRVs) were determined at each flow set point following the procedure presented by M. G. Cox and the χ^2 consistency check. The degree of equivalence with the KCRV was calculated for each flow and laboratory.

1. Introduction

The first key comparison of liquid flow covering the smallest liquid flow calibration measurement capability (CMC) entries is registered as CCM.FF-K1.2022 (EURAMET Project 1852) at the Bureau International des Poids et Mesures (BIPM) and will be finalized in 2024. The pilot laboratory is METAS and the participants are METAS, NIST, NMIJ, IPQ, CETIAT and CMS. The covered flow range is 0.1 μL/min to 10.0 μL/min. Two transfer standards were selected and extensively characterized by METAS. The first one is a Coriolis flow meter ML120 from Bronkhorst High-Tech B.V.,[1] which covers the range from 5 mg/min to 10 mg/min.[2] The second one is a thermal flow meter SLG64-0075 from Sensirion AG, which covers the range from 0.1 μL/min to 5.0 μL/min. All the measurements were performed between March 2023 and December 2023 and the analysis of the measurement results and calculation of the key comparison reference are complete. Draft A of the comparison report is under review [1].

The preliminary testing of the transfer standards, their repeatability and reproducibility will be discussed in this paper. The results of the laboratories will be treated anonymously and are not extensively described in this paper as the final report of the key comparison is still under review.

2. List of participants

Six laboratories participated in the comparison, selected according to the uncertainty listed in CMC entries or peer-reviewed publications, their regional representation, and their experience in measuring low flows. Each laboratory had one week for the calibration of the Coriolis flow meter ML120 (three flows) and two weeks for the calibration of the thermal flow meter SLG64-075, because six flows were measured with this flow meter in the lower flow range. Three weeks were allowed for transportation to the next participating laboratory.

The participants and the type of reference standards used are listed in Table 1. Eight measurement standards were used by the 6 participants. Five of the primary standards were gravimetric, using the change of mass with respect to time of water collected on a weigh scale to calculate flow. Three laboratories used the displacement of water along a cylinder of known diameter (by tracking a piston in a syringe pump or a liquid interface) to measure flow. The uncertainty[3] of the participants' reference flow measurements at the 9 comparison set points ranged between 0.04 % and 4 %, with a median value of 0.7 %. Details of the operating principles and uncertainty of the participants' primary standards can be found in the references listed in Table 1.

3. Transfer standards (TS)

The transfer standards were provided by METAS: a Coriolis flow meter ML120 from Bronkhorst High-Tech B.V. (TS1) and a thermal flow meter SLG64-075 from Sensirion AG (TS2).

[1] Certain commercial entities, equipment, or materials may be identified in this document in order to describe an experimental procedure or concept adequately. Such identification is not intended to imply recommendation or endorsement, nor is it intended to imply that the entities, materials, or equipment are necessarily the best available for the purpose.

[2] For water, 1 μL/min ≅ 1 mg/min. Herein, we use mass flow units for the Coriolis meter and volume flow units for the thermal flow meter to be consistent with their operating principles.

[3] All uncertainties stated herein ar approximately 95 % confidence level ($k = 2$) values unless otherwise stated.

https://doi.org/10.1016/j.measen.2024.101560

Available online 8 January 2025

Table 1
The participants and type of Reference or Primary Standard used to calibrate the Transfer Standard (TS).

Participant	TS: Type of reference or Primary Standard
METAS (Switzerland)	TS1: Piston Prover
	TS2: Piston Prover [2–4]
CETIAT (France)	TS1: Gravimetric [2,4,5]
	TS2: Optical front track [2,5]
IPQ (Portugal)	TS1: Gravimetric [2]
	TS2: Interferometer [2]
NIST (USA)	TS1: Gravimetric
	TS2: Gravimetric [6]
CMS (Taiwan, R.O.C.)	TS1: Gravimetric
	TS2: Gravimetric
NMIJ (Japan)	TS1: Gravimetric
	TS2: Gravimetric [7,8]

3.1. TS1 (Coriolis mass flow meter)

TS1 is a Coriolis flow meter ML120 manufactured by Bronkhorst High-Tech B.V. (see Fig. 1). The maximum flow is 83.3 mg/min and the minimum flow is 0.83 mg/min. The internal volume is approximately 30 μL and it has 1/16″ Swagelok connectors. TS1 was calibrated at 10 mg/min, 8 mg/min and 5 mg/min.

3.2. TS2 (thermal flow meter)

TS2 is a thermal flow meter SLG64-0075 manufactured by Sensirion AG (see Fig. 2). Its maximum flow is 5000 nL/min and the minimum flow is 20 nL/min. The internal volume is approximately 0.35 μL and it has 10–32 coned, finger-tight connectors. TS2 was calibrated at 5000 nL/min, 2000 nL/min, 1000 nL/min, 500 nL/min, 200 nL/min and 100 nL/min.

Fig. 1. Coriolis flow meter ML120 from Manufacturer Bronkhorst High-Tech B.V.

Fig. 2. Thermal flow meter SLG64-0075 from Sensirion AG.

4. Comparison protocol

4.1. General information

The comparison protocol was finalized and accepted by all partners in March 2023. To determine the key comparison reference value (KCRV) the formula of the weighted mean was used, using the inverses of the squares of the associated standard uncertainty of the participants' results as the weights [1]. A $\chi 2$ consistency check was used, to ensure the overall consistency of the set of the results from the laboratories used to calculate the comparison reference value [1]. If the consistency check passed, the participant's results at that flow set point were accepted for the calculation of the reference value. If it failed, the result of the laboratory with the largest contribution $\chi 2_{obs}$ was omitted from the calculation of the reference value. The normalized degrees of equivalence E_n were also determined.

4.2. Measurement conditions

The requirements given in the comparison protocol for calibration conditions were:

- upstream pressure: 0.1 bar–1.0 bar.
- water temperature: between 17 °C and 23 °C.
- at least three repetitions per flow set point.

The means of generating the upstream pressure used to drive the flow through the transfer standards was left up to each participant. Most used a syringe pump, but two applied a regulated gas pressure to drive water out of a sealed reservoir. The flow measurements of the transfer standards were used to establish flow at the set points prescribed by the comparison protocol. The flow stabilization time prior to collecting measurements necessary to avoid temperature effects and the minimum measurement time were also decided by each participant.

4.3. Importance of zero-flow indication

Mechanical stresses and the environmental conditions surrounding the transfer standard flow meter can change their zero-flow indication. Therefore, it is important to determine the zero-flow of the flow meter in each participant's installation and make zero corrections. Any drift in the zero-flow may cause serious deviations in the flow measurements at these low flows. Zero corrections were mandatory for this key comparison.

As prescribed in the comparison protocol, zero flow was established at the transfer standard by filling the meter with water and closing valves upstream and downstream from the meter. Recording the zero-flow over a long period allows one to see if the zero-flow conditions are actually achieved and that the indicated value is not changing

anymore. The zero-flow measurements were performed prior to and after the calibration in order to verify its stability. Each participant corrected the transfer standard flow readings by subtracting the transfer standard zero flow values measured in their laboratory from the transfer standard flow readings.

TS2 has the option for zeroing the flow meter by means of the Bronkhorst software FlowDDE and FlowPlot. TS1 does not have an option for zeroing the flow meter, so zero corrections were implemented in a spreadsheet.

4.4. Cleaning procedure for the TS's

It was important to clean the flow meter prior and after the calibration. Once the flow meter was taken out of the facility, it had to be cleaned and dried. Using clean water does not mean that the water passing through the flow meter is still clean, as the water passes through all the tubing, fittings, and sensors. It is likely that a thin biological film is deposited on the wall of the glass pipe in the thermal flow meter. This film must be removed by cleaning to maintain stable flow meter calibration.

Any contamination on the glass pipe of the thermal flow meter causes a different reaction of the sensing element, which is recording the heat contribution from an electric heater. It is known from prior studies that without cleaning, the thermal flow meter can show a clear drift in the calibration curve. All these effects are mainly affecting the performance of the flow meter at their lower flow range.

To clean and dry the meter, the following procedure was recommended:

1. Flush the meter with isopropyl alcohol for at least half an hour. It may be beneficial to use a dedicated syringe pump to be able to make a close connection to the flow meter. Avoid overpressure with a pressure relief valve for an active flow generator.
2. Flush the meter with nitrogen gas. It is possible to use dry air as well (if no other choice). But make sure that it is an oil-free supply (have an oil filter in place!)

5. Characterisation of the TS's

METAS performed extensive repeatability and reproducibility tests of the transfer standards over several months to check the suitability and stability of these transfer standards for this key comparison. The preliminary evaluation tests follow the approach established by the CIPM Consultative Committee for Mass and the Working Group for Fluid Flow to quantify uncertainty contributions related to the transfer standard (U_{TS}) caused by its repeatability, reproducibility, or the conditions under which it is used [9,10].

As for the comparison itself, the deviation (ε) between the flow indicated by the transfer standard and the flow measured by the laboratory's primary standard, expressed in percent of reading, was used as the measurand.

5.1. Calculation of repeatability uncertainty

The repeatability of the deviations at a flow set point was determined with a series of measurements on several days under the same installation conditions and where the TS was not removed from the facility. The representative repeatability uncertainty ($k = 2$) is calculated according to:

$$U_{\text{Repeat}} = 2\,s/\sqrt{n} \tag{1}$$

where s is the standard deviation of the deviations (ε) and n is the number of measurements.

5.2. Calculation of reproducibility uncertainty

The reproducibility of the deviations at a flow set point was determined with a series of measurements performed under the same installation conditions, but after removing the TS from the facility and installing it again several days or months later. For each series of measurement, the average deviation was calculated. The scatter of ε_{ave} over time represents the reproducibility. The representative reproducibility uncertainty ($k = 2$) is calculated according to:

$$U_{\text{Reprod}} = \frac{\left(\varepsilon_{\text{ave,max}} - \varepsilon_{\text{ave,min}}\right)}{\sqrt{3}} \tag{2}$$

5.3. Extensive characterisation of TS1

The calibration results performed at METAS between October 2022 and November 2023 are shown in Fig. 3. The results of the deviations at the flows generally show consistent results within the manufacturer's specified uncertainty, although there are some outliers. All the results were used to calculate the repeatability and the reproducibility of the flow meter.

5.4. Repeatability of TS1

Four different series of measurements were performed leading to four repeatability values, which were averaged to get the representative repeatability of TS1 listed in Table 2.

5.5. Reproducibility of TS1

Four different series of measurements were used to calculate the representative reproducibility uncertainty listed in Table 3.

5.6. Total expanded uncertainty of TS1

The uncertainty contributed to the comparison by TS1 consists of the contributions of the repeatability and the reproducibility and is reported in Table 4.

5.7. Extensive characterisation of TS2

The calibration results performed at METAS between August 2020 and December 2023 are shown in Fig. 4. The deviations are consistent results within the stated uncertainty, although there are some outliers. These results were used to calculate the repeatability and the reproducibility of the flow meter. The deviation at 5000 nL/min shows larger reproducibility effects as it is the upper limit of the flow meter. The sensitivity of the thermal flow meter is worse in this range.

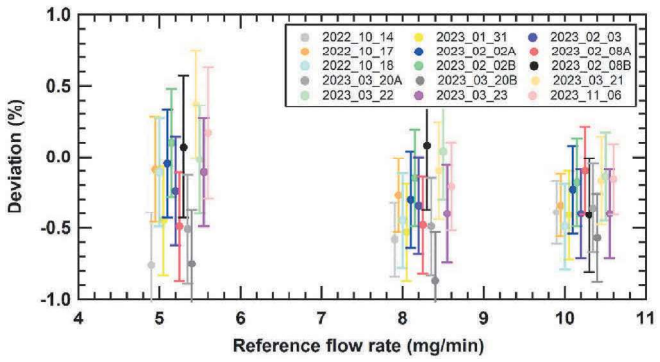

Fig. 3. Calibration of TS1 at METAS. The results for the flows calibrated between 2022 and 2023 are consistent within the manufacturer's specifications, although there are some outliers.

Table 2
Repeatability of TS1.

Nominal flow	U_{Repeat} ($k = 2$)
10 mg/min	0.15 %
8 mg/min	0.29 %
5 mg/min	0.38 %

Table 3
Reproducibility of TS1.

Nominal flow	U_{Reprod} ($k = 2$)
10 mg/min	0.14 %
8 mg/min	0.13 %
5 mg/min	0.29 %

Table 4
Transfer standard uncertainty of TS1.

Nominal flow	U_{TS1} ($k = 2$)
10 mg/min	0.21 %
8 mg/min	0.32 %
5 mg/min	0.48 %

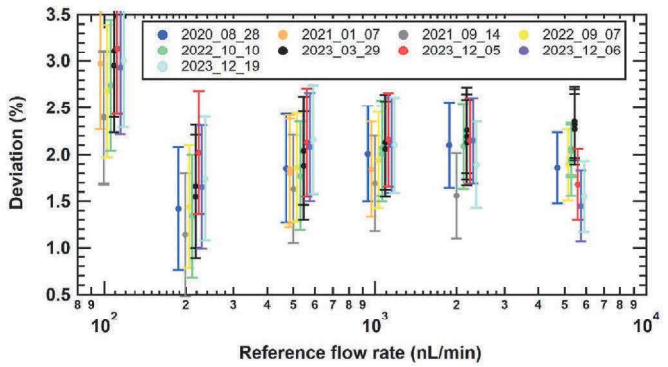

Fig. 4. Calibration of SLG64-0075 at METAS. The results for the flows calibrated between 2020 and 2023 are consistent within the transfer standard uncertainty.

5.8. Repeatability of TS2

Seven different series of measurements were performed leading to seven repeatability values, which were averaged to get the representative repeatability of TS2 listed in Table 5.

5.9. Reproducibility of TS2

Seven different series of measurements were used to calculate the representative reproducibility uncertainty listed in Table 6.

5.10. Total expanded uncertainty of TS2

The total expanded uncertainty contributed to the comparison by TS2 consists of the contributions of the repeatability and the reproducibility and is reported in Table 7.

6. Normalized degree of equivalence

The normalized Degree of Equivalence (E_n) between the results of each laboratory and the key comparison reference value (KCRV) is calculated according to Refs. [1,11,12].

The interpretation of the absolute value of E_n is as follows:

Table 5
Repeatability of TS2.

Nominal flow	U_{Repeat} ($k = 2$)
5000 nL/min	0.06 %
2000 nL/min	0.08 %
1000 nL/min	0.04 %
500 nL/min	0.06 %
200 nL/min	0.12 %
100 nL/min	0.08 %

Table 6
Reproducibility of TS2.

Nominal flow	U_{Reprod} ($k = 2$)
5000 nL/min	0.44 %
2000 nL/min	0.37 %
1000 nL/min	0.23 %
500 nL/min	0.19 %
200 nL/min	0.27 %
100 nL/min	0.36 %

Table 7
Transfer standard uncertainty of TS2.

Nominal flow	U_{TS2} ($k = 2$)
5000 nL/min	0.44 %
2000 nL/min	0.38 %
1000 nL/min	0.24 %
500 nL/min	0.20 %
200 nL/min	0.30 %
100 nL/min	0.37 %

- $|E_n| < 1$: the result of the laboratory is consistent with KCRV.
- $1.0 < |E_n| < 1.2$: the result of the laboratory might indicate a possible warning in the measurement process.
- $|E_n| > 1.2$: the result of the laboratory is not consistent with KCRV.

The normalized Degree of Equivalence E_n for TS1 and TS2 are shown in Figs. 5 and 6 respectively. An extensive discussion of the results is not possible due to the status of the comparison report, which is currently under review.

7. Explanations for discrepant results

Several E_n values show inconsistent results with the KCRV. Possible explanations for the discrepant results of the laboratories are given in this section.

One laboratory reported that their temperature control facilities had some issues during the measurements. The room temperature exceeded 24 °C for some time and so the technicians waited until the room temperature fell below 23 °C again to perform the measurements. The lack of time could have led to an improper procedure for the measurements, which could have affected the determination of the zero-flow correction and the stabilization time of the system for the measurements.

Two laboratories used flow generators with strong pulsations leading to a cut-off effect of TS2, because the fluctuations of the flow exceeded the manufacturer's high flow cut-off limit at 5500 nL/min when tested at the maximum flow set point of 5000 nL/min, shown in Fig. 7. Thus, time-averaged values of the TS2 readings were underestimated and led to discrepant deviations.

One laboratory reported a drift of the indication of the zero-flow. The knowledge of the indication of the zero-flow of the flow meter is very important as the correction for the zero-flow was mandatory for this key comparison. Usually, the zero-flow is not drifting and stable after a stabilization time that guarantees the "no flow conditions" at the flow meter.

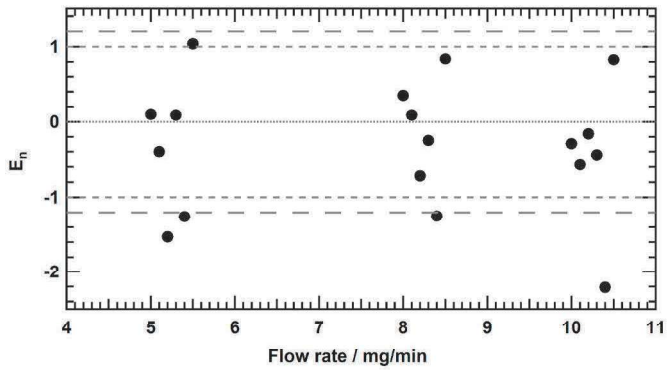

Fig. 5. The E_n values for TS1. The dotted line represents the $E_n = 0$, the short-dashed line represents $E_n = \pm 1$ and the long-dashed line represents $E_n = \pm 1.2$.

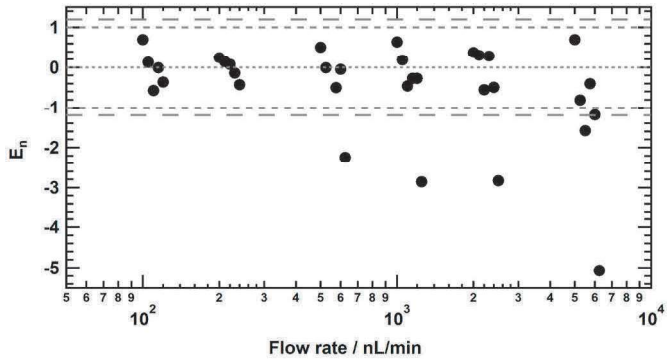

Fig. 6. The E_n values for TS2. The dotted line represents the $E_n = 0$, the short-dashed line represents $E_n = \pm 1$ and the long-dashed line represents $E_n = \pm 1.2$.

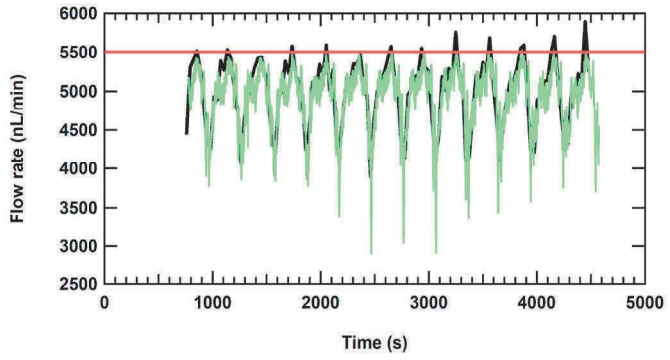

Fig. 7. Cut-off issue at the flow of 5000 nL/min for the TS2 due to fluctuating input flow. The TS2 has a cut-off limit at 5500 nL/min (red line). Reference flow (black line) and TS2 data (green line).

Incomplete cleaning was suspected to cause contamination and drift in the flow sensor. Therefore, the pilot laboratory performed an improper cleaning procedure to test the significance of this possible source of drift. The flow meter was flushed with isopropyl alcohol, but it was not dried with nitrogen prior to the flushing with water and the flushing with water was performed much shorter than usual. The indication of the zero-flow of the flow sensor was not stable even after 6 h, as shown in Fig. 8.

8. Conclusions

The CCM.FF-K1.2022 comparison was performed with the calibration of two transfer standards in the range from 0.1 µL/min to 10.0 µL/min. The results were analyzed following the procedure presented by M. G. Cox and the χ^2 consistency check [1].

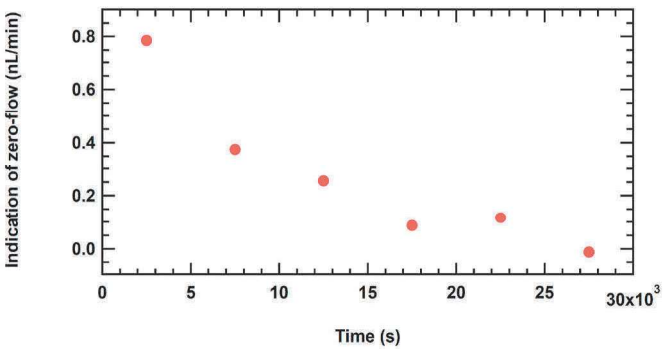

Fig. 8. Instability of the zero-flow after cleaning TS2 without drying it.

Several *En* values show inconsistent results with the KCRV. Possible explanations for the discrepant results of the laboratories are: time issues affecting the determination of the zero-flow corrections and the stabilization time of the system for the measurements; cut-off effect of the TS2 signal due to pulsating flows; instabilities of the zero-flow due to contamination or cleaning issues.

The results have not been discussed extensively and in detail due to the status of the key comparison report, which is currently under review.

This was the first key comparison of microflows and therefore some variability between the participants was expected. It is now important to investigate the sources of the differences and improve the microflow standards.

This research did not receive any specific grant from funding agencies in the public, commercial, or not-for-profit sectors.

References

[1] M. Cox, The evaluation of key comparison data: determining the largest consistent subset, Metrologia 44 (3) (2007) 187–200, https://doi.org/10.1088/0026-1394/44/3/005.

[2] C. Mills, E. Batista, H. Bissig, F. Ogheard, A.W. Boudaoud, Calibration methods for flows down to 5 nL/min and validation methodology, + another 10 authors, Biomed. Eng./Biomed. Tech. 68 (1) (2023) 13–27, https://doi.org/10.1515/bmt-2022-0049.

[3] H. Bissig, M. Tschannen, M. de Huu, Dynamic vs constant liquid flow calibrations down to 20 nL/min, in: 19th International Flow Measurement Conference FLOMEKO, Chongqing, China, 2022, pp. 1–5. Online, https://www.imeko.org/publications/tc9-2022/IMEKO-TC9-2019-135.pdf. (Accessed 28 March 2024).

[4] H. Bissig, H.T. Petter, P. Lucas, E. Batista, E.A. Filipe, Primary standards for measuring flows from 100 nl/min to 1 ml/min – gravimetric principle, + another 9 authors, Biomed. Eng./Biomed. Tech. 60 (4) (2015) 301–316, https://doi.org/10.1515/bmt-2014-0145.

[5] F. Ogheard, S. Margot, J. Savary, Recent improvements of the French liquid micro-flow reference facility, Meas. Sci. Technol. 29 (2) (2018) 024007, https://doi.org/10.1088/1361-6501/aa97ef.

[6] J.D. Wright, J.W. Schmidt, Reproducibility of liquid micro-flow measurements, in: 18th International Flow Measurement Conference FLOMEKO, Lisbon, Portugal, 26.-28. June 2019, pp. 1–19. Online, https://tsapps.nist.gov/publication/get_pdf.cfm?pub_id=928073. (Accessed 28 March 2024).

[7] R. Doihara, T. Shimada, K.H. Cheong, N. Furuichi, Weighing system with low evaporation error for liquid microflow down to 1 mg/min, Flow Meas. Instrum. 81 (2021) 1012030, https://doi.org/10.1016/j.flowmeasinst.2021.102030.

[8] R. Doihara, K.H. Cheong, N. Furuichi, Evaluation of microflow calibration rig using static weighing system with flying start-and-finish method, in: 19th International Flow Measurement Conference FLOMEKO, Chongqing, China, 2022, pp. 1–5. Online, https://www.imeko.org/publications/tc9-2022/IMEKO-TC9-2019-141.pdf. (Accessed 28 March 2024).

[9] Consultative Committee for Mass and Related Quantities, Key comparison report template, version 1.4, Online, https://www.bipm.org/documents/20126/30125929/CCM+Key+Comparison+Report+Template/cf0a4b60-2ece-819c-e50f-f91972f29901, 24/02/2022. (Accessed 27 April 2024).

[10] J. Wright, B. Toman, B. Mickan, G. Wubbeler, O. Bodnar, C. Elster, Transfer standard uncertainty can cause inconclusive inter-laboratory comparisons, Metrologia 53 (October, 2016) 1243–1258. Online, https://tsapps.nist.gov/publication/get_pdf.cfm?pub_id=918285. (Accessed 28 March 2024).

[11] BIPM JCGM 200, International vocabulary of metrology - basic and general concepts and associated terms (VIM), third ed.. Online, https://www.bipm.org

/documents/20126/2071204/JCGM_200_2012.pdf/f0e1ad45-d337-bbeb-53a6-15fe649d0ff1, 2012. (Accessed 28 March 2024).
[12] K. Beissner, On a measure of constancy in comparison measurements, Metrologia 39 (1) (2002) 59–63, https://doi.org/10.1088/0026-1394/39/1/8.

Hugo Bissig[a,*], John Wright[b], Kevin Romieu[c], Elsa Batista[d], Kun-Chih Tsai[e], Ryouji Doihara[f]
[a] *METAS, Bern-Wabern, Switzerland*
[b] *NIST, Gaithersburg, USA*
[c] *CETIAT, Villeurbanne, France*
[d] *IPQ, Caparica, Portugal*
[e] *CMS, Hsinchu, Taiwan*
[f] *NMIJ, Tsukuba, Japan*

[*] Corresponding author.
E-mail addresses: hugo.bissig@metas.ch (H. Bissig), john.wright@nist.gov (J. Wright), kevin.romieu@cetiat.fr (K. Romieu), ebatista@ipq.pt (E. Batista), kctsai@itri.org.tw (K.-C. Tsai), r-doihara@aist.go.jp (R. Doihara).

Measurement: Sensors 38 (2025) 101551

Contents lists available at ScienceDirect

Measurement: Sensors

journal homepage: www.sciencedirect.com/journal/measurement-sensors

Development of measurement procedures for volume and flow related quantities in microfluidic devices

ARTICLE INFO

Keywords:
Microfluidic
Flow
Volume
Liquid proprieties
Calibration
Uncertainty

ABSTRACT

The precise control of fluids within channels is the common feature of the microfluidic systems, which endows them with innovative applications and makes them widely applied in multidisciplinary areas. This work carried out under the EMPIR project 20NRM02 MFMET has the focus on the development of procedures regarding volume and flow related quantity measurements using liquids such as water, simulated body fluid (SBF), and phosphate buffer saline (PBS), used for microfluidic and medical applications. The results and uncertainties obtained in the tested microfluidic devices made of glass, Cyclic Olefin Copolymer (TOPAS®) and Polydimethylsiloxane (PDMS) demonstrate the importance of traceable and comparable measurements to the characterization of microfluidic systems and their subsequent validation.

1. Introduction

Microfluidics, concerned with fluid-handling in the millilitre to nanolitre scale, has major applications in biomedical and chemical analysis, and recently specific applications of microfluidics, such as organ-on-chip, have had exponential growth. The development of microfluidics, and nanofluidics benefits from the advancements of engineering techniques, especially in the aspect of high resolution, low cost, easy processing, flexible design, and high throughput. Inspired by microelectromechanical systems, essential components, including channel, filter, valve, mixer, and pump, could be standardized and incorporated in a single chip to design highly portable innovative fluidic devices [1,2]. Therefore, the integrated fluidic devices are able to provide a versatile platform for the manipulation of flows at different length scales, and the advancements of microfluidics, and nanofluidics have stimulated the discoveries of novel materials and new sciences but so far, quality control of microfluidic devices has mainly derived from manufacturer and/or academia expertise, without reliance on well-established calibration procedures or standards that could potentially streamline and accelerate production [3,4]. Despite the expected impact of microfluidics (societal, health, well-being, environment, etc.), commercial success stories are rare in comparison with the number of laboratorial developments. The main reason for this is the gap between microfluidics advancements made with custom-made devices and the lack of reliable and reproducible products in the market. This is because chips and connections are often developed and fabricated in-house, the test protocols are customized, the materials are not compatible with high volume production, etc. Therefore, it is fundamental to develop guidelines as future standards in the areas of design, materials, and tests, which are of direct relevance to industrial players and end-users in this area.

This work, carried out under the EMPIR project 20NRM02 MFMET – Establishing Metrology Standards in Microfluidic Devices [4], had the purpose of testing different microfluidic devices concerning flow and volume quantities and develop the corresponding technical procedures. The methodologies developed are expected to be used in regulatory documents and standards and thus highly benefit the characterization of microfluidic devices, the accuracy of their physical and chemical functionality, and all metrological operations involved in their lifetime, from manufacturing to its application by the end-user.

2. Methods and procedures

The determination of volume and flow in a microfluidic device can be done using several measurements techniques. These will be explained in the following sections.

2.1. Flow measurements

Flow describes the unit quantity delivered over a unit time. Fluid flow related to the gravimetric method consists of mass flow rate [kg/s] and volume flow rate [m^3/s].

There are various methods for determining the flow rate, e.g. gravimetric method, front tracking, displacement methods (piston prover as flow generator, interferometry), μPIV and others [5]. In addition, there are also secondary methods (e.g. flow meters) which are not included in this report.

2.1.1. Gravimetric method

The gravimetric method is used to determine a delivered mass of a liquid over a time interval. The method can be used for measurements of both inline flow sensors and flow generators. To achieve the measurements a weighing vessel, placed on a balance, collects the liquid to determine the mass delivered. While the delivery time interval for the collection of the mass is determined as well.

The mass flow rate relates the delivered mass and the delivery time

https://doi.org/10.1016/j.measen.2024.101551

Available online 26 December 2024

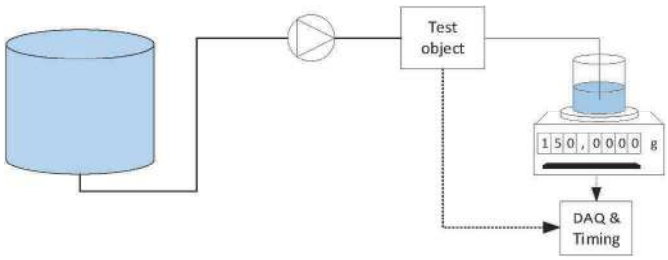

Fig. 1. Scheme of a gravimetric setup.

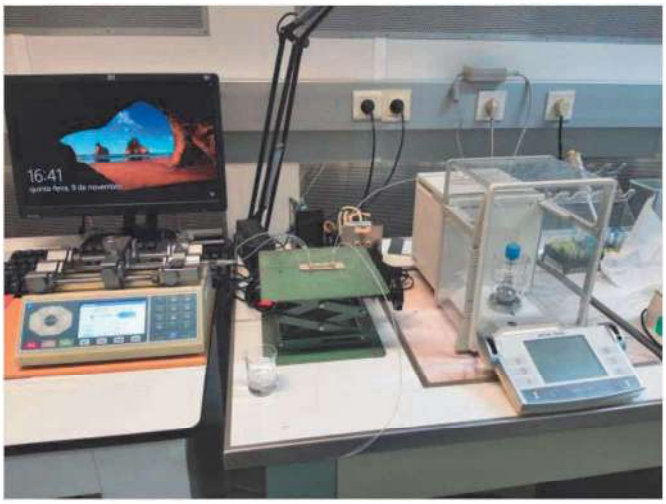

Fig. 2. IPQ gravimetric setup with glass chip.

and the volume flow rate relates to the mass flow rate and the liquid density as presented in Eq. (1) and Eq. (2) respectively:

$$q_m = \frac{m}{t} = \frac{I_L - I_E}{t}\left(\frac{1-\frac{\rho_0}{\rho_B}}{1-\frac{\rho_A}{\rho_L}}\right) . \quad (1)$$

$$q_V = \frac{Q_m}{\rho_L t} = \frac{I_L - I_E}{\rho_L t}\left(\frac{1-\frac{\rho_0}{\rho_B}}{1-\frac{\rho_A}{\rho_L}}\right) . \quad (2)$$

Where:

q_m Mass flow rate
q_v Volume flow rate
m Mass
I_L Balance indication of the weighing vessel with final amount of liquid
I_E Balance indication of the weighing vessel with initial amount of liquid
t Time
ρ_L Density of liquid
ρ_A Density of air
ρ_0 Density at reference conditions for weighing (1.2 kg/m^3)
ρ_B Density of the mass pieces (8000 kg/m^3)

In microfluidic applications flow measurements other corrections should be applied, namely the needle/tube buoyancy effect over the weighing vessel (since the needed is immersed in the water), evaporation, and surface tension between the needle and the liquid. The calculation of these effects is described in detail in the work of Bissig et al. [6] and in TIR 101 [7].

In a gravimetric microfluidic setup (Fig. 1), an electronic balance is used in most cases to determine the delivered mass of a fluid from/through a test object (can be a flow generator, a microfluidic device, or a flow meter). The time interval in which the mass is delivered is determined by a timing module to derive the mass flow rate. The climatic conditions such as air temperature, relative humidity and pressure are determined to correct for buoyancy effects on the balance in AAMI TIR 101 [7]. The liquid temperature is determined to convert the mass flow rate into a volumetric flow rate, considering the density of the liquid used. Often a layer of oil is applied on top of the water surface in the weighing tank (beaker) to reduce evaporation, especially at low flow rates and the needle is immersed in the liquid of the weighing vessel to avoid the drop count effect.

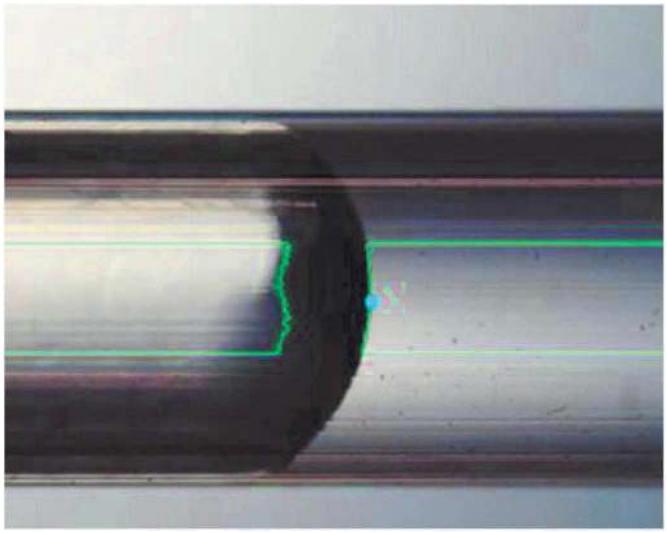

Fig. 3. Example of a meniscus reading inside a capillary.

In this work the flow will be measured gravimetrically with and without the microfluidic chips in order to access the influence of the microfluidic channels is the accuracy and stability of the imposed flow.

The gravimetric used setup at IPQ with a glass chip is presented in Fig. 2.

2.1.2. Front track method

The front tracking method [8,9] for flow measurements is an optical method that consists of tracking the position of the meniscus of a liquid (liquid/air or liquid/liquid interface) inside a (typically) capillary tube over time. An optical image acquisition system and image processing software is used to achieve the position over time of the meniscus. Knowing the displacement of the meniscus over time and the cross-section area of the capillary, it is possible to calculate the flow rate. Alternatively, the front tracking method can be applied directly in a microfluidic channel if the inner dimensions of the channel are known along with their associated uncertainties.

The fluid flowrate related to the front tracking method relates the optically acquired velocity of the fluid $\left(\frac{x_2-x_1}{\Delta t}\right)$ to the dimensions of the capillary tube (πr^2). If the flow is measured inside a channel, replace (πr^2) by the channel's cross-section (Eq. (3)).

$$q_v = \frac{x_2 - x_1}{\Delta t}\,\pi r^2 . \quad (3)$$

Where:

x_1 Initial position of the meniscus
x_2 Final position of the meniscus
Δt Time interval between the positions
r Capillary section radius.

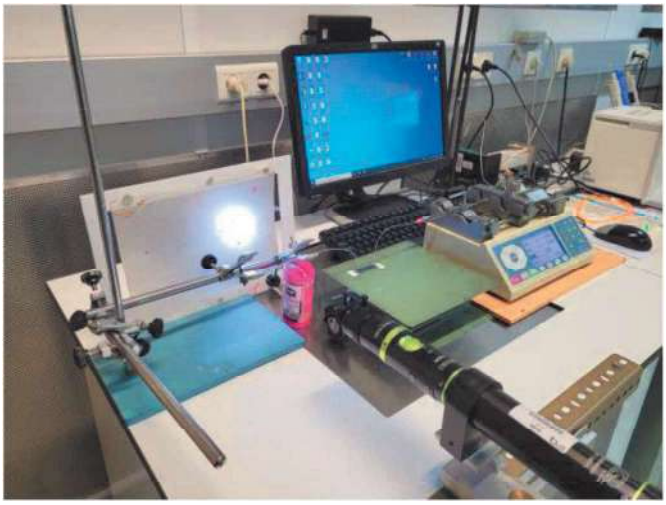

Fig. 4. IPQ front track setup with PDMS chip.

The test method includes calibration of the camera (determining the pixel size), image processing, and determination of position of the meniscus (Fig. 3).

- The calibration of the camera determines the relationship between dimensions of a known and calibrated object (for example the outer diameter of the capillary) and pixels of an image. Usually, the output of the camera's calibration is the pixel size in microns (μm).

The front track method used setup at IPQ with the PDMS chip is presented in Fig. 4.

2.2. Volume measurements

The volume of a microfluidic channel can be determined gravimetrically according to the formula described in ISO 4787 [10]:

$$V_{20} = (I_L - I_E) \times \frac{1}{\rho_L - \rho_A} \times \left(1 - \frac{\rho_0}{\rho_B}\right) \times [1 - \gamma(t - 20)] \,. \quad (4)$$

Where:

V_{20} vol at a reference temperature of 20 °C
I_L Balance indication of the vessel with the contained liquid
I_E Balance indication of the vessel with empty vessel
ρ_L Density of liquid
ρ_A Density of air
ρ_0 Density at reference conditions for weighing (1,2 kg/m^3)
ρ_B Density of the mass pieces (8000 kg/m^3)
t Temperature
γ is the coefficient of cubical thermal expansion of the material of which the chip tested is made

Each microfluidic channel is tested separately. The difference obtained in the weighing measurements gives the mass of the liquid contained in a particular channel, converted to volume using equation (4).

For the residual volume determination, the chips are weighted with the contained liquid and afterword the liquid is removed by aspiration. The difference between the two masses gives the residual volume, converted to volume using equation (4).

3. Microfluidic CHIPS

Three specific examples of microfluidic chips were used for the experiments:

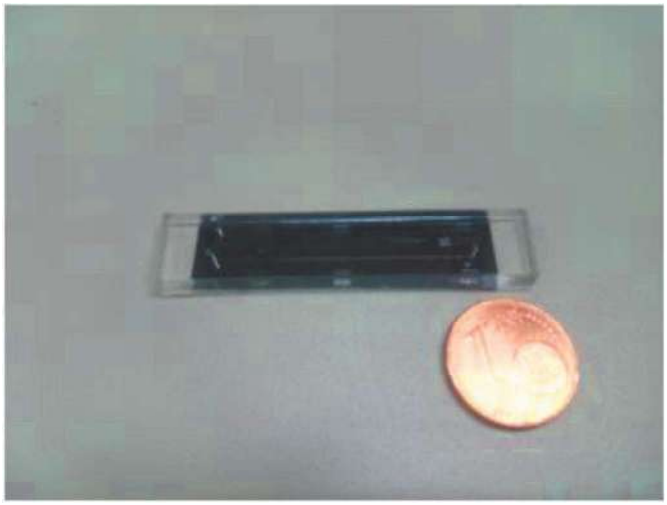

Fig. 5. PDMS chip.

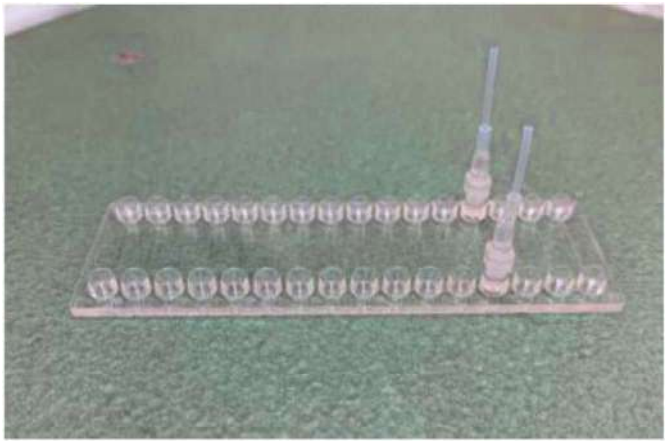

Fig. 6. TOPAS chip.

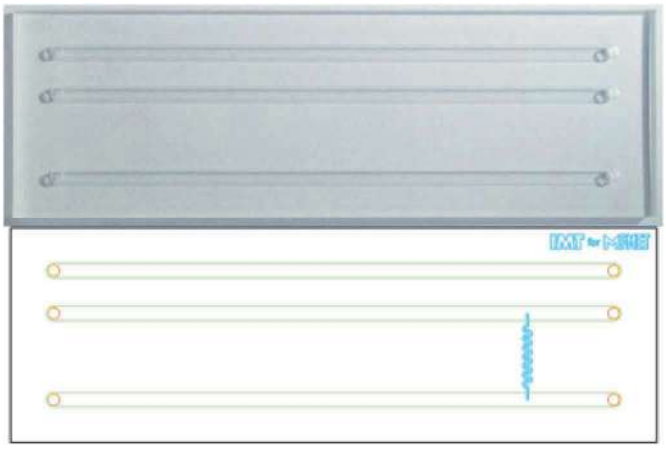

Fig. 7. Glass chip.

(i) Polydimethylsiloxane (PDMS) chip with one channel of 100 μm width and 50 μm depth, with two 0,9 mm inlet holes; material: PDMS; dimensions: 40 × 10 mm; manufactured by INESC MN (Fig. 5).

Table 1
Dimensions of the glass chip.

Dimensions	Width (mm)	Depth (mm)	Length (mm)
Main channels (green)	1.000	0.100	≈40
Leakage channels (blue)	0.150	0.002	≈10
Inlets and outlets	0.800		

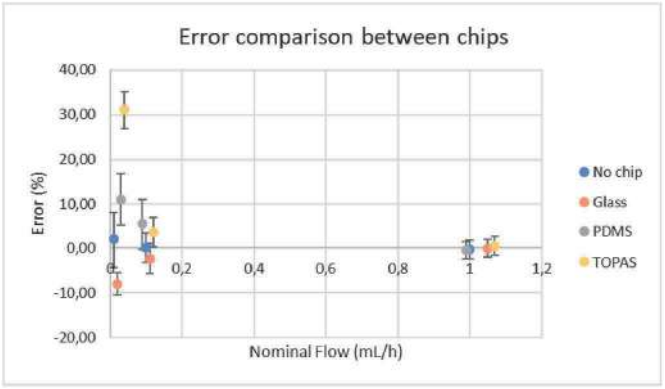

Fig. 8. Gravimetric flow results using different chips.

(ii) Topas Chip (see Fig. 6): parallel channels with mini Luer fluidic interface; material: TOPAS® (Cyclic Olefin Copolymer for medical use); dimensions: 75,5 mm x 25,5 mm × 4 mm; with eight parallel channels of 100 μm width, 100 μm depth, 18 mm length. Luer fluidic interface, similar to "female mini luer port" integrated directly on the chip, manufactured by microfluidic chip shop.

(iii) Glass chip (see Fig. 7): dimensions 45 × 15 × 2 mm (Table 1) material: glass; manufactured by IMTAG (Fig. 7).

4. Measurement results

4.1. Flow

Measurements of flow rate were performed in the 3 microfluid chips using the gravimetric method and the front track method. Three liquids were used, water, simulated body fluid (SBF), and phosphate buffer saline (PBS). Tests were performed at three different flow rates. The results are presented below:

4.1.1. Influence of the chip

In this test 3 different chips were tested at 0,01 mL/h, 0,1 mL/h and 1 mL/h. The results of the flow without the chip and with the different chips are presented in Fig. 8:

The error obtained is the difference between the flow set in the pump and the value determined in the balance.

From the results it can be observed the results and uncertainties at the large flow rate for all chips are very similar. At lower flow rate the error of the measurement with the chips are larger than the value of flow without the chip, meaning that there is an influence of the artifact in the results of flow rate (Fig. 8).

4.1.2. Influence of the liquid

Two different chips, PDMS and TOPAS were tested with 3 different liquids, water, PBS and SBF at 0,01 mL/h, 0,1 mL/h and 1 mL/h using the gravimetric method and a Nexus flow generator. The determined errors are obtained by the difference between the flow results obtained with and without the chip. The results are presented in Figs. 9 and 10:

It can be verified that the SBF and PBS liquid have larger errors than the water. The uncertainties are very similar for all liquids and flow rates.

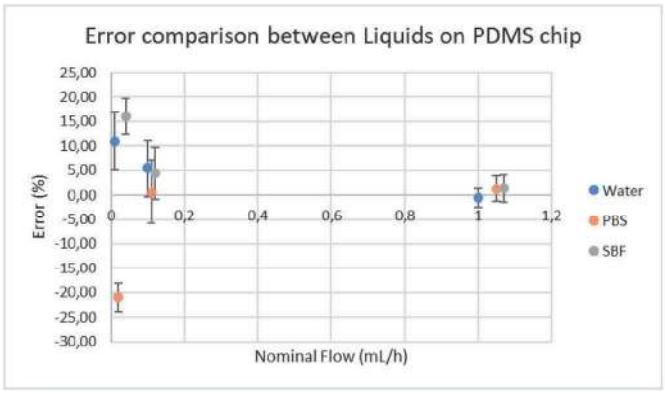

Fig. 9. PDMS chips flow results.

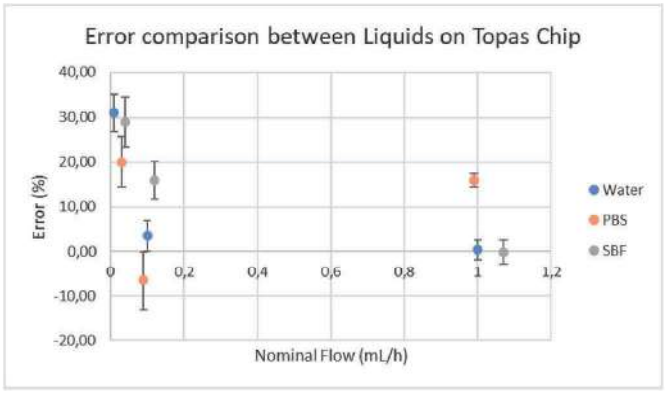

Fig. 10. TOPAS chips flow results.

Table 2
Method comparison results.

Method	Generated Flow (ml/h)	Tested Flow (ml/h)	Error (%)	*U* (%)
Gravimetric	0,1	0,097	2,6	3,4
	1	1,017	−1,7	3,0
Front track	0,1	0,0996	0,5	1,9
	1	1,0259	−2,5	4,0

The liquid variation effect in the flow rate is smaller in the PDMS chip compared with the TOPAS chip.

4.1.3. Different methods

The TOPAS chip was used in the method comparison. Two flow rates were tested with water as refence liquid. The results are presented in Table 2.

It can be seen from the results that the error and uncertainty obtained for each method is quite similar, with a En value of 0,55 for the 0,1 mL/h and 0,18 for 1 mL/h, therefore the two methods are consistent.

4.2. Hydrodynamic resistance

In a microchannel, it is possible to drive a flow by applying a pressure difference, for example using a pump. Here, the hydrodynamic resistance R_{hyd} is defined as the ratio of the pressure difference to the flow rate. For a given microchannel, R_{hyd} is a constant parameter that quantitatively describes the flow characteristics of the microchannel.

Using a Sensirion SLI-1000 flowmeter and Fluigent pressure unit S,

Table 3
Results from paired measurements of flow rate and pressure difference for chip 4-1.

Setup	Flow (μL/min)	Flow unc. ($k = 1$) (μL/min)	Pressure (mbar)	Pressure unc. ($k = 1$) (mbar)
System	50.7	1.5	12.1	1.7
	209.7	5.5	21.4	1.6
	420.	11.	32.3	1.6
	625.	16.	42.4	1.8
	828.	21.	54.6	2.4
	1027.	26.	68.2	2.
System	1028.	27.	70.5	2.8
	828.	21.	56.8	2.1
	628.	17.	41.3	2.5
	417.	11.	31.4	2.2
	210.2	5.9	20.7	1.8
	51.5	1.5	12.6	1.8
Main	50.7	1.5	15.5	1.8
	209.8	5.5	44.8	1.5
	421.	11.	72.7	1.5
	624.	16.	103.2	1.6
	827.	21.	128.7	1.6
	1026.	26.	157.2	1.6
Main	1029.	26.	155.8	1.7
	827.	22.	128.9	1.8
	624.	16.	100.3	1.7
	420.	11.	69.	1.9
	209.7	5.6	45.2	2.8
	50.7	1.4	13.3	1.5
Leakage	0.04711	0.00034	1989.	21.
	0.0856	0.00057	3900.	38.
	0.1181	0.0014	4128.	72.
	0.1457	0.0021	4173.	68.
Leakage	0.12927	0.00089	3750.	20.
	0.0985	0.0017	2937.	22.
	0.07	0.0011	2275.	20.
	0.04256	0.00031	1632.	32.
	0.0248	0.00041	1118.	22 (see Fig. 10).

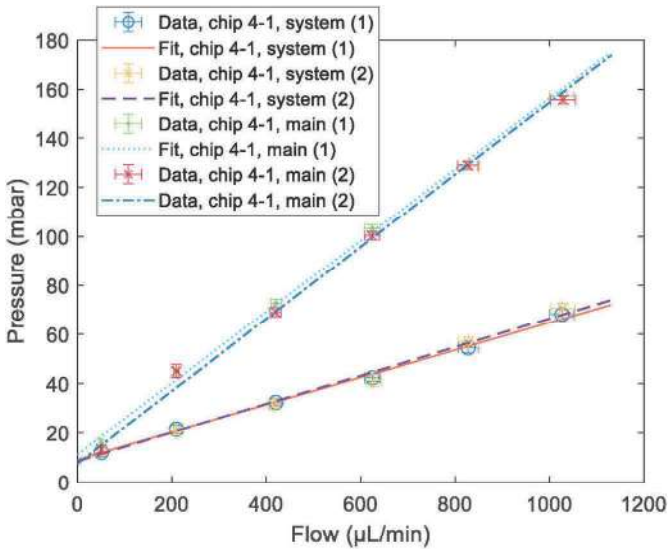

Fig. 11. Plot of flow rate and pressure data of the microfluidics test system and the system plus the main channel of chip 4-1. Also shown are associated linear fits.

measurements of flow rate and pressure were performed for larger flows through a main channel of chip 4-1, see Fig. 7. These sensors were also used to measure flow and pressure for the system, i.e. the microfluidic test system without the chip. Using the gravimetric method and a Fluigent pressure unit XL, measurements of flow rate and pressure were performed for smaller flows through the leakage channel of chip 4-1, see Fig. 7. The results are presented in Table 3.

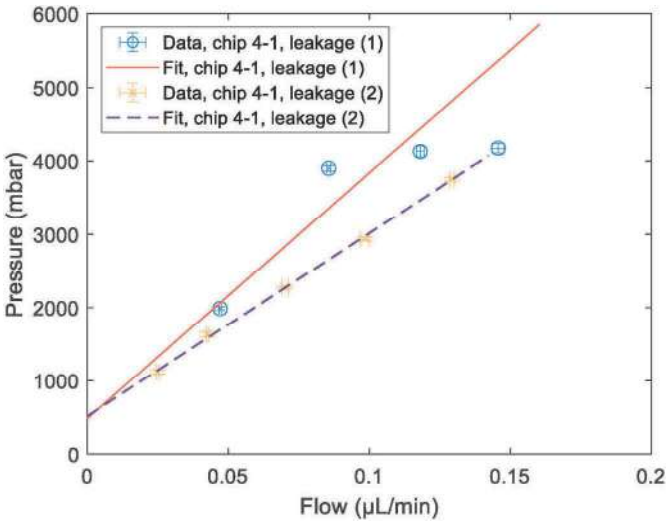

Fig. 12. Plot of flow rate and pressure data of the microfluidics test system plus the leakage channel of chip 4-1. Also shown are associated linear fits.

Table 4
Chi-square goodness of fit tests (Gof-test) for linear fits to the results in Table 3. Interpreted values of R_{hyd} are presented for fits where the Gof-test passed.

Setup	Statistics (χ^2, dof, p-value)	Gof-test (p-value>0.05)	R_{hyd} (mbar/μL/min)	R_{hyd} unc. ($k = 1$) (mbar/μL/min)
System	1.3, 4, **0.86**	Pass	0.0556	0.0025
System	3.0, 4, **0.55**	Pass	0.0574	0.0028
Main	7.4, 4, **0.12**	Pass	0.1449	0.0034
Main	7.4, 4, **0.12**	Pass	0.1471	0.0033
Leakage	335, 2, **0,0**	Fail	N/A	N/A
Leakage	3.8, 3, **0.29**	Pass	24972.	345.

Linear fits were attempted for the results in Table 3. If the fits passed a chi-square goodness of fit test (Gof-test), the slope of the fit was interpreted as the hydrodynamic resistance R_{hyd}. The data and fits are illustrated in Figs. 11 and 12. The resulting Gof-tests and possible hydraulic resistances are presented in Table 4.

In Table 4, the hydrodynamic resistance was well reproduced for the system and for the main channel. It was not possible to reproduce the hydrodynamic resistance for the leakage channel, and thus the reliability of the determined value for the leakage channel is more uncertain. Notice that the hydrodynamic resistance of the main channel and the leakage channel alone could be inferred by subtracting hydrodynamic resistance from elements to be excluded, i.e. the system or the system and the main channel.

Table 5
Results of the contained volume in different chips.

Chip	Liquid	Volume (mL)	U (mL)
PDMS	Water	0,00241	0,00013
	SBF	0,002329	0,000046
	PBS	0,002332	0,000066
TOPAS	Water	0,00368	0,00010
	SBF	0,003624	0,00011
	PBS	0,003531	0,000073
GLASS	Water	0,00423	0,00011
	SBF	0,004167	0,000072
	PBS	0,004157	0,000067

Table 6
Results of the residual volume in different chips.

Chip	Liquid	Volume (mL)	*U* (mL)
PDMS	Water	0,00023	0,00017
	SBF	0,000135	0,000034
	PBS	0,00039	0,00027
TOPAS	Water	0,000040	0,000048
	SBF	0,000191	0,000051
	PBS	0,000080	0,000030
GLASS	Water	0,000174	0,000036
	SBF	0,000201	0,000072
	PBS	0,000161	0,000072

4.3. Volume

Measurements of contained and residual volume in one microfluidic channel were performed in the 3 microfluidic chips using the gravimetric method.

4.3.1. Contained volume

The results of the contained volume can be observed in Table 5:

It can be verified that the contained volume and uncertainty with water is larger than for SBF and PBS liquid for all chips and this is probably due to evaporation effect of the water being larger than for the other liquids.

4.3.2. Residual volume

The results of the contained volume can be observed in Table 6:

It can be verified that the residual volume for glass is very similar for the 3 liquids. For PDMS there is a big variability in the residual volume depending on the liquid use, maybe due to the elasticity of the chip material.

5. Conclusions

In order to assess the accuracy of flow measurements and volume (contained and residual) in different types of microfluidic chips tests were performed using various liquids and calibrations methods.

It was observed a clear influence of the chips in the flow rate probably due to the channel flow resistance. Also, different liquids influence the flow rate depending on the type of material used for the chip. This also happens for volume determination.

From the two methods used, the gravimetric and the front track there were no significant variation found and the uncertainty were very similar.

The results and uncertainties obtained in the tested microfluidic devices made of glass, TOPAS and PDMS demonstrate the importance of traceable and comparable measurements to the characterization of microfluidic systems and their subsequent validation.

Acknowledgments

This project (20NRM02 MFMET) has received funding from the EMPIR programme co-financed by the Participating States and from the European Union's Horizon 2020 research and innovation programme.

References

[1] P. Johan, K. Mattias, C. Daniel, Microfluidic technologies in drug discovery, Drug Discov. Today 10 (20) (2005).
[2] V. Silverio, S. Cardoso, Lab-on-a-chip: systems integration at the microscale, Chapter E, in: Drug Delivery Devices and Therapeutic Systems, Elsevier Science, 2021. ISBN: 978-0-12-819838-4.
[3] D.R. Reyes, H. van Heeren, J. Res. Natl. Inst. Stand Technol. 124 (2019) 1–22, https://doi.org/10.6028/jres.124.001, 2019.
[4] https://MFMET.eu.
[5] EURAMET cg 27, Guidelines for the Calibration of Drug Delivery Devices and Infusion Device Analysers, 2024.
[6] H. Bissig, E. Batista, et al., Primary standards for measuring flow rates from 100 nl/min to 1 ml/min – gravimetric principle, Biomed. Eng. 60 (4) (2015) 301–316.
[7] AAMI TIR 101, Fluid Delivery Performance Testing for Infusion Pumps, 2021.
[8] E. Batista, J. Sousa, M. Álvares, J. Afonso, R. Martins, Application of the front tracking method in micro flow measuring devices, Meas. Sens. 23 (2022) 100397, https://doi.org/10.1016/j.measen.2022.100397.
[9] E. Batista, J. Sousa, M. Álvares, J. Afonso, R. Martins, Development of an experimental setup for micro flow measurement using the front tracking method, Meas. Sens. 18 (2021) 100152, https://doi.org/10.1016/j.measen.2021.100152.
[10] ISO 4787, Laboratory Glass and Plastic Ware - Volumetric Instruments - Methods for Testing of Capacity and for Use, 2021.

Elsa Batista[a,*], Vania Silverio[b,c], Kevin Romieu[d], João Alves e Sousa[a], Thomas Schrøder Daugbjerg[e]
[a] *IPQ, Caparica, Portugal*
[b] *INESC MN, Lisboa, Portugal*
[c] *IST-UL, Lisboa, Portugal*
[d] *CETIAT, Villeurbanne, France*
[e] *DTI, Aahrus, Denmark*

[*] Corresponding author.
E-mail addresses: ebatista@ipq.pt (E. Batista), vania.silverio@tecnico.ulisboa.pt (V. Silverio), kevin.romieu@cetiat.fr (K. Romieu), jas@ipq.pt (J. Alves e Sousa), tsda@teknologisk.dk (T.S. Daugbjerg).

Talanta 298 (2026) 128834

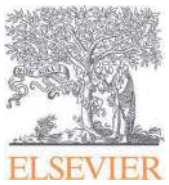

Contents lists available at ScienceDirect

Talanta

journal homepage: www.elsevier.com/locate/talanta

Inter-instrument definition of valid criteria for the automatic identification of microplastics by micro-Raman spectroscopy

Rafaela Fernandes [a], Paul-Tiberiu Miclea [b], Marta Fadda [c], Mara Putzu [c], A. Sacco [c], Andrea M. Rossi [c], Andrea M. Giovannozzi [c], Marta Barbaresi [d], Matteo Masino [d], Monica Mattarozzi [d], Maria Careri [d], Carla Palma [e], José Almeida [e], Claudia Drago [f], Olivier Pellegrino [g], Raquel Quendera [g], Ulrike Braun [f], Ricardo J.N. Bettencourt da Silva [a,*]

[a] Centro de Química Estrutural, Institute of Molecular Sciences, Departamento de Química e Bioquímica, Faculdade de Ciências, Universidade de Lisboa, Campo Grande, 1749-016 Lisboa, Portugal
[b] Fraunhofer Center for Silicon Photovoltaics (CSP), Germany
[c] Istituto Nazionale di Ricerca Metrologica (INRiM), Italy
[d] Department of Chemistry, Life Sciences and Environmental Sustainability, University of Parma, Parma, Italy
[e] Instituto Hidrográfico, Portugal
[f] Umweltbundesamt, German Environment Agency, Germany
[g] Instituto Português da Qualidade, Portugal

ARTICLE INFO

Handling editor: A Campiglia

Keywords:
Microplastics
Automatic identification
μ-Raman spectroscopy
Match threshold
Method validation
True results rate

ABSTRACT

The assessment of the impact of microplastic contamination on the environment and human health requires a reliable identification of the polymer type of these particles. μ-Raman spectroscopy is a popular technique for identifying microplastics by comparing the reference spectra with those of the particles analysed. Automatic identification of microplastics requires defining an algorithm for the match between these spectra and setting a minimum match above which identification is performed with adequately high true and low false results rates. Ideally, the algorithm and match threshold should apply to different spectrometers and spectra collection parameters. This research presents a methodology to determine the best match algorithm for polymer identification using μ-Raman spectroscopy data collected on different instruments and laboratories, associated with a true positive rate (*TP*) of 95 % and a false positive rate (*FP*) lower than 5 %. Determining the match threshold (*P*5»P) by the bootstrap method does not require assumptions regarding match distribution. The normal distribution of the match between the reference and a particle's spectra from a different material allows *FP* determination. Identifying PET microparticles was optimal using Pearson's correlation coefficient (*P*5»P = 0.6244, *TP* = 95 %, $FP = 4.9 \times 10^{-7}$ %). Identification quality was tested based on three unweighted and three weighted correlation coefficients. Spectra with signal-to-noise ratios lower than 10 were forwarded to manual identifications. The MS Excel files used in the research are available as supporting information. The developed methodology for setting up identification criteria of microplastics by spectroscopy proved to be adequate for μ-Raman assessments and robust to different spectrometers and spectra collection conditions.

1. Introduction

The characteristics of plastic materials that drive their commercial success, namely low cost and high chemical and physical resistance, combined with the inadequate disposal of these inexpensive materials, contribute to the ubiquitous presence of long-lasting plastic particles in the environment. The type, size, and shape of plastic materials influence their environmental impact, with smaller particles even able to travel inside living organisms. While significant research has evaluated the abundance of plastic waste [1,2], its impact on ecosystems and human health remains largely unknown due to the diversity and unpredictable consequences of this type of pollution. Plastic particles can be classified according to their size as macroplastics (>25 mm), mesoplastics (from 5 mm to 25 mm), microplastics (from 1 μm to 5 mm) and nanoplastics (<1

* Corresponding author.
E-mail address: rjsilva@ciencias.ulisboa.pt (R.J.N. Bettencourt da Silva).

https://doi.org/10.1016/j.talanta.2025.128834
Received 3 July 2025; Received in revised form 4 September 2025; Accepted 6 September 2025
Available online 9 September 2025

μm) [3].

Parallel to determining the toxicological impact of these particles, it is necessary to determine their abundance, respective trends, and the most relevant sources of contamination by these materials. This information should support the establishment and monitoring of policies to mitigate the environmental and health impacts of plastic pollution.

The harmonisation of procedures for monitoring plastic contamination in food products and environmental matrices is still lacking. Additionally, further developments are needed to assess the performance and evaluate the uncertainty associated with these monitoring methods [4,5].

When analysing food or environmental samples, it is necessary to identify which particles are indeed plastic before counting them. μ-FTIR (Fourier-transform infrared spectroscopy) and μ-Raman are the most popular tools for plastic particle identification before characterising their size and shape [6].

Compared to μ-FTIR spectroscopy, μ-Raman allows for the identification of smaller particles — down to the micrometer and even submicrometer scale — that are beyond the capabilities of FTIR [7]. Raman spectroscopy is also largely unaffected by the strong water absorption that constrains FTIR, making it particularly well suited for the analysis of aquatic samples [8]. In addition, it produces sharp and polymer-specific vibrational spectra, which facilitates better differentiation of chemically similar polymers than FTIR. Despite these advantages, Raman spectroscopy can be affected by fluorescence interference arising from dyes, additives, or biofilms, which may mask characteristic signals and hinder accurate polymer identification [9,10].

The spectroscopic identification of microplastics involves comparing the unknown particle spectrum with reference polymer spectra. Reference and particle spectra can be compared manually or automatically. While manual identifications are time-consuming and must be performed by qualified analysts, automatic identifications are faster and require less analytical expertise. Given the large number of plastic particles observed in some samples, automatic identifications are thus recommended. The most common method for quantifying the similarity between particle and reference spectra is the determination of their correlation using a correlation coefficient, such as the Pearson or Spearman correlation coefficient. The popularity of this method stems from its computational efficiency and the ease of interpreting the coefficients. However, the decrease in correlation values due to fluorescence interferences, baseline variations, signal noise, and particle weathering must be considered in data interpretation. Weighted correlation coefficients can be used to highlight relevant spectra features, improving identification reliability.

Spectral similarity can also be assessed using more complex chemometric tools, such as Principal Component Analysis (PCA) and Partial Least Squares Discriminant Analysis (PLS-DA). More recently, machine learning (ML), through techniques such as Neural Networks (NN), has been used to establish flexible and accurate methods for identifying microplastics even in the presence of noise and spectral overlap. Nevertheless, ML approaches require substantial computational resources, large training datasets, careful validation, and computational expertise, and they are often less transparent than traditional correlation methods. Therefore, the overcome of correlation coefficient fragilities in microplastics identification is particularly welcome.

A study by Jin et al. [11] used Raman spectra combined with PCA-LDA (LDA - Linear Discriminant analysis) followed by Support Vector Machine (SVM) classification to differentiate seven common polymers, i.e. polypropylene (PP), polyethylene terephthalate (PET), polyvinyl chloride (PVC), polycarbonate (PC), polyamide (PA), high density polyethylene (HDPE), and low density polyethylene (LDPE), reporting fitting accuracies over 98 % (ratio between true and total performed identifications) for most polymers and around 70 % for HDPE and LDPE. A study published by Xie et al. [12] extended these methods to nanoplastics, using Raman data with Random Forest (RF) classification to achieve an average accuracy of 98.8 % in identifying individual nanoplastic particles.

A more recent work by Zhang et al. [13] introduced a one-dimensional Convolutional Neural Network (1DCNN) trained on Raman spectra from ten polymer types, achieving a classification accuracy of approximately 96.4 %. Additionally, a CNN model applied to Surface-Enhanced Raman Scattering (SERS) spectra of six common microplastics demonstrated a mean identification accuracy of 99.5 %, outperforming classical classifiers such as SVM, PCA-LDA, PLS-DA, RF, and K-Nearest Neighbours [14].

Studies using hyperspectral Raman imaging paired with multivariate curve resolution have enabled visual mapping of microplastic particles in complex matrices, though classification metrics are less frequently reported [15]. Recent comprehensive reviews confirm that combining Raman spectroscopy with ML techniques — especially PCA, RF, SVM, and deep learning architectures — yields robust identification across varying environmental matrices [16].

Regarding performance statistics, supervised chemometric models consistently achieve high true positive rates (*TP*) (≥98 %) and low false positive rates (*FP*) (≤1 %), while deep learning approaches maintain strong *TP* (around 96 % to 99 %) with comparably low *FP*. Techniques based on SERS combined with CNNs have shown exceptional accuracy (~99.5 %) even with unpreprocessed data.

However, the listed chemometric tools require extensive data preprocessing, which is performed by complex software that consumes relevant computational resources. On the other hand, correlation coefficients are straightforward and computationally efficient, making them the preferred tool for rapid comparisons. Correlation determination is also easier to disseminate in harmonised analysis protocols.

Some guidelines and standards designate the quantified spectral similarity as a Match or Hit Quality Index (HQI) with a maximum value of 100 %. Unfortunately, HQIs are frequently presented and discussed without specifying the algorithm or computational tool used. This omission makes it impossible to compare values determined by different authors and to discern which spectral characteristics contribute most to the similarity value. Some documents even define thresholds for reliable identifications, such as HQI >60 % [17] or HQI >80 % [18], without specifying how HQI should be determined and what data and statistics support the threshold. The harmonisation of protocols is only effective if supported by adequately described and performing protocols applicable to data collected in various laboratories using different instruments. To protect match determinations from noisy signals, a signal-to-noise ratio (S/N) threshold can be defined, below which spectra should be assessed manually or using an alternative tool.

Morgado et al. [4,5] developed a strategy for the automatic identification of microparticles isolated from river and marine sediments based on μ-FTIR, where reference and particle spectra were collected using the same equipment and spectral parameters. Microparticles were manually identified and designated as positive or negative cases based on whether they were from the specific polymer type being studied or not, respectively. For instance, when identifying PET particles, all particles from this polymer were considered positive cases, while all non-PET particles were considered negative cases. After selecting a specific match algorithm and reference spectrum, match values between the reference and positive or negative case spectra were determined. The 5^{th} percentile of match values for positive cases, determined by the bootstrap method [19], was used as the minimum match for polymer identification, with a true positive rate (*TP*) of 95 %. When the particle and reference are from the same polymer, in 95 % of cases, the match exceeds the threshold. This threshold was subsequently tested for the chance of a particle from a material different from the reference polymer producing a spectrum with a match with the reference spectra above the threshold, i.e. the false positive rate (*FP*). Assuming the normal distribution of the match with negative cases, this probability was estimated using regular parametric statistics. An identification method applicable to microplastic identification in environmental samples is considered adequate if associated with a $TP = 95$ % and $FP \leq 5$ % [20]. Various

algorithms for match determination were tested to identify signal transformations and correlation formulas that drive lower *FP*. Since spectral comparison is affected by the low intensity of FTIR bands and the absorbance band from non-oxidised biofilm, a minimum value for the most intense spectral band and a maximum intensity for biofilm bands were defined to exclude spectra from automatic identification. Such spectra should undergo manual identification due to observed signal fragilities.

This paper advances the state-of-the-art in microplastic identification by establishing identification criteria applicable to μ-Raman spectra collected using different instruments and experimental conditions. The μ-Raman spectra improve identification due to their high selectivity and narrow peaks, compared with the broader spectral bands observed in FTIR. An algorithm for determining the S/N was developed to identify spectra that require manual identification by experienced analysts. In this study, PET was chosen as a representative polymer to assess the viability of the approach to determine match thresholds and evaluate match methods, as a result of its extensive use in food packaging and its limited stability under hard oxidative treatments, high temperatures or strong alkaline conditions. Furthermore, the reference material provides a realistic representation of the morphological variability of microplastics, including different shapes and size distribution, commonly found in environmental and food samples. Spectra collected from three different laboratories and in two matrices, ultrapure water and milk, were studied to assess the robustness of the methodology for these factors. The assessment of the ability of the developed method to identify other polymers and weathered particles requires collecting additional spectra and applying a method development and validation equivalent to that performed in this research.

2. Experimental

2.1. Particles and spectra collection conditions

From the 175 particles analysed, 93 were PET and 82 were non-PET. PET particles were provided by the German Federal Institute for Materials Research and Testing (BAM) within the framework of the EU-funded PlasticTrace project. These reference materials were in the form of soluble tablets containing secondary PET microparticles, with irregular shapes and sizes ranging from 10 μm to 100 μm.

Non-PET plastic polymers were analysed in different physical forms (e.g., pellets, powders, films) with a size distribution from 0.05 mm to 5 mm.

While most PET tablets analysed were dissolved in ultrapure water, some were dissolved in powdered milk (infant formula) after reconstitution in ultrapure water. As a result, 4 out of the 175 Raman spectra were acquired from particles in the milk-derived matrix.

The Raman spectrometers and their instrumental conditions used by the three laboratories (Lab. 1 to Lab. 3) are listed in Table 1. The table specifies the wavenumber interval and number of spectral points (Detector pixels) of the original spectra.

Although the Diffraction Grating expresses the dispersion of wavenumber per length unit, since detector pixels can have different lengths, this parameter is not directly related to the spectral resolution. Instead, the ratio between the spectral range (cm^{-1}) and the number of detector pixels, the Spectral Sampling Interval, $\Delta\nu$, is a better way to express spectral resolution. In this work, the spectra were collected with a $\Delta\nu$ between 1.19 cm^{-1} and 5.22 cm^{-1}, subsequently converted to $\Delta\nu$ = 6.51 cm^{-1} in the interval 856 cm^{-1} and 1787 cm^{-1}, considering 143 equidistant points/pixels to allow for spectrum comparison. An Excel spreadsheet was used for spectra harmonisation. No obvious resolution loss was observed when comparing spectra sampled at $\Delta\nu$ = 1.19 cm^{-1} and 6.51 cm^{-1}.

Since the Raman shift is referenced to the excitation wavelength (in this work, 514 nm, 532 nm, or 633 nm), although different lasers can produce the same Raman shift peaks, their relative intensities can differ due to resonance effects, fluorescence background, or absorption. Therefore, the different laser wavelengths of the used spectrometers impact the comparability of the spectra.

Though the Raman signal is proportional to the laser output power, excessively high power may excite fluorescence that can overwhelm the Raman peaks. Too much power can also cause photodegradation of the sample. Therefore, this parameter should be optimized to achieve an acceptable S/N without damaging the sample.

The microscope objective magnification (*MOM*) affects the collection of spectra from particles smaller than the scanned area, but it does not influence the Raman shift positions, the relative intensities of the peaks, or the spectral resolution. Depending on the *MOM*, the numerical aperture determines how tightly the laser is focused and how efficiently scattered light is collected, and thus requires optimization to achieve a better S/N ratio.

Longer acquisition times and signal accumulation reduce the signal's noise. Very short acquisition times can hinder peak detectability, while excessively long acquisition times may cause detector saturation, nonlinearity, or sample damage, which can compromise polymer identification [21].

2.2. Method validation strategy

The validation of the method for identifying PET microparticles by μ-Raman spectroscopy involved collecting spectra from PET and non-PET particles using the spectrometers and instrumental conditions listed in Section 2.1. The particles were manually identified, considering at least the three most intense characteristic Raman spectra peaks of PET occurring at 1615 cm^{-1}, 1120 cm^{-1}, and 1000 cm^{-1}. The Raman shift range for spectra comparison was limited between 856 cm^{-1} and 1787 cm^{-1}. All collected spectra are made available as Supplementary Material 01 being identified with the following code: "A B (C)", where A identifies the polymer type ("PET", "non-PET" or specified polymer acronym such as "PE" [22]), B is a sequential number, and (C) specifies the laboratory that produced the spectra (F – Fraunhofer CSP, I – Istituto Nazionale di Ricerca Metrologica (INRiM) and UP – University of Parma).

After selecting a match algorithm identified by the code presented in

Table 1
Raman spectrometers and relevant instrumental conditions used by the three laboratories. Lab.1 – Fraunhofer CSP (two equipment used, Sp. 1 and Sp. 2), Lab.2 – INRiM and Lab.3 – University of Parma.

Lab.	Spectrometer	*DF*/ (gr. nb./mm)	*LW*/nm| *OP*/mW	*MOM* |*NA*	Detector	*DP*	*WI*/cm^{-1}	*AT*/s| *AN*
1 (Sp. 1)	Triple 557 TriVista	1500	514|100	50 × |0.75	LN2| Si-CCD	450	850 to 3200	1 to 10| 5 to 10[a]
1 (Sp. 2)	HORIBA LabRAM HR Evolution	1800	532|100	50 × |0.75	LN2| Si-CCD	450	850 to 3200	1 to 10|5 to 10[a]
2	HORIBA LabRAM Odyssey	600	633|15	10 × |0.25	LN2| Si-CCD	1024 or 512	664 to 1786	1| 1
3	HORIBA LabRAM HR Evolution	600	532|25	50 × |0.50	LN2| Si-CCD	1024	415 to 2060	1 to 5| 3 to 20[a]

DF – Diffraction grating in groove number by mm; *LW* – Laser wavelength in nm; *OP* – Output power in mW; *MOM* – Microscope objective magnification; *NA* – Numerical aperture; *DP* – Number of detector pixels; *WI* – Wavenumber interval in cm^{-1}; *AT* – Acquisition time in s; *AN* – Accumulation number; LN2\| Si-CCD - silicon-based charge-coupled device cooled with liquid nitrogen.

[a] Optimized according to the specific polymer type and its physical characteristics.

Table 2
Match algorithm identification code, where *CC* is the studied correlation coefficient [4]. "*S*" specifies the type of signal considered (*I*, 1/*I* and (1-I_N) for original, inverse and complementary intensity after signal normalisation – numbers 1, 2 or 3 from code "*S*|#|*CC*|#|#"). The "*d*" specifies the use of the original signal, *S*, or its first or second derivative ($f'(S)$ and $f''(S)$) (*S*|*d*|*CC*|#|#) (*d* = 1, 2 or 3). For weighted *CC*, the signal was weighed (*SW* equal to *y* for yes – Code "*S*|*d*|*CC*|1|#"), and the wavenumber of the Raman shift was weighted directly, $\tilde{\nu}$, ("1") or inversely, $1/\tilde{\nu}$ ("2")) (*S*|*d*|*CC*|*SW*|*RW*).

Match	*S*	*d*	*SW*	*RW*	Match	*S*	*d*	*SW*	*RW*
1|1|*CC*|1|1	*I*	*S*	*y*	$\tilde{\nu}$	1|1|*CC*|1|2	*I*	*S*	*y*	$1/\tilde{\nu}$
2|1|*CC*|1|1	(1/*I*)	*S*	*y*	$\tilde{\nu}$	2|1|*CC*|1|2	(1/*I*)	*S*	*y*	$1/\tilde{\nu}$
3|1|*CC*|1|1	(1 - I_N)	*S*	*y*	$\tilde{\nu}$	3|1|*CC*|1|2	(1- I_N)	*S*	*y*	$1/\tilde{\nu}$
1|2|*CC*|1|1	*I*	$f'(S)$	*y*	$\tilde{\nu}$	1|2|*CC*|1|2	*I*	$f'(S)$	*y*	$1/\tilde{\nu}$
2|2|*CC*|1|1	(1/*I*)	$f'(S)$	*y*	$\tilde{\nu}$	2|2|*CC*|1|2	(1/*I*)	$f'(S)$	*y*	$1/\tilde{\nu}$
3|2|*CC*|1|1	(1 - I_N)	$f'(S)$	*y*	$\tilde{\nu}$	3|2|*CC*|1|2	(1 - I_N)	$f'(S)$	*y*	$1/\tilde{\nu}$
1|3|*CC*|1|1	*I*	$f''(S)$	*y*	$\tilde{\nu}$	1|3|*CC*|1|2	*I*	$f''(S)$	*y*	$1/\tilde{\nu}$
2|3|*CC*|1|1	(1/*I*)	$f''(S)$	*y*	$\tilde{\nu}$	2|3|*CC*|1|2	(1/*I*)	$f''(S)$	*y*	$1/\tilde{\nu}$
3|3|*CC*|1|1	(1 - I_N)	$f''(S)$	*y*	$\tilde{\nu}$	3|3|*CC*|1|2	(1 - I_N)	$f''(S)$	*y*	$1/\tilde{\nu}$

Table 2, including the considered correlation coefficient (*CC*), the match between the reference spectra (PET 01 (F)) and the spectra of all PET or non-PET particles was determined. The studied *CC* are *r*, ρ, and C_{PE} for unweighted Pearson, Spearman, and alternative correlation coefficients, and r_w, ρ_w, and C_{PEW} are the weighted versions of the first [4]. The total number of studied matches is 81 (9 × 3 matches involving unweighted *CC* and 18 × 3 matches involving weighted *CC*).

For the unweighted *r* and ρ, the identification performance is the same for signal (*I*) or (1 - I_N). For the unweighted C_{PE}, and the weighted correlation coefficients, both signal types ((*I*) or (1 - I_N)) can produce different identification performance due to algorithm features.

Positive cases correspond to PET particles, and negative cases refer to non-PET particles. The 5th percentile of the match values for positive cases was determined using the bootstrap resampling method, which simulates its distribution [4,5]. The *P*5»P, the 5th percentile of the 5th percentile distribution of positive cases, is the minimum value of the specific match algorithm above which a particle can be defined as PET with a true positive rate of not less than 95 %, meaning that, in studied PET spectra, there is at least a 95 % probability that a PET microparticle spectrum has a match with "PET 01 (F)" spectrum above *P*5»P. Afterwards the mean, *M*, standard deviation, *s*, and total number, *n*, of match values between "PET 01 (F)" and negative cases is calculated being the false positive rate, *FP*, the complementary of the cumulative t-distribution of (*P*5»P – *M*)/*s* for *n* - 1 degrees of freedom. The *FP* is the estimated chance of a non-PET particle, from the studied non-PET population, producing a match with the "PET 01 (F)" spectra above *P*5»P, therefore being wrongly identified as PET. All match algorithms (Table 1) were tested and considered adequate for PET identification if, together with the *TP* set at 95 %, the *FP* is not larger than 5 %. In this case, the identification performance quantified as a likelihood ratio *LR* (*LR* = *TP*/*FP*) or accuracy, *A* [*A* = (*TP* + *TN*)/(*TP* + *TN* + *FP* + *FN*); where *TN* and *FN* are true and false negative rates complementary to *FP* and *TP* respectively], should not be lower than 19 [4,5,20] or 95 %, respectively.

An *FP* of 5 % is considered adequate for the analysis of environmental and food samples with one microplastic, given the number of required identifications and the health impact of microplastic contamination [4,5,20].

Since the reliability of particle identification is affected by the low intensity of peaks compared to the signal's noise, an algorithm was developed to determine the S/N. This algorithm, described in Section 2.2.1, is applicable regardless of the scale of absolute peak intensities, which vary depending on the spectrometers and spectral collection conditions used. Spectra with S/N lower than 10 should be forwarded to manual identification.

2.2.1. *Determination of signal-to-noise ratio*

To characterise Raman spectra regarding the spectral information clarity, the highest S/N was determined as the ratio between the most intense peak of the spectrum and the background noise. The intensity of the most intense peak was determined as the difference between the maximum signal observed in the spectrum and the minimum signal predicted at the wavenumber of the maximum signal by a regression line. This regression line, referred to as "baseline", is defined from minimum signals of 20 wavenumber segments with equal wavenumber ranges. The absolute difference between the average signal and the minimum signal within each segment is calculated and then averaged across all segments, yielding a value that quantifies the spectrum noise. Fig. 1 presents examples of spectra collected by three laboratories with S/N equal to 15.

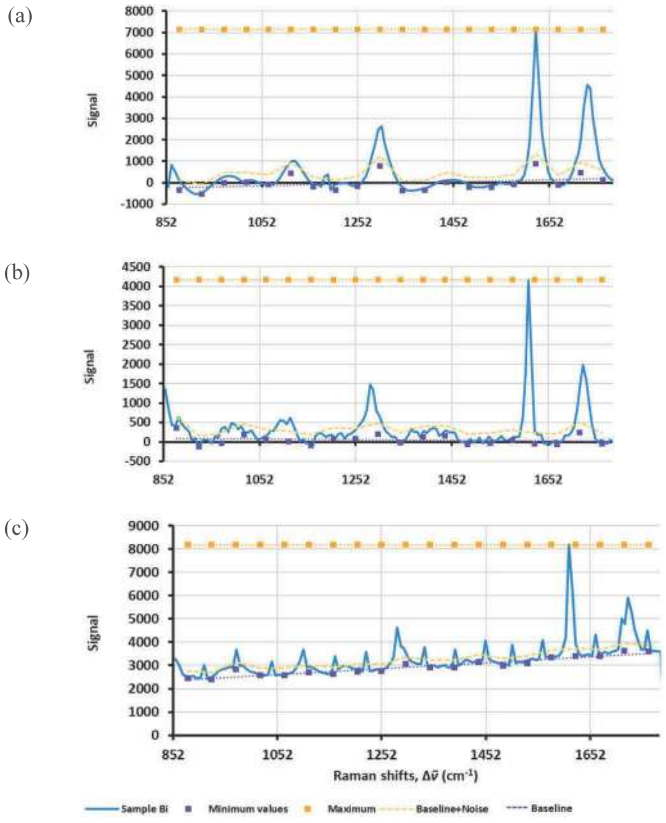

Fig. 1. Spectra (a), (b) and (c) present spectra with S/N of 15 obtained from Fraunhofer CSP, INRiM and the University of Parma, respectively. The mean, minimum and base regression lines of 20 wavenumber ranges are also presented. The developed algorithm was implemented in the MS Excel file used to quantify the match between the studied spectra (Supplementary Material 02).

3. Results and discussion

Table 3 presents the best-performing match algorithms, i.e. those associated with lower *FP*, considering all collected spectra and spectra with a S/N greater than 10. For r and ρ, only I and $1/I$ signals were considered because I and $(1 - I_N)$ produce the same results. The *P*5»P estimated by the resampling bootstrap method slightly varies with the simulation run, with an impact on estimated *FP* and *LR*. It is reported the *P*5»P, *FP*, *LR* and the number of positive, n_P, and negative, n_N, cases considered. For the unweighted correlation coefficients, *SW* and *RW* are not specified.

Supplementary Material 03 presents the S/N of all spectra, match values determined for positive and negative cases for the 81 studied match methods and the *FP* and *LR* for the match methods.

As expected, identification performance improves and *P*5»P raises when considering a S/N threshold. Several match algorithms enable identification with an *LR* larger than 19 and an accuracy larger than 95 %, where the unweighted Pearson's correlation of the original signals distinguishes between positive and negative cases more effectively when a S/N threshold of 10 is considered.

Several weighted correlation coefficients can support valid PET identifications. The weighted alternative correlation coefficient, C_{PE_w}, for complementary normalised signals $(1 - I_N)$ and the two studied types of weighing are the most successful weighted algorithms ($3|1|\ C_{PE_w}\ |1|1$ and $3|1|\ C_{PE_w}\ |1|2$).

The *TP* of 95 % and *FP* of 4.90×10^{-7} % of identifications based on Person's correlation coefficient and S/N > 10 are converted into an identification accuracy of 97.5 %, comparable to the observed accuracy using advanced chemometrics tools that require significantly more computational resources.

The identification criteria can be implemented for new spectra using the Excel file available as Supplementary Material 04. Detailed instructions of how to use this spreadsheet are available in video file Supplementary Material 05.

Supplementary data related to this article can be found online at https://doi.org/10.1016/j.talanta.2025.128834

Fig. 2 presents a graphical representation of Match values for positive and negative cases and the *P*5»P for the Match methods listed in Table 3 considering (a) all spectra or (b) only signals with a S/N > 10. The Match of positive and negative cases are rather distinct being worth highlighting the very low dispersion of Match values of both positive and negative cases for the Match method $3|1|\ C_{PE}$ valid for S/N > 10.

4. Conclusions

The proposed methodology to develop a valid procedure for the automatic identification of microplastics using μ-Raman spectroscopy applicable to spectra collected from different spectrometers and spectra collection conditions was successfully applied to the identification of PET microplastics. Different match algorithms were tested, considering the use of original or inverse signals, before or after derivatisation, and based on unweighted Pearson's, Spearman's, an alternative algorithm, or weighted versions of these correlation coefficients. For the more complex weighted coefficients, signal and two types of wavenumber weightings were considered. The minimum match value (*P*5»P) for identifying a PET particle corresponds to the 5th percentile of the match between spectra of the PET reference and particle, and it is determined by the resampling bootstrap method. The bootstrap method does not require match distribution normality. The match values between the PET reference spectrum and particle spectra proved not to be PET allowed estimating the probability of a non-PET particle producing a match value with the PET reference above *P*5»P. This probability is the false positive rate. A methodology for quantifying the signal-to-noise ratio was developed, and spectra with an S/N lower than 10 were

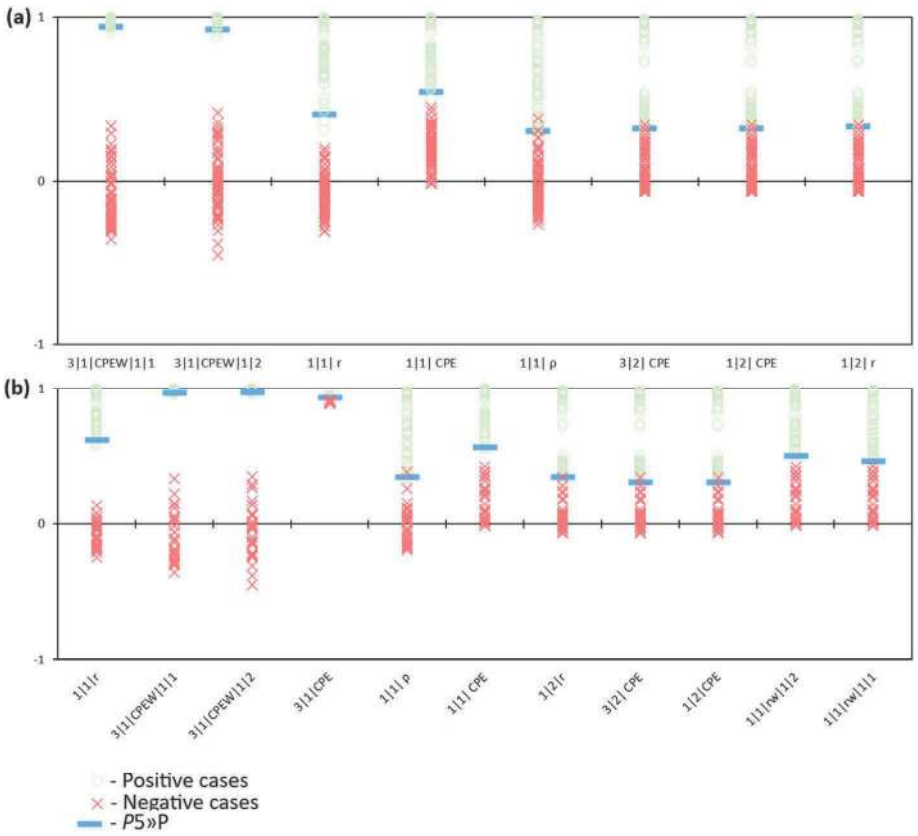

Fig. 2. Graphical representation of Match values for positive and negative cases and the 5th percentile for positive cases, *P*5»P, for the Match methods presenting *LR* larger than 19. (a) All spectra considered; (b) Only spectra with S/N > 10 are considered.

Table 3
Best-performing match algorithms, considering all collected spectra and spectra with S/N larger than 10. The *P5*»P is the match threshold, *FP* the false positive rate, *LR* the likelihood ratio (*LR* = *TP/FP*; *TP* is the true positive rate), and n_P and n_N the number of considered PET and non-PET cases.

All spectra (n_P = 92 and n_N = 82)				Spectra with S/N > 10 (n_P = 80 and n_N = 33)			
Match	*P5*»P	*FP*/%	*LR*	Match	*P5*»P	*FP*/%	*LR*
3|1| C_{PE_w} |1|1	0.9386	4.46×10^{-7}	2.13×10^{8}	1|1|r	0.6244	4.90×10^{-7}	1.94×10^{8}
3|1| C_{PE_w} |1|2	0.9212	5.15×10^{-5}	1.85×10^{6}	3|1| C_{PE_w} |1|1	0.9664	8.09×10^{-5}	1.17×10^{6}
1|1|*r*	0.4049	0.00660	1.44×10^{4}	3|1| C_{PE_w} |1|2	0.9734	0.000537	1.77×10^{5}
1|1| C_{PE}	0.5418	0.190	501	3|1| C_{PE}	0.9325	0.282	336
1|1|ρ	0.3000	0.985	96.5	1|1|ρ	0.3471	0.507	188
3|2| C_{PE}	0.3167	1.30	73.2	1|1| C_{PE}	0.5703	0.620	153
1|2| C_{PE}	0.3167	1.30	73.2	1|2|*r*	0.3438	0.627	151
1|2|*r*	0.3166	1.32	71.9	3|2| C_{PE}	0.3089	1.33	71.2
				1|2| C_{PE}	0.3051	1.45	65.6
				1|1| r_w |1|2	0.5072	1.68	56.5
				1|1| r_w |1|1	0.4692	2.93	32.4

excluded from the automatic identification. The unweighted Pearson's correlation coefficient of the original signal proved to be the most adequate match algorithm for PET particle identification for a match threshold, *P5*»P, of 0.6244. The identification with this match is associated with a true positive rate of 95 % and a very low false positive rate of 4.90×10^{-7} %, fit for microplastic identifications in environmental and food samples. This performance, which guarantees an accuracy of 97.5 %, is equivalent to that observed using complex chemometric tools that require extensive data processing of a large number of spectra.

The user-friendly spreadsheets used to set the *P5*»P and for the subsequent identification of microparticles are made available as supplementary material.

Although promising, the developed methodology should be evaluated for its ability to produce a reliable method for the identification of other polymer types, aged polymers, and particles contaminated with biofilm. Ideally, the identification approach should also be tested considering spectra collected by additional spectrometers.

CRediT authorship contribution statement

Rafaela Fernandes: Writing – review & editing, Writing – original draft, Visualization, Validation, Software, Resources, Methodology, Investigation, Formal analysis, Data curation, Conceptualization. **Paul-Tiberiu Miclea:** Writing – review & editing, Writing – original draft, Resources, Investigation, Funding acquisition, Data curation, Conceptualization. **Marta Fadda:** Writing – review & editing, Resources, Investigation, Data curation. **Mara Putzu:** Writing – review & editing, Resources, Investigation, Data curation. **A. Sacco:** Writing – review & editing, Resources, Investigation, Data curation. **Andrea M. Rossi:** Writing – review & editing. **Andrea M. Giovannozzi:** Writing – review & editing, Writing – original draft, Supervision, Resources, Project administration, Investigation, Funding acquisition, Conceptualization. **Marta Barbaresi:** Writing – review & editing, Writing – original draft, Investigation, Data curation. **Matteo Masino:** Writing – review & editing, Investigation, Data curation. **Monica Mattarozzi:** Writing – review & editing, Supervision, Investigation, Data curation, Conceptualization. **Maria Careri:** Writing – review & editing, Supervision, Resources, Project administration, Investigation, Funding acquisition, Data curation, Conceptualization. **Carla Palma:** Writing – review & editing, Methodology, Funding acquisition, Conceptualization. **José Almeida:** Writing – review & editing. **Claudia Drago:** Writing – review & editing, Supervision, Project administration, Conceptualization. **Olivier Pellegrino:** Writing – review & editing, Funding acquisition, Conceptualization. **Raquel Quendera:** Writing – review & editing. **Ulrike Braun:** Writing – review & editing, Resources, Funding acquisition. **Ricardo J. N. Bettencourt da Silva:** Writing – review & editing, Writing – original draft, Visualization, Validation, Supervision, Software, Resources, Methodology, Investigation, Funding acquisition, Formal analysis, Data curation, Conceptualization.

Declaration of competing interest

The authors declare that they have no known competing financial interests or personal relationships that could have appeared to influence the work reported in this paper.

Acknowledgment

The authors thank the European Commission for funding the PlasticTrace project (21GRD07) from the European Partnership on Metrology (Funder ID: 10.13039/100019599), co-financed from the European Union's Horizon Europe Research and Innovation Program and by the Participating States. This work was supported by Fundação para a Ciência e a Tecnologia (FCT) (Projects UIDB/00100/2020 and UIDP/00100/2020), and Institute of Molecular Sciences (Project LA/P/0056/2020).

Appendix B. Supplementary data

Supplementary data to this article can be found online at https://doi.org/10.1016/j.talanta.2025.128834.

Data availability

Data available as supplementary material and deposited in Zenodo with DOI 10.5281/zenodo.17079479.

References

[1] V. Redko, L. Wolska, M. Potrykus, E. Olkowska, M. Cieszyńska-Semenowicz, M. Tankiewicz, Environmental impacts of 5-Year plastic waste deposition on municipal waste landfills: a Follow-up study, Sci. Total Environ. 906 (2024) 167710, https://doi.org/10.1016/J.SCITOTENV.2023.167710.
[2] Y. Yang, M. Jalalah, S.A. Alsareii, F.A. Harraz, N. Thakur, Y. Zheng, M. Koutb, Y. Yoon, E.S. Salama, Plastic wastes (PWs) and microplastics (MPs) formation: management, migration, and environmental impact, J. Environ. Chem. Eng. 12 (3) (2024), https://doi.org/10.1016/J.JECE.2024.112926.
[3] N.B. Hartmann, T. Hüffer, R.C. Thompson, M. Hassellöv, A. Verschoor, A. E. Daugaard, S. Rist, T. Karlsson, N. Brennholt, M. Cole, M.P. Herrling, M.C. Hess, N.P. Ivleva, A.L. Lusher, M. Wagner, Are we speaking the same language? Recommendations for a definition and categorization framework for plastic debris, Environ. Sci. Technol. 53 (3) (2019) 1039–1047, https://doi.org/10.1021/acs.est.8b05297.
[4] V. Morgado, L. Gomes, R.J.N. Bettencourt da Silva, C. Palma, Validated spreadsheet for the identification of PE, PET, PP and PS microplastics by Micro-ATR-FTIR spectra with known uncertainty, Talanta 234 (April) (2021) 122624, https://doi.org/10.1016/j.talanta.2021.122624.
[5] V. Morgado, C. Palma, R.J.N. Bettencourt da Silva, Microplastics identification by infrared spectroscopy – evaluation of identification criteria and uncertainty by the bootstrap method, Talanta 224 (October 2020) (2021) 121814, https://doi.org/10.1016/j.talanta.2020.121814.
[6] J.L. Xu, K.V. Thomas, Z. Luo, A.A. Gowen, FTIR and raman imaging for microplastics analysis: state of the art, challenges and prospects, TrAC, Trends Anal. Chem. 119 (2019), https://doi.org/10.1016/j.trac.2019.115629.
[7] C.F. Araujo, M.M. Nolasco, A.M.P. Ribeiro, P.J.A. Ribeiro-Claro, Identification of microplastics using raman spectroscopy: latest developments and future prospects,

Water Res. 142 (2018) 426–440, https://doi.org/10.1016/J.WATRES.2018.05.060.
[8] L. Cabernard, L. Roscher, C. Lorenz, G. Gerdts, S. Primpke, Comparison of Raman and fourier transform infrared spectroscopy for the quantification of microplastics in the aquatic environment, Environ. Sci. Technol. 52 (22) (2018) 13279–13288, https://doi.org/10.1021/ACS.EST.8B03438/SUPPL_FILE/ES8B03438_SI_002.XLSX.
[9] A. Käppler, D. Fischer, S. Oberbeckmann, G. Schernewski, M. Labrenz, K. J. Eichhorn, B. Voit, Analysis of environmental microplastics by vibrational microspectroscopy: FTIR, raman or both? Anal. Bioanal. Chem. 408 (29) (2016) 8377–8391, https://doi.org/10.1007/S00216-016-9956-3/TABLES/3.
[10] N.P. Ivleva, A.C. Wiesheu, R. Niessner, Microplastic in aquatic ecosystems, Angew. Chem. Int. Ed. 56 (7) (2017) 1720–1739, https://doi.org/10.1002/ANIE.201606957.
[11] N. Jin, Y. Song, R. Ma, J. Li, G. Li, D. Zhang, Characterization and identification of microplastics using raman spectroscopy coupled with multivariate analysis, Anal. Chim. Acta 1197 (2022) 339519, https://doi.org/10.1016/j.aca.2022.339519.
[12] L. Xie, S. Luo, Y. Liu, X. Ruan, K. Gong, Q. Ge, K. Li, V.K. Valev, G. Liu, L. Zhang, Automatic identification of individual nanoplastics by Raman spectroscopy based on machine learning, Environ. Sci. Technol. 57 (46) (2023) 18203–18214, https://doi.org/10.1021/ACS.EST.3C03210/ASSET/IMAGES/LARGE/ES3C03210_0005.JPEG.
[13] W. Zhang, W. Feng, Z. Cai, H. Wang, Q. Yan, Q. Wang, A deep one-dimensional convolutional neural network for microplastics classification using raman spectroscopy, Vib. Spectrosc. 124 (2023) 103487, https://doi.org/10.1016/J.VIBSPEC.2022.103487.
[14] Y. Luo, W. Su, D. Xu, Z. Wang, H. Wu, B. Chen, J. Wu, Component identification for the SERS spectra of microplastics mixture with convolutional neural network, Sci. Total Environ. 895 (2023) 165138, https://doi.org/10.1016/J.SCITOTENV.2023.165138.
[15] K. Liu, X. Pang, H. Chen, L. Jiang, Visual detection of microplastics using raman spectroscopic imaging, Analyst 149 (1) (2023) 161–168, https://doi.org/10.1039/D3AN01270K.
[16] M. Sunil, N.N. Pallikkavaliyaveetil, I. Mi, A. Gopinath, S. Chidangil, S. Kumar, J. Lukose, Machine learning assisted raman spectroscopy: a viable approach for the detection of microplastics, J. Water Proc. Eng. 60 (2024) 105150, https://doi.org/10.1016/J.JWPE.2024.105150.
[17] European Commission, MSDF guidance on monitoring marine litter. https://doi.org/10.2788/99475, 2013.
[18] ISO/FDIS 16094-2 - water quality — analysis of microplastic in water — part 2: vibrational spectroscopy methods for waters with low content of suspended solids including drinking water. https://www.iso.org/standard/84460.html. (Accessed 20 June 2025).
[19] B. Efron, R.J. Tibshirani, An introduction to the bootstrap method, in: An Introduction to the Bootstrap Method, Chapman & Hall/CRC, 1993.
[20] R. Bettencourt da Silva, S.L.R. Elison, EURACHEM/CITAC Guide Assessment of Performance and Uncertainty in Qualitative Chemical Analysis, 2021.
[21] R.L. McCreery, Raman spectroscopy for chemical analysis, Raman Spectroscopy for Chemical Analysis (2005) 1–420, https://doi.org/10.1002/0471721646.
[22] R.G. Jones, J. Kahovec, R. Stepto, E.S. Wilks Michael Hess, T. Kitayama, W. Val Metanomski, A. Jenkins, P. Kratochvíl, Compendium of polymer terminology and nomenclature IUPAC recommendations 2008 with advice from, Compendium of Polymer Terminology and Nomenclature IUPAC Recommendations (2008).

Measurement: Sensors 38 (2025) 101830

Contents lists available at ScienceDirect

Measurement: Sensors

journal homepage: www.sciencedirect.com/journal/measurement-sensors

Interlaboratory comparison on the verification of fuel dispensers

ARTICLE INFO

Keywords:
Metrological verification
Comparison
Fuel dispensers
Pump
Diesel
Gasoline
Liquefied petroleum gas

ABSTRACT

The metrological control of fuel dispensers measurement systems is an essential activity to promote consumer protection and provide society in general and citizens in particular with a guarantee of the accuracy of the measurements carried out. As the metrological verification bodies are entities recognized and qualified by the Portuguese Institute for Quality (IPQ) for the delegated exercise of the legal metrological control, it was organized by IPQ an interlaboratory comparison in the field of the verification of fuel dispensers (diesel and gasoline) and LPG (Liquefied Petroleum Gas) with the participation of four national verification bodies (NVB). Two different instruments were tested, a fuel dispenser pump (with gasoline and diesel) and an LPG pump. Two volumes were tested for each instrument and each fuel at two different flow rates. The analysis of the results, using the normalized error statistics, evidenced satisfactory values, for the majority of the national entities for all the tested instruments. The uncertainty components were provided and evaluated.

1. Introduction

Fuel dispensers (commonly known as petrol pumps) and Liquefied Petroleum Gas (LPG) dispensers, are submitted to metrological control in order to assure consumer protection and provide to society in general and citizens in particular the guarantee of accurate measurements.

The Portuguese Institute for Quality (IPQ), as the National Metrology Institution, ensures and manages the legal metrological control system of measuring instruments, recognizes competent entities for the delegated exercise of this control, whenever this proves necessary to guarantee the effective coverage at national level.

The legal metrological control in Portugal is widely decentralized in approximately 300 entities, among governmental, regional and local authorities, in the public sector and in private companies.

The process of qualification and recognition of metrological verification bodies follows certain requirements, which are described by IPQ Resolution, one of these requirements being accreditation in accordance with the NP EN ISO/IEC 17025 standard, for the technical domain of qualification. The majority of the national verification bodies (NVB) are accredited laboratories and certified companies (NP EN ISO 9001) involved in the verification of the measuring instruments. Two of these measuring instruments are the fuel dispensers and liquefied petroleum gas dispenser.

In Portugal the fuel and LPG dispenser approved under the Measuring Instruments Directive (MID) are subject to metrological control in service thought its annual verification by the verification bodies, following internal procedures, according to the specific national regulations [1] and OIML R117 [2]. There are approximately 51 800 hoses of the fuel dispensers and 600 of LPG dispensers in Portugal, verified by several verification bodies equally distributed in the national territory.

Accredited laboratories often perform interlaboratory comparisons as an essential tool for demonstrating their competence, evaluate the competence of their laboratory and in order to verify the comparability of the technical procedures used and the agreement of the measurement results obtained. As the metrological verification bodies are entities recognized and qualified by the Portuguese Institute for Quality for the delegated exercise of the legal metrological control in Portugal, it was organized by IPQ an interlaboratory comparison.

2. National comparisons in legal metrology

Accredited laboratories often perform comparisons to verify the agreement of results and procedures.

In this context IPQ organize comparisons between qualified metrological verification bodies. One of these comparisons was in the field of the verification of fuel distributors (diesel and gasoline) and LPG (liquefied petroleum gas) with the participation of four verification bodies. IPQ prepared the protocol, including all the experimental details and a form sheet for the results, sent to all participants before the beginning of the comparison. A diesel pump, a gasoline pump and an LPG pump were tested at two volumes and two different flow rates. Each participant used there one verification instruments and procedures. The measurements have been performed in September 2023 and November 2023 and the analysis of the measurement results have been completed using the normalized error statistics.

3. Measuring instruments

The instruments under test were supplied by the pump's owners and

This article is part of a special issue entitled: Supp: IMEKO 2024 published in Measurement: Sensors.

https://doi.org/10.1016/j.measen.2025.101830

Available online 17 February 2025

the measurements were performed on site with IPQ supervision. For the fuel pump IPQ performed the initial and final measurements to access the stability of the instrument.

3.1. Fuel dispensers

The fuel dispenser (Fig. 1) used in the comparison was supplied by a national company and had the following characteristics:Table 1.

3.2. LPG dispenser

The LPG dispenser (Fig. 2) used in the comparison was supplied by a national company and had the following characteristics:Table 2.

4. Comparison protocol

4.1. General procedure

The experimental procedure was included in the protocol sent to the participants. The main parts are briefly described in the following:

Each participant had to verify the delivered volume of the fuel pump at maximum flow using a 20 L calibrated volume standard and the delivered volume of the fuel at minimum flow using a 5 L calibrated volume standard. The verification liquids used were diesel and petrol, by this order due to residual volume increase. For the LPG pump the volumes tested were 5 L at the minimum flow rate and 50 L at the maximum flow rate using a calibrated LPG meter.

Each participant was asked to use the normal work routine, meaning the operator, the procedure and the equipment. Three measurements were performed for each tested volume, the average values were given by each participant and used in the follow up calculation.

4.2. Instruments and ambient conditions

Its standard capacity measure used by all participants in the verification of the fuel pumps were from Pumpwatch, model CFX (Fig. 3), resolution 0,01 % for 20 L and 0,02 % resolution for 5 L. All instruments were calibrated at IPQ.

The LPG meters (Fig. 4) used by the participants were from Tokyo Tatsuno, 0,01 L resolution and traceable to NMI accredited laboratory in the Netherlands.

The ambient conditions remained within the information of the characteristics plaque of the dispensers for all participants in all tests performed.

Fig. 1. Fuel pump used in the comparison.

Table 1
Fuel dispenser.

Brand	PETROTEC
Model	1P10H
Class	0,5 according to the National Regulation n.° 19/2007, 5th of January
Type	P5000
Resolution	0,01 L
Serial number	11007861702/2011
Diesel hose	5
Petrol hose	1

Fig. 2. LPG dispenser used in the comparison.

Table 2
LPG dispenser.

Brand	Dresser Wayne
Model	1P10H
Class	1 according to the National Regulation n.° 19/2007, 5th of January
Type	Global Century S11-110
Resolution	0,01 L
Serial number	46–1020766

5. Statistical analysys

5.1. Reference value

The reference value used for the fuel dispenser was the mean value of the two measurements performed by IPQ, the first one at the beginning and the other at the end of the comparison. The uncertainty of the

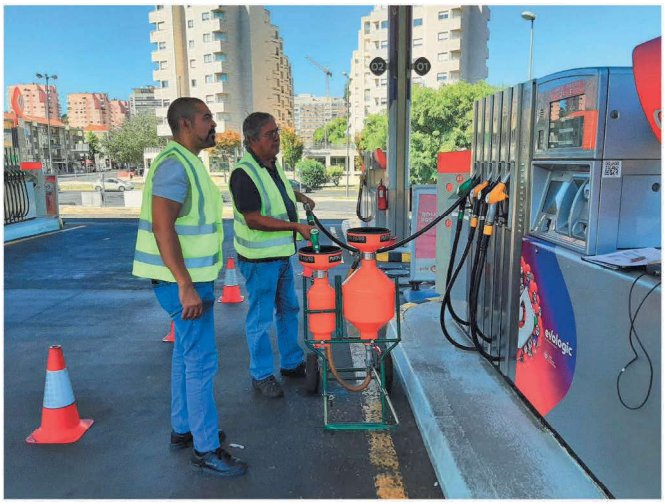

Fig. 3. Measurements performed by IPQ using Pumpwatch measures.

Fig. 4. Measurements performed by one of the participants using an LPG meter.

reference value considered was the largest value of both IPQ measurements.

In case of the LPG dispenser the reference value was the weighing mean of the four participants determined according to Cox method [3].

5.2. Normalize error

The consistency evaluation between the results of each laboratory and the reference value (RV) was calculated according to the normalized error (E_n) [4,5].

The interpretation of the absolute value of E_n is as follows:

- $|E_n| \leq 1$: the result of the laboratory is consistent with RV.
- $|E_n| > 1$: the result of the laboratory is not consistent with RV.

5.3. Temperature correction for the fuel dispenser

In order to obtain comparable measurement results obtained from the fuel dispenser the values were corrected to a reference temperature of 20 °C using the standard calculation model [6]:

$$V_{20} = V_t[1 + \gamma(20 - t)]$$

Where, γ is the cubic thermal expansion coefficient of the volume standard material of the standard capacity measure and t the liquid temperature.

6. Results

6.1. Volume results for the fuel dispenser

The volume delivered by the fuel dispenser determined by the participants using diesel and petrol at a maximum flow (20 L) and minimum flow (5 L) are presented in the following figures (Figs. 5–8):

The majority of the results are very similar and the variation between participants is smaller than 0,2 % which is less than the maximum permissible error (MPE) of these instruments. Indeed, and according to the Portuguese national regulation [1] and the Measuring Instruments Directive [7] the MPE for fuel dispensers is 0,5 %. The worst cases obtained by the participants are for petrol using the 5 L volume standard, which was expected, due to the volatility of the fuel and the small quantity of fluid delivered.

6.2. Normalized error for the fuel dispenser

The normalized errors, E_n numbers as defined previously, obtained for the measurement results of each participant entity, are displayed in Table 3.

6.3. Results for the LPG dispenser

The errors obtained by the participants at a maximum flow (50 L) and minimum flow (5 L) for the LPG dispenser are presented in the Figs. 9 and 10.

The majority of the results are very similar and the variation between participants is smaller than 0,6 % which is less than the maximum permissible error (MPE) of these instruments. Indeed, and according to the Portuguese national regulation [1] and the Measuring Instruments Directive [7] the MPE for LPG dispensers is 1 %.

6.4. Normalized error for the LPG dispenser

The normalized errors, E_n numbers as defined previously, obtained for the measurement results of each participant entity, are displayed in Table 4.

7. Uncertainty calculation

The uncertainty values obtained by each participant according to the "Guide to the Expression of Uncertainty in Measurement" [8] are presented in the following figures. One example is presented for one volume of each type of dispenser.

The uncertainty values for the fuel dispenser at 5 L is presented in Fig. 11.

The uncertainty components for fuel dispenser verification are:

- Repeatability of the measurements
- Calibration of the standard capacity measure
- Resolution of the standard capacity measure
- Meniscus reading
- Resolution of the dispenser
- Temperature of the liquid
- Expansion coefficient of the material od the standard capacity measure
- Other.

The larger component of uncertainty is the resolution of the dispenser, as expected for the small volume.

The uncertainty values for the LPG dispenser at 5 L is presented in

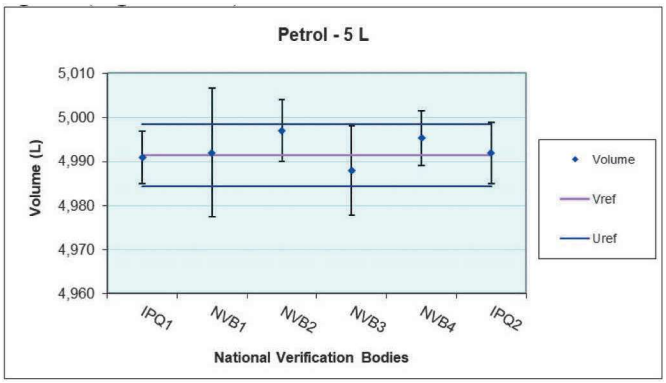

Fig. 5. Volume results for fuel dispenser, petrol, 5 L.

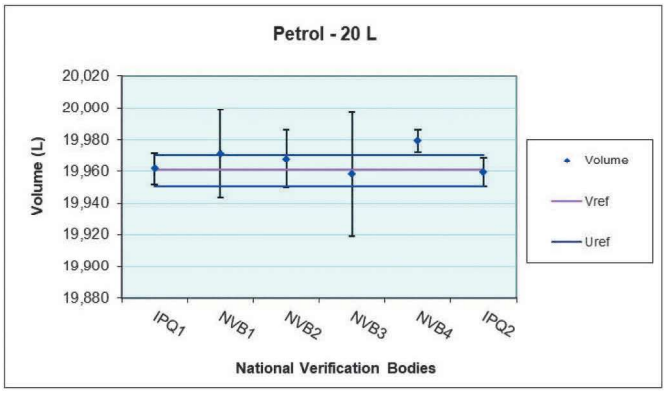

Fig. 6. Volume results for fuel dispenser, petrol, 20 L.

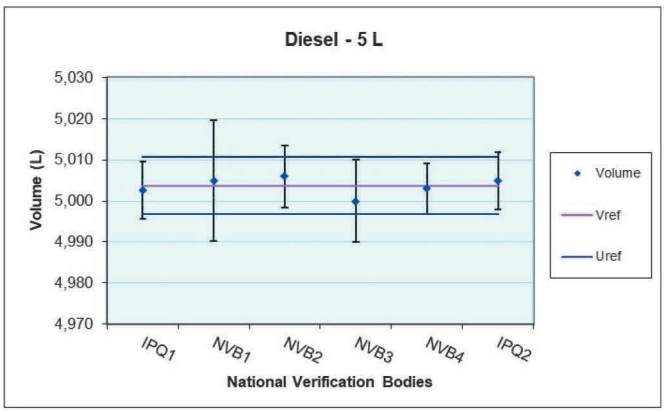

Fig. 7. Volume results for fuel dispenser, diesel, 5 L.

Fig. 12.

The uncertainty components for LPG dispenser verification are:

- Repeatability of the measurements
- Calibration of the reference standard meter
- Resolution of the reference standard meter
- Resolution of the dispenser
- Drift of the reference standard meter
- Uncertainty of the fluid temperature
- Other.

The uncertainty values are very similar except for one participant that overestimated the uncertainty values because the reference meter

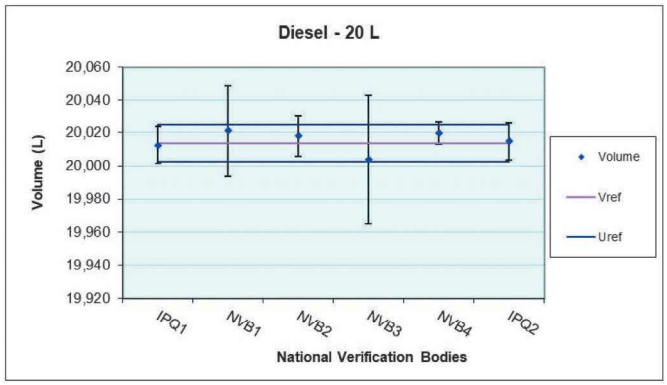

Fig. 8. Volume results for fuel dispenser, diesel, 20 L.

Table 3
Normalized error E_n for fuel dispenser.

Participant	5 L *Petrol* E_n	20 L *Petrol* E_n	5 L *Diesel* E_n	20 L *Diesel* E_n
NVB1	0,04	0,36	0,08	0,25
NVB2	0,57	0,37	0,22	0,26
NVB3	−0,28	−0,06	−0,31	−0,24
NVB3	0,42	1,66	−0,08	0,45

Inconsistent results are only found for petrol at 20 L and possible due to uncertainty underestimation.

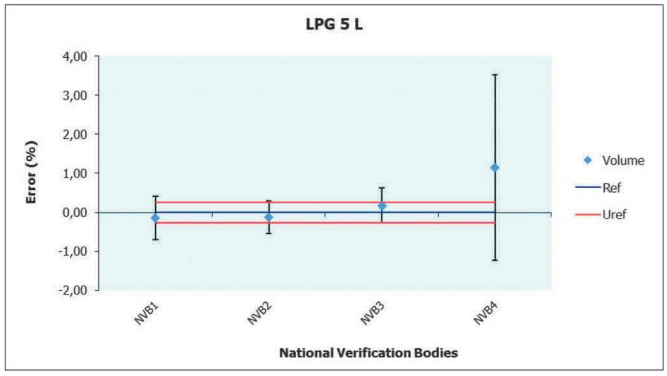

Fig. 9. Error values for 5 L, LPG dispenser.

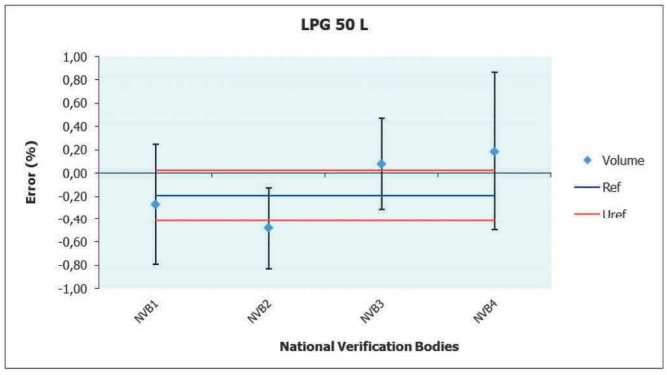

Fig. 10. Error values for 50 L, LPG dispenser.

Table 4
Normalized error E_n for LPG dispenser.

Participant	5 L E_n	50 L E_n
NVB1	−0,27	−0,16
NVB2	−0,35	−1,05
NVB3	0,48	0,85
NVB3	0,48	0,59

Inconsistent results are only found for 50 L but the value is very close do 1.

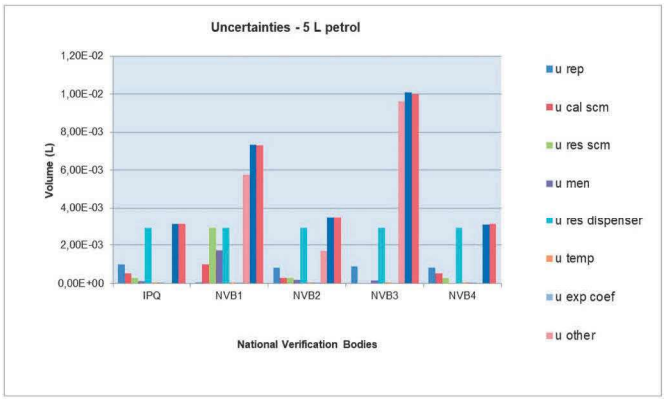

Fig. 11. Uncertainty values for 5 L, fuel dispenser.

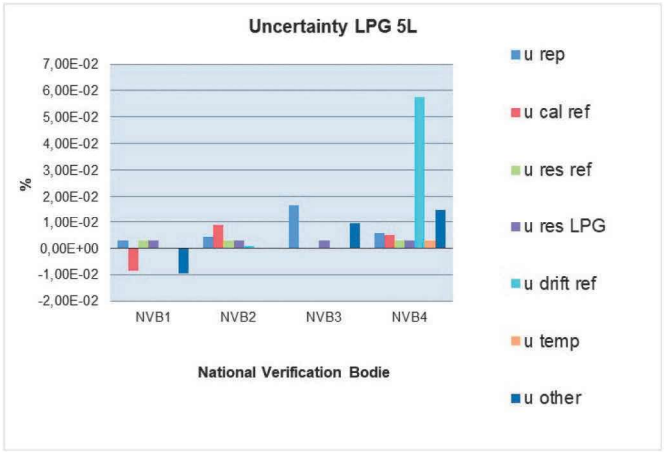

Fig. 12. Uncertainty values for 5 L, LPG dispenser.

used has the same metrological characteristics and it's calibrated in the same institute.

8. Conclusions

A national comparison in field of verification of fuel dispensers and LPG dispenser was organized between four qualified entities for metrological control. IPQ, as the National Metrology Institute, has piloted this interlaboratory comparison, providing the reference value for the fuel dispenser. For the LPG meter the reference value was determined based on the weighing mean of the participants results.

Considering that the measurements were performed on-site, at different days and hours, by different entities using volume standards with different characteristics, the results of the comparisons can be seen as positive.

Although two participants had one unsatisfactory results, but their E_n values were very close to 1. Such situations occurred possible because underestimation of uncertainty.

Interestingly, the volume values measured by the participants had a maximum variation between each other of 0,2 % for the fuel pump and 0,6 % for the LPG pump. This value is smaller than the correspondent MPE and indicates a good reproducibility of the whole measurements.

Concerning the evaluation of the measurement uncertainty, we can verify that, for 5 L with both kinds of fuels, the largest component of uncertainty of all participants was the resolution of the device under test. For LPG meter, there was no evidence regarding the largest source of uncertainty and correspondingly the value of the expanded uncertainty was very similar among all the participants because they used the same type of reference meter.

Acknowledgments

The authors would like to thank all the entities that participated in this comparison: ISQ, SERVIMETRO, OVERMETRON and METROQUALIBEIRAS.

References

[1] Portaria n.° 321, 2019 de 19 de setembro.
[2] OIML R 117-1, Dynamic Measuring Systems for Liquids Other than Water, 2007.
[3] M. Cox, The evaluation of key comparison data: determining the largest consistent subset, Metrologia 44 (3) (2007) 187–200, https://doi.org/10.1088/0026-1394/44/3/005.
[4] ISO/IEC 17043, Conformity Assessment — General Requirements for Proficiency Testing, 2010.
[5] ISO 13528, Statistical Methods Used in Proficiency Testing by Interlaboratory Comparisons, 2005.
[6] ISO 4787, Laboratory glass and plastic ware Volumetric instruments. Methods for testing of capacity and for use, 2021.
[7] DIRECTIVE 2004/22/EC of the European Parliament and of the Council, of 31 March 2004, on Measuring Instruments.
[8] BIPM, IEC, IFCC, ILAC, ISO, IUPAC, IUPAP, and OIML, Evaluation of measurement data | Guide to the expression of uncertainty in measurement, Joint Committee for Guides in Metrology, JCGM 100 (2008). URL: https://www.bipm.org/documents/20126/2071204/JCGM_100_2008_E.pdf/cb0ef43f-baa5-11cf-3f85-4dcd86f77bd6.

Elsa Batista*, António Capela, Mário Condeço, Isabel Godinho
IPQ, Caparica, Portugal

* Corresponding author.
E-mail address: ebatista@ipq.pt (E. Batista).

Measurement: Sensors 38 (2025) 101645

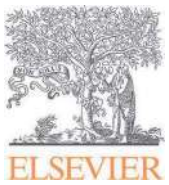

Contents lists available at ScienceDirect

Measurement: Sensors

journal homepage: www.sciencedirect.com/journal/measurement-sensors

Investigations on the performance of a newly developed pressure-driven flow controller used in microfluidic applications

ARTICLE INFO

Keywords:
Microflow
Syringe pump
Pressure-driven flow controller
Microfluidic chip
Flow resistivity

ABSTRACT

This paper gives an overview of investigations with a newly developed pressure-driven flow controller, which has no mechanical components and can therefore provide pulsation-free flows. The performance of the pressure-driven flow controller is compared with high-precision syringe pumps used as reference systems in most laboratories and National Metrology Institutes.

The results show an astonishing performance of the pressure-driven flow controller, but also a strong dependence on the associated flow sensor. In contrast to a high-precision syringe pump, the system with a flow sensor is much more dependent on fluid properties, pressure and temperature.

However, the strength of the pressure-driven flow controller lies in rapid flow changes and flow stability. Here the system gives excellent results.

Another advantage of the system is that direct access to pressure values makes it easy to measure hydrodynamic resistances, which are important for lab-on-a-chip and organ-on-a-chip applications.

1. Introduction

Microfluidics is the technology of designing and manufacturing miniaturised devices consisting of chambers and channels. It is the science of manipulating and controlling fluids within them. The ability to control small flow rates very precisely is used in a wide range of applications, particularly in many areas of biology, medicine and engineering [1,2]. These include diagnostics, cell culture, drug discovery, rapid testing, organ-on-a-chip systems, single cell processing and sequencing, and other technical applications, particularly in the sensor, process and food industries [3]. In microfluidics, the effects of viscosity and capillarity are very important, and inertia and gravity are negligible. This condition affects the behaviour of the fluid and the way its flow is controlled. Flow in a microfluidic system is typically generated by peristaltic or syringe pumps, which are mechanical systems. Consequently, they cannot provide a completely pulsation-free flow and are limited in terms of response time and flow stability.

An alternative method of generating flow is the relatively new pressure-driven flow system, in which the liquid from a sealed container is forced into a more uniform motion by a gas supplied from an external pressure source, resulting in a pulsation-free flow that allows better flow control. Pressure-driven flow controllers only provide direct access to pressure by setting a setpoint pressure. To access flow values, a flow sensor must be added to the setup so that the inlet pressure is automatically adjusted to achieve the desired flow rate. The generated flow rate is proportional to the pressure difference with the microfluidic resistance as the proportional coefficient, which is a characteristic of the fluidic system and depends on the device geometry and liquid properties. This study investigated a novel pressure-driven flow controller and a fast-responding in-line flow sensor capable of measuring liquid flows down to 0.4 µL/min. In contrast to conventional pressure-driven flow controllers, this prototype has a slightly lower response but very low gas consumption. The investigations included pressure control with flow monitoring and flow control with pressure monitoring measurements and simultaneous calibration of the entire microfluidic system, i.e. in this case the flow sensor was calibrated with a balance using the dynamic weighing method. In this context, different microfluidic resistance configurations were investigated using a thermoplastic polymer microfluidic chip (TOPAS chip) containing 8 different channel configurations accommodated on the same chip. To compare the results, the same microfluidic resistance measurements were also performed using high-precision syringe pumps and calibrated glass syringes, which are used as reference systems in most microflow laboratories. All these measurements were carried out using water as the test fluid, but also Simulated Body Fluid (SBF) and Phosphate Buffer Saline (PBS) at two different National Metrology Institutes under the scope of EMPIR project MFMET [4].

There are a variety of microfluidic applications that require fast dynamic response and precise flow rate control. The performance of the pressure-driven flow controller was investigated in terms of its dynamic behaviour by applying various predefined flow profiles (ramp, sine, square and triangular) and comparing them with the response behaviour of the fast-responding flow sensor.

2. Methods and procedures

The gravimetric method [5] is used to determine a delivered mass of a liquid over a time interval. This method can be used for testing inline flow sensors and flow generators. In a gravimetric microfluidic setup, an electronic balance is used to determine the delivered mass of a liquid from or through the test object, which can be a flow generator, a microfluidic device or a flow meter. In general, the desired flow rate is

https://doi.org/10.1016/j.measen.2024.101645

Available online 31 December 2024

Fig. 1. NEXUS pump system measurement setup at IPQ.

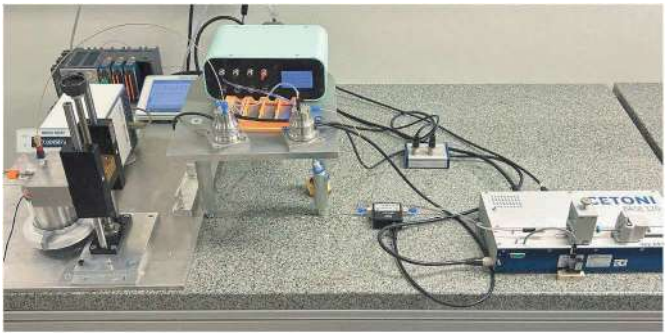

Fig. 2. Cetoni pump system measurement setup at RISE. In the configuration shown, the pressure drop over a channel of the microfluidic chip is measured.

generated using a high-precision syringe pump with a calibrated syringe of known size, material and volume and compared against the weighing scale. The calibrated system can then be used as a reference even without a weighing scale.

2.1. High-precision syringe pump

High-precision syringe pumps are dedicated syringe pumps that are often used in laboratories, medical research centres and other areas where extremely accurate fluid delivery is required due to the need of very reliable and reproducible results. These types of pumps have a very high accuracy and allow extremely accurate delivery of liquids with precise control over the flow rate, especially at low flow rates and volumes. These devices are suitable for a wide range of fluids and applications and often have programmable functions and recording capabilities.

2.1.1. NEXUS pump system at IPQ

At the Portuguese Quality Institute (IPQ) [6] flow is generated with a Nexus 3000 syringe pump (Fig. 1), from Chemyx, using a 1 mL ILS glass syringe connected to polyethylene (PE) tube of 1.26 mm (0.05") inner diameter which is immersed in the water in the weighing vessel on the balance (Mettler AX26, resolution 1 μg). In addition, this particular setup uses an evaporation trap to reduce evaporation, especially useful at low flow rates, and the connecting tube was inserted below the water surface inside the weighing vessel of the balance to avoid the drop impact effect. Thus, the mass flow rate is determined, and the volume flow rate can be calculated with the appropriate density of the liquid.

The time interval in which the mass is delivered is determined by a timing module to derive the mass flow rate. The data are collected from the balance every 250 ms during 60 min using a LabVIEW application. The flow rate is determined every 30 seconds.

The climatic conditions such as air temperature, relative humidity and pressure are determined to correct for buoyancy effects on the balance. The liquid temperature is measured in the beginning and at the end of the tests and used to convert the mass flow rate into a volumetric flow rate, considering the density of the liquid used.

At start of each measurement, it is required to put the system on charge, and after that let it run for 10 minutes to stabilise.

2.1.2. Cetoni pump system at RISE

For the measurements, the Nanoflow Test Facility at the Research Institutes of Sweden (RISE) was used, Fig. 2. A very detailed description and operating principle of the facility can be found in Ref. [7]. The main part of the test facility is a Mettler Toledo XPR10 microbalance (weighing scale) with a capacity of 10.1 g and a readability of 1 μg. The measuring principle of the test facility is based on the dynamic weighing method and has a flow rate range of 0.25 μL/h to 1 mL/h, which is adapted to the specifications of the weighing scale.

The weighing scale can be operated and read out using a Personal Computer (PC) and a self-written LabVIEW programme. For all measurements, the weighing scale was read out at 1 Hz.

The AAMI Technical Information Report (TIR) TIR101:2021 [8] gives recommendations for minimising evaporation. As described in Ref. [7], for all measurements the weighing vessel (beaker) was first filled with about 10 mm of water and then with about 5 mm of paraffin oil to minimise the effects of evaporation. The paraffin oil is denser than water and prevents evaporation on the surface. In addition, an evaporation trap was used.

A 27G needle with a nominal outer diameter (OD) of 0.413 mm, a nominal inner diameter (ID) of 0.210 mm and a length of 90 mm was used for all measurements as the focus is on very low flow rates. This is a Whitacre spinal needle (pencil point) which, unlike a standard Quincke spinal needle (cutting), has the opening on the side (at the end of the needle) and not directly at the end of the needle. The advantage is that this needle does not exert any direct forces when filling the weighing scale.

For all measurements, the tubing in the measuring range is 1/16″ OD Polyether Ether Ketone (PEEK) mostly with an ID of 0.13 mm but also some with an ID of 0.50 mm.

All tests were carried out at an ambient and water temperature of (23.0 ± 0.5) °C. The temperature of the test liquid was measured indirectly at various spots using type K thermocouples (TC) connected to a National Instruments compactRIO Data Acquisition (DAQ) system. The air pressure, room temperature and humidity in the laboratory were measured separately and recorded by a Vaisala PTU300.

Table 1
Manufacturer specifications of the Elveflow Microfluidic Flow rate Sensor (MFS) MFS2.

Specifications MFS2	
Flow rate range	0 to ± 7 μL/min
Accuracy (bi-directional)	5 % m.v. between (0.42–7 μL/min)
Repeatability (bi-directional)	0.5 % m.v. between (0.70–7 μL/min)
Pressure drop at full scale flow rate, 23 °C	3 mbar
Total internal volume	1.5 μL
Sensor inner diameter	150 μm
Operating pressure	200 bar
Fitting type	UNF 1/4″-28

Fig. 3. MIC system measurement setup at IPQ.

2.2. Pressure-driven flow generator

A pressure-driven flow controller is a method to generate flow in microfluidics. The pressure driven flow controller is connected to an external pressure source. The device applies a precise gas pressure to a sealed reservoir filled with liquid. The pressure difference between the outside pressure (atmospheric pressure in an open system) and the pressure inside the reservoir forces the liquid to flow through the microfluidic device. The flow rate generated is therefore directly proportional to the difference in pressure between the inlet and outlet, known as the differential pressure.

The pressure-driven flow controller is operated by the software supplied, which allows to regulate the pressure by setting a target pressure. The higher the pressure difference, the higher the flow rate. The pressure-driven flow controller only provides direct access to pressure. To access flow values, a flow sensor (flow meter) must be added to the setup. The combination of a pressure-driven flow controller and a flow sensor offers the advantage of either working in pressure control with flow monitoring, or in flow control where the inlet pressure is automatically adjusted to achieve the target flow. In this case, a feedback loop is established between the flow sensor and the pressure controller via the control software.

The system provided by the Microfluidics Innovation Center (MIC) consists of the prototype pressure-driven flow controller and a commercially available Elveflow Microfluidic Flow Sensor (MFS). The MFS2 used is a thermal mass flow (TMF) time-of-flight (ToF) conductivity flow sensor with the specifications given in Table 1. The operating principle of the flow sensor is based on local heating of the liquid passing through a capillary inside the sensor and measuring the temperature upstream and downstream of the heater. The difference in temperature between the two spots allows the MFS to determine the flow rate. The relationship between the temperature difference and the flow rate depends on the properties of the liquid. Therefore, the sensor must be calibrated according to the liquid. The MFS2 comes with two different

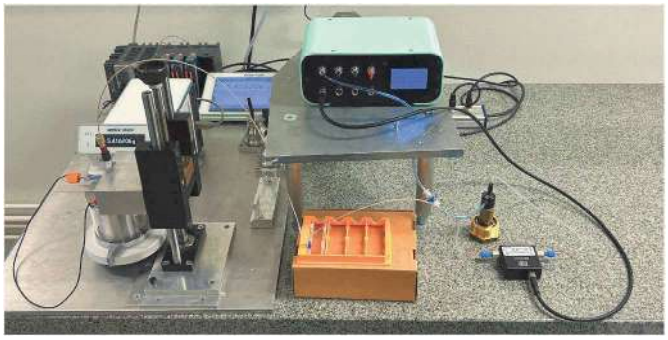

Fig. 4. MIC measurement setup at RISE.

preset calibrations available: water (H_2O) and isopropyl alcohol (IPA) at 23 °C.

The supplied MFS2 has a flow rate specification of 0.42 μL/min to 7 μL/min (0.0252 mL/h to 0.42 mL/h). In order to cover as wide a flow rate range as possible, three flow rates of 0.025 mL/h, 0.1 mL/h and 0.4 mL/h (a factor of 4 in between each) were selected for the measurement campaign.

In principle it is possible to calibrate the flow sensor for other liquids. However, all measurements shown in the following have been made using the factory calibration for water.

2.2.1. MIC system at IPQ

The measurement setup is shown in Fig. 3. First, the pump is connected to a pressure source (50 L, 200 bar nitrogen cylinder) and then positioned higher than the reservoir to prevent backflow. The reservoir is filled with the test fluid which flows through the tube and past the Elveflow MFS. The MFS is positioned slightly above the microchip, which is at the same level as the outlet. The Elveflow software can be used to select the desired flow rate, display it graphically in the software and store the results for further analysis.

It is recommended that the system is primed before starting measurements, then the pump is allowed to run for 10 minutes to stabilise before starting the measurement. After completing the first measurement, set the new flow rate, allow the pump to run for approximately 5 minutes to stabilise and then start the measurement; this step is recommended for each measurement.

2.2.2. MIC system at RISE

In order to obtain consistent results, a similar measurement setup to IPQ, as shown in Fig. 4, was realized. The pressure-driven flow controller allows the control of the output pressure value of 4 independent channels from 0 to 2000 mbar. The pressure source was provided by an Air Liquide ALPHAGAZ™ 1 nitrogen cylinder (50 L, 200 bar) connected by 6mm OD pneumatic tubing with push-in fittings. For the 2000 mbar pressure channel, the pressure source was set at a constant 5 bar using a pressure regulator. The pressure-driven flow controller was connected to the pressure reservoir with 4 mm OD, 2.7 mm ID clear tubing. The flow sensor was placed flat on the granite table as recommended by the supplier.

One difference to the IPQ setup was the measuring time. In this case, the measuring time was selected so that about 1 mL (one full syringe) was delivered in each measurement, regardless of the flow rate.

2.3. Microfluidic chip

Microfluidic chips are used for the precise manipulation and analysis of small amounts of liquid. These include analytical chips, micromixer chips, cell culture chips, lab-on-chip and organ-on-chip. Microfluidic chips contain microscopic channels through which fluids can flow in a very precise and controlled way. The three most common materials used to make these chips are silicon, glass and polymer. The fabrication of the

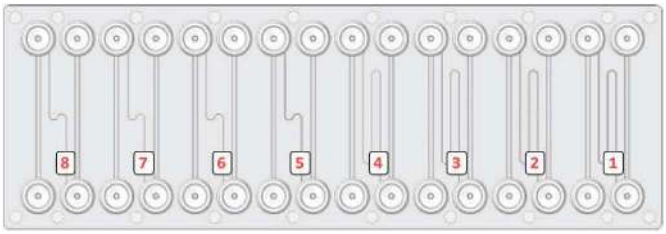

Fig. 5. Microfluidic polymer chip with 8 different channels, chip dimensions 75.5 × 25.5 mm, mini-luer access holes.

channels requires a high degree of precision and control to ensure that fluids can flow properly through the channels.

In this study, measurements were made using the TOPAS microfluidic chip shown in Fig. 5. This chip has 8 different channels. TOPAS (Thermoplastic Olefin Polymer with Amorphous Structure) is a special thermoplastic polymer used in the manufacture of microfluidic chips due to its unique properties such as high transparency, chemical resistance and biocompatibility.

Due to the maximum pressure of the pump of 2000 mbar, only channel numbers 1, 2 and 5 could be considered for the envisaged flow range (Table 2). As channel no. 1 has the lowest pressure drop, this channel was deselected.

Measurements were performed with two configurations of channel no. 5 at IPQ and channel no. 2 at RISE. Herby the direct connection of the inlet and outlet with a height and weight of around 500 µm has the designation "large" and the configuration with the given height and width and length in Table 2 has the has the designation "small". The pressure drop over the "large" configuration is negligible for the given flow rates due to the dimensions.

3. Results and discussion

In the first step, measurements with a high-precision syringe pump are carried out and then compared with measurements with the pressure-driven flow controller.

3.1. High-precision syringe pump

For the measurements with the Nexus pump at IPQ and the Cetoni pump at RISE, with and without the chip, care was taken to ensure that the measurement set-up, test time, start position and syringe remained the same for tests.

The measurements were carried out in two stages:

- In the first stage (section 3.1.1), the test was carried out directly against the balance, without the microfluidic chip. In this stage, the test was performed at 0.025 mL/h, 0.1 mL/h and 0.4 mL/h. At RISE these tests were performed with water only but at IPQ with three test fluids: water, Simulated Body Fluid (SBF) and Phosphate Buffered Saline (PBS).
- In the second stage (section 3.1.2), the same test was carried out but with the microfluidic chip.

3.1.1. Calibration of the high-precision syringe pump against the weighing scale

The later calibrated system consisting of syringe pump and then calibrated syringe can then itself be used as a reference for flow generation (see e.g. section 3.3).

3.1.1.1. Measurements with the Nexus system at IPQ. As can be seen in Table 3, the error decreased as the flow rate increased and the uncertainty varied between 1.4 and 2.0 %. These values are consistent with the claimed Calibration and Measurement Capabilities (CMCs) of IPQ.

3.1.1.2. Measurements with the Cetoni system at RISE. The measurements were carried out using the manufacturer's specifications regarding the dimensions of the syringe. As can be seen in Table 4, the measured values correspond very well with these specifications. The measurements at all three flow points provide consistent results.

Table 3
Measurements with the Nexus system (1 mL ILS syringe) against the weighing scale using water as test liquid.

Calibration results at IPQ (Nexus system)		
1	Set flow rate: 0.025 mL/h	
	Measurement time:	2h 00 min
	Measured flow rate:	0.0257 mL/h
	Measurement error:	−2.80 %
	Uncertainty $U(k = 2)$	1.40 %
2	**Set flow rate: 0.100 mL/h**	
	Measurement time:	2h 00 min
	Measured flow rate:	0.0994 mL/h
	Measurement error:	+0.60 %
	Uncertainty $U(k = 2)$	2.00 %
3	**Set flow rate: 0.400 mL/h**	
	Measurement time:	2h 00 min
	Measured flow rate:	0.3985 mL/h
	Measurement error:	+0.38 %
	Uncertainty $U(k = 2)$	1.70 %

Table 4
Measurement results ($U(k = 2) \leq 0.5$ %) with the CETONI system (1 mL syringe) against the weighing scale.

Syringe calibration results at RISE		
1	0.025 mL/h	
	Measurement time:	39h 45 min
	Weighing scale (Ref.):	0.992708 mL
	Cetoni logfile (syringe):	0.993802 mL
	Measurement error:	+0.11 %
2	**0.100 mL/h**	
	Measurement time:	9h 45 min
	Weighing scale (Ref.):	0.974543 mL
	Cetoni logfile (syringe):	0.975058 mL
	Measurement error:	+0.05 %
3	**0.400 mL/h**	
	Measurement time:	2h 25 min
	Weighing scale (Ref.):	0.966534 mL
	Cetoni logfile (syringe):	0.966722 mL
	Measurement error:	+0.02 %

Table 2
Dimensions of the eight channels available on the microfluidic chip.

Channel no.	1	2	3	4	5	6	7	8
Height (µm)	100	50	20	10	50	20	10	5
Width (µm)	100	50	20	10	50	20	10	5
Length (mm)	40	40	40	40	20	20	20	20
Pressure drop (mbar) at 0.025 mL/h	0.79	12.6	493	7890	6.3	246	3940	6310
Pressure drop (mbar) at 0.400 mL/h	12.6	202	7890	126000	101	3940	63100	1010000

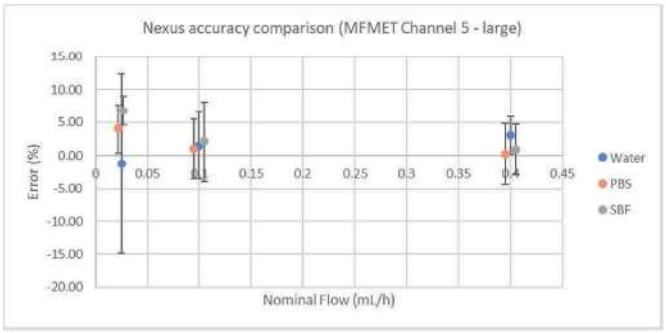

Fig. 6. Error difference in the large configuration of channel 5 with and without the chip with the Nexus system at IPQ.

3.1.2. *Measurements with the high-precision syringe pump and the microfluidic chip against the weighing scale*

3.1.2.1. Measurements with the Nexus system at IPQ. The differences between the results with and without the chip ("large" configuration of channel 5) for water, SBF and PBS using the Nexus pump as flow generator are shown in Fig. 6.

It can be verified that in general the uncertainty and the error values obtained with the different liquids are similar.

Unfortunately, due to the high pressure the Nexus system had to generate, IPQ was unable to measure the flow in the "small" configuration of channel 5.

3.1.2.2. Measurements with the Cetoni system at RISE. Table 5 below shows the measurement results with the Cetoni system for the measurements with the "small" and "large" configuration of Chip 5 at RISE.

In comparison to Table 4, the results show a slight shift in the calibration curve of all flow points in a positive direction. The measurement deviation is higher at low flow rates (longer measurement times) and slightly higher in the "small" configuration of channel 5 (higher pressure). This could speculatively indicate evaporation or leakage, e.g. at the mini-luer connections on the microfluidic chip. From a fluidic point of view, these connections are not ideal. However, the results are still very good, especially for microflow.

Table 5
Measurement results ($U(k = 2) \leq 0.5$ %) of the "small" and the "large" configuration of channel 2 on the microfluidic chip with the Cetoni system at RISE.

Channel 2: "large" and "small" configuration			
		"large"	"small"
1	**0.025 mL/h**		
	Measurement time:	39h 30 min	39h 30 min
	Weighing scale (Ref.):	0.977142 mL	0.972392 mL
	Cetoni logfile (syringe):	0.987557 mL	0.987564 mL
	Measurement error:	+1.07 %	+1.56 %
2	**0.100 mL/h**		
	Measurement time:	9h 45 min	9h 45 min
	Weighing scale (Ref.):	0.973220 mL	0.968468 mL
	Cetoni logfile (syringe):	0.975064 mL	0.975036 mL
	Measurement error:	+0.19 %	+0.68 %
3	**0.400 mL/h**		
	Measurement time:	2h 20 min	2h 25 min
	Weighing scale (Ref.):	0.931187 mL	0.963585 mL
	Cetoni logfile (syringe):	0.933389 mL	0.966734 mL
	Measurement error:	+0.24 %	+0.33 %

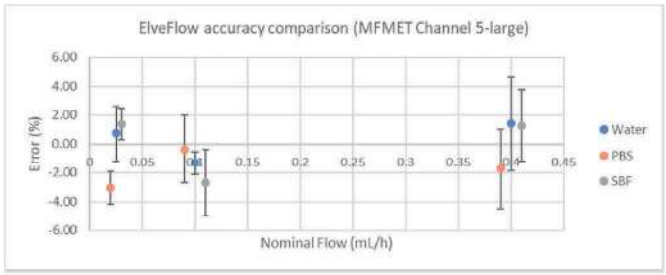

Fig. 7. Error difference in the large configuration of channel 5 with and without the microfluidic chip with the MIC system at IPQ.

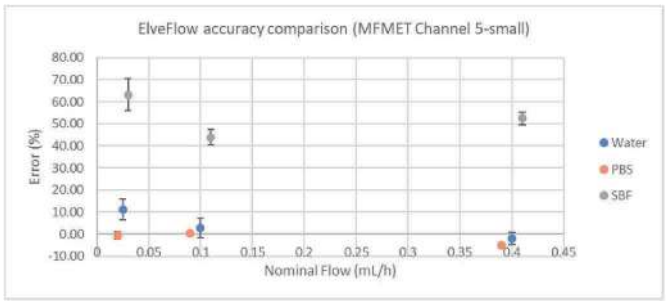

Fig. 8. Error difference in the small configuration of channel 5 with and without the microfluidic chip with the MIC system at IPQ.

3.2. *Pressure-driven flow generator*

For the measurements with the MIC system with and without chip, it was again taken into account that the setup and test time remained the same for all measurements.

The measurements were carried out in two stages:

- In the first stage (section 3.2.1), tests were performed against the weighing scale with the microfluidic chip. Measurements were made at 0.025 mL/h, 0.1 mL/h and 0.4 mL/h with three test fluids (water, SBF and PBS) at IPQ and with water at RISE.
- In the second stage (section 3.2.2), dynamic measurements were performed at RISE with the MIC system.

3.2.1. *Measurements with the MIC system and the microfluidic chip against the weighing scale*

3.2.1.1. Measurements with the MIC system at IPQ. The differences between the results with and without the chip ("large" configuration of channel 5) for water, SBF and PBS using the MIC as flow generator are described in Fig. 7.

In this case there are some variations in the results using different liquids. TMFs are strongly dependent on the thermal properties of the liquid, such as specific heat capacity and thermal conductivity. It should be noted that all the results were obtained with the preset calibration for water at 23 °C.

In general, the uncertainty values of the MIC system are smaller than for the Nexus pump. The differences between the results with and without the chip of the channel 5, "small" configuration, for water, SBF and PBS using the MIC as flow generator are described in Fig. 8.

In this situation the uncertainty is larger than for the larger configuration, but the error values are similar, except for the SBF were some anomalies occurred during the tests.

What can be recognised, however, is that in general the uncertainties obtained at IPQ from the MIC system are smaller than for the Nexus pump. The error variation between the values with and without the chip

Table 6
Measurement results of the "small" and the "large" configuration of channel 2 on the microfluidic chip with the MIC system at RISE.

Channel 2: "large" and "small" configuration			
		"large"	"small"
1	**0.025 mL/h**		
	Measurement time:	39h 30 min	39h 30 min
	Weighing scale (Ref.):	0.945410 mL	0.958790 mL
	MFS logfile:	0.024992 mL/h	0.024988 mL/h
	Pressure	39.64 mbar	58.74 mbar
	Measurement error:	+4.42 %	+2.94 %
2	**0.100 mL/h**		
	Measurement time:	10h 00 min	10h 00 min
	Weighing scale (Ref.):	1.005302 mL	1.010770 mL
	MFS logfile:	0.099994 mL/h	0.099986 mL/h
	Pressure	70.28 mbar	123.33 mbar
	Measurement error:	−0.53 %	−1.08 %
3	**0.400 mL/h**		
	Measurement time:	2h 30 min	2h 30 min
	Weighing scale (Ref.):	1.115796 mL	1.129715 mL
	MFS logfile:	0.400063 mL/h	0.399951 mL/h
	Pressure	198.92 mbar	426.20 mbar
	Measurement error:	−10.36 %	−11.49 %

is similar for both pumps for the large configuration.

3.2.1.2. Measurements with the MIC system at RISE. As can be seen in Table 6, at the lowest flow rate the Elveflow MFS2 delivers a lower flow than is displayed. In contrast, the flow sensor delivers more than it indicates at the maximum flow rate. In the medium flow rate, the two values match more closely.

The flow values with the "small" chip configuration are similar values to those with the "large" ship configuration, possibly with a small shift of the entire calibration curve.

It should be mentioned that there are other influencing factors that can affect the measurement in the MIC system. For example, the inlet pressure changes depending on the filling volume of the reservoir. In the Eppendorf lid used with a filling volume of 2 mL, the first millilitre (from 2 ml to 1 ml filling volume) makes a difference of 1.6 mm and the second millilitre (from 1 mL to 0 mL filling volume due to the conical shape) makes a difference of 1.8 mm. Assuming that a water column of 100 cm represents a pressure of 100 mbar, this already means a pressure difference of 1.6 mbar for a measurement in which a volume of 1 mL is delivered, respectively a necessary increase in inlet pressure. At the same time, the weighing scale is filled and the back pressure increases. In the case of measurements at RISE (about 5.35 mm/ml), this means an additional 5.35 mbar per millilitre.

In order to maintain a constant pressure, the difference at the beginning of the measurement (2 mL in the reservoir) to the end of the measurement (1 mL in the reservoir) is about 7 mbar.

These considerations probably do not make much difference for large flow rates and the associated higher pressures. However, the situation is different with low flow rates and lower pressures.

3.2.2. Dynamic measurements with the MIC system at RISE

Flow control is achieved by a Proportional-Integral-Derivative (PID) controller feedback loop in the MIC system. The software supplied allows the PI parameters to be changed to achieve the desired response. The change of the PI values is usually sufficient for most applications. As a rule of thumb, if the system is slow to react or overshoots, P should be changed and if there is oscillation or the system slows as it approaches the target, I should be changed. The default parameters for P and I are 0.001, which means a quite sluggish system.

The most common test signal for characterising the transmission behaviour of a system is the step function. For this reason, it was examined to what extent the system can follow desired rapid flow changes. For this purpose, the pump (P:0.012, I:0.012) was subjected to

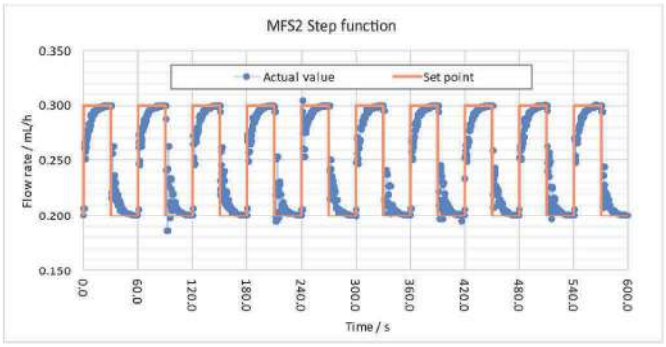

Fig. 9. Result of the step response tests with adjusted amplification factor.

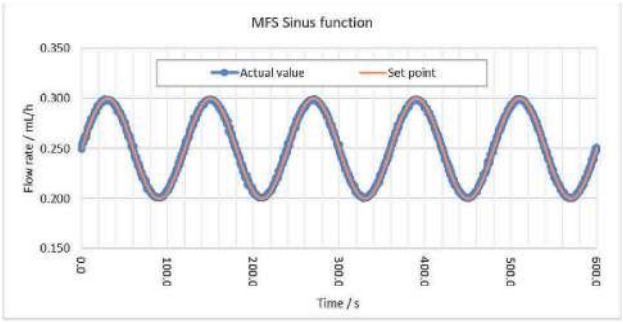

Fig. 10. Result of the sine excitation test with adjusted amplitude and phase.

a rectangular function between 0.2 mL/h and 0.3 mL/h with a period length of 60 s (step up, hold for 30 s, step down, hold for 30 s), Fig. 9.

In addition to the step function and pulse function, periodic input functions are also used as test signals to determine the transfer behaviour of dynamic systems. The frequency response is the relationship between the input and output signal of a linear time-invariant system with sinusoidal excitation in terms of amplitude and phase. Due to the linear behaviour of the system, the output signal has the same frequency as the input signal. However, the two signals differ in amplitude and phase. The ratio of the amplitudes of the input signal and the output signal as a function of the frequency is the amplitude response. The difference in phase between the input signal and the output signal as a function of frequency is the phase response. This means after a transient phase, the system also responds to a sinusoidal signal with a sinusoidal signal of the same frequency, but with a different amplitude and phase depending on the frequency.

As can be seen in Figs. 9 and 10, the MIC system is able to follow rapid changes. The period duration of the rectangular functions is already at the limit, at least for the setup at RISE. The response during excitation with the sine function is on the other hand extremely smooth.

3.3. Flow resistivity/Hydraulic resistance measurements

Microfluidic flows are characterised by their laminar nature and therefore viscous effects dominate over inertia. This leads to a simplification of the Navier-Stokes equations to the Poiseuille equation, which describes the pressure drop due to the viscosity of an incompressible fluid. The flow rate is then proportional to the pressure drop:

$$\Delta p = R_h \cdot Q \tag{1}$$

The flow resistance R_h, also called hydraulic resistance or hydrodynamic resistance, is a crucial parameter in microfluidic experiments. The flow resistance can be defined as the resistance that all microfluidic components in a measurement setup (tubing, valves, flow sensor, etc.) and the microfluidic chip present to the flow. When a fluid is

Table 7
Measurement results of the large configuration of channel 2 on the microfluid chip with the Cetoni system at RISE.

Cetoni system – Channel 2: "large" configuration			
Target flow (mbar)	Cetoni set flow (mL/h)	MFS log (mL/h)	Δp (mbar)
0.000	0.000	0.000474	0.00
0.025	0.024	0.025865	0.38
0.100	0.100	0.099685	0.48
0.200	0.200	0.197413	1.63
0.300	0.312	0.293645	2.22
0.400	0.450	0.403838	2.24

Table 8
Measurement results of the small configuration of channel 2 on the microfluid chip with the Cetoni system at RISE.

Cetoni system – Channel 2: "small" configuration			
Target flow (mbar)	Cetoni set flow (mL/h)	MFS log (mL/h)	Δp (mbar)
0.000	0.000	0.000606	0.00
0.025	0.024	0.025325	18.02
0.100	0.100	0.095104	57.72
0.200	0.200	0.202950	111.27
0.300	0.312	0.294966	161.33
0.400	0.445*	0.397255	225.61

Table 9
Measurement results of the large configuration of channel 2 on the microfluid chip with the MIC system at RISE.

MIC system – Channel 2: "large" configuration			
	MFS flow	Ref. flow	Pressure
	mL/h	mL/h	mbar
0.400	0.400063	0.446319	198.96
0.100	0.099994	0.100530	70.28
0.025	0.024992	0.023934	39.64
0.000	−0.000930	0	27.96

pressurised, the flow resistance determines the corresponding flow rate. The range and precision of the flow rate can be controlled by adjusting the flow resistance of the system.

In lab-on-a-chip experiments, for example, it is important to calculate the microfluidic flow resistance of a chip to understand the system and define the flow parameters (e.g. shear stress). This is determined by the design of the microchip. As a side note, by adjusting the material, length and diameter of the tubing, the flow resistance can be influenced to adapt or improve the performance of the flow control system.

Table 10
Measurement results of the small configuration of channel 2 on the microfluid chip with the MIC system at RISE.

MIC System – Channel 2: "small" configuration			
	MFS flow	Ref. flow	Pressure
	mL/h	mL/h	mbar
0.400	0.399951	0.451886	426.20
0.100	0.099986	0.101077	123.33
0.025	0.024988	0.024273	58.74
0.000	0.000856	0	27.75

3.3.1. *Measurements with the Cetoni system at RISE*

The flow was generated using the high-precision syringe pump (Cetoni) and the 1 mL syringe which was calibrated for this purpose in section 3.1 (section 3.1.1). For the pressure drop measurement over the chip, two external pressure sensors (Cetoni) with a flat ceramic membrane and a nominal pressure of 500 kPa (5.0 bar) were used to measure the pressure before and after the microfluidic chip. The pressure sensors were connected directly to the Cetoni syringe pump via a Cetoni input/output (I/O) port splitter and the pressure values were recorded by the Cetoni software.

The measurement set-up was designed that the syringe pump was connected to the MFS, then the MFS to the upstream pressure sensor. After the downstream pressure sensor, the measuring line ends at an infusion needle that protrudes into the beaker.

For this application, the MFS was used as a flow sensor and not as a regulator as in the MFS system. As can be seen in Tables 7 and 8, the flow rate of the Cetoni pump was set in such a way that the MFS display shows the desired flow rate value in the software. This procedure enables better comparability with the MIC system, as the value of the MFS there is used as the flow reference. As can be seen in Table 7, for example, the flow rate value of the Cetoni pump need to be set to 0.450 mL/h so that the MFS displays a flow rate of 0.400 mL/h. According to the measurements and the evaluation of the MFS log file, the average value in this case was actually 0.403838 mL/h. Incidentally, this finding also corresponds very well with the measurements of the MFS against the weighing scale (Tables 6 and 9).

The pressure sensors have a resolution of 1.25 mbar and are therefore completely unsuitable for measuring such small pressure differences. However, the results shown in Table 7 confirmed that the pressure drop over the "large" configuration of channel 2 is negligible, as already mentioned in section 2.3.

Table 8 and Fig. 11 summarise the results of the pressure drop measurements with the Cetoni pump over the small configuration of channel 2 ($R_h = 518.0$ mbar h/mL). The results correspond well with the theoretical values ($R_h = 505.8$ mbar h/mL) which can be calculated using the channel width, channel height and channel length. The measured value is slightly larger, which could indicate that the actual

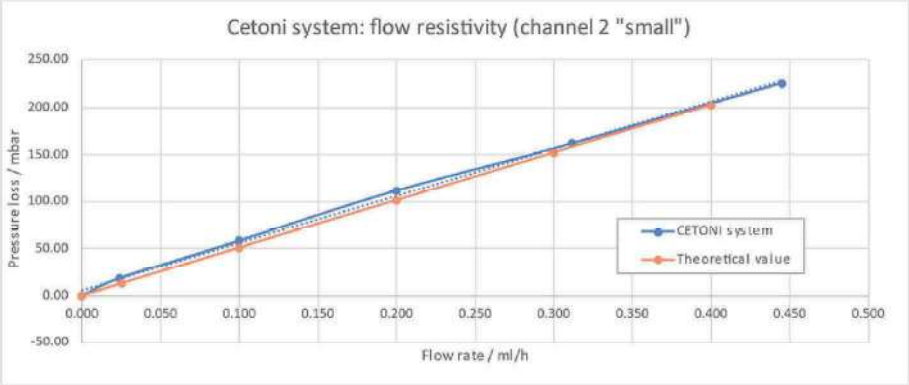

Fig. 11. Comparison of the results of the measurements with the Cetoni system with the theoretical value.

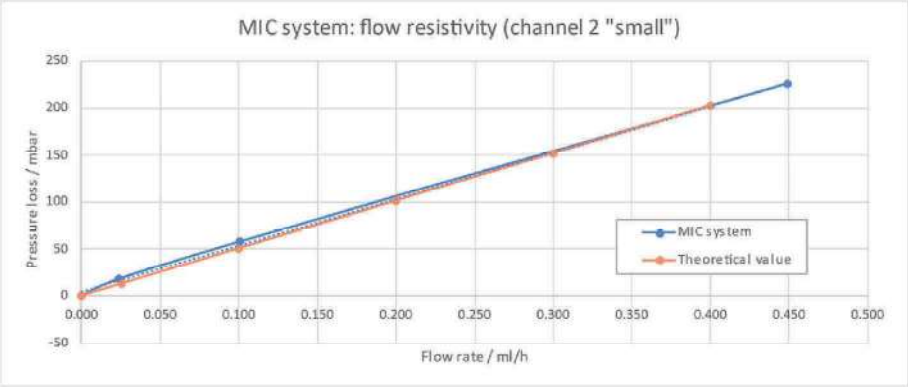

Fig. 12. Comparison of the results of the measurements with the MIC system with the theoretical value.

channel length and/or the channel width is slightly smaller, or the channel is slightly longer.

3.3.2. Measurements with the MIC system at RISE

The same measurements were made using the MIC system. The advantage of the MIC system is that, due to the nature of the operating principle, the pressure is directly available as a value provided by the system.

As the pressure drop over the large configuration of channel 2 is negligible, the pressure drop over the small configuration of channel 2 can be determined. If the measurement setup is identical in both configurations, the only difference is that the pressure drop over the chip plays a role in one case (small configuration of channel 2) and not in the other (large configuration of channel 2). This means that a much higher inlet pressure is required in one case than in the other. The back pressure is also the same in both cases. The difference between these two measurements should therefore only represent the pressure drop over the small configuration of channel 2.

The pressure drop measurements for both configurations are shown in Table 9 (large configuration of channel 2) and Table 10 (small configuration of channel 2).

It is noted that the pressure drop measurements were not taken at exactly the same flow rates. The results are presented by differentiating the pressure values and averaging the respective reference flow values obtained from the measurement against the weighing scale. As can be seen in Fig. 12, the measured value ($R_h = 506.4$ mbar h/mL) agrees very well with the theoretical value ($R_h = 505.8$ mbar h/mL). Again, the measured R_h value is slightly larger than the theoretical R_h value.

4. Conclusions

This study compares the performance of a pressure-driven flow system, comprising a novel pressure-driven flow controller and a commercial thermal mass flow meter, with that of established high-precision syringe pumps, which are typically employed as the reference for flow generation in most medical research and National Metrology Institutes.

The set pressure in a pressure-driven flow controller is proportional to the flow rate, with the microfluidic resistance serving as the proportionality factor. This factor depends on the measurement setup and the properties of the test fluid used. In microfluidic applications, such as lab-on-a-chip experiments, the microfluidic resistance of the microchip is essential because it defines the parameters for the experiment. For this reason, these measurements were realized with a microfluidic chip that can create different pressure conditions at the same flow rate by simply changing the channels or access holes on this chip. It should be noted that the flow sensor was not calibrated for the other test liquids under investigation, and the factory calibration for water was used. This offers potential for further investigation. Finally, pressure-driven flow systems are regarded as fast-responding systems that produce pulsation-free flow. Due to fast pressure changes, it is theoretically possible to generate fast flow changes. For this reason, the dynamic behaviour was also investigated. The system showed a favourable performance.

With water as the test liquid, it was demonstrated that a pressure-driven flow system with a calibrated flow sensor can achieve excellent results. In particular, in the context of lab-on-a-chip experiments, such systems offer significant advantages, as they provide immediate feedback in the event of modifications to the chip design or other changes to the measurement setup. This is of paramount importance for medical research and development.

Funding statement

This project (EMPIR JRP 20NRM02 MFMET) has received funding from the EMPIR programme co-financed by the Participating States and from the European Union's Horizon 2020 research and innovation programme. The pressure-driven flow controller was developed in the Horizon 2020 project "Tumor and Lymph Node on Chip for cancer studies". This project has received funding from the European Union's Horizon 2020 research innovation programme under grant agreement No. 953234 (TUMOR-LN-oC).

Acknowledgments

The authors would like to thank microfluidic ChipShop for providing the microfluidic chips for the measurements.

References

[1] N. Azizipour, R. Avazpour, D.H. Rosenzweig, M. Sawan, A. Ajji, Evolution of biochip technology, A review from lab-on-a-chip to organ-on-a-chip, Micromachines (Basel) 11 (6) (2020 Jun 18) 599.
[2] V. Silverio, S. Cardoso, Lab-on-a-chip: systems integration at the microscale, in: E. Chapter (Ed.), Drug Delivery Devices and Therapeutic Systems, Elsevier Science, 2021. ISBN: 978-0-12-819838-4.
[3] M. Engin, A. Demirel, E. Engin, M. Fedakar, Recent developments and trends in biomedical sensors, Measurement 37 (2) (2005) 173–188.
[4] Project website MFMET project: https://mfmet.eu/.
[5] H. Bissig, E. Batista, et al., Primary standards for measuring flow rates from 100 nl/min to 1 ml/min – gravimetric principle, Biomed. Eng. 60 (4) (2015) 301–316.
[6] E. Batista, J. Alves e Sousa, S. Cardoso, V. Silverio, Experimental testing for metrological traceability and accuracy of liquid microflows and microfluidics, Flow Meas. Instrum. 71 (2021).
[7] O. Büker, K. Stolt, RISE test facilities for the measurement of ultra-low flow rates and volumes with a focus on medical applications, Appl. Sci. 12 (16) (2022) 8332, https://doi.org/10.3390/app12168332.
[8] AAMI TIR101:2021, Fluid Delivery Performance Testing for Infusion Pumps, American National Standards Institute (ANSI), Washington, DC, USA, 2021.

Oliver Büker[a,*], Krister Stolt[a], Elsa Batista[b], Julia Sepulveda[c], Camila Betterelli Giuliano[c], Alan Morin[c], Diogo Nobre[d], Helena Navas[d]

[a] *RISE – Research Institutes of Sweden, Brinellgatan 4, 504 62, Borås, Sweden*

[b] *IPQ – Portuguese Quality Institute, R. António Gião 2, 2825-002, Caparica, Portugal*

[c] *Microfluidics Innovation Center, 172 rue de Charonne, 75011, Paris, France*

[d] *NOVA University Lisbon, Largo da Torre, 2829-516, Caparica, Portugal*

[*] Corresponding author.
E-mail address: oliver.buker@ri.se (O. Büker).

Int. J. Metrol. Qual. Eng. **16**, 2 (2025)

https://doi.org/10.1051/ijmqe/2024021

International Journal of Metrology and Quality Engineering

Available online at:
www.metrology-journal.org

RESEARCH ARTICLE OPEN ACCESS

Measurement of wettability and surface roughness for metrology and quality control in microfluidics

Thomas Schrøder Daugbjerg[1,*], Loïc Crouzier[2], Alexandra Delvallée[2], Florestan Ogheard[3], Christina Pecnik[4], Kevin Romieu[3], Fernanda Saraiva[5], and Elsa Batista[5]

[1] Danish Technological Institute (DTI), 8000 Aarhus C, Denmark
[2] Laboratoire National de Métrologie et d'Essais (LNE), 78190 Trappes, France
[3] Centre Technique des Industries Aérauliques Et Thermiques (CETIAT), 69100 Villeurbanne, France
[4] IMT Masken und Teilungen AG (IMTAG), 8606 Greifensee, Switzerland
[5] Instituto Português da Qualidade (IPQ), 2829-513 Caparica, Portugal

Received: 25 April 2024 / Accepted: 16 December 2024

Abstract. Microfluidics is a rapidly growing technology with applications in biochemistry and life sciences. To support the ongoing growth there is a need for common metrology, quality control, and standardisation. Here measurements of wettability and surface roughness can contribute, and these quantities affect flow characteristics of devices, bonding processes in manufacturing, and special microfluidic mechanisms such as droplet formation and spreading of fluids on surfaces. To quantify wettability, an optical laboratory setup was used to measure liquid drop contact angles of three liquids on a microfluidic surface. To further quantify wettability, the Owens, Wendt, Rabel, and Kaelble model was applied to contact angle measurements to determine the total surface free energy. To quantify surface roughness, atomic force microscopy and stylus profilometry measured area roughness parameter and profile roughness parameter for four samples of microfluidic surfaces. The wettability methods successfully demonstrated measurements of contact angles, and these methods were applied to determine a value for the total surface free energy. AFM and stylus profilometry successfully determined surface roughness parameters, and the determined values agreed with the expected for the material. In conclusion, the demonstrated methods can contribute to metrology, quality control and standardisation in microfluidics.

Keywords: Microfluidics / wettability / surface roughness / metrology / quality control / standardisation

1 Introduction

Microfluidics is the technology of manipulating small amounts of fluid using microchannels where one of the transverse dimensions are smaller than 1000 µm [1,2]. The microchannels are typically embedded in a thin slide, often denoted a chip, and often made of polymer or glass. Noteworthy applications of microfluidics are inkjet printing [3,4], a microscale system for gas chromatography [5], an array of capillary electrophoresis channels for DNA sequencing [6,7], contributions to the Human Genome Project [8,9], and organ-on-a-chip systems with cultures of living cells in channels to simulate organ tissue in drug trials [1]. Further examples of applications and technology are available in the review by Convery and Gadegaard [1].

Different materials are used in microfluidic chips, and the capabilities of microfluidic devices depend on materials and their properties [10]. Thermoplastic polymers are an often-used material, for example cyclic olefin copolymers (COC) and copolyester thermoplastic elastomer (COP), and these are suitable for mass production techniques such as injection moulding [11]. Glass types, e.g. borosilicate glass D236® bio or D236® T eco, are also commonly used with advantages for devices requiring chemical stability, high temperature, or high pressure [12]. The manufacturing of glass chips can involve techniques such as glass substrates, wet etching, and bonding of multiple glass plates [12].

Wettability and surface roughness, both defined in materials and methods, are relevant material properties that can influence the operation and manufacturing of microfluidic devices. Wettability describes the ability to maintain contact between a liquid and a solid surface [13].

* Corresponding author: tsda@dti.dk

Table 1. Samples of glass slides investigated in this study.

Sample	Material	Width (mm) x length (mm)	Description
Sample 1	D263® bio	25 × 75	Flat surface for liquid drops
Sample 2	D263® bio	25 × 52.6	Two open channels
Sample 3	D263® bio	25 × 52.6	Two open channels
Sample 4	D263® bio	25 × 52.6	Two open channels
Sample 5	D263® bio	9.5 × 52.6	Bonding area only

In microfluidic devices associated with droplet mechanisms the surface wettability is a fundamental characteristic affecting the dynamic behaviour of droplet generation and evolution [14]. Greater wettability has been shown to enhance the flow of a fluid displacing another fluid, in a microfluidic system with multiple fluid phases and a porous medium [15]. Wettability is also an important characteristic for microfluidic devices relying on spreading of a fluid for chemical or biological reactions on a surface or in a microchannel [16]. According to the classical description of a stable laminar flow, wettability has no effect on the flow in a microchannel [17]. However, multiple studies have reported an experimental microchannel friction factor higher than that predicted by the classical description [18–20]. Li et al. propose a modified apparent viscosity model for microscale flows based on molecular theory and wetting theory [18]. In that model, the friction factor increases with increasing wettability, and a greater pressure difference would be needed to drive a flow in a microchannel with greater wettability.

Surface roughness may be loosely described as the surface irregularities that makes a surface not smooth. For definitions of surface texture and surface roughness parameters see ISO 25179-2 [21] and ISO 21920-2 [22]. According to the classical description of a stable laminar flow, surface roughness does not affect the flow in a microchannel [17]. However, there are studies where the pressure difference needed to drive a flow in a microchannel is larger than expected from classical laminar flow theory [23–25]. These studies refer that the observed excess flow resistance is an effect of the surface roughness of a microchannel. Thus, higher surface roughness may increase the pressure difference needed to drive a given flow through a microchannel.

In summary, different values of wettability may help facilitate special mechanisms in different types of microfluidic devices. Smooth surfaces and low wettability can lead to microchannels where lower pressure differences are needed to drive the flow, which may improve flow performance, and reduce risks of leaks and burst of microfluidic devices and interfaces [26]. Furthermore, surface roughness is important for microfluidic manufacturing involving bonding of multiple glass or polymer layers, where it can be more difficult to bond rougher surfaces successfully [27]. The goal of this study is to demonstrate accurate measurement and evaluation of wettability and surface roughness, and thus help optimising and standardising the performance of microfluidic devices. Stakeholders from industry, academia and government have recognized that microfluidics has unanswered needs regarding universally accepted metrology, quality control, and standardisation [28,29]. Thus, this study makes a novel contribution to the important effort of advancing quality control, standardisation and harmonisation in the field of microfluidics [28,29].

The experimental results presented in this study have also been communicated in reports of the MFMET project, and these reports are available on the Zenodo general purpose open repository [30–35]. Furthermore, this work was inspired by some of these reports [30–32].

2 Materials and methods

2.1 Samples

Table 1 lists the five samples of glass slides used in this study. Sample 1 was used for wettability measurements, and it had a flat surface of the material D263® bio, with thickness 1 mm, width 25 mm, and length 75 mm. IMTAG in Greifensee, Switzerland, provided sample 1 in a sealed box.

Table 1 also lists sample 2–sample 5, which were used for surface roughness measurements, and these were glass slides of D263® bio with width 25 mm and length 52.6 mm provided by IMTAG in Greifensee, Switzerland. From the perspective of microfluidic manufacturing these glass slides are unbonded glass substrates. Sample 2–sample 4 had two open channels made by wet etching, see Figure 1. These three samples had the surface types bonding surface and channel surface. Sample 5 was a glass slide with only bonding area and no channels.

2.2 Measurements of wettability on microfluidic surfaces

ISO 19403-1 [13] defines quantitative measures of wettability, i.e. the contact angle θ of a liquid drop resting on a solid surface, and the total surface free energy of a solid surface σ_s. The contact angle is the angle between the drop base and the tangent of the liquid-atmosphere interface at the three-phase point, see Figure 2. The total surface free energy of a solid surface is energy or tension arising from forces on the solid surface from interactions between molecules, see Figure 2. While not used as a direct measure of wettability, the total surface tension of the liquid σ_l is an important quantity, which describes energy or tension arising from forces on the liquid surface from interactions between molecules, see Figure 2. As explained below, the contact angle θ depends on both the liquid and the solid surface, while the total surface free energy of a solid surface is a material quantity that depends only on the surface.

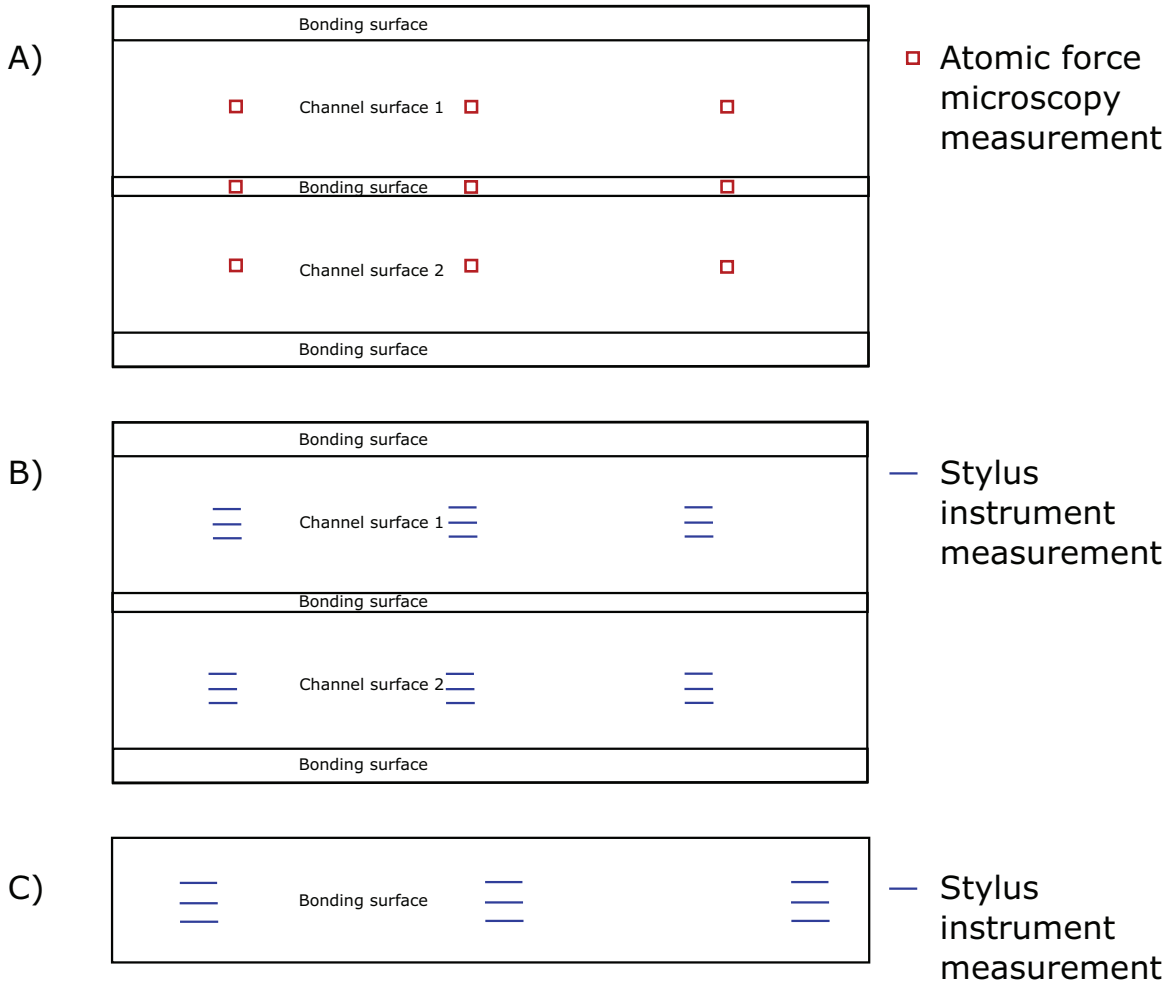

Fig. 1. Selected glass slides from Table 1, and locations of surface roughness measurements. The open channels in sample 2–sample 4 are 100 μm deep and 9.5 mm wide. Sample 1 is not shown in this figure, because it was used for wettability measurements only. A) Sample 2–sample 4 had measurements with atomic force microscopy made at the indicated locations. B) Sample 2–sample 4 had stylus instrument measurements made at the indicated locations. C) Sample 5 had stylus instrument measurements made at the indicated locations.

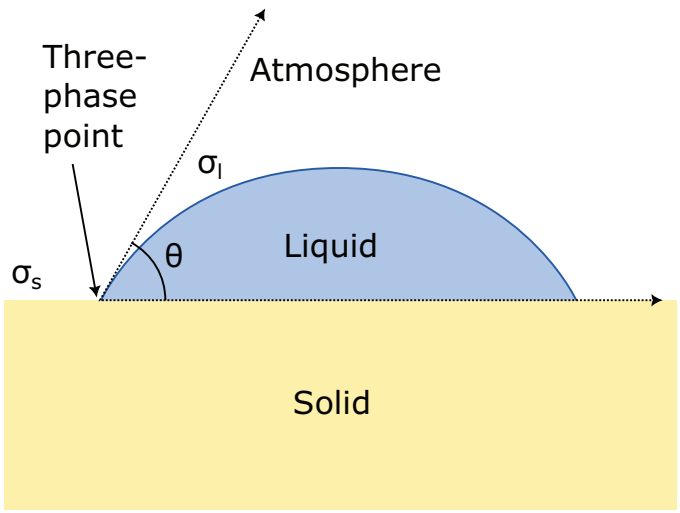

Fig. 2. Illustration of a liquid drop resting on a solid surface. In the three-phase point the solid, liquid, and atmosphere (containing vapour) are in contact. Also shown in the illustration are the contact angle θ, the surface tension of the liquid is σ_l, and the surface free energy of the solid surface σ_s. Source: Redrawn from ISO 19403-1 [13].

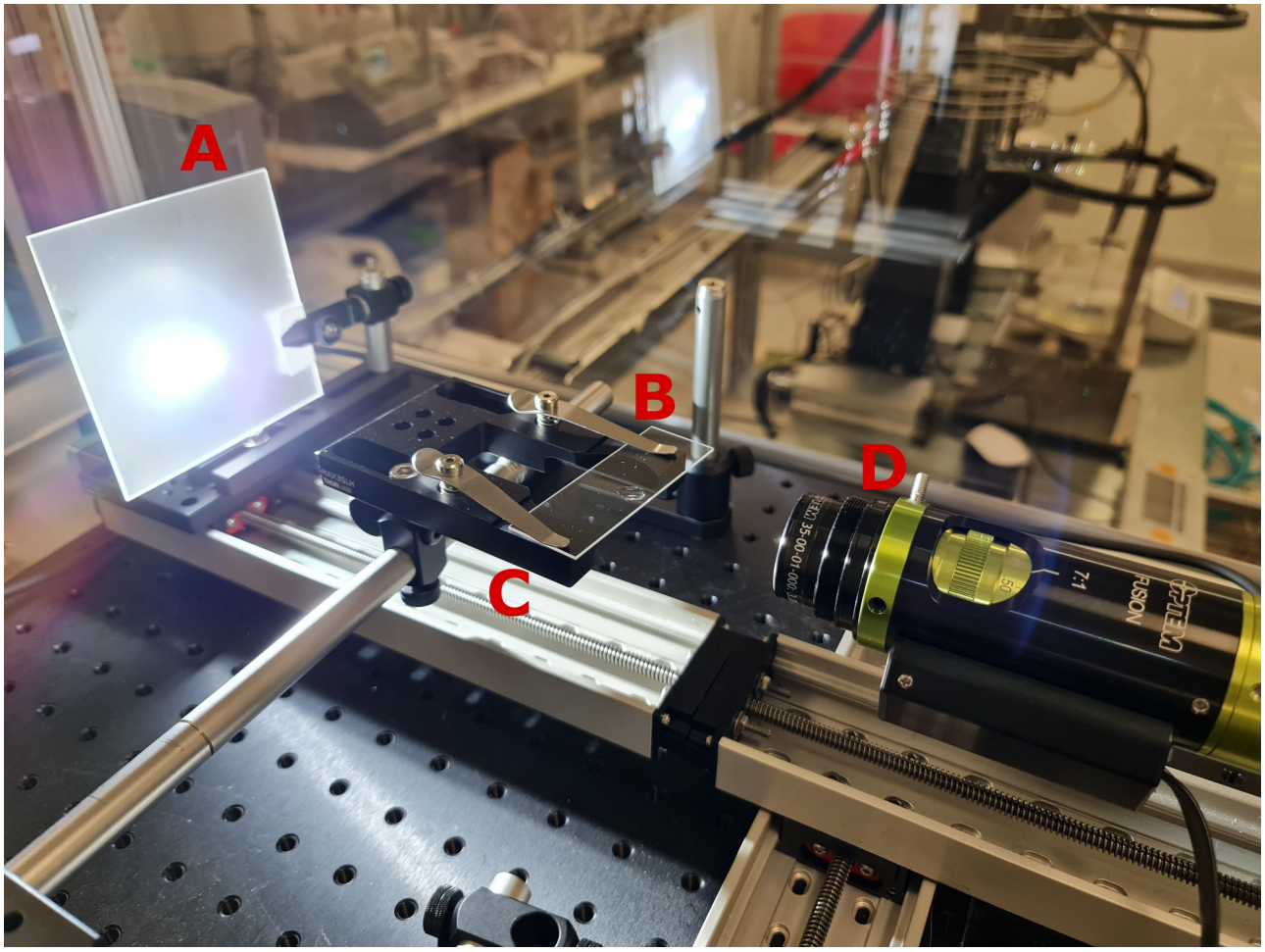

Fig. 3. The laboratory setup at CETIAT in Villeurbanne, France, for measuring contact angles on a flat surface. A − white diffused lighting, B − slide under test, C − slide holder, D − high resolution microscope camera. Image credit: CETIAT.

ISO 19403-1 [13] and ISO 19403-2 [36] describe a method to measure the contact angle, and a method to determine the total surface free energy. In the context of microfluidic chips, it is worth noting that these methods address a drop on a flat surface, and not inside a microchannel. As such, the contact angle and total surface free energy in this study characterise liquids and surfaces, rather than the geometry of a channel. There exists research and publications which discuss measuring the contact angle inside channels or tubes [37–42]. However, at the time of this study there was heterogeneity and ambiguity among these methods, and to support wide applicability and standardisation this study did not use them.

The measurements of contact angle were performed at the liquid flow laboratory at CETIAT in Villeurbanne, France. The measurements used sample 1, see Table 1, and three liquids were used: water, di-iodomethane, and ethylene glycol. Figure 3 shows the laboratory setup that measured the contact angles on a flat surface. To comply with the test conditions described in ISO 19403-2 [36], the laboratory setup operated not exposed to vibrations, intense air flows, or intense light from the outside. Furthermore, the setup was oriented horizontally, equilibrated with the room temperature that was within (23 ± 2) °C, and the room's relative humidity was within $(50 \pm 5)\%$.

The glass slide was placed in a sample holder, and the position adjusted to place it in the lower half of the image of the microscope camera. The slide holder was positioned between the microscope camera and a source of white diffused lighting, see Figure 3. The test liquid was prepared and filled in a clean and bubble-free syringe. The cannula of the syringe was moved to the top of the image, and the image was adjusted for focus, contrast, and brightness. Carefully, the syringe placed a drop on the glass slide, and the microscope magnification was adjusted to make the drop take up about 2/3 of the image.

The laboratory setup was calibrated with the calibration standards CP24 from KRÜSS [43]. The standards are a set of contact angle shapes printed on glass slides, and they accurately follow theoretical drop shapes according to Young-Laplace. The Young-Laplace equation can be found in ISO 19403-1 [13]. The calibration standards allow calibration of contact angles with an accuracy of $U_{\text{angle standard}} = 0.1°$ [43]. Contact angles were measured by manually evaluating captured images with the software

ImageJ [44]. For this calibration three measurements of the contact angle were made for each of the three standards with reference contact angle values 30°, 60°, and 120°.

This study used the Owens, Wendt, Rabel, and Kaelble (OWRK) model to determine the total surface free energy of the solid surface [13,36]. The OWRK model originates from application of adsorption theory to describe the wettability of a solid surface with a liquid [13,45,46]. The theory formulates a state of equilibrium for the three-phase point, see Figure 2. This equilibrium involves quantities such as the contact angle, the total surface free energy of the solid surface, and the total surface tension of the liquid [13].

The OWRK model assumes that polar interactions and disperse interactions dominate other molecular interactions [13,45,46]. Thus, the model describes the total surface free energy of the solid surface σ_s, as the sum of the polar surface free energy of the solid surface $\sigma_s{}^p$ and the disperse surface free energy of the solid surface $\sigma_s{}^d$ [13,45,46]. Likewise, it describes the total surface tension of the liquid σ_l as the sum of the polar surface tension of the liquid $\sigma_l{}^p$ and the disperse surface tension of the liquid $\sigma_l{}^d$ [13,45,46]:

$$\sigma_s = \sigma_s^p + \sigma_s^d$$

$$\sigma_l = \sigma_l^p + \sigma_l^d. \tag{1}$$

Finally, the OWRK model formulates the equilibrium with the following linear equation [13,36]:

$$y = m{\cdot}x + b \tag{2}$$

where [13,36]:

$$y = \frac{(1+\cos\theta){\cdot}\sigma_l}{2\sqrt{\sigma_l^d}}$$

$$m = \sqrt{\sigma_s^p}$$

$$x = \sqrt{\frac{\sigma_l^p}{\sigma_l^d}}$$

$$b = \sqrt{\sigma_s^d}. \tag{3}$$

In summary, application of the OWRK model enabled determination of the total surface free energy of the solid surface σ_s as follows. Two or more liquids with known values of total surface tension σ_l, disperse surface tension $\sigma_l{}^d$ and polar surface tension $\sigma_l{}^p$, were placed on the solid surface and contact angles θ were measured. In this study, the surface tension values were obtained from ISO 19403-2 [36,47]. The literature and measured values enabled calculation of x and y, as stated in equation (3), and a linear equation of the form in equation (2) was fitted to x and y. From the fit parameters m and b, the polar surface free energy of the solid surface was derived as $\sigma_s{}^p = m^2$, and the disperse surface free energy of the solid surface was derived as $\sigma_s{}^d = b^2$. As stated in Equation 1 the total surface free energy of the solid surface was found by adding the disperse and polar contributions. It can be inferred from equations (2) and (3) that if all else is equal, a drop will have a smaller contact angle on a solid surface with a greater total surface free energy. The contact angle is illustrated in Figure 2.

2.3 Measurements of surface roughness on microfluidic surfaces

The area roughness parameter S_a is defined as the arithmetic mean of the absolute value of the height $z(x,y)$ over the investigated surface A [21], see equation (4).

$$S_a = \frac{1}{A}\iint_A |z(x,y)|dxdy. \tag{4}$$

Similarly, the profile roughness parameter R_a is defined as the arithmetic mean of the absolute value of the height $z(x)$ over a line l_e on the investigated surface [22,48], see equation (5).

$$R_a = \frac{1}{l_e}\int_0^{l_e} |z(x)|dx. \tag{5}$$

Notice that equations (4) and (5) use the absolute value of the height, so peaks and valleys of a surface do not cancel each other out. Furthermore, the height in equations (4) and (5) is referenced with the mean of the surface, and ISO 25178 describes filters applied to surface data prior to calculation of roughness parameters [21].

2.3.1 Atomic force microscopy

Atomic force microscopy (AFM) is a technique for imaging three-dimensional surface topographies at the nanometre scale [49–51]. AFM scans a sample by moving a sharp physical probe over the surface, while measuring the interaction forces between the probe and the surface [49,51]. In AFM an important force for this interaction is the interatomic weak force called van der Waals force [50,51]. The sharp probe is attached to a small arm denoted a cantilever, and during a scan either the cantilever or the sample is moved by a very precise positioning system, e.g. a piezoelectric scanner [52]. The interaction between the probe and the surface is determined by measuring the vertical motion of the probe, e.g. using a laser beam deflection system [49,52]. In one operating mode the probe is in contact with the sample, and this so-called contact-mode could damage the surface or the tip. A special operating mode of AFM is denoted tapping-mode, where the cantilever vibrates vertically above the surface (~300 kHz typically), probing the interaction forces by the changes in amplitude and phase of the oscillation can reveal information about the vertical height of the sample surface [49,50,52]. This mode is preferred for surface roughness measurements, avoiding the smoothing of the tip or the surface during acquisition of images.

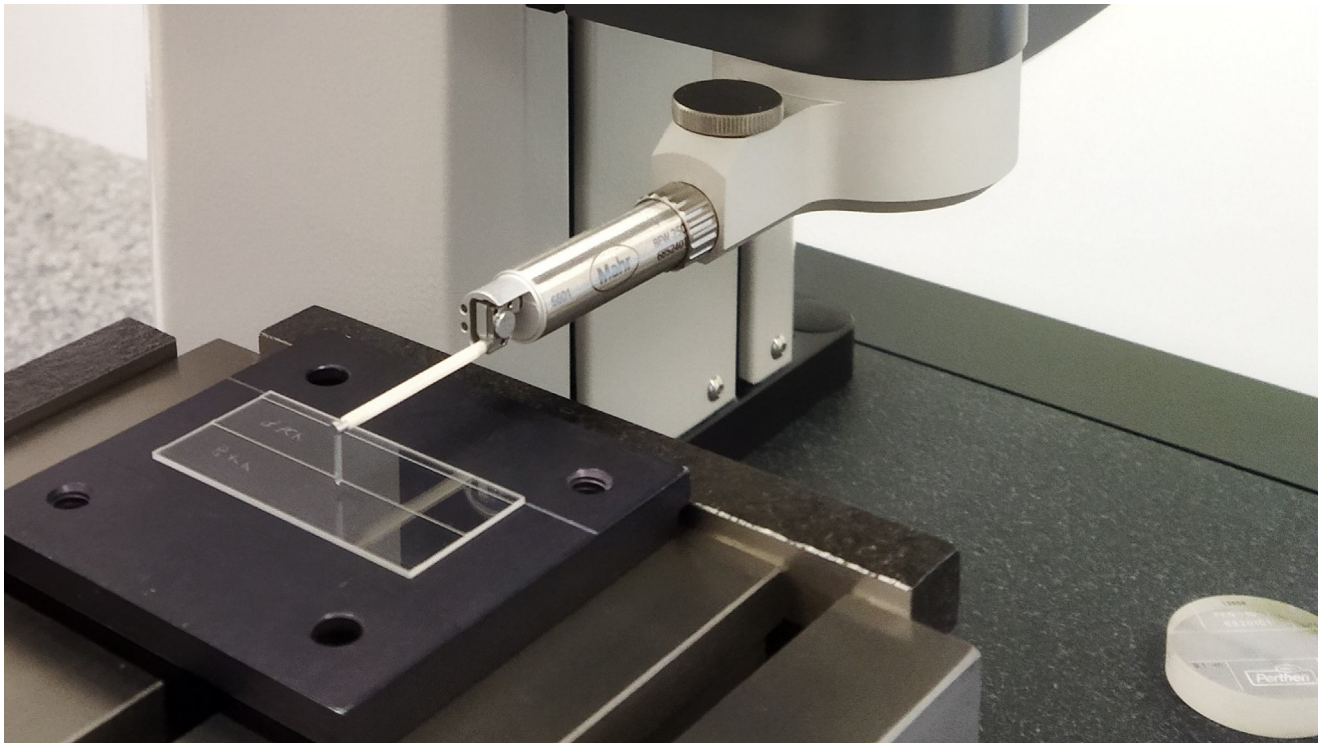

Fig. 4. The MarSurf GD 140 stylus instrument at IPQ, Caparica, Portugal, during the measurement of surface roughness parameters of a sample. Image credit: IPQ.

Table 2. Results from calibration of the laboratory setup for measuring contact angle. This result was also communicated in a report of the MFMET project [33].

Angle of standard (°)	Measured angle (°)	Error (°)
30	30.55	0.55
30	29.35	–0.65
30	29.77	–0.23
60	59.84	–0.16
60	59.70	–0.30
60	59.32	–0.68
120	119.932	–0.068
120	120.20	0.20
120	120.13	0.13
Average of errors $\overline{E}$ (°)		–0.13
Standard deviation of errors σ_E (°)		0.40

This study employed a Veeco Dimension 3100 atomic force microscope [52] and a Bruker AFM probe OTESPA R3 [53], and these measurements were made at LNE in Trappes, France. The typical tip radius of OTESPA R3 is 7 nm. The NanoScope software controlled the acquisition of measurements [52]. The AFM was in tapping-mode with cantilever amplitude, cantilever frequency, gain, and resolution adjusted according to manufacturer recommendations [52]. The measurement campaign was carried out after and before a calibration check to ensure the traceability of the height measurement. This calibration was realised with a P900H60 standard (nominal pitch 900 nm, nominal height 60 nm) [54]. Furthermore, the measurements were made after a few hours of thermalisation, and the protective housing closed. The AFM scans were made in a scan area of 5 µm by 5 µm, 1024 pixels by 1024 pixels (pixel size 4.9 nm), and scan speed 4 µm/s (scan rate 0.5 Hz).

Following measurements, the software MountainsLab (Digital Surf) processed the raw images with the following operations [55]: line to line levelling, thresholding to exclude possible dust or residue on the surface, and calculation of the area roughness parameter S_a according to ISO 25178 [56,57]. No additional filters were used.

Sample 2 to sample 4 were used for surface roughness measurements with AFM. Each sample had three measurements in channel 1, the bonding area, and channel 2, see Figure 1.

2.3.2 Stylus profilometry

Stylus profilometry measures the topography of a surface by physically probing the surface with a stylus tip mounted on a probe arm [58–60]. The stylus profilometer operates with the application of a small force, which makes the stylus tip physically touch the surface [60]. The stylus is typically in the shape of a cone ending in a spherical tip, and typically the tip is made of diamond and has radius of a few micrometres [59,60]. The stylus scans the surface of a sample by movement

provided by a drive unit, typically comprising a motor and gearbox [60]. The vertical motion of the stylus is electrically detected, e.g. with a transducer device [60].

This study employed a Mahr reference measuring station MarSurf GD 140, which scans surfaces with constant velocity and constant force between surface and stylus tip [61] to give quantitative information on heights with respect to position. These measurements were made at IPQ in Caparica, Portugal. Figure 4 shows the MarSurf probe arm with the stylus scanning over the channel surface of one of the samples at the IPQ laboratory. To comply with the MarSurf GD 140 instrument's specifications, the parameters were set to probe arm length 45 mm, measuring force 0.030 N, spherical tip radius 2 µm, vertical measuring range −250 µm to +250 µm, maximum vertical resolution 0.2 nm, and measuring speed 0.10 mm/s [61].

Following the measurements, data analysis was made with the MarWin EasyRoughness software from Mahr. The settings for the evaluation of the surface texture of the profile of the samples were based on the informative annex D of ISO 21920-3:2021 [62], as the samples were produced in a research framework and therefore have no nominal values. Furthermore, the following measurement configuration parameters were used: total profile length 0.56 mm, section length 0.08 mm, and evaluation length $l_e = 0.4$ mm [22]. That analysis enabled the evaluation of several parameters besides profile roughness parameter R_a. These were the height parameters: root mean square height R_q, skewness R_{sk}, kurtosis R_{ku}, and total height R_t [22], and these were the feature parameters maximum height R_z, mean peak height R_p, and mean pit depth R_v [22]. ISO 21920-2:2021 explains these parameters in greater detail [22].

Sample 2 to sample 5 were used for surface roughness measurements with stylus profilometry. Sample 2 to sample 4 had nine profile measurements made in channel 1 and channel 2, see Figure 1. Finally, sample 5 had nine profile measurements made in the bonding area, see Figure 1. The choice of nine measurements was based on, and exceeded, the recommendation of five sections in the informative annex D of ISO 21920-3:2021 [62].

3 Results

3.1 Measurements of wettability on microfluidic surfaces

Table 2 shows results from calibration of the laboratory setup for contact angle measurements.

From the results in Table 2, the measurement uncertainty of contact angle measurements was determined to $U(k=2)_{\text{contact angle}} = 1°$, using the below formula:

$$U(k=2)_{\text{contact angle}} = 2\sqrt{\left(\frac{U_{\text{angle standard}}}{2}\right)^2 + (\sigma_E)^2 + |\overline{E}.|} \quad (6)$$

In equation (6), $U_{\text{angle standard}}$ is the accuracy of the angle standard as defined in materials and methods, $\overline{E}$ and σ_E are respectively the average of errors and standard deviation of errors, as defined in Table 2. In equation (6), $k = 2$ is the coverage factor, and its value implies a 95% confidence level for the uncertainty.

Table 3 presents the results from contact angle measurements of the three liquids on the surface of sample 1. For each average contact angle $\overline{\theta}$, the uncertainty was evaluated following JCGM [63], and the contributors to the uncertainty evaluation were: the standard deviation of the contact angles θ for each liquid and $U_{\text{contact angle}}$ from equation (6).

Table 4 shows values of x and y, see equations (1)–(3), calculated from the average contact angles in Table 3 and liquid surface tensions tabulated in ISO 19403-2 [36,47]. The uncertainty of y was determined following JCGM by propagating uncertainty for y in equation (3) [63], and the contributor to the uncertainty evaluation was: the uncertainty of the average contact angle $\overline{\theta}$ from Table 3.

Figure 5 shows fitting of a linear equation to the values of x and y, and the caption of Figure 4 presents the fit parameters. The R-squared value is close to 1 and indicates a decently successful fit [64], though it is important to notice that the R-squared statistic does not consider the uncertainty of data. If one compares data uncertainty and the fitted linear equation in Figure 5, there is a clear discrepancy between data and fit. The fitting procedure aimed to mitigate this by using *scale_ covar=True* in LMFIT, so the width of the confidence band and uncertainties of the fit parameters were scaled according to the discrepancy [65].

Using equation (1), equation (3), and the fit parameters from Figure 5, calculations were made of the polar surface free energy of the solid surface σ_s^p, and the disperse surface free energy of the solid surface σ_s^d, and the total surface free energy of the solid surface σ_s. The associated uncertainties were evaluated following JCGM by propagating uncertainty for σ_s^p, σ_s^d, σ_s in equations (1) and (3) [36,63], and the contributors to the uncertainty evaluation were: the fit parameter b and m from Figure 5. Table 5 displays the results.

3.2 Measurements of surface roughness on microfluidic surfaces

Table 6 shows results from surface roughness measurements with AFM, and given the resulting uncertainties this method effectively resolved the nanometre scale of the observed surface roughness. The uncertainty of S_a was evaluated following JCGM [63], and the contributor to the uncertainty evaluation was: the standard deviation of three measurements from the same surface, see Figure 1. Figure 6 shows topographic 2D surfaces from selected measurements with AFM.

Table 6 shows the results from surface roughness measurements with stylus profilometry, and given the resulting uncertainties the profile roughness parameter R_a effectively resolved the nanometre scale of the observed surface roughness. Apart from R_a, Table 6 also shows the parameters R_q, R_{sk}, R_{ku}, R_t, R_z, R_p, and R_v from stylus profilometry, and these were introduced in the materials and methods section, and they will be discussed further in the discussion section. The uncertainty of all parameters associated with stylus profilometry was evaluated following JCGM [63], and the contributor to the uncertainty evaluation was: the standard deviation of nine measurements from the same surface, see Figure 1.

Table 3. Contact angle measurements of three liquids on the surface of sample 1. Uncertainties in this table are stated with a 95% confidence level ($k=2$). These results were also communicated in reports of the MFMET project [32–34].

Contact angles θ (°)	Water	Di-iodomethane	Ethylene glycol
	27 ± 1	38 ± 1	41 ± 1
	22 ± 1	34 ± 1	33 ± 1
	21 ± 1	41 ± 1	35 ± 1
Average contact angle $\overline{\theta}$ (°)	23 ± 6	38 ± 7	36 ± 8

Table 4. Values of x and y. The uncertainties U_y are stated with a 95 % confidence level ($k=2$). These results were also communicated in reports of the MFMET project [32,33]. Also shown are values, y_{fit}, from the fit in Figure 5 and a comparison of y and y_{fit} with Z-score [64] using $u_y = U_y/2$. The discussion has further details on the Z-score comparison.

	Water	Di-iodomethane	Ethylene glycol
x	1.53	0.00	0.74
$y \pm U_y$ ((mN/m)$^{1/2}$)	15.0 ± 0.3	6.4 ± 0.3	7.7 ± 0.4
y_{fit} ((mN/m)$^{1/2}$)	14.1	5.8	9.8
Z-score $(y\text{-}y_{\text{fit}})/u_y$	4.9	4.2	–11.1

4 Discussion

The materials and methods described methodology that can be used as test protocols in microfluidics. A test protocol to determine the wettability of a surface was demonstrated on sample 1, a surface of D263® bio glass, and with three liquids: water, di-iodomethane and ethylene glycol. The measurement system for contact angles was calibrated using traceable angle standards. The results of measured contact angles are presented in Table 3, and the determined surface free energy of sample 1 is presented in Table 5. Notice the relatively large uncertainties of the surface energies, which derived from the discrepancy between fit and data, see Figure 5. Here, LMFIT was used with *scale_ covar=True*, so the discrepancy contributed to the uncertainties of fit parameters and in turn to the uncertainties of the determined surface free energies in Table 5. Given the discrepancy, it is important to be critical towards the reliability of the result in Table 5, and it was not possible to make precise claims about the values of surface free energies.

The discrepancy between fit and data could be explained by an underestimation of measurement uncertainties. The uncertainty of y derived from propagation of the uncertainty of contact angle θ. In turn, the uncertainty of θ was estimated using the standard deviation of reproduced measurements and the measurement uncertainty from the calibration of the contact angle laboratory setup. Table 4 quantitatively compares y uncertainties and y values from data and fit. Assuming the fit is correct and considering the values of Z-score, the uncertainties of y may have been underestimated by a factor of 4.2 to 11.1. Considering the values and uncertainties in Table 3, it seems doubtful that all this underestimated uncertainty could come from the contact angle measurements. Indeed, uncertainties greater by a factor of 4.2 to 11.1 could exceed

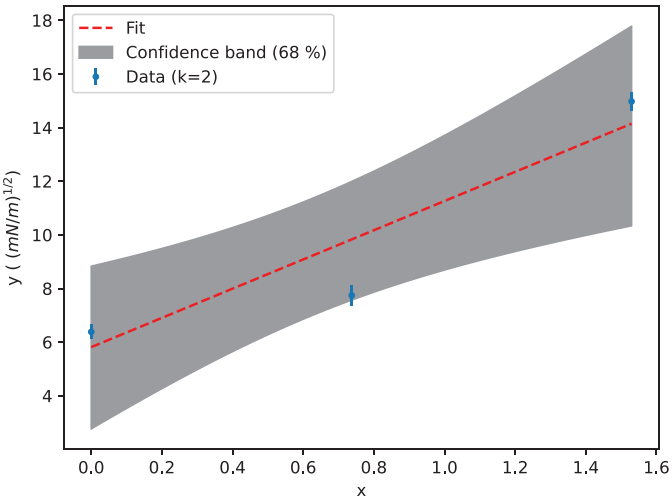

Fig. 5. Plot of values of x and y. Uncertainties of y, b and m have a 95 % confidence level (k=2). A linear equation with confidence band was fitted using LMFIT [65], and the fit parameters are: intercept $b = (6 \pm 3)$ (mN/m)$^{1/2}$ and slope $m = (5 \pm 4)$ (mN/m)$^{1/2}$. The R-squared of the fit is R^2=0.87. These results were also communicated in reports of the MFMET project [32–34].

Table 5. Calculated values for σ_s^p, σ_s^d, and σ_s for sample 1 from Table 1. See equations (1) and (3) for definitions, and this table shows uncertainties with 95% confidence level ($k=2$). These results were also communicated in reports of the MFMET project [32–34].

Parameter	Value $\pm$ uncertainty (mN/m)
σ_s^p	30 ± 40
σ_s^d	34 ± 38
σ_s	63 ± 55

Table 6. Results of surface roughness measurements by AFM and stylus profilometry. The samples and locations of measurements are shown in Figure 1. The uncertainties have a 95 % confidence level (k = 2). No AFM results were available from the channel surfaces of sample 4, or from sample 5. No stylus profilometry results were available from the bonding surface of sample 2 − sample 4. These results were also communicated in reports and a data set of the MFMET project [31,32,34,35].

		AFM	Stylus profilometry							
Sample	Location	S_a (nm)	R_a (nm)	R_q (nm)	R_z (nm)	R_t (nm)	R_p (nm)	R_v (nm)	R_{sk}	R_{ku}
2	Channel surface 1	0.60 ± 0.04	1.4 ± 0.2	1.7 ± 0.4	8 ± 2	12 ± 6	4 ± 1	4.0 ± 0.8	–0.1 ± 0.6	4 ± 2
	Channel surface 2	0.60 ± 0.06	1.3 ± 0.6	1.6 ± 0.7	8 ± 3	10 ± 6	4 ± 2	4 ± 2	–0.4 ± 0.7	3 ± 2
	Bonding surface	0.51 ± 0.04	–	–	–	–	–	–	–	–
3	Channel surface 1	0.56 ± 0.06	1.3 ± 0.2	1.6 ± 0.4	8 ± 2	11 ± 6	4 ± 2	4 ± 1	–0.1 ± 0.8	4 ± 2
	Channel surface 2	0.56 ± 0.02	1.3 ± 0.6	1.7 ± 0.7	8 ± 4	12 ± 6	4 ± 2	4 ± 2	–0.2 ± 0.6	3 ± 2
	Bonding surface	0.49 ± 0.04	–	–	–	–	–	–	–	–
4	Channel surface 1	–	1.4 ± 0.3	1.8 ± 0.6	8 ± 2	13 ± 9	4 ± 1	4 ± 1	0 ± 1	5 ± 5
	Channel surface 2	–	1.5 ± 0.7	1.9 ± 0.9	9 ± 4	13 ± 9	4 ± 2	4 ± 2	0 ± 1	5 ± 5
	Bonding surface	0.46 ± 0.02	–	–	–	–	–	–	–	–
5	Bonding surface	–	1.4 ± 0.4	1.8 ± 0.5	8 ± 2	11 ± 3	4 ± 1	4 ± 1	–0.4 ± 0.4	3.3 ± 0.6

the values of θ in Table 3, and that large uncertainties cannot be justified by observations. Another possibility is that the uncertainties in Figure 5 were underestimated because the values used for surface tension of liquids did not account for uncertainty. Analysis of propagation of error [63] for y in equation (3), using values applicable to water for θ, σ_l, ${\sigma_l}^d$, suggested that surface tension uncertainties of order of magnitude ≈1 mN/m (corresponding to a relative uncertainty of ≈1%) would dominate the uncertainty contributions to y, and exceed the uncertainties reported in Table 4. However, the widespread practise of reporting and using surface tension values without uncertainty makes it difficult to investigate this further [36,66–68]. It is also possible that some data in Figure 4 is an outlier due to an experimental mishap related to the cleanliness of the surface, placing the drops, or issues with liquids or photographs. This study made measurements of wettability in the fall of 2022. While this study was in review, ISO 19403-2:2017 [47] was updated to ISO 19403-2:2024 [36], and this update removed the use of ethylene glycol as a test liquid. It is possible that the data from ethylene glycol was an outlier, because of an issue with ethylene glycol. For example, ethylene glycol is hydroscopic and it changes surface tension with increasing water content [47]. Future studies may investigate further underestimated sources of uncertainty or practises to reduce the occurrence of outliers.

IMTAG communicated that the glass of sample 2–sample 5 was produced to have a surface roughness below 0.5 nm. The surface roughness was however expected to increase from various steps during manufacturing, so values larger than 0.5 nm were expected. The AFM measurements produced surface roughness values in the range 0.46–0.60 nm, which was similar to the surface roughness specified by IMTAG. Looking in Table 6, the bonding surface appeared to have slightly lower surface roughness than the channel surface. Looking at Figure 6, it appeared that the channel areas were more homogenous, while the bonding area had more changes in surface topography over smaller distances. Based on the AFM results, it can be argued that manufacturing steps associated with the channels, e.g. wet etching, increased the surface roughness by a low amount (≈0.1 nm). Low surface roughness is a positive situation for later steps in manufacturing, e.g. bonding processes, and it is positive for the later applications where a microfluidic flow is contained by the channel surfaces.

The measurements with stylus instrument in Table 6 showed slightly higher values of profile roughness parameter R_a than area roughness parameter S_a with AFM in Table 6. However, it was not possible to directly compare the two parameters because of some key differences between the AFM method and the stylus profilometry method. First, AFM measured the surface roughness as a

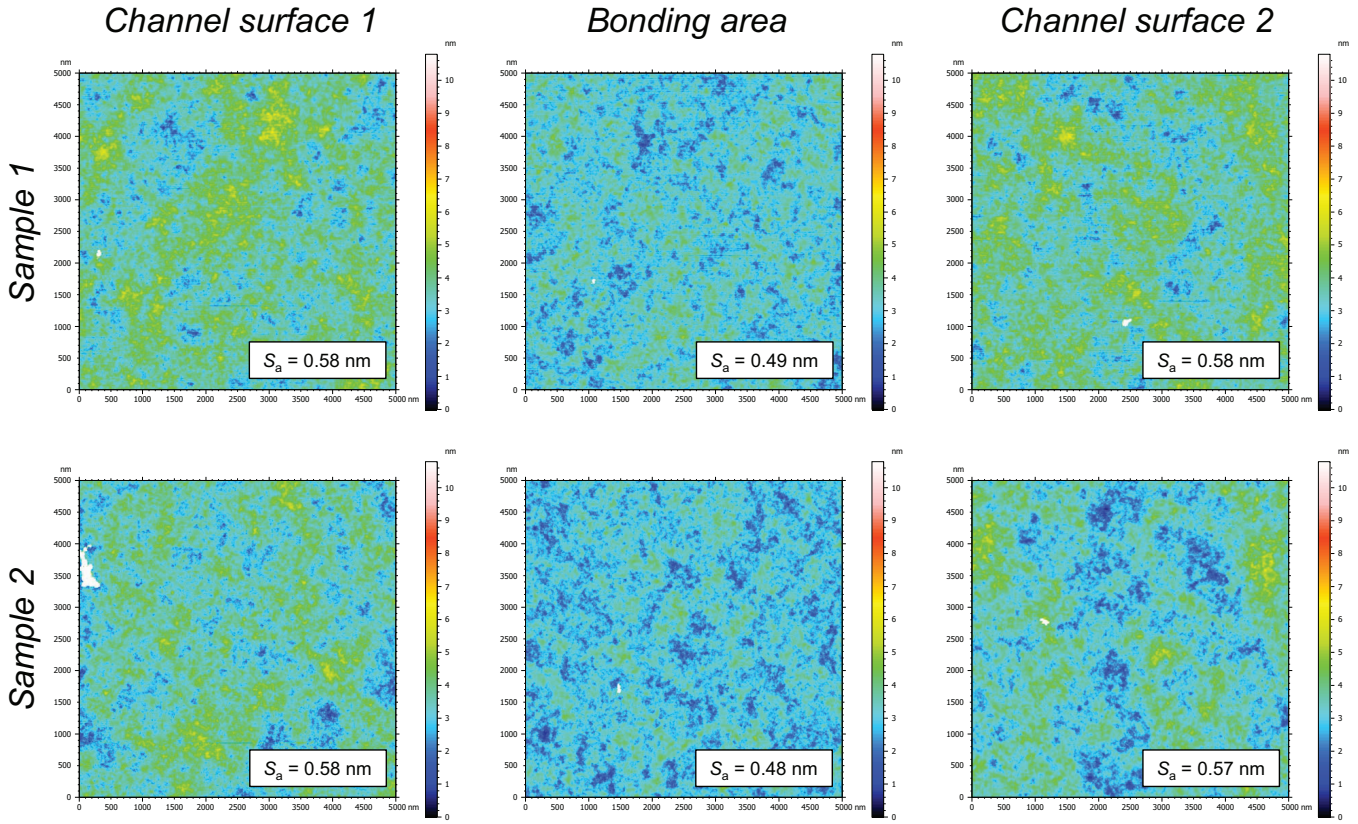

Fig. 6. Topographic surfaces of selected measurements with AFM. Samples and surface types can be compared with Table 1 and Figure 1. For each pair of sample and surface, three AFM measurements contributed to the AFM averages presented in Table 6. These results were also communicated in reports of the MFMET project [31,34].

mean over two dimensions, while stylus profilometry measured it as a mean over one dimension. Second, the scanning ranges were different with AFM scanning 5 µm by 5 µm, and stylus profilometry scanning 560 µm. Hence, the two methods measured surface roughness on different scales. Finally, the tip radius of AFM was 7 nm, while the tip radius of stylus profilometry was 2 µm, and thus the two methods see the surface roughness with different levels of detail. With these considerations, differences are expected between the two methods.

Models exist for the relationship between surface roughness and wettability [69–71]. Wenzel stated that wettability is affected by surface roughness and introduced the Wenzel roughness factor accordingly [69,70]. In that model, a higher surface roughness is associated with an increased contact angle for otherwise chemically similar surfaces. The work by Cassie and Baxter extended the relationship between wettability and surface roughness to porous surfaces, where the liquid drop and solid surface may not be in full contact, but leave small pockets of air [71]. Cassie and Baxter discussed examples where a surface with a regular grid of fibres was associated with a large contact angle and water-repellency [71]. In this study, the feature parameters R_z, R_p, and R_v, see Table 6 and the materials and methods section, partly described the mean peaks and pits of the surfaces, and this was partly related to the relationship between surface roughness and wettability. In that perspective, Hongru et al. evaluated the Wenzel roughness factor of several surfaces using laser scanning confocal microscopy, albeit not they did not measure wettability which was the objective of this study [72].

In conclusion, this study presented methods which can be used as test protocols for wettability and surface roughness in microfluidic manufacturing of devices. These quantities are important in microfluidics, and they may affect flow characteristics, bonding processes, and special mechanisms such as droplet generation, multiple fluid phases in a porous medium, and spreading of fluid. Such test protocols can help the microfluidic industry in facilitating robust quality control, characterisation of devices, validation of devices, and standardised metrology.

Acknowledgments

The authors would like to acknowledge all administrative and technical support for the MFMET project at DTI, LNE, IPQ, CETIAT, and IMTAG.

Funding

This project 20NRM02 MFMET has received funding from the EMPIR programme co-financed by the Participating States and from the European Union's Horizon 2020 research and innovation programme. Funder name: European Metrology Programme for Innovation and Research. Funder ID: 10.13039/100014132. Grant number: 20NRM02 MFMET.

Conflicts of interest

We have no conflicts of interest to disclose.

Data availability statement

Processed data associated with this article is available in two reports and a deliverable on the Zenodo general purpose open repository [30–32].

Author contribution statement

Conceptualization, Loïc Crouzier, Florestan Ogheard, Christina Pecnik and Elsa Batista; Methodology, Loïc Crouzier, Alexandra Delvallée, Pedro Neves, Florestan Ogheard, Kevin Romieu and Fernanda Saraiva; Software, Thomas Schrøder Daugbjerg, Alexandra Delvallée, Florestan Ogheard and Kevin Romieu, Fernanda Saraiva; Validation, Thomas Schrøder Daugbjerg, Florestan Ogheard, Kevin Romieu, Fernanda Saraiva and Elsa Batista; Formal Analysis, Thomas Schrøder Daugbjerg, Loïc Crouzier, Alexandra Delvallée, Florestan Ogheard, Kevin Romieu, Fernanda Saraiva and Elsa Batista; Investigation, Thomas Schrøder Daugbjerg, Loïc Crouzier, Alexandra Delvallée, Florestan Ogheard, Kevin Romieu, Fernanda Saraiva and Elsa Batista; Resources, Loïc Crouzier, Alexandra Delvallée, Pedro Neves, Florestan Ogheard, Christina Pecnik, Kevin Romieu, Fernanda Saraiva, Elsa Batista; Data Curation, Thomas Schrøder Daugbjerg, Alexandra Delvallée, Florestan Ogheard, Kevin Romieu, Fernanda Saraiva and Elsa Batista; Writing – Original Draft Preparation, Thomas Schrøder Daugbjerg; Writing – Review & Editing, Thomas Schrøder Daugbjerg, Alexandra Delvallée, Florestan Ogheard and Elsa Batista; Visualization, Thomas Schrøder Daugbjerg and Alexandra Delvallée; Supervision, Florestan Ogheard and Elsa Batista; Project Administration, Thomas Schrøder Daugbjerg, Florestan Ogheard and Elsa Batista; Funding Acquisition, Elsa Batista.

References

1. N. Convery, N. Gadegaard, 30 years of microfluidics, Micro Nano Eng. **2**, 76–91 (2019)
2. D. Qin, Y. Xia, J.A. Rogers, R.J. Jackman, X.-M. Zhao, G.M. Whitesides, Microfabrication, microstructures and microsystems, in Microsystem Technology in Chemistry and Life Science, edited by A. Manz and H. Becker (Springer Berlin Heidelberg, Berlin, Heidelberg, 1998), pp. 1–20
3. R.G. Sweet, High frequency recording with electrostatically deflected ink jets, Rev. Sci. Instru. **36**, 131 (1965)
4. E. Bassous, H.H. Taub, L. Kuhn, Ink jet printing nozzle arrays etched in silicon, Appl. Phys. Lett. **31**, 135 (1977)
5. S.C. Terry, J.H. Jerman, J.B. Angell, A gas chromatographic air analyzer fabricated on a silicon wafer, IEEE Trans. Electron Dev. **26**, 1880 (1979)
6. P. Simpson, D. Roach, A. Woolley, T. Thorsen, R. Johnston, G. Sensabaugh, R. Mathies, High-throughput genetic analysis using microfabricated 96-sample capillary array electrophoresis microplates, Proc. Natl. Acad. Sci. USA **95**, 2256 (1998)
7. A.T. Woolley, R.A. Mathies, Ultra-high-speed DNA fragment separations using microfabricated capillary array electrophoresis chips, Proc. Natl. Acad. Sci. USA **91**, 11348 (1994)
8. H. Kambara, Development of capillary array DNA sequencers for genome analysis, Chem. Record **10**, 8 (2010)
9. Q. Xiong, J. Cheng, Chapter 2 Chip Capillary Electrophoresis and Total Genetic Analysis Systems, in *Perspectives in Bioanalysis*, edited by Keith R. Mitchelson, Publisher Elsevier Vol. 2 (2007), pp. 45–95
10. X. Hou, Y.S. Zhang, G.T. Santiago, M.M. Alvarez, J. Ribas, S.J. Jonas, P.S. Weiss, A.M. Andrews, J. Aizenberg, A. Khademhosseini, Interplay between materials and microfluidics, Nat. Rev. Mater. **2**, 17016 (2017)
11. C.-W. Tsao, Polymer microfluidics: simple, low-cost fabrication process bridging academic lab research to commercialized production, Micromachines **7**, 225 (2016)
12. T. Tang, Y. Yuan, Y. Yalikun, Y. Hosokawa, M. Li, Y. Tanaka, Glass based micro total analysis systems: materials, fabrication methods, and applications, Sens. Actuat. B **339**, 129859 (2021)
13. ISO 19403-1:2022 Paints and Varnishes — Wettability — Part 1: Terminology and General Principle (2022)
14. A. Venkateshwarlu, R.P. Bharti, Effects of surface wettability and flow rates on the interface evolution and droplet pinch-off mechanism in the cross-flow microfluidic systems, Chem. Eng. Sci. **267**, 118279 (2023)
15. B. Zhao, C. MacMinn, R. Juanes, Wettability control on multiphase flow in patterned microfluidics, Proc. Natl. Acad. Sci. USA **113**, 10251–10256 (2016)
16. S. Saxena, R. Joshi, Microfluidic devices: applications and role of surface wettability in its fabrication, in *Surface Science*, edited by Phuong Pham, Pratibha Goel, Samir Kumar, and Kavita Yadav, Publisher IntechOpen (2020)
17. H. Bruus, *Theoretical Microfluidics* (Oxford University Press, 2008)
18. X. Li, X. Chen, Y. Huang, X. Zhang, Effect of interface wettability on the flow characteristics of liquid in smooth microchannels, Acta Mech. **230**, 2111–2123 (2019)
19. L. Zhigang, G. Ning, Z. Chengwu, Z. Xiaobao, Experimental study on flow and heat transfer in a 19.6-Mm microtube, Exp. Heat Transfer **22**, 178 (2009)
20. F. Wang, X. Yue, S. Xu, L. Zhang, R. Zhao, J. Hou, Influence of wettability on flow characteristics of water through microtubes and cores, Chin. Sci. Bull. **54**, 2256 (2009)
21. ISO 25178-2:2021 Geometrical Product Specifications (GPS) Surface Texture: Areal Part 2: Terms, Definitions and Surface Texture Parameters (2021)
22. ISO 21920-2:2021 Geometrical Product Specifications (GPS) Surface Texture: Profile Part 2: Terms, Definitions and Surface Texture Parameters (2021)
23. Y.-M. Kim, W.-S. Kim, S.-H. Lee, J.-Y. Baek, Effects of surface roughness on the flow characteristics in PDMS microchannels, in *2005 3rd IEEE/EMBS Special Topic Conference on Microtechnology in Medicine and Biology*, Vol. 2005 (2005), pp. 292–295
24. X. Yuan, Z. Tao, H. Li, Y. Tian, Experimental investigation of surface roughness effects on flow behavior and heat transfer characteristics for circular microchannels, Chin. J. Aeronaut. **29**, 1575 (2016)

25. P. Ranjan, Investigations on the flow behaviour in microfluidic device due to surface roughness: a computational fluid dynamics simulation, Microsyst. Technolog. **25**, 3779–3789 (2019)
26. V. Silverio, S. Guha, A. Keiser, R. Natu, D. Reyes, H. Heeren, N. Verplanck, L. Herbertson, Overcoming technological barriers in microfluidics: leakage testing, Front. Bioeng. Biotechnol. **10**, 958582 (2022)
27. T. Wang, J. Wu, T. Chen, F. Li, T. Zuo, S. Liu, Surface roughness analysis and thermal bonding of microfluidic chips fabricated by CD/DVD manufacturing technology, Microsyst. Technolog. 23, (2017)
28. E. Batista, V. Silverio, F. Ogheard, C. Pecnik, H. Becker, A. Niemann, MFMET project – establishing metrology standards in microfluidic devices, in *Conference: 19th International Flow Measurement Conference* 2022 (2023)
29. E. Batista, J. Sousa, F. Saraiva, A. Lopes, V. Silverio, R. Martins, L. Martins, The importance of dimensional traceability in microfluidic systems, Metrology **4**, 240 (2024)
30. L. Crouzier, C. Pecnik, MFMET A3. 2.4: Test Protocol for Surface Roughness (2022)
31. C. Pecnik, L. Crouzier, F. Saraiva, E. Batista, P. Neves, V. Silverio, MFMET A3. 2.7 Documented Example of Surface Roughness Measurements (2023)
32. C. Pecnik et al., MFMET Deliverable 5 – Guidelines for the Measurement of Key Performance Parameters of Microfluidic Connections Including the Identification of Key Properties in an Interface (2024)
33. F. Ogheard, MFMET A3. 2.5. Documented Example of Wettability Test Protocol (2024)
34. K. Romieu, A. Dalvallée, MFMET Webinar – 03. Wettability and Surface Roughness (2024)
35. C. Pecnik, L. Crouzier, F. Saraiva, E. Batista, P. Neves, V. Silverio, MFMET A3. 2.7 Documented Example of Surface Roughness Measurements [Data Set], (2024)
36. ISO 19403-2:2024 Paints and Varnishes — Wettability — Part 2: Determination of the Surface Free Energy of Solid Surfaces by Measuring the Contact Angle (2024)
37. M. Heshmati, M. Piri, Experimental investigation of dynamic contact angle and capillary rise in tubes with circular and noncircular cross sections, Langmuir **30**, 14151 (2014)
38. S. Ehlers, J. Könemann, O. Ott, H. Wolf, J. Šetina, A. Furtado, W. Sabuga, Selection and characterization of liquids for a low pressure interferometric liquid column manometer, Measurement **132**, 191 (2019)
39. A.O. Olanrewaju, M. Beaugrand, M. Yafia, D. Juncker, Capillary microfluidics in microchannels: from microfluidic networks to capillaric circuits, Lab Chip **18**, 2323 (2018)
40. S. Son, L. Chen, Q. Kang, D. Derome, J. Carmeliet, Contact angle effects on pore and corner arc menisci in polygonal capillary tubes studied with the pseudopotential multiphase lattice boltzmann model, Computation **4**, 12 (2016)
41. V. Heiskanen, K. Marjanen, P. Kallio, Machine vision based measurement of dynamic contact angles in microchannel flows, J. Bionic Eng. **5**, 282 (2008)
42. M. Jafari, J. Jung, Direct measurement of static and dynamic contact angles using a random micromodel considering geological CO2 sequestration, Sustainability **9**, 2352 (2017)
43. KRÜSS, Calibration Standards CP24, https://www.kruss-scientific.com/en/products-services/accessories/cp24
44. ImageJ Image Processing and Analysis in Java, https://imagej.net/ij/index.html
45. D.K. Owens, R.C. Wendt, Estimation of the surface free energy of polymers, J. Appl. Polym. Sci. **13**, 1741 (1969)
46. D.H. Kaelble, Dispersion-polar surface tension properties of organic solids, J. Adhesion **2**, 66 (1970)
47. ISO 19403-2:2017 Paints and Varnishes — Wettability — Part 2: Determination of the Surface Free Energy of Solid Surfaces by Measuring the Contact Angle (2017)
48. ANSI, DIN EN 10049:2014 Measurement Of Roughness Average Ra And Peak Count RPc On Metallic Flat Products (2014)
49. N. Jalili, K. Laxminarayana, A review of atomic force microscopy imaging systems: application to molecular metrology and biological sciences, Mechatronics **14**, 907 (2004)
50. R. García, R. Pérez, Dynamic atomic force microscopy methods, Surf. Sci. Rep. **47**, 197 (2002)
51. F. Marinello, Atomic force microscopy, in *CIRP Encyclopedia of Production Engineering* (Springer, 2014), pp. 62–66.
52. Veeco, Veeco Dimension 3100 Manual (2004)
53. BRUKER, OLTESPA-R3, https://www.brukerafmprobes.com/p-3865-oltespa-r3.aspx
54. L. Crouzier, A. Delvallee, S. Ducourtieux, L. Devoille, G. Noircler, C. Ulysse, O. Tache, E. Barruet, C. Tromas, N. Feltin, Development of a new hybrid approach combining AFM and SEM for the nanoparticle dimensional metrology, Beilstein J. Nanotechnol. **10**, 1523 (2019)
55. Digital Surf, What's inside MountainsLab® (n.d.)
56. ISO 25178-6:2010 Geometrical Product Specifications (GPS) Surface Texture: Areal Part 6: Classification of Methods for Measuring Surface Texture (2010)
57. ISO 25178-602:2010 Geometrical Product Specifications (GPS) Surface Texture: Areal Part 602: Nominal Characteristics of Non-Contact (Confocal Chromatic Probe) Instruments (2010)
58. A. Mínguez Martínez, P. Maresca, J. Caja, J. de Vicente y Oliva, Results of a surface roughness comparison between stylus instruments and confocal microscopes, Materials **15**, 5495 (2022)
59. T. Vorburger, H.-G. Rhee, T. Renegar, J.-F. Song, X. Zheng, Comparison of optical and stylus methods for measurement of surface texture, Int. J. Adv. Manufactur. Technol. **33**, 110 (2007)
60. R. Leach, The Measurement of Surface Texture Using Stylus Instruments (2001)
61. Mahr, MarSurf The Newest Generation of Tactile Measuring Technology (2019)
62. ISO 21920-3:2021 Geometrical Product Specifications (GPS) – Surface Texture: Profile – Part 3: Sepcification Operators (2021)
63. JCGM, JCGM 100:2008 GUM 1995 with Minor Corrections Evaluation of Measurement Data — Guide to the Expression of Uncertainty in Measurement (2008)
64. D. Freedman, R. Pisani, R. Purves, Statistics, 4th edition (W.W. Norton & Company, 2007)
65. M. Newville, T. Stensitzki, R. Otten et al., LMFIT, https://lmfit.github.io/lmfit-py/
66. R. Borah, A. Kumar, M. Das, A. Ramteke, Surface functionalization-induced enhancement in surface properties and biocompatibility of polyaniline nanofibers, RSC Adv. **5**, 48971–48982 (2015)

67. Y. He, I. Dobryden, J. Pan, A. Ahniyaz, T. Deltin, R. Corkery, P. Claesson, Nano-scale mechanical and wear properties of a waterborne hydroxyacrylic-melamine anti-corrosion coating, Appl. Surf. Sci. **457**, 548–558 (2018)
68. G. Ström, M. Fredriksson, P. Stenius, Contact angles, work of adhesion, and interfacial tensions at a dissolving hydrocarbon surface, J. Colloid Interface Sci. **119**, 352 (1987)
69. R.N. Wenzel, Resistance of solid surfaces to wetting by water, Ind. Eng. Chem. **28**, 988 (1936)
70. R.N. Wenzel, Surface roughness and contact angle, J. Phys. Colloid Chem. **53**, 1466 (1949)
71. A.B.D. Cassie, S. Baxter, Wettability of porous surfaces, Trans. Faraday Soc. **40**, 546 (1944)
72. A. Hongru, L. Xiangqin, S. Shuyan, Z. Ying, L. Tianqing, Measurement of wenzel roughness factor by laser scanning confocal microscopy, RSC Adv. **7**, 7052 (n.d.)

Cite this article as: Thomas Schrøder Daugbjerg, Loïc Crouzier, Alexandra Delvallée, Florestan Ogheard, Christina Pecnik, Kevin Romieu, Fernanda Saraiva, Elsa Batista, Measurement of wettability and surface roughness for metrology and quality control in microfluidics, Int. J. Metrol. Qual. Eng. **16**, 2 (2025), https://doi.org/10.1051/ijmqe/2024021

ISSN: 2834-4928

Research Article

Journal of Electrical Electronics Engineering

Multicomponent Mixtures - Stability Study to Support Carbon Metrology

Florbela A. Dias*, Cristina Palma and Carlos J. Costa

Portuguese Institute for Quality, Portugal

***Corresponding Author**
Florbela A. Dias, Portuguese Institute for Quality, Portugal.

Submitted: 2025, Jul 02; **Accepted:** 2025, Aug 04; **Published:** 2025, Aug 11

Citation: Dias, F. A., Palma, C., Costa, C. J. (2025). Multicomponent Mixtures - Stability Study to Support Carbon Metrology. *J Electrical Electron Eng, 4*(4), 01-09.

Abstract

The European project EPM SRT-v01 – MetCCUS (Metrology for Carbon Capture, Utilization and Storage) represents the first metrology-focused initiative dedicated specifically to CCUS (Carbon Capture, Utilization, and Storage). Developed within the scope of the European Green Deal, this project addresses the urgent need for accurate and traceable measurements to support the deployment of CCUS technologies. CCUS is identified as a strategic area for achieving the EU's climate objectives, namely the reduction of greenhouse gas emissions by 55 % by 2030 and the attainment of carbon neutrality by 2050. By strengthening the metrological infrastructure related to CO_2 measurement and analysis, MetCCUS plays a key role in enabling reliable monitoring, verification, and regulation of carbon capture processes. Funded by EURAMET, the MetCCUS project addresses the metrological challenges identified by industry. It aims to provide primary standards, measurement methods, and good practice guides to support the essential measurements required in this field. Additionally, it seeks to develop a robust metrological infrastructure for monitoring and detecting carbon dioxide leaks in energy and industrial processes, as well as in transport networks. This infrastructure will also contribute to a better understanding of the carbon dioxide life cycle. As part of the project, four binary gas mixtures were successfully characterized: two of SO_2 in a CO_2 matrix and two of H_2S in a CO_2 matrix. Moreover, four multicomponent mixtures were also characterized: two containing $SO_2 + CO + O_2$ in a CO_2 matrix, and two with $H_2S + CO + CH_4 + O_2$ in a CO_2 matrix. All mixtures were prepared in cylinders at approximately 40 bar and subjected to a one-year stability study. This stability assessment was conducted using statistical analysis based on the Normalized Error (En) function, in accordance with ISO 13528:2022, which specifies statistical methods for interlaboratory comparisons and performance evaluation.

Keywords: Carbon Metrology, Multicomponent Mixtures, Gravimetric Method, Certification, Stability Study

1. Introduction

Climate change has driven a significant expansion of environmental monitoring efforts worldwide. To ensure the reliability of collected data and to minimize measurement uncertainties, the demand for traceable measurements has increased considerably. In this context, reliable gas mixtures play a crucial role, as they are essential for the calibration of analytical instruments used to measure atmospheric pollutants and greenhouse gases (GHGs). These calibrated instruments enable accurate determination of the amount fraction of GHGs in the atmosphere, which is fundamental for climate research and policy development. The excessive accumulation of GHGs, particularly carbon dioxide (CO_2), contributes to global warming, ocean acidification, extreme weather events, and loss of biodiversity. In response to these environmental challenges, decarbonization has emerged as a key strategy. It involves the progressive reduction of CO_2 emissions resulting from human activities, with the objective of achieving a low-carbon or carbon-neutral economy. An important technological pathway to support decarbonization is Carbon Capture, Utilization, and Storage (CCUS). This set of technologies is designed to capture CO_2 emissions from industrial and energy-related sources, enabling either its utilization in industrial processes or its permanent storage in suitable geological formations, thereby preventing its release into the atmosphere. Decarbonization and CCUS represent fundamental components of global efforts to mitigate climate change. Despite existing technological, economic, and regulatory

challenges, continuous innovation, supportive policy frameworks, and international collaboration provide a viable path forward. Together, these initiatives aim to significantly reduce carbon emissions and promote a sustainable, low-carbon future [1].

The European initiative EPM (European Partnership on Metrology) SRT-v01 - MetCCUS (Metrology for Carbon Capture Utilization and Storage) [1] represents the first metrology project dedicated to CCUS (Carbon Capture Utilization and Storage) in Europe. This initiative is a key element of the European Commission's Green Deal, an ambitious plan outlined in the European ecological pact. CCUS is identified as one of the priority areas for achieving the overarching goals of a 55 % reduction in greenhouse gas emissions by 2030 and achieving carbon neutrality by 2050. The project, funded by EURAMET, addresses significant metrological challenges faced by industry stakeholders. It aims to develop primary standards, methodologies and best practice guidelines to ensure precise and reliable measurements essential to support CCUS projects. A critical aspect of this initiative lies in the preparation and use of primary gas mixtures, which plays a key role in environmental monitoring and decarbonization research. Reliable gas mixtures are essential for calibrating instruments that measure atmospheric pollutants and greenhouse gases, ensuring accuracy and consistency in data collection. Decarbonization itself refers to the process of significantly reducing carbon dioxide (CO_2) emissions resulting from human activities, with the goal of transitioning to a low-carbon or carbon-neutral economy. This transformation is a key strategy for mitigating climate change by directly reducing greenhouse gas concentrations in the atmosphere.

The MetCCUS project is a collaborative European initiative aimed at developing advanced metrological techniques to support the accurate measurement and monitoring of carbon dioxide (CO_2) emissions, as well as the processes of its capture, utilization, and storage. Launched on October 1, 2022, the project involves 21 partners and will run for a duration of 36 months. It responds to the growing need for reliable and precise data to ensure the effectiveness and safety of carbon management technologies, which are crucial in addressing climate change. The main objectives of the project include the development of accurate CO_2 measurement techniques, the improvement of calibration procedures and metrological standards, the support of carbon capture and storage (CCS) technologies, and the promotion of CO_2 utilization, particularly in chemical manufacturing and enhanced oil recovery. The project encompasses several key activities, such as research and development, field testing and validation, standardization and harmonization of methodologies, as well as stakeholder engagement and training initiatives. MetCCUS represents a significant advancement in the metrology of CO_2 measurement, with important implications for the performance and credibility of carbon capture, utilization, and storage technologies. By enhancing the accuracy and reliability of CO_2 measurements, the project contributes to the broader goal of reducing greenhouse gas emissions and combating climate change [1].

As part of the MetCCUS project, the Reference Gas Laboratory (LGR) at the Portuguese Institute for Quality (IPQ) is collaborating in the development of gas metrological capabilities. Specifically, the laboratory is preparing Certified Reference Materials (CRMs) to enable precise measurement of impurities in CO_2 with full metrological traceability [1-5]. These materials are vital for validating analytical methods and calibrating the instruments used in carbon capture and storage processes.

The production of the mixtures is done according to a primary method that is a highly accurate technique for preparing standard gas mixtures. It involves accurately measuring the mass of each gas component and combining them with well-defined ratios to achieve the target amount fraction. Ensuring accuracy and precision throughout the preparation process is essential, which requires meticulous calibration of the equipment and careful handling of the gases to minimize errors and ensure the reliability of the resulting standards. This method enables metrological traceability, which guarantees that measurements are consistent and comparable over time and across different locations. Such traceability is vital for maintaining accuracy in a wide range of scientific and industrial applications [3-5].

To date, the LGR has prepared eight gas mixtures. These include four bicomponent mixtures (two consisting of SO_2 in a CO_2 matrix and two of H_2S in a CO_2 matrix) and four multicomponent mixtures (two containing SO_2, CO, and O_2 in a CO_2 matrix, and two with H_2S, CO, CH_4, and O_2 in a CO_2 matrix). These mixtures were successfully characterized to measure four pollutant gases and oxygen in a CO_2 matrix under high pressure, approximately 40 bar. The analysis of these gas mixtures employs analytical techniques such as gas chromatography (GC), paramagnetic sensor, non-dispersive infrared (NDIR), and non-dispersive ultraviolet (NDUV) spectroscopy.

The certification of these mixtures required an extensive stability study. The stability of these mixtures was evaluated over one year using statistical methods. The Normalized Error (En) function, as specified by the ISO 13528 standard for statistical analysis, was employed to ensure accuracy and reliability in the results [6]. This rigorous approach underscores the project's commitment to providing industry and research sectors with robust and reliable metrological solutions.

2. Production of Reference Gas Mixtures

The standard ISO 17034 ensures that the gas mixtures produced are of high quality, reliable, and suitable for use in calibration and analytical applications [7]. The production of reference gas mixtures follows the requirements set out in this standard, which defines the criteria for the development of Certified Reference Materials (CRMs). The process includes comprehensive documentation, strict quality control procedures, and adherence to traceability principles aligned with the International System of Units (SI) [7-9].

Producers are required to validate their preparation methods, evaluate measurement uncertainties, and perform stability studies

to confirm the long-term reliability of the mixtures. By complying with ISO 17034, the CRMs produced are recognized as meeting internationally accepted standards, supporting consistency and comparability in calibration, testing, and measurement processes across different sectors and laboratories.

2.1. Preparation of Gas Mixtures

The process of preparation of gas mixtures involves the use of gravimetric methods, which rely on the accurate weighing of each component in accordance with ISO 6142-1 [10]. The procedure begins with the careful selection of an appropriate gas cylinder, which must be meticulously cleaned and evacuated to eliminate any potential contaminants. This step is critical to ensure the purity and integrity of the final mixture. The gravimetric approach allows for high accuracy in determining the composition of the mixture, contributing to its traceability and reliability as a reference material. The cylinder is then filled with the desired gas components, introduced sequentially, starting with the minor components (trace gases) and finishing with the balance gas, often nitrogen (N_2) or carbon dioxide (CO_2).

The mixture is prepared by gravimetric addition of each component. The mole fractions of the components in the final mixtures are calculated using the following equation [10]:

$$x_i = \frac{\sum_{A=1}^{P}\left(\frac{x_{i,A}\cdot m_A}{\sum_{i=1}^{n} x_{i,A}\cdot M_i}\right)}{\sum_{A=1}^{P}\left(\frac{m_A}{\sum_{i=1}^{n} x_{i,A}\cdot M_i}\right)} \quad (1)$$

Where: x_i is the mole fraction of the component i in the final mixture, $i = 1,\ldots, n$; P is the total number of the parent gases; n is the total number of the components in the final mixture; m_A is the mass of parent gas A determined by weighing, $A = 1,\ldots\ldots, P$; M_i is the molar mass of the component i; $x_{i,A}$ is the mole fraction of the component i.

Each gas is added using a high-precision mass comparator balance capable of measuring mass with a very low uncertainty. The mass of each component is calculated, considering the buoyancy effect of the surrounding air on the balance. Once all components are added, the total composition of the mixture is determined from the masses of the individual components and their respective molar masses.

The method described in the relevant section of ISO 6142 standard applies specifically to mixtures composed of gaseous or fully vaporized components, which can be introduced into the cylinder in either gaseous or liquid form. These mixtures may consist of either two components (binary mixtures) or multiple components (multicomponent mixtures).

The calculation of the associated uncertainty with the amount fraction of each component involves evaluating contributions from several key factors, namely the weighing of the source gases, the purity of the source gases, and the molar masses. Once the uncertainties related to these three categories have been assessed, they are combined to determine the overall uncertainty associated with the mole fraction, using the following expression:

$$u^2(x_i) = \sum_{i=1}^{n}\left(\frac{\partial x_i}{\partial M_i}\right)^2 \cdot u^2(M_i) + \sum_{A=1}^{p}\left(\frac{\partial x_i}{\partial m_A}\right)^2 \cdot u^2(m_A) + \sum_{A=1}^{p}\sum_{i=1}^{n}\left(\frac{\partial x_i}{\partial x_{iA}}\right)^2 \cdot u^2(x_{iA}) \quad (2)$$

where:
$u(M_i)$ - uncertainty in molar mass
$U(m_A)$ - uncertainty in weighing
$u(x_{iA})$ - uncertainty in purity analysis

To obtain the expanded uncertainty, the combined standard uncertainty is multiplied by a coverage factor k, which, for a *t-distribution* with v_{e_f} (effective degrees of freedom), corresponds to a coverage probability of approximately 95 %.

During the preparation of gas mixtures, aluminium cylinders with a special internal coating are used to minimize the adsorption of mixture components onto the inner walls, thereby preserving the integrity and stability of the gas composition.

Following the selection of the cylinder, a rigorous cleaning procedure is carried out to eliminate any potential residues that could affect the composition and, consequently, the uncertainty of the final gas mixture. This step is especially critical when preparing mixtures with very low concentration levels.

Another essential stage in the filling process involves the transfer of each component gas from its respective parent cylinder to the target cylinder where the mixture is being prepared. The addition of each gas is performed at a dedicated filling station, which is equipped with electropolished tubing, high-purity valves, vacuum and pressure gauges, and oil-free turbomolecular vacuum pumps (Figure 1).

Figure 1: Filling Station

The precise mass of each gas component introduced into the cylinder is determined using a mass comparator, with reference to calibrated weights that are traceable to the national standard. Traceability of gas measurements to the International System of Units (SI) is ensured through the use of calibrated and verified

instrumentation. By combining the results from the purity certificates of the source gases with the data obtained from the weighing process, the exact composition of the gas mixture can be calculated, along with the associated uncertainties related to the amount fractions of each component (Figure 2).

Figure 2: Mass Comparator Balance

After preparation, the mixture undergoes a homogenization process (Figure 3), which typically involves rotating the cylinder to ensure uniform distribution of gases within the cylinder.

Figure 3: Rolling Cylinder System

2.2. Certification of Gas Mixtures

The prepared gas mixture is calibrated with others gas standards, by a suitable analytical method, to confirm its composition and validate the gravimetric calculations. The multi-point calibration method [11, 12] involves measuring the response of an analytical instrument against a series of calibration gas mixtures with precisely known compositions, known as reference standards, according to the international standard ISO 6143 [11]. The purpose is to create a dependable correlation between the instrument's signal and the concentrations of the target gases in the sample. This ensures accurate, consistent, and traceable measurements during gas analysis.

The process begins by selecting reference gas mixtures that cover the range of concentrations expected in the sample. These reference standards must be traceable to SI and prepared with high accuracy, often using gravimetric methods according to ISO 6142-1 [10]. The instrument response to each reference mixture is recorded, typically using signals such as peak areas or voltages, depending on the type of analyzer is used. The specific analytical methods used were GC, paramagnetic sensor, NDIR, and NDUV.

A mathematical model, such as a linear or polynomial regression, is then applied to describe the relationship between the instrument response and the concentration of the analyte. ISO 6143 [11, 12] emphasizes the evaluation of uncertainties for both the reference mixtures and the instrument response, ensuring the calibration curve is accurate and reliable.

Finally, the established calibration curve is used to determine the composition of unknown gas mixtures by measuring their instrument response and interpolating within the range of the calibration standards.

The certification process is carried out using an automated multichannel sampling system, to which all the cylinders scheduled for analysis are connected (Figure 4).

Figure 4: Certification of Gas Mixtures Facility

During the analysis, the system automatically selects each cylinder, allowing the individual flow of gas through the analyzer. The entire sampling and measurement process is managed by the custom-developed *IPQAnaliseQui* software, which controls the system operation and records all measurement data obtained by the analyzer. All collected data, including standard and sample analysis records, are subsequently compiled into a spreadsheet. The final results are corrected using zero readings and pressure data.

The determination of the calibration function is performed using *XGENLINE*, a software tool developed by the National Physical Laboratory (NPL). This software identifies the most appropriate low-degree polynomial calibration function (first-, second-, third-, or fourth-order) for a given set of measurement data (*X, Y*), taking into account the associated uncertainties. In this case, *XGENLINE* identified a first-order polynomial as the most suitable calibration function for each calibration performed.

The resulting calibration function is then used to calculate the estimated amount fraction values of the analyzed samples, along with their associated uncertainties. *XGENLINE*, which complies with the ISO 6143 standard, handles the propagation of uncertainty and provides a standard uncertainty value for each analytical result.

The final results are presented together with their respective uncertainties in accordance with the Guide to the Expression of

Uncertainty in Measurement [13].

Traceable gas mixtures are widely used for applications requiring high precision such as equipment calibration, environmental monitoring, and industrial quality control.

The quality control of these measurements is enhanced through active participation in projects and international comparisons [14-19]. Furthermore, recognition and inclusion in the Bureau International des Poids et Measures (BIPM) database of Calibration and Measurement Capabilities (CMC) strengthens the commitment to quality [9].

3. Stability Study

Gas mixtures are often used in calibration and analytical processes where accuracy is critical. The stability study of the eight bi-component and multi-component gas mixtures conducted over approximately one year were essential to ensure the accuracy and reliability of these reference materials over time. A one-year study allows for the assessment of potential chemical interactions, adsorption effects, or decomposition within the cylinders. This helps determine shelf-life, proper storage conditions, and suitability for long-term use. Stability data supports the certification of gas standards, ensuring traceability to international references. It also minimizes measurement uncertainty in critical applications such as environmental monitoring, industrial safety, and laboratory analysis. Detecting any instability early avoids risks in operational settings. Overall, the study confirms the integrity and usability of the mixtures throughout their intended lifespan.

The analyzed parameters included H_2S, CO, O_2, CH_4, and SO_2 in a CO_2 matrix. This research aimed to assess the chemical interactions and long-term stability of these gas combinations. Understanding their behavior is crucial for industrial applications, storage, and transportation safety.

This study was conducted using Primary Reference Material (PRM) of several multicomponent mixtures (Table 1, Table 2, Table 3, Table 4, Table 5). All these reference gas mixtures were prepared in carbon dioxide matrix. The calibration curves were done using primary standards in nitrogen matrix. With these primary standards we can have traceability to the standards of these impurities in CO_2. In this case, the matrix will not influence the analysis because the analyzers in question do not detect CO_2 just as they do not detect nitrogen. Each of them detects only the respective gas.

The purpose is to determine the shelf life of this type of mixtures, that is, the actual period during which a mixture can be considered stable concerning its original metrological specifications.

The study was conducted according to ISO 13528 standard [6], which provides various statistical evaluation methods that can be used in specific tests or measurements and for monitoring the ongoing performance of laboratories. In this context, it will be used to compare two concentrations: the concentration resulting from the initial certification and the concentration obtained in subsequent certifications according to the international standard ISO 6143 [11], over the lifetime of the standard.

In this study, we used the normalized error (E_n) statistical tool that is typically applied in comparison of measurement systems, calculated according to the following equation:

$$\boldsymbol{E_n} = \frac{x_{\mathrm{cer1}} - x_{\mathrm{cern}}}{\sqrt{U_{\mathrm{cer1}}{}^2 + U_{cern}{}^2}} \quad (3)$$

Where x_{Cer1} is the concentration value from the first certification and x_{Cern} is the concentration value resulting from the n^{th} certification. U_{Cer1} represents the uncertainty associated with x_{Cer1} while U_{Cern} is the expanded uncertainty associated with x_{Cern}. With this statistical tool, the results are considered satisfactory if $|E_n| \leq 1$ and unsatisfactory if $|E_n| > 1$.

4. Results

The objective of this preparation was to enable a comprehensive characterization of these gas mixtures, supporting their use as accurate reference materials in analytical applications. Four binary gas mixtures, classified as Primary Reference Materials (PRM), were meticulously prepared for analysis. Among them, two were binary combinations of hydrogen sulfide (H_2S) in a carbon dioxide (CO_2) matrix, designated as PRM108595 and PRM108596. Additionally, two mixtures of sulfur dioxide (SO_2) in CO_2 were prepared, identified as PRM408326 and PRM108593. Each of these four mixtures was stored in individual cylinders, maintained at an approximate pressure of 40 bar, allowing for proper containment and stability during the study [20].

Furthermore, four multicomponent mixtures were prepared in a CO_2 matrix, PRM608395 and PRM308978 with the impurities SO_2, CO and O_2; and two, PRM202557 and PRM302530, with the impurities H_2S, CO, O_2, and CH_4. These mixtures were contained within four cylinders at an approximate pressure of 40 bar each. No stability study was conducted on PRM308978 because this cylinder was sent for analysis to one of the participants of the MetCCUS project.

Each of these multicomponent mixtures was stored in individual cylinders, also at approximately 40 *bar*. Nevertheless, it is important to note that no stability study was carried out for PRM308978, as this specific cylinder was sent to a participant laboratory, Research Institutes of Sweden (RISE) from Sweden, involved in the MetCCUS project for immediate analysis in March 2024. The remaining seven gas mixtures were retained for long-term monitoring and characterization. However, two of them, PRM408326 and PRM202557, were requested for analysis by two participants of the project, Technical University of Denmark (DTU) and Danish National Metrology Institute (DFM) from Denmark, in March 2025.

PRM10859	H_2S/CO_2		
Date	***x*** µmol/mol	***U*** µmol/mol	E_n
2023-09-11	9,64	0,47	-
2024-04-23	10,22	0,42	0,92
2024-11-08	10,02	0,34	0,66
PRM10859	H_2S/CO_2		
Date	***x*** µmol/mol	***U*** µmol/mol	E_n
2023-09-11	9,97	0,48	-
2024-04-23	9,87	0,35	-0,17
2024-11-08	9,61	0,29	-0,64

Table 1: Results of the Stability Study for the Prepared Binary Mixtures of H_2S/CO_2

PRM408326	SO_2/CO_2		
Date	***x*** µmol/mol	***U*** µmol/mol	E_n
2023-09-04	19,52	0,51	-
2024-04-18	20,16	0,57	0,84
2024-11-18	19,9	1,1	0,31
PRM108593	SO_2/CO_2		
Date	***x*** µmol/mol	***U*** µmol/mol	E_n
2023-09-04	20,71	0,50	-
2024-04-18	20,71	0,58	0,00
2024-11-18	20,5	1,0	-0,19

Table 2: Results of the Stability Study for the Prepared Binary Mixtures of SO_2/CO_2

PRM60839	SO_2+CO+O_2 / CO_2		
	SO_2		
Date	***x*** µmol/mol	***U*** µmol/mol	E_n
2024-04-18	14,24	0,77	-
2024-11-18	14,1	1,3	-0,09
	CO		
Date	***x*** µmol/mol	***U*** µmol/mol	E_n
2024-04-17	660,7	1,6	-
2024-11-22	653,5	1,6	-3,2
	O_2		

Date	x cmol/mol	U cmol/mol	E_n
2024-04-16	0,568	0,048	-
2025-01-23	0,572	0,017	0,08

Table 3: Results of the Stability Study for the Prepared Multicomponent Mixture of SO_2 + CO + O_2 / CO_2

PRM20255	**H_2S+CO+O_2+CH_4 / CO_2**		
	H_2S		
Date	***x*** **µmol/mol**	***U*** **µmol/mol**	E_n
2023-09-20	9,83	0,48	-
2024-04-23	9,73	0,33	-0,17
2024-11-08	9,61	0,28	-0,40
	CO		
Date	***x*** **µmol/mol**	***U*** **µmol/mol**	E_n
2023-09-15	669,5	2,7	-
2024-04-17	662,3	1,6	-2,3
2024-11-22	654,4	1,6	-4,8
	O_2		
Date	***x*** **cmol/mol**	***U*** **cmol/mol**	E_n
2023-09-15	0,586	0,027	-
2024-04-16	0,582	0,048	-0,07
2025-01-23	0,586	0,017	0,00
	CH_4		
Date	***x*** **cmol/mol**	***U*** **cmol/mol**	E_n
2023-09-14	1,9685	0,0060	-
2024-04-17	1,9686	0,0061	0,01
2024-11-28	1,9706	0,0062	0,24

Table 4: Results of the Stability Study for the Prepared Multicomponent Mixture of H_2S +CO+O_2+CH_4 / CO_2

PRM30253	**H_2S+CO+O_2+CH_4 / CO_2**		
	H_2S		
Date	***x*** **µmol/mol**	***U*** **µmol/mol**	E_n
2023-12-04	9,92	0,40	-
2024-04-23	9,60	0,36	-0,59
2024-11-08	9,16	0,33	-1,5
	CO		
Date	***x*** **µmol/mol**	***U*** **µmol/mol**	E_n
2023-12-14	677,0	1,8	-
2024-04-17	674,3	1,5	-1,1
2024-11-22	666,5	1,6	-4,3
	O_2		

Date	x cmol/mol	U cmol/mol	E_n
2023-12-18	0,602	0,051	-
2024-04-16	0,591	0,058	-0,14
2025-01-23	0,585	0,017	-0,32
	CH_4		
Date	x cmol/mol	U cmol/mol	E_n
2023-12-05	1,915	0,015	-
2024-04-17	1,9270	0,0059	0,74
2024-11-28	1,9284	0,0060	0,83

Table 5: Results of the Stability Study for the Prepared Multicomponent Mixture of H_2S +CO+O_2+CH_4 / CO_2

5. Summary

As part of the MetCCUS project, LGR plays a key role in the preparation of Certified Reference Materials (CRM) designed to support stability studies of CO_2-based gas mixtures with full metrological traceability. This work supports the calibration and validation of analytical instruments used in carbon capture processes, ensuring accurate and reliable measurements. By developing traceable and stable reference mixtures, LGR helps enhance the quality and comparability of data across laboratories and monitoring systems involved in CO_2 capture, transport, and storage.

In conclusion, IPQ has demonstrated its ability to prepare and certify reference materials (CRM) for measuring impurities of H_2S, SO_2, CO, O_2 and CH_4 in CO_2, within the requested concentration with metrological traceability. The uncertainties obtained were as expected.

The stability study has confirmed that, except for CO, all components remain stable for about one year within the associated uncertainties. To further refine our understanding, a longer study will be conducted to determine the stability period of each type of mixture.

This work is being carried out in collaboration with project partners, involving a joint study in which some of the prepared multicomponent mixtures were sent to participating laboratories (RISE, DTU, DFM) for analysis. The results obtained by the different laboratories will be compared to assess consistency and reliability on measurement. Based on this comparative analysis, conclusions will be drawn regarding the performance and stability of the mixtures, and the findings will be published as part of the project's outcomes.

Looking ahead, this research may be extended to mixtures containing additional components. Additionally, to enhance the scope of the project, these mixtures will be analyzed using alternative analytical methods to gather more data for further characterization of the mixtures.

These standard multicomponent gas mixtures are essential tools for calibrating the analyzers used to measure the purity of carbon dioxide throughout the entire carbon capture and storage (CCS) process. This includes the stages of CO_2 capture, compression, transport, and final storage, as well as its application in industrial processes. Accurate monitoring of CO_2 purity is critical to ensure the safety, efficiency, and compliance of CCS operations with environmental and technical standards.

The use of these reference mixtures allows for more reliable and comparable measurements across different laboratories and facilities. By providing metrological traceability, they help reduce uncertainties and improve the overall quality of the analytical results. Furthermore, the implementation of such standards supports harmonization at the international level, promoting confidence in data reporting and regulatory verification. Ultimately, these mixtures contribute to the advancement of carbon management technologies and to the effectiveness of climate mitigation strategies.

Acknowledgment

This project (21GRD06 MetCCUS) has received funding from the EPM program co-financed by the Participating States and from the European Union's Horizon 2020 research and innovation program.

This article is a revised and expanded version of a conference oral presentation “Stability Study of Multicomponent Mixtures to Support Carbon Metrology”, which was presented at CIM2025, Lyon, 11-14 March 2025.

Conflicts of Interest

Declare conflicts of interest or state “The authors declare no conflicts of interest.”

References

1. MetCCUS Project. (2025).
2. Dias, F. A., Palma, C., & Costa, C. J. (2025). Preparation of multicomponent mixtures to support carbon metrology. *Measurement, 239*, 115453.
3. Amico di Meane, E., Plassa, M., Rolle, F., & Sega, M. (2009). Metrological traceability in gas analysis at IN Ri. M: gravimetric primary gas mixtures. *Accreditation and quality*

assurance, 14(11), 607-611.
4. Milton, M. J. T., Guenther, F., Miller, W. R., & Brown, A. S. (2006). Validation of the gravimetric values and uncertainties of independently prepared primary standard gas mixtures. *Metrologia, 43*(3), L7.
5. Milton, M. J. T., Vargha, G. M., & Brown, A. S. (2011). Gravimetric methods for the preparation of standard gas mixtures. *Metrologia, 48*(5), R1.
6. ISO, I. (2005). ISO 13528: 2005. Statistical methods for use in proficiency testing by interlaboratory comparisons.
7. ISO. (2016). General requirements for the competence of reference material producers.
8. ISO. (2017). General requirements for the competence of testing and calibration laboratories.
9. KCDB. (2025).
10. ISO. (2015). Gas analysis Preparation of calibration gas mixtures Part 1: Gravimetric method for Class I mixtures. 6142-1:
11. ISO. (2001). Gas analysis. Comparison methods for determining and checking the composition of calibration gas mixtures. 6143.
12. Guenther, F. R., & Possolo, A. (2011). Calibration and uncertainty assessment for certified reference gas mixtures. *Analytical and bioanalytical chemistry, 399*(1), 489-500.
13. Evaluation of measurement data. (2008). Guide to the expression of uncertainty in measurement JCGM 100:(GUM 1995 with minor corrections).
14. Kim, D., Kim, Y., Lee, S., Kang, J., Smeulders, D., Wu, H., & Murugan, A. (2021). International comparison CCQM-K41. 2017, hydrogen sulfide in nitrogen. *Metrologia, 58*(1A), 08010.
15. Van der Hout, J. W., van der Veen, A. M., Ziel, P. R., Kipphardt, H., Tuma, D., Maiwald, M., & Engin, E. (2017). International comparison Euramet. QM-K111—propane in nitrogen. *Metrologia, 54*(1A), 08020.
16. Dias, F. A. (2013). Final report on international comparison EURO.QM-S5/1166: Carbon dioxide mixtures in nitrogen, Metrologia. 50 1A 08017.
17. Guenther, F. R. (2011). International comparison CCQM-K76: Sulphur dioxide in nitrogen, Metrologia, 48, Tech. Suppl. 08015.
18. Botha, A. (2010). International comparison CCQM-K51: Carbon monoxide (CO) in nitrogen (5 µmol mol–1), Metrologia, 47, Tech. Suppl. 08008.
19. Nieuwenkamp, G. (2010). Final report on international comparison CCQM-K71: Measurement of stack gas, Metrologia, 47 Tech. Suppl. 08021.
20. Dias, F. A., Palma, C., Costa, C. J. (2025). "Stability Study of Multicomponent Mixtures to Support Carbon Metrology". CIM 2025, Lyon, France, 11-14 March.

Journal of Radiation Research and Applied Sciences 19 (2026) 102159

Contents lists available at ScienceDirect

Journal of Radiation Research and Applied Sciences

journal homepage: www.journals.elsevier.com/journal-of-radiation-research-and-applied-sciences

Performance assessment of commonly used active radiation protection dosimeters for individual and area workplace monitoring

Jelena Vlahović [a,b,*], Nikola Kržanović [b], Miloš Živanović [b], Ivana Stojanović [b,c], Luka Bakrač [d], Argiro Boziari [e], Miloš Đaletić [b], Ana Fernandes [f], Liviu-Cristian Mihailescu [g], Erinc Reyhanoglu [h], Siarhei Saroka [i], Teemu Siiskonen [j], Jana Šmoldasová [k], Vladimir Sochor [k], Maria do Ceu Ferreira [l], Nataša Todorović [a]

[a] Department of Physics, Faculty of Sciences, University of Novi Sad, Novi Sad, Serbia
[b] Department of Radiation and Environmental Protection, Vinča Institute of Nuclear Sciences, National Institute of the Republic of Serbia, University of Belgrade, Belgrade, Serbia
[c] Faculty of Physical Chemistry, University of Belgrade, Belgrade, Serbia
[d] Ruđer Bošković Institute, Zagreb, Croatia
[e] Elliniki Epitropi Atomikis Energeias, Athens, Greece
[f] Instituto Superior Técnico, Lisbon, Portugal
[g] SCK CEN Belgian Nuclear Research Centre, Boeretang 200, B-2400, Mol, Belgium
[h] Türkiye Enerji, Nükleer ve Maden Araştırma Kurumu, Ankara, Turkey
[i] Institutul Național de Metrologie, Chisinau, the Republic of Moldova
[j] Radiation and Nuclear Safety Authority, Vantaa, Finland
[k] Cesky Metrologicky Institut, Brno, Czech Republic
[l] Portuguese Institute for Quality Services (Instituto Portugues de Qualidade - IPQ), Lusofona University RCM2+ Asset Management and Systems Engineering Research Centre, Lisbon, Portugal

ARTICLE INFO

Keywords:
Active area dosimeters
Active personal dosimeters
Dosimeter performance
Individual monitoring
Workplace monitoring

ABSTRACT

Background: Improvement in radiation protection practice may be achieved by acquisition of reliable and accurate dosimetry data. Use of dosimeters with known properties provides insight into their performance in real radiation fields encountered in radiation monitoring practice.
Aim: Performance evaluation in a wide range of radiation conditions provides insight into dosimeter behaviour, providing input for revision, update and harmonization of IEC type testing standards.
Methods: A total of 32 active dosimeters were investigated, of which 26 are used for area workplace, and 6 for individual monitoring. Dosimeter performance was evaluated against the IEC 60846–1:2009 standard for portable workplace and environmental meters and monitors and the IEC 61526:2024 standard for active personal dosimeters in a wide range of photon energies, angles of incidence and dose equivalent rates. Performance was examined beyond the minimum rated range: 33.3 keV–1.25 MeV photon energy; (0°; ±75°) angle of incidence for personal dosimeters and (0°; ±120° with 180°) for area dosimeters; 3 μSv h^{-1} – 7 Sv h^{-1} dose rate range. In addition, dosimeter short-term stability and overload properties were investigated.
Results: State-of-the-art and commonly used dosimeters complied with the standard defined limits of variation with respect to the manufacturer stated specifications. Some dosimeters had significantly lower variations in terms of relative response than the current standard stated requirements.
Conclusion: Potential update of the relevant IEC type testing standards was considered, with the possibility of introducing two distinct dosimeter classes, one of which would comply with reduced limits of variation.

* Corresponding author. Department of Radiation and Environmental Protection, Vinča Institute of Nuclear Sciences, National Institute of the Republic of Serbia, University of Belgrade, P.O. Box 522, 11000, Belgrade, Serbia.
E-mail address: jelena.vlahovic@vin.bg.ac.rs (J. Vlahović).

https://doi.org/10.1016/j.jrras.2026.102159
Received 30 October 2025; Received in revised form 30 December 2025; Accepted 1 January 2026
Available online 7 January 2026

1. Introduction

Radiation protection of exposed workers and the general public is regulated by various national acts, decrees and additional regulations with respect to the established exposure limits which are internationally recognized. In practice, this is achieved through individual and area monitoring programs (IAEA, 2018; Vanhavere & Van Hoey, 2022). Accurate and reliable dosimetry data can be acquired by using dosimeters which comply with relevant international standards (Calvacante et al., 2025; Yasar et al., 2017).

According to European regulations (Euratom, 2013), individual monitoring is mandatory for category A radiation workers, whereas individual monitoring is optional in the case of category B radiation workers. However, sufficient measurements need to be performed to adequately classify exposed workers. Monitoring is realized either through individual monitoring of exposed workers or through workplace area monitoring. In most countries, legal dosimetry data is obtained by passive dosimetry systems for both area and individual monitoring applications, which are commonly based on thermoluminescent dosimeters (TLDs) or optically stimulated luminescence dosimeters (OSLDs) (Stanković Petrović et al., 2021; Vanhavere & Van Hoey, 2022). Some countries require the use of active personal dosimeters (abbreviated as PDs) in addition to passive ones, in certain exposure scenarios, where the dose rate is sufficiently high, surpassing the established national threshold (Abuelhia & Alghamdi, 2020; Ciraj-Bjelac et al., 2018; O'Connor et al., 2021; Ramadhan et al., 2024).

PDs are usually based on semiconductor Si-diode detectors or Geiger-Müller (G-M) detectors. Their main advantage is the possibility of real-time dose indication, accompanied with audio and/or visual signal if a certain threshold is surpassed, as well as the measurement of doses below the detection limit of most passive dosimeters (Pavelić et al., 2019). Existing research has highlighted that PDs exhibit unreliable performance in low-energy and/or pulsed radiation fields (Ankerhold et al., 2009; Cui et al., 2024; Hupe et al., 2019; Kržanović et al., 2017; Li et al., 2025; Yasar et al., 2017). These irradiation conditions are encountered in medical applications of X-rays, particularly in interventional radiology procedures. Taking these findings into consideration, further testing under such conditions would provide more insight into the state-of-the-art dosimeter performance, optimizing the radiation protection of exposed workers.

Area monitoring can be categorized into workplace monitoring, which is used for evaluation of the effective doses to exposed workers, and environmental monitoring, essential for monitoring of background radiation and possible variations due to the release of artificial man-made radiation sources in the environment. Active area dosimeters (abbreviated as ADs) commonly utilize detectors based on G-M tubes. Additionally, semiconductor detectors, pressurized ionization chambers and scintillation detectors are often encountered in workplace monitoring practice (Alomairy, 2023; Pavelić et al., 2019). Workplace monitoring covers a wide range of applications and photon energies, spanning from low-energy medical applications to high-energy nuclear technology applications. Besides focusing on different workplace monitoring exposure scenarios, the relevant type testing standards also pertain to installed/mounted equipment and portable monitoring devices. Previously conducted research evaluated the performance of several commonly used ADs for workplace monitoring, showcasing strong energy dependence at low photon energies for some of the G-M tube-based devices, highlighting their inadequate energy compensation (Ćeklić et al., 2014). In the case of environmental area monitoring G-M tubes are commonly used in non-governmental radiation monitoring networks, including detectors with different geometries and volumes, measurement ranges, sensitivity, and different radiation-based characteristics. Even though these devices may comply with the relevant standard in the minimum rated range, they displayed significant over-response when exposed to low-energy radiation fields (Morosh et al., 2021).

There are several IEC standards which provide requirements for different types or uses of radiation protection dosimeters, such as IEC 60846–1:2009 (IEC, 2009) for workplace area dosimeters and IEC 61526:2024 (IEC, 2024) for personal dosimeters. This research is part of a larger effort to propose updates and harmonization of IEC standards for type testing of radiation protection dosimeters, initiated already in the 17RPT01 DOSEtrace project (Kržanović et al., 2022). The effort of IEC standard update and harmonization is pursued by 22NRM07 GuideRadPROS project (GuideRadPROS, 2025) and European Metrology Network for radiation protection (Alves et al., 2024). Data necessary for the update of standards include overview of the existing standards, collection of existing calibration and type testing data, data on dosimeter use, overview of the current state-of-the-art and upcoming technologies.

In order to test the dosimeter performance against the IEC requirements, 32 active dosimeters have been examined in this work. A measurement protocol was derived and implemented in the Secondary Standard Dosimetry Laboratories (SSDL) participating in the project. The protocol was drafted to collect missing data on dosimeter performance, following the survey of existing papers on dosimeter testing (Kržanović et al., 2019; Morosh et al., 2021; Ćeklić et al., 2014; Đaletić et al., 2025) and the historical calibration data of the 22NRM07 GuideRadPROS participants. Performance of ADs and PDs was evaluated against the requirements defined in IEC 60846–1:2009 (IEC, 2009) and IEC 61526:2024 (IEC, 2024) standards, respectively.

Following the IEC type testing methodology, the influence quantity minimum rated ranges, as well as the performance requirements in terms of variation in dosimeter response, this research aimed to investigate the performance of selected active radiation protection dosimeters in an expanded test range covering various ionizing radiation practices. Testing beyond manufacturer stated ranges would provide the knowledge on their usability in specific scenarios (such as low-energy radiation fields characteristic for diagnostic and interventional radiology applications, or the use of area workplace dosimeters for environmental monitoring applications). Additionally, performance characteristics could provide input in future revisions of the IEC standards by re-evaluation of the current performance requirements, the influence quantity test ranges and/or by exploring the prospect of introducing two distinct dosimeter classes.

2. Materials and Methods

2.1. Secondary Standard Dosimetry Laboratories

Several SSDLs participated in the data collection using the developed measurement protocol presented below in section 2.4. The SSDLs which took part in this study include the Vinča Institute of Nuclear Sciences (*VINS*), the Turkish Energy, Nuclear and Mineral Research Agency (*TENMAK*), Czech Metrology Institute (*CMI*), Institute Ruđer Bošković (*IRB*), Greek Atomic Energy Commission (*EEAE*), National Institute of Metrology (*INM*) and the Belgian Nuclear Research Centre (*SCK CEN*). All SSDLs have established Quality Management Systems according to ISO/IEC 17025:2017 (ISO/IEC, 2017) and have their calibration and measurement capabilities published in the key comparison database of BIPM (BIPM, 2025).

All of the SSDLs have established traceability to the primary standards

in terms of air kerma, while the secondary standard reference values are determined either in terms of the operational dosimetry quantity directly (i.e., by employing the secondary standard for $H_p(10)$ or $H^*(10)$), or in terms of air kerma, where conversion coefficients from air kerma to the operational dosimetry quantity are used to determine the reference value of the operational quantity. These conversion coefficients depend on the photon energy and angle of incidence (ISO, 2019c).

All the SSDLs employ reference radiation fields which are established according to the requirements of ISO 4037–1:2019, including radionuclide-based radiation fields (Cs-137 and Co-60, abbreviated as S-Cs and S-Co) and N-series radiation qualities (narrow-spectrum X-ray radiation fields) (ISO, 2019a). Dosimeter testing was performed using either the substitution method, the known radiation field method or the substitution method with the use of the monitoring ionization chamber (IAEA, 2000). A schematic of the setup is presented in Fig. 1.

2.2. Active radiation protection dosimeters

The investigated dosimeters were selected to collect additional data needed for the update of the relevant IEC standards (IEC, 2009; IEC, 2024). The dosimeters are commercially available models, including both new models, which reflect the current state-of-the-art, as well as older models which are still in use. In this research the performance of 26 ADs and 6 PDs was evaluated. The manufacturer specifications of ADs and PDs are listed in Tables 1 and 2, respectively.

Most ADs utilize detectors based on G-M tubes, whereas a small portion uses a high-pressure ionization chamber, organic/plastic scintillator or a semiconductor detector. Additionally, most dosimeters, as stated by the manufacturers, are suitable for measurement of low-dose rates starting from the background radiation level (e.g., 10 nSv h^{-1}), and cover a broad energy range (Table 1).

Evaluated PDs utilize G-M tube-based detectors, except for one semiconductor-based dosimeter. They operate in a wide range of dose rates, up to 3 Sv h^{-1}, in a broad energy range, with mean photon energies going from 10 keV to 20 MeV (Table 2).

2.3. Dosimeter response and influence quantities

Influence quantities are defined as quantities which are not the subject of the measurement, but can affect the measurement result. The effects of these quantities are evaluated during specialized performance tests within the rated ranges of the influence quantities for which the dosimeter is designed to be used. The influence quantities can have a multiplicative or additive effect on the measurand, and they are categorized as type F and type S, respectively. The IEC standards define the minimum rated ranges for the influence quantities for which the dosimeter performance should be in line with the standard requirements, usually defined as limits of variation in terms of relative response (type F) or deviation (type S). The most important radiation-based influence quantities (photon energy, angle of incidence and non-linearity) are classified as type F influence quantities (IEC, 2009; IEC, 2024).

The response of an active dosimeter, R, is defined as the quotient of the measured value and the reference (conventional true) value of the operational dosimetry quantity, obtained with a reference class standard instrument:

$$R = \frac{M}{H_r} \tag{1}$$

where M is the mean measured value, and H_r is the reference value under specific irradiation conditions.

Relative response, r, is defined as the dosimeter response normalized to the dosimeter (reference) response, which is determined under reference conditions:

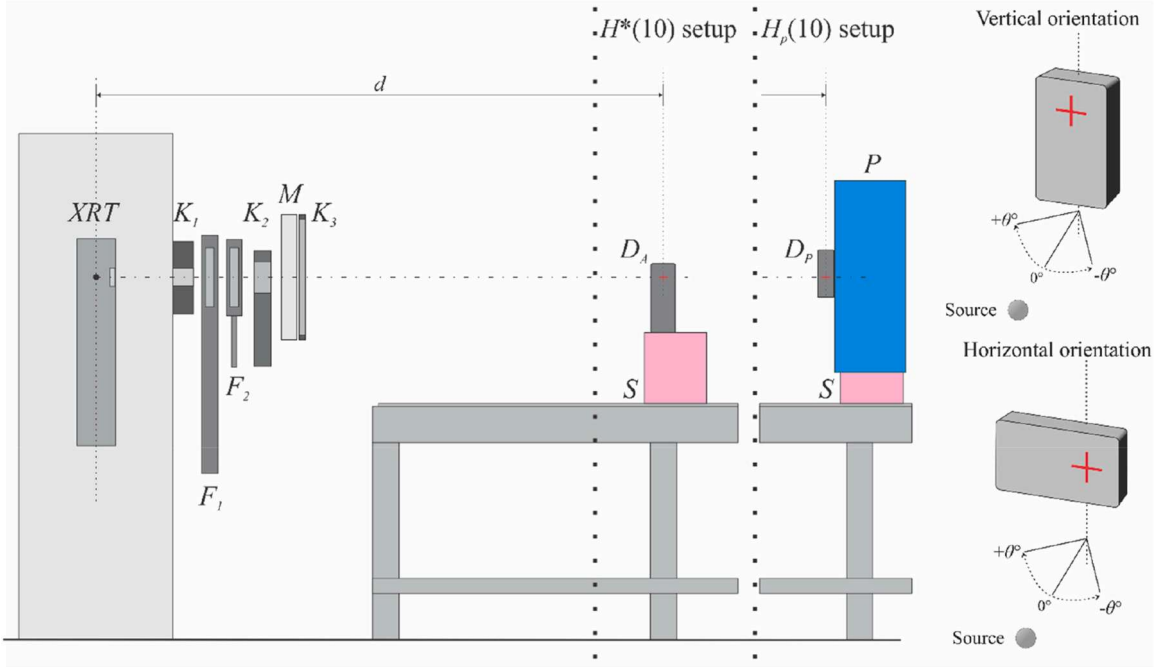

Fig. 1. Schematic representation of the experimental setup. (left): XRT - X-ray tube; K1, K2 and K3 - apertures; F1 and F2 - additional filtration; M - monitor ionization chamber; d - source-to-detector distance; P – ISO slab phantom (used with PDs); S – positioning support (low Z material); D_A – AD; D_P – PD. (right): Dosimeter orientation and rotation for the angular dependence test.

Table 1
Manufacturer specifications of tested ADs in terms of detector type, dose rate and photon energy measurement range.

Manufacturer and Model	Detector type	Dose rate measurement range		Photon energy range		AD No. (DL)	Symbol
		Min [μSv h^{-1}]	Max [mSv h^{-1}]	Min [keV]	Max [MeV]		
Atomtex AT6130	G-M tube	0.1	10	20	3	AD1	●
Atomtex AT1123	Plastic scintillator	0.05	10 000	15	10	AD2	●
						AD3	●
Automess 6150 AD3	G-M tube	1	1000	45	3	AD4	▲
						AD5	▲
Automess 6150 AD6/H	G-M tube	0.1	10	60	1.3	AD6	▲
Canberra Radiagem 2000	G-M tube	0.3	100	40	1.5	AD7	★
						AD8	★
						AD9	★
						AD10	★
						AD11	★
Fluke 451P	High Pressure Ionization chamber	0	50	25	1.25	AD12	■
Ludlum 9DP	High Pressure Ionization chamber	0	50	60	1.25	AD13	▼
Polimaster PM1401K-3P	CsI(Tl), G-M tube	0.1	100	15	15	AD14	▶
Raysafe 452	G-M tube	0	0.02	20	1	AD15	◀
	Si – diode	20	1000	20	5	AD16	◀
						AD17	◀
Mirion RDS-30	G-M tube	0.01	100	48	3	AD18	◆
Mirion RDS-200	G-M tube	0.01	10 000	50	3	AD19	◆
Thermo Fisher RadEye B20 ER	G-M tube	0.2	100	17	3	AD20	⬟
						AD21	⬟
Thermo Fisher FH40G-L10	Proportional counter	0.01	100	30	4.4	AD22	⬢
						AD23	⬢
						AD24	⬢

(*continued on next page*)

Table 1 (*continued*)

Manufacturer and Model	Detector type	Dose rate measurement range		Photon energy range		AD No. (DL)	Symbol
		Min [μSv h^{-1}]	Max [mSv h^{-1}]	Min [keV]	Max [MeV]		
VINS DMRZ-M15	G-M tube	0.1	1	59	1.3	AD25 AD26	◧ ◧

$$r = \frac{R}{R_0} \tag{2}$$

Reference conditions are defined by the type testing standards for each of the influence quantities (IEC, 2009; IEC, 2024). During the performance tests all the influence quantities which are not the subject of a certain test should be within their respective reference conditions.

The multiplicative correction factors, which are derived from the beforementioned radiation-based influence quantity tests, can be directly used to correct the indicated value and obtain the measured value with reduced measurement uncertainty. The measured value can be represented with the following model equation:

$$M = N_H \cdot \frac{I - \sum_{i=1}^{n} D_i}{\prod_{j=1}^{m} r_j} \tag{3}$$

where M represents the corrected measured value, I the indicated value, N_H the calibration coefficient (derived under reference or standard test conditions), while D_i and r_j represent the additive (type S) and multiplicative (type F) corrections, respectively (IEC, 2009; IEC, 2024).

2.4. Measurement protocol

Based on dosimeter manufacturer specifications, analysis of historical calibration data and the previous research on radiation protection dosimeter performance and applications, the measurement protocol was developed to test the effects of radiation-based influence quantities. The focus of the protocol was on dosimeter response energy dependence, angular dependence and non-linearity, as well as overload and stability. The protocol was designed in a way to collect data in a wide range of influence quantity values, in order to assess dosimeter performance even outside their respective manufacturer-stated specifications. Data collection in standardized reference conditions can provide insight into their performance in real workplace poly-energetic and multidirectional radiation fields. The dosimeter performance was evaluated against the limits of variation defined in the respective IEC standards for testing of ADs and PDs (IEC, 2009; IEC, 2024).

2.4.1. Variation in dosimeter response due to photon energy

Photon energy is one of the most important radiation-based influence quantities, and variation in dosimeter response due to its effect could produce unreliable and erroneous data. The performance of ADs and PDs was investigated in a wider energy range than the minimum rated range stated in relevant standards (IEC, 2009; IEC, 2024), as well as the manufacturer stated measurement range. The minimum rated range stated by the standards (IEC, 2009; IEC, 2024), for both operational quantities ($H^*(10)$ and $H_p(10)$), covers mean photon energies from 80 keV to 1.25 MeV, which corresponds to general industrial applications of ionizing radiation. The expanded photon energy range used in this test covered mean photon energies from 33.3 keV to 1.25 MeV, including low-energy applications such as diagnostic radiology modalities and Am-241 photon radiation field. X-ray Narrow spectrum radiation qualities (N-series), from N-40 up to N-200, and radionuclide radiation fields Cs-137 and Co-60, termed as S-Cs and S-Co, respectively, were used (ISO, 2019a). The dose rate was kept constant during all irradiations in the energy dependence test. Both AD and PD type testing standards state the limits of variation from −29 % to +67 %, defined for the minimum rated range. The dosimeter relative energy response curve was determined by normalizing the response value at a specific photon energy to the response value obtained for S-Cs (IEC, 2009; IEC, 2024).

2.4.2. Variation in dosimeter response due to angle of incidence

High angles of incidence accompanied with low photon energies can have a great effect on the dosimeter response (Kržanović et al., 2017;

Table 2
Manufacturer specifications of tested PDs in terms of detector type, dose rate and photon energy measurement range.

Manufacturer and Model	Detector type	Dose rate measurement range		Photon energy range		PD No. (DL)	Symbol
		Min [μSv h^{-1}]	Max [Sv h^{-1}]	Min [keV]	Max [MeV]		
Graetz GPD150G	G-M tube	0.1	1	55	1.3	PD1 PD2	● ●
Mirion Rad-60S	Si – diode	5	3	60	6	PD3 PD4	▲ ▲
Polimaster RadFlash	G-M tube	0.1	1	15	1.5	PD5	★
Polimaster PM1621A	G-M tube	0.1	1	10	20	PD6	■

Ćeklić et al., 2014). Dosimeter angular dependence was evaluated for the three lowest energy radiation qualities for which the energy dependence of the response was in line with the IEC standards (IEC, 2009; IEC, 2024) and for the S-Cs radiation quality. The dose rate was kept constant within the standard test conditions defined by the respective standards. This test was done in both vertical and horizontal dosimeter orientations. The angular dependence test was conducted in a broader range of angles, than the minimum rated range stated by the standards (IEC, 2009; IEC, 2024). In the case of ADs, the minimum rated range stated by the standard covers angles of incidence from 0° to ±45° from the reference direction. This range is defined with respect to the area workplace monitors. For area dosimeters, the following angles were used, 0°, ±45°, ±60°, ±90°, ±120°, and 180°. In this way, the potential of area dosimeters to be used in conditions specific for environmental monitoring was explored. In the case of PDs, the minimum rated range covers angles of incidence from 0° to ±60°. For personal dosimeters the angular dependence test was performed in both directions of rotation for the angles 0°, ±30°, ±45°, ±60°, and ±75°. Relative response for a specific energy and angle of incidence was determined by normalizing the specific response value to the response obtained at S-Cs and 0°. Limits of variation for the energy and angular dependence test are set from −29 % to +67 % in both standards (IEC, 2009; IEC, 2024).

2.4.3. Variation in dosimeter response due to dose rate – non-linearity

Based on the ionizing radiation practice, the range of encountered dose (rate) values can significantly differ. Due to dead-time effects which can occur at high dose rate rates (respective to the tested dosimeter measurement range), and the low-dose rate effects related to dosimeter resolution and detection limits, it is important to test the non-linearity of the dosimeter response. This test was performed over the dosimeter measurement range based on the manufacturer specifications at least at two dose rate values per order of magnitude. The test was conducted in S-Cs and S-Co reference radiation fields. In the cases when S-Co was used for the non-linearity test, type F correction factor was introduced to account for the energy dependence of dosimeters, relative to S-Cs. In the case of ADs, dosimeter performance was evaluated in the dose rate range from 3 μSv h^{-1} to 7 Sv h^{-1}, whereas in the case of PDs the dose rate range spanned from 3 μSv h^{-1} to 2 Sv h^{-1}. The IEC 60846–1:2009 (IEC, 2009) sets the limits of variation for this test from −15 % to +22 %, whereas the IEC 61526:2024 (IEC, 2024) sets the limits of variation from −13 % to +18 %.

2.4.4. Stability and overload

The stability test was performed for five consecutive days in order to evaluate the reproducibility and consistency of measurements under constant irradiation conditions. All measurements were performed utilizing the same radiation source (S-Cs), dose-rate of.

100 μSv h^{-1}, source to detector distance and dosimeter positioning. Cs-137 decay during this period was negligible. The stability test was performed for 20 ADs and 2 PDs, due to time constraints and the availability of tested units. Dosimeter behaviour in the overload conditions was investigated by irradiating the dosimeter with a dose rate which is at least ten times above the upper limit of the measurement range, if such a dose rate was attainable in the SSDL. Following this exposure, measurements under reference conditions (100 μSv h^{-1} at S-Cs) were performed, and the post-overload dosimeter response was recorded. The dosimeter overload test was performed for 12 ADs.

2.4.5. Interpretation of the results and decision rules

Both standards (IEC, 2009; IEC, 2024) state that the limits of variation for each test should be enlarged by the measurement uncertainty of the conventional quantity value. Due to different measurement uncertainties reported by different laboratories and for different quantity values, graphic representations of the limits of variation in the figures all use the limits with zero uncertainty. Measurement uncertainties for the calibration of radiation protection dosimeters in terms of operational dosimetry quantities are similar for all SSDLs (e.g., 4.5–4.8 %, $k = 2$). The largest contributions to the overall measurement uncertainty are attributed to the calibration coefficient of the secondary standard, the secondary standard stability, and the conversion coefficient from air kerma to the operational dosimetry quantity. According to the ISO 4037–3:2019 (ISO, 2019c) standard, the conversion coefficient measurement uncertainty for matched reference fields is estimated as 2.0 % ($k = 1$). In the case of characterized reference fields, the conversion coefficient measurement uncertainties are estimated either by using dosimetry or spectrometry methods defined in the ISO 4037–2:2019 (ISO, 2019b). Detailed uncertainty budgets can be found in Živanović et al. (2023).

Results on dosimeter performance for each test were obtained through multiple measurements. Measurement uncertainty (with $k = 2$) is added to the data points, and, for data points outside the limits, a result is considered acceptable if any part of the uncertainty bar crosses the limit. Correlations in measurement uncertainty are not considered in this work, because of the quantity of measured data and many different laboratories using different equipment and procedures, causing slightly larger limits of variation in some cases. However, this is not considered important for the purpose of this paper, because fail/pass status of single dosimeters is not of special interest, but instead the general state-of-the-art and the possibility to update the standards. Also, differences in practices between laboratories may point toward further needs to improve the type testing protocols.

3. Results and Discussion

The results of AD and PD relative response to the radiation-based influence quantities are presented in Figs. 2–9 and Figs. A1-A7. In Figs. 2 and 3 the energy dependence of ADs and PDs is displayed, respectively. Figs. 4 and 5 show the angular dependence of ADs in N-40 and N-100 radiation qualities, respectively. Figs. 6 and 7 display the angular dependence of PDs in radiation qualities N-40 and N-60, and N-100 and N-120, respectively. Figs. 8 and 9 present the non-linearity response of ADs and PDs, respectively. Figs. A1 – A7 are provided in Appendix A, with additional information on performance of tested dosimeters. Data points outside the dosimeter manufacturer specified range are represented as hollowed out symbols.

3.1. Variation in dosimeter response due to photon energy

For the most part, the performance of ADs is in line with the standard defined limits of variation for this test (−29 %, +67 %), for the minimum rated range from 80 keV to 1.5 MeV mean photon energies (IEC, 2009). As previously mentioned, the dosimeters were tested in a broader range of photon energies, going down to N-40 (mean photon energy 33.3 keV). In case of some dosimeters, such as AD18, AD19, AD25 and AD26, a more pronounced energy dependence in the range of lower photon energies was observed. This under response was observed for the N-40 and N-60 radiation qualities, which are outside of the manufacturer-stated photon energy range. On the other hand, dosimeters AD4 and AD5 showcased a steady under response throughout the entire tested energy range in X-ray fields. This could possibly be attributed to the fact that Automess 6150 AD3 was designed to measure the predecessor of $H^*(10)$, and is a discontinued model replaced with newer ones, such as Automess

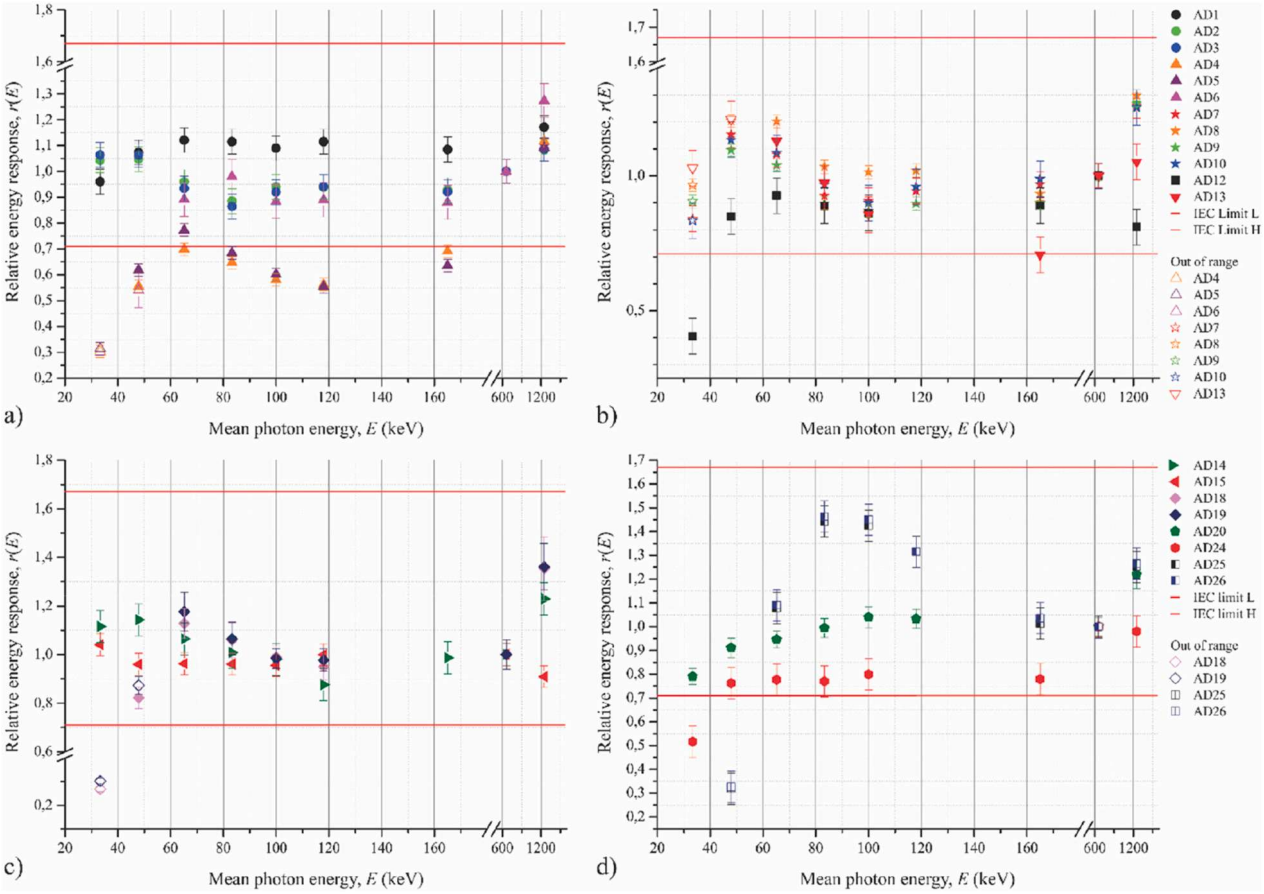

Fig. 2. Energy dependence of active area dosimeter (AD) response in the range from 33 keV (N-40) to 1.25 MeV (S-Co): a) AD1-AD6; b) AD7-AD13; c) AD14-AD19; d) AD20-AD26. The limits of variation (−29 %; +67 %) in terms of relative energy response are displayed (IEC, 2009).

6150 AD6. Some end-users still request calibration for this dosimeter model, which is why dosimeter verification, in addition to regular calibration is important. Additionally, AD12 and AD24 showed a large deviation from the reference response of −59.4 % and −48.4 %, respectively, for the radiation quality N-40, even though that radiation quality is within their manufacturer stated measurement range. The noted under response could be associated with the age of the specific device unit under test and could indicate degradation of its electronic components or possible gas leakage, when it comes to Fluke 451P (AD12), which is not uncommon for pressurized ionization chambers. Most of the devices do not have a significant energy dependence at high photon energies, e.g., making them suitable for environmental monitoring at nuclear facilities. The summarized response energy dependence of ADs is presented in Fig. 2.

Based on the tested ADs it can be concluded that the dosimeters exhibit performance in line with the area workplace type testing standard (IEC, 2009). The tested AD sample included mostly area workplace monitors. It should be noted that in the case of environmental area monitoring many ADs fail to comply with relevant IEC standards. This is especially present in environmental monitoring activities done by laymen and in non-governmental networks, where low-cost devices are utilized (Morosh et al., 2021). To adequately assess the performance of ADs for environmental monitoring, the IEC standard related to area workplace monitoring could additionally include specific tests and requirements for area environmental monitoring. In terms of energy dependence, the IEC test methods could include the standard L-series radiation qualities (ISO, 2019a), as an alternative to the N-series radiation qualities, suitable for low-dose rate applications (Kržanović et al., 2022).

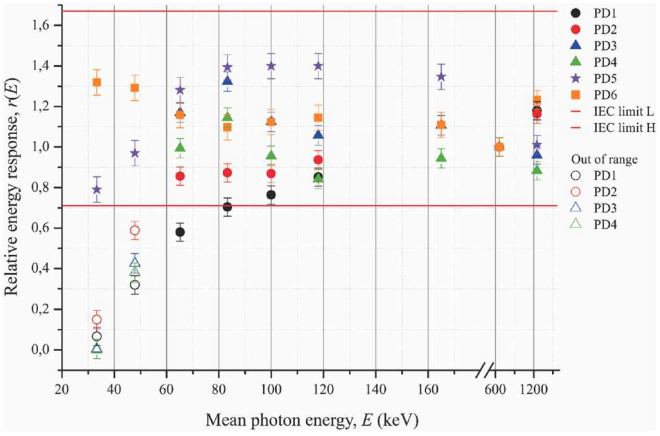

Fig. 3. Energy dependence of active personal dosimeter (PD) response in the range from 33 keV (N-40) to 1.25 MeV (S-Co). The limits of variation (−29 %; +67 %) in terms of relative energy response are displayed (IEC, 2024).

When observing the tested PDs, it can be noted that exhibited performance is mostly in line with the standard defined limits of variation in the minimum rated range (IEC, 2024). PD1 showcased a significant under response up until N-120, which is not in line with the manufacturer stated photon energy range. On the contrary, PD2 exhibited a satisfactory energy dependence, in line with the manufacturer specifications. Considering that PD1 and PD2 are different units of the same dosimeter model, they exhibit similar energy dependence trend at low-photon energies. Therefore, dosimeter recalibration and/or adjustment could be required. This observation can be used to emphasize the importance of individual dosimeter unit verification in addition to the type testing of the dosimeter model (which may be based on the manufacturer selected sample from a given production series). In some countries the legal requirements on radiation protection dosimeters are fulfilled if singular dosimeter units used in practice are regularly calibrated, and/or if the dosimeter model is IEC type tested by designated laboratories, while verification is not a very common requirement. For PD2, PD3 and PD4, an under response can be observed for the radiation qualities N-40 and N-60. These radiation qualities are outside the scope of their respective photon energy ranges, which should be considered if these dosimeters are to be used in certain exposure scenarios (such as interventional radiology or similar medical applications where high doses to exposed workers can be recorded), to prevent the acquisition of unreliable dosimetry data. PD5 and PD6 exhibited good performance across the entire tested energy range, with the maximum deviation from the reference response being +39.9 % for the radiation qualities N-120 and N-150, and +31.9 % for the radiation quality N-40, respectively. Response energy dependence of PDs is presented in Fig. 3.

The observed PD performance in this work is in line with the findings of previous research, where the applications of active personal dosimeters in low-energy continuous radiation fields were considered (Kržanović et al., 2017; Lee et al., 2016). Further examination of the dosimeter performance in low-energy radiation fields, regarding the effects of photon energy, could be done by utilizing real poly-energetic radiation fields encountered in diagnostic radiology (such as the standardized RQR radiation quality series). Such performance tests, focused on fluoroscopy modalities were previously done, where dosimeters, which had their energy response in line with the IEC standard in the medical energy range, were identified. Even though the energy dependence criteria were fulfilled, the non-linearity effect at very high (pulsed field) dose rates caused performance issues (Clairand et al., 2011; Struelens et al., 2011).

Considering the current developments in individual monitoring, hybrid dosimeters which incorporate properties of both active and passive dosimeters are being proposed as an alternative to the existing technologies. Performance tests of novel dosimeter models have also been done, and their characteristics are on par with the commercially available PDs and TLDs/OSLDs (Garzon et al., 2019; Haag et al., 2021; Vlahović et al., 2025).

3.2. Variation in dosimeter response due to angle of incidence

Angular dependence of AD response is in line with the IEC 60846–1:2009 (IEC, 2009) standard requirements in the minimum rated range. Therefore, these dosimeters are suitable for general area workplace applications where the encountered angles of incidence are less than ±45°. The angular response test for ADs included a wider range of angles, to consider irradiation conditions which are encountered when the dosimeters are used for area environmental monitoring. The angular response of ADs in N-40 and N-100 radiation qualities, in both dosimeter orientations is presented in Figs. 4 and 5, respectively. N-40 was highlighted as low photon energies and high angles of incidence present unfavourable irradiation conditions (often encountered in medical applications of ionizing radiation). N-100 represents the lowest energy radiation quality within the IEC stated minimum rated range of photon energy (IEC, 2009; IEC, 2024). Additional information on angular dependence of ADs in other investigated radiation fields is presented in the Appendix (Figs. A1 – A5).

As the geometry of the dosimeter (the position of its active volume relative to the associated electronics, any additional filtration, the structure of the dosimeter casing etc.) has an important role in its angular dependence, sufficient information regarding the dosimeter reference point, orientation and positioning should be clearly stated by the manufacturers. In the S-Cs radiation field it was observed that some of the AD models had their angular response within the standard limits even for the whole test range (0°, ±45°, ±60°, ±90°, ±120°, and 180°), exhibiting potential for applications in environmental monitoring. In the low-energy radiation fields (N-40 and N-60) for the angles of incidence larger than ±45° the angular dependence is more pronounced. It should also be noted that in the manufacturer specifications there is no sufficient information on the angular rated range.

As the minimum rated range in (IEC, 2009) is defined for a narrow angle range, specific to area workplace monitors, the current standard test criteria could be updated by introducing the dosimeter requirements

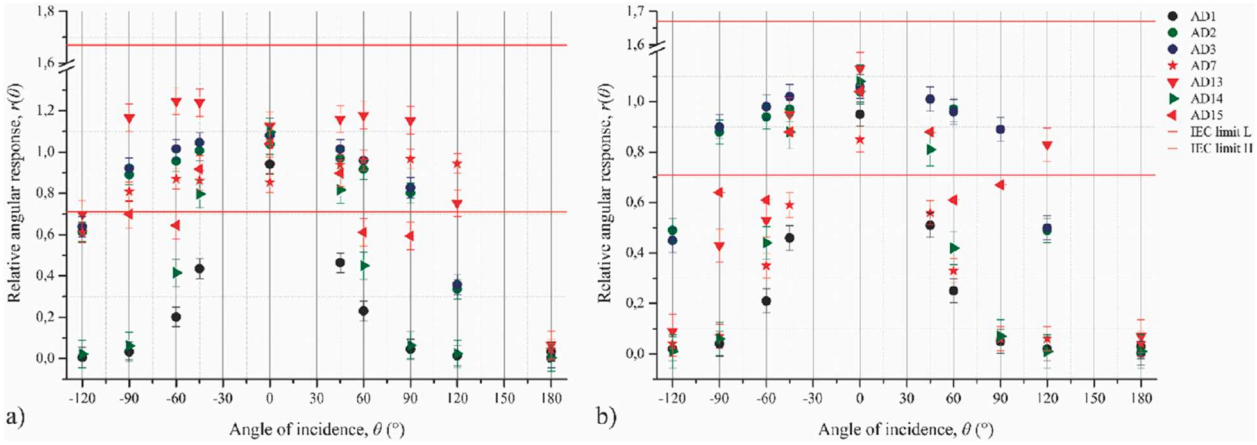

Fig. 4. Angular dependence of active area dosimeter (AD) response in the N-40 (mean photon energy 33.3 keV) radiation quality. a) vertical dosimeter orientation; b) horizontal dosimeter orientation. The limits of variation (−29 %; +67 %) in terms of relative energy and angular response are displayed (IEC, 2009).

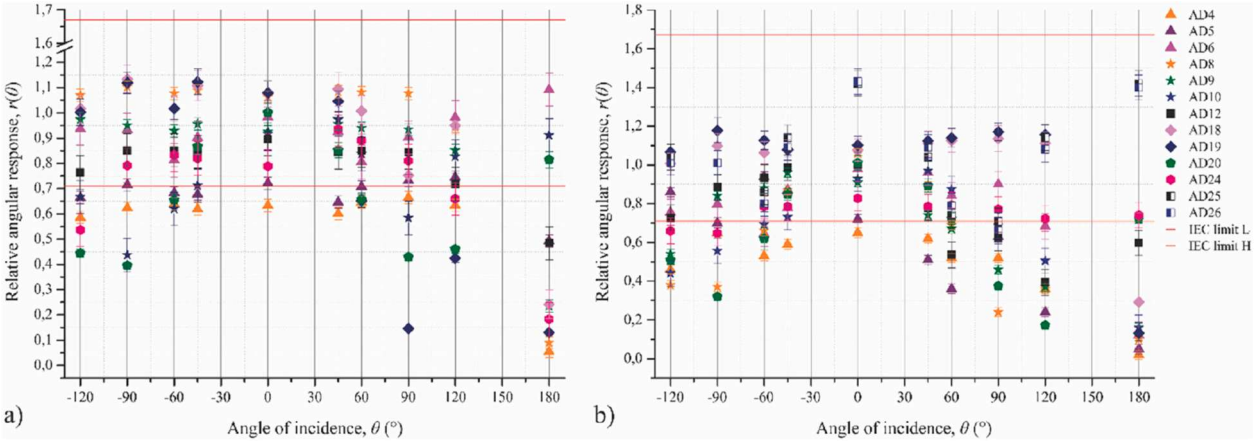

Fig. 5. Angular dependence of active area dosimeter (AD) response in the N-100 (mean photon energy 83.3 keV) radiation quality. a) vertical dosimeter orientation; b) horizontal dosimeter orientation. The limits of variation (−29 %; +67 %) in terms of relative energy and angular response are displayed (IEC, 2009).

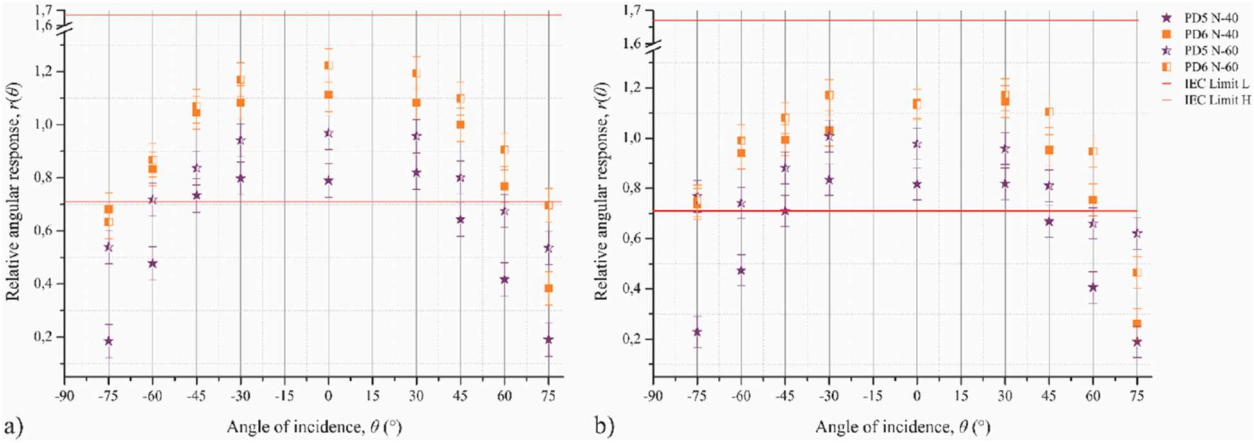

Fig. 6. Angular dependence of active personal dosimeter (PD) response in the N-40 and N-60 (mean photon energies 33.3 keV and 47.9 keV) radiation qualities. a) vertical dosimeter orientation; b) horizontal dosimeter orientation. The limits of variation (−29 %; +67 %) in terms of relative energy and angular response are displayed (IEC, 2024).

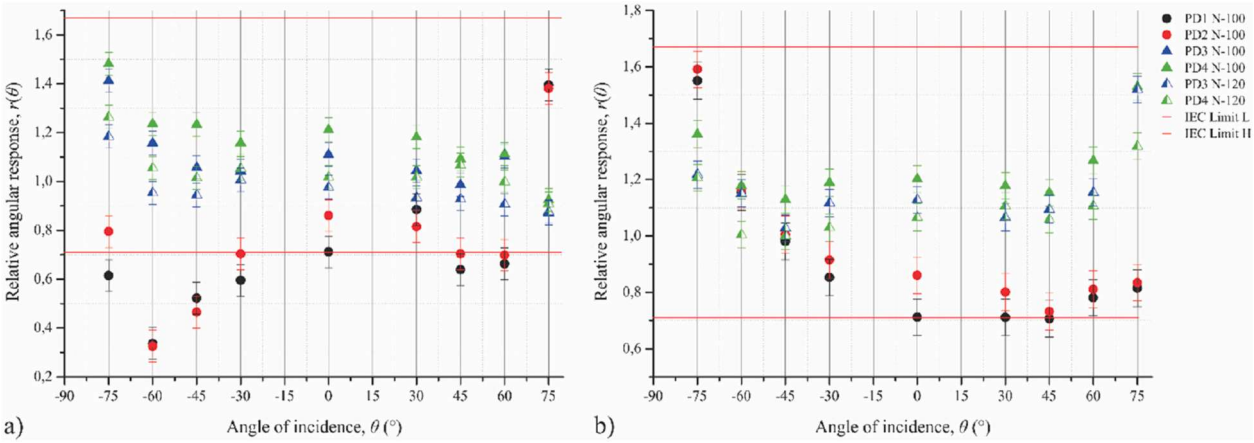

Fig. 7. Angular dependence of active personal dosimeter (PD) response in the N-100 and N-120 (mean photon energies 83.3 keV and 100 keV) radiation qualities. a) vertical dosimeter orientation; b) horizontal dosimeter orientation. The limits of variation (−29 %; +67 %) in terms of relative energy and angular response are displayed (IEC, 2024).

in a broader angular range, specific to environmental monitoring, with adapted limits of variation for larger angles.

In the case of PDs, it was observed that the angular dependence criteria are fulfilled for the S-Cs radiation quality. Considering the manufacturer specifications of the tested dosimeters (Table 2), only two dosimeter models (PD5 and PD6) are designed for low-energy applications. As the photon energy decreases the angular dependence becomes more prominent, with significant under response at higher angles of incidence. In the N-40 and N-60 radiation fields they have displayed alignment with the standard criteria up to approximately ±45°. It

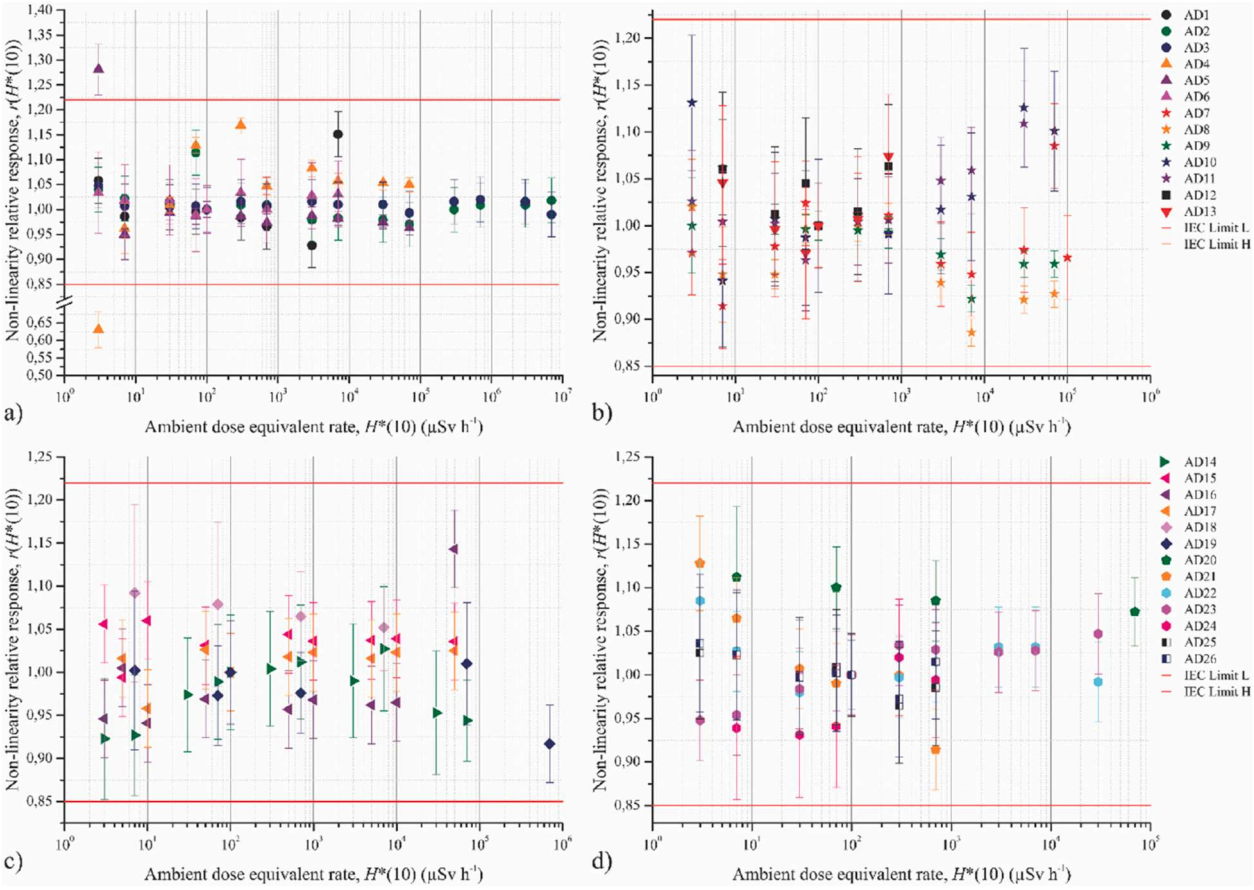

Fig. 8. Non-linearity of active area dosimeter (AD) response in the dose rate range from 3 μSv h $^{-1}$ to 7 Sv h $^{-1}$: a) AD1-AD6; b) AD7-AD13; c) AD14-AD19; d) AD20-AD26. The limits of variation (−15 %; +22 %) in terms of relative response are displayed (IEC, 2009).

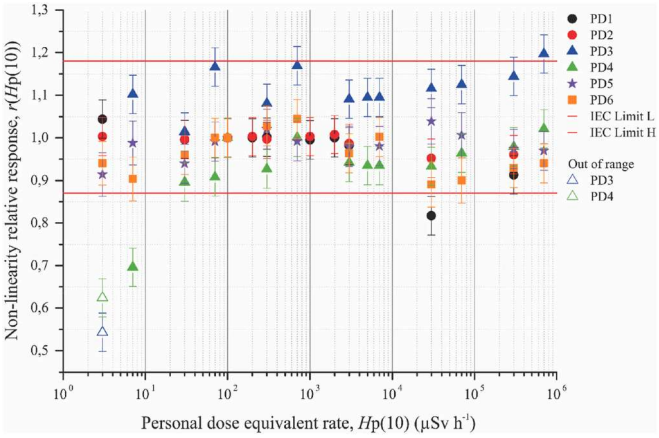

Fig. 9. Non-linearity of active personal dosimeter (PD) response in the dose rate range from 3 μSv h $^{-1}$ to 2 Sv h $^{-1}$. The limits of variation (−13 %; +18 %) in terms of relative response are displayed (IEC, 2024).

should be noted that very low photon energies and high angles of incidence represent unfavourable irradiation conditions. Also, the PD sample sizes are not well representative of the dosimeter type. PD1 and PD2 have displayed a pronounced angular dependence, which could possibly be attributed to their geometry and instrument design. PD3 and PD4 have performed within the standard requirements in line with the manufacturer's specifications. The angular response of PDs in N-40 and N-60, and N-100 and N-120 radiation qualities, in both dosimeter orientations is presented in Figs. 6 and 7 respectively. Additional information on angular dependence of PDs in S-Cs and N-80 radiation qualities is presented in the Appendix (Figs. A6 – A7). Angular dependence tests on current state-of-the-art hybrid dosimeters for individual monitoring proves that some of the new dosimeter models have commendable angular dependence even at very low energies (Garzon et al., 2019; Haag et al., 2021; Vlahović et al., 2025).

Table 3
Dosimeter stability in terms of Coefficient of Variation (CoV).

AD/PD	CoV (%)	AD/PD	CoV (%)
AD1	0.8	AD13	0.7
AD2	0.8	AD14	1.1
AD3	0.9	AD21	0.4
AD4	9.0	AD22	0.6
AD5	4.1	AD23	0.4
AD6	0.9	AD24	3.0
AD7	0.4	AD25	0.2
AD8	2.5	AD26	0.3
AD9	1.8	PD3	4.4
AD10	1.2	PD4	4.7
AD11	2.8		
AD12	0.9		

3.3. *Variation in dosimeter response due to dose rate (non-linearity)*

All the tested ADs have complied with the standard requirements on non-linearity of the response. Over the whole tested dose rate range, relative responses within ±10 % were observed for most dosimeters, making them suitable for various exposure scenarios in both industrial and medical applications. AD4 and AD5 had displayed pronounced non-linearity at the lowest dose rate included in the test (3 μSv h^{-1}), which

Table 4
Overload message indication and post-overload response.

AD	Message	Response
AD4	999 mSv h^{-1}, screen blink	0.868
AD5	999 mSv h^{-1}, screen blink	0.987
AD6	999 mSv h^{-1}, screen blink	1.001
AD8	9999 Sv h^{-1}, screen blink	1.015
AD9	9999 Sv h^{-1}, screen blink	0.964
AD10	9999 Sv h^{-1}, screen blink	1.001
AD14	OVL mSv h^{-1} (overload)	1.001
AD18	OFL (overflow)	0.963
AD19	OFL (overflow)	0.968
AD20	Overload	0.945
AD25	Overload	0.995
AD26	Overload	0.997

may be attributed to the resolution of the instrument reading. Non-linearity of ADs is presented in Fig. 8.

Similar behaviour is observed with PDs where most of the devices fulfil the criteria over the whole tested dose rate range. For the lowest dose rates of 3 μSv h^{-1} and 7 μSv h^{-1}, PD3 and PD4, which represent the same dosimeter model, have exhibited pronounced non-linearity. As with the AD4 and AD5, this behaviour might be attributed to the instrument resolution. This dose rate value is outside of the manufacturer stated measurement range. Non-linearity of PDs is presented in Fig. 9.

Most of the dosimeters included in the study have behaved in accordance with the standards in the tested dose rate ranges, with respect to the manufacturer specifications. In previous studies focused on dosimeter performance the effects of dose rate were investigated in the radiation fields where very high dose rates are encountered, specifically in the pulsed radiation fields. Under these extreme irradiation conditions many of the devices fail to provide any indication. It was observed that in general the non-linearity effect becomes very significant at dose rates approximately above 1 Sv h^{-1} (Clairand et al., 2011; Hupe et al., 2019).

3.4. Stability and overload

Out of the 20 ADs, for which the stability test was conducted, more than half of them exhibited excellent stability, with the Coefficient of Variation (CoV) below 1 %. For the remaining ADs, the CoV was below 5 %, except for AD4, which showed a CoV of 9 % (Table 3). Overall, the dosimeters showcased good stability, indicating that they provide reliable and precise measurements, which is essential when performing dosimetry measurements.

In the case of PDs, only two dosimeters were evaluated in this test, both exhibiting CoV values below 5 % (Table 3), making them suitable for the acquisition of reliable and precise dosimetry data.

For the dosimeter overload test all of the 12 tested ADs either displayed an overload indication message or a numerical value indicating over range (Table 4). The maximum deviation from the reference value of −13.2 % was reported for AD4, which could be attributed to the age of the device. For the rest of the ADs the deviation was less 6 %, which demonstrates that even after being exposed to dose rates beyond the manufacturer stated measurement range, the devices functionality is not compromised and they still provide accurate measurements.

3.5. Possibilities for the update of IEC standards

State-of-the-art radiation protection dosimeters are designed in such a way that they are able to measure within a wide range of photon energies and doses (dose rates). The performance indicators presented in previous sections showcase overall good dosimeter performance, in line both with the standard stated minimum rated ranges, as well as the manufacturer specifications. Additionally, some dosimeters exhibited good performance even beyond their respective manufacturer-stated measurement ranges.

The current standard defined minimum rated ranges and limits of variation are defined to accommodate various ionizing radiation applications. Literature review, everyday practice and state-of-the-art technology overview have shown that the current limits of variation are achievable by various dosimeter manufacturers for different detector technologies. In this way, a variety of dosimeters are available on the market, at different price points, in order to accommodate different end-user needs.

The limits are derived based on the allowed variation of the calibration coefficient of ±40 % (IEC, 2009; IEC, 2024). Current limits of variation lead to higher measurement uncertainties in real poly-energetic and multi-directional radiation fields. These uncertainties are sufficient for most common dosimeter applications and most routine measurements. Measurements of operational quantities are usually performed to estimate effective dose, which is only an approximation of the risk for stochastic effect (ICRP, 2021). However, when high precision measurements are required, with a lower measurement uncertainty (e.g., when comparing different methods, equipment or procedures, transfer instruments for dosimeter comparisons), it could be beneficial to introduce another class of instruments, with lower limits of variation.

Currently, there is no distinction between dosimeters which have small variations in relative response and those which have more pronounced dependence on radiation based influence quantities. Based on the performance test results two dosimeter classes are proposed (Table 5). In the case of the energy and angular dependence test, limits

Table 5
Overview of the minimum rated ranges for radiation-based influence quantities, and their proposed limits of variation in terms of relative response for class A and class B dosimeters.

IEC standard	Influence quantity	Minimum rated range	Limits of variation	
			Class A	Class B
IEC 60846–1:2009	Photon energy	80 keV–1.25 MeV 20 keV–150 keV	0.83–1.25	0.71–1.67
	Angle of incidence	80 keV–1.25 MeV 20 keV–150 keV 0 - ±45°	0.83–1.25	0.71–1.67
	Non-linearity	three orders of magnitude including 10 μSv h^{-1}	0.91–1.11	0.85–1.22
IEC 61526:2024	Photon energy	80 keV–1.25 MeV 20 keV–150 keV	0.83–1.25	0.71–1.67
	Angle of incidence	80 keV–1.25 MeV 20 keV–150 keV 0 - ±60°	0.83–1.25	0.71–1.67
	Non-linearity	0.5 μSv h^{-1} – 1 Sv h^{-1}	0.91–1.11	0.83–1.25

of variation, which would pertain to class B dosimeters, should remain unchanged (0.71–1.67). Such limits are valid for two application based minimum rated ranges, medical, which covers mean photon energies from 20 keV to 150 keV, and industrial, with mean photon energies from 80 keV to 1.25 MeV, with the respective angle of incidence minimum rated ranges for PDs (0°; ±60°) (IEC, 2024), and for ADs (0°; ±45°) (IEC, 2009). Proposed class A dosimeters would comply with more strict limits of variation, 0.83–1.25, which correspond to the ±20 % variation in the calibration coefficient. Observed performance test results indicate that some current and novel dosimeters exhibit small response variations relative to reference conditions, being <±10 %, even outside the minimum rated range. It should be noted that the number of tested personal dosimeters in this study is not sufficiently large, however novel dosimeters exhibit good performance across the entire tested range (Garzon et al., 2019; Haag et al., 2021; Vlahović et al., 2025). Observed dosimeter response variation due to dose rate was within ±10 % for most of the tested dosimeters, which suggests that the limits of variation could be stricter than currently stated in the standard. For class A dosimeters limits of variation could be set to 0.91–1.11, whereas the limits set for proposed class B dosimeters would remain unchanged (IEC, 2009; IEC, 2024).

Considering the proposed distinct dosimeter classes, evaluation of dosimeter performance against stricter criteria was performed to assess the number of ADs and PDs which could be considered class A dosimeters.

Based on the energy dependence test results 12 out of 20 ADs fulfil the newly proposed criteria in the minimum rated range (Fig. 2) (IEC, 2009). If the performance is assessed within the respective manufacturer-stated energy ranges 10 out of 12 ADs fulfil the class A criteria. In the case of PDs, it was observed that 3 out of 6 dosimeters can be considered class A dosimeters within the minimum rated range (Fig. 3).

The angular dependence of the response was evaluated for the three lowest photon energy radiation qualities for which the energy dependence complies with the standard. For the minimum rated range (N-100 radiation quality, mean photon energy 83.3 keV) 8 out of 11 and 6 out of 13 ADs in vertical and horizontal orientation, respectively, satisfy class A requirements (Fig. 5). For the N-80 radiation quality (65.2 keV mean photon energy) 10 out of 17 and 13 out of 19 ADs in vertical and horizontal orientation, respectively, met the newly proposed criteria (Fig. A4) (IEC, 2009). In the case of PDs 2 out of 4 dosimeters comply with the class A requirements in the minimum rated range (N-100) (Fig. 7), whereas 4 out of 6 PDs met the requirements in the N-80 radiation quality (Fig. A7), for both orientations (IEC, 2024).

In the case of non-linearity test nearly all (24 out of 26) ADs can be categorized as class A dosimeters (Fig. 8), while 3 out of 6 PDs fulfil the newly proposed criterion (Fig. 9) (IEC, 2009; IEC, 2024).

4. Conclusion

In this work a measurement protocol was developed based on the IEC type testing standards (IEC, 2009; IEC, 2024) to evaluate the performance of commonly used radiation protection dosimeters, in terms of variation in response caused by radiation-based influence quantities. The test ranges used in this study were extended beyond the minimum rated ranges and manufacturer-stated ranges. ADs and PDs exhibited overall good performance in terms of relative response within the standard defined limits of variation and manufacturer specifications for all the conducted tests (IEC, 2009; IEC, 2024). Some of the dosimeters showcased small variations in response even beyond these ranges, while others exhibited more pronounced variations under these irradiation conditions: low-energy photons (such as N-40 and N-60 radiation fields), high angles of incidence (such as ±75° for PDs, or ±90°/±180° for ADs depending of geometry) and very low dose rates (where device resolution is the limiting factor) or very high dose rates (where devices can be in overload or can be affected by detector dead time). The presented results emphasize the possibility for introducing two dosimeter classes. Class A dosimeters would have to comply with more strict limits of variation than the current standard stated ones, whereas the limits of variation for Class B dosimeters would remain as they are. The aim of these proposed updates is to enhance the quality and reliability of dosimetry data and to reinforce radiation protection of both the exposed workers and the general public. Due to the insufficient number of PDs included in this study, it is necessary to extend the sample size in future work, to provide supporting evidence for the proposed classification. Complementary to this study, future research is needed towards performance tests in pulsed-radiation fields.

CRediT authorship contribution statement

Jelena Vlahović: Writing – review & editing, Writing – original draft, Visualization, Methodology, Investigation, Formal analysis, Data curation, Conceptualization. **Nikola Kržanović:** Writing – review & editing, Writing – original draft, Validation, Supervision, Methodology, Investigation, Formal analysis, Conceptualization. **Miloš Živanović:** Writing – review & editing, Validation, Formal analysis. **Ivana Stojanović:** Validation, Investigation, Data curation. **Luka Bakrač:** Writing – review & editing, Validation, Investigation, Data curation. **Argiro Boziari:** Writing – review & editing, Validation, Investigation, Data curation. **Miloš Đaletić:** Writing – review & editing, Validation, Investigation, Data curation. **Ana Fernandes:** Writing – review & editing, Formal analysis. **Liviu-Cristian Mihailescu:** Writing – review & editing, Validation, Investigation, Data curation. **Erinc Reyhanoglu:** Writing – review & editing, Validation, Investigation, Formal analysis, Data curation. **Siarhei Saroka:** Writing – review & editing, Validation, Formal analysis, Data curation. **Teemu Siiskonen:** Writing – review & editing, Project administration, Formal analysis, Data curation, Conceptualization. **Jana Šmoldasová:** Validation, Investigation, Formal analysis, Data curation. **Vladimir Sochor:** Writing – review & editing, Validation, Investigation, Formal analysis, Data curation. **Maria do Ceu Ferreira:** Writing – review & editing, Investigation. **Nataša Todorović:** Writing – review & editing, Supervision.

Declarations of interest

None.

Acknowledgement

The project (22NRM07 GuideRadPROS) has received funding from the European Partnership on Metrology, co-financed by the European Union's Horizon Europe Research and Innovation Programme and by the Participating States.

Funded by the European Union. Views and opinions expressed are, however, those of the author(s) only and do not necessarily reflect those of the European Union or EURAMET. Neither the European Union nor the granting authority can be held responsible for them.

This research presented in this paper received funding by The Ministry of Science, Technological Development, and Innovation of the Republic of Serbia under contract 451-03-136/2025-03/200017.

Appendix A. Results on the performance of Active Area Dosimeter (AD) and Active Personal Dosimeter (PD) in terms of response to radiation-based influence quantities

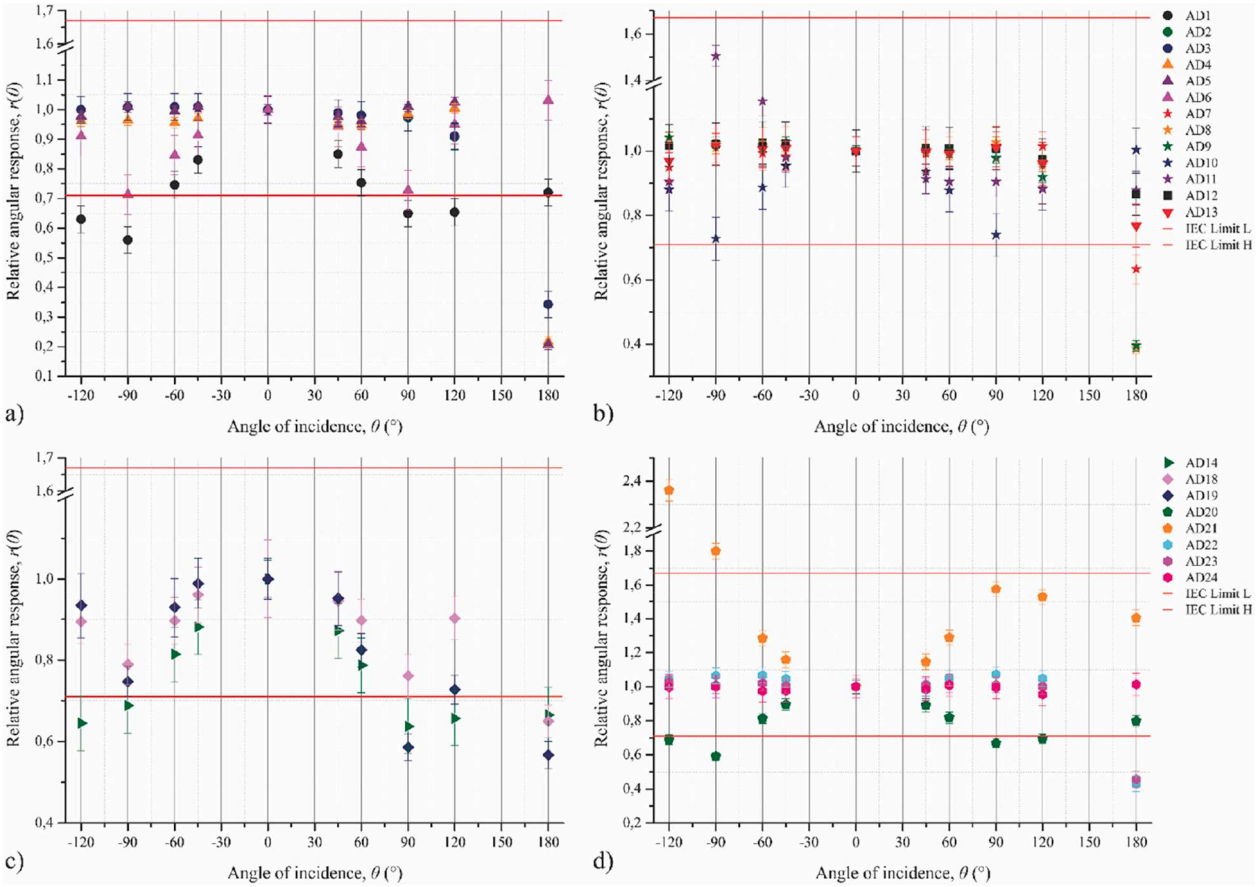

Fig. A1. Angular dependence of active area dosimeter (AD) response in the S-Cs (mean photon energy 662 keV) radiation quality in vertical dosimeter orientation. a) AD1-AD6; b) AD7-AD13; c) AD14-AD19; d) AD20-AD26. The limits of variation (−29 %; +67 %) in terms of relative energy and angular response are displayed (IEC, 2009).

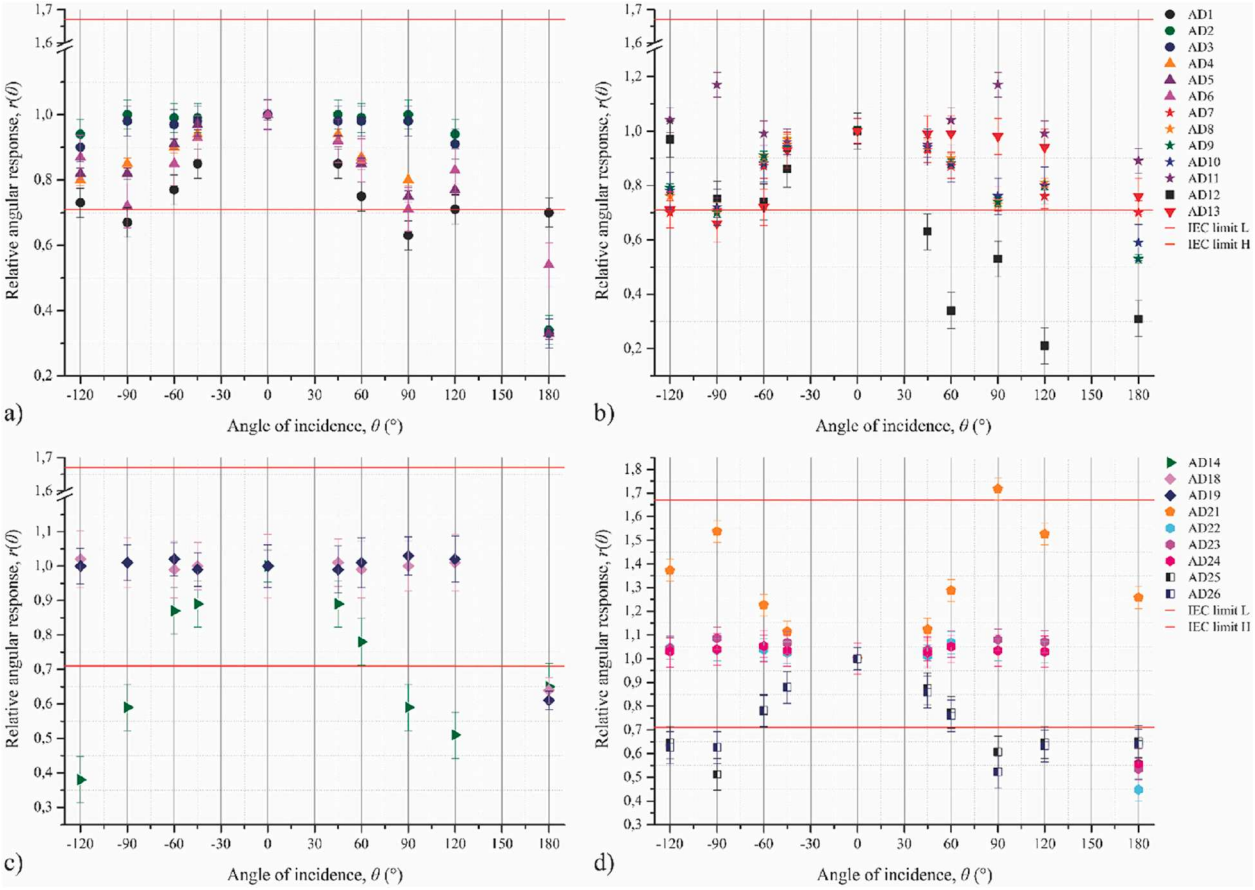

Fig. A2. Angular dependence of active area dosimeter (AD) response in the S-Cs (mean photon energy 662 keV) radiation quality in horizontal dosimeter orientation. a) AD1-AD6; b) AD7-AD13; c) AD14-AD19; d) AD20-AD26. The limits of variation (−29 %; +67 %) in terms of relative energy and angular response are displayed (IEC, 2009).

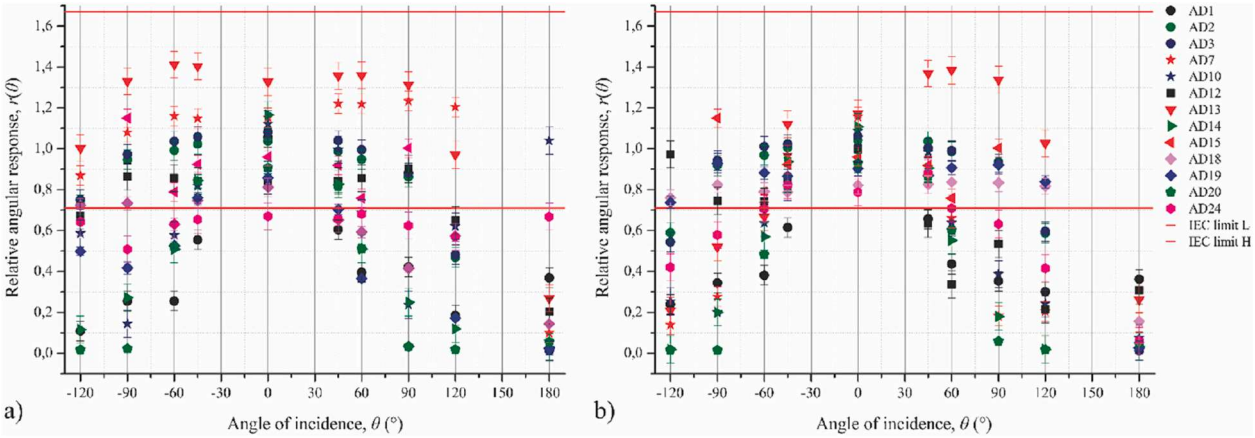

Fig. A3. Angular dependence of active area dosimeter (AD) response in the N-60 (mean photon energy 47.9 keV) radiation quality. a) vertical dosimeter orientation; b) horizontal dosimeter orientation. The limits of variation (−29 %; +67 %) in terms of relative energy and angular response are displayed (IEC, 2009).

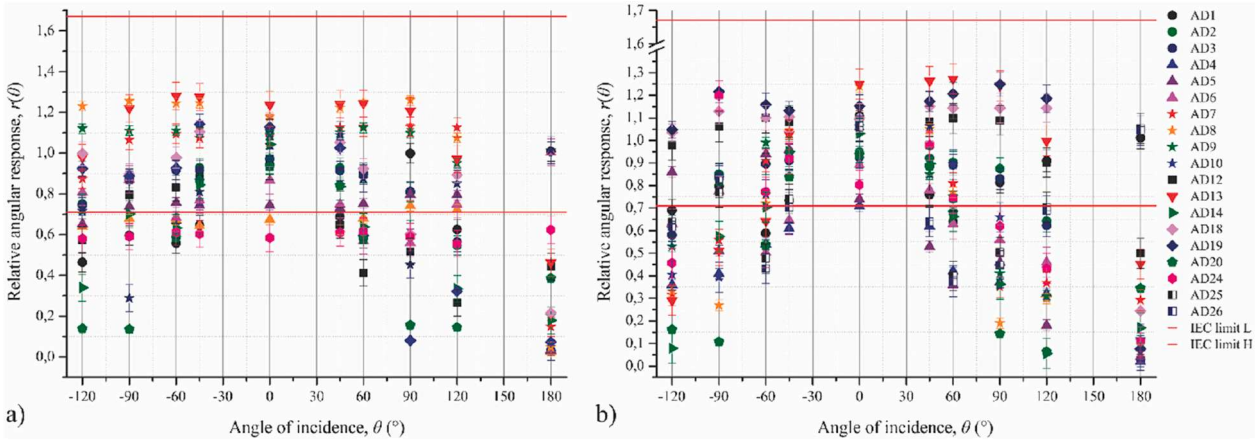

Fig. A4. Angular dependence of active area dosimeter (AD) response in the N-80 (mean photon energy 65.2 keV) radiation quality. a) vertical dosimeter orientation; b) horizontal dosimeter orientation. The limits of variation (−29 %; +67 %) in terms of relative energy and angular response are displayed (IEC, 2009).

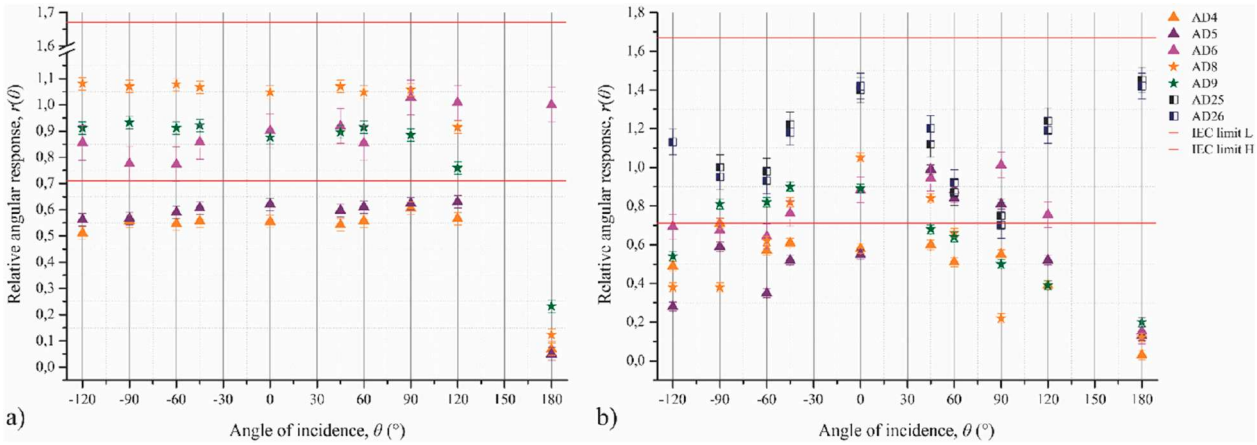

Fig. A5. Angular dependence of active area dosimeter (AD) response in the N-120 (mean photon energy 100 keV) radiation quality. a) vertical dosimeter orientation; b) horizontal dosimeter orientation. The limits of variation (−29 %; +67 %) in terms of relative energy and angular response are displayed (IEC, 2009).

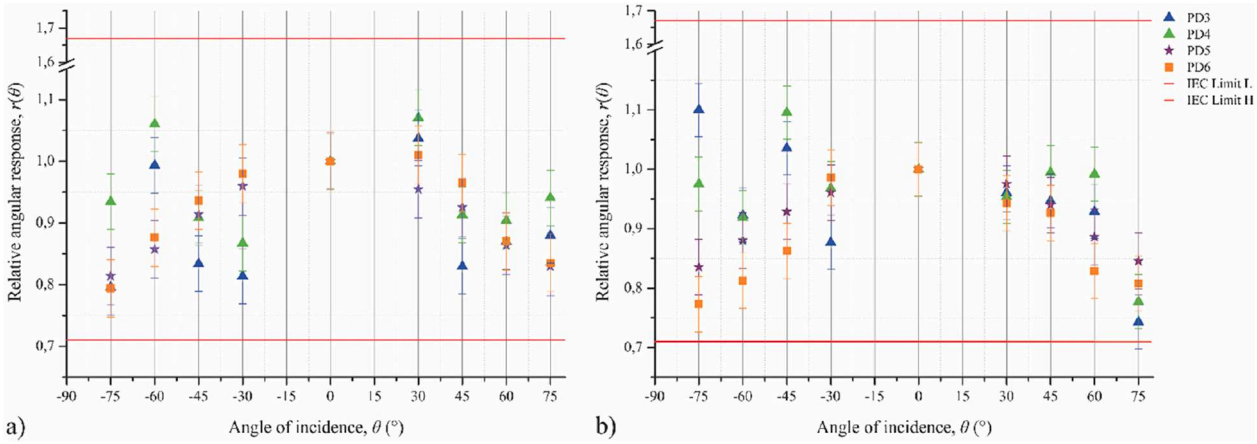

Fig. A6. Angular dependence of active personal dosimeter (PD) response in the S-Cs (mean photon energy 662 keV) radiation quality. a) vertical dosimeter orientation; b) horizontal dosimeter orientation. The limits of variation (−29 %; +67 %) in terms of relative energy and angular response are displayed (IEC, 2024).

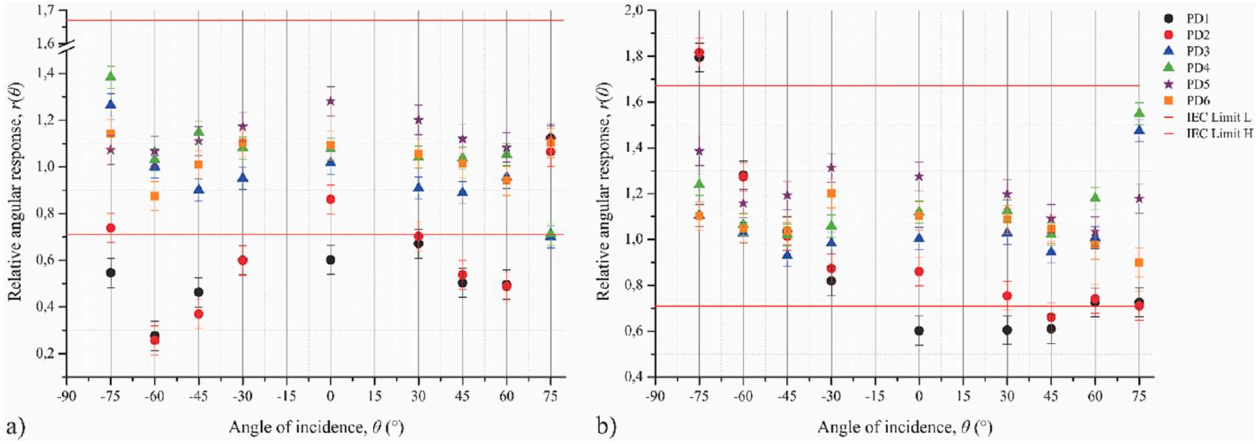

Fig. A7. Angular dependence of active personal dosimeter (PD) response in the N-80 (mean photon energy 65.2 keV) radiation quality. a) vertical dosimeter orientation; b) horizontal dosimeter orientation. The limits of variation (−29 %; +67 %) in terms of relative energy and angular response are displayed (IEC, 2024).

References

Abuelhia, E., & Alghamdi, A. (2020). Evaluation of arising exposure of ionizing radiation from computed tomography and the associated health concerns. *Journal of Radiation Research and Applied Sciences, 13*(1), 295–300. https://doi.org/10.1080/16878507.2020.1728962

Alomairy, N. A. (2023). Assessment of secondary radiation dose in radiology departments. *Journal of Radiation Research and Applied Sciences, 16*(4), Article 100726. https://doi.org/10.1016/j.jrras.2023.100726

Alves, J., Caldeira, M., Röttger, A., Khanbabaee, B., Adam-Guillermin, C., Siiskonen, T., Živanović, M., Šabeta, A., & Glavič-Cindro, D. (2024). Metrology supporting the European regulation for radiation protection. *Radiation Protection Dosimetry, 200*(2), 155–163. https://doi.org/10.1093/rpd/ncad289

Ankerhold, U., Hupe, O., & Ambrosi, P. (2009). Deficiencies of active electronic radiation protection dosimeters in pulsed fields. *Radiation Protection Dosimetry, 135*, 149–153. https://doi.org/10.1093/rpd/ncp099

Bureau International des Poids et Mesures (BIPM). (2025). Key comparison database. https://www.bipm.org/kcdb/. (Accessed 4 August 2025).

Calvacante, F. R., Reynaldo, S. R., Soares, C. R., Engler, C., da Silva Lima, S. S., da Silva, T. A., & do Socorro Nogueira, M. (2025). Characterization of active personal dosimeter in terms of Hp(10) for X and gamma radiation beams. *Applied Radiation and Isotopes, 225*, Article 112117. https://doi.org/10.1016/j.apradiso.2025.112117

Ćeklić, S., Arandić, D., Živanović, M., Ciraj-Bjelac, O., & Lazarević, Đ. (2014). Performance of radiation survey meters in X- and gamma-radiation fields. *Radiation Protection Dosimetry, 162*(1–2), 139–143. https://doi.org/10.1093/rpd/ncu246

Ciraj-Bjelac, O., Carinou, E., & Vanhavere, F. (2018). Use of active personal dosimeters in hospitals: EURADOS survey. *Journal of Radiological Protection, 38*, 702–715. https://doi.org/10.1088/1361-6498/aabce1

Clairand, I., Bordy, J.-M., Carinou, E., Daures, J., Debroas, J., Denoziere, M., Donadille, L., Ginjaume, M., Itie, C., Koukorava, C., Krim, S., Lebacq, A.-L., Martin, P., Struelens, L., Sans-Merce, M., & Vanhavere, F. (2011). Use of active personal dosemeters in interventional radiology and cardiology: Tests in laboratory conditions and recommendations - ORAMED project. *Radiation Measurements, 46*(11), 1252–1257. https://doi.org/10.1016/j.radmeas.2011.07.008

Cui, L., Feng, Z., Jin, G., Ma, Y., Ma, X., & Ma, X. (2024). Performance and use of active personal dosimeters in pulsed radiation field. *Chinese Journal of Radiological Health, 33*(4), 353–357. https://doi.org/10.13491/j.issn.1004-714X.2024.04.001

Daletić, M., Kržanović, N., Radumilo, V., Živanović, M., & Komatina, I. (2025). Ambient dose equivalent monitoring in the vicinity of a nuclear facility with dosemeters based on geiger-müller tubes. *Nuclear Engineering and Technology, 57*(5), Article 103363. https://doi.org/10.1016/j.net.2024.103363

Euratom. (2013). Council directive 2013/59/Euratom of 5 December 2013. Laying Down basic safety standards for protection against the dangers arising from exposure to ionizing radiation. *Official Journal of the European Union L, 13*, 1–73.

Garzon, W. J., Khoury, H., Ovalle, S. A. M., & Medeiros, R. B. (2019). Performance of the InstaDose dosemeter for interventional radiology and cardiology application. *Radiation Protection Dosimetry, 183*, 522–528. https://doi.org/10.1093/rpd/ncy172

GuideRadPROS (22NRM07). European partnership on metrology, EURAMET. https://lmri-met.github.io/sites-guideradpros/. (Accessed 3 September 2025).

Haag, D., Schmdt, S., Hufschmidt, P., Eberle, F., Michel, T., Anton, G., Hupe, O., Roth, J., Fuhg, C., Zutz, H., Behrens, R., Campbell, M., Llopart, X., Ballabriga, R., Tlustos, L., & Wong, W. (2021). Personal dosimetry in continuous photon radiation fields with the dosepix detector. *IEEE Transactions on Nuclear Science, 68*(5). https://doi.org/10.1109/TNS.2021.3068832

Hupe, O., Friedrich, S., Vanhavere, F., & Brodecki, M. (2019). Determining the dose rate dependence of different active personal dosemeters in standardized pulsed and continuous radiation fields. *Radiation Protection Dosimetry, 187*(3), 345–352. https://doi.org/10.1093/rpd/ncz173

ICRP. (2021). Use of dose quantities in radiological protection. ICRP Publication 147. *Ann. ICRP, 50*(1). Authors on behalf of ICRP J.D. Harrison, M. Balonov, F. Bochud, C. Martin, H.-G. Menzel, P. Ortiz-Lopez, R. Smith-Bindman, J.R. Simmonds, R. Wakeford.

International Atomic Energy Agency, IAEA. (2000). Calibration of radiation protection monitoring instruments. *Safety Reports Series*. IAEA SRS 16.

International Atomic Energy Agency, IAEA. (2018). *Occupational radiation protection - General safety guide no. GSG-7*.

International Electrotechnical Commission (IEC). (2009). Radiation protection instrumentation – Ambient and/or directional dose equivalent (rate) meters and/or monitors for beta. *X and gamma radiation – Part 1: Portable workplace and environmental meters and monitors*. IEC 60846-1:2009.

International Electrotechnical Commission, (IEC). (2024). *Radiation protection instrumentation - Measurement of personal dose equivalents for X, gamma, neutron and beta radiations - Active personal dosemeters - IEC 61526*. Geneva: IEC.

International Organization for Standardization, (ISO). (2019c). Radiological protection—X and gamma reference radiation for calibrating dosimeters and doserate meters for determining their response as a function of photon energy - Part 3: Calibration of area and personal dosimeters and the measurement of their response as a function of. *Photon energy and angle of incidence*. Geneva: ISO, 4037-3; 2019.

International Organization for Standardization, (ISO). (2019b). *Radiological protection—X and gamma reference radiation for calibrating dosimeters and doserate meters for determining their response as a function of photon energy - Part 2: Dosimetry for radiation protection over the energy ranges from 8 keV to 1,3 MeV and 4 MeV to 9 MeV*. Geneva: ISO, 4037-2; 2019.

International Organization for Standardization, (ISO). (2019a). Radiological Protection - X and gamma reference radiation for calibrating dosimeters and doserate meters for determining their response as a function for photon energy - Part 1. *Radiation characteristics and production methods*. Geneva: ISO, 4037-1; 2019.

International Organization for Standardization/International Electrotechnical Commission (ISO/IEC). (2017). *General requirements for the competence of testing and calibration laboratories – ISO/IEC 17025*.

Kržanović, N., Stanković, K., Živanović, M., Đaletić, M., & Ciraj-Bjelac, O. (2019). Development and testing of a low cost radiation protection instrument based on an energy compensated Geiger-Müller tube. *Radiation Physics and Chemistry, 164*, Article 108358. https://doi.org/10.1016/j.radphyschem.2019.108358

Kržanović, N., Živanović, M., Ciraj-Bjelac, O., Lazarević, Đ., Ćeklić, S., & Stanković, S. (2017). Performance testing of selected types of electronic personal dosimeters in X- and gamma radiation fields. *Health Physics, 113*, 252–261. https://doi.org/10.1097/HP.0000000000000704

Kržanović, N., Zutz, H., Hupe, O., Živanović, M., Ketelhut, S., & Luchkov, M. (2022). Harmonization of IEC type testing requirements and test methods for active area dosimeters in environmental monitoring. *Radiation Physics and Chemistry, 198*, Article 110291. https://doi.org/10.1016/j.radphyschem.2022.110291

Lee, Y., Won, Y., & Kang, K. (2016). Performance test results of active personal dosemeters (APDs) used in nuclear power plant in Korea: A comparison with thermos-luminescence dosimeters (TLDs). *Radiation Protection Dosimetry, 174*(3), 431–437. https://doi.org/10.1093/rpd/ncw174

Li, F., Lv, S., Qi, S., Cheng, P., Zeng, G.-Q., Xiao, M., & Sempau, J. (2025). Optimization of energy compensation layered structure of Geiger- Müller counters. *Nuclear Engineering and Technology, 57*(4), Article 103300. https://doi.org/10.1016/j.net.2024.11.002

Morosh, V., Röttger, A., Neumaier, S., Krasniqi, F., Živanović, M., Kržanović, N., Pantelić, G., Iurlaro, G., Mariotti, F., Sperandio, L., Bell, S., Ioannidis, S., Kelly, M., & Sangiorgi, M. (2021). Investigation into the performance of dose rate measurement instruments used in non-governmental networks. *Radiation Measurements, 143*, Article 106580. https://doi.org/10.1016/j.radmeas.2021.106580

O'Connor, U., Carinou, E., Clairand, I., Ciraj-Bjelac, O., De Monte, F., Domienik-Andrzejewska, J., Ferrari, P., Ginjaume, M., Hrsak, H., Hupe, O., Knezevic, Z., Sans Merce, M., Sarmento, S., Siiskonen, T., & Vanhavere, F. (2021). Recommendations for the use of active personal dosemeters (APDs) in interventional workplaces in hospitals. *Physica Medica, 87*, 131–135. https://doi.org/10.1016/j.ejmp.2021.05.015

Pavelić, L., Lacković, I., Surić Mihić, M., & Prlić, I. (2019). A technology overview of active ionizing radiation dosemeters for photon fields. *Radiation Protection Dosimetry, 188*(3), 361–371. https://doi.org/10.1093/rpd/ncz294

Ramadhan, R. A., Etzel, R., & Fiebich, M. (2024). Estimation of the backscatter radiation level in occupational interventional radiography. *J. Radiat. Res. App. Sci., 17*(2), Article 100865. https://doi.org/10.1016/j.jrras.2024.100865

Stanković Petrović, J., Knežević, Ž., Kržanović, N., Majer, M., Živanović, M., & Ciraj-Bjelac, O. (2021). Review of the thermoluminescent dosimetry method for the environmental dose monitoring. *Nuclear Technology & Radiation Protection, 36*(2), 150–162. https://doi.org/10.2298/NTRP2102150S

Struelens, L., Carinou, E., Clairand, I., Donadille, L., Ginjaume, M., Koukorava, C., Krim, S., Mol, H., Sans-Merce, M., & Vanhavere, F. (2011). Use of active personal dosemeters in interventional radiology and cardiology: Tests in hospitals – ORAMED project. *Radiation Measurements, 46*(11), 1258–1261. https://doi.org/10.1016/j.radmeas.2011.08.002

Vanhavere, F., & Van Hoey, O. (2022). Advances in personal dosimetry towards real-time dosimetry. *Radiation Measurements, 158*, Article 106862. https://doi.org/10.1016/j.radmeas.2022.106862

Vlahović, J., Kržanović, N., Stanković Petrović, J., Živanović, M., Bakrač, L., Nikolov, J., & Todorović, N. (2025). Examination of a hybrid dosimeter: Response to the radiation based influence quantities. *Radiation Physics and Chemistry, 235*, Article 112847. https://doi.org/10.1016/j.radphyschem.2025.112847

Yasar, D., Kapdan, E., & Korkmaz, M. (2017). Performance tests of active personal dosemeter developed by CNRTC/NEL. *Radiation Protection Dosimetry, 176*(4), 380–387. https://doi.org/10.1093/rpd/ncx021

Živanović, M., Hupe, O., Zutz, H., Šabeta, A., Sandtner, S., & Kržanović, N. (2023). EURAMET DOSEtrace supplementary comparison in terms of the ambient dose equivalent/rate for photon radiation (EURAMET.RI(I)-S18). *Metrologia, 60*(1A), Article 06017. https://doi.org/10.1088/0026-1394/60/1A/06017

Marine Chemistry 273 (2025) 104573

Contents lists available at ScienceDirect

Marine Chemistry

journal homepage: www.elsevier.com/locate/marchem

pH_T measurements of TRIS buffer solutions in artificial seawater matrix in the salinity range 5–40 and temperature range 5–40 °C. Part 2: Uncertainty of pH_T values

Rieke Schäfer [a,*], Gaëlle Capitaine [b,c], Frank Bastkowski [a], Daniela Stoica [b], Olivier Pellegrino [d], Raquel Quendera [d], Eric P. Achterberg [e], Simon L. Clegg [f], Paola Fisicaro [b], Steffen Seitz [a]

[a] Physikalisch-Technische Bundesanstalt (PTB), Bundesallee 100, 38116, Braunschweig, Germany
[b] Laboratoire National de Métrologie et d'Essais, 1 Rue Gaston Boissier, 75015, Paris, France
[c] Aix Marseille Université, CNRS, IRD, MIO, 13288, Marseille, France
[d] Departamento de Metrologia, Instituto Português da Qualidade, R. António Gião, 2, Caparica, 2829-513, Portugal
[e] GEOMAR Helmholtz Centre for Ocean Research Kiel, Wischhofstraße 1-3, Geb. 12, 24148, Kiel, Germany
[f] School of Environmental Sciences, University of East Anglia, Norwich, NR4 7TJ, United Kingdom

ARTICLE INFO

Dataset link: 10.5281/zenodo.14964822, 10.5281/zenodo.14964817

Keywords:
Weighted RMSE
Harned cell measurements
Metrology
Monte Carlo simulation
Total pH

ABSTRACT

In the first part of this study, we determined a fit function which allows the calculation of the total pH (pH_T) value of an artificial seawater/2-amino-2-(hydroxymethyl)-1,3-propanediol (TRIS) buffer, extrapolated to 0 mol kg^{-1} H_2O TRIS molality (i.e. to a true pH_T scale), in terms of temperature and practical salinity. In this second part, we present a method to quantify the uncertainty of that function. The uncertainty plays an important role in the characterization of the indicator dye used for the routine spectrophotometric pH_T measurement in seawater. However, it has not been determined previously. We assigned uncertainties to measured input quantities, and propagated them through the calculation steps described in the first part. Both, analytical uncertainty calculation and Monte Carlo simulations have been applied to adequately consider the various steps of the procedure needed to calculate pH_T values of artificial seawater. The combined standard uncertainty of $pH_T(S, T, b(\mathrm{TRIS}) = 0\,\mathrm{mol\,kg^{-1}\,H_2O})$ for artificial seawater/TRIS buffers was 0.0011 over the practical salinity range 5 to 40 and temperature range 5 °C to 40 °C. This uncertainty can now be used to determine, the uncertainties of the characterization of the indicator dye used for seawater pH_T measurements.

1. Introduction

In part 1 of this study (Capitaine et al., 2025), we presented pH_T primary measurements of artificial seawater (ASW)/2-amino-2-(hydroxymethyl)-1,3-propanediol (TRIS) buffers in the nominal practical salinity S range from 5 to 40 and temperature T range from 5 °C to 40 °C. The results were used as a basis to fit a function describing the dependence of pH_T on temperature and salinity in artificial seawater. This function can be used for the characterization of meta-Cresol Purple, an indicator dye for seawater pH_T measurements. With the uncertainties associated with the pH_T reference material used for the characterization, uncertainties can be propagated to the final pH_T measurements of seawater. This topic is of interest because anthropogenic emissions of CO_2 decrease the pH value of the ocean (Calvin et al., 2023; Friedlingstein et al., 2023) which needs to be monitored. Reliable measurements with adequately determined measurement uncertainties are essential to accurately assess ocean acidification (Newton et al., 2015).

The Harned cell measurement of pH_T in artificial seawater at different temperatures T and salinities S with a TRIS buffer of molality b(TRIS) (see Buck et al., 2002 for detailed information on primary pH measurements), and the determination of the fit function involve a variety of measurements and calculation steps. This makes the determination of appropriate uncertainties a difficult and complex task. In this part 2, we demonstrate and discuss in detail how the uncertainties of the measured pH_T values were quantified and how these uncertainties are considered to assign an uncertainty to the fit function. In the future,

* Corresponding author.
E-mail addresses: rieke.schaefer@ptb.de (R. Schäfer), gaelle.capitaine@lne.fr (G. Capitaine), frank.bastkowski@ptb.de (F. Bastkowski), daniela.joubertstoica@cea.fr (D. Stoica), opellegrino@ipq.pt (O. Pellegrino), rquendera@ipq.pt (R. Quendera), eachterberg@geomar.de (E.P. Achterberg), s.clegg@uea.ac.uk (S.L. Clegg), paola.fisicaro@lne.fr (P. Fisicaro), steffen.seitz@ptb.de (S. Seitz).

https://doi.org/10.1016/j.marchem.2025.104573
Received 12 March 2025; Received in revised form 2 September 2025; Accepted 12 October 2025
Available online 17 October 2025

Table 1
Overview of the key packages and package bundles used in R with their version number and respective main use. A full list of package versions is included with the code (doi:10.5281/zenodo.14964817).

Package	Use	Version	Citation
`MASS`	stepwise model selection by AIC[a]	7.3.65	Venables and Ripley (2002)
`metafor`	uncertainty of extrapolations	4.8.0	Viechtbauer (2010)
`metRology`	uncertainties following (BIPM et al., 2008a)	0.9.29.2	Ellison (2018)
`mltools`	weighted RMSE[b]	0.3.5	Gorman (2018)
`tidymodels` bundle	leave-one-out cross-validation	1.3.0	Kuhn and Wickham (2020)
`tidyverse` bundle	data processing	2.0.0	Wickham et al. (2019)

[a] AIC – Akaike Information Criterion.
[b] RMSE – root-mean-squared error.

those uncertainties can be used to determine the uncertainties in the characterization of the indicator dye meta-Cresol Purple (specifically the uncertainty of $pK_2^T e_2$) which is used in seawater pH_T measurements. As far as we are aware, the uncertainty of the fit function was not available previously thus interrupting the uncertainty propagation for spectrophotometric seawater pH_T measurements. As such the uncertainty value presented in this work, constitutes an important step on the way to establishing full metrological traceability for those measurements.

The complete model to determine the fit function from the measured input quantities involved a variety of steps. While the uncertainties of some of the intermediate results were better calculated by uncertainty propagation according to the "Guide of the expression of uncertainty in measurement" (GUM) (BIPM et al., 2008a), the use of a Monte Carlo approach (BIPM et al., 2008b) was more suitable for others, i.e., the involved fitting procedures. The main challenges to address were: (i) the determination of reasonable uncertainties of extrapolated values; and (ii) the determination of the uncertainty of a pH_T value at a specific temperature and salinity calculated from the fit function. To tackle these challenges, we have employed a step-wise approach in which we calculated the uncertainties of each step individually by different methods. This approach combined analytical and numerical methods from the GUM and its supplements.

2. Uncertainty of primary $pH_T(S,T,b(\mathrm{TRIS}))$ values of ASW/TRIS buffers

The measurement model used to determine the fit function $pH_T(S,T,b(\mathrm{TRIS}))$ has been detailed in part 1 (Capitaine et al., 2025). From that model, the $pH_T(S,T,b(\mathrm{TRIS}) = 0\,\mathrm{mol\,kg^{-1}\,H_2O})$ value of a given artificial seawater standard at nominal practical salinity S and temperature T, referred to a TRIS molality of $0\,\mathrm{mol\,kg^{-1}\,H_2O}$, was calculated. In summary, the model involved the following fundamental steps:

1. calculation of water mass fraction, ω_{H_2O}, of the buffer and equimolal TRIS and TRIS hydrochloride (TRIS.HCl) molality, b(TRIS), in water,
2. determination of the standard potential, E^{0*}, of the silver-silver chloride electrodes in artificial seawater media,
3. calculation of the ASW/TRIS buffer $pH_T(S,T,b(\mathrm{TRIS}))$ value and
4. fitting of the function.

Each step required a specific approach to determine the associated uncertainties which are needed to propagate the uncertainties of the measured input quantities to the combined uncertainty of $pH_T(S,T)$. In the following section, the uncertainty calculation and data processing are described and discussed for each step to determine the primary $pH_T(S,T,b(\mathrm{TRIS}))$ value of the ASW/TRIS buffer. The next section describes the uncertainty determination for the last step, the fitting of the function.

Calculations were done in R version 4.3.2 (R Core Team, 2023). Table 1 lists key packages with their versions. The data and code can be found in doi:10.5281/zenodo.14964822 and doi:10.5281/zenodo.14964817, respectively. Additionally, a custom R package was developed to combine many of the main functions needed. It is available as part of the code.

2.1. Uncertainties of ASW/TRIS buffer preparation

Stock solutions for ASW/TRIS buffer and HCl solutions were prepared gravimetrically at the Physikalisch-Technische Bundesanstalt (PTB, Germany). The purities of all salts were measured by coulometric titration at the Slovak Institute of Metrology (purities are shown in Table 2). The HCl solutions were characterized with coulometry at the Danish National Metrology Institute (under DANAK accreditation reg. No. 255). The ASW/TRIS buffer solutions were prepared at PTB, while the ASW/HCl solutions needed to determine the standard potential of the silver-silver chloride electrodes in artificial seawater, E^{0*}, were prepared from the stock solutions by Instituto Português da Qualidade (IPQ, Portugal), Laboratoire National de Métrologie et d'Essais (LNE, France) and PTB individually. The measured masses were corrected for air buoyancy (for details see Supplementary Material 1). The water mass fraction, ω_{H_2O}, was calculated from the nominal practical salinity, S, as defined in part 1 section 2.3 (Capitaine et al., 2025) with

$$\omega_{H_2O} = 1 - 0.0010047 \cdot S \tag{1}$$

(Clegg et al., 2022). This was used to convert from the molality-based to the amount-content-based pH_T scale based on the reference composition of seawater and its practical salinity. The factor with the value of 0.0010047 was established by Clegg et al. (2022) (as opposed to 0.00106 used by DelValls and Dickson (1998)). The uncertainty of the nominal practical salinity was calculated as the combined uncertainty of the mass measurements needed for the preparation of stock solutions and subsequent preparation of ASW/TRIS buffers, as well as the difference between the measured mass and the target mass of the artificial seawater recipe (for details see Supplementary Material 2). The uncertainties of the TRIS molality were determined from the uncertainties of the measured masses and their impurities. Propagation of uncertainties was performed within the GUM (BIPM et al., 2008a) framework, using the `metRology` package (Ellison, 2018) with the uncertainties of the molar masses assumed to be $0\,\mathrm{kg\,mol^{-1}}$ (Meija et al., 2016).

Table 3 shows an example uncertainty budget for a nominal practical salinity of 35. The main uncertainty contributors were the molalities of NaCl and $MgCl_2$. A visual summary of the uncertainty calculation and the relative contribute of the different components is given in Supplementary Material 3.

2.2. Uncertainties of potential and temperature measurements

At IPQ, the potential difference between the electrodes was measured using a Keithley 2700 digital multimeter (Keithley Instruments, Solon, United States) and recorded with XLinx software. Measurements were recorded every minute. pH_T calculations were based on the mean

Table 2
Characterization of salts and solutions by the Slovak Institute of Metrology and the Danish National Metrology Institute.

(a) Purity characterizations of salts and solutions with their absolute standard uncertainty.

Substance	Purity / %	Standard uncertainty / %
KCl	99.880	0.018
NaCl	99.842	0.018
Na_2SO_4	99.999	0.0135
TRIS	99.925	0.027

(b) Amount contents of solutions.

Substance	Amount content / mol kg^{-1}	Standard uncertainty / mol kg^{-1}
$CaCl_2$	0.51586	0.00009
HCl	0.106494	0.000019
	0.106470	0.000019
$MgCl_2$	1.42292	0.00029

Two different batches of HCl were used.

Table 3
Example uncertainty budget for an ASW/TRIS buffer of nominal practical salinity 35 and b(TRIS) = 0.025 mol kg^{-1} H_2O, made from stock solutions (PTB). The uncertainty of the molality already includes both the weighing uncertainty and the component from the difference to target weight. The last column shows the individual uncertainty contributions to the combined standard uncertainty of the nominal practical salinity (in the last row). A visual summary of the uncertainties is given in Supplementary Material 3. For the equation to calculate the salinity, see Supplementary Material 2. The shown numbers were rounded for presentation. For precise numbers, please see the original calculations provided in doi:10.5281/zenodo.14964817.

Substance	Molality / mol kg^{-1} H_2O	Standard uncertainty / mol kg^{-1} H_2O	Sensitivity coefficient / kg H_2O mol^{-1}	Uncertainty contribution
NaCl	0.40253	$2.2 \cdot 10^{-4}$	46.74431	0.010086
$MgCl_2$	0.054736	$3.0 \cdot 10^{-5}$	140.2329	0.004182
Na_2SO_4	0.029262	$1.5 \cdot 10^{-5}$	140.23294	0.0021464
HCl	0.025097	$4.2 \cdot 10^{-5}$	46.74431	0.0019647
$CaCl_2$	0.010501	$5.7 \cdot 10^{-6}$	140.23294	0.0008060
KCl	0.0105793	$5.8 \cdot 10^{-6}$	46.74431	0.0002701
combined standard uncertainty for the nominal practical salinity				0.011

potential data collected over one hour, after reaching a stable potential (standard deviation below $5 \cdot 10^{-5}$ V).

The potential difference between the electrodes at LNE was measured using an Agilent 34972 A data acquisition system (Agilent, Santa Clara, United States) and recorded with Agilent Benchlink Data Logger software (Agilent, Santa Clara, United States). Measurement results were recorded every 2 min. pH_T calculations were made from the mean of potential data acquired over one hour with a stable potential signal (i.e., standard deviation below $2 \cdot 10^{-5}$ V).

At PTB, the potential was measured with a digital multimeter (3458 A, Agilent, Santa Clara, United States). The system was stabilized for 45 min. The potential was recorded every five minutes and averaged over 50 min once a stable potential (standard deviation below $5 \cdot 10^{-5}$ V over 11 measurements) was reached.

Potentials were measured with a mean standard uncertainty of $5.4 \cdot 10^{-6}$ V (IPQ), $6.1 \cdot 10^{-6}$ V (LNE) and $2 \cdot 10^{-5}$ V (PTB) after the correction to a hydrogen pressure of 1 atm. The main uncertainty components were the uncertainty of the electrode potentials, the uncertainty of the multimeter and the repeatability of the measurement.

At IPQ, Harned cell measurements were performed at 20 °C, 25 °C, and 30 °C. The cells were placed in a Lauda Proline PV36 thermostatic bath with the temperature measured by three Pt100 probes.

Harned cell measurements at LNE were conducted at 15 °C, 25 °C, and 30 °C. Cells were placed in a TAMSON thermostatic bath with five Pt100 probes to measure temperature. Measurement results were recorded every 2 min. The temperature was averaged within each condition across the time the potential was measured and then averaged across the five temperature probes.

At PTB, temperature was measured with four PT100 temperature probes connected to a F250 MKII thermometer (Automatic Systems Laboratories (ASL), Sevenoaks, United Kingdom) evenly distributed inside the temperature bath. The temperature result was averaged within each condition across the time the potential was measured and then averaged across the four temperature probes. Calibration uncertainty and stability of the temperature measurement (standard deviation) had similar values of 0.0017 K and 0.0014 K. Their combined contribution was about one order of magnitude smaller (mean of 0.000692 K) than the value of the temperature inhomogeneity within the bath (mean of 0.00776 K).

Temperatures were measured with a mean standard uncertainty of 0.021 °C (IPQ), 0.011 °C (LNE) or 0.0045 °C (PTB).

As mentioned in part 1, the pH_T values at a nominal practical salinity 20 were excluded from the analysis. As can bee seen in figure 2 in part 1 especially for a TRIS molality of 0.025 mol kg^{-1} H_2O, they were lower compared to the values of the adjacent salinities. As a consequence, the residuals from the fit are likewise unusually large at nominal practical salinity 20. The deviation has been measured by PTB and LNE. Therefore, a defect of the measurement system can be excluded. However, a similar anomaly was not seen in the works of DelValls and Dickson (1998) and Müller et al. (2018). Therefore, and because PTB and LNE have measured samples from the same batch, it is much more likely that an unnoticed error occurred during the preparation of salinity 20 solutions than that an unusual physicochemical effect caused the observed anomaly, for which there is no explanation. Therefore, we decided to exclude the values at nominal practical salinity 20. We have conducted repeated fits in which we

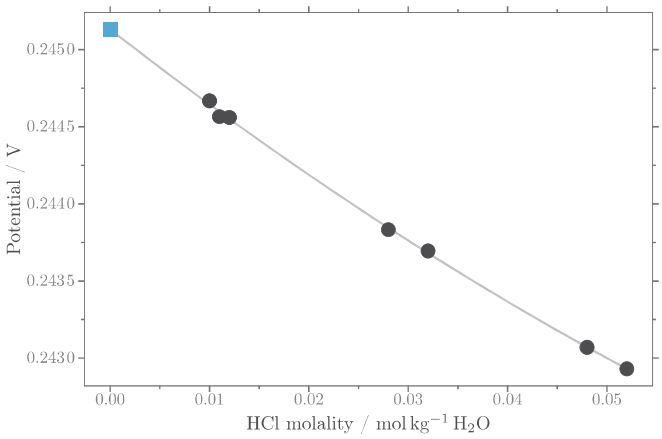

Fig. 1. Example extrapolation of measured potentials (E', black points) to determine an extrapolated value for b(HCl) equal to zero (E^{0*}, blue square) at 25 °C, nominal practical salinity 25 from measurements carried out at PTB. The thin black line shows the quadratic fit used to determine the extrapolated value.

have removed the data at a single condition to investigate the effect on the fit function. They showed that the fit was robust against removal, especially for salinities in the middle of the salinity range.

2.3. Uncertainties of the standard potential E^{0*}

E^{0*} values (see equations (7) and (8) in part 1) have been determined for each salinity and temperature condition from the potential measurements of the corresponding ASW/HCl solutions. They were calculated from a quadratic extrapolation of the measured potentials to 0 mol kg^{-1} H$_2$O HCl molality as in Dickson (1990) (see Fig. 1 as an example). The extrapolation and uncertainty of this extrapolated value were determined with the `metafor::rma` function (Viechtbauer, 2010). We chose this method because we wished to propagate the uncertainties of the potential to the extrapolated value. The `metafor::rma` function uses the covariance matrix the uncertainties of the input potentials to include them in the determination of the uncertainty at 0 mol kg^{-1} H$_2$O. The distribution of HCl molalities was chosen to minimize the expected uncertainty of the extrapolated value.

The uncertainties of E^{0*} and residuals of the fit did not vary significantly across measurement conditions. The average uncertainty was $2.9 \cdot 10^{-5}$ V, and the root-mean-squared error (RMSE) of all residuals was $3.4 \cdot 10^{-5}$ V. For the measurements at PTB, the RMSE of the residuals of the fit was always smaller compared to the uncertainty determined for E^{0*}. For the measurements at LNE and IPQ, the residuals were generally higher compared to the uncertainty, and also compared to the residuals of the PTB data (absolute residual up to $2.3 \cdot 10^{-4}$ V compared to the maximum of $5.7 \cdot 10^{-5}$ V in PTB measurements).

2.4. Uncertainties of measured $pH_T(S, T, b(TRIS))$ values

Uncertainties of the measured $pH_T(S, T, b(TRIS))$ values at nominal practical salinity S, temperature T and TRIS molality b(TRIS) were calculated according to the GUM framework (BIPM et al., 2008a) by propagating the uncertainties of the above-mentioned input quantities through

$$pH_T = \frac{E - E^{0*}}{(R \cdot T \cdot \ln(10)) \cdot F^{-1}} + \log\left(\frac{b(Cl^-)}{b_0}\right) - \log(\omega_{H_2O}). \quad (2)$$

E is the measured potential of the ASW/TRIS buffer corrected to 1 atm H_2 pressure, R is the molar gas constant, T is temperature in kelvin, F is the Faraday constant, $b(Cl^-)$ is the molality of Cl^- ions, b_0 is the standard molality (b_0 = 1 mol kg^{-1} H$_2$O and ω_{H_2O} is the water mass fraction (Clegg et al., 2022, equation 1). The `metRology` package (Ellison, 2018) was used for the uncertainty propagation.

Table 4 shows an exemplary uncertainty budget of a $pH_T(S, T, b(TRIS))$ value. The uncertainty components with the highest contribution were those of E and E^{0*}, followed by temperature, molality of Cl^- and ω_{H_2O}. A visual summary of the uncertainty calculation is given in Fig. 2 and the relative contribution of the different components is shown in Supplementary Material 3.

The uncertainty contribution of E to pH_T was almost constant across the temperature and salinity range with only a slight decrease at higher temperatures. The uncertainty contribution of E^{0*} showed little variation but had some outliers with higher uncertainties at nominal practical salinity 5 and 30 and lower uncertainties at nominal practical salinity 35. The uncertainty contribution of the molality of Cl^- increased for all temperatures with increasing salinity from around $4.8 \cdot 10^{-5}$ mol kg^{-1} H$_2$O to $5.7 \cdot 10^{-5}$ mol kg^{-1} H$_2$O. The uncertainty contribution of the temperature increased slightly with increasing temperature and decreasing salinity. And the uncertainty contribution of ω_{H_2O} was constant across temperatures but decreased with increasing salinity. The combined uncertainty of $pH_T(S, T, b(TRIS))$ values was stable across all conditions with a few outliers resulting from variations in the uncertainties of E^{0*}.

2.5. Uncertainties of consensus $pH_T(S, T, b(TRIS))$ values

If measured $pH_T(S, T, b(TRIS))$ values were provided by more than one institute for a combination of (nominal) salinity, temperature and TRIS molality, we calculated the weighted mean of the $pH_T(S, T, b(TRIS))$ results and their uncertainties using the Graybill-Deal estimator with dispersion (CCQM, 2013). We chose the uncertainty-weighted mean to account for different uncertainties of the individual measurements and included dispersion correction to include interlaboratory differences. This step was not necessary and therefore skipped if the condition was measured by only one institute.

Fig. 3 illustrates the distribution of the standard uncertainties of the $pH_T(S, T, b(TRIS))$ measurement results as a function of temperature and salinity. The uncertainty of $pH_T(S, T, b(TRIS))$ for conditions where measurements were taken at more than one institution was between $1.2 \cdot 10^{-5}$ and $2 \cdot 10^{-3}$ in pH_T units. If only measurements from PTB were available, the uncertainties were between $2.8 \cdot 10^{-4}$ and $1.6 \cdot 10^{-3}$ in pH_T units.

As uncertainties of the pH_T values for TRIS buffer solutions have not been routinely determined previously, limited literature is available for comparison. The uncertainties for the measurements by Müller et al. (2018) were mostly in the range between $1 \cdot 10^{-3}$ to $2.1 \cdot 10^{-3}$ in pH_T units. Our maximum uncertainties had similar values. However, our minimum uncertainties were lower. This was caused by the combination of measurements from different institutes and, in the case of PTB, lower uncertainties of the determined E^{0*}.

In the data by Müller et al. (2018), a tendency for higher uncertainties at higher temperatures and lower salinities can be observed. We did not observe this trend. This is likely due to improved temperature stability of the measurement set-up and the correction of the ASW/TRIS buffer composition.

3. Uncertainty of the fitted equation $pH_{T,c}(S, T, b(TRIS) = 0$ mol kg^{-1} H$_2$O)

3.1. Fitting procedure

We used the equation proposed by Müller et al. (2018) to calculate a fit function describing the dependence of pH_T on salinity, temperature and TRIS molality. However, since we have omitted the $pH_T(S, T, b(TRIS))$ results at TRIS molality b(TRIS) = 0.01 mol kg^{-1} H$_2$O

Table 4
Example uncertainty budget for nominal practical salinity 35, temperature 25 °C and TRIS molality 0.025 mol kg^{-1} H_2O at PTB, before averaging. The last column shows the uncertainty contribution of the individual components to the combined uncertainty. A visual summary of the uncertainties is given in Fig. 2 with the relative contributions of each visualized in Supplementary Material 3. The shown numbers were rounded for presentation. For precise numbers, please see the original calculations provided in doi:10.5281/zenodo.14964817.

Component	Value	Standard uncertainty	Sensitivity coefficient	|Uncertainty contribution|
E	0.738154 V	$2.0 \cdot 10^{-5}$ V	16.902875 V^{-1}	$3.38 \cdot 10^{-4}$
E^{0*}	0.245972 V	$2.0 \cdot 10^{-5}$ V	−16.902875 V^{-1}	$3.377 \cdot 10^{-4}$
T	298.16 K (25.01 °C)	$4.7 \cdot 10^{-3}$ K	−0.0279 K^{-1}	$1 \cdot 10^{-4}$
$b(Cl^-)$	0.569177 mol kg^{-1} H_2O	$7.7 \cdot 10^{-5}$ mol kg^{-1} H_2O	0.763022 kg H_2O mol^{-1}	$5.83 \cdot 10^{-5}$
ω_{H_2O}	0.964836 g/kg sol	$1.1 \cdot 10^{-5}$ g/kg sol	−0.4501228 kg sol g^{-1}	$5.12 \cdot 10^{-6}$
combined standard uncertainty of the pH_T value				$4.993 \cdot 10^{-4}$

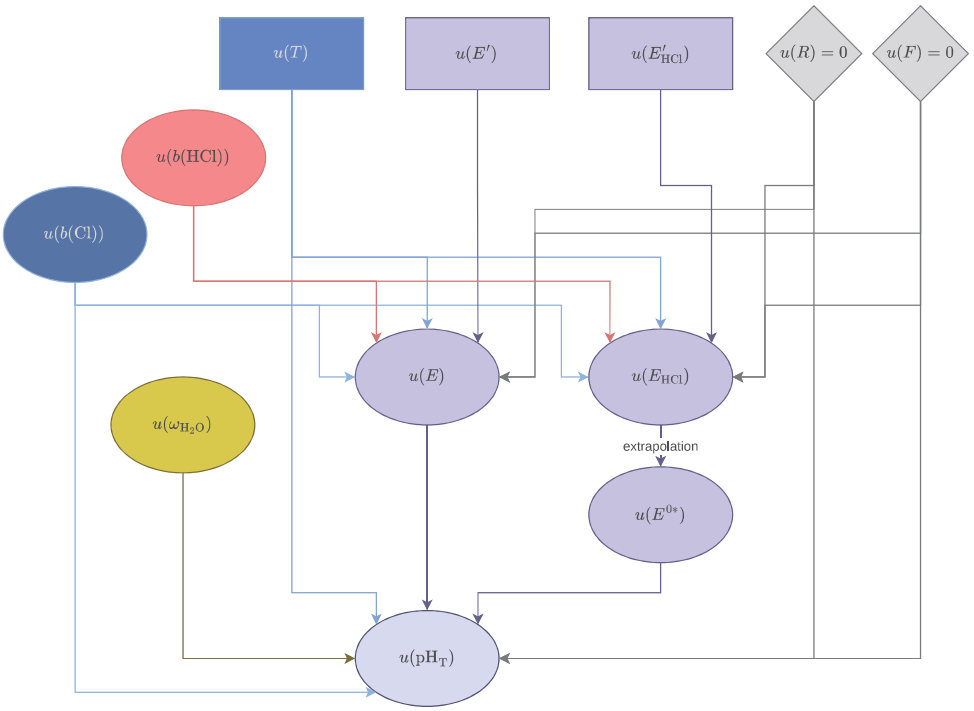

Fig. 2. Contributions to the uncertainty of a single pH_T value. Gray boxes indicate constants. The blue and green reference the corresponding contributions in Supplementary Material 3. The lighter the blue/purple, the larger the contribution.

and expected a linear relationship across TRIS molalities, we have considered only the linear term of TRIS molality in the equation:

$$\begin{aligned} \mathrm{pH}_{\mathrm{T},c}(S,T,b(\mathrm{TRIS})) = {} & g + h_1 \cdot S + h_2 \cdot S^2 + h_3 \cdot S^3 + i_1 \cdot T_d + i_2 \cdot \ln(T_d) \\ & + i_3 \cdot \frac{1}{T_d} + j_1 \cdot S \cdot T_d + j_2 \cdot S^2 \cdot T_d + j_3 \cdot S^3 \cdot T_d \\ & + j_4 \cdot S \cdot \ln(T_d) + j_5 \cdot S^2 \cdot \ln(T_d) + j_6 \cdot S^3 \cdot \ln(T_d) \\ & + k_1 \cdot S \cdot \frac{1}{T_d} + k_2 \cdot S^2 \cdot \frac{1}{T_d} + k_3 \cdot S^3 \cdot \frac{1}{T_d} \\ & + l_1 \cdot b_d(\mathrm{TRIS}) + l_2 \cdot b_d(\mathrm{TRIS}) \cdot S \\ & + l_3 \cdot b_d(\mathrm{TRIS}) \cdot T_d + l_4 \cdot b_d(\mathrm{TRIS}) \cdot S \cdot T_d, \end{aligned} \tag{3}$$

where temperature and TRIS molality are of dimension one, given as

$$T_d = \frac{T}{T_0} \tag{4}$$

and

$$b_d(\mathrm{TRIS}) = \frac{b(\mathrm{TRIS})}{b_0} \tag{5}$$

and with nominal practical salinity S, temperature T in kelvin, standard temperature $T_0 = 1$ K, TRIS molality b(TRIS) in mol kg^{-1} H_2O and standard molality $b_0 = 1$ mol kg^{-1} H_2O. We have fitted the equation to the dataset with TRIS molalities of 0.025 and 0.04 mol kg^{-1} H_2O. The $pH_{T,c}(S,T,b(\mathrm{TRIS}))$ value of artificial seawater at 0 mol kg^{-1} H_2O TRIS molality was then calculated by inserting $b(\mathrm{TRIS}) = 0$ mol kg^{-1} H_2O.

We used a generalized linear model with the `glm` function (R Core Team, 2023) to fit the data and weighted them with the uncertainty of the $pH_T(S,T,b(\mathrm{TRIS}))$ values: $\frac{1}{u(\mathrm{pH_T})^2}$. The `stepAIC` function was used to perform a stepwise model selection based on the Akaike Information Criterion (AIC) (Venables and Ripley, 2002). The numbers of relevant digits of the coefficients were determined by checking with how many digits the calculated $pH_{T,c}(S,T,b(\mathrm{TRIS}))$ value of the function stabilized compared to the standard uncertainty.

3.2. Uncertainty determination

The uncertainty of $pH_{T,c}(S,T,b(\mathrm{TRIS}) = 0\,\mathrm{mol\,kg^{-1}}\ H_2O)$ was determined from the weighted RMSE of the fit (u_{RMSE}) and from the variation of the $pH_{T,c}(S,T,b(\mathrm{TRIS}))$ values at 0 mol kg^{-1} H_2O TRIS molality in three Monte Carlo simulations (u_{MC}). This combination allowed us to consider the goodness of fit and the robustness of the extrapolation with respect to uncertainty.

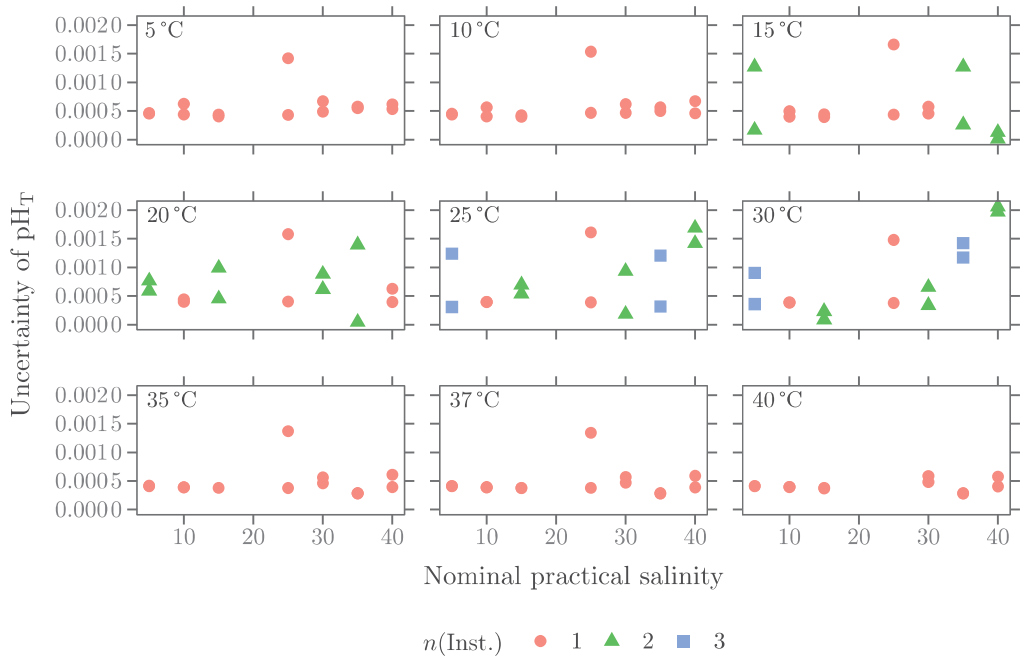

Fig. 3. Standard uncertainties of the $pH_T(S,T,b(\text{TRIS}))$ values calculated from the measurements of the individual institutes. The differently colored shapes indicate how many institutes (n(Inst.)) measured under the specific condition. The two TRIS molalities did overall not differ in their uncertainties significantly and are not distinguished here, therefore, there are two points for each salinity-temperature combination (though sometimes so similar in value that they are indistinguishable). Each plot shows the data for the temperature indicated at the top.

The weighted RMSE of the fit was calculated with the `mltools::rmse` function (Gorman, 2018). The weights were the same as for the fit: $\frac{1}{u(pH_T)^2}$. The weighing of the RMSE with uncertainties meant that values with a higher uncertainty contributed less to the RMSE. This was chosen to adequately account for the different levels of confidence in the values as indicated by the uncertainties.

In each Monte Carlo simulation run, a new dataset was generated by random draws from the measurement value distributions of pH_T, temperature, salinity and TRIS molality data. The starting points of the simulations were pH_T data at 0.025 mol kg^{-1} H_2O and 0.04 mol kg^{-1} H_2O TRIS molality, with their respective temperature, salinity and TRIS molality data. We assumed normal distributions for all input data. Since the main contribution to uncertainties of the $pH_T(S,T,b(\text{TRIS}))$ values are the statistical variation of the potential measurements and the interlaboratory reproducibility, correlation of the input data have not been considered in the determination of the uncertainty of the fit.

We used the function coefficients from the stepwise selected model of the original fit in the Monte Carlo simulation. It was fitted in each run to the generated dataset. Using the fit function of a single run, the $pH_{T,c}(S,T,b(\text{TRIS}) = 0\,\text{mol kg}^{-1}\,H_2O)$ values for all nominal temperatures and salinities were calculated and saved. For each combination of temperature and salinity, the standard deviation of the $pH_{T,c}(S,T,b(\text{TRIS}) = 0\,\text{mol kg}^{-1}\,H_2O)$ values was finally calculated across all runs. A Monte Carlo simulation involved 30,000 runs, which was sufficient to let the standard deviations of the three independent simulations converge. The uncertainty component u_{MC} for the variation of $pH_{T,c}(S,T,b(\text{TRIS}) = 0\,\text{mol kg}^{-1}\,H_2O)$ was calculated as the average standard deviation from three independent Monte Carlo simulations.

The combined uncertainty u_c was then calculated as

$$u_c = \sqrt{u_{RMSE}^2 + u_{MC}^2}. \tag{6}$$

u_c estimates the uncertainty of the $pH_{T,c}(S,T,b(\text{TRIS}) = 0\,\text{mol kg}^{-1}\,H_2O)$ value of an artificial seawater standard at a given salinity and temperature.

3.3. Uncertainty of $pH_{T,c}(S,T,b(TRIS) = 0\,mol\,kg^{-1}\,H_2O)$

We have presented the fit function describing pH_T depending on salinity and temperature in part 1 (Capitaine et al., 2025). Fig. 4 visualizes the fit function with the uncertainty. The two uncertainty contributions had values in the same order of magnitude: 0.000 42 from the RMSE of the fit (u_{RMSE}) and 0.000 99 from the variation of the extrapolated values in the Monte Carlo simulation (u_{MC}; the variations for other molalities up to 0.04 mol kg^{-1} H_2O were smaller than this value for 0 mol kg^{-1} H_2O). u_{RMSE} is smaller than the goodness-of-fit value reported by DelValls and Dickson (1998) which was 0.000 71. As the RMSE is calculated across the whole salinity, temperature and TRIS molality range and the extrapolated values did not show a relevant pattern across all conditions either, we have decided to use a single uncertainty estimate for $pH_{T,c}(S,T,b(\text{TRIS}) = 0\,\text{mol kg}^{-1}\,H_2O)$ for all temperature and salinity conditions. Thus, the combined standard uncertainty of the $pH_{T,c}(S,T,b(\text{TRIS}))$ value at 0 mol kg^{-1} H_2O TRIS molality (u_c) is 0.001 1 in pH_T units.

To assess the quality of the fit function, we have applied a leave-one-out cross-validation, which showed less variation (maximum: 0.000 11) than the uncertainty we have assigned to $pH_{T,c}(S,T,b(\text{TRIS}) = 0$ mol kg^{-1} $H_2O)$ (Fig. 5). This demonstrates the stability of the fit. It further justifies that leaving out the results at salinity 20 for the reason mentioned in part 1 (see section 2.6.1) has little effect on the reliability of the fit function.

In this work, we have decided to fit a function through the measured $pH_T(S,T,b(\text{TRIS}))$ values and calculate $pH_{T,c}(S,T,b(\text{TRIS}) = 0\,\text{mol kg}^{-1}\,H_2O)$ at zero TRIS molality. Alternatively, it would have been possible to extrapolate $pH_T(S,T,b(\text{TRIS}))$ for each temperature-salinity combination to 0 mol kg^{-1} H_2O TRIS molality first, and use the extrapolated results to calculate the pH_T at 0 mol kg^{-1} H_2O TRIS molality as a function of salinity and temperature. The weighted RMSE was 0.001 4. However, even though that function did represent the extrapolated values well the dependence on salinity and temperature seen at 0.025 mol kg^{-1} H_2O and 0.04 mol kg^{-1} H_2O TRIS molality was not well reflected. This was due to variations in the measurement data that were amplified in the extrapolation to 0 mol kg^{-1} H_2O

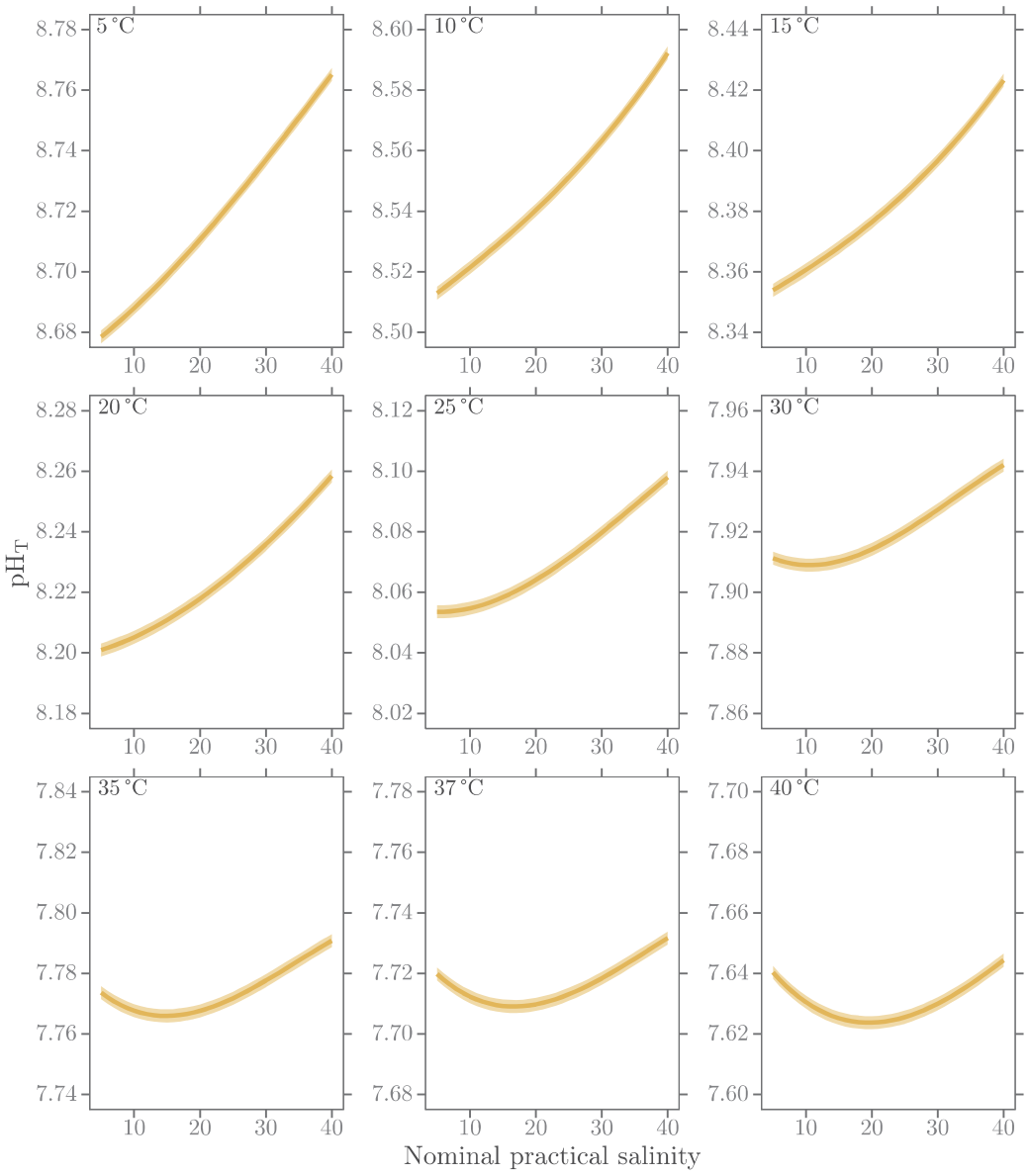

Fig. 4. Fit function at 0 mol kg^{-1} H_2O TRIS molality with uncertainty. The lines show the fit function at 0 mol kg^{-1} H_2O TRIS molality, the shaded area is the expanded uncertainty ($k = 2$). Each plot shows the data for the temperature indicated at the top. Note that the y-axis ranges are different between the individual plots.

TRIS molality. Locally extrapolated values amplified the effect of the measurement variation on the extrapolation, while global extrapolation smoothed local variations. For example, in some cases the $pH_T(S, T, b(\text{TRIS}))$ value for 0.04 mol kg^{-1} H_2O TRIS molality was lower than for 0.025 mol kg^{-1} H_2O, which does not comply with the expectation that it should be the other way round (Clegg et al., 2022). As a consequence, the fit function was distorted to some extent. In contrast, the fit presented in this work smoothed such irregularities and did not affect the dependence on salinity and temperature seen at 0.025 mol kg^{-1} H_2O and 0.04 mol kg^{-1} H_2O TRIS molality significantly.

4. Role of ASW/TRIS buffer standards for the characterization of the indicator dye meta-Cresol Purple and its uncertainty

We have described the uncertainty of the pH_T value of ASW/TRIS buffers, having a nominal practical salinity between 5 and 40, a temperature between 5 °C and 40 °C and for $b(\text{TRIS}) = 0$ mol kg^{-1} H_2O. Currently, such ASW/TRIS buffers are used to characterize the $pK_2^T e_2$ value of the indicator dye meta-Cresol Purple (Liu et al., 2011; Müller and Rehder, 2018). This characterization is essential for conducting spectrophotometric pH_T measurements. Traceability of spectrophotometric pH_T measurement is basically given through published $pK_2^T e_2$ values of meta-Cresol Purple, or rather through a function of $pK_2^T e_2$ depending salinity and temperature. The uncertainties described here can henceforth be used to also assign uncertainties to the $pK_2^T e_2$ values of the indicator dye, which was not possible before because the uncertainty of the $pH_T(S, T, b(\text{TRIS}) = 0 \text{ mol kg}^{-1} H_2O)$ was not known. This is needed to establish, by propagation, a complete uncertainty budget of the spectrophotometric measurement of pH_T for a seawater sample.

Due to the time-consuming experimental process, $pK_2^T e_2$ values are currently not determined for each new batch of meta-Cresol Purple, instead, published values are used for each batch, independently from the actual provider. Therefore, uncertainties in the replicability, mainly because of varying unknown impurities, increase the uncertainty of the assigned $pK_2^T e_2$ values and, consequently, of subsequent pH_T measurements to an unknown extent. Ideally, each new batch of meta-Cresol Purple should be calibrated by measuring the pH_T of

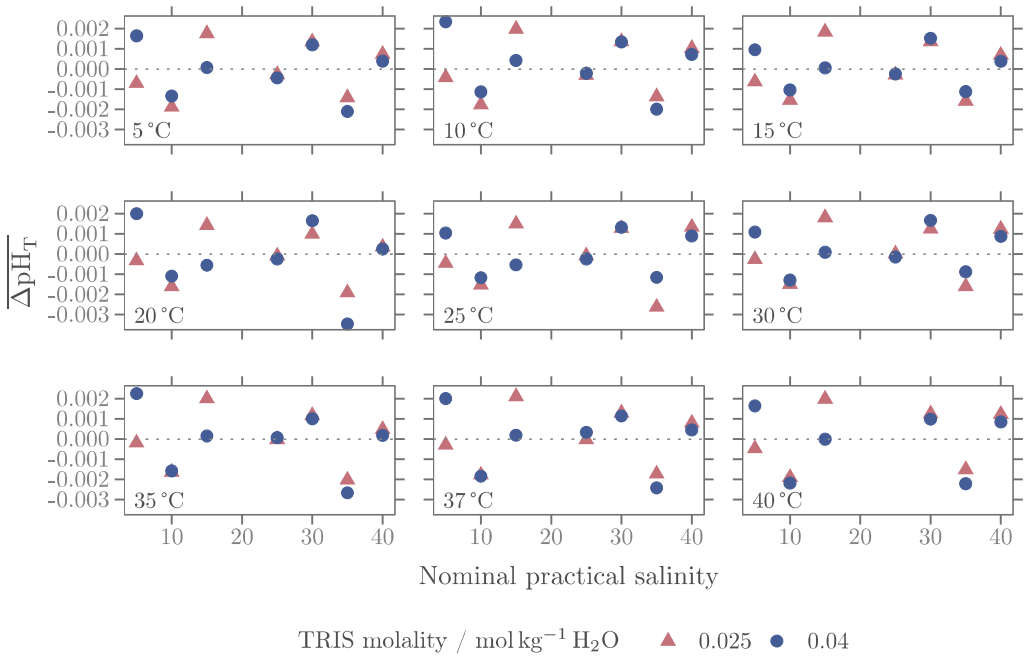

Fig. 5. Mean residuals under each condition from the leave-one-out cross-validation. Each point represents the mean of the results from the 124 runs (triangular for 0.025 mol kg^{-1} H_2O and round for 0.04 mol kg^{-1} H_2O). Standard deviations were below $1.15 \cdot 10^{-4}$ in pH_T units and are not shown here. The dotted line indicates a difference of 0 in pH_T units. Each plot shows the data for one temperature shown in the bottom left.

certified ASW/TRIS buffer standards with a spectrophotometer. The $pK_2^T e_2$ can be calculated from the spectrophotometrical measurement of an ASW/TRIS buffer standard, its certified pH_T value, and the temperature measurement following the procedure in Müller and Rehder (2018). The fit function $pH_{T,c}(S, T, b(\text{TRIS}) = 0\,\text{mol kg}^{-1}\,H_2O)$ presented here can be used to calculate the pH_T value of the reference material (i.e., ASW/TRIS buffer standard) and its uncertainty directly impacts the uncertainty the determined $pK_2^T e_2$.

Ideally, each batch of meta-Cresol Purple should be accompanied with a certificate stating its $pK_2^T e_2$ value and its uncertainty for a range of salinity and temperature relevant for oceanographic measurements. In this way, batch to batch variations due to impurities could be compensated for. Such a certified meta-Cresol Purple can then be used by oceanographers to do their measurements on unknown samples, with adequate uncertainty calculations. However, such certification of meta-Cresol Purple demands time and resources as ASW/TRIS buffers over a wide range of salinity need to be analyzed by spectrophotometry for a wide range of temperature. Alternatively, it could be recommended for meta-Cresol Purple producers to determine $pK_2^T e_2$ at a specific salinity (i.e., for only one ASW/TRIS buffer) and temperature. This would allow a limited quantification of the variations due to impurities.

The uncertainty goal for seawater pH_T measurements is a standard uncertainty of 0.003 for climate research (Newton et al., 2015). The standard uncertainty of 0.001 1 for artificial seawater presented here, is a valuable step towards this goal. It provides important insight into the attainable accuracy of spectrophotometric pH_T measurements. The uncertainty of the $pK_2^T e_2$ term, as well as other terms coming from the characterization of the molar extinction coefficients of the dye, still need to be assessed.

However, the uncertainty of the function presented here applies only if the uncertainties of salinity and temperature from the original measurements (the electrochemical measurements of the artificial seawater) are achieved in the calibration measurements. If that is not the case, these uncertainties should be considered in the calculation. This could, for example, be done by propagating them through the functions. In essence, this would lead to an additional uncertainty contribution u_{TS} of

$$u_{TS} = \sqrt{\left(\frac{\partial \text{pH}_{T,c}(S,T,b(\text{TRIS}))}{\partial T}\right)^2 \cdot u(T)^2 + \left(\frac{\partial \text{pH}_{T,c}(S,T,b(\text{TRIS})}{\partial S}\right)^2 \cdot u(S)^2}. \quad (7)$$

The uncertainty of temperature has a much larger effect on the combined uncertainty compared to the uncertainty of salinity since the sensitivity of pH_T on temperature is higher. An increase of the uncertainty of temperature by 0.01 °C results in an increase of the uncertainty of pH_T by about 0.000 04 (at 25 °C and nominal practical salinity 35) while the effect of a salinity uncertainty increase of 0.01 is about two orders of magnitude lower. Sensitivity is somewhat affected by temperature and salinity, but the overall pattern remains. We estimate that uncertainties in temperature below 0.015 °C and in salinity below 0.1 are negligible. Fig. 6 shows how much the uncertainty of $pH_{T,c}(S, T, b(\text{TRIS}) = 0\,\text{mol kg}^{-1}\,H_2O)$ is affected by the uncertainty of salinity and temperature for one example condition.

This is in agreement with the results from the sensitivity analysis method where we found that the primary source of uncertainty was the uncertainty of the temperature with more than 99 % of the value of the combined uncertainty. In this method the minimum and maximum value of salinity, temperature and TRIS molality are calculated based on their uncertainties (value minus or plus the uncertainty) (Bernardini et al., 2024). We used the fitted coefficients to calculate a pH_T value at zero TRIS molality for those conditions, and then estimated an uncertainty from the resulting variation of the result. The resulting standard uncertainties for $pH_{T,c}(S, T, b(\text{TRIS}) = 0\,\text{mol kg}^{-1}\,H_2O)$ were between 0.000 20 and 0.000 28 in pH_T units if the mean uncertainties for all three input quantities were used. Which is lower than the uncertainty we propose because only the effect of input uncertainties is determined and not the effect of the fitting. However, it does reveal the sensitivity of the function towards temperature.

While our measurements covered most of the oceanographically relevant temperature and salinity range, we were unable to measure

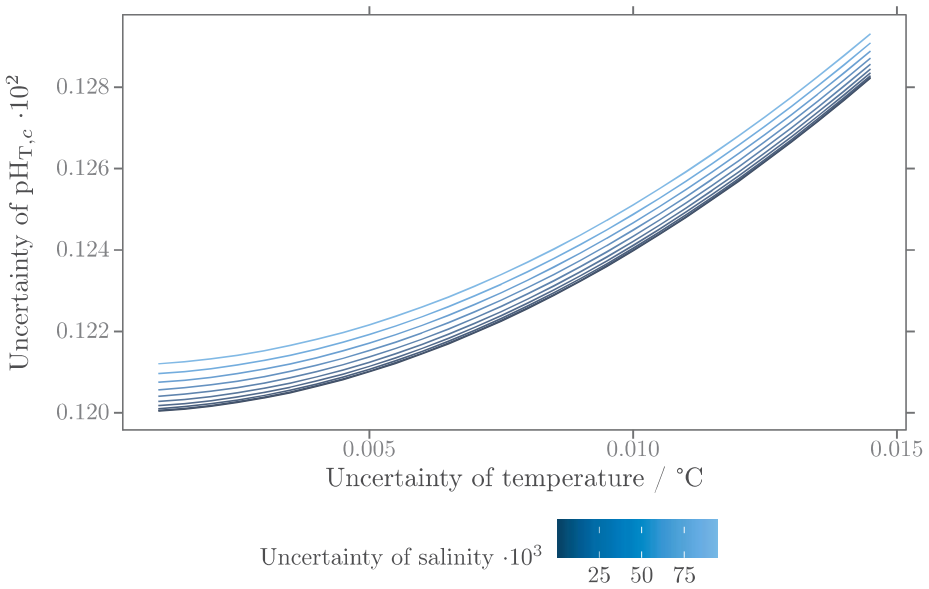

Fig. 6. Dependence of the combined uncertainty of pH_T on the uncertainties of temperature ($u(T)$) and practical salinity ($u(S)$) ($S = 35$ and $T = 25\,°C$). In the calibration where the ASW/TRIS buffer is used, temperature and salinity might be known with a larger uncertainty than in our measurements. The effect of a larger temperature uncertainty is higher than a larger salinity uncertainty. The plot gives an indication how high the uncertainty of the calculated pH_T value of the ASW/TRIS buffer is when the uncertainty of the temperature increases. It also shows that the effect of an increase in salinity uncertainty has a smaller effect (though for a given buffer the salinity should be known from the preparation).

at 0 °C due to technical constraints. Application of the results to values below 5 °C should therefore be carefully considered and the extrapolation added in the uncertainty budget. Similar caution should apply to higher temperatures and salinities outside the range covered by our measurements.

As discussed in part 1, the artificial seawater is the best approximation of the acid-base equilibria in natural seawater available for the measurements. Even so, artificial seawater does not exactly represent the behavior of acid-base equilibria in natural seawater and this should be taken into account when determining the uncertainty of a measurement of natural seawater when the calibration was done with artificial seawater.

5. Conclusion

After determining the fit function to describe the pH_T value of an ASW/TRIS buffer at $b(\text{TRIS}) = 0\,\text{mol}\,\text{kg}^{-1}\,H_2O$ in a practical salinity range from 5 to 40 and temperature range from 5 °C to 40 °C in Capitaine et al. (2025), this study added the uncertainty determination for the final values. This value is an important step towards traceable spectrophotometric pH_T measurements of seawater because with it, the indicator dye can be characterized with uncertainties. We determined that the combined standard uncertainty is 0.001 1 in pH_T units with analytical procedures following GUM (BIPM et al., 2008a) and a Monte Carlo simulation (BIPM et al., 2008b). This is an important step towards the climate measurement objective established by Newton et al. (2015).

The main open questions regarding the uncertainty of spectrophotometric pH_T seawater measurements remain in the context of the uncertainties related to the impurities in meta-Cresol Purple and the effect of practical salinity not being traceable to the International System of Units (SI) (Seitz et al., 2011). However, the results in this paper present a first step towards fully traceable seawater pH_T measurements.

CRediT authorship contribution statement

Rieke Schäfer: Writing – original draft, Visualization, Software, Formal analysis, Data curation. **Gaëlle Capitaine:** Writing – review & editing, Investigation, Formal analysis. **Frank Bastkowski:** Writing – review & editing, Investigation, Formal analysis, Data curation. **Daniela Stoica:** Writing – review & editing, Project administration, Funding acquisition, Conceptualization. **Olivier Pellegrino:** Writing – review & editing, Investigation. **Raquel Quendera:** Writing – review & editing, Investigation. **Eric P. Achterberg:** Writing – review & editing, Supervision. **Simon L. Clegg:** Writing – review & editing. **Paola Fisicaro:** Writing – review & editing, Project administration, Funding acquisition, Conceptualization. **Steffen Seitz:** Writing – review & editing, Project administration, Funding acquisition, Conceptualization.

Funding

This work was supported by the Joint Research Project EMPIR 20NRM06 SApHTIES, which received funding from the EMPIR programme co-financed by the Participating States and from the European Union's Horizon 2020 Research and Innovation programme.

Acknowledgments

We would like to thank Thomas Schmelter for his help with determining the most appropriate distribution of HCl concentrations for the determination of E^{0*}. We thank Gerd Wübbeler in his support to develop the uncertainty determination of the fit function and Thibaut Wagener for his input on the Harned cell measurements.

The color scheme used in Figs. 4 and 5 was created by Paul Tol (https://personal.sron.nl/~pault/).

We thank two anonymous reviewers for their valuable feedback.

Appendix A. Supplementary data

Supplementary material related to this article can be found online at https://doi.org/10.1016/j.marchem.2025.104573.

Data availability

Data (DOI: 10.5281/zenodo.14964822) and code (DOI: 10.5281/zenodo.14964817) are shared on Zenodo.

References

Bernardini, L., McLinden, M.O., Yang, X., Richter, M., 2024. How accurate are your experimental data? A more accessible GUM-based methodology for uncertainty evaluation. Int. J. Thermophys. 45, http://dx.doi.org/10.1007/s10765-024-03446-9.

BIPM, IEC, IFCC, ILAC, ISO, IUPAC, IUPAP, OIML, 2008a. Evaluation of measurement data — Guide to the expression of uncertainty in measurement. JCGM URL: https://www.bipm.org/documents/20126/2071204/JCGM_100_2008_E.pdf/cb0ef43f-baa5-11cf-3f85-4dcd86f77bd6, jCGM 100:2008, GUM 1995 with minor corrections.

BIPM, IEC, IFCC, ILAC, ISO, IUPAC, IUPAP, OIML, 2008b. Evaluation of measurement data — Supplement 1 to the guide to the expression of uncertainty in measurement — Propagation of distributions using a Monte Carlo method. JCGM URL: https://www.bipm.org/documents/20126/2071204/JCGM_101_2008_E.pdf/325dcaad-c15a-407c-1105-8b7f322d651c. jCGM 101:2008.

Buck, R.P., Rondinini, S., Covington, A.K., Baucke, F.G.K., Brett, C.M.A., Camoes, M.F., Milton, M.J.T., Mussini, T., Naumann, R., Pratt, K.W., Spitzer, P., Wilson, G.S., 2002. Measurement of pH. Definition, standards, and procedures (IUPAC recommendations 2002). Pure Appl. Chem. 74, 2169–2200. http://dx.doi.org/10.1351/pac200274112169.

Calvin, K., Dasgupta, D., Krinner, G., Mukherji, A., Thorne, P.W., Trisos, C., Romero, J., Aldunce, P., Barrett, K., Blanco, G., Cheung, W.W., Connors, S., Denton, F., Diongue-Niang, A., Dodman, D., Garschagen, M., Geden, O., Hayward, B., Jones, C., Jotzo, F., Krug, T., Lasco, R., Lee, Y.Y., Masson-Delmotte, V., Meinshausen, M., Mintenbeck, K., Mokssit, A., Otto, F.E., Pathak, M., Pirani, A., Poloczanska, E., Pörtner, H.O., Revi, A., Roberts, D.C., Roy, J., Ruane, A.C., Skea, J., Shukla, P.R., Slade, R., Slangen, A., Sokona, Y., Sörensson, A.A., Tignor, M., van Vuuren, D., Wei, Y.M., Winkler, H., Zhai, P., Zommers, Z., Hourcade, J.C., Johnson, F.X., Pachauri, S., Simpson, N.P., Singh, C., Thomas, A., Totin, E., Alegría, A., Armour, K., Bednar-Friedl, B., Blok, K., Cissé, G., Dentener, F., Eriksen, S., Fischer, E., Garner, G., Guivarch, C., Haasnoot, M., Hansen, G., Hauser, M., Hawkins, E., Hermans, T., Kopp, R., Leprince-Ringuet, N., Lewis, J., Ley, D., Ludden, C., Niamir, L., Nicholls, Z., Some, S., Szopa, S., Trewin, B., van der Wijst, K.I., Winter, G., Witting, M., Birt, A., Ha, M., 2023. IPCC, 2023: Climate change 2023: Synthesis report. In: Core Writing Team, Lee, H., Romero, J. (Eds.), Contribution of Working Groups I, II and III To the Sixth Assessment Report of the Intergovernmental Panel on Climate Change. IPCC, Geneva, Switzerland, http://dx.doi.org/10.59327/ipcc/ar6-9789291691647.

Capitaine, G., Schäfer, R., Bastkowski, F., Pellegrino, O., Quendera, R., Achterberg, E., Wagener, T., Seitz, S., Fisicaro, P., 2025. pH_T measurements of TRIS buffer solutions in an artificial seawater matrix in the salinity range 5–40 and temperature range 5–40 °C. Part 1: Measurements and data fitting Mar. Chem. 273, 104551. http://dx.doi.org/10.1016/j.marchem.2025.104551.

CCQM, 2013. CCQM guidance note: Estimation of a consensus KCRV and associated degrees of equivalence. Version 10.

Clegg, S.L., Humphreys, M.P., Waters, J.F., Turner, D.R., Dickson, A.G., 2022. Chemical speciation models based upon the pitzer activity coefficient equations, including the propagation of uncertainties. II. tris buffers in artificial seawater at 25° C, and an assessment of the seawater 'total' pH scale. Mar. Chem. 244, 104096. http://dx.doi.org/10.1016/j.marchem.2022.104096.

DelValls, T., Dickson, A., 1998. The pH of buffers based on 2-amino-2-hydroxymethyl-1, 3-propanediol ('tris') in synthetic sea water. Deep. Sea Res. Part I: Ocean. Res. Pap. 45, 1541–1554. http://dx.doi.org/10.1016/s0967-0637(98)00019-3.

Dickson, A.G., 1990. Standard potential of the reaction: $AgCl(s)+1/2\ H_2(g)=Ag(s)+HCl(aq)$, and the standard acidity constant of the ion HSO_4^- in synthetic sea water from 273.15 to 318.15 K. J. Chem. Thermodyn. 22, 113–127. http://dx.doi.org/10.1016/0021-9614(90)90074-z.

Ellison, S.L.R., 2018. metRology: Support for metrological applications. URL: https://CRAN.R-project.org/package=metRology. R package version 0.9-28-1.

Friedlingstein, P., O'Sullivan, M., Jones, M.W., Andrew, R.M., Bakker, D.C.E., Hauck, J., Landschützer, P., Le Quéré, C., Luijkx, I.T., Peters, G.P., Peters, W., Pongratz, J., Schwingshackl, C., Sitch, S., Canadell, J.G., Ciais, P., Jackson, R.B., Alin, S.R., Anthoni, P., Barbero, L., Bates, N.R., Becker, M., Bellouin, N., Decharme, B., Bopp, L., Brasika, I.B.M., Cadule, P., Chamberlain, M.A., Chandra, N., Chau, T.T.T., Chevallier, F., Chini, L.P., Cronin, M., Dou, X., Enyo, K., Evans, W., Falk, S., Feely, R.A., Feng, L., Ford, D.J., Gasser, T., Ghattas, J., Gkritzalis, T., Grassi, G., Gregor, L., Gruber, N., Gürses, O., Harris, I., Hefner, M., Heinke, J., Houghton, R.A., Hurtt, G.C., Iida, Y., Ilyina, T., Jacobson, A.R., Jain, A., Jarníková, T., Jersild, A., Jiang, F., Jin, Z., Joos, F., Kato, E., Keeling, R.F., Kennedy, D., Klein Goldewijk, K., Knauer, J., Korsbakken, J.I., Körtzinger, A., Lan, X., Lefèvre, N., Li, H., Liu, J., Liu, Z., Ma, L., Marland, G., Mayot, N., McGuire, P.C., McKinley, G.A., Meyer, G., Morgan, E.J., Munro, D.R., Nakaoka, S.I., Niwa, Y., O'Brien, K.M., Olsen, A., Omar, A.M., Ono, T., Paulsen, M., Pierrot, D., Pocock, K., Poulter, B., Powis, C.M., Rehder, G., Resplandy, L., Robertson, E., Rödenbeck, C., Rosan, T.M., Schwinger, J., Séférian, R., Smallman, T.L., Smith, S.M., Sospedra-Alfonso, R., Sun, Q., Sutton, A.J., Sweeney, C., Takao, S., Tans, P.P., Tian, H., Tilbrook, B., Tsujino, H., Tubiello, F., van der Werf, G.R., Ooijen, E.van., Wanninkhof, R., Watanabe, M., Wimart-Rousseau, C., Yang, D., Yang, X., Yuan, W., Yue, X., Zaehle, S., Zeng, J., Zheng, B., 2023. Global carbon budget 2023. Earth Syst. Sci. Data 15, 5301–5369. http://dx.doi.org/10.5194/essd-15-5301-2023.

Gorman, B., 2018. mltools: Machine learning tools. URL: https://CRAN.R-project.org/package=mltools. R package version 0.3.5.

Kuhn, M., Wickham, H., 2020. Tidymodels: a collection of packages for modeling and machine learning using tidyverse principles. URL: https://www.tidymodels.org.

Liu, X., Patsavas, M.C., Byrne, R.H., 2011. Purification and characterization of meta-cresol purple for spectrophotometric seawater pH measurements. Environ. Sci. Technol. 45, 4862–4868. http://dx.doi.org/10.1021/es200665d.

Meija, J., Coplen, T.B., Berglund, M., Brand, W.A., De Bièvre, P., Gröning, M., Holden, N.E., Irrgeher, J., Loss, R.D., Walczyk, T., Prohaska, T., 2016. Atomic weights of the elements 2013 (IUPAC technical report). Pure Appl. Chem. 88, 265–291. http://dx.doi.org/10.1515/pac-2015-0305.

Müller, J.D., Bastkowski, F., Sander, B., Seitz, S., Turner, D.R., Dickson, A.G., Rehder, G., 2018. Metrology for pH measurements in brackish waters—part 1: Extending electrochemical pHT measurements of TRIS buffers to salinities 5–20. Front. Mar. Sci. 5 (176), http://dx.doi.org/10.3389/fmars.2018.00176, URL: https://www.frontiersin.org/article/10.3389/fmars.2018.00176.

Müller, J.D., Rehder, G., 2018. Metrology of pH measurements in brackish waters—part 2: Experimental characterization of purified meta-cresol purple for spectrophotometric pHT measurements. Front. Mar. Sci. 5 (177), http://dx.doi.org/10.3389/fmars.2018.00177, URL: https://www.frontiersin.org/article/10.3389/fmars.2018.00177.

Newton, J., Feely, R.A., Jewett, E.B., Williamson, P., Mathis, J., 2015. Global ocean acidification observing network: Requirements and governance plan. URL: http://www.goa-on.org/docs/GOA-ON_plan_print.pdf. GOA-ON.

R Core Team, 2023. R: A Language and Environment for Statistical Computing. R Foundation for Statistical Computing, Vienna, Austria, URL: https://www.R-project.org/.

Seitz, S., Feistel, R., Wright, D.G., Weinreben, S., Spitzer, P., Bièvre, P.D., 2011. Metrological traceability of oceanographic salinity measurement results. Ocean. Sci. 7, 45–62. http://dx.doi.org/10.5194/os-7-45-2011.

Venables, W.N., Ripley, B.D., 2002. Modern Applied Statistics with S, fourth ed. Springer, New York, ISBN: 0-387-95457-0, URL: https://www.stats.ox.ac.uk/pub/MASS4/.

Viechtbauer, W., 2010. Conducting meta-analyses in R with the metafor package. J. Stat. Softw. 36, 1–48. http://dx.doi.org/10.18637/jss.v036.i03.

Wickham, H., Averick, M., Bryan, J., Chang, W., McGowan, L.D., François, R., Grolemund, G., Hayes, A., Henry, L., Hester, J., Kuhn, M., Pedersen, T.L., Miller, E., Bache, S.M., Müller, K., Ooms, J., Robinson, D., Seidel, D.P., Spinu, V., Takahashi, K., Vaughan, D., Wilke, C., Woo, K., Yutani, H., 2019. Welcome to the tidyverse. J. Open Source Softw. 4 (1686), http://dx.doi.org/10.21105/joss.01686.

Marine Chemistry 273 (2025) 104551

Contents lists available at ScienceDirect

Marine Chemistry

journal homepage: www.elsevier.com/locate/marchem

pH_T measurements of TRIS buffer solutions in an artificial seawater matrix in the salinity range 5–40 and temperature range 5–40 °C. Part 1: Measurements and data fitting

Gaëlle Capitaine [a,b,*,1], Rieke Schäfer [c,1], Frank Bastkowski [c], Daniela Stoica [a,2], Olivier Pellegrino [d], Raquel Quendera [d], Eric P. Achterberg [e], Thibaut Wagener [b], Simon L. Clegg [f], Steffen Seitz [c], Paola Fisicaro [a]

[a] Laboratoire National de Métrologie et d'Essais (LNE), 1 Rue Gaston Boissier, 75015 Paris, France
[b] Aix Marseille Université, CNRS, IRD, MIO, 13288 Marseille, France
[c] Physikalisch-Technische Bundesanstalt (PTB), Bundesallee 100, 38116 Braunschweig, Germany
[d] Instituto Português da Qualidade, (IPQ), R. António Gião, 2, 2829-513 Caparica, Portugal
[e] GEOMAR Helmholtz Centre for Ocean Research Kiel, 24148 Kiel, Germany
[f] School of Environmental Sciences, University of East Anglia, Norwich NR4 7TJ, UK

ARTICLE INFO

Keywords:
Ocean acidification
Total pH
TRIS buffer
Traceability

ABSTRACT

Spectrophotometric measurements of seawater total pH (pH_T) contribute to the knowledge of the oceanic carbonate system, and hence to the assessment of the ocean carbon cycle and the monitoring of ocean acidification. Spectrophotometric measurements rely on the characterization of the indicator dye's second dissociation constant, obtained from measurements on solutions of known pH_T. Therefore, Harned cell potentiometric measurements were performed on equimolal TRIS buffers (i.e. buffers containing equal molalities of 2-amino-2-(hydroxymethyl)-1,3-propanediol (TRIS, CAS reference number 77–86-1) and TRIS hydrochloride (TRIS.HCl)), made in an artificial seawater (ASW) matrix. Buffer solutions were prepared in an ASW matrix of nominal practical salinities from 5 to 40, and Harned cell measurements were performed on these solutions at temperatures from 5 °C to 40 °C. This provides, for the first time, pH_T values of ASW/TRIS buffers that are consistent for the entire ranges of salinity relevant for oceanographic measurements, and for a wide range of temperature. The work presented includes a comparison of results from three National Metrology Institutes to assess reproducibility, and provides a function allowing the calculation of equimolal ASW/TRIS buffers pH_T as a function of salinity, temperature and TRIS buffer molality. This function can be used to derive pH_T values for zero TRIS molality, thus representing a pure ASW (i.e. a chemical environment unaffected by the presence of TRIS and TRIS.HCl), and referring to a true pH_T scale. These values are needed for the characterization of the second dissociation constant of the dye with perspective of traceability to the International System of units.

1. Introduction

It is estimated that 10.8 gigatonnes of carbon (GtC) per year were emitted in the decade 2014–2023 by anthropogenic activities such as fossil fuel burning, land-use change and cement production (Friedlingstein et al., 2024). Of the total amount of carbon dioxide (CO_2) emitted, (2.9 ± 0.4) GtC per year were absorbed by the ocean, representing about 27 % of anthropogenic CO_2 global emissions. The absorption of CO_2 by seawater causes changes in the oceanic carbonate system, leading to an acidification of seawater and to a decrease of the carbonate ion concentration (IPCC, 2019). By affecting the stability of mineral forms of calcium carbonate, the decreasing carbonate

* Corresponding author at: Laboratoire National de Métrologie et d'Essais (LNE), 1 Rue Gaston Boissier, 75015 Paris, France.
E-mail addresses: gaelle.capitaine@lne.fr (G. Capitaine), rieke.schaefer@ptb.de (R. Schäfer), frank.bastkowski@ptb.de (F. Bastkowski), daniela.joubertstoica@cea.fr (D. Stoica), opellegrino@ipq.pt (O. Pellegrino), rquendera@ipq.pt (R. Quendera), eachterberg@geomar.de (E.P. Achterberg), thibaut.wagener@univ-amu.fr (T. Wagener), s.clegg@uea.ac.uk (S.L. Clegg), steffen.seitz@ptb.de (S. Seitz), paola.fisicaro@lne.fr (P. Fisicaro).
[1] Co-first authorship.
[2] Present address: CEA, 17 Avenue des Martyrs, 38000 Grenoble, France.

https://doi.org/10.1016/j.marchem.2025.104551
Received 10 March 2025; Received in revised form 5 August 2025; Accepted 12 August 2025
Available online 26 August 2025

concentrations leads to lower calcification rates, malformation and dissolution of carbonate structures, and are therefore impacting marine biodiversity (Rastelli et al., 2020). To study ocean acidification, the modification of the oceanic carbonate system, as well as the ocean carbon cycle, four independently measurable parameters can be monitored: pH on the total scale (pH_T), total alkalinity (A_T), total dissolved inorganic carbon (C_T) and equilibrium fugacity of CO_2 (fCO_2) (Dickson et al., 2007). These parameters are the basis of the ocean carbon observation system, with uses in data management, analysis, and biogeochemical models.

Among the four parameters aforementioned, pH_T has been widely used by oceanographers following the development of the spectrophotometric measurement method (Byrne and Breland, 1989; Clayton and Byrne, 1993) and later spectrophotometric in-situ autonomous sensors (Seidel et al., 2008; Yin et al., 2021). It is of major importance to guarantee the reliability and comparability of these measurement results, which requires the use of metrological principles such as uncertainty estimation, validation of measurement processes and establishment of metrological traceability.

The spectrophotometric pH_T measurement method is based on the use of the indicator dye meta-cresol purple (mCP). It consists of measuring the absorbance ratio R at the wavelengths corresponding to the peak of absorbances of the basic and acidic form of the indicator dye in a seawater sample. This, together with the second dissociation constant and molar extinction coefficients of the dye, allows for the calculation of pH_T (eq. 1). To be suitable for spectrophotometric pH_T measurements of natural seawater samples, these parameters need to be characterized over appropriate ranges of salinities and temperatures (Douglas and Byrne, 2017; Liu et al., 2011; Loucaides et al., 2017; Müller and Rehder, 2018).

$$pH_T = -\log\left(K_2^T e_2\right) + \log\left(\frac{R - e1}{1 - R \times \frac{e3}{e2}}\right) \quad (1)$$

where K_2^T is the second dissociation constant of the indicator dye, R the ratio of the absorbance at 578 nm (i.e. mCP basic form absorbance wavelength) on the absorbance at 434 nm (i.e. mCP acid form absorbance wavelength), and e_1, e_2 and e_3 are ratios of the dye molar extinction coefficients (Liu et al., 2011).

The characterization of the molar extinction coefficients has been described by Liu et al. (2011) and Loucaides et al. (2017). The term $K_2^T e_2$ is characterized by spectrophotometric measurements of artificial seawater (ASW) solutions of known pH_T (Liu et al., 2011; Loucaides et al., 2017; Müller and Rehder, 2018).

The solutions used for that purpose are equimolal TRIS buffers (buffer of 2-amino-2-(hydroxymethyl)-1,3-propanediol (TRIS) and TRIS hydrochloride (TRIS.HCl)) made in ASW solutions of the desired salinities. The pH_T values of these solutions are commonly characterized with the Harned cell potentiometric measurement method (DelValls and Dickson, 1998; Pratt, 2014; Papadimitriou et al., 2016; Müller et al., 2018; Capitaine et al., 2023b). Harned cell measurements are the primary measurement procedure for aqueous pH measurements. They provide the lowest standard uncertainty for pH measurement results, typically below 0.002 (Buck et al., 2002). From such measurements, a function giving the pH_T of equimolal ASW/TRIS buffers at each studied salinity and temperature can be computed and used for the subsequent determination of $K_2^T e_2$. Thus, traceability of spectrophotometric pH_T results can be considered established to the Harned cell potentiometric measurement method.

However, in ASW/TRIS buffers, the TRIS and protonated TRIS (the $TrisH^+$ ion) contribute to a significant extent to the composition of the buffer, especially at low salinities, and these buffers do thus not accurately represent a seawater matrix. Indeed, the activity coefficients of the ions involved in acid-base equilibria will differ slightly from their values in pure ASW and seawaters of the same nominal salinity. Values of pH_T of those buffers, which are measured with Harned cells, do not correspond to the true total pH scale in seawater, which applies to saline waters having ionic strengths similar to those of the open ocean (Clegg et al., 2022). To overcome this, Nemzer and Dickson (2005) recommended that the $K_2^T e_2$ characterization should be made from equimolal ASW/TRIS buffers with pH_T values extrapolated to zero TRIS molality, thus to a pure ASW matrix. The extrapolation is done with measurements of equimolal ASW/TRIS buffers at various TRIS molalities.

The characterization of the ASW/TRIS buffers used for the $K_2^T e_2$ characterization has, up to now, only been made in separate ranges of salinity: 5–20 in Müller and Rehder (2018) and 20–40 in DelValls and Dickson (1998). It must be mentioned that Müller and co-workers provide an equation for the whole salinity range 5–40 and temperature range 5–45 °C that is, however, based on their measurements for salinities 5–20 combined with DelValls and Dickson measurements to establish the fit up to salinity 40. Particularly important is the fact that the preparation of ASW/TRIS buffers by Müller et al. differed from the one commonly used and the extrapolation to zero TRIS molality resulted in an incorrect ASW composition which affects the resulting pH_T (Clegg et al., 2022). Unfortunately, Müller et al. (2018) was the only study providing ASW/TRIS buffers with pH_T values extrapolated to zero TRIS molality for ranges of salinity and temperature, as well as subsequent $K_2^T e_2$ characterization (Müller and Rehder, 2018). Dye characterizations provided in Liu et al. (2011) and Loucaides et al. (2017) did not refer to a pure ASW, thus to a true pH_T scale. New measurements of ASW/TRIS buffers as well as subsequent dye characterization are therefore needed.

The aim of this work is to provide pH_T data for equimolal ASW/TRIS buffers measured with the common Harned cell methodology and to compute a suitable fitted function for pH_T for the salinity and temperature ranges relevant for seawater spectrophotometric measurements (i.e., salinity range 5–40 and temperature range 5–40 °C). This function is suitable for the computation of pH_T values at the limit of zero TRIS molality. This work aims thus to provide a consistent function usable for the characterization of mCP in the salinity and temperature ranges most relevant for oceanography. The fitted function provided will enable for the dye characterization, itself allowing for spectrophotometric pH_T measurements (1) traceable for wider ranges of salinity and temperature and (2) that are consistent with a true pH_T scale.

Our work is divided into two parts. In this work we determine the variation in pH_T of equimolal ASW/TRIS buffers, for varying buffer molalities, for the salinity range 5–40 and temperature range 5–40 °C. A further study (Schäfer et al., 2025) describes for the first time the estimation of the uncertainty of the fitted function, which is necessary to establish the uncertainty budget for spectrophotometric measurement of pH_T that is lacking up to now (Fong, 2021).

This paper details the preparation of equimolal ASW/TRIS buffers and the measurement of their pH_T values, as well as the data processing method used to establish the fitted function. Harned cell measurements of the pH_T values of the ASW/TRIS buffer solutions were conducted at three National Metrology Institutes (NMIs): the Physikalisch-Technische Bundesanstalt (PTB, Germany), the Laboratoire National de Métrologie et d'Essais (LNE, France) and the Instituto Português da Qualidade (IPQ, Portugal). Our results are compared with the earlier work of DelValls and Dickson (1998), and of Müller et al. (2018). In addition, spectrophotometric measurements of some of the equimolal ASW/TRIS buffers have been conducted at LNE to check the compatibility of the fitted function presented in this work with the dye characterization of Müller and Rehder (2018). The metrological traceability of pH_T values of ASW/TRIS buffers is finally discussed.

2. Materials and methods

2.1. General approach

Harned cell measurements of ASW/TRIS buffer solutions were performed at nominal practical salinities 5, 10, 15, 20, 25, 30, 35 and 40, and at nine temperatures between 5 °C and 40 °C with steps of 5 °C, with an additional measurement at 37 °C performed at PTB. In accordance with former work, three equimolal ASW/TRIS buffers were measured for each salinity, having molalities of $b(\mathrm{TRIS}) = b(\mathrm{TRIS.HCl}) = 0.01$, 0.025 and 0.04 mol kg^{-1} H_2O. Measurements were carried out by the three NMIs involved in this study: PTB, LNE and IPQ (Fig. S1, Supplementary Material).

The pH_T values of equimolal ASW/TRIS buffers within the whole ranges of nominal practical salinity 5–40 and temperature 5–40 °C were calculated from the measurements as described in section 2.3. An equation giving the pH_T of equimolal ASW/TRIS buffers as a function of nominal practical salinity, temperature and molality of TRIS was computed (section 2.6). For a molality of $b(\mathrm{TRIS}) = b(\mathrm{TRIS.HCl}) = 0$ mol kg^{-1} H_2O, the function yields the pH_T values extrapolated to pure ASW (i.e. an ASW matrix without TRIS and TRIS.HCl), which has important practical applications.

Spectrophotometric measurements have been conducted at LNE on equimolal ASW/TRIS buffers of salinities 5, 20, 35 and 40 using $K_2^T e_2$ determined by Müller and Rehder (2018). The spectrophotometric pH_T values obtained in that way were compared to the fitted function presented in this work to check their equivalence. Details of these comparisons are given in section 2.7.

2.2. ASW/TRIS buffer pH_T preparation

The composition of the ASW used for ASW/TRIS buffers preparation was based on the reference seawater composition of the International Association for the Physical Sciences of the Oceans (IAPSO) for a practical salinity of 35 (Millero et al., 2008). From that reference composition, adjustments were made, as recommended by Dickson (1990) to simplify the composition and thus the preparation of the solutions, and to replace bromide ions that damage silver-silver chloride electrodes, giving the composition presented in Pratt (2014). The ASW composition referred to as a nominal practical salinity of 35 (i.e. with an equivalent chemical environment to the reference natural seawater composition of practical salinity 35). When referring to ASW/TRIS buffers, the use of the word "salinity" corresponds to the aforementioned "nominal practical salinity" throughout the paper.

Table 1 presents the way of obtaining all equimolal ASW/TRIS buffers compositions for nominal practical salinities 5, 10, 15, 20, 25, 30 and 40 from the reference composition of Pratt (2014) at a nominal practical salinity of 35. They are calculated by changing the amount content of all salts proportionally, based on the ionic strength of the desired salinity.

For each salinity, three equimolal buffers were prepared at $b(\mathrm{TRIS}) = b(\mathrm{TRIS.HCl}) = 0.01$, 0.025 and 0.04 mol kg^{-1} H_2O. To keep the ionic strength constant, the amount of HCl added was compensated by removing the same amount of NaCl from the initial composition (Table 1, footnote a), see DelValls and Dickson (1998). The practical effect of this is to substitute Na^+ for equal moles of $TrisH^+$ in the buffer solution.

The ASW/TRIS buffer recipe is defined for a nominal practical salinity, such that the artificial seawater (without the buffer) is expected to provide the same chemical environment – in terms of the activity coefficients of the species involved in acid-base equilibria – as natural seawater of the same practical salinity. Thus the difference in stoichiometric dissociation constants, such as that of HSO_4^-, for ASW and natural seawater, is negligible.

Substituting TRIS.HCl for NaCl in artificial seawater is expected to minimise changes in the thermodynamic properties of the buffer solutions relevant to acid-base equilibrium relative to those for a pure artificial seawater, and the approach has been used in this study to salinities as low as 5. However, it must be emphasized that the proportion of TRIS and TRIS.HCl in the artificial solution is significant for low salinities, and this leads to greater changes in the acid-base properties of the solution compared to higher salinity buffers (Clegg et al., 2022). The elimination of this effect can be achieved by an extrapolation of the measured property, and of pH_T, to zero TRIS buffer molality. Note that such a pH_T is not the same as the total pH of a solution composed only of artificial seawater which, if no TRIS is added, would likely have a neutral pH_T. This behaviour, and other aspects of pH_T, have been investigated using a chemical speciation model by Clegg et al. (2022).

The ASW/TRIS buffers were prepared gravimetrically at PTB using the compositions given in Table 1 and using the following chemical compounds: TRIS (*NIST Standard Reference Material 723e*), NaCl (*Merck KGaA, 99.842 %*), KCl (*Merck KGaA, 99.988 %*), Na_2SO_4 (*Merck KGaA, 99.999 %*), $CaCl_2.2H_2O$ (*Merck KGaA*), $MgCl_2.6H_2O$ (*Merck KGaA*), HCl (*Danish Institute of Fundamental Metrology, amount content of 0.1 mol per kilogram of solution*) and ultrapure water. $MgCl_2$ and $CaCl_2$ stock solutions were prepared from the hydrated salts at around 1.4 mol kg^{-1}-sol and 0.5 mol kg^{-1}-sol, respectively. All salts, and the stock solutions of $MgCl_2$, $CaCl_2$ and HCl, were characterized for purity or amount content, respectively, by coulometric acid-base or argentimetric titrations (S2, Supplementary Material). NaCl, KCl and Na_2SO_4 salts were dried before use (S2, Supplementary Material) and the buffers were prepared by gravimetry from stock solutions of the different components.

An offset of 0.4 % excess in the HCl molality was added

Table 1
Computation of the composition of the different TRIS buffers (i.e. various nominal practical salinities, noted S, and TRIS molalities) from the reference composition of Pratt (2014).

Salts	Molar mass M / g mol^{-1}		Pure ASW reference composition (Pratt, 2014)	TRIS buffer composition (This study)
			Molality b / mol kg^{-1} H_2O	Molality b / mol kg^{-1} H_2O
NaCl	58.4428		0.42753	a
Na_2SO_4	142.0421		0.02926	b
KCl	74.5513		0.01058	b
$MgCl_2$	95.2110		0.05474	b
$CaCl_2$	110.9840		0.01075	b
HCl	36.4609		–	c
TRIS	121.1352		–	d
		Nominal Practical Salinity, S	35	
		Ionic Strength, I	0.72236	I_S

Note: Where the Ionic strength I_S of a specific salinity is calculated with the formula $I_S = \frac{0.72236 \bullet S}{35}$ and where b expresses the molality of the solute entities, i.e. their amount divided by the mass of the solvent, which is water in this study, noted mol kg^{-1} H_2O. The subscript "S" corresponds to a TRIS composition at one specific salinity and the subscript "*Ref*" to the reference composition of Pratt (2014).

[a] $b(Nacl)_{S,b(Hcl)} = \frac{I_S \bullet b(Nacl)_{Ref}}{I_{Ref}} - b(Hcl)$.

[b] $b(Salt)_S = \frac{I_S \bullet b(Salts)_{Ref}}{I_{Ref}}$.

[c] $b(HCl)$ of respective equimolal ASW/TRIS buffers (i.e. 0.01, 0.025 or 0.04 mol kg^{-1} H_2O)

[d] $b(TRIS) = 2 \bullet b(Hcl)$.

unintentionally in the preparation of some ASW/TRIS buffers (S3, Supplementary Material). Additional studies were conducted to investigate the potential impact on the pH_T values. To this end, solutions with varying excess HCl molalities (0 %, 0.13 %, 0.26 %, 0.4 %, 0.8 %, 1.5 % and 5 %) were prepared for a buffer of salinity 35 and at $b(\text{TRIS}) = b(\text{TRIS.HCl}) = 0.01$ mol kg^{-1} H_2O, and their pH_T values were measured at several temperatures. The raw data of this experiment are presented in the Zenodo Repository (https://doi.org/10.5281/zenodo.14964822; details about the repositories are given in S4, Supplementary Material). An offset of −0.003 could theoretically be calculated for the pH_T value at 0.4 % from a linear extrapolation of the results to 0 % offset, as well as from eq. 8 of Clegg et al. (2022). However, no significant dependence of the pH_T values on the excess HCl molality could be noted in the range up to 0.8 % (i.e. within their spread of 0.004 pH_T units). Additionally, equimolal ASW/TRIS buffers of salinity 40 were prepared again with the correct HCl molality, and sent to LNE for comparison with the original buffers. These investigations showed that the error led to a bias of around −0.001 pH_T units, which is fairly small compared to the reproducibility of the pH_T Harned cell measurement results (around 0.003 pH_T units). As a consequence of these experimental findings, it was decided that the uncertainty of pH_T due to the excess in HCl molality of some ASW solutions is covered by the overall uncertainty of the measurements. This is presented in more details in S5, Supplementary Material. Moreover, it is expected that the overall fitted function will not be significantly impacted. Therefore, pH_T values obtained from ASW solutions affected from the HCl offset have not been corrected.

Each solution was stored in 500 mL borosilicate glass bottles. Before closing with screw caps and sealing with Parafilm, the headspace (around 1 % of the total volume) was filled with humidified Argon gas. The bottles were shipped to LNE and IPQ. The masses of the bottles were measured at PTB and at the recipient laboratory to check the integrity of the solutions during transport.

2.3. *Definition of* pH_T *and potentiometric measurement model for ASW/TRIS buffers*

In metrology, the measurement model corresponds to the mathematical relation among all quantities known to be involved in a measurement (JCGM 200:2012, 2012). The value of the measurand (i.e. output quantity, or quantity intended to be measured) is to be inferred from information about input quantities in the measurement model. Here, the measurand is the pH_T value, which is inferred from potentiometric measurements conducted with Harned cells, as well as other measurements or information. The subsections below present the measurement model of the pH_T obtained by potentiometry.

Operational pH_T definition:

The operational pH_T defined on a molality basis, denoted $pH_{T,m}$, is defined as follows:

$$pH_{T,m} = \frac{E - E^{0*}}{k} + \lg(b(Cl^-)) \quad (2)$$

where:

- E (V), is the potential difference measured between a silver-silver chloride electrode (noted $Ag_{(s)}/AgCl_{(s)}$) and a Standard Hydrogen Electrode (noted Pt,H_2) in the electrochemical cell *I*, and corrected to a pressure of H_2 equal to 1 atm.

$Pt|H_2(g)|$ASW/TRIS buffer solution$|AgCl|Ag$ Cell I

- E^{0*} (V), is the standard potential of the $Ag_{(s)}/AgCl_{(s)}$ electrode in ASW media (corresponding to extrapolation to infinite dilution). It is determined from potential measurements (E') made with the electrochemical cell *II* in at least 5 solutions with HCl molalities varying between 0.005 and 0.05 mol kg^{-1} H_2O, made in an ASW matrix of a given salinity.

$Pt|H_2(g)|HCl\ (0.005 < b < 0.05$ mol kg^{-1} $H_2O)$ in ASW solution$|AgCl|Ag$ Cell II

The E^{0*} term is obtained by extrapolating E' values to an HCl molality of zero using a quadratic polynomial function.

- k is the Nernstian term, given by eq. 3.

$$k = \frac{RT\ln(10)}{F} \quad (3)$$

where F is the Faraday constant (C mol^{-1}), R the Gas constant (J mol^{-1} K^{-1}), and T the measured temperature (K).

- Finally, $b(Cl^-)$ is the molality of chloride ions in the TRIS buffer solution (mol kg^{-1} H_2O)

Conversion to an amount content basis:

The operational molality based $pH_{T,m}$ is converted to an amount content basis (pH_T) to be suitable for oceanographers using the following expression.

$$pH_T = pH_{T,m} - \lg(\omega_{H_2O}) \quad (4)$$

where ω_{H_2O} is the water mass fraction (g kg^{-1} sol) of natural seawater at the practical salinity of interest.

To establish the conversion to amount content (amounts per kg of seawater), as used by oceanographers, the water mass fraction must be relative to a natural seawater composition and not to the TRIS buffer composition itself. The value of ω_{H_2O} is obtained from eq. 5, coming from equation A.4 of Clegg et al. (2022), which is itself established based on the natural seawater reference composition of Millero et al. (2008).

$$\omega_{H_2O} = 1 - 0.0010047 \bullet S \quad (5)$$

where S is the nominal practical salinity.

The numerical factor corresponds to the ratio 0.03516504/35, where 0.03516504 is the solute content of the reference seawater composition of the International Association for the Physical Sciences of the Oceans (IAPSO) for a practical salinity of 35 (Clegg et al., 2022; Millero et al., 2008).

The numerical factor in eq. 5 differs from the value of 0.00106 used by DelValls and Dickson (1998) and in related studies. Their use of another value appears likely to be an inadvertent error. This leads to a discrepancy in calculated pH_T of, for example, +0.0009 for a practical salinity of 35 and + 0.0004 for a practical salinity of 15, compared to pH_T values where the water mass fraction is computed using eq. 5. This error is carried over into related studies focusing on dye characterization (Liu et al., 2011; Loucaides et al., 2017; Müller et al., 2018; Müller and Rehder, 2018; Papadimitriou et al., 2016). While applying a correction may be an appropriate solution, as it could help mitigate the error, this approach must be thoroughly investigated and carefully discussed within both the metrological and oceanographic communities. It is also important to note that the error falls within the standard uncertainty range of the spectrophotometric method used for dye characterization (0.005–0.01 pH_T units).

We also note that Pratt (2014), in his metrological study of the pH_T of TRIS buffers, used values of ω_{H_2O} calculated for the buffer solution itself, however, it is thus not representative of a natural seawater composition.

Link to the conventional thermodynamic definition:

The molality-based conventional thermodynamic total pH, noted $pH^*_{T,m}$, is defined by Eqs. (6) and (7).

$$pH^{*}_{T,m} = -\lg\left\{\frac{b^{T}(H^{+})}{mol\ kg^{-1}\ H_2O}\right\} \quad (6)$$

$$b^{T}(H^{+}) = b^{f}(H^{+}) + b\left(HSO_4^{-}\right) = b^{f}(H^{+})\left(1+\frac{b_S}{K_S}\right) \approx b^{f}(H^{+})\left(1+\frac{b_{ST}}{K_S}\right) \quad (7)$$

where $b^{f}(H^{+})$ is the molality of free protons, b_S is the free sulphate molality, b_{ST} is the total sulphate molality ($b(HSO_4^{-}) + b\left(SO_4^{2-}\right)$), and K_S is the molality based dissociation constant of HSO_4^{-} at the salinity and temperature of interest (Dickson et al., 2007). Although this definition is the most rigorous one, being traceable to the international system of units (SI), $pH^{*}_{T,m}$ cannot be measured directly in seawater.

The $pH_{T,m}$ values of TRIS buffer solutions, relying on Harned cell potentiometric measurements, include approximations that vary with both temperature and salinity and are not yet fully quantified. These approximations arise because of the combination of Harned cell results for two solutions (TRIS buffer vs ASW only) that differ slightly in composition and therefore acid-base thermodynamic properties (Clegg et al., 2022). Even if the approximations can be considered negligible, the definition of the potentiometric operational $pH_{T,m}$ obtained experimentally differs from the thermodynamic definition.

In this paper, we focus on the pH_T of ASW/TRIS buffer according to the operational definition based in amount content (eq. 4). The implication of the difference with the thermodynamic definition are discussed in the last section (Section 4) of this paper as well as in Clegg et al. (2022).

2.4. Instrumentation

2.4.1. LNE Harned cell set-up

Harned cell measurements at LNE were conducted at 15 °C, 25 °C, and 30 °C. Cells were placed in a TAMSON thermostatic bath with accurate temperature control, within 0.01 °C. Five Pt100 probes facilitated temperature stability in the bath. The potential difference between the electrodes was measured using an Agilent 34972A data acquisition system and recorded with the Agilent Benchlink Data Logger software. The atmospheric pressure was measured with a Druck DPI 740 sensor. Measurement results, including potential difference, temperature, and pressure, were recorded every 2 min. The cell potentials used in the calculations were means of values acquired over one hour with a stable potential signal (i.e. standard deviation below 20 μV). Electrodes were prepared according to Bates (1973) methods for primary pH measurements. LNE internal quality procedure plans the calibration for potential, temperature and pressure measurements, respectively every 4 years, 1 year and 2 years. They are made by accredited laboratories.

2.4.2. PTB Harned cell set-up

Harned cell measurements at PTB were conducted between 5 °C and 40 °C in 5 °C steps. Cells were placed in a Lauda Proline PV36 thermostat, connected to a Lauda DLK45 cooling thermostat. Potential difference between electrodes was measured using an Agilent 3458A digital multimeter and recorded via self-programmed measurement software. Atmospheric pressure was measured with a Setra Digital Pressure Gauge. The temperature was measured with a ASL F250 MKII thermometer connected to four RTD PT100 temperature probes which were placed in the Lauda Proline PV36 thermostat bath. The digital multimeter and the thermometer (including temperature probes) are calibrated at PTB every year and the digital pressure gauge is calibrated at PTB every 5 years. Data, including potential difference (for each of the twelve cells), temperature, and pressure, were recorded for each of 21–30 measurement runs (depending on voltage stability). The cell potentials used in the calculations were means of the last eleven potential data acquired. Electrodes were prepared according to Bates (1973), methods for primary pH measurements.

2.4.3. IPQ Harned cell set-up

Harned cell measurements at IPQ were conducted at 20 °C, 25 °C, and 30 °C. Cells were placed in a Lauda Proline PV36 thermostatic bath with accurate temperature control (standard uncertainty of 0.021 °C in temperature measurement). The potential difference between the electrodes was measured using a Keithley 2700 digital multimeter and recorded with XLinx software. The atmospheric pressure was measured with a Vaisala digital pressure sensor. The Pt100 temperature probes, the pressure sensor and the multimeter are calibrated at IPQ annually. Measurement results, including potential difference, temperature, and pressure, were recorded every 1 min. The cell potentials used in the calculations were means of values acquired over one hour with a stable potential signal (i.e. standard deviation below 50 μV). Electrodes were prepared according to Bates (1973) methods for primary pH measurements.

2.4.4. LNE spectrophotometric pH_T measurement set-up

pH_T spectrophotometric measurements were conducted using an Agilent Cary 60 UV–vis spectrophotometer and Starna quartz cells of 10 cm path-length. Cells were pre-thermostated and a Lauda Loop L100 circulation thermostat was connected to the internal support of the cell of the spectrophotometer to allow maintaining a temperature of 25.0 ± 0.1 °C inside the cell. The two PTFE plugs of the spectrophotometric cell contained a calibrated temperature probe allowing for precise measurements of the temperature inside the cell during the pH_T measurement.

The spectrophotometer was checked for linearity and wavelength accuracy using neutral density filters and holmium filters, respectively. The procedure followed for calibration was based on the Spectrophotometer calibration guide of the French College of Metrology (CFM, 2017).

2.5. ASW/TRIS buffers potentiometric characterization

The three NMIs used the electrochemical *cell I* to measure the potentials E of the three equimolal buffers at each salinity and temperature (see supplementary materials S1). Each institute performed duplicate or triplicate measurements. Values of E^{0*} were obtained by each institute for all measured salinities and temperatures using *cell II* and following the method described in Section 2.3. The solutions used for the determination of the E^{0*} terms were prepared by each institute in its own laboratory. The same salts and stock solutions used by PTB for the preparation of the ASW/TRIS buffers were distributed to LNE and IPQ for the preparation of these solutions. Seven ASW solutions with $b(HCl)$ of 0.005, 0.01, 0.012, 0.028, 0.032, 0.048 and 0.052 mol kg^{-1} H_2O were measured for each salinity, some outliers were discarded. This is further discussed in section 2.6.2.

Homogeneity between $Ag_{(s)}/AgCl_{(s)}$ electrodes used for the determination of E^{0*} was checked at each institute either by characterization of their standard potential E^{0} in HCl solution of molality 0.01 mol kg^{-1} H_2O, or by computing standard deviation of potentials acquired between the various $Ag_{(s)}/AgCl_{(s)}$ electrodes in a NaCl solution of molality 0.01 mol kg^{-1} H_2O.

Comparison measurements were made at 25 °C and 30 °C on the three ASW/TRIS equimolal buffers for both salinities 5 and 35 to demonstrate the compatibility of the results of the three NMIs. Instrumentations available at LNE and IPQ prevented from making the comparison at the lowest temperatures, which were only investigated at PTB.

2.6. Data processing and fitted function

The data processing described in the following subsections was done with R (R Core Team, version: 4.3.2 (R Core Team, 2023)). Key packages with their versions are listed in Table 1 of Schäfer et al. (2025). The full

code can be found in the Zenodo Repository (https://doi.org/10.5281/zenodo.14964817). A custom R package, that combined many of the functions needed, was developed and is available with the code.

2.6.1. Evaluation of anomalous results

Three equimolal ASW/TRIS buffers, in which *b*(TRIS) and *b*(TRIS.HCl) are equal to 0.01, 0.025, and 0.04 mol kg^{-1} H_2O, have up to now been studied and reported one time in literature to allow extrapolation of the corresponding pH_T values linearly to zero TRIS concentration (Müller et al., 2018). However, our results suggest that the assumption of linearity is not entirely justified in this molality range. Non-linear behaviour was observed at all salinities and temperatures studied and the non-linearity is more pronounced at low temperatures and high salinities (Fig. 2). In Fig. 2, at each salinity and temperature, the discrepancy between pH_T values for *b*(TRIS) = 0.01 and 0.025 mol kg^{-1} H_2O versus the discrepancy between pH_T values for *b*(TRIS) = 0.025 and 0.04 mol kg^{-1} H_2O is significant, showing the non-linearity in all the conditions. It leads to differences in the extrapolated pH_T values of around 0.002.

The reason for the deviation from linearity, which suggests that the pH_T values at 0.01 mol kg^{-1} H_2O become smaller in a non-linear way for decreasing TRIS and TRIS.HCl molalities, has been illustrated by Clegg et al. (2022). They suggest that for molalities lower than 0.02 mol kg^{-1} H_2O the amounts become too low for effective buffering, so that the pH_T drops and tends toward neutrality. Consequently, Clegg and co-workers suggest to work at a lower limit of *b*(TRIS) and *b*(TRIS.HCl) equal to 0.02 mol kg^{-1} H_2O. Because the value of 0.01 mol kg^{-1} H_2O used in this study is below this limit, non-linearity has been observed in the experiments to differing degrees. However, we note that this non-linear behaviour, which cannot be neglected but is still small in relation to the absolute pH_T value, has not always been reported in literature (e.g., Fig. 1 of DelValls and Dickson, 1998; Müller et al., 2018). In DelValls and Dickson (1998) the drop in pH_T values is only visible for *b*(TRIS) below 0.01 mol kg^{-1} H_2O and at temperatures below 20 °C. The small magnitude of this change appears to be comparable to the minor deviations that can occur in Harned cell measurements, which may explain why it is not always detectable.

We decided to use only the results of the ASW/TRIS buffers at 0.025 mol kg^{-1} H_2O and 0.04 mol kg^{-1} H_2O for the computation of the fitted function. Furthermore, we suggest that future measurements should be conducted with a 0.02 mol kg^{-1} H_2O ASW/TRIS buffer at the lower end, in agreement with the suggestions by Clegg et al. (2022).

The deviation of the measured pH_T values from the fitted function was significantly larger at salinity 20 for all temperatures compared to the pH_T values at all other salinities. A thorough analysis of the available measurement parameters failed to reveal any obvious errors. The measurements that exhibited issues were specifically the one measured for *b*(TRIS) = 0.025 mol kg^{-1} H_2O at all temperatures. Including the results at salinity 20 in the regression distorted the fitted function significantly compared to a regression without these results. We therefore removed the results at salinity 20, assuming that they were subject to an unnoticed measurement error, more details are given in Schäfer et al. (2025).

Finally, the measurements at 40 °C were excluded for salinity 25 because a voltage peak interfered in the measured potential and affected the results.

2.6.2. Determination of E^{0*}

Measurements of ASW at seven different HCl molalities (without TRIS buffer) were made for each salinity and temperature value to determine E^{0*} values (see section 2.5).

Each measured potential $E'_{ASW+HCl}$, corrected to a pressure of H_2 equal to 1 atm, was used to calculated E' with eq. 8.

$$E' = E'_{ASW+HCl} + \frac{RT\ln(10)}{F} \lg(b(\mathrm{HCl}) \bullet b(\mathrm{Cl})) \quad (8)$$

where *F* is the Faraday constant (C mol^{-1}), *R* the Gas constant (J mol^{-1} K^{-1}), *T* the measured temperature (K), and *b*(HCl) is the molality of HCl, *b*(Cl) the molality of Cl^- (Müller et al., 2018).

Each E^{0*} value was determined from a quadratic fitted function fitted through the E' values and the corresponding molalities *b*(HCl):

$$E' = \alpha_0 + \alpha_1 \bullet b(\mathrm{HCl}) + \alpha_2 \bullet b(\mathrm{HCl})^2 \quad (9)$$

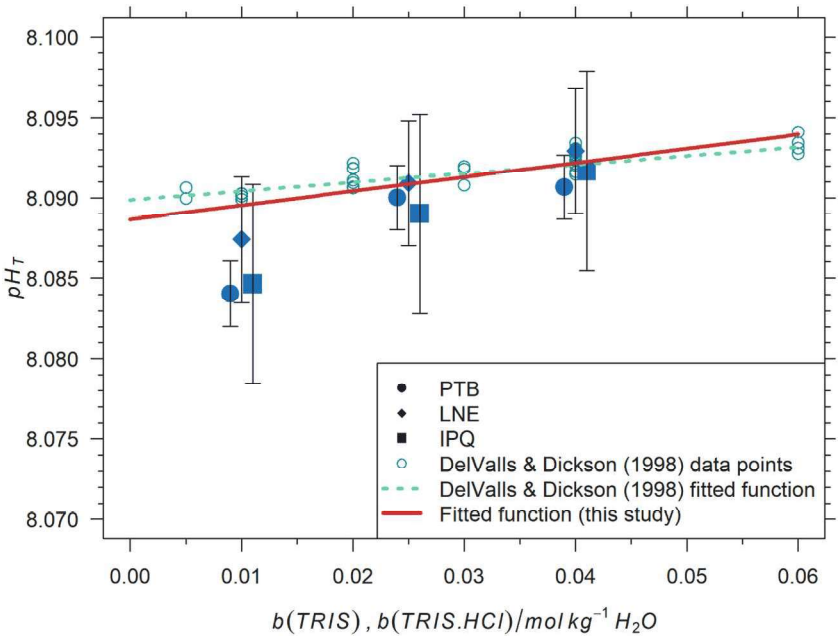

Fig. 1. Harned cell measurements conducted by the three NMIs at 25 °C for the three equimolal TRIS buffers of nominal practical salinity 35. Where ●, ◆ and ■ represent measurements conducted by PTB, LNE and IPQ, respectively. The data points are slightly staggered from the actual TRIS molality in the x axis in order to visualize the error bars correctly. Error bars correspond to their respective expanded uncertainties (i.e. with a coverage factor, k, of 2). The straight line represents the values calculated with the fitted function, while the dotted line represents values obtained by DelValls and Dickson (1998). The measurement data points of DelValls and Dickson (1998) are also included (○). (color only in the online version).

with α_0, α_1, and α_2 being the fitted parameters. E^{0*} was then determined as the value of the fitted function at $b(HCl) = 0$ mol kg^{-1} (i.e., α_0). The E' values were weighted with $\frac{1}{u(E')^2}$, $u(E')$ being the standard uncertainties of the measured E' values (details of the uncertainty calculation are given in Schäfer et al. (2025)). Eq. 9 was fitted with metafor::rma (Viechtbauer, 2010).

2.6.3. Calculation of pH_T values of ASW TRIS buffers

The pH_T values were calculated at each salinity and temperature with eq. 4 (DelValls and Dickson, 1998). The input values are:

- The potentials E of the respective equimolal ASW/TRIS buffers at each combination of nominal practical salinity, S, and temperature, T, obtained as described in section 2.5.
- The corresponding E^{0*} value, obtained as described in section 2.6.2.
- The molality $b(Cl^-)$, calculated from the gravimetric preparation of the TRIS buffer from the added mass of salts containing chloride ions (Table 1).
- The Nernstian term k, according to eq. 3.
- The water mass fraction, ω_{H_2O}, calculated with eq. 5.

Additional to the input values needed to calculate pH_T, temperature must be known for each pH_T value for the subsequent fitting (see below). Temperatures were measured during the Harned cell measurements.

Finally, the Graybill-Deal estimator with dispersion was used to calculate the mean pH_T value with uncertainty if more than one institute had measured at the same salinity and temperature (CCQM, 2013). This ensured that no condition had more influence in the fit just because it was measured more often.

2.6.4. Model fitting

The equation proposed by Müller et al. (2018) (eq. 9 of that publication) was used to describe the relationship between salinity, temperature, TRIS molality and pH_T. However, since the pH_T results at 0.01 mol kg^{-1} H_2O TRIS molality were excluded, so that there are just two pH_T values at the two remaining TRIS molalities for each salinity and temperature, the quadratic b(TRIS) terms were omitted, giving:

$$\begin{aligned} pH_T = {} & g + h_1 \bullet S + h_2 \bullet S^2 + h_3 \bullet S^3 + i_1 \bullet T + i_2 \bullet \ln(T) + i_3 \bullet \frac{1}{T} + j_1 \bullet S \\ & \bullet T + j_2 \bullet S^2 \bullet T + j_3 \bullet S^3 \bullet T + j_4 \bullet S \bullet \ln(T) + j_5 \bullet S^2 \bullet \ln(T) + j_6 \\ & \bullet S^3 \bullet \ln(T) + k_1 \bullet \frac{S}{T} + k_2 \bullet \frac{S^2}{T} + k_3 \bullet \frac{S^3}{T} + l_1 \bullet b(\mathrm{TRIS}) + l_2 \\ & \bullet b(\mathrm{TRIS}) \bullet S + l_3 \bullet b(\mathrm{TRIS}) \bullet T + l_4 \bullet b(\mathrm{TRIS}) \bullet S \bullet T \end{aligned} \quad (10)$$

where T is the temperature in Kelvin in the interval $278.15 \leq T \leq 313.15$ (i.e. 5–40 °C), $b(TRIS)$ the TRIS molality in mol kg^{-1} H_2O, and S the nominal practical salinity in the interval $5 \leq S \leq 40$.

The extrapolated pH_T value at 0 mol kg^{-1} H_2O TRIS molality can then simply be calculated by inserting b(TRIS) = 0 mol kg^{-1} H_2O. We used the stats::glm function and weighted the pH_T values with $\frac{1}{u(pH_T)^2}$ for the fit. The MASS::stepAIC function was used to do stepwise model selection based on the Akaike Information Criterion (AIC) (Venables and Ripley, 2002). The number of necessary digits in the coefficients was determined by checking with how many digits the calculated pH_T value of the function stabilised.

The uncertainty of the fitted function is discussed in Schäfer et al. (2025).

The fitted function allows computing pH_T values of an ASW sample at a given practical salinity and temperature and zero TRIS molality. Additionally, it can be used to calculate the pH_T at zero TRIS molality from the measured pH_T value of an ASW/TRIS buffer at a given TRIS buffer molality.

Alternatively, it would have been possible to calculate a fitted function $pH_T(S, T)$ at zero TRIS molality from pH_T values received from a linear extrapolation of the pH_T values measured at molalities 0.025 and 0.04 mol kg^{-1} H_2O for each salinity and temperature individually. However, this approach was less robust against statistical variations of the measurements results and was therefore discarded.

2.7. Spectrophotometric measurements

Spectrophotometric measurements were performed to check the values of $K_2^T e_2$ obtained by Müller and Rehder (2018) agreed with the results of this work, even though there are reasons to expect that the former will differ, this is further discussed in section 3.3. The measurements were performed at LNE on equimolal ASW/TRIS buffers of nominal practical salinities 5, 20, 35 and 40 with b(TRIS) = b(TRIS.HCl) = 0.025 and 0.04 mol kg^{-1} H_2O. Three replicates were performed for each buffer.

The indicator dye, a purified mCP solution at 2 mmol/L in ultrapure water with a pH close to that of natural seawater, was injected using a micropipette with a volume of 60 µL. The indicator solution was made at GEOMAR (Helmholtz Centre for Ocean Research Kiel), who purified the dye using HPLC, and prepared the solution following the recommendations of Dickson et al. (2007). Absorbance values were acquired at 434 nm and 578 nm wavelengths for the dye's acidic and basic forms, and at a non-absorbing wavelength of 730 nm as a baseline check. Two dye additions were performed to correct for any pH_T perturbation coming from the dye solution, by extrapolation of the ratio R (eq. 1) to zero dye addition. The final pH_T value was calculated following the method described in Liu et al. (2011). The $K_2^T e_2$ of the indicator dye was calculated using coefficients given in Müller and Rehder (2018).

The spectrophotometric pH_T values were corrected to 25 °C to compare them. To this end, the potentiometric characterization of the buffers made at temperatures between 5 °C and 40 °C was used to determine relations of pH_T dependence on temperature for all the studied salinities. These relations were used for the correction at 25 °C.

3. Results and discussion

3.1. Equivalence of results between the three NMIs

Fig. 1 illustrates the pH_T results at three TRIS molalities, salinity 35 and 25 °C that have been measured by the three NMIs to estimate the equivalence of the measurements. Measurement points of each NMI represent the mean of repeated measurements, with its associated expanded uncertainty (k = 2). The values and associated expanded uncertainties were computed and provided by each institute. From the compatibility tests performed at 25 °C and 30 °C, both for salinities 5 and 35, the maximum standard deviation between the three NMIs for specific TRIS molalities is 0.0048 pH_T units with a mean standard deviation of 0.0020. These data are within the expanded uncertainties of the measurements, presented as error bars in Fig. 1 for salinity 35 and 25 °C, which demonstrates the equivalence among NMIs.

DelValls and Dickson (1998) also conducted measurements on TRIS buffers of various TRIS molalities for a nominal practical salinity of 35 and at 25 °C. They derived from their results a function represented by the dotted line in Fig. 1 (which has here been adjusted to use the same conversion to an amount content basis as in eq. 5, about −0.0008 in pH_T).

Fig. 1 demonstrates the equivalence of measurements between the three NMIs, and shows the results are consistent with the non-linear behaviour predicted by Clegg et al. (2022) for TRIS buffers at low buffer molalities (below 0.02 mol kg^{-1} H_2O). Their calculation indeed suggests that pH_T for buffers with a molality of TRIS of 0.01 mol kg^{-1} H_2O should be less than at 0.025 mol kg^{-1} H_2O by about 0.0008 at salinity 35 and 25 °C. Here the non-linearity seems to be more pronounced with a discrepancy in the extrapolated value of about −0.003

pH_T units if the values at $b(\text{TRIS}) = b(\text{TRIS.HCl}) = 0.01$ mol kg^{-1} H_2O are included. In contrast, the non-linear behaviour is observed in only a few of the results of DelValls & Dickson, who conducted measurements with TRIS buffers having TRIS molalities as low as 0.005 mol kg^{-1} H_2O.

3.2. Fitted function

The fitted function which gives equimolal TRIS buffer pH_T as a function of salinity, temperature and TRIS molality (eq. 10) was computed from Harned cell measurements of TRIS buffers with $b(\text{TRIS}) = b(\text{TRIS.HCl}) = 0.025$ and 0.04 mol kg^{-1} H_2O, as described in Section 2.6. All pH_T measurement results can be found in the Zenodo Repository (https://doi.org/10.5281/zenodo.14964822). The coefficients to be used in eq. 10 are given in Table 2. The coefficients l_2, l_3 and l_4 in eq. 10 have a value of zero, and are thus not reported in Table 2.

It should be noted that to convert the pH_T values given by the fitted function, (1) to $pH_{T,m}$ values (i.e. in molality-basis), or (2) to the pH_T values obtained with the ω_{H_2O} conversion factor presented by DelValls and Dickson (1998), an adjustment on only the salinity term $h_1 \bullet S$ is needed (eq. 10). For (1), add $+\lg(1 - 0.0010047 \bullet S)$ and for (2), add $+\lg\left(\frac{1-0.0010047\bullet S}{1-0.00106\bullet S}\right)$.

Fig. 2 shows, for each temperature, the fitted function as a function of salinity calculated with eq. 10 for $b(\text{TRIS}) = b(\text{TRIS.HCl}) = 0.025$ and 0.04 mol kg^{-1} H_2O, together with the measured pH_T values, excluding the discarded values (see section 2.6.1).

The pH_T of TRIS buffers for a pure artificial seawater matrix were then obtained by applying $b(\text{TRIS}) = b(\text{TRIS.HCl}) = 0$ mol kg^{-1} H_2O to the fitted function. Fig. 3 shows these extrapolated pH_T values obtained in that way as a function of nominal practical salinity for each of the eight temperatures studied (5–40 °C).

Fig. 4 shows, for all salinities and at 5 °C, 25 °C and 40 °C, the comparison of the fitted function obtained in this study with previous work available in the literature. The fitted functions from DelValls and Dickson (1998) and Müller et al. (2018) studies were corrected to take into account the different way of converting the pH_T values to amount content. The figure shows good agreement between studies for pH_T values above salinity 20. However, discrepancies occur for lower salinities.

Müller and co-workers studied pH_T of TRIS buffers, having the same TRIS molalities, but deviating ASW compositions, in the interval of salinity 5–20 with an added measurement at salinity 35, and in the temperature interval 5–45 °C. DelValls and Dickson (1998) studied the equimolal TRIS buffer for $b(\text{TRIS}) = b(\text{TRIS.HCl}) = 0.04$ mol kg^{-1} H_2O in the salinity interval 20–40 and temperature interval 0–45 °C. Müller and co-workers combined their results with those of DelValls and Dickson to compute a fitted function giving pH_T values of TRIS buffers as a function of salinity, temperature and molality of TRIS in the whole interval of nominal practical salinity 5–40. This function, from Müller et al. (2018), is illustrated by large dashes in Fig. 4.a-c.

Mosley et al. (2004) also studied pH_T of TRIS buffers of $b(\text{TRIS}) = b(\text{TRIS.HCl}) = 0.04$ mol kg^{-1} H_2O at 25 °C for estuarine waters, i.e. for low salinities. They computed their function with that from DelValls and Dickson (1998) for $S > 20$ and from Bates and Hetzer (1961a, 1961b) that performed measurements on TRIS buffers made in pure water. However, lack of measurements in-between low salinities and $S > 20$, as well as high standard deviation between measurements of Bates and Hetzer (1961a, 1961b), raises questions about the robustness of the resulting fitted function. It is thus not presented in Fig. 4.a-c, nor further discussed.

Fig. 4.a-c shows good agreement between all fitted functions presented for salinities between 20 and 40 (i.e. discrepancies ≤0.003 pH_T units). Moreover, the pH_T of ASW/TRIS buffer with a molality of $b(\text{TRIS}) = b(\text{TRIS.HCl}) = 0.04$ mol kg^{-1} H_2O at salinity 35 and 25 °C has previously been reported in literature many times. Our fitted function also shows good agreement with these studies with a maximum discrepancy of 0.002 (Capitaine et al., 2023b; Papadimitriou et al., 2016; Pratt, 2014).

However, the discrepancy between our model and the one of Müller et al. (2018) increases for salinities below 20, especially at high temperatures. Müller et al. (2018) computed the composition of their equimolal TRIS buffers with $b(\text{TRIS}) = b(\text{TRIS.HCl}) = 0.025$ and 0.01 mol kg^{-1} H_2O taking as reference the composition at salinity 20 of DelValls and Dickson for $b(\text{TRIS}) = b(\text{TRIS.HCl}) = 0.04$ mol kg^{-1} H_2O. They also computed the composition of TRIS buffers at lower salinities from this reference composition. To this end, they have used eq. 1 of Müller et al. (2018). However, this equation leads to a difference of the composition of ASW compared to the reference composition of ASW (Clegg et al., 2022). To keep the salinity of a TRIS buffer constant when adding HCl, all salt molalities were changed to compensate for the addition of HCl instead of only changing the molality of NaCl. This results in different sulphate molalities between the three equimolal buffers at a given salinity and affects the chemical equilibria defining pH_T. Using those pH_T values to extrapolate to $b(\text{TRIS}) = b(\text{TRIS.HCl}) = 0$ mol kg^{-1} H_2O leads to biases in the range − 0.005 to −0.01 pH_T units at the extrapolated composition of pure ASW, and at 25 °C, according to Clegg et al. (2022). The maximum bias observed for extrapolated values between the function presented in this study and the one of Müller et al. (2018) is of −0.014 for salinity 15 at 40 °C.

In contrast, Müller and co-workers used the same composition as DelValls and Dickson for their measurement at salinities 20 and 35, where good agreement is found. This proves the overall equivalence of the quality of the measurements of all these studies.

Likewise, the present study reproduces the measurements of DelValls and Dickson (1998) for the equimolal TRIS buffer of $b(\text{TRIS}) = b(\text{TRIS.HCl}) = 0.04$ mol kg^{-1} H_2O for salinities from 20 to 40 and temperatures from 5 °C to 40 °C. The maximum discrepancy between pH_T values presented in Fig. 4.d-f for this study and one of DelValls and Dickson (1998) is −0.0022, being within expanded uncertainties of measurements. No significant dependence of the discrepancy on temperature and salinity can be observed. Additionally, our results are in agreement with the measurements of DelValls and Dickson (1998) performed on a TRIS buffer of $b(\text{TRIS}) = b(\text{TRIS.HCl}) = 0.01$ mol kg^{-1} H_2O at salinity 35 and 25 °C. Since we have used the same procedures as DelValls and Dickson (1998) for sample preparation, this agreement in the range of salinity 20–40 validates the approach to obtain the pH_T values for lower salinities (5–20), giving confidence in the final fitted function.

The preparation and characterization methods for ASW/TRIS buffers can be considered reproducible, as they show good agreement with previous studies when the same methodology is applied (Fig. 4). A future application of this work would be to characterize the dye using freshly prepared ASW/TRIS buffers, assigning pH_T values derived from the

Table 2
Coefficients to be used in the fitted function given by eq. 10.

Coefficient	Multiplier	Value
g	1	−8.3693859548•10^2
h_1	S	1.8652734033•10^2
h_2	S^2	−1.3605760271•10^1
h_3	S^3	2.4396571566•10^-1
i_1	T	−2.4105706890•10^-1
i_2	$\ln(T)$	1.4637804352•10^2
i_3	$1/T$	2.4705268460•10^4
j_1	$S \bullet T$	5.4254155700•10^-2
j_2	$S^2 \bullet T$	−4.0142626000•10^-3
j_3	$S^3 \bullet T$	7.2290700000•10^-5
j_4	$S \bullet \ln(T)$	−3.2690135916•10^1
j_5	$S^2 \bullet \ln(T)$	2.3891658058•10^0
j_6	$S^3 \bullet \ln(T)$	−4.2866503610•10^-2
k_1	S/T	−4.9041626737•10^3
k_2	S^2/T	3.5485055280•10^2
k_3	S^3/T	−6.3457349499•10^0
l_1	$b(\text{TRIS})$	8.8398941470•10^-2

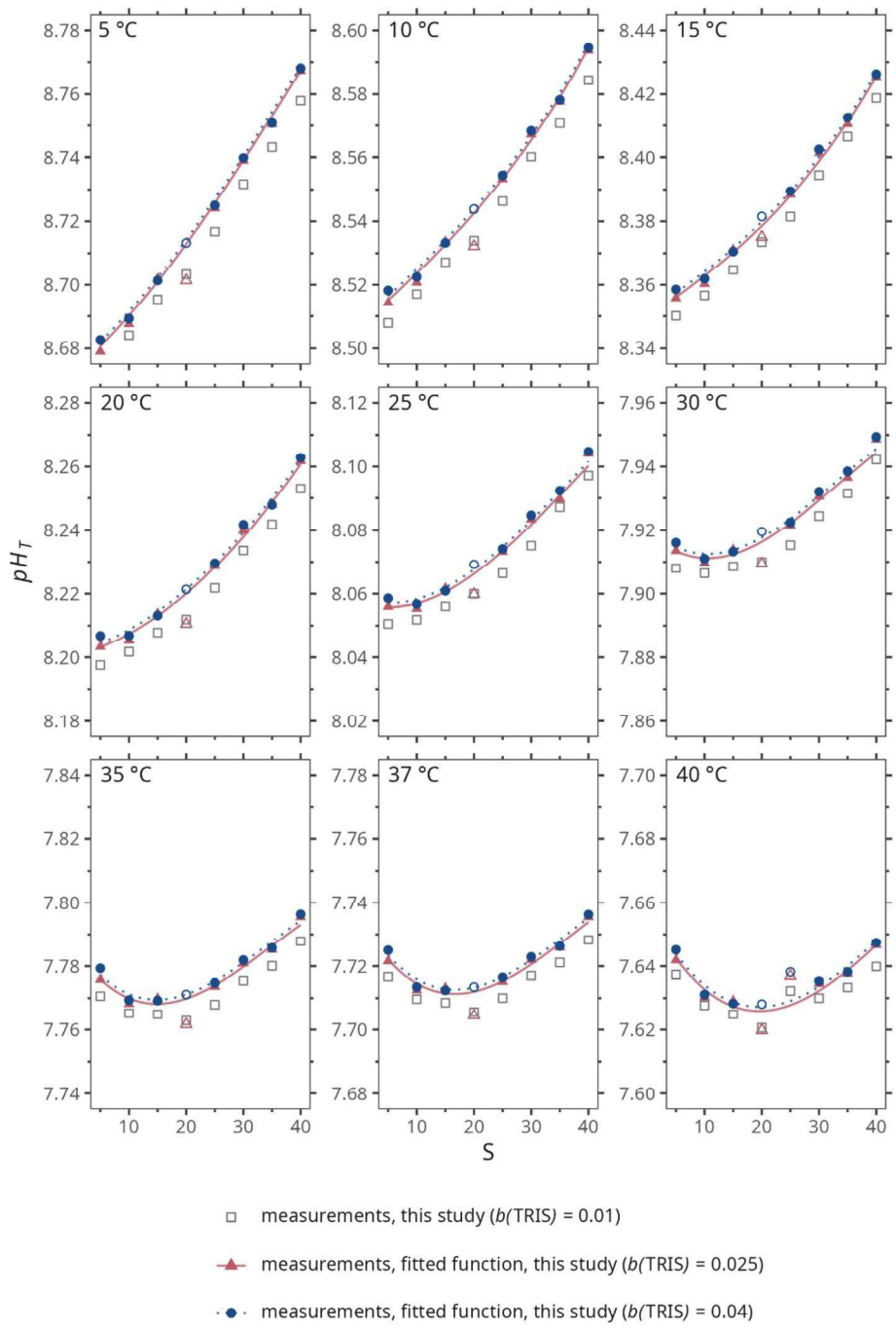

Fig. 2. Fitted function given by eq. 10 and coefficients from Table 2 as a function of temperature and nominal practical salinity. (1) red (▲) and blue (●) represent Harned cell measurements data points made for b(TRIS) = b(TRIS.HCl) = 0.025 and 0.04 mol kg^{-1} H_2O, respectively. (2) thin red and dotted blue lines represent the fitted function for b(TRIS) = b(TRIS.HCl) = 0.025 and 0.04 mol kg^{-1} H_2O, respectively. The excluded data are also presented with grey (□) representing Harned cell measurements data points made for b(TRIS) = b(TRIS.HCl) = 0.01 mol kg^{-1} H_2O; (Δ) and (○) representing excluded data points at salinity 20 for all temperatures, and at salinity 25 at 40 °C; more details are given in section 2.6.1. (color only in the online version). (For interpretation of the references to color in this figure legend, the reader is referred to the web version of this article.)

fitted function presented here.

It should be noted, however, that using updated coefficients for dye characterization may affect the comparability of spectrophotometric pH_t measurements. For instance, the pH_T of ASW/TRIS buffers at *b*(TRIS) = *b*(TRIS·HCl) = 0.04 mol $kg^{-1}H_2O$—used in earlier dye characterizations (Liu et al., 2011)—appears to be approximately 0.0035 units higher than the value extrapolated to zero TRIS molality. This suggests a systematic bias across salinity and temperature, which could potentially be corrected. Nevertheless, the application of any such correction must be thoroughly investigated and carefully discussed within both the metrological and oceanographic communities.

3.3. Spectrophotometric measurements

Fig. 5 shows the difference between the fitted function (eq. 10) and spectrophotometric measurements performed at LNE at 25 °C on the two equimolal TRIS buffers of *b*(TRIS) = *b*(TRIS.HCl) = 0.025 and 0.04 mol kg^{-1} H_2O for salinities 5, 20, 35 and 40. The mean deviation between the

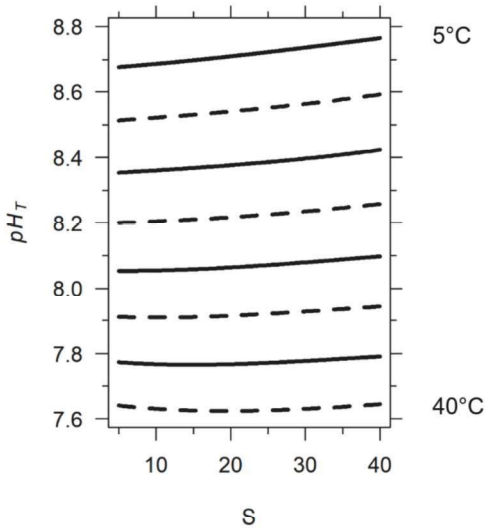

Fig. 3. Fitted function given by eq. 10 and coefficients from Table 2 as a function of nominal practical salinity for equimolal b(TRIS) and b(HCl) equal to 0 mol kg^{-1} H_2O, at each studied temperature. The results go in order of increasing temperature from the top to the bottom of the plot with alternating dashed and straight lines for more clarity.

fitted function and the spectrophotometric pH_T value is of −0.0009.

The spectrophotometric measured pH_T values are calculated from $K_2^T e_2$ values from Müller and Rehder (2018) which corresponds to values at b(TRIS) = 0 mol kg^{-1} H_2O. The coefficients given in Müller and Rehder (2018) for the calculation of $K_2^T e_2$ seem to give pH_T values that are in agreement with the fitted function presented in this paper for the four buffers tested at 25 °C, even for salinity 5. The maximum discrepancy is −0.0051 pH_T units, which is lower than the expanded uncertainty (k = 2) of the spectrophotometric pH_T results, estimated to be around 0.01 (Capitaine et al., 2023a; Carter et al., 2013; DeGrandpre et al., 2014). For comparison, from the same spectrophotometric measurements, pH_T values were calculated with the coefficient given in Liu et al. (2011) for salinities 20, 35 and 40 (as they do not provide coefficients for salinities below 20). It gave a maximum discrepancy of 0.0037 pH_T units.

The TRIS buffer composition made by Müller et al. (2018) is not the one commonly used, and resulting values do not extrapolate truly to pure ASW. The use of $K_2^T e_2$ values from Müller and Rehder (2018) might thus introduce an inconsistency in the subsequent spectrophotometric pH_T calculation. $K_2^T e_2$ values were computed based on the knowledge of TRIS buffers pH_T values, themselves computed from their fitted function for a pure ASW (b(TRIS) = 0 mol kg^{-1} H_2O). The discrepancy between the pH_T values obtained from the fitted function presented in our study and the one of Müller et al. (2018) for a pure ASW at 25 °C and in the range of salinities 5–40, vary between −0.004 and 0.010. The suitability of coefficients given in Müller and Rehder (2018) must be investigated on a large data set, for example for a TRIS buffer of salinity 15 at 40 °C, where the biggest discrepancy was obtained in extrapolated pH_T values compared to our study, as well as on natural seawater samples. It should indeed be noted that $K_2^T e_2$ values extrapolated to b(TRIS) = 0 mol kg^{-1} H_2O are highly relevant for spectrophotometric measurements on natural seawater, while measurements on TRIS buffers could benefit from $K_2^T e_2$ values for specific TRIS molalities or from corresponding corrections. This may explain the observation outlined in Fig. 5 that spectrophotometric pH_T values for equimolal TRIS buffers of the highest molality (i.e. 0.04 mol kg^{-1} H_2O) seem to give systematically lower values compared to TRIS buffers at molalities 0.025 mol kg^{-1} H_2O. This should be further investigated. All the more, as the deviation of the fitted function for pH_T of Müller et al. (2018) shows a larger, positive deviation for TRIS buffer at 0.04 mol kg^{-1} H_2O in the low salinity interval (see Fig. 4.a-c).

4. Traceability of potentiometric pH_T measurements

The work presented, by linking TRIS buffers pH_T values to a pure artificial seawater matrix, and thus to a true pH_T scale, offers improved metrological traceability of pH_T measurements.

Metrological traceability is defined as the "property of a measurement whereby the result can be related to a reference through a documented unbroken chain of calibrations, each contributing to the measurement uncertainty" (JCGM 200:2012, 2012). Metrological traceability is ideally established to the International System of Units (SI) as it is the most stable reference. There are certain cases where this cannot be achieved, for example, if the measurement procedure requires making approximations that are not fully mastered or do not have quantified uncertainties. In this case, the reference can either be a reference material or a common procedure.

The route of traceability of routine seawater pH_T spectrophotometric measurement results is currently established to the commonly accepted measurement procedure of the primary pH potentiometric measurement method, i.e. Harned cell measurement method. This is achieved through the ASW/TRIS buffer solutions that allow the characterization of the indicator dye (Liu et al., 2011; Loucaides et al., 2017; Müller and Rehder, 2018).

This measurement method lacks direct metrological traceability to the SI units, due to the assumptions required for the interpretation of the measurements, as expressed in section 2.3. Indeed, the conventional thermodynamic and operational total pH definitions ($pH^*_{T,m}$ and $pH_{T,m}$, respectively) differ as shown by Fig. 6 (Dickson et al., 2016).

In Fig. 6, γHCl is the mean activity coefficient of HCl, $b(SO_4^{2-})$ the molality of sulphate ions (mol kg^{-1} H_2O) and $Kb(HSO_4^-)$ the molality-based dissociation constant of bisulphate ions.

The two components with the "trace" superscripts in Fig. 6 indicate quantities in a pure artificial seawater composition and $b^T(SO_4^{2-})$ is the total sulphate molality in pure ASW.

If it is assumed that, in TRIS buffers, $1+\frac{b(SO_4^{2-})}{Kb(HSO_4^-)}$ and γHCl are equivalent to their limiting values in pure ASW (Clegg et al., 2022), the $pH^*_{T,m}$ definition in Fig. 6 can be simplified under this assumption to give the so called operational potentiometric $pH_{T,m}$ (eq. 2).

For simplicity, the $-2\lg\left(\frac{\gamma HCl^{trace}}{\gamma HCl}\right)$ and $-\lg\left(\frac{1+\frac{b(SO_4^{2-})}{Kb(HSO_4^-)}}{1+\frac{b^T(SO_4^{2-})}{Kb(HSO_4^-)^{trace}}}\right)$ terms are below referred to as the "γHCl term" and "$Kb(HSO_4^-)$ term", respectively.

Achieving traceability of pH_T potentiometric measurement results to SI units would require the quantification of the γHCl and $Kb(HSO_4^-)$ terms as well as their uncertainties, which cannot be achieved experimentally.

The difference between conventional thermodynamic and operational potentiometric pH_T (Fig. 6), coming from the γHCl and $Kb(HSO_4^-)$ terms, has been studied by Clegg et al. (2022) using a Pitzer based speciation model. It has been assessed to be 0.0045 ± 0.0014 for an equimolal TRIS buffer with b(TRIS) = b(TRIS.HCl) = 0.04 mol kg^{-1} H_2O in ASW of nominal salinity 35 at 25 °C.

It was suggested by Clegg et al. (2022) that for a pure artificial seawater matrix, $pH^*_{T,m}$ and $pH_{T,m}$ values are identical (i.e. for b(TRIS) = b(TRIS.HCl) = 0 mol kg^{-1} H_2O) (see Fig. 12a of Clegg et al., 2022). They also suggest that the γHCl and $Kb(HSO_4^-)$ terms are expected to tend linearly toward zero as buffer molality is reduced. SI traceability of TRIS buffers might thus be established solely from measurements through

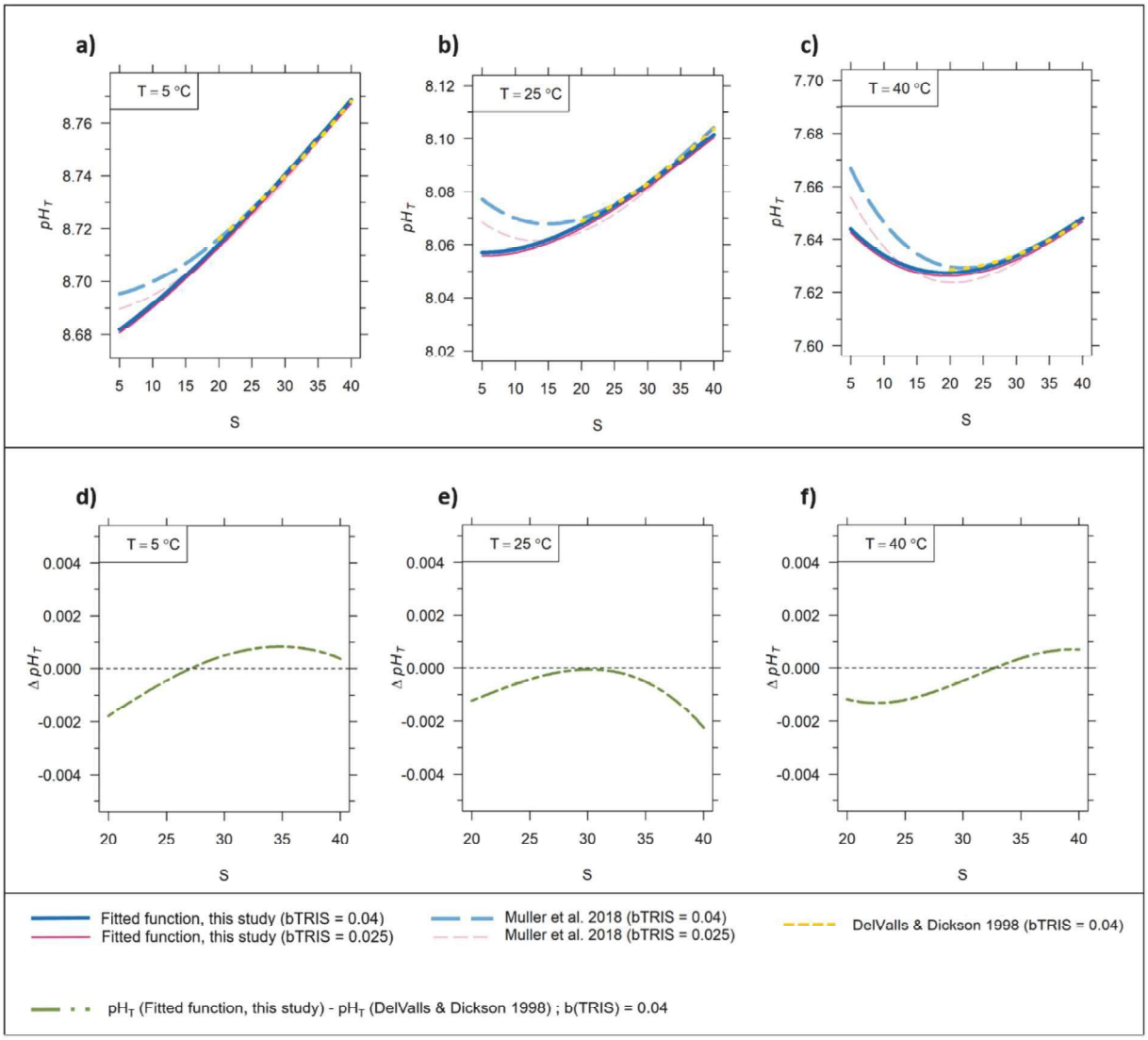

Fig. 4. a-c) pH_T fitted functions at 5 °C, 25 °C and 40 °C computed in this study, in Müller et al. (2018) and in DelValls and Dickson (1998); represented by the straight line, large dashes and dots, respectively. The thin pink and thick blue functions correspond to equimolal buffers of $b(TRIS) = b(TRIS.HCl) = 0.025$ and 0.04 mol kg^{-1} H_2O, respectively. d-f) Discrepancy between the pH_T fitted functions at 5 °C, 25 °C and 40 °C computed in this study and in DelValls and Dickson (1998) for the equimolal buffer of $b(TRIS) = b(TRIS.HCl) = 0.04$ mol kg^{-1} H_2O. (color also in the printed version).

relation to a pure artificial seawater (i.e. without TRIS and TRIS.HCl).

The use of the speciation model may in the future assist this process by providing constraints on, for example, the slope of the relationship between $pH_{T,m}$ and TRIS buffer molality. A sufficiently accurate and validated model would also be able to determine $pH^*_{T,m}$ values for finite buffer molalities, including the hypothetical value for pure artificial seawater. This could be of great help in the objective of making SI traceable reference materials available to the oceanographic community. However, the model defined by Clegg and co-workers needs first to be validated and to be improved for key interactions. Uncertainties associated with the relevant Pitzer interactions parameters must also be thoroughly assessed. Moreover, it should be noted that while the activity coefficients of ions involved in acid-base equilibria in pure artificial seawater (ASW) are the closest approximation, they do not exactly represent those in natural seawater.

5. Conclusion

This paper presents the characterization of equimolal ASW/TRIS buffers in the intervals of nominal practical salinity 5–40 and temperature 5–40 °C with respect to their operational potentiometric pH_T values, performed with Harned cells at three National Metrology Institutes. These measurements allowed the computation of a fitted function giving pH_T values of equimolal ASW/TRIS buffers depending on salinity, temperature and TRIS molality. For the first time, the experimental data covered in the same study (i.e. using a consistent methodology) the ranges of salinities and temperatures that are most relevant in oceanography. This fitted function allows computation of pH_T values of a pure artificial seawater matrix (i.e. without TRIS and TRIS.HCl contribution) for the aforementioned salinity and temperature ranges. These values are relevant to characterize the indicator dye used for spectrophotometric measurements by better representing its response in real seawater. The uncertainties associated to the pH_T values obtained with the fitted function are detailed in the second part of this paper "pH_T measurements of TRIS buffer solutions in artificial seawater matrix in the salinity range 5–40 and temperature range 5–40 °C. Part 2: uncertainty quantification" (Schäfer et al., 2025).

The consistency with the reference work of DelValls and Dickson (1998) gives confidence in the fitted function for nominal practical salinities as low as 5, and the extrapolation to pure artificial seawater. This

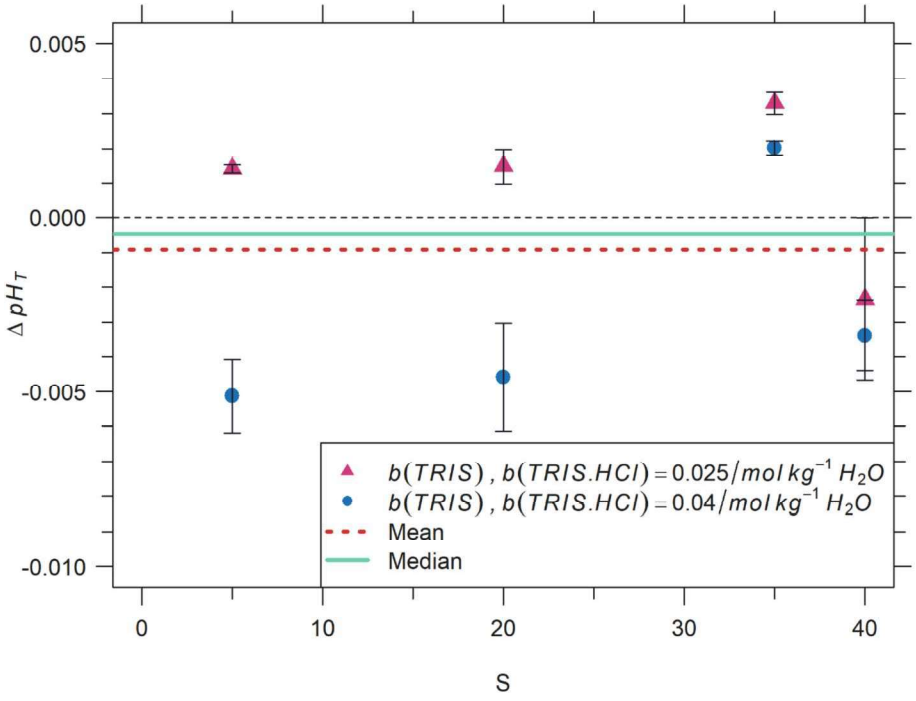

Fig. 5. Difference between the pH_T value given by the fitted function and the mean pH_T obtained from 3 replicates of spectrophotometric measurements made at LNE on equimolal TRIS buffers with $b(TRIS) = b(TRIS.HCl) = 0.025$ (Δ) and 0.04 (○) mol kg^{-1} H_2O of nominal practical salinities 5, 20, 35 and 40 at 25 °C. Error bars represent standard deviations of the three replicates. The thick dashed and solid lines represent mean and median deviations computed from the eight values presented. (color only in the online version).

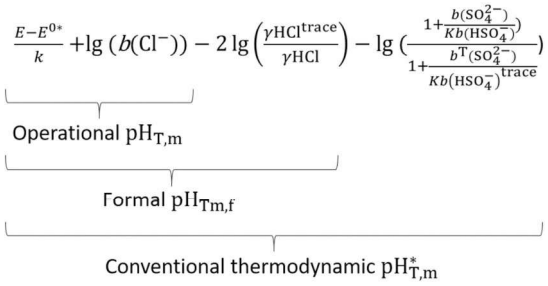

Fig. 6. Differences in the different total pH definitions. (color only in the online version).

work, together with previous study of Clegg et al. (2022) is an important step to establish traceability for potentiometric pH_T measurement results of ASW/TRIS buffers, and, subsequently, for spectrophotometric measurements of natural seawater.

It will subsequently be necessary to characterize the indicator dye based on the fitted function presented. This will support the extension of the spectrophotometric pH_T measurement method to cover a practical salinity range of 5–40 and a temperature range of 5–40 °C, while also laying the groundwork for establishing traceability to SI units in end-user measurements.

However, there are still a few concerns regarding the establishment of traceability of routine spectrophotometric measurements: (1) reference materials used for the spectrophotometric pH_T measurement method are currently not certified for pure artificial seawater, (2) the effect of impurities in mCP and (3) the practical salinity measured of a natural seawater sample and used to calculate the pH_T is not traceable to the SI (Seitz et al., 2011).

The implications of the differences identified in this study compared to previous work—specifically, the definition of water mass fraction in ASW/TRIS buffers and the extrapolation of their pH_T values to zero TRIS molality—must be carefully evaluated and discussed by both the metrological and oceanographic communities. Ultimately, this work provides a valuable foundation for dialogue and collaboration between these two fields.

Data statement

All data involved in the computation of the results are presented either in the manuscript, the Supplementary Material or the Zenodo Repositories (Data: https://doi.org/10.5281/zenodo.14964822; Code: https://doi.org/10.5281/zenodo.14964817). Any other specific information will be made available on demand.

CRediT authorship contribution statement

Gaëlle Capitaine: Writing – original draft, Visualization, Validation, Methodology, Investigation, Formal analysis. **Rieke Schäfer:** Writing – original draft, Visualization, Validation, Software, Methodology, Investigation, Formal analysis, Data curation. **Frank Bastkowski:** Writing – review & editing, Methodology, Investigation, Conceptualization. **Daniela Stoica:** Writing – review & editing, Methodology, Conceptualization. **Olivier Pellegrino:** Writing – review & editing, Methodology, Investigation. **Raquel Quendera:** Writing – review & editing, Methodology, Investigation, Conceptualization. **Eric P. Achterberg:** Writing – review & editing, Supervision. **Thibaut Wagener:** Writing – review & editing, Supervision. **Simon L. Clegg:** Writing – review & editing. **Steffen Seitz:** Writing – review & editing, Supervision, Funding acquisition, Conceptualization. **Paola Fisicaro:** Writing – review & editing, Supervision, Funding acquisition, Conceptualization.

Funding

This work was supported by the Joint Research Project EMPIR 20NRM06 SApHTIES, which received funding from the EMPIR Programme co-financed by the Participating States and from the European

Union's Horizon 2020 Research and Innovation Programme. Gaëlle Capitaine was supported by the CIFRE scholarship n° 2021/0220 provided by ANRT (Association Nationale de la Recherche et de la Technologie).

Acknowledgments

Gaëlle Capitaine acknowledges Anton Petrenko and Vincent Rostaing for their support on conducting the experiments at LNE.

We would like to thank Dr. Thomas Schmelter for his help with determining the best distribution of HCl concentrations for the computation of E^{0*} values.

We thank DFM and SMU for the coulometric characterization of chemical products used in this study.

We also acknowledge the editors and reviewers for their valuable inputs to the paper.

Appendix A. Supplementary data

Supplementary data to this article can be found online at https://doi.org/10.1016/j.marchem.2025.104551.

Data availability

Additional data than ones presented in the manuscript, the SM or the repositories (https://doi.org/10.5281/zenodo.14964822; https://doi.org/10.5281/zenodo.14964817) will be made available on demand.

References

Bates, R.G., 1973. Determination of pH: Theory and Practice. John Wiley&Sons, USA.

Bates, R.G., Hetzer, H.B., 1961. Dissociation constant of the protonated acid form of 2-amino-2-(hydroxyme- thyl)-1,3-propanediol [tris-hydroxymethyl-aminomethane] and related thermodynamic quantities from 0 to 50°. J. Phys. Chem. 65, 667–671. https://doi.org/10.1021/j100822a017.

Buck, R.P., Rondinini, S., Covington, A.K., Baucke, F.G.K., Brett, C.M.A., Camoes, M.F., Milton, M.J.T., Mussini, T., Naumann, R., Pratt, K.W., Spitzer, P., Wilson, G.S., 2002. Measurement of pH. Definition, standards, and procedures (IUPAC recommendations 2002). Pure Appl. Chem. 74, 2169–2200. https://doi.org/10.1351/pac200274112169.

Byrne, R.H., Breland, J.A., 1989. High precision multiwavelength pH determinations in seawater using cresol red. Deep Sea Res. A 36, 803–810. https://doi.org/10.1016/0198-0149(89)90152-0.

Capitaine, G., Demeyer, S., Stoica, D., Alliouane, S., Petton, S., Rimmelin-Maury, P., Savoye, N., Wagener, T., Fisicaro, P., 2023a. Inter-laboratory Comparison on a Reference Material for Seawater Spectrophotometric pHT Measurements. La Valletta, Malta, pp. 11–15. https://doi.org/10.1109/MetroSea58055.2023.10317274.

Capitaine, G., Stoica, D., Wagener, T., Fisicaro, P., 2023b. Production of a reference material for seawater pHT measurements by a National Metrology Institute. Mar. Chem. 252, 104244. https://doi.org/10.1016/j.marchem.2023.104244.

Carter, B.R., Radich, A., Doyle, H.L., Dickson, A.G., 2013. An automated system for spectrophotometric seawater pH measurements. Limnol. Oceanogr. Methods 16–27. https://doi.org/10.4319/lom.2013.11.16.

CCQM, 2013. Guidance Note: Estimation of a Consensus KCRV and Associated Degrees of Equivalence.

CFM, 2017. Guide d'étalonnage des spectrophotomètres (Afnor EDITIONS).

Clayton, T.D., Byrne, R.H., 1993. Spectrophotometric seawater pH measurements: total hydrogen ion concentration scale calibration of m-cresol purple and at-sea results. Deep-Sea Res. I Oceanogr. Res. Pap. 40, 2115–2129. https://doi.org/10.1016/0967-0637(93)90048-8.

Clegg, S.L., Humphreys, M.P., Waters, J.F., Turner, D.R., Dickson, A.G., 2022. Chemical speciation models based upon the Pitzer activity coefficient equations, including the propagation of uncertainties. II. Tris buffers in artificial seawater at 25 °C, and an assessment of the seawater 'Total' pH scale. Mar. Chem. 244, 104096. https://doi.org/10.1016/j.marchem.2022.104096.

DeGrandpre, M.D., Spaulding, R.S., et al., 2014. Considerations for the measurement of spectrophotometric pH for ocean acidification and other studies. Limnol. Oceanogr. Methods 12, 830–839. https://doi.org/10.4319/lom.2014.12.830.

DelValls, T.A., Dickson, A.G., 1998. The pH of buffers based on 2-amino-2-hydroxymethyl-1,3-propanediol ('tris') in synthetic sea water. Deep-Sea Res. I Oceanogr. Res. Pap. 45, 1541–1554. https://doi.org/10.1016/S0967-0637(98)00019-3.

Dickson, A.G., 1990. Standard potential of the reaction: AgCl(s) + 12H2(g) = Ag(s) + HCl(aq), and and the standard acidity constant of the ion HSO4− in synthetic sea water from 273.15 to 318.15 K. J. Chem. Thermodyn. 22, 113–127. https://doi.org/10.1016/0021-9614(90)90074-Z.

Dickson, A.G., Sabine, C.L., Christian, J.R. (Eds.), 2007. Guide to Best Practices for Ocean CO2 Measurements PICES Special Publication, 3, p. 191.

Dickson, A.G., Camões, M.F., Spitzer, P., Fisicaro, P., Stoica, D., Pawlowicz, R., Feistel, R., 2016. Metrological challenges for measurements of key climatological observables. Part 3: seawater pH. Metrologia 53, R26. https://doi.org/10.1088/0026-1394/53/1/R26.

Douglas, N.K., Byrne, R.H., 2017. Spectrophotometric pH measurements from river to sea: calibration of mCP for 0 ≤S≤ 40 and 278.15 ≤T≤ 308.15 K. Mar. Chem. 197, 64–69. https://doi.org/10.1016/j.marchem.2017.10.001.

Fong, M.B., 2021. Uncertainty of Spectrophotometric pH Measurements in Seawater and Implications for Ocean Carbon Chemistry. UC San Diego.

Friedlingstein, P., O'Sullivan, M., Jones, M.W., Andrew, R.M., Hauck, J., Landschützer, P., Le Quéré, C., Li, H., Luijkx, I.T., Olsen, A., Peters, G.P., Peters, W., Pongratz, J., Schwingshackl, C., Sitch, S., Canadell, J.G., Ciais, P., Jackson, R.B., Alin, S.R., Arneth, A., Arora, V., Bates, N.R., Becker, M., Bellouin, N., Berghoff, C.F., Bittig, H.C., Bopp, L., Cadule, P., Campbell, K., Chamberlain, M.A., Chandra, N., Chevallier, F., Chini, L.P., Colligan, T., Decayeux, J., Djeutchouang, L., Dou, X., Duran Rojas, C., Enyo, K., Evans, W., Fay, A., Feely, R.A., Ford, D.J., Foster, A., Gasser, T., Gehlen, M., Gkritzalis, T., Grassi, G., Gregor, L., Gruber, N., Gürses, Ö., Harris, I., Hefner, M., Heinke, J., Hurtt, G.C., Iida, Y., Ilyina, T., Jacobson, A.R., Jain, A., Jarníková, T., Jersild, A., Jiang, F., Jin, Z., Kato, E., Keeling, R.F., Klein Goldewijk, K., Knauer, J., Korsbakken, J.I., Lauvset, S.K., Lefèvre, N., Liu, Z., Liu, J., Ma, L., Maksyutov, S., Marland, G., Mayot, N., McGuire, P., Metzl, N., Monacci, N. M., Morgan, E.J., Nakaoka, S.-I., Neill, C., Niwa, Y., Nützel, T., Olivier, L., Ono, T., Palmer, P.I., Pierrot, D., Qin, Z., Resplandy, L., Roobaert, A., Rosan, T.M., Rödenbeck, C., Schwinger, J., Smallman, T.L., Smith, S., Sospedra-Alfonso, R., Steinhoff, T., Sun, Q., Sutton, A.J., Séférian, R., Takao, S., Tatebe, H., Tian, H., Tilbrook, B., Torres, O., Tourigny, E., Tsujino, H., Tubiello, F., van der Werf, G., Wanninkhof, R., Wang, X., Yang, D., Yang, X., Yu, Z., Yuan, W., Yue, X., Zaehle, S., Zeng, N., Zeng, J., 2024. Global Carbon Budget 2024. Earth System Science Data Discussions, pp. 1–133. https://doi.org/10.5194/essd-2024-519.

IPCC, 2019. 2019: technical summary. In: Pörtner, H.-O., Roberts, D.C., Masson-Delmotte, V., Zhai, P., Tignor, M., Poloczanska, E., Mintenbeck, K., Alegría, A., Nicolai, M., Okem, A., Petzold, J., Rama, B., Weyer, N.M. (Eds.), IPCC Special Report on the Ocean and Cryosphere in a Changing Climate. Cambridge University Press, Cambridge, UK and New York, NY, USA, pp. 39–69. https://doi.org/10.1017/9781009157964.002.

JCGM 200:2012, 2012. International Vocabulary of Metrology (VIM) — Basic and General Concepts and Associated Terms.

Liu, X., Patsavas, M.C., Byrne, R.H., 2011. Purification and characterization of meta-cresol purple for spectrophotometric seawater pH measurements. Environ. Sci. Technol. 4862–4868.

Loucaides, S., Rèrolle, V.M.C., Papadimitriou, S., Kennedy, H., Mowlem, M.C., Dickson, A.G., Gledhill, M., Achterberg, E.P., 2017. Characterization of meta-Cresol Purple for spectrophotometric pH measurements in saline and hypersaline media at sub-zero temperatures. Sci. Rep. 7, 2481. https://doi.org/10.1038/s41598-017-02624-0.

Millero, F., Feistel, R., Wright, D., McDougall, T., 2008. The composition of standard seawater and the definition of the Reference-Composition Salinity Scale. Deep Sea Res. I 55, 50–72. https://doi.org/10.1016/j.dsr.2007.10.001.

Mosley, L.M., Husheer, S.L.G., Hunter, K.A., 2004. Spectrophotometric pH measurement in estuaries using thymol blue and m-cresol purple. Mar. Chem. 91, 175–186. https://doi.org/10.1016/j.marchem.2004.06.008.

Müller, J.D., Rehder, G., 2018. Metrology of pH measurements in brackish Waters—part 2: experimental characterization of purified meta-cresol purple for spectrophotometric pHT measurements. Front. Mar. Sci. 0. https://doi.org/10.3389/fmars.2018.00177.

Müller, J.D., Bastkowski, F., Sander, B., Seitz, S., Turner, D.R., Dickson, A.G., Rehder, G., 2018. Metrology for pH measurements in brackish waters—part 1: extending electrochemical pHT measurements of TRIS buffers to salinities 5–20. Front. Mar. Sci. 5, 176. https://doi.org/10.3389/fmars.2018.00176.

Nemzer, B.V., Dickson, A.G., 2005. The stability and reproducibility of Tris buffers in synthetic seawater. Mar. Chem. 96, 237–242. https://doi.org/10.1016/j.marchem.2005.01.004.

Papadimitriou, S., Loucaides, S., Rérolle, V., Achterberg, E.P., Dickson, A.G., Mowlem, M., Kennedy, H., 2016. The measurement of pH in saline and hypersaline media at sub-zero temperatures: characterization of Tris buffers. Mar. Chem. 184, 11–20. https://doi.org/10.1016/j.marchem.2016.06.002.

Pratt, K.W., 2014. Measurement of pHT values of Tris buffers in artificial seawater at varying mole ratios of Tris:Tris·HCl. Mar. Chem. 162, 89–95. https://doi.org/10.1016/j.marchem.2014.03.003.

R Core Team, 2023. R: A Language and Environment for Statistical Computing. R Foundation for Statistical Computing, Vienna, Austria.

Rastelli, E., Petani, B., Corinaldesi, C., Dell'Anno, A., Lo Martire, M., Cerrano, C., Danovaro, R., 2020. A high biodiversity mitigates the impact of ocean acidification on hard-bottom ecosystems. Sci. Rep. 10, 2948. https://doi.org/10.1038/s41598-020-59886-4.

Schäfer, R., Capitaine, G., Bastkowski, F., Pellegrino, O., Quendera, R., Wagener, T., Achterberg, E., Fisicaro, P., Seitz, S., 2025. pHT Measurements of TRIS Buffer Solutions in Artificial Seawater Matrix in the Salinity Range 5–40 and Temperature Range 5–40 °C. Part 2: Uncertainty Quantification (in preparation).

Seidel, M.P., DeGrandpre, M.D., Dickson, A.G., 2008. A sensor for in situ indicator-based measurements of seawater pH. Mar. Chem. 109, 18–28. https://doi.org/10.1016/j.marchem.2007.11.013.

Seitz, S., Feistel, R., Wright, D.G., Weinreben, S., Spitzer, P., De Bièvre, P., 2011. Metrological traceability of oceanographic salinity measurement results. Ocean Sci. 7, 45–62. https://doi.org/10.5194/os-7-45-2011.
Venables, W.N., Ripley, B.D., 2002. Modern Applied Statistics with S, Fourth ed. Springer, New York. iSBN 0-387-95457-0.
Viechtbauer, W., 2010. Conducting meta-analyses in R with the metafor package. J. Stat. Softw. 36, 1–48. https://doi.org/10.18637/jss.v036.i03.
Yin, T., Papadimitriou, S., Rérolle, V.M.C., Arundell, M., Cardwell, C.L., Walk, J., Palmer, M.R., Fowell, S.E., Schaap, A., Mowlem, M.C., Loucaides, S., 2021. A novel lab-on-chip spectrophotometric pH sensor for autonomous in situ seawater measurements to 6000 m depth on stationary and moving observing platforms. Environ. Sci. Technol. 55, 14968–14978. https://doi.org/10.1021/acs.est.1c03517.

Glossary of symbols

K_2^T: meta-Cresol Purple dissociation constant
e_2: meta-Cresol Purple molar extinction coefficient ratio
T: Temperature (K or °C)
S: Nominal Practical Salinity
I: Ionic strength
pH_T: Operational definition of the total pH, in amount content
$pH_{T,m}$: Operational definition of the total pH, in molality
$pH^*_{T,m}$: Conventional thermodynamic definition of the total pH, in molality
b: Molality, expressed in moles per kilogram of solvent, here water (mol kg^{-1} H_2O)
E: Measured potential between Standard Hydrogen electrode and silver-silver-chloride electrode corrected to a pressure of H_2 equal to 1 atm (V)
E^0: Standard potential of silver-silver chloride electrode in HCl 0.01 mol kg^{-1} H_2O (V)
E^{0*}: Standard potential of silver-silver chloride electrode in ASW media (V)
E': Potential of silver-silver chloride electrode in saline media at a given chloride molality (> 0 mol kg^{-1} H_2O) (V)
k: Nernstian term: $\frac{RTln(10)}{nF}$ (Eq. 4)
F: Faraday constant (C mol^{-1})
R: Gas constant (J mol^{-1} K^{-1})
ω_{H_2O}: Water mass fraction, expressed as grams per kilogram of solution (g kg^{-1} sol)
γ: Activity coefficient

γHCl *term:* $-2\lg\left(\frac{\gamma HCl^{trace}}{\gamma HCl}\right)$

$Kb(HSO_4^-)$ *term:* $-\lg\left(\frac{1+\frac{b\left(SO_4^{2-}\right)}{Kb\left(HSO_4^-\right)}}{1+\frac{b^T\left(SO_4^{2-}\right)}{Kb\left(HSO_4^-\right)^{trace}}}\right)$

Measurement 239 (2025) 115453

Contents lists available at ScienceDirect

Measurement

journal homepage: www.elsevier.com/locate/measurement

Preparation of multicomponent mixtures to support carbon metrology

Florbela A. Dias *, Cristina Palma, Carlos J. Costa

Instituto Português da Qualidade, Rua António Gião, 2, 2629-531 Caparica, Portugal

ARTICLE INFO

Keywords:
Carbon metrology
Multicomponent mixtures
Gravimetric method
Certification

ABSTRACT

The Reference Gas Laboratory (LGR) of Portuguese Institute for Quality (IPQ) is participating in the project – Metrology Support for Carbon Capture Utilization and Storage (MetCCUS) under the new European Partnership on Metrology Program (EPM).

The goal of this project is to develop a metrological infrastructure that enables monitoring and detection of carbon dioxide leaks in energy and industrial processes, in transport networks and also allow the support of a better understanding of the life cycle of carbon dioxide.

The contribution of LGR involves the preparation of certified reference materials (CRM) to allow the measurement of impurities in CO_2 with the associated uncertainties and metrological traceability. The study is focused on the impurities: SO_2, H_2S, CO, O_2 and CH_4. This work also involves the study of interferents based on the analytical methods used. These CRM will provide support for the calibration and validation of instrumentation used in carbon capture processes.

1. Introduction

In recent years, the growing concern surrounding climate change has driven a substantial increase in environmental monitoring efforts. As a result, the demand for measurements with traceability has surged, aiming to ensure the reliability of data and minimize measurement uncertainties. It is important to note the relevance of gas mixtures in environmental monitoring and decarbonization research and how reliable gas mixtures are essential for calibrating instruments that measure atmospheric pollutants and greenhouse gases [1]. Decarbonization refers to the process of reducing carbon dioxide (CO_2) emissions resulting from human activities, with the goal of achieving a low-carbon or carbon–neutral economy. This is a critical strategy in addressing global climate change, driven by the need to reduce the amount fraction of greenhouse gases (GHGs) in the atmosphere. The accumulation of GHGs, particularly CO_2, in the atmosphere leads to global warming and climate change. High levels of CO_2 contribute to ocean acidification, extreme weather events, and loss of biodiversity. Carbon Capture Utilization and Storage (CCUS) is a set of technologies aimed at capturing CO_2 emissions from industrial and energy-related sources, utilizing the captured CO_2 in various applications, or storing it in geological formations to prevent its release into the atmosphere. Decarbonization and CCUS are integral components of global efforts to combat climate change. While there are significant challenges to overcome, advances in technology, supportive policies, and collaborative efforts provide a path forward for reducing carbon emissions and achieving a sustainable, low-carbon future [2,3].

The LGR at IPQ plays a pivotal role in this domain. It is responsible for producing, maintaining, and development of national primary standard gas mixtures in strict accordance with ISO 17034 [4]. These mixtures are meticulously prepared using a gravimetric approach, following an internal procedure aligned with the international standard ISO 6142-1 [5], thereby guaranteeing the utmost accuracy. The gravimetric method is a precise approach to creating standard gas mixtures and involves measuring the mass of each gas component accurately and combining them in specific ratios to achieve the desired amount fraction. It is also important the accuracy and precision in the preparation process and the need for meticulous calibration of equipment and careful handling of gases to minimize errors and ensure the reliability of the standards. With this method we can accomplish the metrological traceability, which ensures that measurements are consistent and comparable across different times and locations. This traceability is crucial for maintaining accuracy in various scientific and industrial applications [1,6,7,8]. The certification of these gas mixtures adheres to the international standard ISO 6143 [9,10], leveraging analytical techniques such as gas chromatography (GC), paramagnetic sensor, non-dispersive infrared spectroscopy (NDIR), and non-dispersive ultraviolet spectroscopy (NDUV).

* Corresponding author at: Instituto Português da Qualidade, Rua António Gião, 2, 2829-513 Caparica, Portugal.
E-mail address: florbelad@ipq.pt (F.A. Dias).

https://doi.org/10.1016/j.measurement.2024.115453
Received 18 January 2024; Received in revised form 2 August 2024; Accepted 3 August 2024
Available online 14 August 2024

The quality control of these measurements is enhanced through active participation in projects and international comparisons [11,12,13,14,15,16]. Furthermore, recognition and inclusion in the *Bureau International des Poids et Mesures* (BIPM) database of Calibration and Measurement Capabilities (CMC) strengthens their commitment to quality [17].

The LGR's latest contribution focuses on preparing multicomponent gas mixtures [18] aimed at enhancing the accuracy, reliability, and traceability of carbon metrology measurements. Specifically, this paper outlines the work undertaken by LGR as part of the MetCCUS project.

The MetCCUS project is a collaborative European initiative aimed at developing advanced metrological techniques to support the accurate measurement and monitoring of carbon dioxide (CO_2) emissions and their capture, utilization, and storage processes. Started on October 1, 2022, with the participation of 21 partners and will lasts for 36 months. This project addresses the growing need for reliable and accurate data to ensure the effectiveness and safety of carbon management technologies, which are critical in mitigating climate change. The primary objectives of the MetCCUS project include development of accurate measurement techniques, improvement of standards and calibration, support for carbon capture and storage (CCS) technologies and utilization of CO_2 mainly in chemical manufacturing or enhanced oil recovery. The project encompasses several key activities namely research and development, field testing and validation, standardization and harmonization and stakeholder engagement and training. MetCCUS represents a critical effort in advancing the metrology of CO_2 measurement, with significant implications for the effectiveness of carbon capture, utilization, and storage technologies. By improving the accuracy and reliability of CO_2 measurements, MetCCUS supports the broader goal of reducing greenhouse gas emissions and combating climate change [19].

Under the MetCCUS project, the contribution of LGR involves the preparation of CRMs to allow the measurement of impurities in CO_2 with metrological traceability, providing support for methods validation and the calibration of instrumentation used in carbon capture processes. LGR had prepared the following bicomponent mixtures: SO_2 in CO_2 matrix and H_2S in CO_2 matrix; and two multicomponent mixtures SO_2+CO+O_2 in CO_2 and H_2S+CO+CH_4+O_2 in CO_2 matrix. This study successfully characterized four polluting gases and oxygen in CO_2 matrix within a cylinder under a pressure of approximately 40 bar, and it entailed an in-depth analysis of interferences and a stability study [20].

2. Gas mixtures preparation

As previously mentioned, reference gas mixtures are prepared according to an internal procedure based on the gravimetric method outlined in ISO 6142-1 [5]. The mixture was prepared by gravimetric addition of each component. The mole fractions of the components in the final mixtures were calculated using the following equation [5]:

$$x_i = \frac{\sum_{A=1}^{P}\left(\frac{x_{i,A}\cdot m_A}{\sum_{i=1}^{n} x_{i,A}\cdot M_i}\right)}{\sum_{A=1}^{P}\left(\frac{m_A}{\sum_{i=1}^{n} x_{i,A}\cdot M_i}\right)} \quad (1)$$

where: x_i is the mole fraction of the component i in the final mixture, $i = 1,\ldots,n$; P is the total number of the parent gases; n is the total number of the components in the final mixture; m_A is the mass of parent gas A determined by weighing, $A=1,\ldots\ldots, P$; M_i is the molar mass of the component i; $x_{i,A}$ is the mole fraction of the component i.

The method described on ISO 6142-1 section used applies specifically to gas mixtures or completely vaporized components, which can be introduced into the cylinder in either the gas or liquid state. The mixtures to be prepared can be either bicomponent or multicomponent.

The calculation of uncertainty associated with the amount fraction of each component requires the evaluation of contributions stemming from factors such weighing of source gases, purity of source gases and molar masses. After these three categories of standard uncertainties have been determined, they are combined to obtain the final uncertainty corresponding to the amount fraction, through the expression:

$$u^2(x_i) = \sum_{i=1}^{n}\left(\frac{\partial x_i}{\partial M_i}\right)^2 \cdot u^2(M_i) + \sum_{A=1}^{p}\left(\frac{\partial x_i}{\partial m_A}\right)^2 \cdot u^2(m_A) + \sum_{A=1}^{p}\sum_{i=1}^{n}\left(\frac{\partial x_i}{\partial x_{iA}}\right)^2 \cdot u^2(x_{iA}) \quad (2)$$

where: $u(M_i)$ – uncertainty in molar mass; $U(m_A)$ – uncertainty in weighing; $u(x_{iA})$ – uncertainty in purity analysis

In order to obtain the expanded uncertainty, the combined uncertainty is multiplied by the coverage factor, k, which for a *t-distribution* with $v_{ef} = y$ effective degrees of freedom corresponds to an expanded probability of approximately 95 %.

During the preparation of gas mixtures, aluminium cylinders with a special coating are used to prevent the adsorption of mixture components on the inner walls.

Following the cylinder selection, a rigorous cleaning process is performed to ensure that any potential residues inside the cylinder do not impact the uncertainty of the composition of the final mixture. This step is particularly important when preparing mixtures with very low amount fractions.

Another critical step in the filling process is the transfer of gases from the parent cylinder, for each component, to the cylinder where the mixture is being prepared. The addition of each gas is carried out at a filling station equipped with electropolished tubes, valves, vacuum and pressure meters, and oil-free turbo molecular vacuum pumps (Fig. 1). The amount of gas added to the cylinder is carefully controlled using a mass comparator (Fig. 1).

The accurate mass of each gas component added to the cylinder is determined using a mass comparator, utilizing calibrated masses that are traceable to the national standard of mass. The traceability of gas measurements to the International System of Units (SI) is ensured using calibrated instrumentation.

By utilizing the results from the purity analysis certificates of the initial gases and the data obtained through the weighing process, the exact composition of the mixture and the associated uncertainties related to the various amount fractions obtained can be accurately calculated.

The gas mixtures were prepared with the following nominal amount fractions: SO_2 (20×10^{-6} mol/mol), H_2S (10×10^{-6} mol/mol) CO (750×10^{-6} mol/mol), CH_4 (2×10^{-2} mol/mol) and O_2 (1×10^{-2} mol/mol) that are the impurities in CO_2 matrix.

The defined limits are based on state-of-the-art knowledge from the latest research findings and available industry expertise. The project partners conducted a literature review and engaged in discussions with stakeholders, including CCS operators, CO_2 end-users, and industry representatives [19]. The CO_2 specification was developed by selecting relevant impurities and concentration levels to ensure material integrity, operability, and considerations for health, safety, and the environment for end-users.

The objective is to prepare standards of these multicomponent mixtures that are as close to reality as possible in order to simulate a real sample. We consider that these types of standards are an advantage for end users who want to carry out the calibration and validation of instrumentation used in carbon capture processes.

The cylinders containing the mixtures were placed in a rolling system for approximately an hour to ensure homogenization (Fig. 2).

3. Gas mixtures certification

The composition of the gas mixture is determined through an individual analysis of the amount fraction of each component. The procedure for determining the amount fraction is described in the international standard ISO 6143 [9]. The analytical method used is a comparative

(a)

(b)

Fig. 1. Filling station and mass comparator.

method, as it employs primary reference standards to establish the calibration curve. The specific analytical methods used were GC, paramagnetic sensor, NDIR, and NDUV. The final results are presented together with their respective uncertainties in accordance with the Guide to the Expression of Uncertainty in Measurement [21].

The produced gas mixtures are certified using specific analysers for SO_2, H_2S, CO, CH_4 and O_2. In each certification, the amount fraction of each component in the prepared mixture is determined by comparing the equipment response to the standards used, and related with the gas under analysis, within appropriate measurement intervals.

Fig. 2. Rolling cylinder system.

The certification process takes place using an automated multi-channel sampling system, to which all the cylinders to be analysed are connected (Fig. 3).

During the analysis, cylinders are automatically selected, enabling individual circulation of gas through the analyser. This system employs the purpose-built *IPQAnaliseQui* software, which manages the sampling process and records all measurements taken by the analyser. Ultimately, all the collected data, including records of standard and sample analyses, are entered into a spreadsheet. The results are corrected with zero and pressure data.

The calibration function determination is carried out using the XGENLINE program developed by the NPL – National Physical Laboratory. This software calculates the most suitable low-degree polynomial calibration function (1, 2, 3 or 4) for a set of measurement data (X, Y), considering the uncertainties associated with the data. In our case XGENLINE program calculated the most suitable low-degree polynomial calibration function of first order for each calibration.

Hence, the determined calibration function is employed to derive estimates of the amount fraction values for the samples under analysis and their corresponding associated uncertainties.

The XGENLINE program, which meets the requirements of the ISO 6143 standard, handles uncertainty, and a standard uncertainty is obtained for each analytical test.

The expanded uncertainty presented is expressed by the combined uncertainty multiplied by the coverage factor k, which for a *t-distribution* with v_{ef} = y effective degrees of freedom corresponds to an expanded probability of approximately 95 %.

4. Interferents study

The study of interferents was conducted using Primary Standard Material (PSM) and CRMs (Table 1). All these standard gas mixtures are prepared in nitrogen matrix. With these primary standards we can have traceability to the standards of these impurities in CO_2. In this case, the matrix will not influence the analysis because the analysers in question do not detect CO_2 just as they do not detect nitrogen. Each of them detects only the respective gas.

4.1. SO_2 analyser

Measurements of SO_2, H_2S, CO, CH_4, O_2, and CO_2 standards were conducted on the SO_2 analyser. The results obtained during the SO_2 analyser tests are presented in Table 2. *Zero* is the reading of the analyser

Fig. 3. Certification of Gas Mixtures Facility.

Table 1
PSM / CRM used for the study of interferents.

Interferent Gas	PSM /CRM (mol/mol)	Analytical method	Model of the analyser
H_2S	CRM412061 (9.2±0,5) x10^{-6}	NDUV	ABB Limas11 AO2020
SO_2	VSL4910 (25.00±0,37) x10^{-6}	NDIR	ABB URAS26 EL3040
CO	CRM034916 (823±4) x10^{-6}	NDIR	ABB URAS26 AO2040
O_2	VSL8612 (1.003±0,019) x10^{-2}	Paramagnetic	HB Magnos16
CH_4 / ar	CRM015377 (2.49±0,02) x10^{-2}	NDIR	ABB URAS26 AO2040
CO_2	CRM034907 (20.01±0,05) x10^{-2}	NDIR	ABB URAS26 AO2040
CH_4 / N_2	PSM202534 (2.501±0,012) x10^{-2}	NDIR	ABB URAS26 AO2040

A different analyser was used for each component.

Table 2
Results of interferents on the SO_2 analyser.

Cylinder	Amount Fraction mol/mol	Zero mV	Reading mV	S mV
CRM412061 (H_2S)	9.2 × 10^{-6}	−2560.95	−2556.61	0.67
VSL4910 (SO_2)	**25.00 × 10^{-6}**	**−2553.19**	**−2249.54**	**0.61**
CRM034916 (CO)	823 × 10^{-6}	−2547.53	−2546.61	0.53
VSL8612 (O_2)	1.003 × 10^{-2}	−2545.11	−2544.24	0.53
CRM015377 (CH_4 / ar)	2.49 × 10^{-2}	***−2543.55***	***7314.06***	0.69
CRM034907 (CO_2)	20.01 × 10^{-2}	−2531.41	−2540.10	0.81
PSM202534 (CH_4 / N_2)	2.501 × 10^{-2}	—	—	—

when the zero gas is passing, which is nitrogen. *Reading* is the value when the sample gas is passing. *S* is the standard deviation of the measurements.

According to ISO 6143, the content determination of a specified gas mixture component (analyte) is performed by measuring an instrumental response of the gas analyser. Thus, *Zero* value of the analyser does not have to be zero because the calculations are carried out with the zero correction.

We can observe that for the gases H_2S, CO, O_2 and CO_2, the zero in the Table 2 is similar to the reading. We consider that the values are similar when the difference between the reading and the zero is less than 10 mV. In this case we have a difference of 8.7 mV (Table 2), on CO_2

Table 3
Results of interferents on the H_2S analyser.

Cylinder	Amount Fraction mol/mol	Zero mV	Reading mV	S mV
CRM412061 (H_2S)	**9.2×10^{-6}**	**−1054.93**	**−548.592**	**4.893**
VSL4910 (SO_2)	25.00×10^{-6}	***−1036.35***	***781.121***	8.379
CRM034916 (CO)	823×10^{-6}	−1030.93	−1028.56	6.31
VSL8612 (O_2)	1.003×10^{-2}	−1027.85	−1025.05	7.16
CRM015377 (CH_4 / ar)	2.49×10^{-2}	—	—	—
CRM034907 (CO_2)	20.01×10^{-2}	−1024.66	−1022.14	4.89
PSM202534 (CH_4 / N_2)	2.501×10^{-2}	−2458.53	−2456.86	8.40

parameter, that is equivalent to 0.71×10^{-6} mol/mol which is within the measurement uncertainties of the used SO_2 primary standards (Table 12). This indicates that these gases do not interfere with the SO_2 gas reading on the SO_2 analyser. On the other hand, we have CH_4 gas interfering with the SO_2 sensor.

4.2. H_2S analyser

Measurements of SO_2, H_2S, CO, CH_4, O_2, and CO_2 standards were conducted on the H_2S analyser. The results obtained during the H_2S analyser tests are presented in Table 3.

We can observe that for the gases CO, O_2, CH_4 and CO_2, the zero in the table is similar to the reading. This indicates that these gases do not interfere with the H_2S gas reading on the H_2S analyser. On the other hand, we have SO_2 gas interfering with the H_2S sensor.

4.3. CO analyser

Measurements of SO_2, H_2S, CO, CH_4, O_2, and CO_2 standards were conducted on the CO analyser. The results obtained during the CO analyser tests are presented in Table 4.

We can observe that for the gases SO_2, H_2S, O_2 and CO_2, the zero in the table is similar to the reading. This indicates that these gases do not interfere with the CO gas reading on the CO analyser. In this case we have a difference of 7.9 mV (Table 4), on CO_2 parameter, that is equivalent to 1.1×10^{-6} mol/mol which is within the measurement uncertainties of the used CO primary standards (Table 12). Methane gas interferes with the CO analyser however the interference is negligible within the measurement uncertainty. This means that we have a difference of 31.3 mV (Table 4), on CH_4 parameter, that is equivalent to 4.6×10^{-6} mol/mol which is within the measurement uncertainties of the used CO primary standards (Table 12).

4.4. O_2 analyser

Measurements of SO_2, H_2S, CO, CH_4, O_2, and CO_2 standards were conducted on the O_2 analyser. The results obtained during the O_2 analyser tests are presented in Table 5.

Table 4
Results of interferents on the CO analyser.

Cylinder	Amount Fraction mol/mol	Zero mV	Reading mV	S mV
CRM412061 (H_2S)	9.2×10^{-6}	2180.90	2179.85	0.38
VSL4910 (SO_2)	25.00×10^{-6}	2179.17	2178.70	0.38
CRM034916 (CO)	**823×10^{-6}**	**2179.00**	**7819.40**	**0.67**
VSL8612 (O_2)	1.003×10^{-2}	2180.19	2178.71	0.42
CRM015377 (CH_4 / ar)	2.49×10^{-2}	*2179.03*	*2147.72*	0.46
CRM034907 (CO_2)	20.01×10^{-2}	2178.36	2170.43	0.36
PSM202534 (CH_4 / N_2)	2.501×10^{-2}	—	—	—

Table 5
Results of interferents on the O_2 analyser.

Cylinder	Amount Fraction mol/mol	Zero mV	Reading mV	S mV
CRM412061 (H_2S)	9.2×10^{-6}	3.7872	3.5922	0.1091
VSL4910 (SO_2)	25.00×10^{-6}	3.5856	3.4970	0.1089
CRM034916 (CO)	823×10^{-6}	3.4521	3.4017	0.1513
VSL8612 (O_2)	**1.003×10^{-2}**	**3.3812**	**13.502**	**0.111**
CRM015377 (CH_4 / ar)	2.49×10^{-2}	—	—	—
CRM034907 (CO_2)	20.01×10^{-2}	3.5417	2.4963	0.1468
PSM202534 (CH_4 / N_2)	2.501×10^{-2}	−5.5571	−6.7359	0.2068

Table 6
Results of interferents on the CH_4 analyser.

Cylinder	Amount Fraction mol/mol	Zero mV	Reading mV	S mV
CRM412061 (H_2S)	9.2×10^{-6}	2079.21	2078.47	0.19
VSL4910 (SO_2)	25.00×10^{-6}	2079.33	2080.43	0.20
CRM034916 (CO)	823×10^{-6}	2079.44	2079.35	0.20
VSL8612 (O_2)	1.003×10^{-2}	2079.87	2079.67	0.22
CRM015377 (CH_4 / ar)	**2.49×10^{-2}**	**2079.72**	**5944.30**	**0.29**
CRM034907 (CO_2)	20.01×10^{-2}	2081.01	2078.70	0.21
PSM202534 (CH_4 / N_2)	2.501×10^{-2}	—	—	—

We can observe that for the gases SO_2, H_2S, CO, O_2 and CO_2, the zero in the table is similar to the reading. The zero of methane standard is slightly different because was not carried out in the same day. This difference is not significant according to ISO 6143. This indicates that these gases do not interfere with the O_2 gas reading on the O_2 analyser.

4.5. CH_4 analyser

Measurements of SO_2, H_2S, CO, CH_4, O_2, and CO_2 standards were conducted on the CH_4 analyser. The results obtained during the CH_4 analyser tests are presented in Table 6.

We can observe that for the gases SO_2, H_2S, CO, O_2 and CO_2, the zero in the table is similar to the reading. This indicates that these gases do not interfere with the CH_4 gas reading on the CH_4 analyser.

Some of the type of the analysers described in this section can be also used for the analysis of impurities of CO_2 in the carbon capture processes in field.

As we can observe all analysers were tested with the amount fraction of 20 % of CO_2 and did not detect CO_2, which means that CO_2 does not interfere with these analysers regardless of the amount fraction of CO_2.

5. Results

Four gas mixtures, Primary Reference Material (PRM), were carefully prepared for analysis, including two binary combinations of SO_2 in a carbon dioxide matrix, designated as PRM408326 and PRM108593. Furthermore, two mixtures composed of H_2S in CO_2, labelled as PRM108595 and PRM108596, were also carefully assembled. This study facilitated the comprehensive characterization of these four mixtures,

Table 7
Standards used for SO_2 Component Certification.

Standards Used	X mol/mol	U mol/mol
VSL9159	2.554×10^{-5}	3.7×10^{-7}
VSL7897	2.992×10^{-4}	9.3×10^{-7}
VSL7886	1.0010×10^{-3}	3.2×10^{-6}

Table 8
Results of the analysis of the SO_2 component, in the prepared binary mixtures.

Results PRM408326 – SO_2		
Date	*X* **10^{-6} mol/mol**	*U* **10^{-6} mol/mol**
2023-09-04	19.52	0.51
Results PRM108593 – SO_2		
Date	*X* **10^{-6} mol/mol**	*U* **10^{-6} mol/mol**
202309-04	20.71	0.50

Table 9
Standards used for H_2S Component Certification.

Standards Used	*X* **mol/mol**	*U* **mol/mol**
NPL0274	4.610×10^{-6}	3.4×10^{-7}
VSL4408	5.000×10^{-6}	3.7×10^{-7}
VSL4982	1.001×10^{-5}	3.2×10^{-7}
VSL4427	5.000×10^{-5}	7.5×10^{-7}

Table 10
Results of the analysis of the H_2S component, in the prepared binary mixtures.

Results PRM108595 – H_2S		
Date	*X* **10^{-6} mol/mol**	*U* **10^{-6} mol/mol**
2023–09-11	9.97	0.48
Results PRM108596 – H_2S		
Date	× **10^{-6} mol/mol**	*U* **10^{-6} mol/mol**
2023–09-11	9.64	0.47

Table 11
Uncertainty budget for an analytical measurement, referring to the mixtures PRM108595 and PRM108596.

Cylinder PRM108595	X_i µmol/mol	Dist.	$u(X_i)$ µmol/mol	$u(y_i) = 1.\ u(X_i)$
run1	9.92×10^{-6}	normal	1.5×10^{-7}	1.5×10^{-7}
run2	10.02×10^{-6}	normal	1.7×10^{-7}	1.7×10^{-7}
Cylinder PRM108596	X_i µmol/mol	Dist.	$u(X_i)$ µmol/mol	$u(y_i) = 1.\ u(X_i)$
run1	9.63×10^{-6}	normal	$1,5 \times 10^{-7}$	$1,5 \times 10^{-7}$
run2	9.64×10^{-6}	normal	$1,6 \times 10^{-7}$	$1,6 \times 10^{-7}$

each contained within individual cylinders maintained at an approximate pressure of 40 bar.

Furthermore, two multicomponent mixtures were prepared in a CO_2 matrix, PRM308978 with the impurities SO_2, CO and O_2; and PRM202557, with the impurities H_2S, CO, O_2, and CH_4 at the previously mentioned amount fractions. These mixtures were contained within two cylinders at an approximate pressure of 40 bar each.

5.1. Results for the SO_2 mixtures

The binary mixtures PRM408326 and PRM108593 were certified using the SO_2 analyser with the standards presented in Table 7.

Table 8 shows the results of the analysis of the SO_2 component, in the two prepared binary mixtures, PRM408326 and PRM108593.

The values of the prepared mixtures for SO_2 are slightly outside the calibration range. However, the validity of the calibration is supported by the *Goodness of Fit* (*GoF*) results for the calibration curves, which are 1.85, 1.64, and 1.46. According to ISO 6143 must be $GoF \leq 2$ for a valid calibration curve.

Table 12
Standards Used for Certification of the Components.

Standards Used	*X* **mol/mol**	*U* **mol/mol**
SO_2		
VSL9159	2.554×10^{-5}	3.7×10^{-7}
PSM502546	5.005×10^{-5}	4.0×10^{-7}
VSL7897	2.992×10^{-4}	9.3×10^{-7}
VSL7886	1.0010×10^{-3}	3.2×10^{-6}
H_2S		
NPL0274	4.610×10^{-6}	3.4×10^{-7}
VSL4408	5.000×10^{-6}	3.7×10^{-7}
VSL4982	1.001×10^{-5}	3.2×10^{-7}
VSL0536	2.000×10^{-4}	3.0×10^{-6}
CO		
PSM402577	5.002×10^{-4}	5.0×10^{-6}
NMI8601	5.501×10^{-4}	5.2×10^{-6}
NMI8622	7.005×10^{-4}	2.0×10^{-6}
NMI3707	8.003×10^{-4}	2.3×10^{-6}
NPL1720	9.994×10^{-4}	3.7×10^{-6}
CH_4		
NPL273	4.999×10^{-3}	1.9×10^{-5}
VSL6039	5.001×10^{-3}	1.8×10^{-5}
PSM202534	2.501×10^{-2}	1.2×10^{-4}
VSL6037	5.006×10^{-2}	1.0×10^{-4}
O_2		
VSL3704	5.00×10^{-3}	4.3×10^{-4}
VSL8612	1.003×10^{-2}	1.9×10^{-4}
VSL8554	1.0029×10^{-1}	2.6×10^{-4}

Table 13
Amount fractions of the multicomponent mixtures in CO_2.

PRM308978 2023-09-19		
Component in a Carbon Dioxide Matrix.	*X* **mol/mol**	*U* **mol/mol**
SO_2	14.26×10^{-6}	0.46×10^{-6}
CO	666.1×10^{-6}	2.7×10^{-6}
O_2	0.594×10^{-2}	0.027×10^{-2}
PRM202557 2023-09-20		
Component in a Carbon Dioxide Matrix.	*X* **mol/mol**	*U* **mol/mol**
H_2S	9.83×10^{-6}	0.48×10^{-6}
CO	669.5×10^{-6}	2.7×10^{-6}
CH_4	1.9685×10^{-2}	0.0060×10^{-2}
O_2	0.586×10^{-2}	0.027×10^{-2}

5.2. Results for the H_2S mixtures

The binary mixtures PRM108595 and PRM108596 were certified using the H_2S analyser with the standards presented in Table 9.

Table 10 shows the results of the analysis of the H_2S component, in the two prepared binary mixtures, PRM108595 and PRM108596.

Below, as an example, we present the uncertainty budget Table 11 for an analytical measurement, referring to the mixtures PRM108595 and PRM108596, with the standard uncertainty ($u(x_i)$, $u(y_i)$), normal distribution and sensitivity coefficient 1.

The expanded uncertainty presented (Table 10) is expressed by the combined uncertainty (Eq. (2)) multiplied by the coverage factor $k = 2.04$, in this case, which for a *t-distribution* with $v_{ef} = 60$ effective degrees of freedom corresponds to an expanded probability of approximately 95 %.

5.3. Results for the multicomponent mixtures

The multicomponent mixtures PRM308978 and PRM202557 were certified using the SO_2, H_2S, CO, CH_4 and O_2 analysers with the standards presented in Table 12.

The number of standards used ranged from 3 to 5, for each component, according to the best calibration curve results based on the goodness of fit, in accordance with ISO 6143. The results of the amount fractions of the multicomponent mixtures PRM308978 (SO_2+CO+O_2 in CO_2) and PRM202557 (H_2S+CO+CH_4 + O_2 in CO_2) are presented in Table 13.

6. Summary

Under the MetCCUS project, the contribution of LGR involves the preparation of CRM to allow the measurement of impurities in CO_2 with metrological traceability, providing support for the calibration and validation of instrumentation used in carbon capture processes.

We can conclude that methane gas interferes with the SO_2 sensor when using the NDIR analytical method. Also, SO_2 gas interferes with the H_2S sensor when using the NDUV analytical method. Methane gas interferes with the CO analyser using NDIR, however the interference is negligible within the measurement uncertainty. Therefore, two multicomponent mixtures were prepared taking this information into account. One mixture does not contain SO_2 and the other does not contain CH_4 and H_2S.

Four bicomponent and two multi-component mixtures in CO_2 matrix were prepared, with uncertainties within expectations.

This work is being a joint study with project partners where some of the prepared multicomponent mixtures will be sent for analysis to some of the participating laboratories and then the results will be compared, and the conclusions will be published.

A stability study will be carried out in order to establish the shelf life of the different mixtures.

In the future, we intend to extend this study to mixtures with more components. To obtain more information regarding what is intended in the project. We intend to analyse these mixtures using other analytical methods to avoid the interferences.

These multicomponent gas mixtures standards can be used to calibrate analysers that measure the purity of carbon dioxide throughout the entire process, from capture to storage, including its industrial applications. The use of such standards is essential, as it promotes more accurate and traceable measurements.

CRediT authorship contribution statement

Florbela A. Dias: Writing – review & editing, Writing – original draft, Validation, Supervision, Project administration, Methodology, Investigation, Formal analysis, Conceptualization. **Cristina Palma:** Software, Methodology, Investigation, Formal analysis. **Carlos J. Costa:** Writing – review & editing, Software, Methodology, Formal analysis.

Declaration of competing interest

The authors declare the following financial interests/personal relationships which may be considered as potential competing interests: [Florbela Dias reports financial support was provided by EPM EURAMET. If there are other authors, they declare that they have no known competing financial interests or personal relationships that could have appeared to influence the work reported in this paper].

Data availability

Data will be made available on request.

Acknowledgements

This project (21GRD06 MetCCUS) has received funding from the EPM programme co-financed by the Participating States and from the European Union's Horizon 2020 research and innovation programme.

References

[1] M. Sega, et al., Reference Materials: gas mixtures to support measurements for climate change studies, J. Phys.: Conf. Ser. 2192 (2022) 012016, https://doi.org/10.1088/1742-6596/2192/1/012016.
[2] https://www.iea.org/reports/ccus-in-clean-energy-transitions/ccus-in-the-transition-to-net-zero-emissions (accessed 20 June 2024).
[3] https://pubs.acs.org/doi/10.1021/acsengineeringau.3c00049 (accessed 20 June 2024).
[4] ISO/IEC 17034:2016 General requirements for the competence of reference material producers.
[5] ISO 6142-1:2015 – Gas analysis – Preparation of calibration gas mixtures – Part 1: Gravimetric method for Class I mixtures.
[6] E. Amico di Meane, M. Plassa, F. Rolle, M. Sega, Metrological traceability in gas analysis at I.N.Ri.M: gravimetric primary gas mixtures, Accred. Qual. Assur. 14 (2009) 607–611, https://doi.org/10.1007/s00769-009-0577-9.
[7] M.J.T. Milton, F. Guenther, W.R. Miller, A.S. Brown, Validation of the gravimetric values and uncertainties of independently prepared primary standard gas mixtures, Metrologia 43 (2006) 7.
[8] M.J.T. Milton, G.M. Vargha, A.S. Brown, Gravimetric methods for the preparation of standard gas mixtures, Metrologia 48 (2011) 5. https://iopscience.iop.org/volume/0026-1394/48.
[9] ISO 6143:2001 – Gas analysis – Comparison methods for determining and checking the composition of calibration gas mixtures.
[10] F.R. Guenther, A. Possolo, Calibration and uncertainty assessment for certified reference gas mixtures, Anal. Bioanal. Chem. 399 (2011) 489–500, https://doi.org/10.1007/s00216-010-4379-z.
[11] D. Kim, et al., International comparison CCQM-K41.2017, hydrogen sulphide in nitrogen, Metrologia 58 (2021) 08010, https://doi.org/10.1088/0026-1394/58/1A/08010.
[12] A. m. h., van der Veen et al, International comparison Euramet.QM-K111—propane in nitrogen, Metrologia 54 (2017) 08020, https://doi.org/10.1088/0026-1394/54/1A/08009.
[13] F.A. Dias, et al., Final report on international comparison EURO.QM-S5/1166: Carbon dioxide mixtures in nitrogen, Metrologia 50 (2013) 1A08017, https://doi.org/10.1088/0026-1394/50/1A/08017.
[14] F.R. Guenther, International comparison CCQM-K76: Sulphur dioxide in nitrogen, Metrologia, Tech. Suppl. 48 (2011) 08015, https://doi.org/10.1088/0026-1394/48/1A/08015.
[15] A. Botha, International comparison CCQM-K51: Carbon monoxide (CO) in nitrogen (5 μmol mol–1), Metrologia, Tech. Suppl. 47 (2010) 08008, https://doi.org/10.1088/0026-1394/47/1A/08008.
[16] G. Nieuwenkamp, Final report on international comparison CCQM-K71: Measurement of stack gas, Metrologia, Tech. Suppl. 47 (2010) 08021, https://doi.org/10.1088/0026-1394/47/1A/08021.
[17] KCDB https://www.bipm.org/kcdb/ (accessed 12 September 2023).
[18] F.A. Dias, C. Palma, C. Costa, Preparation of multicomponent gas mixtures, Revista Medições e Ensaios 17 (2023).
[19] https://metccus.eu/about-the-project/ (accessed 18 June 2024).
[20] ISO 13528:2022 – Statistical methods for use in proficiency testing by interlaboratory comparisons.
[21] Evaluation of measurement data – Guide to the expression of uncertainty in measurement JCGM 100:2008 (GUM 1995 with minor corrections).

Florbela A. Dias, PhD in Chemistry, is the Head of IPQ Reference Gas Laboratory and EURAMET/METCHEM Contact person and member of CCQM Gas Analysis WG. She is working in the gas analysis field since 2002. She participates in EPM MetCCUS project. She is contact person in national and international standardisation committees in the field of gas analysis.

Carlos J. Costa, degree in Physics and Chemistry, Senior scientist in the Amount of Substance and Electrochemistry Laboratory of the Portuguese Institute for Quality. He is currently developing activities in the Reference Gas Laboratory, namely gravimetric preparation and gas analysis.

Cristina Palma, degree in Chemical Engineering. She is a scientist doing research in the field of metrology in chemistry. She is currently developing activities in the Reference Gas Laboratory, namely gravimetric preparation and gas analysis.

22NRM07 GuideRadPROS: Radiation protection dosimeter performance assessment – Aggregated calibration data in the Cs-137 reference radiation field

Nikola Kržanović[1], Miloš Živanović[1], Miloš Đaletić[1], Ivana Komatina[1,2], Luka Bakrač[3], Argiro Boziari[4], Maria Do Ceu Ferreira[5], Lukasz Michalik[6], Reetta Nylund[7], Siarhei Saroka[8], Teemu Siiskonen[7], Vladimir Sochor[9], Srboljub Stankovic[1], Jelena Vlahović[1,10]

1 Vinca Institute of Nuclear Sciences, Belgrade, Serbia
2 Faculty of Physical Chemistry, University of Belgrade, Belgrade, Serbia
3 Ruđer Bošković Institute, Zagreb, Croatia
4 Greek Atomic Energy Commission, Athens, Greece
5 Portuguese Institute for Quality, Lisabon, Portugal
6 Central Office of Measures, Warsaw, Poland
7 Radiation and Nuclear Safety Authority, Vantaa, Finland
8 National Institute of Metrology, Chisinau, Moldova
9 Czech Metrology Institute, Brno, Czech Republic
10 Faculty of Sciences, University of Novi Sad, Novi Sad, Serbia

One of the goals of the GuideRadPROS joint research project (JRP) is the harmonization and update of international standards for type testing of radiation protection dosimeters. This is to be achieved through analysis of the test methods and criteria of evaluation of dosimeters defined in different standards, and through analysis of the performance of radiation protection dosimeters used in different European countries. Within one of the activities under the WP3 of this JRP, most commonly used active radiation protection dosimeters used for area monitoring in the workplace and for individual monitoring of occupationally exposed workers have been identified.

Aggregated calibration data on several radiation protection dosimeter models have been collected from a total of six dosimetry calibration laboratories. The collected calibration data predominantly includes calibration at the radionuclide-based radiation qualities (termed as S-Cs and S-Co in the ISO 4037 standard). The calibrations are usually performed in these radiation fields at various dose rate and dose values. This data can be used to assess the dosimeter performance in terms of response non-linearity. Calibrations in the N-series radiation qualities are either not commonly requested by the end-users or not regularly provided by the calibration laboratories.

In this work, aggregated calibration data in terms of absolute dosimeter response have been presented. The collected calibration data is presented for S-Cs at the reference dose (rate). Inter-variation of dosimeter response within a dosimeter model of up to approximately 10 % can be observed. The cause of this variation can be addressed to the dosimeters being used in different environments, with different frequencies of use, as well as the differences between the data originating from several calibration laboratories. For some dosimeter models the conclusions on the behavior of dosimeter type under reference conditions cannot be clearly deducted due to the low sample size. The response of all the calibrated dosimeters is within ± 40 %.

The aggregated calibration data, along with the data on dosimeter performance from the literature, and the state-of-the-art manufacturer specifications will be used to identify the gaps in the data on radiation protection dosimeters. A measurement program is currently ongoing and being conducted under the scope of the JRP, to collect additional data on dosimeter performance including their energy and angular dependence of the response as well as their non-linearity.

Acknowledgments: The project (22NRM07 GuideRadPROS) has received funding from the European Partnership on Metrology, co-financed from by the European Union's Horizon Europe Research and Innovation Programme and by the Participating States.

Lighting Res. Technol. 2025; **57**: 345–362

The Society of Light and Lighting

Sensitivity evaluation of measurement uncertainty contributions of spectral data for calculated integral quantities

U Krüger[a], A Ferrero[b], A Thorseth[c], O Pellegrino[d], J Dubard[e], E Ikonen[f,g] and A Sperling[h]

[a]TechnoTeam Bildverarbeitung GmbH, Ilmenau, Germany
[b]Instituto de Óptica, Consejo Superior de Investigaciones Científicas, Madrid, Spain
[c]Technical University of Denmark, Roskilde, Denmark
[d]Departamento de Metrologia, Instituto Português da Qualidade, Caparica, Portugal
[e]Laboratoire National de Métrologie et d'Essais, Paris, France
[f]Metrology Research Institute, Aalto University, Espoo, Finland
[g]VTT MIKES, Espoo, Finland
[h]Physikalisch-Technische Bundesanstalt, National Metrology Institute of Germany, Braunschweig, Germany

Received 27 December 2023; Revised 22 September 2024; Accepted 30 March 2025

Integrating spectral data (spectral responsivities of photometers or spectral distributions of light sources) to calculate integrated quantities such as tristimulus values is straightforward at first sight. However, estimating the measurement uncertainty of these integrated quantities is challenging. When calculating integrated photometric quantities, some uncertainty contributions from the spectral data transfer to the final results, some 'cancel out', some 'average out' and others increase or decrease their weight by correlation. The spectral data are usually assumed to be uncorrelated when deriving other quantities by integration, which is typically not justified. A method called the framework approach, applying orthogonal basis functions and Monte Carlo simulations, is introduced. This approach shows that neglecting partial spectral correlations may lead to a significant underestimation of the measurement uncertainty of integrated quantities. Furthermore, this paper shows how information about spectral error correlation structures can be used to obtain better estimations of the measurement uncertainty.

1. Introduction

Integration of spectral data is central to calculating photometric and colorimetric quantities, as well as quantities that are used to assess non-visual effects and photobiological safety. Calculating any of these quantities from spectral data involves determining the value of the measurand by numerical integrals (weighted sums) of source spectral distributions across the spectral range of the weighting functions.

This paper considers spectral integrals of the form:

$$X = \int_{\lambda_{\min}}^{\lambda_{\max}} x(\lambda) S(\lambda)\, \mathrm{d}\lambda \qquad (1)$$

where $x(\lambda)$ is a defined weighting function, $S(\lambda)$ is the spectral distribution of a source or the spectral responsivity of a detector and the

Address for correspondence: E Ikonen, Metrology Research Institute, Aalto University, Maarintie 8, Espoo 02150, Finland.
E-mail: erkki.ikonen@aalto.fi

10.1177/14771535251337364

integral is calculated over the wavelength range $\lambda_{min} \leqslant \lambda \leqslant \lambda_{max}$. A similar spectral integral may be involved when using filtered detectors (including practical photometers). In those cases, the spectral response function, taking the place of $x(\lambda)$, also has associated uncertainties.

While these calculations are straightforward and generally calculated using a trapezium rule, estimating the associated measurement uncertainty becomes complex and challenging, as described in the CIE198-SP2[1] report. In particular, where there is a significant error correlation between measured spectral data at different wavelengths, the combined uncertainty associated with the integrated quantity is affected, as demonstrated by Schmähling *et al*.[2] To describe the effects that can be caused by correlations, one must first understand what 'correlated' means in this context. This paper also provides some assistance in this regard.

A general measurement uncertainty assessment, whether based on the law of propagation of uncertainties in the legacy GUM[3] or Monte Carlo (MC) methods introduced in the JCGM 101[4] document, starts with a measurement model written as an equation. It is common for measurement models to be multi-stage, as described in the JCGM 106[5] document. This means that some of the model's input quantities are based on previous (earlier stage) measurement models.

For photometric and colorimetric quantities as well as quantities that are used to assess non-visual effects and photobiological safety, the measurement model will be in the form of Equation (1) and this is therefore what will be discussed in Section 2. The measurement model can be considered multi-stage in that the spectral quantity itself will be the measurand of a calibration process to determine that spectrum and will have its own measurement model.

In this work, we propagate uncertainties with complex error correlation structures through the measurement model using a method of orthogonal basis functions introduced by Kärhä *et al*.[6] To describe correlations, a framework approach for the estimation of dependencies is developed. This framework approach allows a better insight into the origin of those significant contributions to the measurement uncertainty of an integrated quantity, which come from correlations in the spectral distribution data.

With the framework approach, we introduce an evaluation method; its application (simply to show how it works) is presented based on an example in this paper.

The main contribution of this work is the estimation of sensitivity coefficients. Here, we use MC methods to propagate such error correlation structures, both individually – to evaluate the sensitivity of the integrated quantity to each source of uncertainty – and combined to provide a combined uncertainty for the integrated quantity. In this method, we follow the kind of sensitivity analysis proposed by the JCGM 101, Annex B,[4] which is called 'one factor at a time' by Razavi and Gupta.[7]

Furthermore, this work considers partially correlated contributions associated with both wavelength and the spectral distribution amplitude, alongside with fully correlated and uncorrelated errors.

In spectral integrals, sources of uncertainty that lead to fully correlated errors are simple to propagate (and cancel out if the integrated quantity is normalised). Sources of uncertainty that lead to fully uncorrelated (independent) errors reduce significantly by the effective weighted averaging of the integral. Therefore, the most important sources of uncertainty are those that provide partial error correlation. In general, however, the form of that partial error correlation is unknown. For the description of partial error correlation, this paper builds on a method originally presented by Kärhä *et al*.,[6] and extended by

Vaskuri *et al.*[8] and Maham *et al.*[9] The basis function method uses a set of basis functions to model possible, (realistic) error correlation forms and uses MC methods to explore different possible correlation structures. This paper presents the final modelling equations for the basis function method and examples.

The implementation of the work presented here can be found in the open-source Python package 19nrm02,[10] which uses the LuxPy Python package by Smet.[11] Additional examples of the application of the approach, including animations in the form of mp4 files, are presented in Supplemental Material for this paper (available online).

2. Methods

Integrals of the form of Equation (1) are treated as summations of a spectral quantity over a set of wavelengths λ_i:

$$X = \sum_{i=0}^{N_\lambda - 2} x(\lambda_i) \cdot S_i \cdot (\lambda_{i+1} - \lambda_i) \qquad (2)$$

It is useful to describe the spectral data with vector notation. In this paper, vectors are represented by bold italic symbols, and scalars are represented by thin italic symbols. For spectral data with N_λ elements (e.g. from 360 nm to 830 nm in 5 nm steps, $N_\lambda = 95$), two vectors are used:

- Amplitude vector: $\boldsymbol{S} = [S_0, S_1, S_2, \ldots, S_{N_\lambda - 1}]$
- Wavelength vector: $\boldsymbol{\lambda} = [\lambda_0, \lambda_1, \lambda_2, \ldots, \lambda_{N_\lambda - 1}]$

where the random values of the elements in the vectors, generated during the MC simulation (MCS), can originate from wavelength uncertainty, signal uncertainty or both. Both vectors are used to calculate the spectrally integrated quantity of interest. Initially, to better understand their individual influences, they are simulated independently.

Within this paper, where the elements of the vectors are processed individually, they are written as thin italic symbols with an index (e.g. λ_i) or in functional form (e.g. $S(i)$ or $S(\lambda)$). The symbol S_i in Equation (2) is used instead of $S(\lambda_i)$ to indicate that the i-th element of the signal vector should be used without any interpolation, whereas the $x(\lambda_i)$ means that we have to interpolate the x-function to the specific wavelength λ_i.

The elements of these two vectors are determined experimentally, and the values can be affected by three types of uncertainty that create fluctuations in them:

- Effects that are uncorrelated from one element to another (random effects, noise).
- Effects that are fully correlated from one element to another (systematic effects, bias).
- Effects that are partially correlated, where 'partially correlated' can be interpreted as an infinite variety of different correlation states varying from fully uncorrelated to fully correlated.

In this paper, MCS was used to propagate uncertainties. MCS is a mathematical technique[12,13] that enables a quantitative analysis of a measurement result. The core idea behind an MCS is to represent the propagation of probability density functions (PDFs) for the input quantities (here the measured values of the spectral quantity at different wavelengths) through the measurement model (here the integral given in Equation (1)).

This involves the following steps:

- *Random sampling:* For each input quantity (here the spectral quantity at each wavelength), a set of representative errors are generated by generating random numbers drawn from the distributions.

- *Repeated trials:* In an MCS, a large number (N_{MC}) of trial runs, also known as simulations, using random inputs are performed. These trials are used to generate the PDFs of different outcomes of the model.
- *Aggregation of results:* After running simulations many times, the results are aggregated and analysed to estimate the statistical properties of the system being modelled, such as averages, variances, probabilities of different outcomes, correlations, etc.

2.1 Overview

A general overview of the framework approach is presented in Figure 1. The different parts of the figure will be explained in detail in this section.

Figure 1 shows the calculation during two separate MCSs (MCS1 and MCS2) running each N_{MC} times (the number of MC trials or runs). The first part of the structure, shown in MCS1, starts with a given spectral distribution based on the outcome of a real or simulated measurement, a physical modelling (e.g. the spectral radiance of a blackbody) or a spectral distribution given in a Standard (e.g. CIE Standard Illuminant A,[14] CIE reference spectrum L41,[15] etc.) at a nominal wavelength scale $\boldsymbol{\lambda}$ and at this point without any uncertainty information. The nominal wavelength scale is a set of true wavelength values, used as reference values for the calculation.

In the next step, a general model, explained in Section 2.2, uses this spectral distribution to add the measurement uncertainty by generating different fluctuations around the input spectral distribution. This is done by separately modelling the wavelength and amplitude scales with different types of simulated uncertainty contributions. The uncertainty contributions are modelled as correlated, uncorrelated and partially correlated contributions. At the end, this results in a set of N_{MC} combinations of wavelength and signal vectors $\boldsymbol{M}_{i,\mathrm{SD}} = (\boldsymbol{\lambda}_i, \boldsymbol{S}_i)$.

Besides the correlated and uncorrelated uncertainty contributions, generating partially correlated uncertainty contributions using the basis function technique, as described in Section 2.3, is essential for the evaluation presented here.

In this paper, the data are simulated and do not consider the physical background of a particular measurement setup or device under test to ensure that the application does not cover just one method or describe a specific measurement technique. Possible connections of the model parameter to physical models or real measurements are given in Section 2.4.

Finally, using the N_{MC} generated combinations of wavelength and signal vectors $\boldsymbol{M}_{i,\mathrm{SD}} = (\boldsymbol{\lambda}_i, \boldsymbol{S}_i)$, integrated quantities (see Section 3) can be calculated for every of the generated $\boldsymbol{M}_{i,\mathrm{SD}}$ values. This results in N_{MC} integrated quantities (e.g. relative luminance values Y_{rel}, as shown for the MCS1 example in Figure 1), and a PDF including mean, standard deviation and expanded uncertainty can be calculated from a statistical analysis of this set of output quantities.

Furthermore, the N_{MC} generated combinations of wavelength and signal vectors $\boldsymbol{M}_{i,\mathrm{SD}} = (\boldsymbol{\lambda}_i, \boldsymbol{S}_i)$ can be used to summarise the data using a nominal wavelength scale $\boldsymbol{\lambda}$, a mean spectral distribution $\overline{\boldsymbol{S}_{\mathrm{f}}}$, the associated standard deviation $\boldsymbol{\sigma}(\boldsymbol{S}_{\mathrm{f}})$, and a correlation matrix $\boldsymbol{P}_{\mathrm{f}}$. This set of summarised data is called the 'compressed information' hereafter. The methods used here are explained in Section 3.3. These data can be used to transfer the outcome of the first MCS (MCS1) to other users or to visualise the data.

In parallel to the MCS1 using the framework approach, we can use an MCS2, as shown in the lower part of Figure 1, to calculate a set of integral quantities based on a multivariate

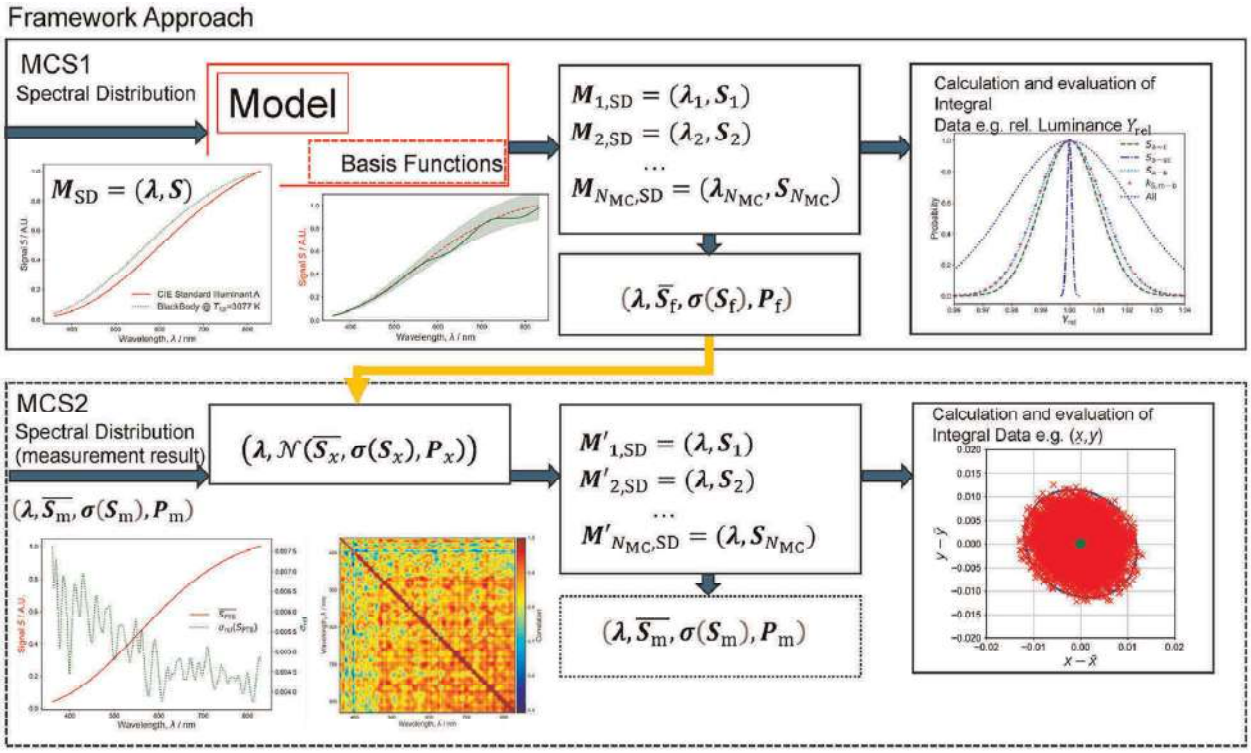

Figure 1 Overview of the framework approach. See Section 2.1 for definitions of the symbols used

normal distribution method. This can be done using either real measurement results, for example, provided by the Physikalisch-Technische Bundesanstalt (PTB) as shown in Section 3.1 or with compressed information from MCS1 (see Section 3.2). With this method, we generate the spectral distribution data from multivariate normal distribution sampling, to again get combinations of wavelength and spectral information $\boldsymbol{M'}_{i,\mathrm{SD}} = (\boldsymbol{\lambda}, \boldsymbol{S}_i)$, but in this case with a nominal wavelength scale only. These are used for calculation and evaluation of integral data in the same manner as for MCS1, yielding compressed information $\overline{\boldsymbol{S}_\mathrm{m}}$, the associated standard deviation, $\boldsymbol{\sigma}(\boldsymbol{S}_\mathrm{m})$, and a correlation matrix, $\boldsymbol{P}_\mathrm{m}$. In Section 3.3, we use chromaticity coordinates as an example to show the correlation analysis for the results using this approach and to validate the data processing from MCS1.

2.2 Model for uncertainty contributions in the framework approach

The framework approach uses additive (subscript 'a') and multiplicative (subscript 'm') model parameters linked to the values as uncertainty components. The uncertainty contributions are implemented during the simulation as follows:

- *Uncorrelated (subscript 'uc'):* Every vector element represents a different realisation of a random process in each of the N_MC MC trials. A vector with random elements is drawn in each trial. Variations of the vector elements are independent.
- *Correlated (subscript 'c'):* All vector element variations behave similarly in any given MC trial. A random number is drawn for every trial only once for the complete vector.

- *Basis function (subscript 'b'):* Partially correlated variations of spectral data points are simulated by the variations of the vector elements with a periodic spectral dependence. The different vectors for the trials are calculated according to the basis function technique introduced by Kärhä *et al.*[6] with Fourier basis functions and by Vaskuri *et al.*[8] with Chebyshev basis functions. See Section 2.3 for details.

2.2.1 Amplitude vector

The model used to calculate the random numbers (subscript 'r') for the signal or amplitude scale is shown in Equation (3).

$$\boldsymbol{S}_\mathrm{r} = \boldsymbol{k}_{S,\mathrm{m\text{-}b}} * \boldsymbol{S} + \boldsymbol{S}_\mathrm{a\text{-}c} + \boldsymbol{S}_\mathrm{a\text{-}uc} + \boldsymbol{S}_\mathrm{a\text{-}b} \quad (3)$$

where $\boldsymbol{S}_\mathrm{r}$ is the random variable for the amplitude scale in the MCS (vector); $\boldsymbol{S}$ is the nominal value of the amplitude (vector, normalised to $\max(\boldsymbol{S}) = 1$); $\boldsymbol{k}_{S,\mathrm{m\text{-}b}}$ is the multiplicative uncertainty component modelled with the basis function technique (vector, systematic and random); $*$ denotes element-wise multiplication of the vector elements; $\boldsymbol{S}_\mathrm{a\text{-}c}$ is the additive fully correlated uncertainty component (vector, systematic); $\boldsymbol{S}_\mathrm{a\text{-}uc}$ is the additive uncorrelated uncertainty component (vector, random); $\boldsymbol{S}_\mathrm{a\text{-}b}$ is the additive partially correlated uncertainty component modelled with the basis function technique (vector, systematic).

2.2.2 Wavelength vector

The model to generate the random numbers for the wavelength scale is described in Equation (4).

$$\boldsymbol{\lambda}_\mathrm{r} = \boldsymbol{F}_\mathrm{d}(\boldsymbol{k}_{\lambda,\mathrm{m\text{-}b}} * \boldsymbol{F}_\mathrm{n}(\boldsymbol{\lambda})) + \boldsymbol{\lambda}_\mathrm{a\text{-}c} + \boldsymbol{\lambda}_\mathrm{a\text{-}uc} + \boldsymbol{\lambda}_\mathrm{a\text{-}b} \quad (4)$$

where $\boldsymbol{\lambda}_\mathrm{r}$ is the random variable for the wavelength scale in the MCS (vector); $\boldsymbol{\lambda}$ is the nominal wavelength (vector); $\boldsymbol{k}_{\lambda,\mathrm{m\text{-}b}}$ is the multiplicative uncertainty component modelled with the basis function technique (vector, systematic and random); $\boldsymbol{\lambda}_\mathrm{a\text{-}c}$ is the additive fully correlated uncertainty component (vector, systematic); $\boldsymbol{\lambda}_\mathrm{a\text{-}uc}$ is the additive uncorrelated random uncertainty or noise component (vector, random); $\boldsymbol{\lambda}_\mathrm{a\text{-}b}$ is the additive partially correlated uncertainty component modelled with the basis function technique (vector, systematic).

The functions $\boldsymbol{\lambda}' = \boldsymbol{F}_\mathrm{n}(\boldsymbol{\lambda})$ and $\boldsymbol{\lambda} = \boldsymbol{F}_\mathrm{d}(\boldsymbol{\lambda}')$, shown in Equation (5), are used to normalise/denormalise the wavelength scale to handle the multiplicative factor for the model in a standard way for the wavelength range $[\lambda_\mathrm{min}, \lambda_\mathrm{max}]$.

$$\begin{aligned} \boldsymbol{\lambda}' &= \boldsymbol{F}_\mathrm{n}(\boldsymbol{\lambda}) = \frac{\boldsymbol{\lambda} - \boldsymbol{\lambda}_\mathrm{min}}{\lambda_\mathrm{max} - \lambda_\mathrm{min}} \\ \boldsymbol{\lambda} &= \boldsymbol{F}_\mathrm{d}(\boldsymbol{\lambda}') = (\lambda_\mathrm{max} - \lambda_\mathrm{min})\boldsymbol{\lambda}' + \boldsymbol{\lambda}_\mathrm{min} \end{aligned} \quad (5)$$

where $\boldsymbol{\lambda}_\mathrm{min}$ and $\boldsymbol{\lambda}_\mathrm{max}$ are vectors containing λ_min or λ_max, respectively, in every vector element.

2.2.3 Combination of amplitude and wavelength scales

Pairs of wavelength vectors $\boldsymbol{\lambda}_\mathrm{r}$ and amplitude vectors $\boldsymbol{S}_\mathrm{r}$ are necessary to define the spectral distribution in a matrix $\boldsymbol{M}_{\mathrm{r,SD}}$, as demonstrated in Equation (6).

$$\boldsymbol{M}_{\mathrm{r,SD}} = (\boldsymbol{\lambda}_\mathrm{r}, \boldsymbol{S}_\mathrm{r}) \quad (6)$$

2.2.4 Parameters for random numbers

For simplicity, the random numbers used for simulating the uncorrelated and correlated contributions introduced above are drawn from normal

distributions with mean value μ, and standard deviation σ (symbol: $\mathcal{N}(\mu;\sigma)$).

- Additive components: $\mathcal{N}(\mu = 0;\sigma)$
- Multiplicative components: $\mathcal{N}(\mu = 1;\sigma)$

The standard deviation parameter σ is selected in a way that one can adapt the result of the simulation conveniently to the situation in a real measurement setup:

- The uncertainty of the wavelength scale parameters is, for example, 1 nm for the additive components ($u_{\lambda,\mathrm{a}}$) and, for example, 1% for the factor in the normalised wavelength scale part ($u_{\lambda,\mathrm{m}}$).
- The uncertainty of the amplitude scale parameters (u_S) is, for example, 1%. The same parameter can also be used for the additive components using normalised data.

These parameters are not used to generate a realistic measurement uncertainty. Rather, they are used to generate easy-to-use sensitivities that can be used in a linear manner for small measurement uncertainties.

Example: If we use 1 nm for the value of the model parameter for the additive fully correlated wavelength uncertainty component $\boldsymbol{\lambda}_{\mathrm{a\text{-}c}}$ and we get an uncertainty of 0.0005 for the chromaticity coordinate x, we can easily calculate that we get an uncertainty contribution of 0.0001 if the real value of the model parameter is 0.2 nm. This means we have made an easy-to-use uncertainty budget that can be used to provide sensitivity information.

2.3 Basis function technique

The basis function technique is explained in detail in Kärhä *et al.*[6] for Fourier basis functions and in Vaskuri *et al.*[8] for Chebyshev basis functions. The implementation can be found in the MC Toolbox of the open-source Python package 19nrm02[10] in the file `FourierNoise.py`. The basis function approach is used inside the MCS1 and also uses random parameters. First of all, a set of basis functions $b_k(\lambda)$ must be generated, where k is the order and $b_k(\lambda)$ is used as a general notation to represent either Fourier basis functions $f_k(\lambda)$, which are generated using Equation (7), or Chebyshev basis functions $c_k(\lambda)$, which are generated using Equation (8).

Fourier basis functions

$$\begin{aligned} f_0(\lambda) &= 1 \\ f_k(\lambda) &= \sqrt{2}\,\sin\left(2\pi k\frac{\lambda-\lambda_{\min}}{\lambda_{\max}-\lambda_{\min}}+\phi_k\right) \end{aligned} \tag{7}$$

Chebyshev basis functions

$$\begin{aligned} g_0(\lambda) &= T_0(\lambda) = 1 \\ T_k(\lambda) &= \cos\left[k\,\arccos\left(\frac{2\lambda-\lambda_{\min}-\lambda_{\max}}{\lambda_{\max}-\lambda_{\min}}\right)\right] \\ g_k(\lambda) &= T_k(\lambda)/\sigma_k \\ c_k(\lambda) &= g_{2k-1}(\lambda)\cos\phi_k + g_{2k}(\lambda)\sin\phi_k \end{aligned} \tag{8}$$

where k is the order of the current basis function, $k \in [0\ \ldots\ N_{\mathrm{B}}-1]$; N_{B} is the number of basis functions (model parameter), $N_{\mathrm{B}} \in [0\ \ldots\ N_\lambda/2-1]$; ϕ_k is a uniformly distributed random number in the range of $[0,\ 2\pi]$; $[\lambda_{\min};\lambda_{\max}]$ is the wavelength range; σ_k is the standard deviation of $T_k(\lambda)$.

Based on the generated basis functions $b_k(\lambda)$ (depending on the method $b_k(\lambda) = f_k(\lambda)$ or $b_k(\lambda) = c_k(\lambda)$) and introducing a random number Y_k, which has a standard normal distribution, $Y_k \sim \mathcal{N}(0;1)$, one calculates the normalised weighting factors γ_k with $\gamma_k = Y_k \Big/ \sqrt{\sum_{j=0}^{N_{\mathrm{B}}-1} Y_j^2}$.

Depending on the Fourier or Chebyshev functions used, different types of basis functions are calculated. A deviation function $\delta(\lambda)$, describing the local deviations over the scale, is then calculated according to Equation (9):

$$\delta(\lambda) = \sum_{k=0}^{N_B-1} \gamma_k b_k(\lambda) \tag{9}$$

The direct influence of a specific basis function order $k = N_B$ can be investigated using the deviation function $\delta_s(\lambda)$, describing the local deviations over the scale using a single basis function only:

$$\delta_s(\lambda) = \gamma_{N_B} b_{N_B}(\lambda) \tag{10}$$

A comparison with correlations in real datasets in Maham *et al.*[9] suggests that the summation of the results of the N_B orthogonal functions should not be equally weighted, but weighted with the reciprocal of the order of the basis functions. Applying this new approach with the one over f weighting according to Ikonen *et al.*[16] and Maham *et al.*,[9] the basis function $\delta_{1f}(\lambda)$ can be calculated according to Equation (11):

$$\delta_{1f}(\lambda) = \sin\phi_{1f} + \frac{\cos\phi_{1f}}{\sum_{k=1}^{N_B-1} 1/k^2} \sum_{k=1}^{N_B-1} \frac{b_k(\lambda)}{k} \tag{11}$$

where $\delta_{1f}(\lambda)$ is the function describing the local deviations over the scale using the one over f weighting; ϕ_{1f} is a uniformly distributed random number in the range of $[0,\ 2\pi]$.

In every trial of the MCS, the random numbers γ_k, ϕ_k and ϕ_{1f} are generated from their distributions.

In the last step, the wavelength (Equation (12)) or amplitude (Equation (13)) data can be modified accordingly by the basis functions:

$$\begin{aligned} k_{\lambda,\mathrm{m-b}}(\lambda) &= (1 + u_{\lambda,\mathrm{m}}\delta(\lambda)) \\ \lambda_{\mathrm{a\text{-}b}}(\lambda) &= u_{\lambda,\mathrm{a}}\delta(\lambda) \end{aligned} \tag{12}$$

$$\begin{aligned} k_{S,\mathrm{m\text{-}b}}(\lambda) &= (1 + u_S\delta(\lambda)) \\ S_{\mathrm{a\text{-}b}}(\lambda) &= u_S\delta(\lambda) \end{aligned} \tag{13}$$

where $u_{\lambda,m}$ is the multiplicative standard uncertainty of the wavelength scale; $u_{\lambda,a}$ is the additive standard uncertainty of the wavelength scale; u_S is the standard uncertainty of the amplitude scale.

The corresponding vectors ($\boldsymbol{k}_{\lambda,\mathrm{m\text{-}b}}$, $\boldsymbol{\lambda}_{\mathrm{a\text{-}b}}$, $\boldsymbol{k}_{S,\mathrm{m\text{-}b}}$ and $\boldsymbol{S}_{\mathrm{a\text{-}b}}$) are formed from the elements given in Equations (12) and (13).

2.4 Connection to physical models

The framework approach can be linked to the physical properties of measurement systems. An overview is given in Table 1 together with the uncertainty components in the framework approach.

3. Comparison of real and modelled results

In Section 3.1, real measurement data, provided by the PTB, are used for the MCS2 path to compare the results with modelled data from the framework approach from the MCS1 path of the simulation as presented in Section 3.2. The reduction of the datasets from the simulation into a form that can be transferred to other users or to other simulation paths is described in Section 3.3. As an example, we calculate tristimulus values and chromaticity data as explained in Section 3.4.

3.1 Real measurement data

During the development of the framework method, the PTB provided a dataset from a real measurement of the spectral irradiance of an

Table 1 Connection of the uncertainty components in the framework approach to physical models, for the example of spectroradiometric measurements of a lamp

Symbol	Description	Origin in other (physical) models
$k_{\lambda,\,m=b}$	Uncertainty of the wavelength calibration factor	The measurement result obtained using several narrowband spectral lamps for the wavelength calibration is the scale factor in nm per pixel or nm per degree of the spectroradiometric system. The uncertainty of this scale factor, for example, from a polynomial regression of different wavelength measurement points, can be used to model $k_{\lambda,\,m=b}$
$\lambda_{a=c}$	Wavelength scale shift of the whole scale	The stability (reproducibility or repeatability) of the homing/initialisation of a monochromator can be used to model $\lambda_{a=c}$
$\lambda_{a=uc}$	Wavelength scale shift of single measurement points	Reproducibility or repeatability of the wavelength setting at a single wavelength position
$\lambda_{a=b}$	General uncertainty of the wavelength scale	A complicated relationship between different wavelength settings can be modelled by $\lambda_{a=b}$. An example of a physical-based modelling for such a parameter can be found in White *et al*.[17] The basis function technique can model the described behaviour if a correction is not possible
$k_{S,\,m=b}$	Uncertainty of the absolute/relative amplitude calibration factor	A sophisticated modelling of the calibration factor can be introduced, for example, ageing of the calibration reference artefact can cause correlations between the calibration factors at different wavelengths
$S_{a=c}$	Correlated uncertainty of a global offset	Modelling the global dark signal offset
$S_{a=uc}$	Uncorrelated uncertainty of the offset signals	Modelling the individual dark signal at every measurement position
$S_{a=b}$	Uncertainty modelling for the offset	A time-dependent offset of a reference voltage can cause wavelength-dependent offset values in the amplitude scale

FEL lamp. The data consisted of a mean spectral distribution vector $\overline{\boldsymbol{S}_{\mathrm{PTB}}}$, the standard deviation $\boldsymbol{\sigma}(\boldsymbol{S}_{\mathrm{PTB}})$ (see Figure 2) and the correlation matrix $\boldsymbol{P}_{\mathrm{PTB}}$ (see Figure 3), all at a nominal wavelength scale $\boldsymbol{\lambda}$. The correlation matrix included the uncertainty information associated with the nominal wavelength scale.

The data from PTB were then used to generate a value matrix $\boldsymbol{M}_{\mathrm{r,\,SD,\,PTB}}$ to describe the spectral characteristics of the lamp, by making draws from a multivariate normal distribution using the nominal wavelength $\boldsymbol{\lambda}$, according to Equation (14).

$$\boldsymbol{M}_{\mathrm{r,\,SD,\,PTB}} = \left(\boldsymbol{\lambda}, \mathcal{N}\left(\overline{\boldsymbol{S}_{\mathrm{PTB}}}, \boldsymbol{\sigma}(\boldsymbol{S}_{\mathrm{PTB}}), \boldsymbol{P}_{\mathrm{PTB}}\right)\right) \quad (14)$$

3.2 Modelled data using the framework approach

In this study, we used the model as described in this section to perform a sensitivity analysis on the calculated relative luminance, chromaticity coordinates and correlated colour temperature (CCT). Separate MCSs were performed for each source of uncertainty with respect to Equations (3) and (4), with the random number parameters described in Section 2.2, so that the sensitivity of

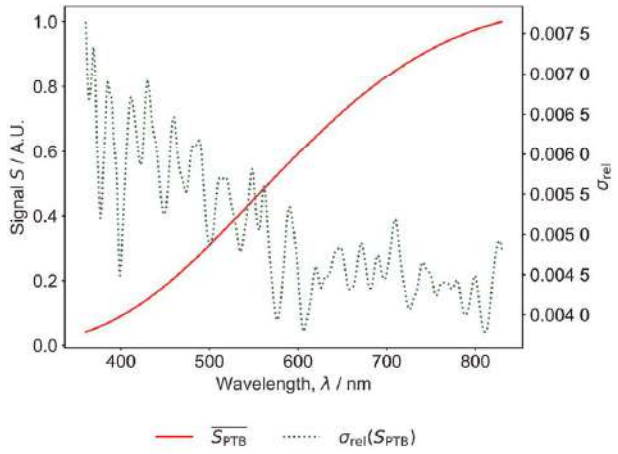

Figure 2 Spectral distribution $\overline{\boldsymbol{S}_{PTB}}$ and standard deviation $\sigma(\boldsymbol{S}_{PTB})$ of a real FEL lamp measurement at PTB

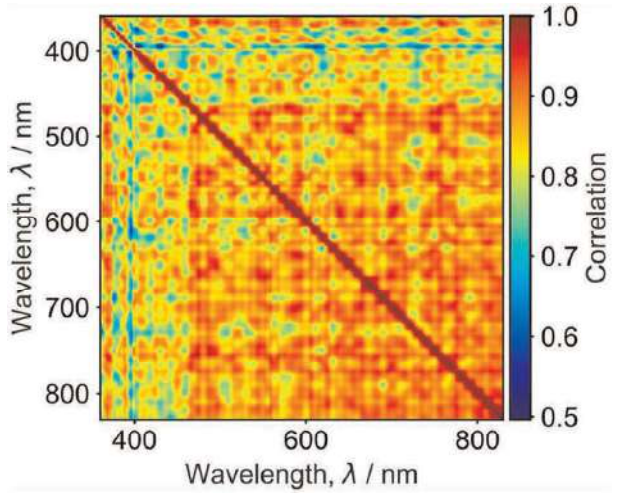

Figure 3 Correlation matrix $\boldsymbol{P}_{PTB}$ of the real spectral distribution measurement of the FEL lamp, shown in Figure 2

the output values to each source of uncertainty in turn could be calculated. This follows the type of sensitivity analysis proposed by Razavi and Gupta.[7]

The spectral distribution of a blackbody at a temperature of 3077 K was used as input quantity for the simulated measurement, to make the simulation as simple as possible. The chosen blackbody temperature is the same as the CCT of the FEL lamp measured at PTB (see Section 3.1) and gives a spectral distribution very close to the relative spectral distribution of the measured lamp. Based on this theoretical blackbody, the amplitude and wavelength values were modified during the MCS as described above (MCS1). With the modified spectral distributions, one can calculate integrated output quantities and study their behaviour during the simulation. Using these simulation data one can estimate the PDFs and statistical parameters for all output quantities, including mean and standard deviation.

Since this assessment is not based on an actual measurement system, we only generate sensitivity values rather than absolute values. This means one can state at the end, for example: The sensitivity coefficient for the chromaticity coordinate x is 0.0006 for every 1 nm correlated error in the wavelength scale.

Starting from a blackbody at 3077 K at a nominal wavelength scale from 360 nm to 830 nm with 1 nm steps, and using the model equations presented previously, we generate N_{MC} pairs of random wavelength $\boldsymbol{\lambda}_r$ and amplitude $\boldsymbol{S}_r$ realisations with defined parameters.

For the amplitude scale, Equation (3), the following parameters are used in the simulation:

$\boldsymbol{S}$ blackbody at 3077 K, normalised to $\max(\boldsymbol{S}) = 1$

$\boldsymbol{k}_{S,\mathrm{m\text{-}b}}$ multiplicative uncertainty component modelled with the basis function technique (used with the cumulative basis function approach and $N_B = 7$ Chebyshev basis functions) with $u_S = 0.01$

$\boldsymbol{S}_{\mathrm{a\text{-}c}}$ additive fully correlated uncertainty component (vector, systematic), $\boldsymbol{S}_{\mathrm{a\text{-}c}} \sim \mathcal{N}(0; 0.01)$

$\boldsymbol{S}_{\mathrm{a\text{-}uc}}$ additive uncorrelated uncertainty component (vector, random), $\boldsymbol{S}_{\mathrm{a\text{-}uc}} \sim \mathcal{N}(0; 0.01)$

$\boldsymbol{S}_{\mathrm{a\text{-}b}}$ additive partially correlated uncertainty component modelled with the basis function technique (vector, systematic), with $u_S = 0.01$

For the wavelength scale, Equation (4), the following parameters are used in the simulation:

$\boldsymbol{k}_{\lambda,\mathrm{m\text{-}b}}$ multiplicative uncertainty component modelled with the basis function technique (used with the cumulative basis function approach and $N_\mathrm{B} = 7$ Chebyshev basis functions, see Equation (10)) with $u_{\lambda,\mathrm{m}} = 0.01$ (description: 'basis c 7')

$\boldsymbol{\lambda}$ nominal wavelength (vector)

$\boldsymbol{\lambda}_{\mathrm{a\text{-}c}}$ additive fully correlated uncertainty component (vector, systematic), $\boldsymbol{\lambda}_{\mathrm{a\text{-}c}} \sim \mathcal{N}(0; 1\ \mathrm{nm})$

$\boldsymbol{\lambda}_{\mathrm{a\text{-}uc}}$ additive uncorrelated random uncertainty or noise (vector, random), $\boldsymbol{\lambda}_{\mathrm{a\text{-}uc}} \sim \mathcal{N}(0; 1\ \mathrm{nm})$

$\boldsymbol{\lambda}_{\mathrm{a\text{-}b}}$ additive partially correlated uncertainty component modelled with the basis function technique (vector, systematic), with $u_{\lambda,\mathrm{a}} = 1$ nm

3.3 Data transfer and interpolation

For data visualisation or the transfer of measurement results to other users, the matrix $\boldsymbol{M}_{\mathrm{r,SD}}$ of spectral distributions can be reduced to a mean vector $\overline{\boldsymbol{S}'}$, a standard deviation $\boldsymbol{\sigma}(\boldsymbol{S}')$ and a correlation matrix $\boldsymbol{P} = \mathrm{Corr}(\boldsymbol{S}'_\mathrm{r})$. To do this, the nominal wavelength scale $\boldsymbol{\lambda}$ is required and not the wavelength scale $\boldsymbol{\lambda}_\mathrm{r}$ from the MC trials described in Section 3.2. Every pair of wavelength and spectral distribution data $(\boldsymbol{\lambda}_\mathrm{r}, \boldsymbol{S}_\mathrm{r})$ is interpolated to the nominal wavelength $\boldsymbol{\lambda}$.

$$\boldsymbol{M}'_{\mathrm{r,SD}} = (\boldsymbol{\lambda}, \boldsymbol{S}'_\mathrm{r}) = \mathrm{Interpolate}(\boldsymbol{\lambda}_\mathrm{r}, \boldsymbol{S}_\mathrm{r}) \quad (15)$$

Using a non-nominal wavelength scale usually requires interpolation for further calculations. This interpolation of the amplitude vector to regular, equidistant wavelength intervals means that the measurement uncertainties of the wavelength vector are converted to the amplitude values and influence the measurement uncertainties and correlations for the amplitude vector. Care is needed when doing the interpolation, particularly if the amplitude vector is noisy, since artificial spectral structure can be introduced if an inappropriate interpolation method is used. Guidance on interpolation is given in CIE 15:2018, Clause 7.2.3.[14] (Rule of thumb: Interpolate the smooth function and not the noisy one.)

New data pairs $\boldsymbol{M}''_{\mathrm{r,SD}}$ for the interpolated data can now be generated based on a multivariate normal distribution $\mathcal{N}$ according to Equation (16):

$$\boldsymbol{M}''_{\mathrm{r,SD}} = \left(\boldsymbol{\lambda}, \mathcal{N}\left(\overline{\boldsymbol{S}'}, \boldsymbol{\sigma}(\boldsymbol{S}'), \boldsymbol{P}\right)\right) \quad (16)$$

3.4 Calculation and evaluation of integral data

As an example, to show the effect of the different measurement uncertainties (with regard to the parameters of the models introduced above), several integrated quantities (tristimulus values, chromaticity coordinates and CCT) are calculated from the simulated spectral distributions.

According to CIE 15:2018, Clause 7[14] the tristimulus values, X, Y, Z, are calculated with Equation (17) using the nominal wavelength scale.

$$\begin{aligned} X &= \sum_{i=0}^{N_\lambda - 1} \bar{x}(\lambda_i) \cdot S(\lambda_i) \cdot \Delta\lambda; \\ Y &= \sum_{i=0}^{N_\lambda - 1} \bar{y}(\lambda_i) \cdot S(\lambda_i) \cdot \Delta\lambda; \\ Z &= \sum_{i=0}^{N_\lambda - 1} \bar{z}(\lambda_i) \cdot S(\lambda_i) \cdot \Delta\lambda \end{aligned} \quad (17)$$

where $\bar{x}\ (\lambda_i)$, $\bar{y}\ (\lambda_i)$, $\bar{z}(\lambda_i)$ are colour-matching functions at wavelength λ_i; $S(\lambda_i)$ is the (relative) spectral distribution of the light source at wavelength λ_i; $\Delta\lambda$ is the step width for the summation; N_λ is the number of elements.

Using the spectral distributions generated with the framework approach, the tristimulus values, $X_\mathrm{r}, Y_\mathrm{r}, Z_\mathrm{r}$, and from these the chromaticity coordinates, x_r and y_r, are calculated according to Equations (18) to (21).

Note that, due to the variation of the wavelength scale in each MC trial depending on the modelling, the wavelength steps are calculated separately for each trial and therefore the integrated values obtained using Equations (18) to (20) are also calculated separately for each trial:

$$X_\mathrm{r} = \sum_{i=0}^{N_\lambda - 2} \bar{x}(\lambda_{\mathrm{r},i}) \cdot S_{\mathrm{r},i} \cdot (\lambda_{\mathrm{r},i+1} - \lambda_{\mathrm{r},i}) \quad (18)$$

$$Y_\mathrm{r} = \sum_{i=0}^{N_\lambda - 2} \bar{y}(\lambda_{\mathrm{r},i}) \cdot S_{\mathrm{r},i} \cdot (\lambda_{\mathrm{r},i+1} - \lambda_{\mathrm{r},i}) \quad (19)$$

$$Z_\mathrm{r} = \sum_{i=0}^{N_\lambda - 2} \bar{z}(\lambda_{\mathrm{r},i}) \cdot S_{\mathrm{r},i} \cdot (\lambda_{\mathrm{r},i+1} - \lambda_{\mathrm{r},i}) \quad (20)$$

$$x_\mathrm{r} = \frac{X_\mathrm{r}}{X_\mathrm{r} + Y_\mathrm{r} + Z_\mathrm{r}};\; y_\mathrm{r} = \frac{Y_\mathrm{r}}{X_\mathrm{r} + Y_\mathrm{r} + Z_\mathrm{r}} \quad (21)$$

The CCT is calculated from the chromaticity coordinates $(x_\mathrm{r}, y_\mathrm{r})$ based on standard algorithms according to Robertson[18] and Baxter *et al.*[19]

4. Results

All diagrams, tables and calculations in the following are based on the open-source Python package 19nrm02[10] and implemented in the Jupyter Notebook `MCSim_PM.ipynb`. The calculations in the MCS were performed with $N_\mathrm{MC} = 20\,000$ trials.

Table 2 shows the result of the MCS1 for the described model settings and the output data relative luminance (Y), chromaticity coordinates (x, y) and CCT (T_cp). In every row of the table, only the parameter described in the first column is used as random. All others are set to their nominal values. For the last row, all parameters are set to their random inputs to evaluate the results of all model parameters together.

Relative luminance: The additive correlated components and the additive partially correlated components (basis functions for both the wavelength and the amplitude scales) have a greater contribution to the uncertainty than the other effects.

Chromaticity coordinates: Uncorrelated contributions of the model average out and correlated additive amplitude component as well as the multiplicative basis function contribution for the wavelength scale and the additive basis function contribution for the amplitude scale are significant.

CCT: Besides all the partially correlated parameters modelled by the basis functions, the correlated additive amplitude component contributes significantly to the uncertainty.

The results of the uncertainty evaluation for the chromaticity coordinates are shown graphically in Figures 4 and 5, in terms of expanded uncertainty ellipsoids. Figure 4 shows the effect of the wavelength scale parameters, and Figure 5 shows the effect of the amplitude scale parameters. The label 'All' is used for the results in the last row of Table 2 containing all modelled uncertainty contributions. In addition to the data in Table 2, these plots allow the chromaticity uncertainty and the correlation to be analysed together.

The correlated additive components result in fully correlated chromaticity uncertainties, displayed as a line. The other contributions result in ellipsoids with different principal axis orientations and lengths. A major contribution is the partially correlated amplitude component, which is modelled as an additive basis function.

Figures 6 to 9 show selected correlation matrices of the generated spectral distributions inside the MCS1 based only on the influence of the model parameter $\boldsymbol{k}_{S,\mathrm{m\text{-}b}}$. This means, after calculating the value pairs $\boldsymbol{M}_{\mathrm{r,SD}} = (\boldsymbol{\lambda}, \boldsymbol{S}_\mathrm{r})$ during the MCS1, we can summarise the data as

Table 2 Evaluation table for the MU calculation using the framework approach in the MCS1

Quantity	Unit	Mean	SD	Distribution	$u(Y)$	$u(x)$	$u(y)$	$u(T_{cp})$/K
$\boldsymbol{\lambda}_{a=c}$	nm	0.0	1.000	Normal	0.0058	0.00056	0.00026	7.8
$\boldsymbol{\lambda}_{a=uc}$	nm	0.0	1.000	Normal	0.00048	0.0001	0.00012	1.7
$\boldsymbol{\lambda}_{a=b}$	nm	0.0	1.000	Basis c 7	0.0067	0.00085	0.00078	14
$\boldsymbol{k}_{\lambda,\,m=b}$	1	1.0	0.010	Normal	0.013	0.0011	0.0011	23
$\boldsymbol{S}_{a=c}$	1	0.0	0.010	Normal	0.021	0.0025	0.0018	30
$\boldsymbol{S}_{a=uc}$	1	0.0	0.010	Normal	0.0017	0.00041	0.0005	6.5
$\boldsymbol{S}_{a=b}$	1	0.0	0.010	Basis c 7	0.024	0.0036	0.0036	52
$\boldsymbol{k}_{S,\,m=b}$	1	1.0	0.010	Basis c 7	0.0065	0.00098	0.00088	20
All					0.037	0.0048	0.0043	70

Mean values: $Y = 1.000$, $(x, y) = (0.43155, 0.40216)$, $T_{cp} = 3077\,\mathrm{K}$.

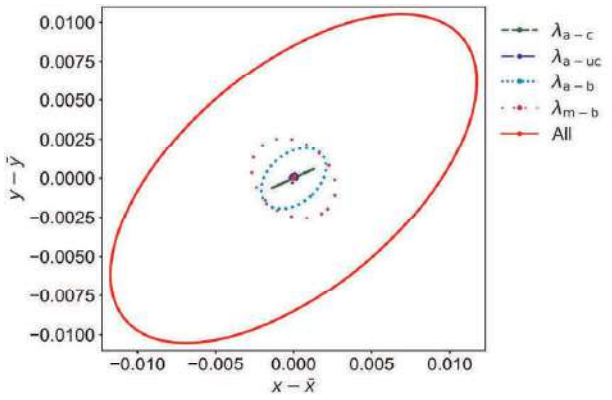

Figure 4 Covariance plots for the chromaticity coordinates based on the wavelength uncertainty contributions

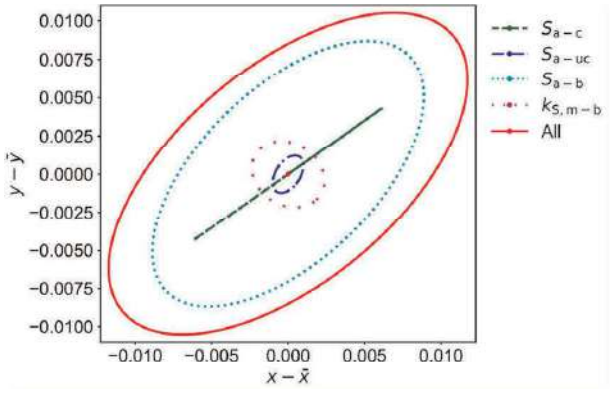

Figure 5 Covariance plots for the chromaticity coordinates based on the amplitude uncertainty contributions

explained in Section 3.3 and display the correlation matrix $\boldsymbol{P}$ to get some insights about the correlation structure of the simulated data. A correlation matrix is a symmetric matrix with values between -1 and 1 and with other specific properties (e.g. all eigenvalues must be non-negative). Therefore, it is almost impossible to generate the correlation matrices directly via an MC simulation. This makes the basis function approach more valuable.

The nominal wavelength scale is used for the ordinate and abscissa axes in these plots. For the following examples, one can see that there is only a partial correlation generated by the basis function approach between different wavelength settings and not a full correlation as could be expected.

Figure 6 shows the correlation matrix for the spectral distribution based on the $\boldsymbol{k}_{S,\,m\text{-}b}$ modelling with $N_B = 7$ and Chebyshev basis functions. Figure 7 shows the same calculation with Fourier basis functions. Figure 8 shows a correlation matrix using Fourier basis functions as in Figure 7, but with a single basis function of order $k = 7$ only. Figure 9 shows a correlation matrix using the same basis functions as in Figure 7 and a one over f weighting.

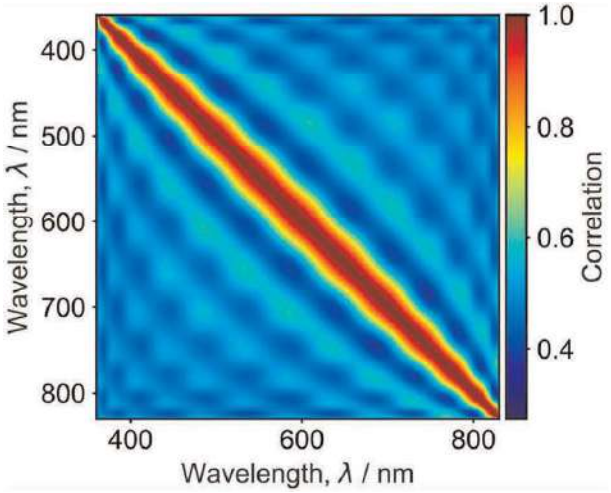

Figure 6 Correlation matrix for the spectral distribution with $N_B = 7$ Chebyshev basis functions ($k_{S,m-b}$ Model parameter only)

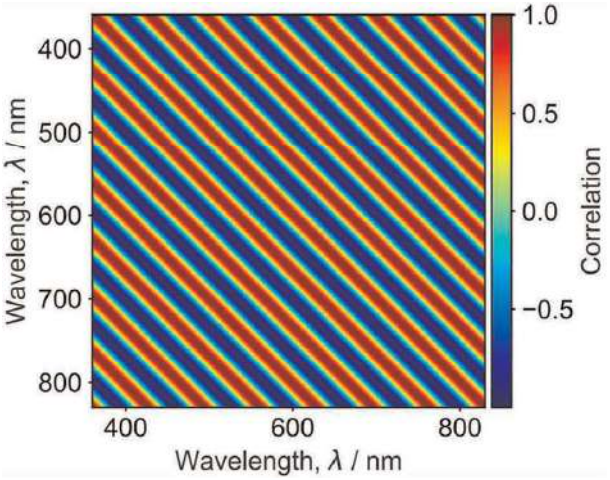

Figure 8 Correlation matrix for the spectral distribution with seventh base function only (Fourier basis functions, $k_{S,m-b}$ Model parameter only)

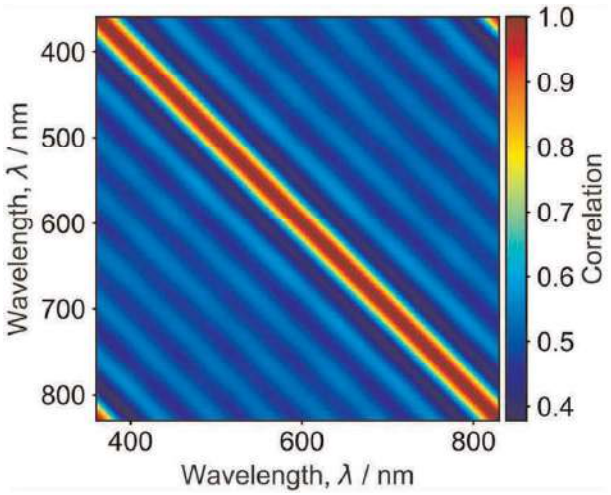

Figure 7 Correlation matrix for the spectral distribution with $N_B = 7$ Fourier basis functions ($k_{S,m-b}$ Model parameter only)

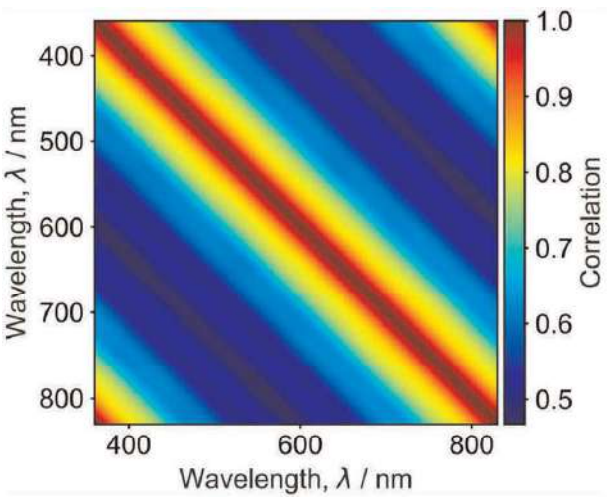

Figure 9 Correlation matrix for the spectral distribution with $N_B = 7$ Fourier basis functions and one over *f* weighting ($k_{S,m-b}$ Model parameter only)

Figures 6 to 9 indicate different correlation matrices that are also structured completely differently from the measurement results of the PTB, which are shown in Figure 3. The authors cannot yet provide general interpretations of the selected correlation matrices displayed here.

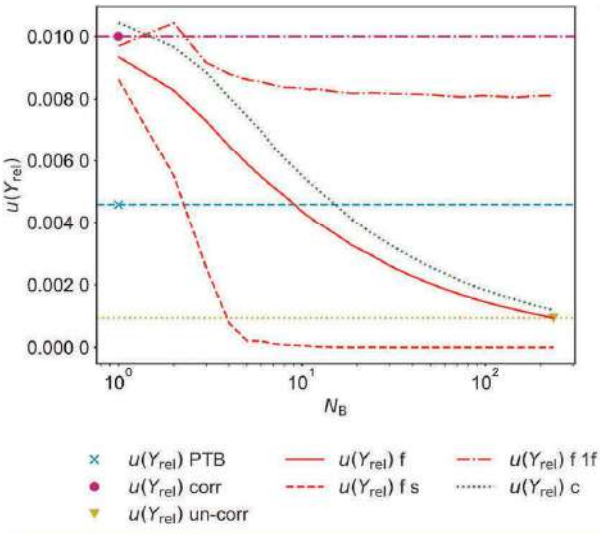

Figure 10 Measurement uncertainty of relative tristimulus value, $u(Y_{rel})$, as a function of the number of basis functions, N_B.

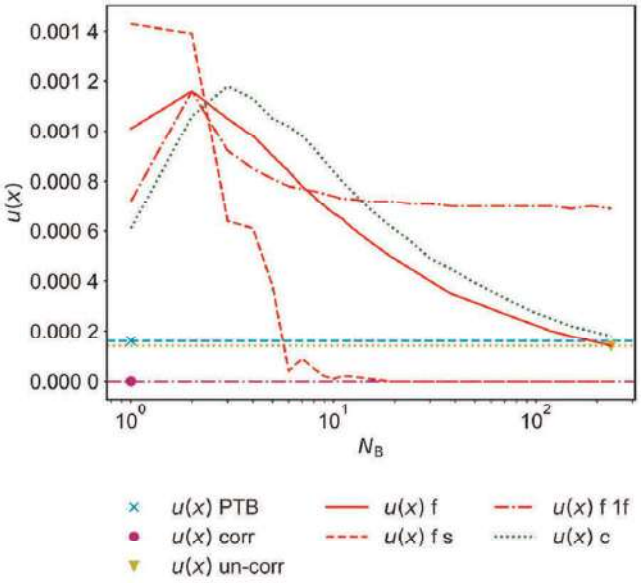

Figure 11 Measurement uncertainty of the chromaticity value, $u(x)$, as a function of the number of basis functions, N_B

4.1 Evaluation of different basis function numbers and types

Iterating the MCS over several basis function numbers ($N_B = 0 \ldots N_\lambda/2 - 1$) and types will result in a lot of information as can be seen in Figures 10 to 13. $N_\lambda/2 - 1$ is the maximum number of basis functions possible, due to the Nyquist rule.

Figures 10 to 13 show the number of basis functions on the horizontal axis (log scale) and on the vertical axis the measurement uncertainty of different quantities (tristimulus value (Y), chromaticity coordinates (x, y) and CCT (T_{cp}) resulting from changes of the model parameter $\boldsymbol{k}_{S,\,\mathrm{m\text{-}b}}$ only.

Besides identifying the basis function number that has the maximum impact on the final uncertainty in each case, three specific points are usually of particular interest and marked separately in Figures 10 to 13:

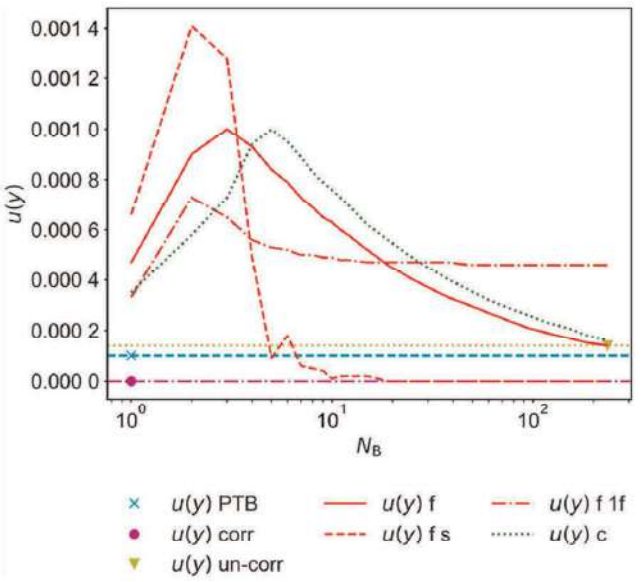

Figure 12 Measurement uncertainty of chromaticity value, $u(y)$, as a function of the number of basis functions, N_B

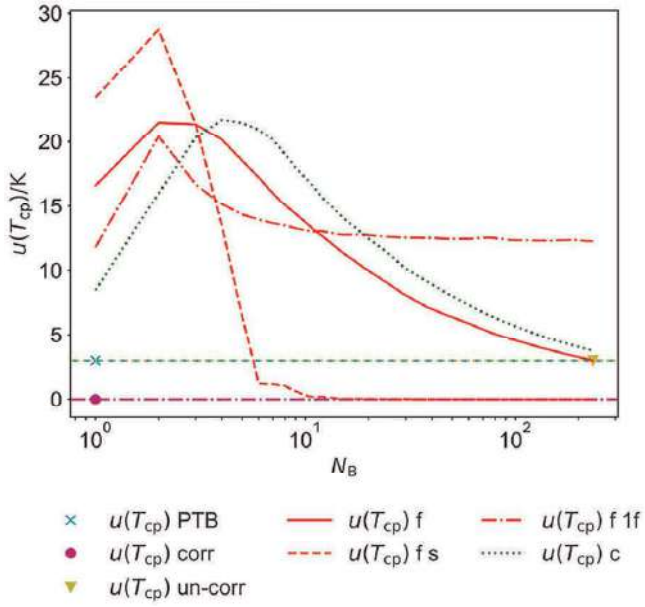

Figure 13 Measurement uncertainty of the correlated colour temperature value, $u(T_{cp})$, as a function of the number of basis functions, N_B

- $N_B = 0$, the fully correlated case, is marked with the label 'corr'.
- $N_B = N_\lambda/2 - 1$, the uncorrelated case, is marked with the label 'un-corr' and a corresponding horizontal line.
- The uncertainties evaluated from the measurement results from PTB are shown as an additional point and a corresponding horizontal line marked with the label 'PTB'.

The different basis function techniques are displayed with different graphs and labelled with 'f' for the cumulative Fourier basis functions (see Equation (9)), 'f s' for a single Fourier basis function (see Equation (10)) and 'c' for cumulative Chebyshev basis functions. The one over *f* approach using Fourier basis functions is labelled with 'f 1f' (see Equation (11)).

5. Discussion

The simulations show that, as expected, uncorrelated and fully correlated contributions generally have no significant influence on chromaticity coordinates and the other evaluated quantities. The exception is the contribution from the additive, fully correlated errors in the values of the wavelengths (e.g. caused by the homing/initialising procedure of a monochromator or by the wavelength adjustment of an array spectroradiometer with a few spectral lines only), which makes significant contributions to nearly all investigated output quantities.

However, it was shown by modelling with orthogonal basis functions that partial correlations contribute significantly to the measurement uncertainty. The tristimulus functions change slowly with wavelength and therefore only the long-wave basis functions (i.e. those where N_B is small) produce effects that do not cancel each other out. Thus, these reflect the possible maximum effects of correlations. This is a possible contribution to the measurement uncertainty that needs to be considered for physical models.

Using single basis functions provides information about the most sensitive frequency for the basis function technique. It is usually observed that ignoring correlations for intermediate spectral frequencies leads to a greater underestimation of the uncertainty. It therefore makes sense to carry out this single basis function analysis and to analyse the results carefully.

6. Conclusion

The framework approach presented in this paper makes it possible to understand the main contributions of the spectral measurement uncertainties to the estimated combined measurement uncertainty and to consider their impact for specific

cases. Additionally, this approach identifies possible correlations among the output quantities.

An MCS1 has shown that when evaluating quantities and uncertainties derived using spectral integrations, the fully correlated and uncorrelated errors contribute much less to the uncertainty than the partially correlated errors modelled by the basis functions. As expected, the basis functions with fewer terms (functions with low spectral frequencies representing errors with short autocorrelation length) provide a larger uncertainty in the evaluation of these spectrally integrated quantities and thus provide a reasonable estimate of the maximum uncertainty.

Acknowledgement

A version of this work was also published in the Proceedings of the CIE 2023 Session. We thank Kevin G. Smet for implementing all the photometric and colorimetric functions in the LuxPy Python package, which we used to implement the calculations presented here. We thank Thorsten Gerloff from PTB Germany for providing the measurement data of the FEL lamp, including the beneficial covariance information. Finally, we would like to thank Peter Zwick, Teresa Goodman and the reviewers for their numerous valuable comments during the final correction of the paper.

Declaration of conflicting interests

The authors declared no potential conflicts of interest with respect to the research, authorship, and/or publication of this article.

Funding

The authors disclosed receipt of the following financial support for the research, authorship, and/or publication of this article: This project 19NRM02 RevStdLED has received funding from the EMPIR programme, co-financed by the Participating States and from the European Union's Horizon 2020 research and innovation programme. Erkki Ikonen wishes to acknowledge support by the Research Council of Finland Flagship Programme, Photonics Research and Innovation (PREIN), decision number: 346529.

ORCID iDs

U Krüger https://orcid.org/0000-0001-7729-4316
A Thorseth https://orcid.org/0000-0003-4344-0770

Supplemental material

Supplemental material for this article is available online.

References

1 Commission International de l'Éclairage. *Determination of Measurement Uncertainties in Photometry, Supplement 2: Spectral Measurements and Derivative Quantities*. CIE 198-SP2:2018. Vienna: CIE, 2018.
2 Schmähling F, Wübbeler G, Krüger U, *et al*. Uncertainty evaluation and propagation for spectral measurements. *Color Research and Application* 2018; 43: 6–16.
3 Joint Committee for Guides in Metrology (JCGM). *Evaluation of Measurement Data – Guide to the Expression of Uncertainty in Measurement*. JCGM 100:2008. Paris: BIPM, 2008.
4 Joint Committee for Guides in Metrology (JCGM). *Evaluation of Measurement Data – Supplement 1 to the 'Guide to the Expression of Uncertainty in Measurement' – Propagation of Distributions Using a Monte Carlo Method*. JCGM 101:2011. Paris: BIPM, 2011.
5 Joint Committee for Guides in Metrology (JCGM). *Guide to the Expression of Uncertainty in Measurement – Part 6: Developing and Using Measurement Models*. JCGM 106:2020. Paris: BIPM, 2020.
6 Kärhä P, Vaskuri A, Mäntynen H, Mikkonen N, Ikonen E. Method for estimating effects of unknown correlations in spectral irradiance data on uncertainties of spectrally integrated colorimetric quantities. *Metrologia* 2017; 54: 524–534.
7 Razavi S, Gupta HV. What do we mean by sensitivity analysis? The need for comprehensive

characterization of 'global' sensitivity in Earth and Environmental systems models. *Water Resources Research* 2015; 51: 3070–3092.
8 Vaskuri A, Kärhä P, Egli L, Gröbner J, Ikonen E. Uncertainty analysis of total ozone derived from direct solar irradiance spectra in the presence of unknown spectral deviations. *Atmospheric Measurement Technology* 2018; 11: 3595–3610.
9 Maham K, Kosonen V, Peltoniemi J, Kärhä P, Ikonen E. Spectral analysis of deviations from key comparison reference values. *Metrologia* 2024; 61: 015002.
10 EMPIR 19NRM02, RevStdLED, Revision and extension of standards for test methods for LED lamps, luminaires and modules. Python package empir19nrm02, https://doi.org/10.5281/zenodo.6860392
11 Smet KAG. Tutorial: The LuxPy Python toolbox for lighting and color science. *LEUKOS* 202; 16: 179–201.
12 Dunn WL, Shultis JK. *Exploring Monte Carlo Methods*, 2nd edition. Amsterdam: Elsevier Science, 2022.
13 Stevens A. *Monte-Carlo Simulation: An Introduction for Engineers and Scientists*. Boca Raton, FL: CRC Press, 2022.
14 Commission International de l'Éclairage. *Colorimetry, 4th Edition*. CIE 015:2018. Vienna: CIE, 2018.
15 Commission International de l'Éclairage. *LED Reference Spectrum for Photometer Calibration*. CIE 251:2023. Vienna: CIE, 2023.
16 Ikonen E, Maham K, Kosonen V, Kärhä P. Spectral analysis of deviations from KCRV. *NEWRAD Conference 2023*, Teddington, UK, 11–15 September 2023.
17 White M, Smid M, Porrovecchio G. Realization of an accurate and repeatable wavelength scale for double subtractive monochromators. *Metrologia* 2012; 49: 779–784.
18 Robertson AR. Computation of correlated color temperature and distribution temperature. *Journal of the Optical Society of America* 1968; 58: 1528.
19 Baxter D, Royer M, Smet K. Modifications of the Robertson method for calculating correlated color temperature to improve accuracy and speed. *LEUKOS* 2024; 20: 55–66.

Stability Study of Multicomponent Mixtures to Support Carbon Metrology

Florbela A. Dias [1*], *Cristina Palma*[1], and *Carlos J. Costa*[1]

[1]Instituto Português da Qualidade, Rua António Gião, 2, 2829-513 Caparica, Portugal

Abstract. The European project EPM SRT-v01 - MetCCUS (Metrology for Carbon Capture Utilization and Storage) is the first metrology project within the scope of CCUS (Carbon Capture Utilization and Storage), which, in the European ecological pact, European Commission's Green Deal, is listed as one of the priority areas to achieve a reduction in greenhouse gas emissions by 55 % by 2030 and carbon neutrality by 2050. This project, financed by EURAMET, aims to respond to the metrological challenges identified by the industry and aims to provide the primary standards, methods, good practice guides that will support the necessary measurements. This study successfully characterized four bicomponent mixtures: SO_2 in CO_2 matrix (two mixtures) and H_2S in CO_2 matrix (two mixtures) and four multicomponent mixtures SO_2+CO+O_2 in CO_2 (two mixtures) and H_2S+CO+CH_4+O_2 in CO_2 matrix (two mixtures) within a cylinder under a pressure of approximately 40 bar, and it entailed a stability study. The stability study was conducted over one year, employing statistical evaluation using the Normalized Error (E_n) function in accordance with the international standard ISO 13528:2022 for statistical methods.

1 Introduction

The European initiative EPM (European Partnership on Metrology) SRT-v01 - MetCCUS (Metrology for Carbon Capture Utilization and Storage) [1] represents the first metrology project dedicated to CCUS (Carbon Capture Utilization and Storage) in Europe. This initiative is a key element of the European Commission's Green Deal, an ambitious plan outlined in the European ecological pact. CCUS is identified as one of the priority areas for achieving the overarching goals of a 55 % reduction in greenhouse gas emissions by 2030 and achieving carbon neutrality by 2050. The project, funded by EURAMET, addresses significant metrological challenges faced by industry stakeholders. It aims to develop primary standards, methodologies and best practice guidelines to ensure precise and reliable measurements essential to support CCUS projects.

A critical aspect of this initiative lies in the preparation and use of primary gas mixtures, which plays a key role in environmental monitoring and decarbonization research. Reliable gas mixtures are essential for calibrating instruments that measure atmospheric pollutants and greenhouse gases, ensuring accuracy and consistency in data collection. Decarbonization itself refers to the process of significantly reducing carbon dioxide (CO_2) emissions resulting from human activities, with the goal of transitioning to a low-carbon or carbon-neutral economy. This transformation is a key strategy for mitigating climate change by directly reducing greenhouse gas concentrations in the atmosphere.

As part of the MetCCUS project, the Reference Gas Laboratory (LGR) at the Portuguese Institute for Quality (IPQ) is collaborating in the development of gas metrological capabilities. Specifically, the laboratory is preparing Certified Reference Materials (CRMs) to enable precise measurement of impurities in CO_2 with full metrological traceability [1, 2]. These materials are vital for validating analytical methods and calibrating the instruments used in carbon capture and storage processes.

To date, the LGR has prepared eight gas mixtures. These include four bicomponent mixtures (two consisting of SO_2 in a CO_2 matrix and two of H_2S in a CO_2 matrix) and four multicomponent mixtures (two containing SO_2, CO, and O_2 in a CO_2 matrix, and two with H_2S, CO, CH_4, and O_2 in a CO_2 matrix). These mixtures were successfully characterized to measure four pollutant gases and oxygen in a CO_2 matrix under high pressure, approximately 40 bar. The certification of these mixtures required an extensive stability study.

The stability of these mixtures was evaluated over one year using statistical methods. The Normalized Error (E_n) function, as specified by the ISO 13528 standard for statistical analysis, was employed to ensure accuracy and reliability in the results [3]. This rigorous approach underscores the project's commitment to providing industry and research sectors with robust and reliable metrological solutions.

* Corresponding author: florbelad@ipq.pt

2 Production of reference gas mixtures

The production of reference gas mixtures is done according to ISO 17034 [4] that specifies the requirements for the production of Certified Reference Materials (CRMs), ensuring high-quality and reliable standard gas mixtures. The process involves detailed documentation, and rigorous quality control to ensures high accuracy and traceability to the International System of Units (SI) [5, 6]. Producers must validate methods, assess uncertainties, and conduct stability studies to guarantee accuracy over time. Compliance with ISO 17034 ensures CRMs meet international standards for calibration, testing, and analytical measurements.

2.1 Preparation of gas mixtures

The preparation of gas mixtures following the ISO 6142-1 standard involves gravimetric methods, which are based on the precise weighing of components [7]. The process starts with the selection of a suitable gas cylinder, which must be thoroughly cleaned and evacuated to prevent contamination. The cylinder is then filled with the desired gas components, introduced sequentially, starting with the minor components (trace gases) and finishing with the balance gas, often nitrogen (N_2) or carbon dioxide (CO_2).

The mixture is prepared by gravimetric addition of each component. The mole fractions of the components in the final mixtures are calculated using the following equation [7]:

$$x_i = \frac{\sum_{A=1}^{P}\left(\frac{x_{i,A}\cdot m_A}{\sum_{i=1}^{n} x_{i,A}\cdot M_i}\right)}{\sum_{A=1}^{P}\left(\frac{m_A}{\sum_{i=1}^{n} x_{i,A}\cdot M_i}\right)} \quad (1)$$

Where: x_i is the mole fraction of the component i in the final mixture, i = 1,…., n; P is the total number of the parent gases; n is the total number of the components in the final mixture; m_A is the mass of parent gas A determined by weighing, A= 1,……, P; M_i is the molar mass of the component i; $x_{i,A}$ is the mole fraction of the component i.

Each gas is added using a high-precision mass comparator balance capable of measuring mass with a very low uncertainty. The mass of each component is calculated, considering the buoyancy effect of the surrounding air on the balance. Once all components are added, the total composition of the mixture is determined from the masses of the individual components and their respective molar masses.

After preparation, the mixture undergoes a homogenization process, which typically involves rotating the cylinder to ensure uniform distribution of gases within the cylinder. Finally, the prepared gas mixture is calibrated with others gas standards, by a suitable analytical method, to confirm its composition and validate the gravimetric calculations.

The traceable gas mixtures are widely used in calibration, environmental monitoring, and industrial applications.


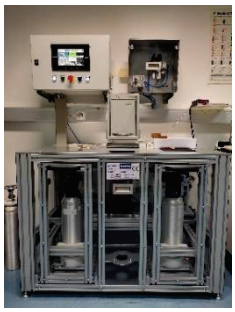

Fig. 1. Filling Station and the mass comparator balance.

2.2 Certification of gas mixtures

The ISO 6143 standard provides a systematic framework for the calibration of gas mixtures using a multi-point method [8]. This approach involves comparing the response of an analytical instrument to a set of calibration gas mixtures with known compositions, referred to as reference standards. The goal is to establish a reliable relationship between the instrument's response and the concentrations of the target components in the mixture being analysed.

Fig. 2. Certification of Gas Mixtures Facility.

The process begins by selecting reference gas mixtures that cover the range of concentrations expected in the sample. These reference standards must be traceable to SI and prepared with high accuracy, often using gravimetric methods according to ISO 6142-1 [7]. The instrument response to each reference mixture is recorded, typically using signals such as peak areas or voltages, depending on the type of analyser is used.

A mathematical model, such as a linear or polynomial regression, is then applied to describe the relationship between the instrument response and the concentration of the analyte. ISO 6143 [8] emphasizes the evaluation of uncertainties for both the reference mixtures and the instrument response, ensuring the calibration curve is accurate and reliable.

Finally, the established calibration curve is used to determine the composition of unknown gas mixtures by measuring their instrument response and interpolating within the range of the calibration standards. This process is essential for applications requiring high precision, such as environmental monitoring and industrial quality control.

3 Stability Study

The stability study of the eight bi-component and multi-component mixtures prepared was conducted over approximately one year. The analysed parameters included H_2S, CO, O_2, CH_4, and SO_2 in a CO_2 matrix. This research aimed to assess the chemical interactions and long-term stability of these gas combinations. Understanding their behaviour is crucial for industrial applications, storage, and transportation safety.

This study was conducted using Primary Reference Material (PRM) of several multicomponent mixtures (Table 1, Table 2, Table 3, Table 4, Table 5). All these reference gas mixtures were prepared in carbon dioxide matrix. The calibration curves were done using primary standards in nitrogen matrix. With these primary standards we can have traceability to the standards of these impurities in CO_2. In this case, the matrix will not influence the analysis because the analysers in question do not detect CO_2 just as they do not detect nitrogen. Each of them detects only the respective gas.

The purpose is to determine the shelf life of this type of mixtures, that is, the actual period during which a mixture can be considered stable concerning its original metrological specifications.

The study was conducted according to ISO 13528 standard [3], which provides various statistical evaluation methods that can be used in specific tests or measurements and for monitoring the ongoing performance of laboratories. In this context, it will be used to compare two concentrations: the concentration resulting from the initial certification and the concentration obtained in subsequent certifications according to the international standard ISO 6143 [8], over the lifetime of the standard.

In this study, we used the normalized error (*En*) statistical tool that is typically applied in comparison of measurement systems, calculated according to the following equation:

$$E_n = \frac{x_{\text{cer1}} - x_{\text{cern}}}{\sqrt{U_{\text{cer1}}{}^2 + U_{cern}{}^2}} \quad (2)$$

Where x_{Cer1} is the concentration value from the first certification and x_{Cern} is the concentration value resulting from the n^{th} certification. U_{Cer1} represents the uncertainty associated with x_{Cer1} while U_{Cern} is the expanded uncertainty associated with x_{Cern}. With this statistical tool, the results are considered satisfactory if $|E_n| \leq 1$ and unsatisfactory if $|E_n| > 1$.

4 Results

Four gas mixtures, Primary Reference Material (PRM), were carefully prepared for analysis, including two binary combinations of H_2S in a carbon dioxide matrix, designated as PRM108595, PRM108596 and two mixtures of SO_2 in CO_2, labelled as PRM408326 and PRM108593, were also carefully assembled. This study facilitated the comprehensive characterization of these four mixtures, each contained within individual cylinders maintained at an approximate pressure of 40 bar.

Furthermore, four multicomponent mixtures were prepared in a CO_2 matrix, PRM608395 and PRM308978 with the impurities SO_2, CO and O_2; and two, PRM202557 and PRM302530, with the impurities H_2S, CO, O_2, and CH_4. These mixtures were contained within four cylinders at an approximate pressure of 40 bar each. No stability study was conducted on the PRM308978 because this cylinder was sent for analysis to one of the participants of the MetCCUS project.

Table 1. Results of the stability study for the prepared binary mixtures of H_2S/CO_2

PRM108596	**H_2S/CO_2**		
Date	***x*** **µmol/mol**	***U*** **µmol/mol**	***E*n**
2023-09-11	9,64	0,47	-
2024-04-23	10,22	0,42	0,92
2024-11-08	10,02	0,34	0,66

PRM108595	**H_2S/CO_2**		
Date	***x*** **µmol/mol**	***U*** **µmol/mol**	***E*n**
2023-09-11	9,97	0,48	-
2024-04-23	9,87	0,35	-0,17
2024-11-08	9,61	0,29	-0,64

Table 2. Results of the stability study for the prepared binary mixtures of SO_2/CO_2

PRM408326	**SO_2/CO_2**		
Date	***x*** **µmol/mol**	***U*** **µmol/mol**	***E*n**
2023-09-04	19,52	0,51	-
2024-04-18	20,16	0,57	0,84
2024-11-18	19,9	1,1	0,31

PRM108593	**SO_2/CO_2**		
Date	***x*** **µmol/mol**	***U*** **µmol/mol**	***E*n**
2023-09-04	20,71	0,50	-
2024-04-18	20,71	0,58	0,00
2024-11-18	20,5	1,0	-0,19

Table 3. Results of the stability study for the prepared multicomponent mixture of SO_2+CO+O_2 / CO_2

PRM608395	**SO_2+CO+O_2 / CO_2**		
	SO_2		
Date	***x*** **µmol/mol**	***U*** **µmol/mol**	***E*n**
2024-04-18	14,24	0,77	-
2024-11-18	14,1	1,3	-0,09
	CO		
Date	***x*** **µmol/mol**	***U*** **µmol/mol**	***E*n**
2024-04-17	660,7	1,6	-
2024-11-22	653,5	1,6	-3,2
	O_2		
Date	***x*** **cmol/mol**	***U*** **cmol/mol**	***E*n**
2024-04-16	0,568	0,048	-
2025-01-23	0,572	0,017	0,08

Table 4. Results of the stability study for the prepared multicomponent mixture of H_2S +CO+O_2+CH_4 / CO_2

PRM202557	**H_2S+CO+O_2+CH_4 / CO_2**		
	H_2S		
Date	***x*** **µmol/mol**	***U*** **µmol/mol**	***E*n**
2023-09-20	9,83	0,48	-
2024-04-23	9,73	0,33	-0,17
2024-11-08	9,61	0,28	-0,40
	CO		
Date	***x*** **µmol/mol**	***U*** **µmol/mol**	***E*n**
2023-09-15	669,5	2,7	-
2024-04-17	662,3	1,6	-2,3
2024-11-22	654,4	1,6	-4,8
	O_2		
Date	***x*** **cmol/mol**	***U*** **cmol/mol**	***E*n**
2023-09-15	0,586	0,027	-
2024-04-16	0,582	0,048	-0,07
2025-01-23	0,586	0,017	0,00
	CH_4		
Date	***x*** **cmol/mol**	***U*** **cmol/mol**	***E*n**
2023-09-14	1,9685	0,0060	-
2024-04-17	1,9686	0,0061	0,01
2024-11-28	1,9706	0,0062	0,24

Table 5. Results of the stability study for the prepared multicomponent mixture of H_2S +CO+O_2+CH_4 / CO_2

PRM302530	**H_2S+CO+O_2+CH_4 / CO_2**		
	H_2S		
Date	***x*** **µmol/mol**	***U*** **µmol/mol**	***E*n**
2023-12-04	9,92	0,40	-
2024-04-23	9,60	0,36	-0,59
2024-11-08	9,16	0,33	-1,5
	CO		
Date	***x*** **µmol/mol**	***U*** **µmol/mol**	***E*n**
2023-12-14	677,0	1,8	-
2024-04-17	674,3	1,5	-1,1
2024-11-22	666,5	1,6	-4,3
	O_2		
Date	***x*** **cmol/mol**	***U*** **cmol/mol**	***E*n**
2023-12-18	0,602	0,051	-
2024-04-16	0,591	0,058	-0,14
2025-01-23	0,585	0,017	-0,32
	CH_4		
Date	***x*** **cmol/mol**	***U*** **cmol/mol**	***E*n**
2023-12-05	1,915	0,015	-
2024-04-17	1,9270	0,0059	0,74
2024-11-28	1,9284	0,0060	0,83

5 Summary

In conclusion, IPQ has demonstrated its ability to prepare and certify reference materials (CRM) for measuring impurities of H_2S, SO_2, CO, O_2 and CH_4 in CO_2, within the requested concentration with metrological traceability. The uncertainties obtained were as expected.

The stability study has confirmed that, except for CO, all components remain stable for about one year within the associated uncertainties. To further refine our understanding, a longer study will be conducted to determine the stability period of each type of mixture.

Looking ahead, this research may be extended to mixtures containing additional components. Additionally, to enhance the scope of the project, these mixtures will be analysed using alternative analytical methods to gather more data for further characterization of the mixtures.

References

1. MetCCUS Project https://metccus.eu/about-the-project/ (accessed 11 February 2025).
2. F. A. Dias, C. Palma, C. J. Costa, Preparation of Multicomponent Mixtures to Support Carbon Metrology, Measurement - Elsevier., **239**, 2025, 115453.
3. ISO 13528:2022 – Statistical methods for use in proficiency testing by interlaboratory comparisons.
4. ISO 17034:2016 – General requirements for the competence of reference material producers.
5. ISO/IEC 17025:2017 – General requirements for the competence of testing and calibration laboratories.
6. KCDB https://www.bipm.org/kcdb/ (accessed 11 February 2025).
7. ISO 6142-1:2015 – Gas analysis — Preparation of calibration gas mixtures — Part 1: Gravimetric method for Class I mixtures.
8. ISO 6143:2001 – Gas analysis — Comparison methods for determining and checking the composition of calibration gas mixtures.

22NRM07 GuideRadPROS: A survey on calibration of radiation protection dosimeters in photon reference fields – current practices and standardization and training needs

Miloš Živanović[1], Ivana Komatina[1,2], Nikola Kržanović[1], Miloš Đaletić[1], Teemu Siiskonen[3], Reetta Nylund[3], Hayo Zutz[4], Steffen Ketelhut[4], Oliver Hupe[4], Argiro Boziari[5], Eirini Trifylli[5], Liviu-Cristian Mihailescu[6], Siarhei Saroka[7], Jean-Marc Bordy[8], Paz Aviles Lucas[9], Vladimir Sochor[10], Jaroslav Šolc[10], Massimo Pinto[11], Lukasz Michalik[12], Amra Šabeta[13], Maria do Ceu Ferreira[14,15], Luka Bakrač[16], Ana Fernandes[17], Erinc Reyhanioglu[18], Matti Vuotila[19], Kowatari Munehiko[20]

1 VINS - Vinča Institute of Nuclear Sciences - National Institute of the Republic of Serbia, University of Belgrade, Belgrade, Serbia
2 Faculty of Physical Chemistry, University of Belgrade, Belgrade, Serbia
3 STUK - Radiation and Nuclear Safety Authority, Vantaa, Finland
4 PTB – Physikalisch-Technische Bundesanstalt, Braunschweig, Germany
5 EEAE – Elliniki Epitropi Atomikis Energeias, Athens, Greece
6 SCK CEN – Belgian Nuclear Research Centre, Mol, Belgium
7 INM – I.P. Institutul Național de Metrologie, Chisinau, Moldova
8 CEA – Commissariat à l'énergie atomique et aux énergies alternatives, Paris, France
9 CIEMAT – Centro de Investigaciones Energéticas, Medioambientales y Tecnológicas, Madrid, Spain
10 CMI – Cesky Metrologicky Institut, Brno, Czech Republic
11 ENEA – Agenzia Nazionale per le nuove tecnologie, l'energia e lo sviluppo economico sostenibile, Rome, Italy
12 GUM – Główny Urząd Miar, Warsaw, Poland
13 IMBiH – Institut za mjeriteljstvo Bosne i Hercegovine, Sarajevo, Bosnia and Herzegovina
14 IPQ – Instituto Português da Qualidade, I.P, Lisbon, Portugal
15 Lusofona University RCM2+, Lisbon, Portugal
16 IRB – Ruđer Bošković Institute, Zagreb, Croatia
17 IST – Instituto Superior Técnico, Lisbon, Portugal
18 TENMAK – Türkiye Enerji, Nükleer ve Maden Araştırma Kurumu, Ankara, Turkey
19 Mirion Technologies (RADOS) Oy, Turku, Finland
20 QST – National Institutes for Quantum Science and Technology, Chiba, Japan

Regular calibration of radiation protection dosimeters is of great importance to ensure accurate measurements and the adequate protection of workers and the public. Calibrations are required by the European Legislation (EURATOM directive) and by many individual countries, both in Europe and in other regions. Some countries have additional requirements, such as verification, testing or type testing of dosimeters. All these requirements improve the confidence in measurements and improve overall radiation protection. Photon dosimeters are typically calibrated and tested in reference radiation fields, which are realized in Primary and Secondary Standards Dosimetry Laboratories according to the standard ISO 4037. The standard was updated in 2019, but early adopters reported problems with its implementation and missing data. Especially smaller laboratories needed additional training. This was one of the main reasons to establish a project within European Partnership on Metrology, with the name 22NRM07 GuideRadPROS "Harmonisation, update and implementation of standards related to radiation protection dosimeters for photon radiation". A survey was organized in the project, and 40 replies were received, with 34 answers from 27 European countries. Considering the small number of calibration laboratories and considering that some countries do not have any calibration laboratories, the coverage of Europe was excellent. The survey showed that only half of the respondents completely implemented the new version of ISO 4037. Setting up gamma reference fields is clear to most respondents, but around half of the respondents have problems (unclear requirements, missing information, difficult to implement) with X-ray reference fields, half-value layer measurements and measurement uncertainty. Only a few respondents stated that X-ray tube voltage, spectrometry and Am-241 fields are adequately covered in the standard. A significant number of laboratories expressed training needs in high voltage measurements (27 respondents), spectrometry (24), setting X-ray reference fields (18), measurement uncertainty (18) and other topics. Survey inputs are used by 22NRM07 GuideRadPROS project to develop training courses and e-training materials, and to collate future research needs. The project will generate guidelines on spectrometry and will investigate conversion coefficients and associated uncertainties allowing for a future edition of the ISO 4037 standard.

Acknowledgments: The project (22NRM07 GuideRadPROS) has received funding from the European Partnership on Metrology, co-financed from the European Union's Horizon Europe Research and Innovation Programme and by the Participating States. Funded by the European Union. Views and opinions expressed are, however, those of the author(s) only and do not necessarily reflect those of the European Union or EURAMET. Neither the European Union nor the granting authority can be held responsible for them.

REVISTAS NACIONAIS

a rastreabilidade das medições no domínio elétrico

Vitor Cabral[1], Isabel Godinho
Instituto Português da Qualidade, I. P. Q.
[1]vcabral@ipq.pt

Em qualquer domínio de atividade (técnico, científico, comercial, entre outros) a rastreabilidade das medições é um aspeto essencial para assegurar o rigor dos resultados e a sua comparabilidade.

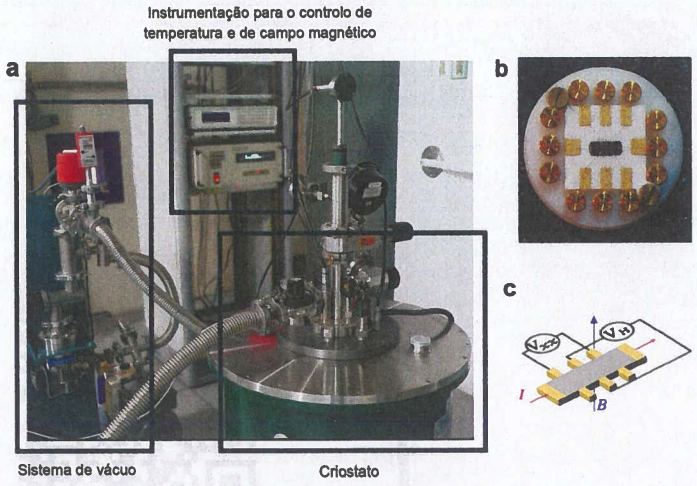

Figura 1. a. Sistema experimental do IPQ para a realização prática da unidade de resistência elétrica - ohm - através do Efeito de Hall Quântico, onde o sistema de vácuo e o crióstato asseguram um valor de temperatura da ordem de 1 kelvin; **b.** Imagem de uma amostra de Hall baseada numa heteroestrutura de GaAs/AlGaAs; **c.** Representação esquemática de uma amostra de Hall, onde V_H corresponde à tensão quântica gerada nos seus terminais quando esta é percorrida por uma corrente elétrica *I*, submetida a um campo magnético *B* e verificando-se um valor de V_{xx} próximo de zero.

A rastreabilidade metrológica é definida como a "*propriedade dum resultado de medição pela qual tal resultado pode ser relacionado a uma referência através duma cadeia ininterrupta e documentada de calibrações, cada uma contribuindo para a incerteza de medição*". Esta cadeia de calibrações, em que o resultado da indicação de um instrumento de medição é relacionado com a indicação de um outro instrumento de medição (padrão) de exatidão superior, assegura a ligação a uma referência comum estabelecida pelo topo da cadeia. Essa referência, ou padrão de referência, materializa uma quantidade expressa, com o maior rigor possível, de acordo com o estado da arte, nas unidades de medida acordadas para a grandeza física ou química em questão, e assegurando, dessa forma, a comparabilidade e uniformidade das medições.

As unidades de medida são estabelecidas por convenção entre os Estados-Membros e sob a responsabilidade do *Bureau International des Poids et Mesures* (BIPM), organização internacional e intergovernamental, criada em 1875, através do tratado da *Convenção do Metro*, da qual Portugal é membro fundador.

Em 2019, o BIPM publicou a última revisão do Sistema Internacional de Unidades (SI), passando as 7 unidades base (kilograma, metro, segundo, ampere, kelvin, candela, mole) a estarem definidas em termos de contantes fundamentais da natureza, com valores imutáveis e exatos (publicada em maio de 2025 a Tradução Luso-Brasileira). As unidades de medida das grandezas derivadas são estabelecidas através de produtos de potências das unidades base.

Os Institutos Nacionais de Metrologia, entre outros aspetos, são responsáveis por estabelecer a realização prática das definições das unidades de medida e por assegurar a rastreabilidade das medições ao SI através da calibração de instrumentos de medição, nomeadamente dos padrões usados pelos Laboratórios de Calibração acreditados que, por sua vez, asseguram a calibração de instrumentos de medição usados na indústria e serviços. Em Portugal, essa missão é assegurada pelo IPQ – Instituto Português da Qualidade.

A definição atual da unidade base da corrente elétrica, ampere, estabelece que 1 A corresponde ao fluxo de $1/(1{,}602\,176\,634 \times 10^{-19})$ cargas elementares por segundo.

Historicamente, a realização da unidade de corrente elétrica apresenta maior dificuldade do que a realização prática do volt e do ohm. Enquanto estas são materializadas, respetivamente, através dos Efeitos Quânticos de Josephson e de Hall, que asseguram a sua rastreabilidade direta às constantes fundamentais da natureza – constante de Planck (*h*) e carga elementar (*e*) – a definição prática do ampere recorreu, durante décadas, à sua determinação indireta pela lei de Ohm. Atualmente, a aplicação universal destes efeitos quânticos torna possível a realização prática do ampere. As Figuras 1 e 2 ilustram, de forma esquemática, os sistemas experimentais implementados no IPQ para a realização prática destas unidades elétricas.

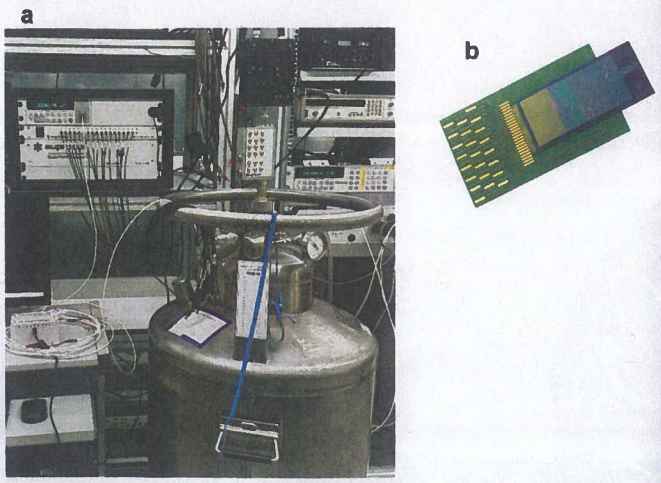

Figura 2. a. Sistema experimental do IPQ para a realização prática da unidade de tensão - volt - através do Efeito Quântico de Josephson, que inclui um *dewar* com hélio líquido, para manter o padrão de tensão a temperaturas criogénicas (da ordem de 4 kelvin), bem como a instrumentação de controlo e medição; **b.** Imagem do padrão de tensão de Josephson, constituído por milhares de junções supercondutor-isolador-supercondutor programáveis para gerar valores quânticos de tensão entre 0 V e 10 V, em regime contínuo e alterando (DC e AC).

Estes padrões primários permitem a realização das respetivas unidades de medida com incertezas típicas na ordem de algumas partes em 10^9 e asseguram a sua transferência para padrões de referência, constituindo o segundo nível na cadeia de rastreabilidade. Estes padrões de referência, por sua vez, são utilizados na calibração de instrumentos de medição multifunção, tais como calibradores ou multímetros de elevada resolução, cuja exatidão é da ordem de algumas partes por milhão. No extremo desta cadeia de rastreabilidade encontram-se os multímetros de mão, cujas especificações são geralmente expressas em termos do erro máximo da sua indicação (Figura 3).

A extensão destas cadeias de rastreabilidade a outras grandezas derivadas no domínio elétrico, como capacidade, indutância, potência e energia e a necessidade de construir escalas para abranger intervalos de medição acima a abaixo dos valores iniciais de materialização das unidades de medida, exigem sistema complexos e de operacionalização demorada. Constituem, por isso, um desafio para os Institutos Nacionais de Metrologia que os procuram implementar e desenvolver continuadamente na procura de sistemas capazes de atingir elevados níveis de exatidão e de operacionalização mais eficiente. Regionalmente, os Institutos Nacionais de Metrologia agrupam-se em associações para coordenar o desenvolvimento de trabalho conjunto. Na Europa, essa entidade é a EURAMET. Nos últimos anos, muitos dos projetos de investigação conjuntos a nível europeu, e em que Portugal tem participado ativamente, têm-se focado no desenvolvimento de aplicações dos padrões de tensão Josephson, para substituir os sistemas de rastreabilidade clássicos de tensão AC, baseados em termo conversores AC-DC e na amostragem digital de sinais elétricos AC com multímetros rastreados diretamente aos padrões Josephson.

> “As unidades de medida são estabelecidas por convenção entre os Estados-Membros e sob a responsabilidade do *Bureau International des Poids et Mesures* (BIPM), organização internacional e intergovernamental, criada em 1875, através do tratado da Convenção do Metro, da qual Portugal é membro fundador.

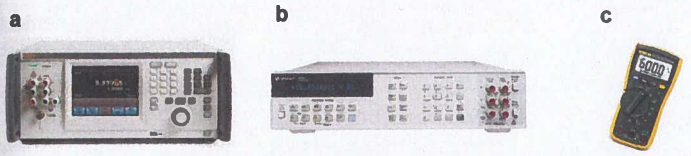

Figura 3. a. Calibrador multifunção com capacidade de gerar valores de tensão e corrente (DC e AC) e resistência; **b.** Multímetro de elevada resolução com oito dígitos e meio; **c.** Multímetro de mão.

Em síntese, a rastreabilidade das medições, em particular no domínio elétrico, é essencial para garantir o rigor e a comparabilidade dos resultados. A Metrologia, ciência da medição e das suas aplicações, está em constante desenvolvimento técnico-científico para assegurar a implementação destas cadeias de rastreabilidade e a melhoria contínua da exatidão das medições, com impacto nos mais diversos aspetos da nossa vida quotidiana.

APLICAÇÕES DA METROLOGIA EM CUIDADOS DE SAÚDE

Maria do Céu Ferreira

1. INTRODUÇÃO

Ao longo das últimas décadas, a crescente consciencialização para a necessidade da melhoria contínua dos serviços e cuidados de saúde tem evoluído de uma forma significativa, permitindo a utilização de instrumentos cada vez mais sofisticados e complexos. Esta evolução tem proporcionado o acesso a novos meios de diagnóstico e de terapêutica, com otimização dos respetivos parâmetros de eficácia e de eficiência, sendo também nesta matéria os resultados das medições parâmetros fundamentais.

Considerando que o valor de qualquer grandeza é determinado através de medições, a sua influência nos processos de decisão, designadamente nos que envolvem a avaliação clínica e, por conseguinte, a evolução do diagnóstico e/ou tratamento, é, indiscutivelmente, uma realidade na sociedade. Nesta vertente, a importância da Metrologia em saúde, como ciência da medição, apresenta-se de uma forma permanente e transversal. Nesta vertente, o subsistema da Metrologia, inserido na estrutura organizacional do Sistema Português da Qualidade que é coordenado pelo Instituto Português da Qualidade, desempenha um papel fundamental na consecução da garantia da Qualidade, enfatizando-se a sua relevância nos serviços e nas instituições de saúde.

2. A IMPORTÂNCIA DA RASTREABILIDADE METROLÓGICA DAS MEDIÇÕES

Entre as várias atribuições da Metrologia, salienta-se a definição das unidades de medida internacionalmente aceites, onde naturalmente se inclui os padrões e os instrumentos de medição, bem como todos os assuntos que estão relacionados com as medições (Ferreira, 2013).

No domínio da saúde, as características metrológicas dos instrumentos médicos com função de medição, habitualmente designados por equipamentos médicos, e o rigor das medições preconizadas pelos mesmos, apresentam-se como fatores determinantes em saúde. A fundamentação para tal, assenta na importância da indicação dos resultados das medições, que influenciam a decisão/evolução do diagnóstico e/ou tratamento. Essas medições contribuem assim de forma significativa para o diagnóstico clínico e processos terapêuticos, com o consequente impacto no doente/utilizador ou cliente (Ferreira, 2011).
Nesta matéria refira-se, como exemplo, a importância da utilização dos equipamentos de ultrassons (ecógrafos) na medição exata do diâmetro de um vaso, amplamente utilizado em protocolos cardiovasculares, ou na determinação das características dimensionais de uma massa num determinado órgão, ou ainda, numa outra vertente, a importância da dosagem exata dos fármacos ministrados através dos sistemas de bombas de perfusão. Refletindo em outras áreas clínicas, outros exemplos de aplicação emergem: no domínio da

hemodiálise, é crucial para o sucesso do processo o rigor da indicação do instrumento de pesagem (balança) utilizado com o paciente, entre outros aspetos. Ao caminharmos para o domínio das radiações ionizantes e respetivos impacto que as mesmas exercerem no corpo humano facilmente é percetível o quão importante é conhecer com a máxima exatidão a quantidade de radiação a debitar.

Ainda na vertente clínica, e apesar de ser um processo relativamente simples, a medição da pressão arterial está sujeita a vários fatores de erro (erros aleatórios e erros sistemáticos) que poderão conduzir a falsos diagnósticos. Em função do estado de saúde do utilizador dos instrumentos de medição, esta ocorrência poderá ter impacto significativo na sua qualidade de vida e, com repercussões económicas e sociais.

Vários outros exemplos poderiam ser elencados, pois em todas as áreas clínicas existem instrumentos médicos com função de medição que são diariamente utilizados. De facto, o que a prática diária evidencia é que, em todos os processos clínicos existe um denominador comum relativamente ao qual, e no atual contexto, se designa por *rastreabilidade metrológica*, e que poderá contribuir para o sucesso ou insucesso dos resultados clínicos.

De acordo com o Vocabulário Internacional de Metrologia (VIM, 2012), rastreabilidade metrológica é uma propriedade do resultado da medição, através da qual esse mesmo resultado pode ser relacionado com uma referência. Assim, no caso de não ser possível relacionar a indicação da medição com um padrão credível e comparável, a probabilidade de ser disseminado um resultado não verdadeiro é real e significativa, com todas as consequências que poderão derivar desse resultado não conforme.
Também nesta vertente, assume especial relevância o controlo da qualidade do equipamento e a garantia do correto funcionamento dentro das suas especificações, sendo de importância vital para a segurança dos utilizadores (profissionais de saúde, doente/utente, terceiros) e para a credibilidade das medições e dos seus resultados (Ferreira, 2015).

2.1 COMO ASSEGURAR A EFETIVA RASTREABILIDADE METROLÓGICA DAS MEDIÇÕES

A medicina estabelece consensos e estratégias para tratamento e diagnóstico de patologias, assumindo que as instituições de saúde e os instrumentos de medição utilizados na obtenção de diagnósticos funcionem em conformidade, com resultados aceites e confiáveis. Por outro lado, uniformizar e integrar verdadeiramente os conceitos da qualidade em saúde entre os vários profissionais da saúde e aproximar a respetiva aplicabilidade de uma forma generalizada, continua a constituir um enorme desafio para várias organizações de saúde.

Na realidade, a implementação de modelos de governação clínica assentes em princípios de gestão pela qualidade, orientados para ganhos (mensuráveis) em saúde são, indiscutivelmente vetores catalisadores de uma efetiva cultura da qualidade.
Assim, uma questão relevante que qualquer profissional de saúde deveria colocar a si próprio antes de aceitar um resultado de uma medição indicado por um equipamento

médico com função de medição, seria questionar-se sobre a sua validade. Obviamente que, a análise critica de qualquer resultado, designadamente o de uma medição, implica uma atitude pró-ativa, mas também um conhecimento prévio dos valores aproximadamente espectáveis, face às referências conhecidas. Em muitos domínios, este comportamento poderá marcar a diferença entre um bom ou um mau diagnóstico.

Considerando que as medições realizadas em contexto clínico estão relacionadas com as grandezas do Sistema Internacional de Unidades, SI (BIPM 2019) tais como a massa, temperatura, comprimento, etc., consideram-se aplicáveis os princípios adotados para as diversas áreas de intervenção na sociedade, onde a atuação da metrologia é uma realidade há muito praticada. Seguindo essa linha de raciocínio, existe uma forte necessidade de conhecer e otimizar a rastreabilidade metrológica dos instrumentos de medição, pois o conhecimento das condições de reprodutibilidade e de repetibilidade de um instrumento de medição é um requisito obrigatório nas boas práticas metrológicas, independentemente da área de atuação.

A utilização de equipamentos médicos com erros desconhecidos (não existe erro nulo, contrariamente ao que frequentemente se assiste) no diagnóstico e no tratamento de doentes, em muitas situações, poderá induzir a alterações nos parâmetros, nos protocolos e nas condições terapêuticas aplicadas e, consequentemente, conduzir a um procedimento inadequado (Barroso, 2021).

Apesar de em Portugal, maioritariamente, os serviços de saúde (públicos e privados) apresentarem Sistemas de Gestão da Qualidade implementados, o cumprimento de requisitos relacionados com a rastreabilidade metrológica dos instrumentos de medição ainda está longe de uma abordagem similar à que é aplicada em outros sectores da sociedade. Inclusivamente, em diversos contextos de avaliação, a abordagem metrológica oscila em função da área de avaliação e dos conhecimentos específicos de quem avalia. Em complemento, como não existe uma monitorização da conformidade metrológica de acordo com os requisitos estabelecidos para cada área clínica, o acesso às características e desempenho metrológico dos equipamentos médicos torna-se uma tarefa dificultada.

No sentido de contribuir para a melhoria continua dos serviços de saúde e minimizar o impacto da ausência de rastreabilidade metrológica, o Instituto Português da Qualidade publicou recentemente legislação para a implementação de controlo metrológico legal em quatro domínios distintos. Assim, a par dos instrumentos de pesagem e do domínio das radiações ionizantes, em novembro de 2023 foram publicados novos diplomas aplicáveis ao controlo metrológico legal de termómetros clínicos, esfigmomanómetros, audiómetros e tonómetros.

Tabela 1: Legislação nacional aplicável ao controlo metrológico legal de instrumentos de medição no âmbito da saúde

Portaria	Âmbito de aplicação
Portaria n.º 351/2023 de 14 de novembro	Controlo metrológico legal de audiómetros
Portaria n.º 368/2023 de 15 de novembro	Controlo metrológico legal de tonómetros
Portaria n.º 367/2023 de 15 de novembro	Controlo metrológico legal de termómetros clínicos

Portaria n.º 354/2023 de 14 de novembro	Controlo metrológico legal dos instrumentos de medição da pressão arterial
Portaria n.º 356/2023 de 14 de novembro	Controlo metrológico legal dos instrumentos de medição de radiações ionizantes
Portaria 320/2019, de 19 de setembro	Controlo metrológico legal dos instrumentos de pesagem não automática

Assim, através da implementação de operações de verificação metrológica realizadas por entidades com qualificações devidamente reconhecidas para os devidos efeitos, o rigor das medições encontra-se assegurado bem como os resultados que fundamentam a medicina baseada na evidência. Encontram-se assim, reunidas as condições iniciais para a efetiva promoção e aplicação de abordagens adequadas do ponto de vista da metrologia, qualidade e rastreabilidade das medições nos diferentes tipos de equipamentos, procedimentos e práticas vigentes na área da saúde, com envolvimento dos profissionais e entidades do setor.

3. CONCLUSÕES

Garantir o rigor e a exatidão das medições é uma condição prévia a assegurar, em prol da qualidade dos serviços e da segurança do utilizador.

O atual cenário permite afirmar que em Portugal, a Metrologia aplicada aos equipamentos médicos tem contribuído para a melhoria continua dos serviços de saúde e dos respetivos procedimentos aplicáveis, contudo, tem ainda um longo caminho de implementação pelas instituições de saúde. Neste enquadramento, qualquer estratégia de desenvolvimento futuro terá de passar por uma maior participação dos utilizadores do sistema, que inclui a atuação governamental através de relações e cooperações interministeriais, permitindo às organizações promover benefícios para a saúde, para a economia e para a Qualidade dos serviços e dos cuidados de saúde.

REFERÊNCIAS BIBLIOGRÁFICAS

Barroso, F., Nurse, H., Sales, L., & Ramos, S. (Eds.). (2021). *Guia prático para a segurança do doente*. Lidel-Edições Técnicas.

BIPM (2019), The Internacional System of Units (SI), 9ª edition, Sèvres:BIPM. V3.01 de 2024.

Ferreira, M. (2011). The role of metrology in the field of medical devices. International Journal of Metrology and Quality Engineering. 2: 135-140. DOI:10.1051/ijmqe/2011101.

Ferreira, M. (2013). *Avaliação da perceção da metrologia em serviços de sáude*. Tese de Doutoramento em Engenharia Industrial. Universidade Nova de Lisboa, Faculdade de Ciências e Tecnologia, Caparica.

Ferreira, M.; Matos, A. *et al*. (2015). Evaluation of the role of metrological traceability in health care: a comparison study by statistical approach. *Accreditation and Quality Assurance*. Volume 20, Issue 6 (2015), Page 457-464.

Portaria n.º 351/2023 de 14 de novembro, Regulamento do Controlo Metrológico Legal dos audiómetros.

Portaria n.º 354/2023 de 14 de novembro, Regulamento do Controlo Metrológico Legal dos Instrumentos de Medição da Pressão Arterial.

Portaria n.º 356/2023 de 14 de novembro, Regulamento do Controlo Metrológico Legal dos Instrumentos de Medição de Radiações Ionizantes

Portaria n.º 367/2023 de 15 de novembro, Regulamento do Controlo Metrológico Legal dos termómetros clínicos.

Portaria n.º 368/2023 de 15 de novembro, Regulamento do Controlo Metrológico Legal dos tonómetros.

Vocabulário Internacional de Metrologia. (2012).1ª edição Luso-Brasileira, Instituto Português da Qualidade. ISBN 972-763-00-6.

Metrologia na terapia de perfusão: desafios e avanços tecnológicos

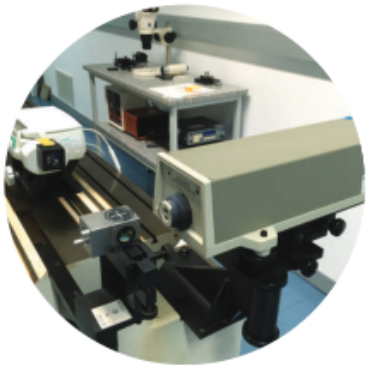

A medição de caudal de líquidos, tanto dentro como fora do corpo humano, desempenha um papel crucial na tecnologia médica. A segurança e a fiabilidade de muitos dispositivos médicos, tais como máquinas de diálise, dispositivos de perfusão e sistemas de manuseamento de líquidos para diagnósticos in vitro, dependem de uma dosagem rigorosa e segura de líquidos.

por ***Elsa Batista, Maria do Céu Ferreira, Isabel Godinho***

A terapia de perfusão é a forma mais comum de administração de medicamentos em doentes nos cuidados de saúde. Devido à sua ampla utilização, especialmente nas Unidades de Cuidados Intensivos (UCI) hospitalares, ocorrem frequentemente erros de perfusão, que podem ter graves consequências em determinadas aplicações, especialmente em doentes vulneráveis, como no domínio da neonatologia. Existem inúmeros casos em que esses incidentes adversos estão associados a dosagens inadequadas ou imprecisas, contribuindo significativamente para o aumento das taxas de morbilidade e mortalidade.

Para aplicações críticas de perfusão em doentes vulneráveis, é essencial garantir uma administração rigorosa e bem controlada de medicamentos, o que pode ser alcançado através da melhoria da exatidão da dosagem e da medição rastreada de todas as grandezas envolvidas, nomeadamente volume, caudal e pressão em dispositivos de administração de medicamentos e sensores em linha que operam a caudais muito baixos.

Nesse contexto, a contribuição das infraestruturas metrológicas recentemente instaladas nos Institutos de Metrologia Europeus, no âmbito dos projetos MeDD e MeDDII, tem sido fundamental para garantir uma terapia de perfusão mais segura em cuidados de saúde, onde o rigor, a rastreabilidade e a comparabilidade das medições são fatores decisivos.

Introdução

A qualidade dos cuidados de saúde é uma verdadeira medida do bem-estar social e da civilização. Ela depende não apenas de recursos económicos, mas também da excelência científica, do desenvolvimento tecnológico e do progresso.

Nas Unidades de Cuidados Intensivos (UCI), a terapia de perfusão é a forma mais comum de tratamento, tornando a administração de medicamentos por esta via um procedimento crucial. A ampla utilização da terapia de perfusão nos cuidados de saúde tem sido recentemente associada a erros de perfusão subestimados, que ocorrem frequentemente, mesmo em condições de

Figura 1 Incubadora num serviço de neonatologia e sistemas de multiperfusão

Figura 2 Calibração de uma seringa perfusora pelo método gravimétrico

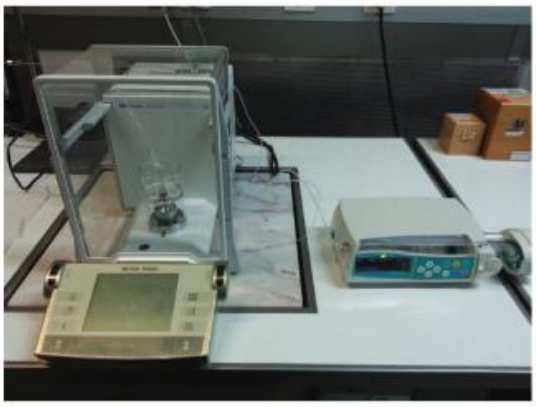

trabalho ideais. Esses erros podem ser a fonte de eventos adversos, especialmente em áreas como a neonatologia, com consequências nefastas para o doente [1-2].

É de extrema importância que a administração de medicamentos e outros líquidos seja controlada de forma rigorosa ao longo do tempo, garantindo que a dose administrada é conhecida com exatidão. Este aspeto é especialmente crucial para medicamentos críticos em alta concentração.

Uma infraestrutura metrológica bem definida é essencial para que os fabricantes de bombas de perfusão possam disponibilizar informações precisas sobre a dose "real" administrada ao doente. Além disso, é também importante que os profissionais de saúde que manuseiam os dispositivos de administração de medicamentos sejam detentores de conhecimentos metrológicos adequados às boas práticas, prevenindo medições incorretas e melhorando significativamente a segurança dos seus utilizadores, com especial foco na segurança do doente.

Nos últimos anos, o Instituto Português da Qualidade (IPQ) participou em três projetos de investigação e desenvolvimento metrológico, financiados pelos programas Horizonte 2020 e Horizonte Europa da Comissão Europeia, na área da saúde: MeDD – *Metrology for Drug Delivery* [3], 15SIP03 – *Infusion Uptake* e MeDDII – *Metrology for Drug Delivery II* da EURAMET [4]. O projeto MeDDII, coordenado pelo IPQ, contou com a participação de vários Laboratórios Nacionais de Metrologia (LNM), fabricantes de bombas de perfusão e universidades. Estes projetos visaram o desenvolvimento de novas capacidades de medição de caudal em intervalos inferiores a 100 nL/min, utilizando diferentes fluidos. Como resultado, o IPQ publicou duas novas capacidades de medição e calibração (CMC) para a medição de caudal. Uma destas CMC possui um intervalo de medição até 5 nL/min, com incertezas associadas de 2 %, utilizando o método interferométrico, sendo esta uma das menores CMC de caudal a nível mundial. Neste âmbito, foram também desenvolvidos novos procedimentos de medição para dispositivos médicos de caudal e caracterizados vários tipos de instrumentos de perfusão, como bombas de insulina, analisadores de caudal, bombas de seringa e sistemas de multiperfusão. Esses resultados foram publicados no guia EURAMET cg 27 - *Calibration of Drug Delivery Devices* [5], desenvolvido durante o projeto MeDDII.

As atividades e os desenvolvimentos técnico-científicos implementados no âmbito destes projetos beneficiaram diretamente a sociedade ao possibilitar a identificação e a redução de erros de dosagem em dispositivos de administração de medicamentos utilizados para tratamento e diagnóstico de doentes.

Riscos da terapia de perfusão

Existem várias tecnologias de perfusão, desde os primeiros sistemas de administração de medicamentos por gravidade até às mais recentes tecnologias, que utilizam bombas de seringa, eletromecânicas ou peristálticas. No entanto, essas tecnologias não estão isentas de riscos, podendo ser suscetíveis a erros humanos ou falhas operacionais, com efeitos potencialmente graves para a saúde do doente. No passado, a utilização de bombas de perfusão esteve associada a inúmeros casos de lesões, efeitos adversos à saúde e até a óbitos, evidenciando questões críticas de segurança [6-7].

De acordo com estudos recentes, a medicação intravenosa está associada ao maior risco de erros de medicação, cujos efeitos negativos são difíceis de mitigar devido à sua distribuição imediata na corrente sanguínea do doente [8]. Entre esses erros, os alarmes de oclusão são considerados de alta prioridade, pois destinam-se a evitar consequências clínicas graves, como extravasação (administração errónea de medicamentos fora dos vasos, podendo causar necrose tecidual).

A perfusão parenteral para neonatos e crianças é particularmente desafiadora devido ao número limitado de locais de acesso venoso, à pequena dimensão dos cateteres e ao reduzido volume de fármacos [9].

Figura 1. Soluções altamente concentradas de medicamentos de alto risco são frequentemente administradas a baixo caudal para evitar sobrecarga de volume, mas através da mesma linha, aumentando assim o risco de incompatibilidades de medicamentos [10]. Diversos estudos indicam que 13,7 % das perfusões simultâneas de medicamentos em UCI Pediátricas e 74 % em UCI Neonatais são incompatíveis ou não foram previamente testadas [11-12]. As oclusões resultantes dessas incompatibilidades de medicamentos podem gerar efeitos adversos graves, incluindo embolias pulmonares, formação de granulomas ou síndrome de resposta inflamatória sistémica [13-16], representando riscos significativos para a segurança dos doentes.

Desconhece-se a existência de estudos de avaliação das incompatibilidades medicamentosas, designadamente no que diz respeito às diferentes propriedades dos fluidos, como a viscosidade, que pode motivar a ocorrência de alarmes de oclusão. Assim, é extremamente importante que a administração de medicamentos e outros fluidos seja rigorosamente controlada ao longo do tempo, e que a dose administrada seja conhecida com exatidão, especialmente para medicamentos críticos em alta concentração [17-18]. Embora a monitorização do doente forneça uma indicação de possíveis erros de dosagem, os sinais vitais dos doentes são influenciados por múltiplos parâmetros, permitindo apenas identificar informações indiretas sobre a qualidade e a quantidade da administração de medicamentos [19]. Da mesma forma, a monitorização da perfusão, conforme indicado pela frequência e duração dos alarmes do dispositivo de perfusão, depende muito do tipo de fluido administrado, mas depende também do local, da hora do dia e da semana, do estado de manutenção do equipamento, etc. [20]. Em aplicações de multiperfusão, as condições reais de dosagem, além do ponto de mistura na linha de perfusão, não são conhecidas e são afetadas por vários parâmetros com interações indefinidas (volume morto, oclusão, ar na linha, entre outras) podendo desviar-se da dose de medicamento pretendida. Assim, a exatidão dos ajustes do ponto de definição do caudal, com base nos sinais vitais do doente e/ou alarmes registados, que constitui a prática estabelecida nas UCI, é insuficiente para garantir a administração segura e rigorosa de medicamentos aos doentes.

Os riscos na terapia de perfusão podem ser atribuídos, principalmente, a quatro razões:

- Falta de dados quantitativos reais e fiáveis sobre a dosagem de medicamentos disponíveis para todos os medicamentos administrados simultaneamente.
- Falta de conhecimento do pessoal médico e/ou dos fabricantes de sistemas de perfusão.
- Compreensão inadequada do funcionamento do sistema de administração de medicamentos.
- Falta de uma infraestrutura metrológica adequada, especialmente para caudais baixos de administração de medicamentos.

Estas deficiências na terapia de perfusão podem ser efetivamente solucionadas utilizando o conhecimento adquirido durante os desenvolvimentos recentes em Metrologia e nos projetos MeDD. Os desenvolvimentos técnico-científicos verificados nos últimos anos na área do microcaudal, aliados a uma infraestrutura metrológica eficiente, podem disponibilizar aos fabricantes de dispositivos de administração de medicamentos dados precisos e confiáveis sobre o desempenho real desses dispositivos em condições de uso, contribuindo para uma maior segurança e eficácia na terapia de perfusão.

Consequentemente, os fabricantes poderão obter uma melhor compreensão sobre a dose de medicamento esperada, permitindo também que os utilizadores de dispositivos de administração de medicamentos tenham um melhor entendimento e conhecimento sobre esses dispositivos através da sua calibração, prevenindo a administração incorreta de medicamentos.

Manutenção, caracterização e calibração de bombas de perfusão

A calibração e a manutenção das bombas de perfusão são essenciais para identificar quaisquer problemas com o equipamento e garantir o estado operacional adequado dos instrumentos, assegurando a dosagem correta aos doentes e minimizando os potenciais riscos de segurança. Protocolos de manutenção apropriados, fornecidos pelos fabricantes de bombas de perfusão, devem ser rigorosamente seguidos pelo pessoal técnico autorizado nos intervalos de serviço recomendados.

É crucial que o pessoal esteja familiarizado com as especificações de desempenho e as características metrológicas deste equipamento para garantir o funcionamento fiável do sistema de perfusão [21,22].

Contudo, importa referir que os programas de manutenção para este tipo de equipamento médico não podem substituir a necessidade de calibrações periódicas. Um método comum de calibração para determinar o erro do caudal de uma bomba de perfusão envolve o uso de um analisador de caudal, que fornece informações sobre o caudal, a volume e a pressão. O analisador serve como padrão de referência para testar rapidamente o desempenho das bombas de perfusão; no entanto, é crucial que este padrão seja também calibrado regularmente. Esses analisadores de dispositivos de perfusão são habitualmente utilizados pelos serviços de manutenção dos hospitais [22].

Por outro lado, o método gravimétrico [23] é amplamente utilizado pelos Institutos Nacionais de Metrologia (INM) e laboratórios acreditados para calibrar e caraterizar as bombas de perfusão e os caudalímetros (Figura 2). Este método primário de determinação de caudal consiste na medição da massa de água [24] escoada da bomba de perfusão ao longo do tempo. Esse valor é então convertido em caudal utilizando fórmulas apropriadas (1), adaptadas da norma ISO 4787 [25], para uma temperatura de referência de 20 °C.

$$Q = \frac{1}{t_f - t_i}\left[\left((I_f - I_i) - \left(\delta m_{imp}\right)\right) \times \frac{1}{\rho_w - \rho_A} \times \left(1 - \frac{\rho_A}{\rho_B}\right) \times [1 - \gamma(T - 20)]\right] + \delta_{evap}$$

Figura 3 Calibração de uma seringa perfusora pelo método interferométrico

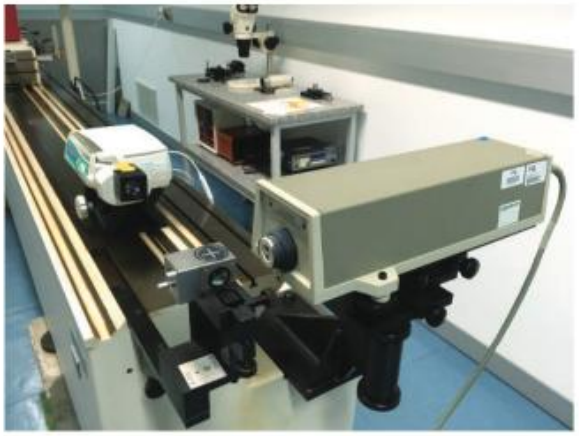

É crucial que o pessoal esteja familiarizado com as especificações de desempenho e as características metrológicas (...) para garantir o funcionamento fiável do sistema de perfusão

Em que:

Q	Caudal volúmico, em mL/s
t_f	Tempo final, em s
t_i	Tempo inicial, em s
l_f	Resultado da pesagem final, em g
l_i	Resultado da pesagem inicial, em g
δm_{imp}	Impulsão, em g
ρ_A	Massa volúmica do ar em g/mL
ρ_B	Massa volúmica de referência das massas da balança, em g/mL
ρ_w	Massa volúmica da água, em g/mL
T	Temperatura da água utilizada no procedimento experimental, em °C
γ	Coeficiente de expansão térmica do material de que é feita a tubagem/ seringa descartável, /°C
δ_{evap}	Taxa de evaporação, em mL/s

Existem vários fatores de influência que devem ser considerados numa calibração gravimétrica, nomeadamente:

- Bolhas de ar: Deve ser passado um volume suficiente de água através das linhas para purgar quaisquer bolhas de ar.
- Estabilidade do caudal e tempo de resposta da bomba: É necessário esperar até que o caudal selecionado seja alcançado, sendo o tempo necessário para isso frequentemente referido como o atraso de doseamento e depende do caudal, tipo de bomba e consumíveis utilizados.
- Diâmetro incorreto da seringa: Pode levar a grandes erros de dosagem. Por exemplo, um erro de 5 % no diâmetro da seringa pode resultar em um erro de 10 % no caudal do medicamento administrado. Diferentes modelos e marcas de seringas podem ter diâmetros diferentes, por isso é sempre importante verificar essa situação.
- Evaporação da água: Se não for controlada adequadamente, pode causar uma subestimação das medições de caudal.
- Conformidade do equipamento: Existem efeitos de expansão nos componentes devido à elasticidade dos materiais. Por exemplo, a expansão de uma seringa de plástico quando a pressão aumenta durante a inicialização da bomba. A expansão dos componentes também pode ocorrer quando o caudal aumenta; este aumento na pressão pode causar a expansão da linha de perfusão, seringa e outros equipamentos. A expansão resulta no aumento do volume interno, podendo causar uma resposta retardada para mudanças no caudal [26].

O método de calibração gravimétrica apresenta limitações ao medir caudais ultrabaixos, pois a incerteza de medição aumenta substancialmente e a evaporação torna-se um fator crítico de erro. Foram implementadas novas melhorias nos métodos gravimétricos existentes em vários LNM, permitindo um aumento do intervalo de medição até 100 nL/min [23]. No entanto, é necessário ir ainda mais longe em termos de aumento de intervalo de medição (até 5 nL/min), o que exigiu o desenvolvimento de outros métodos de medição de caudal baseados em medições óticas. Um exemplo é o método que segue o deslocamento do pistão da seringa ao longo do tempo com um interferómetro (Figura 3) [27], implementado no laboratório de volume e caudal do IPQ.

Harmonização na terminologia

Devido a uma ligação pouco consolidada entre o mundo médico e a Metrologia, existem algumas inconsistências entre as normas utilizadas no setor médico (por exemplo, bombas de perfusão) e a terminologia e a prática metrológica estabelecida, conforme descrito no Vocabulário Internacional de Metrologia (VIM) [28]. Este facto pode motivar a incorreta interpretação de conceitos relevantes para a

prática clínica com eventuais consequências na aplicação de boas práticas durante a utilização de dispositivos médicos pelos serviços de saúde.

Um exemplo típico de falta de harmonização nas práticas e terminologia aplicadas a equipamentos médicos é a definição do erro sistemático de um instrumento de medição. Na Metrologia (VIM) e nas normas médicas (por exemplo, IEC 60601-2-24:2012 [29]), são aplicadas duas definições diferentes. Comparando essas duas definições, o erro sistemático de um instrumento de medição não só tem sinal oposto, como também apresenta diferente valor de amplitude para parâmetros de calibração especificados. Consequentemente, as correções geralmente aplicadas às indicações destes instrumentos de medição utilizando o erro sistemático podem originar resultados diferentes, dependendo da interpretação dos dados de calibração. Os resultados da calibração das bombas de perfusão e a sua interpretação devem ser claramente compreendidos pelos utilizadores finais, dado que é essencial para estabelecer a dosagem recomendada de medicamentos aos doentes. Se não existir um entendimento harmonizado relativo à definição de erro para um determinado dispositivo, as devidas correções a serem aplicadas aos instrumentos podem estar incorretas. Isso comprometeria a dose administrada e, possivelmente, a condição do doente. Esse entendimento terá de estar harmonizado entre todas as partes envolvidas, designadamente entre fabricantes, metrologistas e utilizadores finais.

Assim, o erro relativo do caudal de uma bomba de acordo com o VIM é dado por:

$$Erro = \frac{Q_{selecionado} - Q_{referência}}{Q_{referência}} * 100\,\%$$

Onde: $Q_{selecionado}$ é o caudal selecionado na bomba e $Q_{referência}$ é o caudal real determinado na calibração. Um erro negativo significa que a bomba está a fornecer um caudal acima do valor selecionado e um erro positivo significa que está a fornecer menos caudal do que o desejado. No entanto, é de notar que é utilizada uma definição diferente na norma IEC 60601-2-24:2012 [29], onde o erro é dado por:

$$Erro = \frac{Q_{referência} - Q_{selecionado}}{Q_{selecionado}} * 100\,\%$$

É importante identificar a forma de cálculo do erro, caso contrário, podem ser aplicadas correções erradas. Informações mais detalhadas sobre essas definições conflitantes são apresentadas no relatório MeDDII [31].

Normalização e medição de caudal

O regulamento (UE) 2017/745 especifica quais os requisitos essenciais de segurança e de desempenho sem exigir soluções técnicas específicas [32]. No entanto, recomenda-se que os fabricantes adotem a norma da Comissão Eletrotécnica Internacional (IEC) IEC 60601-2-24:2012 *Medical electrical equipment – Part 2-24: Particular requirements for the basic safety and essential performance of infusion pumps and controllers* [29]. Esta norma está em revisão, pois a tecnologia e a análise de dados foram melhoradas, mas ainda não estão refletidas no documento.

Existem outras normas relevantes que disponibilizam informações sobre a realização de testes de dispositivos de administração de medicamentos. Como exemplo, refere-se a norma ISO 7886-2: 2020 - *Sterile hypodermic syringes for single use – Part 2: Syringes for use with power-driven syringe pumps* [33] e a norma AAMI TIR 101 – *Fluid delivery performance testing for infusion pumps* [34]. Estes documentos foram publicados recentemente e já incluem os novos desenvolvimentos e informações obtidas pelos projetos MeDD e MeDDII. Ambos os projetos apoiaram o desenvolvimento das normas acima mencionadas, bem como a implementação de procedimentos de calibração robustos, a indicação de equipamentos e condições que permitem garantir a exatidão dos resultados de administração de medicamentos e reduzir os riscos de incidentes adversos aos doentes. No entanto, foi identificado pelo projeto MeDD que as normas indicadas são específicas para fabricantes, sendo ainda necessária a elaboração de normas para ensaios de equipamento "em uso". Nesse sentido, foi desenvolvido em 2024 o guia EURAMET cg 27 - *Calibration of Drug Delivery Devices* [5], que contém informações sobre os procedimentos de calibração de vários instrumentos de administração de medicamentos em uso clínico, o que permitirá uma harmonização de resultados entre os vários LNM e laboratórios acreditados nesse âmbito.

Conclusão

Este artigo destaca a importância da manutenção e da calibração regular de bombas de perfusão médicas para reduzir os riscos de segurança, identificar problemas de desempenho e garantir a administração de dose correta aos doentes. O método gravimétrico é o mais comummente utilizado para avaliar o desempenho de várias bombas de perfusão. No entanto, os novos métodos óticos desenvolvidos no âmbito do projeto *European Metrology Programme for Innovation and Research* MeDD II permitem efetuar a medição de caudais inferiores a 100 nL/min, utilizados por exemplo em bombas de insulina.

A análise de desempenho de uma bomba de perfusão deve ser realizada e reportada de acordo com as referências apropriadas para evitar avaliações incorretas, sendo que a terminologia metrológica utilizada deverá ser harmonizada.

As melhores práticas em tecnologia de perfusão têm sido estabelecidas por trabalhos de investigação e desenvolvimento recentes com o objetivo de melhorar a fiabilidade na administração de medicamentos aos doentes, minimizar a incidência de erros de perfusão em tratamentos críticos nas UCI e sensibilizar a comunidade de profissionais de saúde sobre os potenciais riscos associados às técnicas de perfusão.

A melhoria da exatidão dos dispositivos médicos desempenha um papel fundamental na redução de erros de dosagem, contribuindo diretamente para a segurança dos doentes e para salvar vidas. Atualmente, o conhecimento fiável sobre a dose real administrada aos doentes é suportado por infraestruturas metrológicas modernizadas, modelos de simulação e conhecimento técnico e científico avançados, fatores decisivos para a segurança e a eficácia das terapias de perfusão.

Referências

[1] US Food and Drug Administration website accessed 26th March 2020

[2] Fonzo-Christe C, Bochaton N, Kiener A, Rimensberger P, Bonnabry P. Incidence and Causes of Infusion and Pediatric Intensive Care Unit: A Prospective Pilot Study. J Pediatr Pharmacol Ther 2020; Vol. 25 No. 6: 500-506.

[3] Lucas P, Klein S. Metrology for drug delivery. Biomed. Eng.-Biomed. Tech.2015;60(4):271-275.

[4] Batista E., et al, New EMPIR project – Metrology for Drug Delivery, Flow Measurement and Instrumentation 72 (2020) 101716

[5] EURAMET Calibration guideline on the calibration of drug delivery devices nº 27, version 1 (02/2024)

[6] Waterson J, Bedner A. Types and Frequency of Infusion Pump Alarms and Infusion-Interruption to Infusion-Recovery Times for Critical Short Half-life Infusions: Retrospective Data Analysis. JMIR Hum Factors 2019 6 (3). DOI: 10.2196/14123: 10.2196/14123.

[7] Lee PT, Thompson F, Thimbleby H. Analysis of infusion pump error logs and their significance for health care. British Journal of Nursing (Intravenous Supplement) 2012;21(8):S12-S20.

[8] Sutherland A, Canobbio M, Clarke J, Randall M, Skelland T, Weston E. Incidence and prevalence of intravenous medication errors in the UK: a systematic review. Eur J Hosp Pharm 2020;27:3-8.

[9] Leff R, Roberts RJ. Problems in drug therapy for pediatric patients. *Am J Hosp Pharm*. 1987;44(4):865–870.

[10] Sherwin CMT, Medlicott NJ, Reith DM, Broadbent RS. Intravenous drug delivery in neonates: lessons learnt. *Arch Dis Child*. 2014;99(6):590–594.

[11] Gikic M, Di Paolo ER, Pannatier A, Cotting J. Evaluation of physicochemical incompatibilities during parenteral drug administration in a paediatric intensive care unit. *Pharm World Sci*. 2000;22(3):88–91.

[12] Kalikstad B, Skjerdal A, Hansen TW. Compatibility of drug infusions in the NICU. *Arch Dis Child*. 2010;95(9):745–748.

[13] Bradley JS, Wassel RT, Lee L, Nambiar S. Intravenous ceftriaxone and calcium in the neonate: assessing the risk for cardiopulmonary adverse events. *Pediatrics*. 2009;123(4):e609–e613.

[14] Hill SE, Heldman LS, Goo ED, Whippo PE, Perkinson JC. Fatal microvascular pulmonary emboli from precipitation of a total nutrient admixture solution. *JPEN J Parenter Enteral Nutr*. 1996;20(1):81–87.

[15] McNearney T, Bajaj C, Boyars M, Cottingham J, Haque A.. Total parenteral nutrition associated crystalline precipitates resulting in pulmonary artery occlusions and alveolar granulomas. *Dig Dis Sci*. 2003;48(7):1352–1354.

[16] Jack T, Boehne M, Brent BE, Hoy L, Koditz H, Wessel A, et al. In-line filtration reduces severe complications and length of stay on pediatric intensive care unit: a prospective, randomized, controlled trial. *Int Care Med*. 2012;38(6):1008–1016.

[17] Snijder RA, Egberts TCG, Lucas P, Lemmers P, van Bel F, Timmerman A. Dosing errors in preterm neonates due to flow rate variability in multi-infusion syringe pump setups: an in vitro spectrophotometry study. European Journal of Pharmaceutical Sciences 2016; 93:56-63.

[18] Batliner M, Weiss M, Dual SA, Grass B, Mebolet M, Schmid Daners M. Evaluation of a novel flow-controlled syringe infusion pump for precise and continuous drug delivery at low flowrates: a laboratory study. Anaesthesia 2019;74:1425-1431.

[19] Lyons I, Furniss D, Blandford A, Chumbley G, Iacovides I, Wei L, et al. Error and discrepancies in the administration of intravenous infusions: a mixed methods multihospital observational study. BMJ Qual Saf 2018; 27:892-901.

[20] Vitoux R.T, Schuster C, Glover KR, Dekker M. Frequency and Duration of Infusion Pump Alarms: Establishing National Benchmarks. Biomedical Instrumentation & Technology 2018; November/December 2018:433-441.

[21] ISO 15189:2012 - Medical laboratories — Requirements for quality and competence

[22] Guia de Boas Práticas - Parte II, Capítulo III, Bombas de Perfusão, IPQ, 2017

[23] Bissig H, Peter HT, Lucas P, Batista E, Filipe E, Almeida N, et al. Primary standards for measuring flow rates from 100 nL/min to 1 mL/min – gravimetric principle. Biomedizinische Technik (Biomed Tech) 2015;60 (4): 301-316.

[24] ISO 3696:1978. Water for analytical laboratory use -- Specification and test methods

[25] ISO 4787:2021, Laboratory glassware — Volumetric instruments — Methods for testing of capacity and for use

[26] E. Batista, J. A. Sousa, R. F. Martins, Calibration of Insulin Pumps, Journal of Diabetes and Treatment, Vol 4, Issue 03, 2019

[27] Batista, E., Godinho, I., Martins, R., Mendes, R., Robarts, J., (2020). Development of an experimental setup for microflow measurement using interferometry, Flow Measurement and Instrumentation, vol. 75

[28] JCGM 200:212 - International vocabulary of metrology – Basic and general concepts and associated terms (VIM), 3rd edition

[29] IEC 60601-2-24:2012 - Medical electrical equipment – Part 2-24: Particular requirements for the basic safety and essential performance of infusion pumps and controllers.

[30] BIPM, IEC, IFCC, ILAC, ISO, IUPAC, IUPAP, and OIML. Evaluation of measurement data | Guide to the expression of uncertainty in measurement. Joint Committee for Guides in Metrology, JCGM 100:2008 (GUM)

[31] MeDDII report, Measurement error: two opposite definitions in metrology standards and medical standards, 4/2021 https://drugmetrology.com/wp-content/uploads/2021/04/Measurement-error-defenitions_FINAL_04_2021.docx

[32] REGULATION (EU) 2017/745 OF THE EUROPEAN PARLIAMENT AND OF THE COUNCIL of 5 April 2017.

[33] ISO 7886-2:2020 - Sterile hypodermic syringes for single use – Part 2: Syringes for use with power-driven syringe pumps"

[34] AAMI TIR101:2021- Fluid delivery performance testing for infusion pumps

Elsa Batista,
Maria do Céu Ferreira,
Isabel Godinho
Instituto Português da Qualidade, I. P.

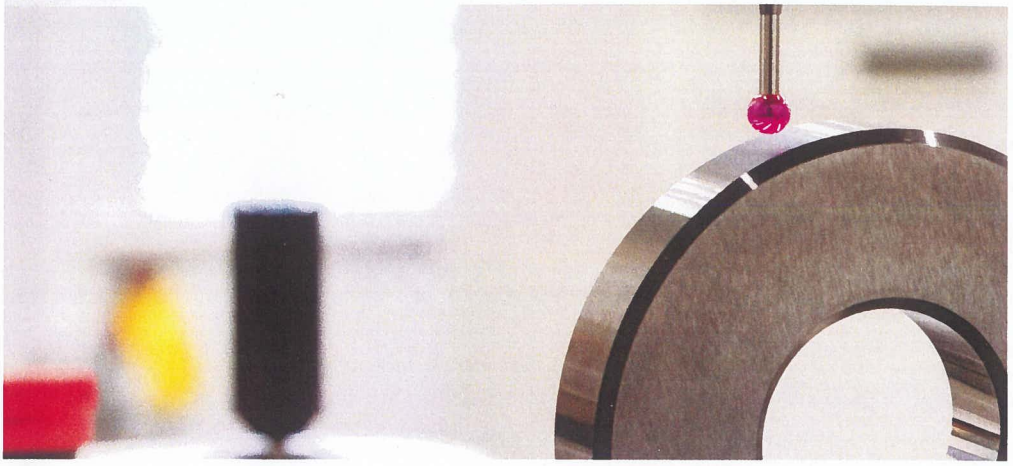

© GREG ROSENKE / UNSPLASH

Isabel Godinho
Diretora do Departamento de Metrologia
do Instituto Português da Qualidade

METROLOGIA NOS DOMÍNIOS DAS RADIAÇÕES IONIZANTES, ENERGIA, ACÚSTICA, EMISSÕES GASOSAS E MATÉRIAS-PRIMAS CRÍTICAS: **PERSPETIVA NACIONAL E INTERNACIONAL**

A ciência da medição impacta em todas as áreas da sociedade moderna, e para além do impacto na investigação científica e no setor industrial e económico, desempenha um papel vital para garantir a segurança, a qualidade e o bem-estar da sociedade.

Enfrentamos atualmente um mundo em grande mudança, onde a Europa enfrenta também uma multiplicidade de desafios e onde são evidentes as necessidades de novas capacidades metrológicas. As áreas onde a Metrologia terá um papel crucial na próxima década incluem as que permitem assegurar sociedades resilientes, indústrias soberanas e competitivas, maior inovação tecnológica, fornecimento de energia a baixo custo, proteção do ambiente, descarbonização, a par da mitigação e adaptação às alterações climáticas, ambição de poluição zero, economia circular, transformação digital, transformação do sistema de saúde e resiliência das infraestruturas europeias, fatores estes que estabelecem confiança através da garantia da qualidade.

De modo a acompanhar todos estes desafios, é imprescindível a plena articulação e forte cooperação europeia e internacional da rede alargada de intervenientes, quer no âmbito da investigação e do desenvolvimento, da normalização, dos fabricantes e dos reguladores. Esta colaboração, orientada pelas necessidades das áreas emergentes, abre caminho para desenvolvimentos inovadores e novos produtos e dispositivos, aperfeiçoando métodos e processos de medição.

A Metrologia disponibiliza a estrutura que assegura o rigor e a comparabilidade das medições e que possibilita a livre circulação dos produtos e a eliminação de barreiras comerciais, atendendo aos mesmos critérios de justiça, transparência, segurança e qualidade, essenciais para o sucesso do mercado único e da competitividade global das indústrias europeias.

Em particular, a Metrologia científica e aplicada enfrenta atualmente um processo de renovação estrutural, impulsionado por fatores como a transição energética, a transformação digital, a sustentabilidade ambiental e a emergência de novas tecnologias. Neste contexto, e considerando, em particular, os domínios das radiações ionizantes, energia, acústica, emissões gasosas e matérias-primas críticas, estes assumem um papel decisivo, exigindo uma abordagem integrada que alia a rastreabilidade metrológica, a interoperabilidade digital e a resposta aos desafios sociais e económicos emergentes.

RADIAÇÕES IONIZANTES

A medição rigorosa no domínio das radiações ionizantes é essencial em diversas áreas e aplicações, tais como na investigação, aplicações médicas (e.g. medicina nuclear, proteção radiológica, radioterapia, radiodiagnóstico), industriais (e.g. esterilização, controlo da qualidade) e ambientais (e.g. monitorização da radioatividade). O Comité Consultivo para Radiações Ionizantes (CCRI) do *Bureau Inter-*

national des Poids et Mesures (BIPM) tem vindo a consolidar os referenciais globais da rastreabilidade das medições aos padrões do Sistema Internacional de unidades (SI), com destaque para os padrões primários de dose absorvida, a expansão dos campos de radiação clínicos e a melhoria das respetivas incertezas associadas.

A nível europeu, a participação nacional em atividades de investigação e desenvolvimento metrológico, em particular no âmbito da *European Metrology Programme for Innovation and Research* (EMPIR), no quadro do Horizonte 2020, da *European Partnership on Metrology* (EPM), do Horizonte Europa, bem como a participação nas *European Metrology Networks* (EMN) da EURAMET (e.g. a *European Metrology Network for Radiation Protection*) têm permitido o desenvolvimento de novas tecnologias, de soluções adequadas para aplicações práticas, novos serviços de calibração e capacidades de medição, bem como a elaboração de normas e de regulamentos técnicos.

Portugal, através do seu Instituto Designado para as Radiações Ionizantes, o Laboratório de Metrologia das Radiações Ionizantes (LMRI) do Instituto Superior Técnico (IST), assegura, em particular, a manutenção e a rastreabilidade das grandezas dose absorvida na água, dose absorvida no tecido, equivalente de dose ambiente, equivalente de dose direcional, equivalente de dose individual e atividade por unidade de superfície, de acordo com as suas capacidades de medição e de calibração publicadas na KCDB do BIPM.

Como investimentos estratégicos determinantes neste âmbito, incluem-se, nomeadamente, o desenvolvimento de padrões primários para o domínio dos radionuclídeos, a consolidação da capacidade laboratorial em dosimetria de elevada exatidão, para fins clínicos e ambientais, bem como o desenvolvimento de sistemas automatizados de calibração e a integração de algoritmos baseados em Inteligência Artificial, designadamente para técnicas de análise espectral e para a estimativa de incertezas de medição.

No âmbito da Metrologia legal, Portugal assegura atualmente o controlo metrológico dos instrumentos de medição de radiações ionizantes e dos seus dispositivos complementares, considerando, em particular, as categorias de instrumentos de medição de radiação para a radioterapia, medicina nuclear, radiologia e a proteção radiológica.

ENERGIA

As áreas onde a Metrologia terá um papel crucial na próxima década incluem as que permitem assegurar sociedades mais resilientes, o fornecimento de energia a baixo custo, a proteção do ambiente, a descarbonização, a par da mitigação e adaptação às alterações climáticas, ambição de poluição zero e a economia circular. São diversos os desafios na área da energia, e incluem, entre outros, as alterações climáticas e as metas de descarbonização, a segurança energética global, as desigualdades no acesso à energia, a dependência de combustíveis fósseis e a urgência para a aceleração da transição energética. Torna-se, assim, premente potenciar um maior desenvolvimento tecnológico e investimento em áreas-chave que permitam o crescimento sustentável da mobilidade elétrica e o armazenamento de energia, o aumento de redes inteligentes (*smart grids*) e a digitalização do setor energético, uma maior aposta no hidrogénio verde como vetor energético estratégico, e o fortalecimento da capacidade de energias renováveis (especialmente eólica e fotovoltaica).

Neste âmbito, o Instituto Português da Qualidade (IPQ), enquanto Instituição Nacional de Metrologia, coordena atualmente a Rede Europeia de Metrologia Clean Energy, área de aposta da União Europeia, com objetivos ambiciosos para a redução das emissões dos gases de efeito de estufa, de 55 % em 2030, face aos valores de 1990, para se tornar climaticamente neutra em 2050. Isto implica que as energias renováveis sejam cada vez mais uma realidade, devendo a sua contribuição crescer de 23 % (em 2022), para pelo menos 43 % em 2030, o que é muitíssimo ambicioso.

A rede *Clean Energy* tem especial enfoque na energia fotovoltaica e na energia eólica, e as atividades de I&D no âmbito da Metrologia estão associadas à geração, armazenamento, conversão e utilização de fontes de energia renováveis, eficiência de utilização e armazenamento temporário de energia em baterias elétricas.

A nível europeu, é também de salientar a atividade desenvolvida pela Rede Europeia de Metrologia *Smart Electricity Grids*, que pretende dar resposta aos principais desafios no âmbito da medição, enfrentados pelas redes elétricas, considerando a necessidade de um fornecimento de energia mais sustentável e abrangendo os seguintes temas: monitorização de rede e análise de dados, qualidade da energia, subestações digitais, transformadores e sensores de instrumentos, ensaios de alta tensão, eficiência e integração de rede.

A nível nacional e no âmbito da metrologia legal, a mobilidade elétrica acolhe também importância estratégica crescente no sentido de atingir as metas climáticas definidas, nomeadamente para a redução das emissões de gases com efeito de estufa e para a neutralidade carbónica. Assim, no apoio ao desenvolvimento da mobilidade elétrica têm vindo a ser efetuados investimentos nas infraestruturas de carregamento, permitindo a instalação de equipamentos de carregamento de veículos elétricos acessíveis a todos os consumidores, pelo que se torna importante regulamentar as condições específicas a observar no exercício do controlo metrológico legal de tais instrumentos de medição destinados à transação comercial da energia elétrica associada ao carregamento de veículos elétricos e estabelecer os requisitos aplicáveis àquele controlo, o que é assegurado através do Regulamento do Controlo Metrológico Legal dos Equipamentos de Carregamento de Veículos Elétricos. No âmbito da preparação de uma infraestrutura técnica metrológica de enquadramento legal para a implementação de estações de carregamento de veículos

elétricos, salienta-se a participação nacional no projeto EURAMET LegalEVcharge - LegalE-Vcharge: *Practical legal metrology framework for electric vehicle charging stations*, recentemente concluído.

Também no que se refere ao uso do gás natural veicular e do hidrogénio, o Regulamento do Controlo Metrológico Legal dos Sistemas de Medição de Combustível Gasoso Comprimido para Veículos assegura as condições específicas a observar no exercício do controlo metrológico legal dos instrumentos de medição associados aos sistemas de medição destinados ao abastecimento de veículos motorizados, pequenas embarcações e aeronaves com gás natural comprimido, hidrogénio, biogás, misturas de gases ou outros combustíveis gasosos comprimidos.

No domínio da energia, em particular no domínio elétrico, o Comité Consultivo de Eletricidade e Magnetismo (CCEM) do BIPM e o comité técnico da Eletricidade e Magnetismo da EURAMET (TC-EM) têm promovido o desenvolvimento das medições elétricas e magnéticas através da redefinição e da materialização das unidades ampere, volt e ohm, através de padrões baseados em constantes fundamentais (capacidades também detidas pelo IPQ), bem como o desenvolvimento de projetos estratégicos para a medição de energia elétrica em redes inteligentes, a caracterização metrológica de dispositivos de conversão de energia (e.g. inversores, carregadores de veículos elétricos) e medições em sistemas de transporte e armazenamento de energia (e.g. baterias, hidrogénio).

Como desenvolvimento estratégico, é de referir como prioridade o desenvolvimento de capacidades metrológicas associadas à eficiência energética, energias renováveis, hidrogénio verde, a modernização das infraestruturas elétricas e as redes inteligentes.

ACÚSTICA

No campo da metrologia acústica, assume especial relevância o rigor e a rastreabilidade metrológica em medições de pressão sonora, vibração e ultrassons, com especial enfoque em aplicações biomédicas e ambientais (saúde ocupacional, controlo ambiental e aplicações industriais).

O Comité Consultivo de Acústica, Ultrassons e Vibrações (CCAUV) e o comité técnico da EURAMET têm promovido a digitalização da metrologia acústica, considerando novas abordagens para a calibração de sensores MEMS, microfones digitais e para a avaliação do desempenho de próteses auditivas.

O IPQ, através do seu Laboratório de Aceleração e Vibrações, assegura a calibração absoluta de acelerómetros padrão, através de interferometria laser com deteção homodina, assegurando a rastreabilidade nacional neste domínio, considerando as capacidades de medição e calibração registadas na base de dados do BIPM. No domínio dos Ensaios de Vibração, efetua a realização de estudos e determinações de características de equipamentos, com capacidade para a realização de simulações de condições adversas de funcionamento ou transporte.

A rede estruturada de laboratórios acreditados com competência técnica para a calibração de sonómetros, microfones, calibradores acústicos e analisadores, bem como para a realização de ensaios acústicos em campo ou em laboratório, permite a realização de medições rastreadas nos domínios do ruído ambiental, caracterização do isolamento acústico, verificação da conformidade dos limites de exposição ao ruído, entre outros.

No âmbito da metrologia legal, o Regulamento do Controlo Metrológico Legal dos Sonómetros assegura que os instrumentos utilizados para medir ou registar as grandezas características dos níveis de pressão sonora no domínio do audível, cumprem os requisitos metrológicos e técnicos definidos na respetiva legislação específica.

Como área prioritária de investimento, salienta-se a necessidade de expansão das atuais capacidades para a medição de ultrassons na área da biomedicina, a medição no âmbito das vibrações a nível industrial e a caracterização acústica de ambientes urbanos.

EMISSÕES GASOSAS

A medição de emissões gasosas constitui um eixo estratégico na mitigação das alterações climáticas, no cumprimento dos regulamentos da qualidade do ar e o cumprimento das metas climáticas.

O Comité Consultivo de Quantidade de Matéria (CCQM) do BIPM e o comité técnico da Metrologia em Química da EURAMET têm coordenado esforços para o desenvolvimento de padrões de referência para gases de efeito de estufa, compostos orgânicos voláteis e poluentes atmosféricos, para o desenvolvimento de misturas gasosas de referência, métodos de espectroscopia avançados (como CRDS – *Cavity Ring-Down Spectroscopy* e FTIR – *Fourier Transform Infrared Spectroscopy*), bem como o desenvolvimento de micro sensores autocalibráveis. Em particular no domínio da metrologia científica, as atividades de I&D têm como foco o desenvolvimento de métodos de medição no âmbito do CO_2, CH_4 e NO_2 em setores industriais e em monitorização ambiental, apoiando o Pacto Ecológico Europeu e a legislação comunitária sobre *ar limpo*.

O Laboratório de Gases de Referência e o Laboratório de Analisadores de Gases do IPQ é responsável pela produção, manutenção e desenvolvimento dos padrões primários nacionais de misturas gasosas, bem como pelo desenvolvimento e implementação de novos métodos e capacidades de medição, e pela calibração de diversas tipologias de analisadores de gases ambientais e poluentes.

Neste domínio, os investimentos futuros devem privilegiar a rastreabilidade de sensores de baixo custo, o desenvolvimento de sistemas móveis de medição e a incorporação de modelos preditivos, suportados por *machine learning*, para a quantificação de incertezas de medição em tempo real.

MATÉRIAS-PRIMAS CRÍTICAS

Por outro lado, a medição rigorosa de elementos críticos como o lítio, cobalto, terras raras ou platina é essencial para garantir a rastreabilidade e a sustentabilidade das cadeias de valor de tecnologias emergentes, incluindo os desenvolvimentos tecnológicos associados aos semicondutores, às baterias, aos painéis solares e para a produção de turbinas e componentes no âmbito da energia eólica. A Metrolo-

gia desempenha também um papel crucial na caracterização exata da composição química e das propriedades físico-químicas destas matérias, garantindo a rastreabilidade e a comparabilidade destas medições, bem como a qualidade dos respetivos dados analíticos.

A nível nacional, existe competência técnica relevante que permite assegurar o mapeamento geológico (face às reservas de lítio e minérios metálicos) e a caracterização de depósitos, garantindo as capacidades laboratoriais de análise destas matérias-primas críticas, em infraestruturas para a calibração analítica avançada, atividades estas que são integradas em projetos europeus multidisciplinares, com enfoque em materiais de referência certificados e contaminação ambiental. No entanto, torna-se ainda relevante considerar um maior desenvolvimento de métodos e técnicas analíticas (tais como a espectrometria de massa ou a fluorescência de raios X), nos domínios da química analítica, geociências, ambiente e saúde, quer na análise de elementos e de materiais, quer para a produção e a certificação de materiais de referência, bem como reforçar a capacidade metrológica nacional nestes domínios e a sua integração em redes europeias de referência.

A criação de bancos de materiais de referência nacionais, com certificação metrológica, é um passo crítico para reforçar a soberania científica e industrial, iniciativas estas que assumem crescente relevância geopolítica e ambiental nos nossos dias, a par de uma maior recuperação e valorização de matérias críticas, contribuindo e estimulando a reciclagem, a circularidade de materiais e uma maior sustentabilidade.

CONSIDERAÇÕES FINAIS

Portugal dispõe de capacidades relevantes em diversas áreas da metrologia, mas a consolidação de uma infraestrutura de metrologia fundamental moderna exige investimento estruturado, formação avançada e cooperação internacional. As áreas identificadas — radiações ionizantes, energia, acústica, emissões gasosas e matérias-primas críticas — representam domínios de elevado impacto socioeconómico e científico. A sua integração com tecnologias digitais e práticas sustentáveis é imperativa para garantir a resposta metrológica aos desafios do futuro, reforçar a sua autonomia estratégica, cumprir com as exigências regulatórias e contribuir ativamente para as agendas europeia e global da sustentabilidade, transição energética e segurança tecnológica. IA

O papel da Física Quântica no desenvolvimento da Metrologia e nos padrões do Sistema Internacional de Unidades

Isabel Godinho[1], Carlos Pires, Olivier Pellegrino, Vitor Cabral

[1]Instituto Português da Qualidade, I. P., Rua António Gião, 2, 2829-513 Caparica

igodinho@ipq.pt[1]

Resumo

A Física Quântica tem desempenhado um papel central na evolução da Metrologia Científica, sustentando a definição moderna do Sistema Internacional de Unidades em constantes fundamentais da natureza. O presente artigo aborda as aplicações atuais e as perspetivas de desenvolvimento futuras no domínio da Metrologia Quântica, com ênfase nos padrões quânticos e nas tecnologias emergentes, como a fotónica, a eletrónica, os relógios ópticos e os sensores de elevada exatidão, considerando as implicações societais destas inovações. Releva o papel do IPQ, enquanto Instituição Nacional de Metrologia, e o seu contributo para assegurar medições fiáveis, rastreáveis e comparáveis a nível internacional, enquanto um pilar de soberania, inovação e competitividade.

Palavras-chave: Física Quântica, Metrologia, Sistema Internacional de Unidades, Padrões Quânticos, Tecnologias Quânticas, IPQ.

Introdução

A Metrologia, ciência da medição e das suas aplicações, tem acompanhado de forma intrínseca os avanços científicos e tecnológicos. A revolução quântica, iniciada no início do século XX, abriu novas perspetivas que culminaram, em 2018 [1], na redefinição do Sistema Internacional de Unidades (SI), constituindo um marco histórico na Metrologia, ancorando as unidades em constantes fundamentais da natureza em vez de artefactos materiais. Estas redefinições, que marcaram uma mudança de paradigma (formulação de "constante explícita" em vez de "unidade explícita"), permitem separar a definição da realização das unidades, utilizando equações da física e abrindo caminho para métodos de medição inovadores com exatidão potencialmente ilimitada, estabelecendo um "SI quântico", representam um marco, consolidando padrões universais e imutáveis, independentes de artefactos materiais.

Esta transformação é indissociável dos avanços da Física Quântica ao longo do século XX e início do século XXI, que permitiram traduzir conceitos teóricos em padrões universais e invariáveis. O ponto de partida pode ser identificado em 1900, quando Max Planck introduziu a quantização da energia ao descrever a radiação do corpo negro. A constante que leva o seu nome tornou-se, mais de um século depois, a base da definição do kilograma através da balança de Kibble [2]. Poucos anos mais tarde, Albert Einstein consolidaria a física quântica emergente ao explicar o efeito fotoelétrico (1905), introduzindo o conceito de fotão, e ao formular a teoria da relatividade restrita, cujas correções são hoje indispensáveis ao funcionamento de relógios atómicos e sistemas de navegação.

O modelo atómico de Niels Bohr (1913), ao introduzir níveis de energia discretos, abriu caminho para a utilização de transições eletrónicas como padrões para a medição do tempo. Este princípio é a base da definição atual do segundo, sustentada pelas transições hiperfinas do átomo de césio-133 e, mais recentemente, pelos relógios ópticos, por exemplo de estrôncio, itérbio ou cálcio. Paralelamente, os contributos de Werner Heisenberg, com o princípio da incerteza, e de Erwin Schrödinger, com a sua equação de onda, permitiram o enquadramento teórico que ainda hoje sustenta a modelação dos sistemas atómicos utilizados em Metrologia.

A contribuição de Paul Dirac foi igualmente determinante, com a formulação da equação relativística do eletrão e a fundamentação da quantização da carga elétrica, que permitiram consolidar a atual definição do ampere com base na carga elementar. Na segunda metade do século XX, emergiram dois contributos experimentais de grande impacto: o Efeito Josephson (EJ), descoberto por Brian Josephson, em 1962, que viabilizou a utilização de padrões quânticos de tensão elétrica, e o Efeito de Hall Quântico (EHQ), descoberto por Klaus von Klitzing, em 1980, que estabeleceu um padrão universal de resistência elétrica através da constante de von Klitzing. Estas descobertas,

reconhecidas com o Prémio Nobel da Física, possibilitaram a materialização destas duas grandezas elétricas através de padrões rastreáveis e invariáveis, dependentes apenas da constante de Planck e da carga elementar.

Finalmente, o trabalho de Bryan Kibble foi decisivo para a redefinição do kilograma. A sua invenção da balança de Kibble (anteriormente designada por balança de Watt) permitiu relacionar diretamente a constante de Planck com a unidade de massa, tendo esta realização experimental permitido substituir a dependência de um protótipo material de platina iridiada, o protótipo internacional do kilograma, guardado no Bureau Internacional dos Pesos e Medidas (BIPM), em Sèvres.

A culminar este percurso, em 2019, o SI passou a basear as suas unidades de base (kilograma, metro, segundo, ampere, kelvin, mole e candela) em constantes fundamentais da natureza, tais como a constante de Planck (*h*), a velocidade de luz no vazio (*c*), a carga elementar (*e*), a constante de Boltzmann (*k*) e a constante de Avogadro (N_A), tal como indicado na Tabela seguinte, em vez de artefactos materiais, propriedades de materiais ou descrições de medições.

Assim, o legado de mais de um século de investigação quântica traduz-se hoje em medições universais, robustas e sustentáveis, que constituem o pilar da ciência e da inovação tecnológica contemporânea. Os desenvolvimentos da ciência e das tecnologias, em particular no domínio da física quântica, têm permitido a realização prática destas unidades, conseguindo alcançar níveis de exatidão, limitada apenas pela estrutura quântica da natureza e pelas capacidades técnicas, e não pelas definições propriamente ditas.

O desenvolvimento de novos sistemas de medição, baseados em padrões quânticos e utilizando supercondutores, semicondutores, amostras de grafeno, entre outros sensores de elevada exatidão, exigem métodos validados e medições rastreáveis e comparáveis, pelo que a Metrologia Quântica não é apenas um suporte, mas também um motor de inovação técnico-científica. Atualmente, o desenvolvimento da Metrologia Científica está intimamente ligado às tecnologias quânticas emergentes, com implicações em setores estratégicos como telecomunicações, defesa, saúde, segurança, energia, indústria e comércio internacional.

Padrões Quânticos no Sistema Internacional de Unidades

Padrões de tempo e frequência

As escalas de tempo formam a base da sociedade moderna, permitindo tecnologias como o GNSS (*Global Navigation Satellite System), radiowave interferometer arrays*, sincronização de redes em telecomunicações e sistemas de energia elétrica. Atualmente, existem 3 métodos primários para medição do tempo: Tempo Universal (UT), baseado no movimento de rotação da Terra; Tempo Efeméride (ET), baseado na órbita da Terra à volta do Sol; e Tempo Atómico (AT), baseado nos efeitos quânticos dos átomos. O Tempo Atómico Internacional (TAI) é uma escala de tempo uniforme, mantida pelo BIPM e baseada na transição atómica do átomo de Cs, de acordo com a definição do segundo do SI. A base de tempo civil, o Tempo Universal Coordenado (UTC), é uma escala atómica com a mesma taxa do TAI mas que se mantém em concordância com o UT em menos de 0,9 s. Desde a primeira observação da transição hiperfina do átomo de Cs-133, na década de 50 do século XX, que se especulou que os relógios atómicos podiam superar todas as referências temporais existentes. A exatidão da referência atómica levou em 1967 à redefinição do segundo do SI, que se tornou a primeira unidade a ter como base da sua definição um princípio da natureza em vez de um artefacto físico. O desenvolvimento dos relógios de Cs atingiu o seu pico com uma estabilidade na ordem dos 10^{-16}. Atualmente, este é o limite que se consegue obter utilizando a atual definição do segundo e a comunidade científica considera pouco realista conseguir melhorar este valor.

Nos últimos vinte anos, os avanços alcançados nos padrões de frequência óptica revelaram níveis de estabilidade e exatidão que ultrapassam, em pelo menos duas ordens de grandeza (10^{-18}), os dos atuais padrões de tempo baseados em micro-ondas. Esta evolução tecnológica levou a comunidade internacional de tempo e frequência a considerar a futura redefinição do segundo do SI, tendo por base padrões de frequência óptica, que oferecem um desempenho significativamente superior. Com esse objetivo, o BIPM elaborou um *roadmap* para orientar o processo de redefinição do segundo. Esse pla-

Grandeza	Unidade	Símbolo	Constante universal	Valor numérico	Unidade
Massa	kilograma	kg	constante de Planck	h - 6,626 070 15 × 10^{-34}	J s
Comprimento	metro	m	velocidade da luz no vazio	c - 299 792 458	m/s
Tempo	segundo	s	frequência de transição hiperfina do estado fundamental do átomo de ^{133}Cs não perturbado	$\Delta\nu_{Cs}$ - 9 192 631 770	Hz
Corrente elétrica	ampere	A	carga elementar	e - 1,602 176 634 × 10^{-19}	C
Temperatura termodinâmica	kelvin	K	constante de Boltzmann	k - 1,380 649 × 10^{-23}	J/K
Intensidade luminosa	candela	cd	eficácia luminosa	K_{cd} - 683	lm/W
Quantidade de matéria	mole	mol	constante de Avogadro	N_A - 6,022 140 76 × 10^{23}	mol^{-1}

Tabela 1

no estabelece critérios, indicadores e marcos de progresso destinados a avaliar a maturidade tecnológica e científica dos diferentes candidatos a padrões ópticos. O Comité International de Pesos e Medidas (CIPM) pretende, na 28.ª Conferência Geral de Pesos e Medidas (CGPM), a realizar em outubro de 2026, analisar propostas e identificar os melhores elementos atómicos a utilizar na construção dos relógios ópticos – tais como o estrôncio (Sr), o alumínio (Al) ou o ítrio (Yb). A adoção oficial da nova definição do segundo SI está prevista para a 29.ª CGPM, em 2035, quando se espera que a comunidade científica disponha de consenso técnico e comprovação experimental suficiente para garantir uma transição segura, estável e universalmente rastreável para os novos padrões óticos de tempo e frequência.

Padrões das grandezas elétricas

Na realização prática das unidades de medida das grandezas elétricas [3] através de métodos primários, os efeitos quânticos de Josephson e de Hall têm sido utilizados há décadas para a realização do volt e ohm, respetivamente.

O volt (V) é realizado utilizando o valor da constante Josephson, $K_J = 2e/h = 483\,597{,}848\,416\,984$ GHz V^{-1}. Os sistemas experimentais atuais (PJVS – *Programmable Josephson Voltage System*) que materializam este efeito utilizam *arrays* de milhares de junções (de materiais supercondutores, e.g. $NbSi_x$) (Figura 1), programadas para associar em série essas junções e gerarem valores de tensão entre 0 V e 10 V, com uma resolução de f/K_J, sendo f a frequência das micro-ondas (de alguns gigahertz) que irradiam essas junções, submetidas a temperaturas de alguns kelvins para assegurar a sua supercondutividade.

O ohm (Ω) é realizado utilizando o valor da constante de von Klitzing, $R_K = h/e^2 = 25\,812{,}807\,459\,3045\ \Omega$. Os sistemas experimentais que materializam este efeito submetem junções de heteroestruturas de materias semicondutores (e.g. GaAs/AlGaAs) (Figura 1), a temperaturas próximas de 1 kelvin e a campos magnéticos elevados (dezenas de tesla) transversais à direção da corrente que percorre a amostra, possibilitando assim a observação de valores quantizados de resistência $R = R_K/n$, onde n é um número inteiro.

Comparações entre estes sistemas demonstram a possibilidade de obter incertezas relativas na ordem de algumas partes em 10^{-9} nos valores gerados.

Através da lei de Ohm, é possível realizar a unidade de corrente elétrica, o ampere (A), com base na relação A = V/ Ω, através do EHQ e do EJ. Paralelamente, o ampere pode também ser realizado de forma direta através de dispositivos que implementam o princípio de *single electron transport*, com base na relação A = C/s, no valor da carga elementar (*e*) fixada na definição do ampere e na realização prática da unidade de tempo segundo. Estes dispositivos recorrem a nanoestruturas concebidas para controlar a passagem individual de eletrões entre contactos metálicos, e ao efeito *quantum tunneling* para permitir a passagem de cargas através de barreiras de potencial em semicondutores. No entanto, esta realização do ampere apresenta ainda níveis de incerteza superiores aos obtidos indiretamente, através da Lei de Ohm e dos efeitos quânticos de Josephson e Hall.

Tecnologias Quânticas em Desenvolvimento na Metrologia

Relógios quânticos

Os relógios atómicos de última geração (Figura 2), baseados em transições ópticas, atingem estabilidades temporais da ordem de 10^{-18}, o que representa um avanço sem precedentes na medição do tempo. Este nível de desempenho tem impacto direto em múltiplos domínios tecnológicos, nomeadamente nas redes de comunicação, sistemas de navegação e posicionamento global e nas missões de exploração espacial. Estes relógios utilizam transições atómicas em frequências superiores às das frequências emitidas pelos átomos de césio, permitindo subdividir o segundo com uma exatidão superior em mais de 2 ordens de grandeza face aos relógios de césio, atualmente em uso como referência do SI. Embora os relógios comerciais utilizados nos satélites do sistema GNSS já incorporem os efeitos da relatividade, a exatidão e a estabilidade de um relógio óptico permite detetar variações de altitude da ordem de 1 cm, demonstrando o seu potencial em geodesia relativística. Entre as suas aplicações mais promissoras destacam-se:

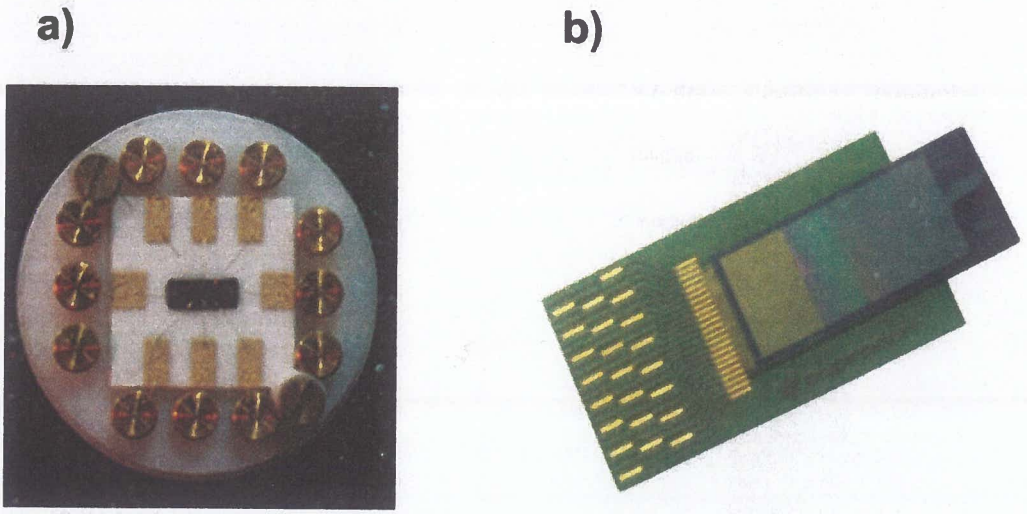

Figura 1: a) Amostra de Hall, com ligações ao longo da heteroestrutura semicondutora (©IPQ). b) *Array* de tensão Josephson com milhares de junções supercondutor-isolador-supercondutor (©Supracon)

- a medição do potencial gravítico da Terra, contribuindo para um mapeamento geodésico de precisão sem precedentes;
- a criação de redes de relógios óticos interligados por fibras ópticas, capazes de detetar variações sísmicas e antecipar terramotos;
- e a monitorização de variações em constantes fundamentais da natureza, o que poderá fornecer indícios de uma nova física, ajudando a compreender a matéria escura e a energia escura (projeto europeu QSNET).

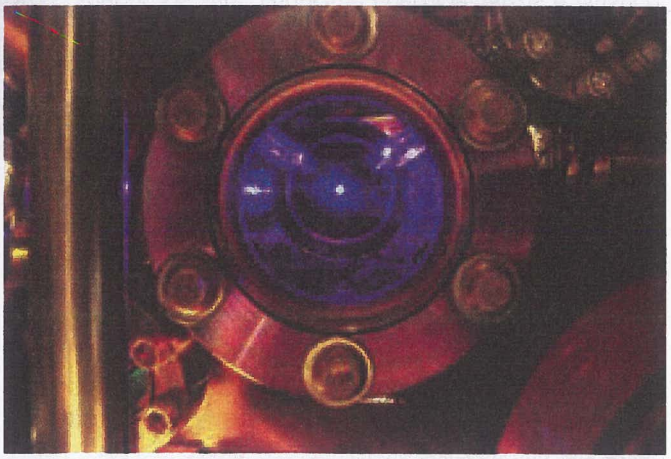

Figura 2: Relógio óptico de Sr, JILA.
(©The Ye group and Brad Baxley, JILA)

Padrões quânticos de resistência elétrica

Atualmente estão a ser estudados sistemas experimentais baseados no "efeito quântico de Hall anómalo", como alternativa ao efeito de Hall clássico, com a vantagem destes sistemas funcionarem sem a necessidade de campo magnético [4]. Estes sistemas baseiam-se em materiais isoladores topológicos (e.g. Bi_2Se_3 e Bi_2Te_3) dopados com átomos magnéticos os quais permitem que surjam efeitos quânticos exóticos.

Outros sensores quânticos como o caso de memristores que podem gerar valores discretos múltiplos da condutância fundamental, à temperatura ambiente, e com a possibilidade de serem incorporados em circuitos integrados, estão a ser estudados com vista à sua utilização como padrões intrínsecos de resistência elétrica. A integração destes padrões na eletrónica dos instrumentos de medição, constituindo a sua referência metrológica, permitirá suportar processos de auto calibração e auto ajuste, com rastreabilidade direta ao SI, materializando o conceito de "NMI on chip" (*National Metrology Institute on a chip*) e eliminando a necessidade de longas cadeias de calibração, permitindo implementar "serviços metrológicos diretamente em microchips" [5].

Óptica quântica

A óptica quântica constitui atualmente um dos domínios mais ativos e inovadores da física fundamental e da física aplicada [6]. O estudo dos estados quânticos da luz, incluindo a sua representação, caracterização, coerência quântica e não separabilidade (emaranhamento) é uma das áreas de investigação mais desenvolvidas, conduzindo naturalmente à criação de fontes monofotónicas, um dos instrumentos essenciais da óptica quântica moderna. Outro campo de grande relevância é o da comunicação quântica, que explora sistemas óticos e métodos avançados para teletransporte quântico, memórias quânticas e criptografia quântica, nomeadamente através da distribuição quântica de chaves (QKD – *Quantum Key Distribution*). Estes avanços possibilitam sistemas de comunicação intrinsecamente seguros, baseados em princípios fundamentais da mecânica quântica.

A produção quântica de imagens constitui igualmente uma área emergente, com aplicações potenciais em metrologia de precisão, biotecnologia e deteção remota, entre outras. Paralelamente, tem-se verificado um crescimento significativo no desenvolvimento de técnicas e dispositivos para metrologia ótica quântica e sensores baseados em coerência ótica quântica, com impacto direto na medição de grandezas físicas com incertezas extremamente reduzidas.

Na radiometria quântica, lidando-se com fluxos fotónicos extremamente baixos — da ordem de 10^6 fotões por segundo — recorrem-se a técnicas de contagem de fotões e a fontes monofotónicas [7].

Estas fontes são essenciais para a calibração de detetores monofotónicos, atualmente já tecnologicamente maduros e disponíveis comercialmente, como o díodo de avalanche monofotónico (SPAD), o sensor de bordo de transição (TES) e o detetor monofotónico de nanofio supercondutor (SNSPD), amplamente utilizados nas aplicações referidas anteriormente.
A fotónica quântica desempenha assim um papel central no desenvolvimento de padrões ópticos de frequência e de sistemas de comunicação invioláveis, sustentando o avanço da Metrologia Quântica e da infraestrutura científica europeia. As fontes monofotónicas são, por isso, objeto de vários projetos de investigação colaborativos que envolvem Institutos Nacionais de Metrologia, centros de investigação e universidades europeias [8].

Na *mise en pratique* para a realização da candela [3], é já explicitamente referida a possibilidade de utilização de fontes monofotónicas, o que permitirá, no futuro, exprimir as grandezas fotométricas e radiométricas em função do número de fotões, reforçando a rastreabilidade quântica das medições de luz.

Implicações Societais

Os desenvolvimentos em Metrologia Quântica têm efeitos diretos em áreas críticas da sociedade, tais como:
- economia digital: comunicações seguras baseadas em criptografia quântica.
- saúde: técnicas de diagnóstico por imagem e sensores biomédicos de alta resolução.
- energia e ambiente: monitorização precisa de gases, campos e fluxos energéticos.
- indústria: padrões rastreáveis que suportam qualidade, inovação e comércio internacional.

A confiança nas medições e a rastreabilidade universal são elementos centrais para a segurança e para a tomada de decisão baseada em dados. Enquanto Instituição Nacional de Metrologia, o IPQ desempenha um papel essencial na implementação e no desenvolvimento dos padrões nacionais das unidades de medida, assegurando o rigor e a exatidão das medições realizadas, bem como a sua comparabilidade e rastreabilidade ao

SI, concretizando o objetivo constitucional de soberania no domínio dos padrões de medição e do controlo dos instrumentos de medição necessários à indústria e à sociedade portuguesa em geral.

No âmbito da Metrologia Quântica, o IPQ além de integrar a *European Metrology Network for Quantum Technologies* (EMN-Q) da EURAMET, participou no projeto de I&D "*Memristive Devices as Quantum Standard for Nanometrology*" para a implementação e desenvolvimento de dispositivos em chip (CMOS), integrados em instrumentação de laboratório, possibilitando a implementação de processos de auto ajuste e de auto calibração de instrumentos de medição ou de geração de grandezas elétricas. Esta nova aproximação para a realização da unidade elétrica de resistência, Ω, à temperatura ambiente e sem necessidade de um campo magnético, como acontece com o sistema primário de EHQ, embora com menor exatidão das medições, tem a grande vantagem de ter uma aplicação muito simplificada, com grande impacto industrial, dada a rastreabilidade imediata ao SI.

Conclusão

A Física Quântica redefiniu a Metrologia e abriu caminho para padrões baseados em constantes fundamentais da natureza. O estado atual da Metrologia Científica demonstra avanços notáveis, nomeadamente no desenvolvimento de relógios ópticos, que irão contribuir para a redefinição do segundo, de sensores e sistemas de fotónica e eletrónica, com perspetivas de impacto transformador em múltiplos setores da sociedade, desde a segurança de dados e a navegação até à saúde, indústria e sustentabilidade ambiental, mas só poderão fazê-lo com base em medições fiáveis, rastreáveis e comparáveis a nível internacional. A colaboração ativa entre Institutos Nacionais de Metrologia (como o IPQ), a academia e a indústria são essenciais para continuar a impulsionar a investigação, a normalização e a transferência de conhecimento, assegurando a liderança europeia neste domínio. A nível nacional, o IPQ desempenha um papel catalisador, promovendo e participando no ecossistema europeu da Metrologia Quântica, nomeadamente em redes europeias e em projetos de I&D, incentivando e acelerando o desenvolvimento e a adoção das tecnologias quânticas através de medições comparáveis e rastreadas. O futuro da Metrologia Quântica dependerá da capacidade de consolidar infraestruturas globais de confiança, capazes de responder aos desafios científicos, tecnológicos e societais.

Referências

[1] "O Sistema Internacional de Unidades", Tradução luso-brasileira do SI - 2.ª edição, INMETRO / IPQ, 2025, ISBN: PT 978-972-763-189-6.

[2] F. Bielsa; K. Fujita; A. Kiss; H. Fang et al., "Development of a beam mechanism for the BIPM Kibble Balance", IEEE, 2024. 10.1109/CPEM61406.2024.10646070

[3] "Mise en pratique for the definition of the ampere and other electric units in the SI", SI Brochure - 9th edition (2019) – Appendix 2, 20 May 2019

[4] Patel et al., "A zero external magnetic field quantum standard of resistance at the 10-9 level", Nat. Electron 7, 1111-1116 (2024). ArXiV preprint: https://arxiv.org/abs/2410.13565

[5] Gianluca Milano, Xin Zheng, Fabio Michieletti, Giuseppe Leonetti, Gabriel Caballero, Ilker Oztoprak, Luca Boarino, Özgür Bozat, Luca Callegaro, Natascia De Leo, Isabel Godinho, Daniel Granados, Itir Koymen, Mariela Menghini, Enrique Miranda, Luis Ribeiro, Carlo Ricciardi, Jordi Suñe, Vitor Cabral, Ilia Valov, "A quantum resistance memristor for an intrinsically traceable International System of Units standard", Nature Nanotechnology, 2025, https://doi.org/10.1038/s41565-025-02037-5

[6] Liñares, J.; Prieto-Blanco, "Quantum Optics: Theory, Methods, and Applications", Appl. Sci. 2025, 15(21), 11691, https://doi.org/10.3390/app152111691

[7] Zwinkels, J.C.; Ikonen, E.; Fox, N.P.; Ulm, G.; Rastello, M.L. "Photometry, radiometry and 'the candela': evolution in the classical and quantum world", Metrologia 47 (2010) R15-R32, DOI:10.1088/0026-1394/47/5/R01

[8] Kück, S. et al., "Single photon sources for quantum radiometry: a brief review about the current state-of-the-art", Applied Physics B 128 (2022) 28, https://doi.org/10.1007/s00340-021-07734-2

Isabel Godinho é licenciada em Física, pela Faculdade de Ciências da Universidade de Lisboa, e doutorada em Física pela mesma Universidade. É, desde 2016, diretora do Departamento de Metrologia do Instituto Português da Qualidade e responsável pelo Subsistema Nacional de Metrologia, nas áreas da Metrologia Científica, Aplicada e Legal. Ingressou no Laboratório de Metrologia Elétrica do Laboratório Nacional de Engenharia, Tecnologia e Inovação (LNETI) em 1991 e esteve envolvida no desenvolvimento e materialização de padrões nas áreas da Metrologia elétrica, quântica e aceleração e em diversos projetos de cooperação e de I&D. É atualmente delegada nacional no âmbito do comité European Partnership on Metrology e representante nacional na EURAMET, no Comité Internacional de Metrologia Legal, da Organização Internacional de Metrologia Legal, e no BIPM.

Carlos Pires é licenciado em Engenharia Física pela Faculdade de Ciências da Universidade de Lisboa e, pela mesma faculdade, fez o mestrado em Engenharia Física. Em 2007, iniciou as suas funções no Laboratório de Velocidade do Laboratório Nacional de Metrologia, do Instituto Português da Qualidade, como Técnico Superior. Em 2015, assume as funções de Responsável Técnico pelo domínio do Tempo e da Frequência, tendo como principal função realizar e disseminar o segundo, bem como dar rastreabilidade à unidade a nível nacional. Atualmente, desempenha as funções de presidente do Comité Técnico de Tempo e Frequência (TC-TF) da EURAMET.

Olivier Pellegrino, PhD em Física, pela Université de Paris 6, Licenciatura de Engenharia Química, técnico superior no Instituto Português da Qualidade (IPQ) onde, desde 2002, é responsável pelos Domínios Metrológicos de Fotometria, Radiometria e Radiofrequências no Departamento de Metrologia, representando o IPQ em Comissões Técnicas de Normalização CTE 01 – Terminologia, CTE 25- Grandezas e Unidades e CT 225 – Aplicações de Métodos Estatísticos, com participações em vários projetos de investigação científica europeus. É membro da equipa editorial da Gazeta de Física, da Sociedade Portuguesa de Física.

Vítor Cabral é licenciado em Engenharia Física pela Faculdade de Ciências e Tecnologia da Universidade de Coimbra. Em 2014, iniciou funções no Laboratório de Eletricidade do Laboratório Nacional de Metrologia, do IPQ - Instituto Português da Qualidade, sendo atualmente Responsável Técnico dos domínios elétrico, termometria e higrometria e representante do IPQ no Comité Técnico da Eletricidade e Magnetismo da EURAMET. Tem participado em diversos projetos de investigação internacionais no âmbito dos programas coordenados pela EURAMET.

POSTERS

A PROGRAMMABLE INTRINSIC QUANTUM STANDARD OF RESISTANCE OPERATING AT ROOM TEMPERATURE AND IMPLEMENTABLE ON-CHIP BASED ON MEMRSITIVE DEVICES

Gianluca Milano*[1], Xin Zheng[2], Fabio Michieletti[3], Giuseppe Leonetti[1,3], Gabriel Caballero[4,5], Ilker Oztoprak[6], Luca Boarino[1], Özgür Bozat[7], Luca Callegaro[8], Natascia De Leo[1], Isabel Godinho[9], Daniel Granados[4], Itir Koymen[7,10], Mariela Menghini[4], Enrique Miranda[11], Luís Ribeiro[9], Carlo Ricciardi[3], Jordi Suñe[11], Vitor Cabral*[9], Ilia Valov*[2,12]

[1]Advanced Materials Metrology and Life Sciences Division, INRiM (Istituto Nazionale di Ricerca Metrologica), Strada delle Cacce 91, 10135 Torino, Italy.
[2]Forschungszentrum Jülich, Peter Grünberg Institute (PGI-7), WilhelmJohnen-Straße, 52428, Jülich, Germany.
[3]Department of Applied Science and Technology, Politecnico di Torino, C.so Duca degli Abruzzi 24, 10129 Torino, Italy.
[4]IMDEA Nanociencia, Cantoblanco, 28049 Madrid, Spain
[5]Facultad de Ciencias Físicas, Universidad Complutense de Madrid, 28040, Madrid
[6]Department of Physics, Gebze Technical University, 41400, Gebze, Kocaeli, Turkey
[7]TUBITAK National Metrology Institute (UME), 41470 Gebze, Turkey
[8]Quantum Metrology and Nanotechnologies Division, INRiM (Istituto Nazionale di Ricerca Metrologica), Strada delle Cacce 91, 10135 Torino, Italy.
[9]Instituto Português da Qualidade, Rua António Gião 2, 2829-513 Caparica, Portugal
[10]Department of Electrical and Electronics Engineering, TOBB University of Economics and Technology, 06510 Ankara, Turkey
[11]Departament d'Enginyeria Electrònica, Universitat Autònoma de Barcelona, 08193 Cerdanyola del Valles, Spain
[12]Institute of Electrochemistry and Energy Systesms, Bulgarian Academy of Sciences (BAS), Acad. G. Bonchev Str., Block 10, 1113 Sofia, Bulgaria

Background

- **National Metrological Institutes services on chip («NMI-on-a-chip»)**

The **revision of the International System of Units** (SI) in 2019 represented a historic change of paradigm for metrology, opening a new perspective on the *mise en pratique* of the SI basic units. SI units are now defined in terms of fundamental constants of nature defined by fixed numerical values.

Any experiment able to correlate measurable physical quantities to one, or a set of, fundamental constants fixed by the SI becomes a direct realization of the corresponding SI unit. Novel devices working according to the principles of quantum physics can enable the realization of reliable SI-traceable self-referenced systems.

- **New horizons for electrical metrology**

The quantum Hall effect, the Josephson effect and single-electron transport effects have been widely explored for the practical realization of resistance, voltage, and current electrical units, respectively. However, they requires **large size and complex experiments**, operating at cryogenic temperatures, vacuum conditions, and/or the presence of high magnetic fields, limiting their acquisition almost exclusively to universities and metrology institutions.

A device exhibiting a physical observable related to the fundamental quantum of conductance G_0 at room temperature, in air and without applying a magnetic field can revolutionize electrical metrology, enabling the realization of an intrinsic resistance standards directly available to the end-user.

Self-calibrating electrical systems with zero-chain traceability

This avoid possible drifts of each measuring standard caused by time, environmental parameters, and/or use calibration cost, long unavailability periods of the measurement equipment and a lot of effort in the management of the calibration process.

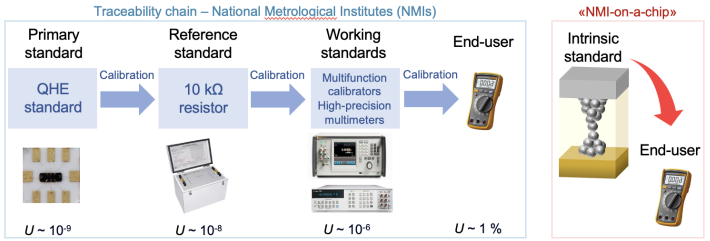

The idea

- **Memristive devices for quantum metrology**

Memristive devices can exhibit conductance levels that are multiple of the fundamental quantum of conductance G_0 in air, enabling the realization of an intrinsic standard of resistance scalable to the nanometer scale and compatible with CMOS technology that can work at room temperature, in air, withouth applying a magnetic field [1].

Working principle

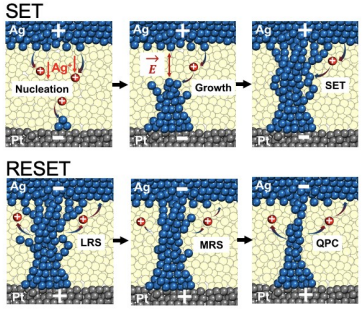

The memristive mechanism relies on resistive switching effects in two-terminal metal-insulator-metal nanoscale devices. This effects rely on the formation/rupture of a nanosized conductive filament bridging the two electrodes during SET/RESET operations, driven by the action of the applied electric field.

Electrical characteristics

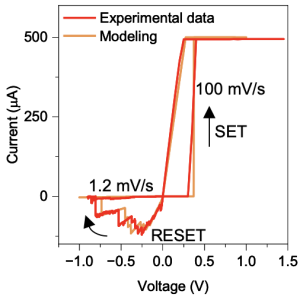

The *I-V* characteristics of memrsitive cells are characterized by a histeretic loops, since the internal state of resistance relies on the history of applied voltage and current.

Quantum conductance effects in air at room temperature

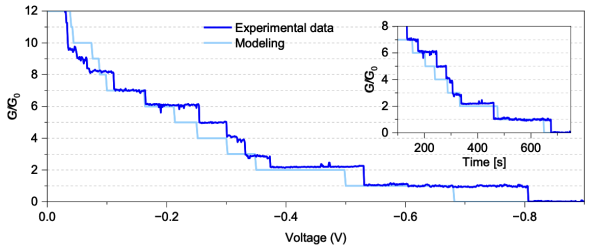

By exploiting the electropolishing effect, it is possible to control the dissolution of the filament nearly atom-by-atom, making possible the observations of quantum conductance effects with step-like behavior during the RESET process. These conductance plateaus are multiple of the fundamental quantum of conductance.

[1] Milano, Gianluca, et al. "Memristive devices for quantum metrology." *Advanced Quantum Technologies* 3.5 (2020): 2000009.

Results

- **A memristive-based resistance standard**

Conductance plateaus of memristive devices operating in the quantum conductance regime have been exploited as quantum reference values for the realization of a programmable standard of resistance [2].

An interlaboratory comparison involving three NMIs and three academic/research laboratories was performed to measure the achieved quantum reference values

Stability

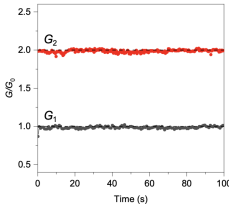

Stability has been evaluated by monitoring the conductance over time after programming the device to the desired quantum level.

Repeatability

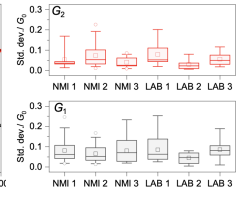

Repeatability has been evaluated in terms of standard deviation over consecutive measurements of the programmed quantum levels.

Reproducibility

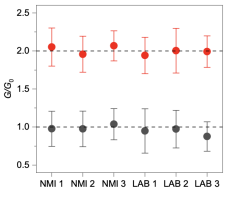

Reproducibility has been defined as the standard deviation of the mean values corresponding to each programming level

Interlaboratory comparison results

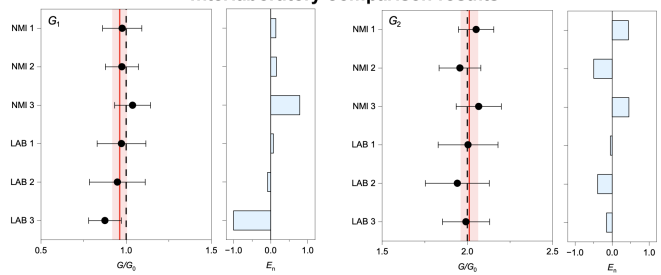

A consensus value G_{cons} and expanded uncertainty $U(G_{cons})$ are $(0.962 \pm 0.043)\ G_0$ and $(2.012 \pm 0.051)\ G_0$ for G_1 and G_2, respectively. The error of the consensus values for G_1 and G_2 is -3.8 % and 0.6 % with respect to expected G_0 and $2G_0$ theoretical values, respectively. The normalized error $E_n \leq 1.0$ for all participants shows that the measured conductance values belong to consistent sets

Our results highlight the possibility of having a quantum resistance standard on a chip that can be incorporated into any type of electronic measurement instrumentation and device.

[2] The MEMQuD consortium, "Intrinsic, room temperature quantum resistance memristor for next generation zero-chain traceability SI standard ", *arxiv preprint*, (2025).

NEXT-GENERATION ZERO-CHAIN TRACEABILITY USING AN INTRINSIC, ROOM-TEMPERATURE QUANTUM RESISTANCE MEMRISTOR SI STANDARD

L. Boarino[1]*, G. Milano[1], X. Zheng[2], F. Michieletti[3], G. Leonetti[1,3], G. Caballero[4,5], I. Oztoprak[6], Ö. Bozat[7], L. Callegaro[8], N. De Leo[1], I. Godinho[9], D. Granados[4], I. Koymen[7,10], M. Menghini[4], E. Miranda[11], L. Ribeiro[9], C. Ricciardi[3], J. Suñe[11], V. Cabral[9], I. Valov[2,12]

[1] *Advanced Materials Metrology and Life Sciences Division, INRiM, Torino, Italy.*

[2] *Forschungszentrum Jülich, (PGI-7), Jülich, Germany.*

[3] *Department of Applied Science and Technology, Politecnico di Torino, Torino, Italy.*

[4] *IMDEA Nanociencia, Madrid, Spain.*

[5] *Facultad de Ciencias Físicas, Universidad Complutense de Madrid, Madrid.*

[6] *Department of Physics, Gebze Technical University, Gebze, Kocaeli, Turkey.*

[7] *TUBITAK National Metrology Institute (UME), Gebze, Turkey.*

[8] *Quantum Metrology and Nanotechnologies Division, INRiM Torino, Italy.*

[9] *Instituto Português da Qualidade, Caparica, Portugal.*

[10] *Department of Electrical and Electronics Engineering, TOBB, Ankara, Turkey.*

[11] *Departament d'Enginyeria Electrònica, Universitat Autònoma de Barcelona, Spain.*

[12] *Institute of Electrochemistry and Energy Systems, Bulgarian Academy of Sciences (BAS), Sofia, Bulgaria*

Email: (l.boarino@inrim.it)

The revision of the International System of Units opens new perspectives for the mise en pratique of SI units, fixing numerical values of fundamental constants of nature. Here, we show the realization of an intrinsic standard of resistance based on memristive devices working in air, at room temperature, directly accessible to the end user1. By fixing numerical values for fundamental constants of nature, the revision of the International System of Units provides new avenues for the use of SI units. Here, we demonstrate the implementation of an intrinsic standard of resistance based on memristive devices that are immediately available to the end user and operate in air at ambient temperature. We report on a programming method based on the electrochemical polishing effects for operating nanoionic cells in the quantum conductance domain. This allows to control quantum conductance levels multiple of the fundamental unit of conductance and implement it as intrinsic standard values. It is confirmed that the results are metrologically consistent with the consensus values, departing from the G_0 and $2G_0$ values by -3.8% and 0.6%, respectively[2]. In order to achieve self-calibrating systems with zero-chain traceability, the results open the door for the on-chip deployment of National Metrological Institute services.

References

1. *Milano, G. et al. Quantum Conductance in Memristive Devices: Fundamentals, Developments, and Applications. Advanced Materials 34, 2201248 (2022).*
2. *Ilia Valov, Gianluca Milano, Xin Zheng et al. Intrinsic, room temperature quantum resistance memristor for next generation zero-chain traceability SI standard, 27 January 2025, PREPRINT (Version 1) available at Research Square [https://doi.org/10.21203/rs.3.rs-5783287/v1]*

The Impact of Metrology on Health Care Quality and Safety: A Focus on Infusion Therapy and Diagnostic

Elsa Batista[a], Isabel Godinho[a], João Alves e Sousa[a], Vania Silverio[b,c], Miroslava Benkova [d], Thomas Schrøder Daugbjerg [e], Oliver Buker[f], Annemoon Timmerman [g], Hugo Bissig[h]

[a] Portuguese Institute for Quality, IPQ; [b] Instituto de Engenharia de Sistemas e Computadores para os Microsistemas e as Nanotecnologias, INESC MN; [c] Department of Physics, Instituto Superior Técnico, Universidade de Lisboa; [d] Czech Metrology Institute, CMI; [e]Danish Technological Institute, DTI ; [f] Research Institutes of Sweden, RISE; [g] Universitair Medisch Centrum Utrecht ; [h] Federal Institute of Metrology, METAS

Contact email: ebatista@ipq.pt

Infusion technology

Metrology, the science of measurement, is crucial for healthcare quality and safety, especially in infusion therapy and diagnostics. Vital signs like heart rate, blood pressure, and blood oxygen levels can indicate dosing errors from infusion pump flow rate adjustments in multi-infusion setups.

Infusion therapy, the most common drug administration method, relies on precise liquid flow. Accurate liquid dosing is essential for the safety and reliability of medical devices like dialysis machines, infusion devices, and in-vitro diagnostic systems. Infusion errors, particularly in ICUs, can have severe consequences, especially with critical drugs or low doses for premature infants. Many adverse incidents, including morbidity and mortality, are linked to inaccurate dosing.

The role of metrology in drug delivery devices

Calibration is crucial for identifying flow rate and dosage errors in multi-infusion systems. Drug delivery can vary with flow rate adjustments and setup configuration, leading to differences between actual and intended doses. Clinicians adjust medications based on vital signs, needing a clear understanding of multi-infusion impacts. Accurate infusion pump delivery is vital to avoid clinical safety risks. Precise control of medication and fluid delivery, especially for critical drugs, is essential. Regular calibration and maintenance of infusion pumps ensure correct dosages and minimize safety risks.

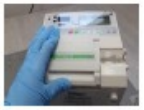

Microfluidics

The diagnostics sector is rapidly advancing, driven by the need to manage infectious diseases like COVID-19. Metrology significantly impacts the commercialization of next-generation microfluidic devices, such as point-of-care diagnostics, lab-on-a-chip, and organ-on-a-chip (OoC).

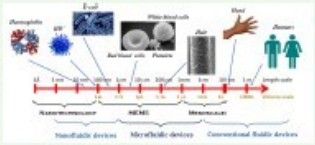

Microfluidics studies fluid behavior through microchannels and involves manufacturing devices with tiny chambers and tunnels. Organ-on-Chip replicates aspects of an organ's dynamics and responses within a non-biological platform.

Despite growth in microfluidics, quality production has relied on manufacturers' expertise without standardized calibration procedures. This gap between laboratory developments and reliable products is due to differences in device production. The MFMET project aims to develop standards and methods for characterizing microfluidic devices, including internal volume, hydraulic resistance, surface roughness, and liquid properties.

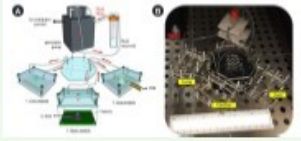

State of the art

A well-defined traceability chain ensures that drug delivery devices meet manufactures and end users specifications. Upgraded metrological infrastructures in European Metrology Institutes, through the MeDD – Metrology for Drug Delivery project, have improved infusion therapy safety by developing reliable test methods and protocols.

Calibration methods of drug delivery devices

Gravimetric method

The gravimetric method is the most common for calibrating DDD, including peristaltic and syringe pumps and flow meters. Gravimetric facilities for micro flow calibrations typically include a flow generator (e.g., piston prover, syringe pump, pump and flow controller system) and a flow rate reference system with a weighing scale and a "stopwatch" to measure liquid mass over time.

Flow rate down to 15 nL/min with uncertainties of the order of 1 %

$$Q = \frac{1}{t_f - t_i}\left[\left((l_f - l_i) - (\delta m_{buoy})\right) \times \frac{1}{\rho_w - \rho_A} \times \left(1 - \frac{\rho_A}{\rho_B}\right) \times [1 - \gamma(T - 20)]\right] + \delta_{evap}$$

Displacement method

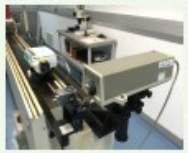

High precision syringe pumps and piston provers generate pulse-free, accurate flow rates by displacing a piston plunger. Syringe pumps use glass or stainless steel syringes, while piston provers are mainly stainless steel. The plunger's position, speed, and the piston's inner diameter can be calibrated for traceability. Length metrology uses interferometry to calibrate the plunger's position, monitoring the distance traveled by the syringe pump's pusher block over time.

Flow rates down to 1,6 nL/min with 2 % uncertainty

$$Q = v \times A = \frac{x_2 - x_1}{\Delta t} \times \pi r^2 = \frac{d\pi r^2}{t}$$

Front Track method

Meniscus (or front) tracking consists of measuring the displacement as a function of time of a liquid/air or liquid/liquid interface moving inside a glass capillary tube that is connected to a flow generating device.

Flow rate down to 1 nL/min with 10 % uncertainty

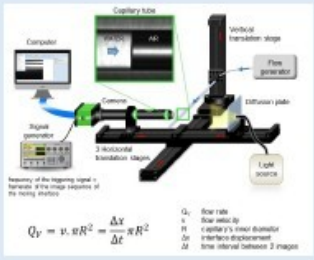

$$Q_V = v.\pi R^2 = \frac{\Delta x}{\Delta t}\pi R^2$$

Micro PIV/Micro PTV method

Alternative methods for micro/nano flows include Particle Tracking Velocimetry (PTV) and Particle Image Velocimetry (PIV). PTV determines flow velocity by tracking individual tracer particles across frames, while PIV calculates velocities by dividing video frames into patches and cross-correlating them in successive frames.

Methods validation

In order to validate the new flow facilities two inter-comparison of the primary standards were conducted. Project 1291 in 2015 and project 1508 in 2022, the results were overall consistent and let to publication of new flow CMCs by 5 different NMIs.

A new EURAMET guide was developed and published in May 2024 - EURAMET Calibration Guide No. 27 - Guidelines for the Calibration of Drug Delivery Devices and Infusion Device Analysers

Results and Research activities drug delivery devices

After the facilities were in place it is was possible to characterize several types of Drug Delivery Devices, like syringe pumps, infusion device analyzers (IDA) and insulin pumps. The results allowed the manufactures and end users to understand better the behavior of the devices after installation and use.

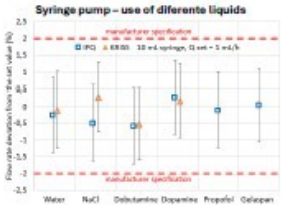

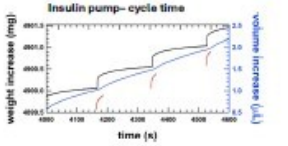

Results and Research activities microfluidics

The development of the new flow facilities also allowed the expansion of the flow measurements to another field – microfluidics. Project MFMET – Establishing standards in microfluidic devices started in 2021. This project investigated the measurement methods of several quantities such as internal volume, hydraulic resistance, surface roughness and liquid properties, among others in different chips (made of glass and TOPAS) specially developed and manufactured in the project and lead to a new EURAMET technical Guide 4 - Evaluation of flow related quantities in microfluidic devices.

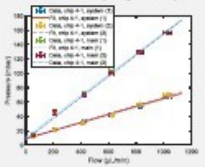

Contained volume in TOPAS and glass chips using different fluids, water, simulated body fluid (SBF) and phosphate buffer saline (PBS)

Chip	Liquid	Volume (mL)	U (mL)
TOPAS	Water	0,00368	0,00010
	SBF	0,003824	0,00011
	PBS	0,003531	0,000073
GLASS	Water	0,00423	0,00011
	SBF	0,004167	0,000072
	PBS	0,004157	0,000067

Conclusions and Future activities

Advances in microfluidics and nanotechnology have enabled the creation of miniaturized, portable labs. While product development has been the focus, new approaches are needed to assess performance and accuracy. Recent work has refined harmonization methods, but standards and regulations are still required for full system qualification.

Progress in Organ-on-Chip (OoC) is driven by the need to replace animal testing, supported by the FDA Modernization Act 2.0. The OoC field grew at a 70% CAGR from 2015 to 2020 and is projected to grow at 31% CAGR from 2020 to 2030, reaching a market size of €1.6B. However, companies lack standard test methods for validating manufacturing steps, performance, material compatibility, and safety.

The MFMET II project aims to develop protocols and guidelines to address gaps in the microfluidics supply chain, including OoC applications, supporting ISO/TC 48/WG 3 and other standardization committees.

References

- H. Bissig, M.T. Pettet, P. Lucas, E. Batista, E.A. Filipe, et al, Primary standards for measuring flows from 100 nl/min to 1 ml/min – gravimetric principle, Biomed. Eng./Biomed. Tech. 60 (4) (2015) 305–316
- C. Mills, E. Batista, H. Bissig, F. Ogheard, A.W. Boudaoud, et al Calibration methods for flows down to 5 nl/min and validation methodology, Biomed. Eng./Biomed. Tech. 68 (1) (2023) 13–27
- A. Niemann, E. Batista, J.Gerst, H. Bissig, O. Büker, SH. Lee, et al, Assessment of drug delivery devices working at microflow rates. Biomed Eng Biomed Tech 2022
- E. Batista, V. Silverio, K. Romieu, J. Alves e Sousa, T. Daugbjerg, Development of measurement procedures for volume and flow related quantities in microfluidic devices, Measurement: Sensors, 2024, 101551

Instituto Português da Qualidade · INESC MN · DF Departamento de Física Técnico Lisboa · CMI Czech Metrology Institute · Danish Technological Institute · RISE · UMC Utrecht · METAS · EMPIR · EURAMET

Improving the accuracy of medical devices will reduce dosing errors and lives can be saved

Instituto Português da Qualidade

RUA ANTÓNIO GIÃO, N.º 2 | 2829-513 CAPARICA
T (+351) 212 948 100
WWW.IPQ.PT